

**Investigation of
Dynamic Sea Ice Processes
In the Weddell Sea
During 1992**

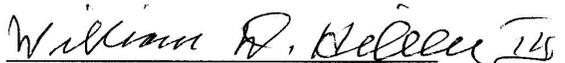
A Thesis Submitted to the Faculty
in partial fulfillment of the requirements for the
degree of
Doctor of Philosophy

by

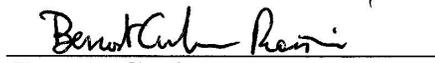
Cathleen A. Geiger
Thayer School of Engineering
Dartmouth College
Hanover, New Hampshire

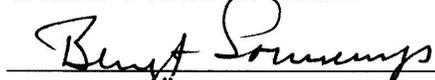
May 1996

Examining Committee:

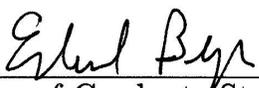

William D. Hibler III, Chairman


Stephen F. Ackley, External


Benoit Cushman-Roisin


Bengt U. Ö. Sonnerup


Eric W. Hansen


Dean of Graduate Studies


Cathleen A. Geiger, Author

Research "... is one percent inspiration and ninety-nine percent perspiration."

Thomas A. Edison (1931)

" The chief source of ideas in oceanography comes, I think, from new observations. Today we take much of ocean knowledge for granted. On the whole, when it comes to the phenomenology of the ocean, there are more discoveries than predictions. Most theories are about observations that have already been made. It is therefore particularly exciting when a theorist comes up with an idea about a feature of the ocean that he is willing to go to sea to look for.

And if some of us somehow manage to avoid getting entangled in the 'Big Science' part of our field, then perhaps we can preserve an innocent, simple approach to our tasks. Our work can seem like a pleasant hobby to us, it can sustain a sense of wonder, and bring us joy and fulfillment. Those of us who entered oceanography [did so because] we preferred the pioneer homesteading model of the scientific life to the glitter of the intellectually fashionable."

Henry Stommel (1990)

Abstract

Through a series of case studies, signal processing and statistical tools, analyses of dynamic sea ice processes of drift, deformation, and ice pack expansion and decay are investigated for the Weddell Sea region during 1992. Cavitating fluid (CAV) and viscous-plastic (VP) models are the most widely used ice models in sea ice, ocean and climate communities. Examination of these and observations are presented in order to identify the external (air/ocean) and internal (ice) forces that affect specific processes. Inconsistencies between processes in models and observations are isolated and examined with suggestions given for the next generation of ice models.

Key findings are as follows. Observationally, from ISW 1992, ice velocity in Western Weddell is found to be driven by low frequency forcing (longer than one day), while sub-daily frequencies drive ice deformation. In the models, annual expansion during winter months is dominated by air temperature at the ice edge and storms in the interior where sensible/latent heat fluxes are large, especially in leads. Coupled with this is divergent advection towards open water regimes which works to expand the ice pack. Thermodynamic processes dominate ice edge retreat in summer, specifically daily/subdaily thermal variations, relative humidity/latent heat and ocean heat flux. Interior thickness and deformation are respectively more sensitive than ice edge extent and velocity. Relative humidity and ocean heat flux are critical climatological variables having their greatest impact near the Antarctic Peninsula. Increased ocean heat flux reduces overall thickness with little effect to the ice edge, leading to catastrophic melting scenarios. Cross-spectral analyses show significant coherence between simulated and 30 hour low pass filter observed velocity and strain rates. Shear is significantly better modeled than divergence. Suggestions for next generation models include a reformulation of the boundary layer and incorporation of high frequency tidal forcing.

Acknowledgments

This work was made possible by grants from NSF (No. OPP-9024809 and DPP-9203470), ONR (No.N0014-93-1-1221), CRREL (No. 5-36686.140), and Thayer School (No. 255402.140 and 420048.140). The Argos buoy data from remote sites of ISW have been provided courtesy of Robin Muench at Science Applications International Corporation (SAIC) to whom I am most grateful. Five of the buoys at remote sites are also from Robin and used here with his permission. Meteorological data, the camp GPS data, access to the buoy data and all remaining data sources were made possible through Steve Ackley at the Cold Regions Research and Engineering Laboratory (CRREL). ECMWF analysis fields were made available through Steve Ackley and Christopher Kottmeier in Bremerhaven (Vielen Dank und viele Grüße). Special thanks goes to W.D. Hibler III for being my advisor, committee chairman, and numerical modeling mentor through my years here at Dartmouth. Special thanks also goes to Steve Ackley for providing funding for at least two terms and financial assistance to attend two conferences (Finland Conference 1994 and AGU Fall Meeting 1995). Also special thanks to Steve for many hours of discussion on observed sea ice processes and lots of common sense thinking. Additional thanks goes to the remaining members of my committee (Professors Cushman-Roisin, Hansen, and Sonnerup) to whom I have frequently popped in on asking all sorts of perplexing questions. Professor Hansen is additionally thanked for being my private tutor in principles of signal processing, to which I am most grateful for. Also much thanks to Jinlun Zhang and Xiyong Song, former students under Hibler, for a number of insightful discussions regarding ice rheology, numerical coding, and how to deal with the Dartmouth Northstar system. To all the staff and faculty at Thayer, thank you very much for making the passage of time here a most bearable existence. Also many HUGE HUGS and thanks to my friends and family without whose support I never would have survived 6 years at Dartmouth. Last, but by all means most importantly, to mein ein und alles LYSM:-).

Contents

1	Introduction	1
2	Overview of Sea Ice	5
2.1	Description of Sea Ice	5
2.2	General Circulation	6
2.2.1	Weddell Sea Circulation	7
2.3	Sea Ice Processes	8
2.3.1	Sea Ice Drift and Deformation	9
3	Field Measurements	13
3.1	Introduction	13
3.2	Data Processing	13
3.2.1	Large Scale Strain Array	13
3.2.2	Meteorological and Oceanographic Data	14
3.3	Results	15
3.3.1	General Ice Drift Features	15
3.3.2	Power Spectra Analysis	20
3.3.3	Centroid Velocity and Deformation Tensor	27
3.3.4	Error Analysis	38
3.4	Discussion	46
3.5	Chapter Summary	59
4	Numerical Model Hierarchy	61
4.1	Governing Equations	61
4.1.1	2D Sea Ice Model	62
4.1.2	1D and 1.5D Sea Ice Models	70
4.2	Boundary and Initial Conditions	72
4.3	Input and Output Fields	77
4.3.1	Atmospheric Forcing Fields	77
4.3.2	Oceanic Forcing Fields	78
4.4	Summary of Numerical Scheme	83
4.4.1	VP Numerical Scheme in Spherical Coordinates	85
4.5	Testing of Numerical Scheme	87
5	Numerical Rheology Behavior	91
5.1	Basic Behavior of Cavitating Fluid Rheology	92
5.1.1	1D Cavitating Fluid Code vs. Analytical Solution	92
5.1.2	Sensitivity of 1D Ice Dynamics	104

5.1.3	Dimensional Sensitivity of Cavitating Fluid Rheology	117
5.2	Basic Behavior of Viscous Plastic Rheology	122
5.2.1	Principal Axes in 2-Space	122
5.2.2	1D Viscous Plastic Code vs. Analytical Solution	127
5.2.3	Sensitivity of 1D Viscous Plastic Rheology	132
5.2.4	Dimensional Sensitivity of Viscous Plastic Rheology	148
5.3	Chapter Summary	156
6	Regional Model Study	158
6.1	Model Sensitivity to External Input	159
6.1.1	Sensitivity to Resolution	159
6.1.2	Sensitivity to Atmospheric Forcing	165
6.1.3	Sensitivity to Ocean	176
6.1.4	Summary of Ice Sensitivity to External Forcing	182
6.2	Model Sensitivity to Ice Components	182
6.2.1	Responses due to Rheology	183
6.2.2	Responses to Internal Ice Parameters	185
6.2.3	Summary of Sensitivity to Ice	186
6.3	Weddell Sea Annual Cycle for 1992	191
6.3.1	Modeled Annual Cycle versus Observed Ice Edge	191
6.3.2	Regional Balance	201
6.3.3	Regional Distribution of Growth and Advection	209
6.3.4	Particle Case Study	217
6.3.5	Summary of Simulated Results	222
6.4	Buoy Comparison	222
6.4.1	Comparison in the Frequency Domain	223
6.4.2	Comparison in the Time Domain	232
6.4.3	Comparing Category Distributions	242
6.4.4	Summary of Buoy Comparison	260
6.5	Chapter Summary	260
7	Summary	263
	Appendices	269
A	Data Processing Tools	269
A.1	Estimate of Instrument Error	269
A.2	FFT Power Spectra	271
A.2.1	Rotary Spectra	275
A.3	Low Pass Filter (LPF)	279
A.4	Ice Deformation using Multiple Regression	282
B	Statistical Methods for Comparison	286
B.1	Probability Density Distribution	286
B.2	Chi-Square Analysis	286
B.3	Correlation Coefficient	287
B.3.1	Correlation of Max Shear	287
B.4	Cross-Spectral Analysis	288

C	Coordinate System Transforms	290
C.1	Distance Transforms	290
C.1.1	Arc Length Distance	290
C.1.2	Local Projection	291
C.1.3	Comparison	292
C.2	Equal Area Transforms	293
C.2.1	Basic Formulation	293
C.3	Non-Orthogonal Transformations	296
C.3.1	Basic Formulation	296
C.3.2	Test Case	297
C.4	Interpolation of Data	297
C.4.1	Basic Formulation	297
C.4.2	Example Case	301
	References	302

List of Tables

3.1	Overview of Large Scale Array Program	14
3.2	Overview of Beta Parameters	27
3.3	Overview of Deformation Parameters	29
3.4	Overview of Beta Parameter Errors	39
3.5	Average Signal to Noise Ratio	40
4.1	List of Variables	63
4.2	List of Variables (cont'd)	64
5.1	Standard Values for Rheology Study	92
5.2	Results from 1D Spherical Case with -10m/s Wind Velocity	99
A.1	Instrument Pairs for Error Estimate	270
A.2	Results of Error Analysis	271
C.1	Navigational versus Great Circle Distance	292

List of Figures

2.1	Schematic of Governing Equations for Sea Ice	10
2.2	Practice Example of Why Sea Ice Research is Needed	11
3.1	Geographical Region of ISW during 1992	16
3.2	Configuration of ISW Large Scale Array	17
3.3	Time Series of ISW Large Scale Buoys	18
3.4	Time Series of Wind and Water Velocities	19
3.5	Spectral Plots of Buoy Drift (U+V) Velocity	23
3.6	Spectral Plots of Buoy Drift U Velocity	24
3.7	Spectral Plots of Buoy Drift V Velocity	25
3.8	Spectral Plots of Wind and Water Velocities	26
3.9	Velocity of ISW Array Centroid	31
3.10	Multiple Linear Regression Results: 9 Hour LPF	32
3.11	Multiple Linear Regression Results: 15 Hour LPF	33
3.12	Multiple Linear Regression Results: 30 Hour LPF	34
3.13	9 Hour LPF Centroid Speed, Max Shear and DKPs	35
3.14	15 Hour LPF Centroid Speed, Max Shear and DKPs	36
3.15	30 Hour LPF Centroid Speed, Max Shear and DKPs	37
3.16	Error Analysis of Multiple Linear Regression	41
3.17	Standard Deviation of Beta Parameters: 9 Hour LPF	42
3.18	Standard Deviation of Beta Parameters: 15 Hour LPF	43
3.19	Standard Deviation of Beta Parameters: 30 Hour LPF	44
3.20	Estimate of Power Spectra Error	45
3.21	Spectral Plots of Centroid Velocity and Invariant Strain-Rates	51
3.22	Spectral Plots of Deformation Components	52
3.23	15 Day Integrated Power Spectra of All Buoys at All 32 Frequencies	53
3.24	Power Distribution for Western Buoys	54
3.25	Power Distribution for Eastern Buoys	55
3.26	15 Day Integrated Spectra of Wind, Ocean Current, and Strain-rate	56
3.27	Power Distribution for Array Centroid Velocity and Ocean Current	57
3.28	Power Distribution of 15 Day Integrated Power Spectra for Strain-Rate	58
4.1	Cloud cover	69
4.2	Relative Humidity	69
4.3	Weddell Sea Region	73
4.4	High Resolution Regional Grid	74
4.5	Low Resolution Regional Grid	75
4.6	Grid Cell Configurations	76

4.7	Ocean Heat Flux and Mixed Layer Depth Distribution	80
4.8	Ocean Circulation for Weddell Sea Region	81
4.9	Ocean Circulation for 50km 2D Models	82
4.10	Kinetic Energy Test for CAV	88
4.11	Kinetic Energy Test for VP	89
5.1	Compressive Stress of 1D CAV	101
5.2	V Velocity of 1D CAV for Linear Drag	102
5.3	Position of Internal Yielding Boundary	103
5.4	V Velocity of 1D CAV for Quadratic Drag	110
5.5	Results of 1D CAV with South Wind in Spherical Coordinates	111
5.6	Position of Internal Free Drift Boundary	112
5.7	Response of 1D CAV to Ice Thickness	113
5.8	Response of 1D CAV to Ice Compactness	114
5.9	Response of Cartesian 1D CAV to Resolution	115
5.10	Response of Spherical 1D CAV to Resolution	116
5.11	Compressive Stress of 1.5D and 2D CAV	119
5.12	V Velocity of 1.5D CAV with Quadratic Drag	120
5.13	V Velocity of 2D CAV with Quadratic Drag	121
5.14	Rheologies in 2D Principal Axis Space	126
5.15	Analytical vs. Numerical 1D VP	130
5.16	Schematic of 1D VP Stress Distribution	131
5.17	Stress State for 1D VP Linear Drag Concentric Ellipse Closure Method	136
5.18	Velocity for 1D VP Linear Drag Concentric Ellipse Closure Method	137
5.19	Stress States for 1D VP Closure Methods in σ_{xx}, σ_{yy} Space	138
5.20	Stress State for 1D VP Linear Drag Replacement Closure Method	139
5.21	Velocity for 1D VP Linear Drag Replacement Closure Method	140
5.22	Stress State for 1D VP Approximation to CAV	141
5.23	Velocity for 1D VP Approximation to CAV	142
5.24	1D VP Spherical with South Wind	143
5.25	1D VP Truncated Ellipse	144
5.26	Stress State for 1D VP Quadratic Drag Replacement Closure Method	145
5.27	Velocity for 1D VP Quadratic Drag Replacement Closure Method	146
5.28	Effects of Resolution on VP	147
5.29	Stress State for 1.5D VP Quadratic Drag Replacement Closure Method	150
5.30	V Velocity for 1.5D VP Quadratic Drag Replacement Closure Method	151
5.31	U Velocity for 1.5D VP Quadratic Drag Replacement Closure Method	152
5.32	Stress State for 2D VP Replacement Closure Method	153
5.33	V Velocity for 2D VP Replacement Closure Method	154
5.34	U Velocity for 2D VP Replacement Closure Method	155
6.1	Resolution Study: Sensitivity to Monthly Input	162
6.2	Resolution Study: Sensitivity to Daily Input	163
6.3	Resolution Study: Sensitivity to Sub-Daily Input	164
6.4	Sensitivity to Air Temperature Input Rate	169
6.5	Control Case for 2D Low Resolution Sensitivity Study	170
6.6	Standard Case for 2D Low Resolution Sensitivity Study	171

6.7	Selected 7 Day Average Wind Fields for Sensitivity Study	172
6.8	Standard Run with Constant Relative Humidity	173
6.9	Bowen Ratio at Low and High Relative Humidity	174
6.10	Sensitivity to Low Relative Humidity Along the Antarctic Peninsula . . .	175
6.11	Control Case vs Variable Mixed Layer for 2D Low Res Sensitivity Study	178
6.12	Sensitivity to Constant Low and High Ocean Heat Fluxes	179
6.13	Sensitivity to Variable Ocean Heat Flux and Ocean Currents	180
6.14	Sensitivity to Combination of Inputs	181
6.15	Sensitivity to Thermodynamics Only Model	187
6.16	Sensitivity to Ice Rheology	188
6.17	Sensitivity to Internal Ice Parameters	189
6.18	Sensitivity to Internal Ice Parameters	190
6.19	Annual Cycle using Free Drift Model - Part 1	194
6.20	Annual Cycle using Free Drift Model - Part 2	195
6.21	Annual Cycle using Cavitating Fluid Model - Part 1	196
6.22	Annual Cycle using Cavitating Fluid Model - Part 2	197
6.23	Annual Cycle using VP with Truncated Ellipse Model - Part 1	198
6.24	Annual Cycle using VP with Truncated Ellipse Model - Part 2	199
6.25	7 Day Mean Wind, Ice Velocity and Energy from 50 km TRU Model . .	200
6.26	Overview of Annual Cycle Regional Mass Balance	205
6.27	Relative Changes in Annual Cycle Regional Mass Balance	206
6.28	Annual Cycle Regional Growth Balance	207
6.29	Annual Cycle Regional Advective Balance	208
6.30	Regional Distribution of Mass Balance Components in January	211
6.31	Regional Distribution of Mass Balance Components in February	212
6.32	Regional Distribution of Mass Balance Components in March	213
6.33	Regional Distribution of Mass Balance Components in July	214
6.34	Regional Distribution of Mass Balance Components in August	215
6.35	Regional Distribution of Mass Balance Components in September	216
6.36	Particle Trajectories using VP with Truncated Ellipse Model (TRU) . . .	219
6.37	Mass Balance Components for Particles 1 and 2	220
6.38	Mass Balance Components for Particles 11 and 12	221
6.39	Spectral Plots from FD Model and Observed	225
6.40	Spectral Plots from CAV Model and Observed	226
6.41	Spectral Plots of Drift and Total Strain-Rate from TRU and Observed .	227
6.42	Spectral Plots of Divergence and Shear from TRU and Observed	228
6.43	Spectral Plots for the Case of TRU+30*Mass	229
6.44	Left Rotary Spectral Plots at Each of the Observed Buoy Sites	230
6.45	Left Rotary Spectral Plots at Each Observed Buoy Site	231
6.46	Time Series of Free Drift Model Deformation Variables	234
6.47	Free Drift Model Centroid Speed, Max Shear and DKPs	235
6.48	Time Series of Cavitating Fluid Model Deformation Variables	236
6.49	Cavitating Fluid Model Centroid Speed, Max Shear and DKPs	237
6.50	Time Series of VP with Truncated Ellipse Model Deformation Variables .	238
6.51	VP with Truncated Ellipse Model Centroid Speed, Max Shear and DKPs	239
6.52	Progressive Vector Plots from Observed, FD, and CAV	240
6.53	Progressive Vector Plots from Observed, TRU, and TRU+DRAG	241

6.54	VP Models at ISW Centroid in Principal Axis Space	246
6.55	Time Series of Ice Thickness at ISW under Ductile and Brittle States . .	247
6.56	Scatter Plot Correlation of OBS vs. FD	248
6.57	Scatter Plot Correlation of OBS vs. CAV	249
6.58	Scatter Plot Correlation of OBS vs. TRU	250
6.59	Scatter Plot Correlation of OBS vs. Z/100	251
6.60	Scatter Plot Correlation of OBS vs. DRAG	252
6.61	Cross-Correlations of Velocity and Deformation: OBS vs. Models	253
6.62	Probability Distribution and Chi-Square of Velocity	254
6.63	Prob Distribution and Chi-Square of Deformation: FD and CAV	255
6.64	Prob Distribution and Chi-Square of Deformation: TRU and DRAG . .	256
6.65	Chi-Square for Velocity Magnitude: OBS vs. Models	257
6.66	Chi-Square for Velocity Direction: OBS vs. Models	258
6.67	Chi-Square for Deformation Terms: OBS vs. Models	259
A.1	Power Spectrum Verification Test	277
A.2	Rotary Spectra Verification Test	278
A.3	Low Pass Filter Verification Test	281
A.4	Test of Multiple Regression Strain Algorithm	285
C.1	Test of Coordinate Transformation from Geographical to Cartesian Grid	295
C.2	Transformation for Interpolating Data	300

Chapter 1

Introduction

The air-sea interface of polar seas is complicated by the presence of frozen sea water, i.e. sea ice, resulting in an air-ice-sea interface. The addition of sea ice as a solid phase medium between the gaseous atmosphere and aqueous ocean affects the heat, mass and momentum/energy transfer between the air and ocean. In order to understand sea ice and its effect in the polar regions, principles based on the physics of sea ice must be used in concert with atmospheric and oceanic studies.

Sea ice is the thinnest member of this coupled system making one think that its involvement at the interface is a rather passive one reacting to the conditions imposed on it by the larger atmospheric and oceanic systems. However, the ice is a solid medium located **in** the boundary layer making it logistically and physically very different from its neighboring media. Because of this, a distinction arises when one tries to quantify events in the air-ice-sea interfacial region for each phase. Descriptions of the atmosphere near the interface include the addition of an atmospheric boundary layer (ABL) to the atmosphere while an ocean mixed layer (OML) describes the ocean thermohaline circulation close to the boundary. Several variations of these boundary layer formulations have been developed and have demonstrated a number of feedback mechanisms between the atmosphere and ocean. However, the presence of sea ice in the boundary layer requires more than an extension of physical principles near a boundary such that an entirely new set of principles within the interface must be incorporated in the description of the system.

Keeping these necessities in mind, consider the Southern Ocean; a region bound by the continent of Antarctica to the south and the Circumpolar Current to the north (Zwally et al., 1983). The seasonal sea ice extent for the Southern Ocean ranges from $3 \times 10^6 \text{ km}^2$ to $20 \times 10^6 \text{ km}^2$ (Breitenberger and Wendler, 1990) which is considerably more variable than its northern counterpart, the Arctic, which varies from $11 \times 10^6 \text{ km}^2$ to $15 \times 10^6 \text{ km}^2$ (Lewis and Weeks, 1970). Sea ice freezing, melting and advection influence the atmosphere's lower layer thermal budget and the ocean's upper layer thermal and salt budgets. Alterations of these properties have a direct effect on the density of nearby air and water masses and thus impact the stratification and dynamic stability (i.e. the "weather") of the air and ocean. In a global context, the southern seasonal sea ice field accounts for approximately 3% of the global surface area, making the Southern Ocean air-ice-sea region a significant contributor to the total atmosphere-ocean system. A proper description of the sea ice cover in this region and the factors influencing its growth and

decay are thus essential.

The physical extremes in the Antarctic region (both the Southern Ocean and Antarctica) and the recent advances in computer technology greatly encourage the use of numerical simulations to study the air-ice-ocean system in this region, particularly with the current interest of Antarctic studies to global climate change. A review of the literature shows that the first real effort to model sea ice cover in the Southern Ocean was done by Parkinson and Washington (1979) who used rather comprehensive atmospheric input and ice thermodynamics together with very simple sea ice dynamics and oceanic heat flux inputs. Using the more realistic Hibler (1979) sea ice formulation, Hibler and Ackley (1983) looked at the sea ice thermodynamics and dynamics in a sea ice model of the Weddell Sea. Later, Semtner (1986) looked at an one dimensional thermodynamic ice model using a simplified formulation of Maykut and Untersteiner (1971). Following these is a whole series of ice-ocean coupled models (e.g. van Ypersele, 1986; Lemke et al., 1990; Owens and Lemke, 1990; Stössel et al., 1990), atmospheric-ice coupled models (e.g. Koch, 1988), and others which are currently being developed.

Sea ice characteristics analyzed in these models are generally ice thickness distribution, compactness, and velocity field. These quantities are relatively easy to measure and provide quite a bit of information about the basic features of ice circulation, growth and decay. Most of the numerical models for the Southern Ocean make use of these quantities when comparing model results to observations. In most cases, however, there is little assessment of the ice directly and instead, the air and ocean constituents and their impact on the general circulation become the more focused topics. Contrary to this, investigations dealing with the role of sea ice in these coupled models are rare, particularly studies of sea ice response to imposed conditions. The main lack of focus is due to the relatively crude horizontal resolution and simplified thickness distribution of most models which precludes a detailed investigation of different processes on sea ice variations. One exception to this was the Hibler and Ackley (1983) study which focused on the role of sea ice processes (including frazil ice formulations) on the advance and retreat of the ice margin. An important conclusion of the study was that the inclusion of sea ice dynamics produces a realistic seasonal cycle of sea ice extent without the need for the large oceanic heat fluxes used in previous investigations. This result further substantiates the need to include sea ice dynamics in polar region models.

One very important process not included above is sea ice deformation. Deformation is the mechanical process responsible for ice events such as ridge and lead formation, which have an enormous impact on ice thickness, distribution, compactness and air-sea heat and momentum transfer. It is the main process through which physical properties (e.g. salinity, temperature, crystalline structure, strength) are linked to the mechanical response of the ice. In order to achieve this link, a constitutive relation or ice rheology is needed. To date there is no formulation to describe the rheology of ice in general, even in its simplest form. Two types of complications prevent us from achieving this. First, ice (both fresh and salt) is a very complicated, non-linear behaving material and second, sea ice fields consist of variable size floes of different thicknesses, an assortment of impurities and ice strengths, all subject to dynamic fluctuating inputs. Because of these difficulties, a number of rheologies are currently postulated in the literature which serve as good approximations for ice as a material but they are only successful in specific cases or when examining general features such as ice thickness or drift.

Recent data collected in the Weddell Sea under winter conditions from 1986 (Wadhams et al., 1987), 1989 and 1992 (Ackley, personal communication) further suggest that there are a number of sea ice interaction and thermodynamic processes which significantly affect sea ice extension in the Southern Ocean but which may not be adequately represented in the current sea ice model formulations. Availability of data from the Weddell Sea cruise in 1992 (through Steve Ackley at CRREL) and the accessibility to a variety of numerical sea ice codes (from the Hibler Ice-Ocean Dynamics Lab at Thayer School) provide a unique opportunity to study sea ice processes on an annual cycle using the Weddell Sea as a testing ground. The central part of the Weddell is fairly representative of the Southern Ocean ice cycle with its 2 to 8×10^6 km² seasonal ice coverage (Zwally et al. 1983). Additionally its edges provide some of the less frequent Southern Ocean features of multiyear ice, ridging, high shear (western edge) and the Weddell Polynya (eastern edge) making the Weddell Sea a robust choice for studying different types of ice processes on all scales.

The approach of this study is to compare observed sea ice events, specifically ice drift and more critically ice deformation, with a hierarchy of sea ice models. Using sensitivity studies we will investigate the dynamic response of sea ice to specific forcing and assess these responses in order to understand the processes of drift and deformation from an observational, numerical and analytical perspective. An outline of the study is as follows. First an overview of sea ice and sea ice processes is given in Chapter 2 followed, in Chapter 3, by a description of the primary observations used for this study and the results of the data analysis performed on them. An overview of the model hierarchy will be given in Chapter 4 followed by an assessment of the mechanical behavior of this hierarchy in Chapter 5. Finally a regional numerical study is presented in Chapter 6 and compared to observations (Chapter 3). The main focus of this research is observed and numerical dynamic sea ice response of seasonal variability, drift and deformation to specific inputs and not the development of numerical codes. Hence, the models will be described in a condensed summary (Chapter 4), and technical aspects on material developed specifically for this study will be presented in the Appendices.

Chapter 2

Overview of Sea Ice

The intention of the chapter is to provide a brief synopsis of sea ice features relevant to this study. The discussion will begin with a fundamental introduction to sea ice and circulation followed by a description of what is meant by sea ice processes. An overview of the specific processes of drift and deformation, which are the main foci of this study, is then presented.

2.1 Description of Sea Ice

In brief, sea ice is different from fresh water ice found on land in that it is composed primarily of frozen sea water which contains salt. The presence of salt makes the ice structurally weaker and thermally more complicated than fresh water ice. According to Wadhams (1986), the geographical distribution of sea ice can basically be divided into three sectors:

- a) fast ice zone
 - sea ice attached to land
 - too fixed to move much, lots of ridging
- b) shear zone/main pack ice
 - isolated from both land and open ocean
 - potentially a high shear zone, ridging, leads
- c) marginal ice zone or MIZ
 - within range of the open water ($\leq 200\text{-}300\text{km}$ from ice edge)
 - low resistance to movement, wave and wind effects

The physical size of sea ice can be categorized into several ice types ranging from very small ($<10\text{ cm}$) to large (kilometer range) as one proceeds from open water regions (such as the ice edge) into the ice pack. The ice types forming in closest contact with the

open water include a whole range of translucent ice types (ice needles, grease ice, frazil ice, and others). Under wind and wave action these small crystalline structures combine to form pancake ice, less than 1 meter in diameter. Further wind and wave action induce collisions of the pancake ice forming small floes of congealed pancakes (meter range). Deeper into the ice pack wave effects are damped out by the larger floe sizes allowing freezing between floes, resulting in floe size increases to 100m-1km. At this size ocean currents, damped wave interaction and wind alter the structure of the floes through ridging and lead (open water) formation.

For each of the above mentioned ice types, properties of salinity, temperature, ice strength, and conductivity (to name but a few) are dependent on the amount of contact with surrounding ocean, water and other ice crystals, as does their age (i.e. how long they have survived as a certain ice type), the internal and external forces, processes they have been exposed to, and many other factors. In short, the description of sea ice characteristics and properties encompasses an entire research area within the study of sea ice. Hence for further in-depth descriptions on this topic, the reader can refer to, for example, Untersteiner (1986).

2.2 General Circulation

Sea ice is predominantly confined to two major regions on the planet: north of the Arctic Circle in the northern hemisphere, and between the circumpolar current and Antarctica (Antarctic continent) in the southern hemisphere. One aspect of sea ice in these regions is that its constituents are visible surface tracers which allow researchers to physically see circulation patterns at the surface. One of the early Arctic explorers, Fridtjof Nansen, was the first to take advantage of sea ice as a tracer. Through observations (Nansen, 1906), he discovered that ice drifted on the surface of the ocean at an angle to the right of the wind rather than parallel to it. Theoretical work by Vilhelm Ekman based on these observations led to the development of the Ekman Theory wherein he showed (Ekman, 1908) that the angular difference between wind and surface current is caused by the rotational force of the planet (i.e. the Coriolis force). This theoretical work also led to the identification of the so-called Ekman layer (approximately 10 m or so above to some 30 m below the ice/ocean surface) which is the region of transfer between the air and sea; in this context it is also referred to as the boundary layer. In more recent years, advances in satellite communication and instrumentation allow researchers to utilize sea ice as a research platform. Thus, due to the presence of sea ice, considerable gain has been made in understanding heat, mass and momentum/energy transferring processes that occur at the air-sea interface.

As alluded to in the introduction, the fact that sea ice is a solid located at a gas-liquid interface creates a whole range of dynamic-thermodynamic problems not encountered in air-sea interfaces where freezing does not occur. One problem of particular importance to this study is that the presence of a flexible solid at a dynamic gas-liquid interface introduces a number of non-linear processes into the transfer of heat, energy and momentum. The main impact of these non-linear processes is that they are able to transfer quantities such as momentum from one scale size to multiple scales making it difficult to keep track of the evolution of a given event.

In both northern and southern regions, wind and storms generate a variable force above the ice while the ocean circulates with a more or less steady flow below the ice. Additionally, the ocean is driven by the wind circulation from above and steered by the bottom topography from below. Sea ice contributes its own internal forces of resistance to flow and deformation. In the Arctic, sea ice is confined in a mediterranean sea (sea surrounded by land) located primarily north of 75°N . The circulation pattern consists mainly of the Beaufort Gyre rotating clockwise (when looking down at the north pole from above) connecting to the Transpolar Drift Stream which crosses from the Beaufort Sea through the North Pole across the Eurasian Basin then southward out of the Arctic Ocean through the Fram Strait located between Northern Norway and Greenland.

In the Antarctic, a land mass (Antarctica) sits at the pole while the sea ice is held bound against the continent by the circumpolar current which traverses around the planet between about 40°S and 60°S . Lack of land masses in the circumpolar region allows the wind driven ocean circulation to maintain a strong eastward current which acts as a barrier separating surface circulation patterns to the north and south of it. The most outstanding difference between the northern and southern regions is the variability in sea ice extent. In the north the annual ice cover varies by about 25% versus an 85% change in the south. The location of these regions relative to land (land locked in the north versus continent surrounding in the south) creates two different circulation fields.

2.2.1 Weddell Sea Circulation

The Weddell Sea is bound by land on two sides, the Antarctic Peninsula to the west and Antarctica to the south. To the north the circumpolar current maintains its strong eastward flow from which the Weddell Sea Gyre forms as a secondary circulation pattern. Thus, the circumpolar current defines the northern boundary of the Weddell Sea Gyre while the eastern extent of the Weddell Sea Gyre defines its eastern boundary located along 0° to 10°E approximately.

A number of subregional circulation patterns occur in the Weddell Sea making it a very interesting place to study. Along the western part of the gyre there is a build up of ice due to the presence of the Antarctic Peninsula. The buildup creates a situation where ice can survive from one year to the next resulting in a multiyear ice type which survives through the summer melt and then continues to freeze with the onset of winter. Because of this build up and the constraints of the peninsula, shear becomes the dominant stress type in this part of the field. Very close to the peninsula, however, and along the coast of Antarctica a narrow region along the shelf often experiences periods of open water due to katabatic winds (cold dry continental surface winds) and tidal forcing (Foldvik and Gammelsröd, 1988). The cold air temperatures combine with open water lead formation, creating ideal conditions for producing high density bottom water. The bottom water process arises when new ice freezes over the shallow cold shelf water. Salt is ejected from the freezing ice and mixes into the shelf water increasing its density. This heavier water sinks along the shelf slope into the abyssal region. The combination of cold high saline water located near a deep abyssal region creates the best conditions for the heaviest water making the Weddell Sea western corner one of the best bottom water generators on the planet.

To the east, the Weddell polynya serves as another bottom water generator resulting from a different type of circulation structure. The Weddell polynya is an intermittent large opening in the middle of the ice pack near Maud Rise. The formation process of this polynya is believed to be connected with the water circulation and mixed layer depth adjustment from below (Gordon, 1978). Once formed the polynya has a great impact on air-sea transfer due to the creation of a large open water source in the presence of strong atmospheric cooling. The result is an oceanic convective process similar to the one described above. In terms of sea ice, this transient process precludes the steady state ocean structure thereby complicating the surface heat, mass and momentum transfer processes.

A final interesting circulation feature in this region is the effect of the roaring 50's wind and circumpolar ocean current at the northern reaches of the gyre. The strong transient storms and the circumpolar current's strong eastward movement produce a stormy wave field which on the one hand rapidly cools the surface, especially during the onset of winter, and on the other hand, enhances mixing in the ocean, hence hindering surface freezing. The result is the creation of sea ice over a vast region in a fairly short time span (can be several kilometers in less than a day). It is the presence of such a torrent boundary that sustains the rapidly growing and decaying ice fields seen in the south.

2.3 Sea Ice Processes

From the descriptions above, we see that the sea ice field is exposed to a range of air, ice and sea properties together with velocities, undulations, collisions and other mechanical interactions all of which impact the development of the different ice types and their adjustment to lateral boundaries (land, open water). It is these features which are studied under the heading of sea ice processes. More formally, sea ice processes are the thermodynamic and dynamic events occurring in sea ice as a result of external (air, ocean) and internal (ice) forcing. The impact of these processes on the air-ice-sea system includes a large range of heat, mass and momentum/energy transfers between the atmosphere and ocean. Understanding the involvement of sea ice in this transfer is a key focus of this study.

In the above sections a number of air-ice-sea processes were already alluded to. Some of them include sea ice processes involving growth, decay, drift and deformation while others (such as deep water formation) include processes resulting from the combined influence of air, ice and sea. Sea ice processes make up a very large research area within the field of sea ice. Only a small subset of these processes can be dealt with in any given study with the confines of such a study being limited by scale sizes, time lengths and the number of measurable variables which can be used to quantify specific events. In order to best utilize the resources available for this study, the focus here will be on dynamic processes mainly occurring in the sea ice itself as a result of air, ice and ocean forces. Furthermore we will reduce our interest to those dynamic events related to the drift and deformation of the ice with a focus on how these processes affect movement, growth and decay of the annual ice extent in the Weddell Sea region. We will limit ourselves to scales ranging from 10's (mesoscale) to 100's (large scale) of kilometers and time scales between

a few hours to a few months. Finally we will regard only those processes which can both be measured from the available field data and calculated in numerical simulations.

2.3.1 Sea Ice Drift and Deformation

Beginning with velocity, the movement of ice is often referred to as ice “drift” because of the historical notion that ice is a passive recipient of the surrounding air and water motion. Today, however, we recognize that the ice moves with a velocity resulting from both internal and external forces as follows.

$$m \frac{D\vec{v}}{Dt} = -m f \hat{k} \times \vec{v} + \vec{\tau}_a + \vec{\tau}_w - m g \nabla H + \vec{\mathbf{F}}_{ice}. \quad (2.1)$$

(Description of each variable in Tables 4.1 and 4.2.) The external air and ocean forces, as noted above, are complicated by the earth’s rotation while the internal ice forces complicate matters by resisting in a non-linear manner any alteration in shape. When the shape of the ice does change, deformation ensues and the shape is said to “yield” to the stresses/forces imposed on it. Stress and strain are the two principal categories governing these processes of resistance and yielding.

Stress is the internal force per unit area within any given material and strain is relative displacement within the object as a result of the imposed stress. Load is the external or far field force applied per unit area. Mathematically this relationship is linked to formulate stress as a function of strain through the constitutive relation (or constitutive law). Since stress is a force per unit area, the resultant stress from the constitutive relation times the area of the surface exposed to that stress results in the internal force of the ice. We complete a circle linking deformation back to velocity by realizing that the internal ice stress computed using the constitutive relation is the force (per unit area) which is used in the momentum balance to define how the internal ice forces work in concert with the external forces imposed by the air and water to produce the reaction forces which drive the ice velocity (Figure 2.1). In terms of the importance of the internal ice force to the momentum balance, the size of the internal ice force per unit area is of the order of 10^{-3}N/m^2 or so. This compared with terms such as the wind and water drag forces (per unit area) (10^{-1}N/m^2) are small but compared to terms like the Coriolis force (10^{-3}N/m^2) and inertial term (10^{-4}N/m^2) is significant to the overall momentum and energy transfer within the air-ice-sea system.

In terms of understanding these processes through numerical computations there are a number of things to consider among which is, how well does the model reproduce the effect being studied. One way of determining how well a model works (i.e. how well we can describe and predict local field variables) is through its ability to reproduce both the spatial and temporal evolution of, for example, an observed field’s drift. Deformation, including strain, shear, divergence and similar processes, consists essentially of spatial derivatives of the drift field. As a result they are of higher order than the drift field and hence more sensitive to spatial differences. In quantitative terms, typical ice velocity is of the order of 10^{-1} m/s while on scales of 10 to 100 km or so a divergence rate of 10^{-7} to 10^{-6} s^{-1} (1 to 10%/day) is representative for deformation. The ability to correctly simulate such small deformation rates mandates a more critical understanding of the dynamic processes in the field than is expected for ice drift alone. Hence, deformation terms

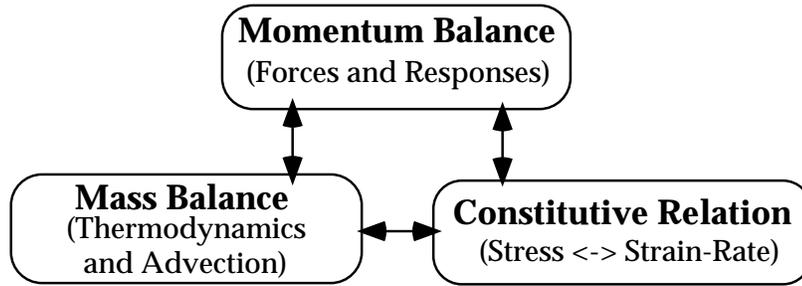


Figure 2.1: Schematic of Governing Equations for Sea Ice.

provides more stringent criterion for evaluating a model's ability to simulate observed field events. In the following study we will examine this sensitivity of the deformation field and investigate to what degree it is more sensitive than the ice drift.

In theoretical and numerical work, devising mathematical functions for stress-strain relationships is straightforward. In the field, however, measuring strain-rates on the order of 10^{-7} s^{-1} is to say the least, difficult. Measuring the stresses responsible for those strain-rates is even more than difficult to the point that reliable methods for doing so on a geophysical scale are not available to date. Although stress and strain can be examined in numerical and theoretical studies, the primary focus here will be on the strain-rate activity (displacement per unit time) as this is a quantity which can be computed using both observed and numerical information.

In practical terms, the scales and processes considered in this study are useful for understanding the basic mechanical behavior of sea ice at scales which directly impact human activity. A simple illustration of this is the example of an oil platform designed to withstand thousands of tons of pressure. As illustrated in Figure (2.2), proper understanding of the ice field through modeling efforts and field experiments can make the difference between the platform resisting the converging onset of seasonal ice or looking like a twisted bread stick as a result of the ice field not uniformly converging but twisting in shear around it. This example sets the precedent for understanding the drift and deformation of sea ice in its natural environment at scales considered here.

In summarizing, we have used this chapter to become more familiar with sea ice, its basic properties and processes, and the dynamic processes of particular interest to this study. We have found that the processes of drift and deformation are critical to understanding the relationship between the reaction of forces from the air, water and ice in the polar seas. In particular we found from both this and the previous chapter that our current ability to measure and understand the processes of deformation are limited and that more research is needed in this area in order to better predict and correctly simulate events occurring at the air-ice-sea interface. Questions arising include those aimed at better understanding ice drift and deformation and its contribution to the system at large, in this case the variability of the sea ice field in the Weddell Sea. Two specific questions will be addressed throughout this study in light of what has been discussed so far. First, what external forces are responsible for the development of specific drift

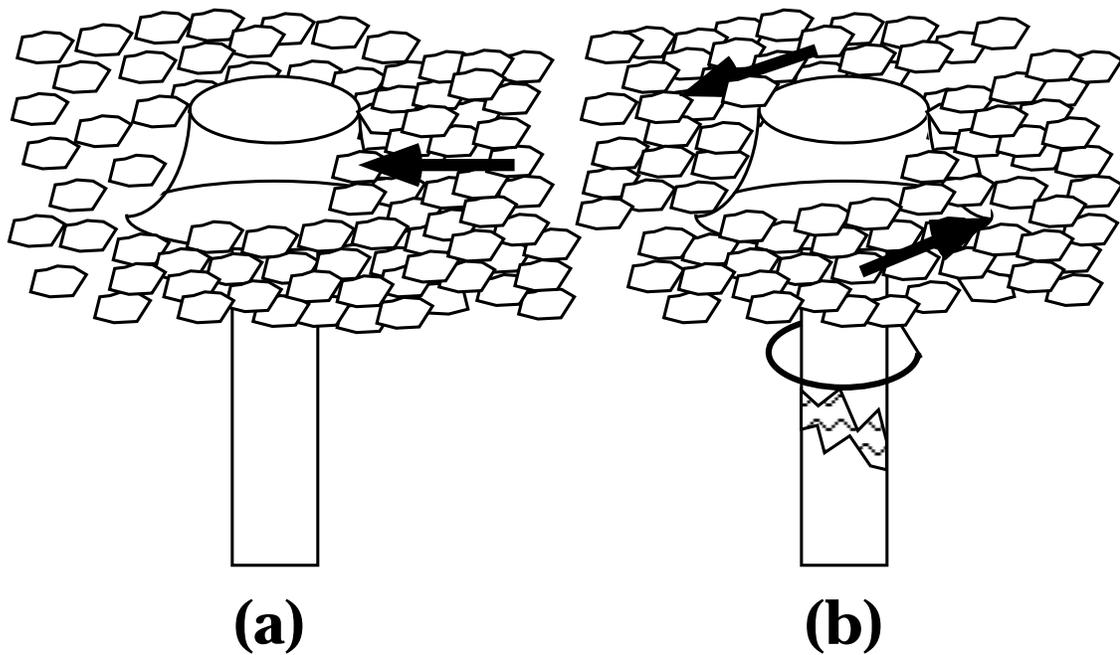


Figure 2.2: Example illustrating sea ice drift and deformation processes.

and deformation processes, and how well can we simulate (and eventually predict) such events? Second, how do the external forces and internal ice dynamic processes affect the ice expansion and decay cycle in a region as variable as the Weddell Sea? There are certainly a number of factors both thermodynamic and dynamic which enter into such complicated questions. The task here is to reduce the focus to a limited range of issues in terms of scale and region, in order to understand the air-ice-sea interface through case studies.

Chapter 3

Field Measurements

3.1 Introduction

In this chapter we will examine the processes of sea ice drift and deformation as observed in the field. We will also identify some of the external forces driving the different processes in order to gain an understanding of the forces and responses of these observed events. The knowledge gained in this chapter will then serve as a test case to assess the capability of numerical models for simulating these processes.

From the resources available, the observations from the February to June 1992 Ice Station Weddell program (ISW) in the Western Weddell Sea are the best suited. Specifically, data from the ISW large scale (150 km) array allow us to examine sea ice responses to air and ocean forcing. The selected data include a four month time series of surface wind, ocean current and positions from 6 ice sites in the array.

3.2 Data Processing

3.2.1 Large Scale Strain Array

During the 1992 ISW program (Gordon et al., 1993), a large scale array spanning 150 km was set up in the Western Weddell Sea. The array included 6 Argos buoys at remote sites located 25 to 100 km from the central camp and a GPS unit at the camp. Positions for these sites were recorded at the camp every three hours, on average, via satellite. An overview of the buoy names and their deployment dates is given in Table 3.1. Figures (3.1) and (3.2) show the general track of the buoys and their relative configuration within the array, respectively. One of the buoys, Martinson, is considerably shorter in duration than the others and actually resides on site Chris (i.e. on the same ice floe). Because of the brevity and redundancy of this information, the Martinson buoy will be used for instrument error and spectral analyses but not for strain-rate estimates.

Processing of these data began with the conversion of asynchronous satellite information into a common time series database which retained the instrument number, date, time, and geographical position from each site. The data were then linearly interpolated

Table 3.1: Overview of Large Scale Array Program

Instrument Site (No.)	Activated (Jul. Day)	Deployed (Jul. Day)	Stopped (Jul. Day)	Total (hours)
Camp (1400)	43.44		158.66	2766.17
Alex (1430)	41.58	48.71 to 48.92	151.55	2640.45
Brent (1431)	41.72	61.75 to 62.04	153.71	2688.57
Dimitri (1432)	41.57	61.46 to 61.75	153.52	2687.92
Ed (1433)	41.57	50.67 to 51.00 63.46 to 63.83	182.95	3395.10
Chris (1435)	62.05	62.05	182.95	2902.73
Martinson (6440)	116.44	116.44	154.58	916.22

to hourly positions and analyzed for instrument error (Appendix A.1). The positions were found to be accurate to about a half kilometer with the largest relative error between GPS and Argos units. Errors in distance due to instrument accuracy propagate to errors in velocity which, because of its presence at every time step, shows up as a high frequency signal. In order to minimize this and other high frequency influences, the position data were passed through a 4 pole Butterworth low pass filter (Roberts et al., 1978) at selected cut-off times before computing the ice drift velocity (Appendix A.3). Buoy velocity is computed from the hourly geographical positions using a simple local Cartesian projection (Appendix C.1.2) followed by the simple linear calculation $\Delta x_i / \Delta t$ for each velocity component at each site. Following this, the data were subject to power spectra, strain-rate analysis, and additional error analyses all of which are discussed below. Descriptions of the analysis techniques are given in Appendix A.

3.2.2 Meteorological and Oceanographic Data

Meteorological stations were located at three of the sites in the large scale array: site Chris (west of camp), site Dimitri (east of camp), and the main camp (Figure 3.2). From the data recorded, readings of surface (1m) air pressure, hourly averaged wind magnitude and direction, and temperature profiles from the top, 1m above the ice, to the bottom were made available to the author through S.F. Ackley (USA Cold Regions Research and Engineering Laboratory (CRREL), Hanover, N.H). Analyses performed at CRREL (S.F. Ackley, personal communication) show that the meteorological data are very similar at each of the sites and that two of the sites had inoperative sensors for short periods of time. Based on these preliminary findings the longest most continuous record, which is from site Chris, was chosen to represent meteorological readings for the array.

Current meter arrays were deployed by Robin Muench (SAIC, Seattle, Wa.) at sites Alex, Chris, and Dimitri each at 50 and 100 meter depths, site Ed at 50 meters and the main camp at 25, 50 and 200 meter depths (Muench et al., 1992). Due to the strong barotropic nature of the current in this area (Muench et al., 1992) and the presence of only one site with current measurements less than 50 meters deep, a single site, the main camp, was chosen to represent the overall local current structure for the array.

Both the above described data sets were converted into the same format as the buoy information and subject to the same spectral analysis. In order to retain as much of the original information as possible, and given the high sampling rates and accuracy of the velocity and pressure sensors, these data were not subject to low pass filtering. Time series of the selected meteorological and oceanographic data are shown in Figure (3.4).

3.3 Results

3.3.1 General Ice Drift Features

An overview of the buoy drift pattern is shown in Figures (3.1) and (3.3) in the form of geographic and time series plots, respectively. There was some erratic behavior at the beginning and end of the drift due to deployment activity. As a result the time series has been limited for this study between Julian days 63 and 150. Within this time frame there are a few notable features. First, the general drift pattern in the Western Weddell is primarily northward and very slightly eastward. Second, relative to the bathymetry, the array configuration and ice drift proceed northward along the shelf slope with the western most sites (Ed and Chris) tracking along the 1500 to 2000m isobaths and the remaining sites tracking closer to the 2500 to 3500m isobaths to the east. The depth of the water column below the array is decreasing by about half from east to west. Third, at the beginning of the drift there is a large convergence that moves, for example, site Alex from east to south of the camp (some of this activity occurred before day 63 while the array was being deployed). Fourth, between 1. April (day 92) and 1. May (day 123), the entire array undergoes at least two complete cyclonic (clockwise) loops. The largest of these, between day 116 and 121, coincides with the passage of a 5 day atmospheric low pressure system as seen in the surface wind in Figure (3.4) and as noted from the field experiment. The wind shift from northeast to southeast to northwest during that time period produced a corresponding sea ice response as seen in both Figures (3.1) and (3.3). A final general feature to note is that the buoy tracks contain a significant amount of drift perturbation activity (Figure 3.3) which results from local deformation processes in the ice. We will investigate this activity in considerable detail below.

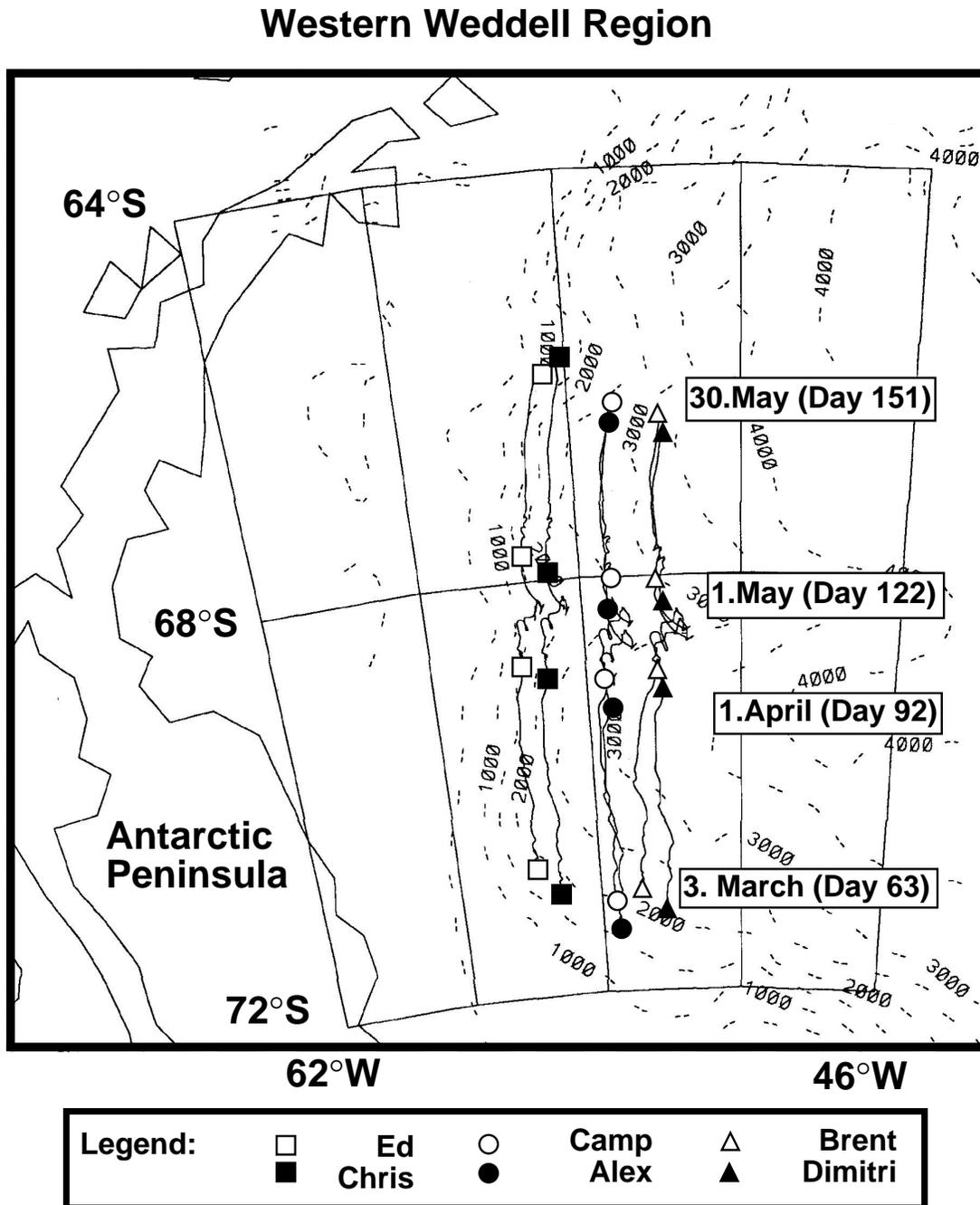


Figure 3.1: Western Weddell Sea Region with ISW buoy track and local bathymetry.

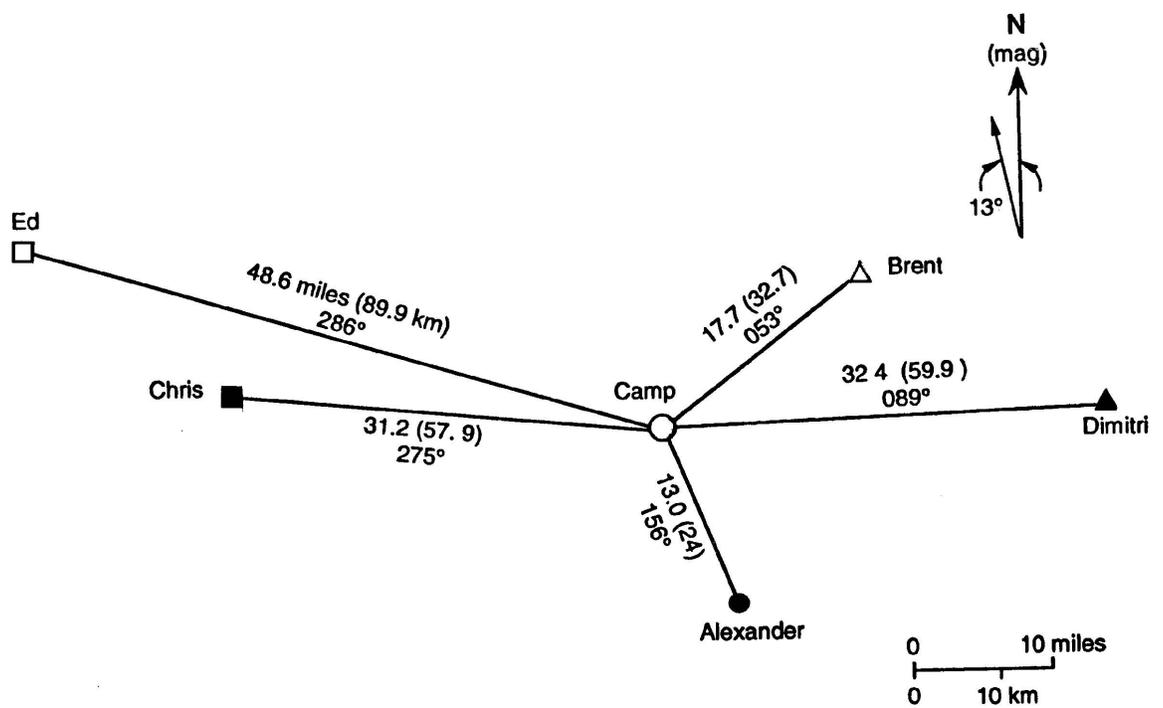


Figure 3.2: Initial configuration of Argos sites relative to ISW Camp during 1992. Used with permission from Ackley et al., 1992 with some modification.

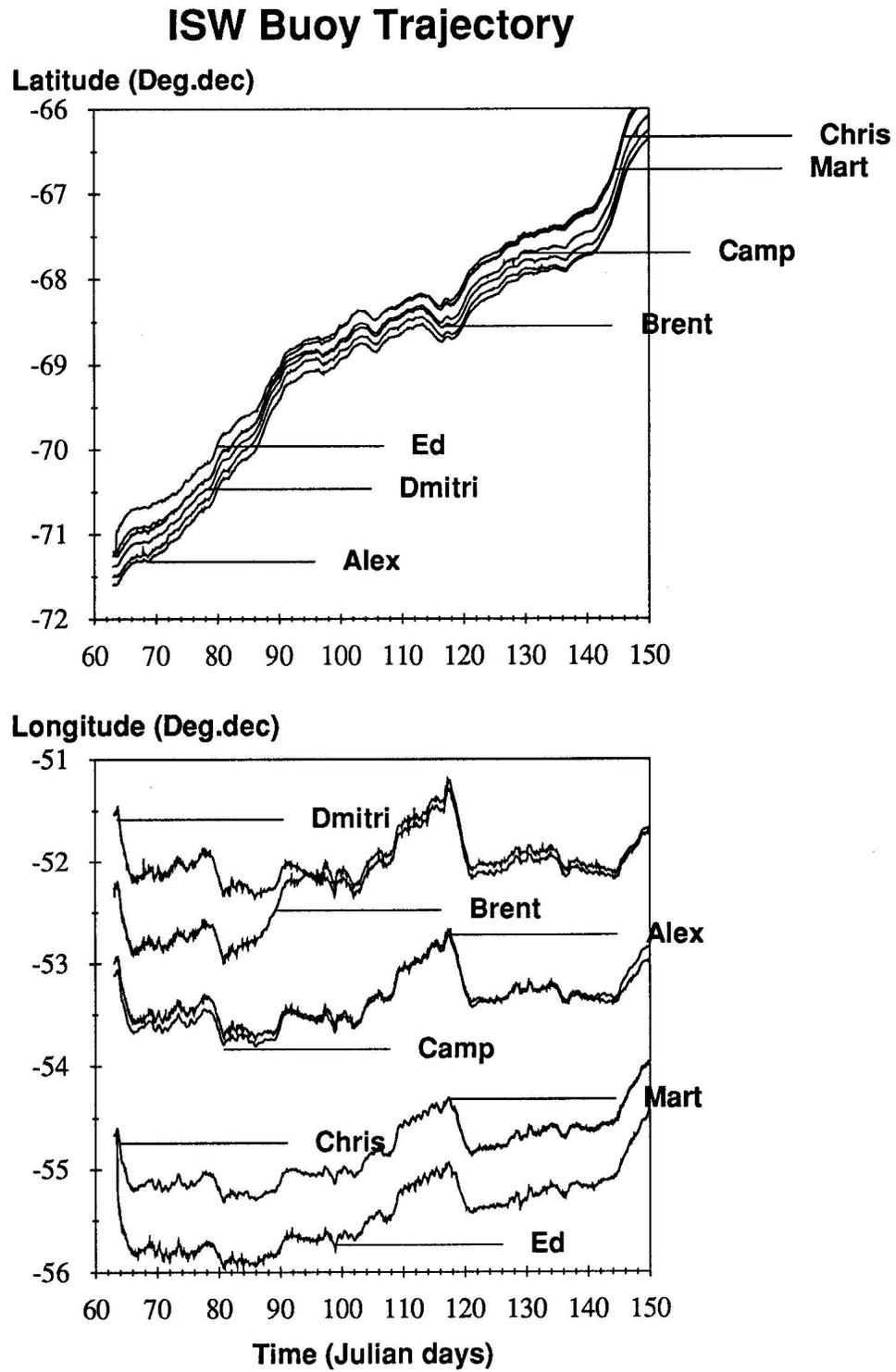


Figure 3.3: Time series of ISW Argos and GPS units from day 63 to 150 during 1992.

Wind and Water Velocities

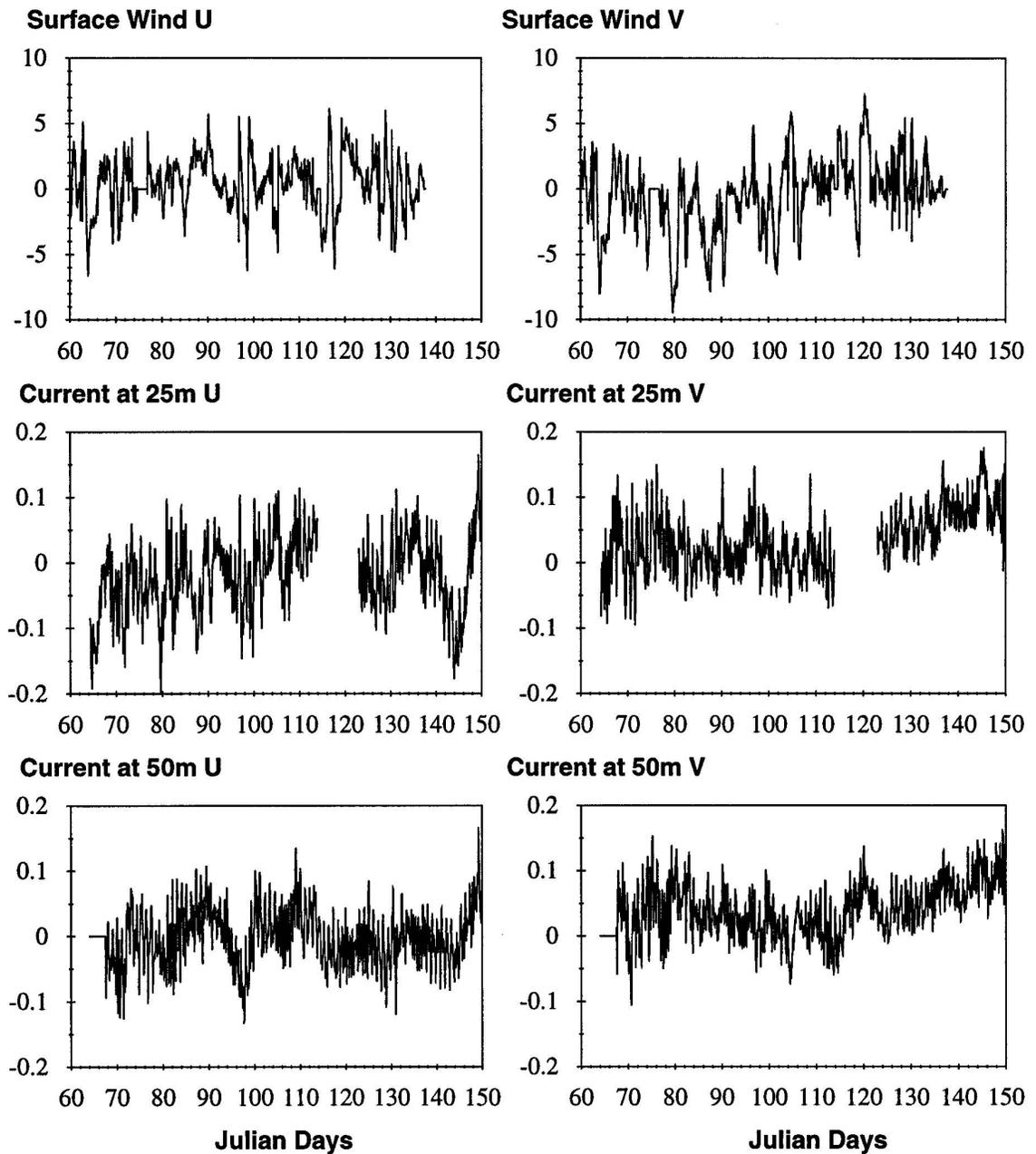


Figure 3.4: Time series of surface wind from site Chris and ocean currents from camp at 25 and 50 m depths. Wind and current data used here with permission from Ackley and Muench, respectively. Velocities are in units of [m/s] with U oriented positive eastward and V oriented positive northward.

3.3.2 Power Spectra Analysis

The results of a power spectra investigation using all the buoys and both velocity components are shown in Figure (3.5). The plots show power density (normalized power per frequency binwidth) resolved to 64 and 128 frequency bins ranging from the DC signal at 0 cycles/day down to the Nyquist frequency of 4 cycles/day (6 hour period). The frequency resolution is $\Delta f = 0.06$ cycles/day for 64 bins and 0.03 cycles/day for 128 bins. From this figure we note two general trends. First, the largest power signal is seen in a linear log (i.e. exponential) increase in power density (so called “red shift”) towards lower frequencies (<0.8 cycles/day). This means that most of the kinetic energy associated with the velocity drift is coming from lower frequency sources (e.g. 3 to 5 day storm fronts, ocean eddies, weekly oceanic and atmospheric current patterns, and other events of similar duration). Second, there are prominent power spikes near 1, 2, and 3 cycles/day (24, 12, and 8 hour periods, respectively). From the literature (Rowe et al., 1989, Foldvik et al., 1990), the 12 and 24 hour power spikes are believed, at least for this part of the Weddell Sea region, to be associated with ocean tides and possibly sea ice inertial oscillations. The collection of power spikes near 3 cycles/day are believed to be associated with high frequency non-linear ice interaction possibly due to inertial oscillation activity. Given the size of the instrument error, however, these high frequency 3 cycles/day signals are not being considered in detail in this investigation.

In addition to these general trends, there is a considerable amount of regional variability. At sites Alex (southeast), Brent (northeast), and Dimitri (east) the 12 hour power spike is fairly strong but the 24 hour spike is quite weak, while at the camp (center), Martinson (west), Chris (west) and Ed (northwest), both 12 and 24 hour power spikes are quite pronounced and of about equal magnitude. Relative to the topography in the area, the eastern sites are more in the deep basinal area while the western sites are located along the continental slope (Figure 3.1). The increased power density in both the diurnal (24 hour) and semidiurnal (12 hour) frequencies in the western section is associated with this rise in bathymetry. More specifically, there is an increase in ice activity along the slope region due to topographically enhanced ocean circulation patterns.

If we look at the power spectra of the individual velocity components (u and v) we see some very interesting dichotomies in energy/power distribution. First, the low frequency power density of the u component (Figure 3.6) is at most the same order of magnitude (between 10^2 and 10^3 (m/s)²) as the power spikes at 12 and 24 hours. Contrary to this the strong low frequency signal seen in the total velocity power density appears in the v component of the power spectra (Figure 3.7). Second, the strong 12 hour power spike seen in the total velocity power density at the eastern sites is quite visible in the v component but nearly indistinguishable from the rest of the signal in the u component, except at site Alex. Contrary to this the strong 12 and 24 hour spikes (2 and 1 cycles/day, respectively) in the western sites are very pronounced in the u component but almost indistinguishable in the v component. Only at site Ed, furthest up the shelf slope, do we see a strong 12 and 24 hour signature in both the u and v components.

We can identify potential sources for these signals by examining the power density of the wind and current meter data. As seen in Figure (3.8) the same strong exponential increase toward low frequency power density seen with the buoy data for frequencies below 1 cycle/day is present in both the wind and current meter data. Taking into

account the fact that the ocean is 1000 times more dense (3 orders of magnitude) than air the low frequency contribution from both ocean and air in terms of kinetic energy become comparable with the ocean power spikes at 12 and 24 hours having a greater impact at these frequencies than the wind. We also see in the current data the presence of two prominent power spikes at 1 and 2 cycles/day corresponding to the same 24 and 12 hour power spikes seen in the ice drift data. The kinetic energy power signature at these higher frequency 24 and 12 hour periods is about an order of magnitude more than the wind forcing at the same frequencies. From this information it becomes evident that at low frequencies both the wind and current are comparable external forces on the ice while at diurnal and semi-diurnal frequencies the ocean seems to be dominating. The strong dichotomy between u and v velocity components seen in the buoy data is not nearly as pronounced in the current data. There is only a slightly lower power density in the v component at 12 and 24 hour than in the u component but given the topography some difference is expected. One interesting dichotomy that does exist in the ocean current is the reduced low frequency signature in the u component of the current compared to the strong low frequency signature in the v component (four lower plots in Figure 3.8). This same situation was observed in the buoy data indicating that the dominantly northward ocean current is contributing substantially to the northward drift of the array. Figures not included here confirm that no such directional dependence was seen in the wind signature.

With respect to ocean current regional variability, an overview of the ocean circulation around ISW is given in a preliminary report from Muench et al. (1992) wherein three relevant circulation conditions are described. First, results from all four current meter sites indicate that the mean ice drift is about 7 cm/s northward indicating a primarily barotropic flow locally. Second, a western boundary intensification is observed in the 50m measurements which average from 5 cm/s at the westernmost site to at least 1 cm/s at the easternmost site. Third, fluctuations of 10-20 cm/s superimposed on the mean flow consist of semi-diurnal, diurnal, inertial and low frequency mesoscale signals. This information coincides very closely with the power spectra information described above. The mean northward ice drift described by Muench corresponds to the strong low frequency power signature in the v velocity component. The orientation of the continental slope is responsible for the western boundary intensification and also the main source of the increased diurnal and semi-diurnal activity at the western end of the array. Finally, the diurnal and semi-diurnal power spikes from the spectral plots correspond to the 10-20 cm/s superimposed fluctuations observed in the current meter data which further supports the assumption that ocean circulation patterns are driving these high frequency features.

In summarizing this section we note the following. In comparing the wind and current results with the buoy spectra, we find that the mean ice drift is being driven by low frequency wind and ocean circulation patterns. At first glance, the ocean appears to have the most direct influence on the northward drift of the ice. However caution must be taken in interpreting these results since the internal ice resistance may also be acting in such a way that the ice resists compacting southward due to the continent then when the wind blows northward it provides a force complementary with the ocean current. Additionally as described in Chapter 2, it is important to realize that the large scale ocean circulation responsible for the mean ocean current is driven by the large scale wind

circulation from above and steered by the bottom topography below. With regard to the higher frequency activity, the 12 and 24 hour power spikes seen in the ice drift are driven primarily due to the diurnal and semi-diurnal ocean oscillations which in turn must be driven largely by tidal forcing. With regard to total ice drift forcing, these higher frequencies (greater than one cycle per day) contribute about an order of magnitude less power to the ice drift than the low frequency forcing. Comparing results here with the general drift results from Section (3.3.1) we also find that a considerable amount of low frequency response must be coming from the variable passage of storms such as the one identified around day 120 and that this storm activity contributes substantially to deviations in drift trajectory. Finally, it is important to note that the ice response contains a considerable amount of high frequency activity and directional variability that neither the wind nor the ocean exhibit. Through process of elimination this additional activity must be a result of internal ice interaction.

Spectral Plots of Buoy Velocity

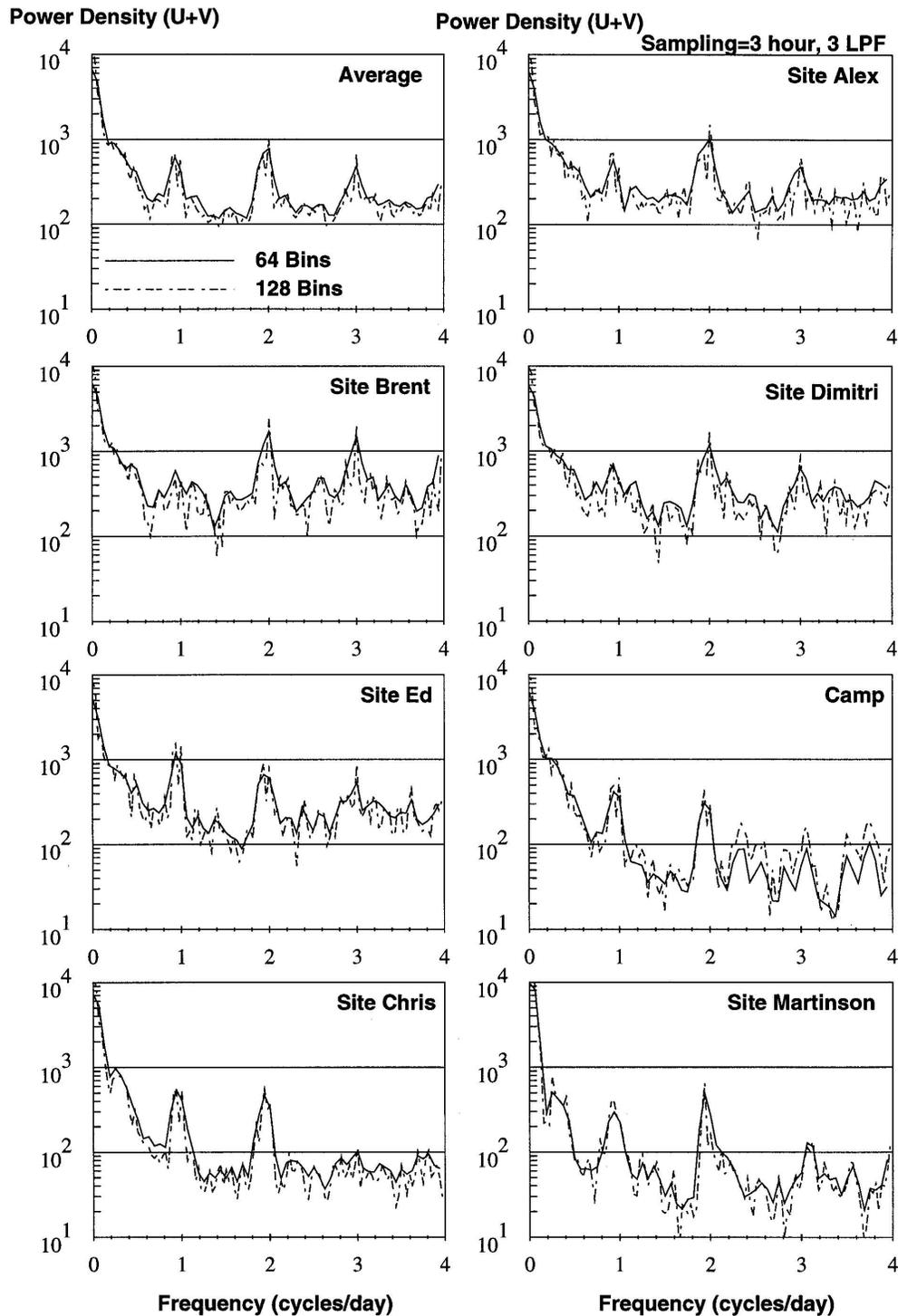


Figure 3.5: Plots of power density for Argos buoys and camp drift U and V velocity components resolved to 64 and 128 frequency bins. Power spectral density in units of $[(\text{m/s})^2/\Delta f]$.

Spectral Plots of Buoy Velocity

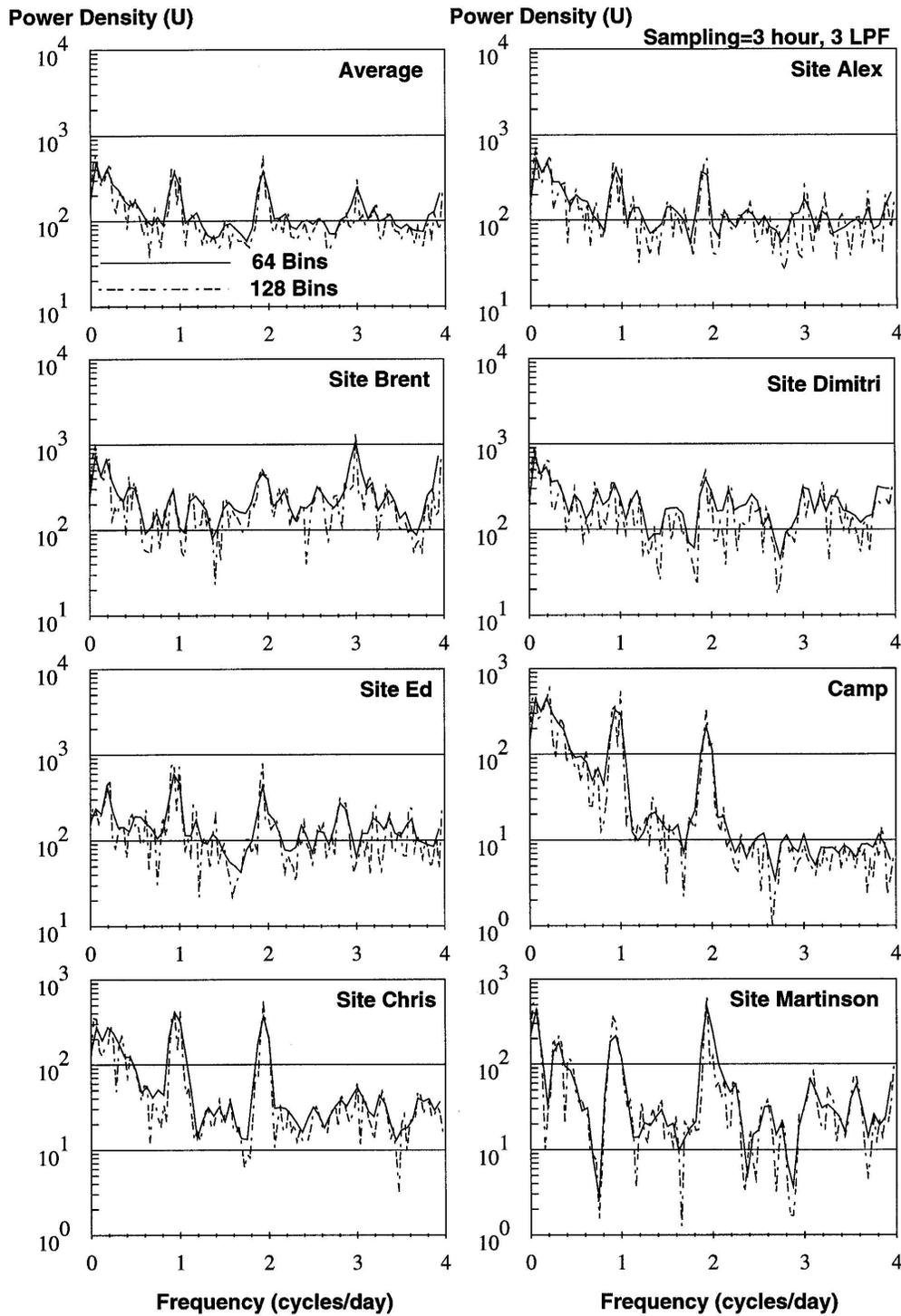


Figure 3.6: Plots of power density for Argos buoys and camp drift U velocity component resolved to 64 (solid) and 128 (dashed) frequency bins. Power spectral density in units of $[(\text{m/s})^2/\Delta f]$. Note change in Y-scale of last three panels.

Spectral Plots of Buoy Velocity

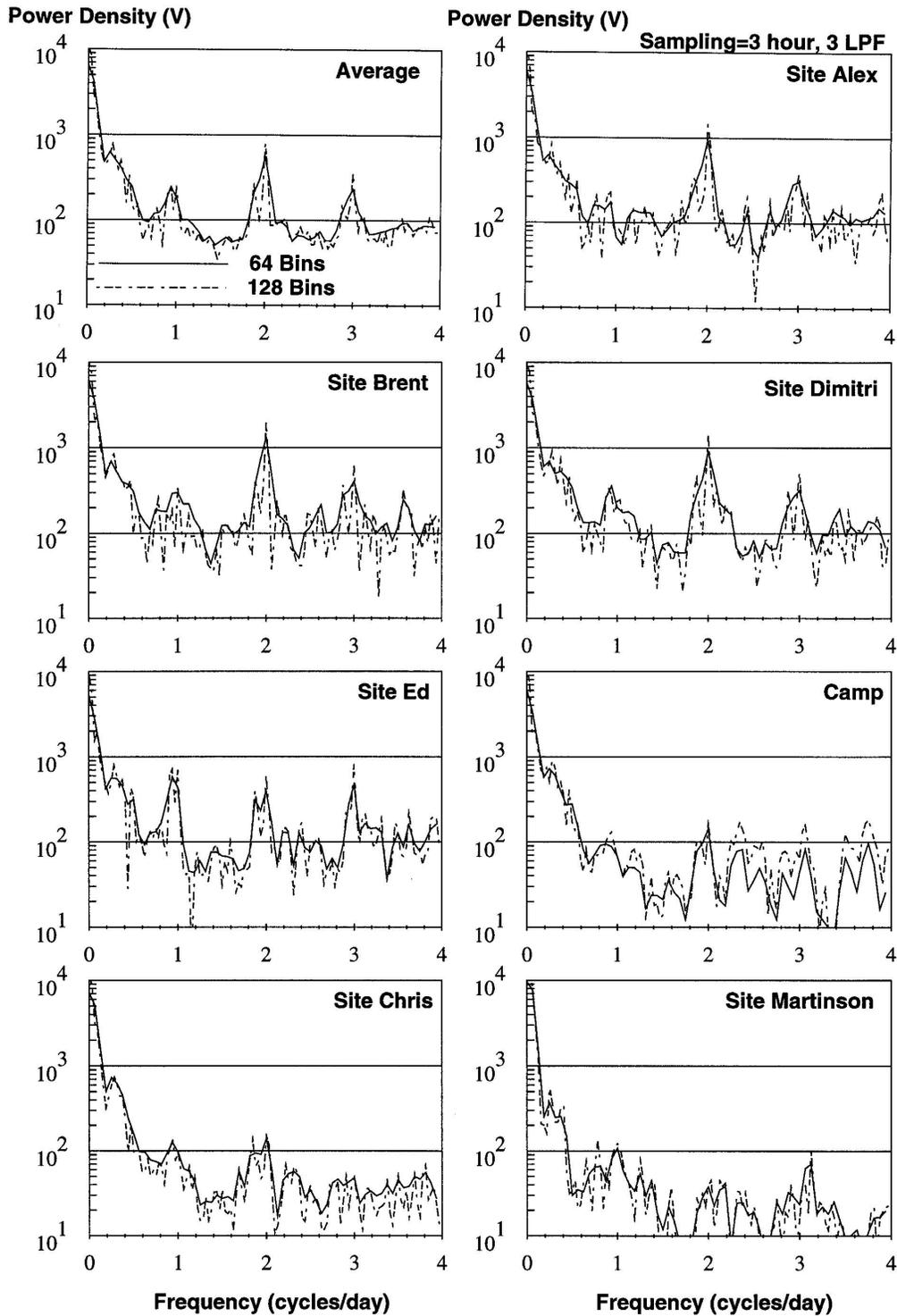


Figure 3.7: Power density for Argos buoys and camp V velocity component resolved to 64 and 128 frequency bins. Power spectral density in units of $[(\text{m/s})^2/\Delta f]$.

Spectral Plots of Wind and Water Velocities

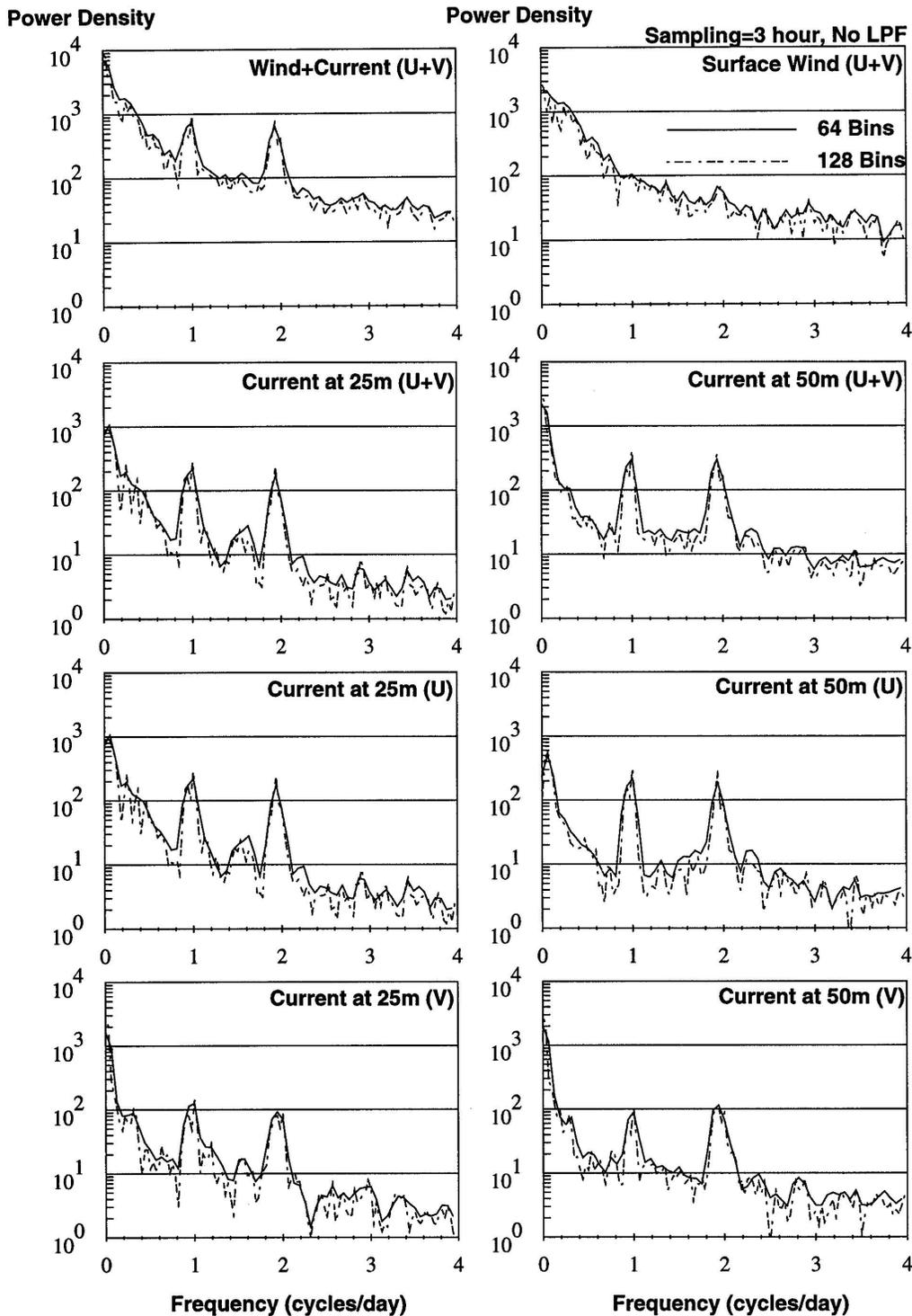


Figure 3.8: Power density for wind and water velocities resolved to 64 and 128 frequency bins. Power spectral density of wind in units of $[(\text{m/s})^2/(1000\Delta f)]$ ocean in units of $[(\text{m/s})^2/\Delta f]$. Wind divided by 1000 to compare kinetic energy with ocean.

Table 3.2: Overview of Beta Parameters

Beta Term	9 Hour LPF		15 Hour LPF		30 Hour LPF	
	Average	RMS Spread	Average	RMS	Average	RMS
u (cm/s)	0.3205	5.4858	0.3761	4.8420	0.4448	3.8537
v (cm/s)	7.7342	8.7131	7.6958	8.5188	7.4969	8.4100
$\frac{\partial u}{\partial x} \times 10^6$ (1/s)	0.0228	0.3704	0.0256	0.2627	0.0278	0.1825
$\frac{\partial u}{\partial y} \times 10^6$ (1/s)	0.1010	0.7325	0.0969	0.4674	0.0991	0.3264
$\frac{\partial v}{\partial x} \times 10^6$ (1/s)	-0.0204	0.4432	-0.0191	0.3560	-0.0255	0.2313
$\frac{\partial v}{\partial y} \times 10^6$ (1/s)	-0.0406	0.7180	-0.0383	0.4531	-0.0498	0.3124
Avg. Divergence	-0.0178		-0.0127		-0.0220	
Avg. Shear	0.0806		0.0778		0.0736	

3.3.3 Centroid Velocity and Deformation Tensor

From the power spectra analysis we noted that internal ice interaction must be responsible for some of the low and high frequency activity and directional variability in the ice response. We will investigate this statement by examining some of the sea ice deformation processes contributing to internal ice interaction. Using a multiple linear regression model on the buoy data we can compute the deformation tensor of the local ice field and from that derive quantities describing the different deformation processes of divergence, shear, and vorticity. The regression procedure solves for the unknown centroid velocity, u and v , and deformation tensor components $\frac{\partial u}{\partial x}$, $\frac{\partial v}{\partial x}$, $\frac{\partial u}{\partial y}$ and $\frac{\partial v}{\partial y}$. For more information on the multiple regression procedure see Appendix (A.4).

A series of multiple linear regressions were made using different low pass filter (LPF) cut-off times from 3 to 35 hours. Time series plots of the centroid velocity from these runs are shown in Figure (3.9). The general trend (i.e. the low frequency signal) is similar for low pass filter cut-off times between 7 and 35 hours which supports the earlier spectral analyses showing the main drift of the ice to be dominated by the low frequency signal. Contrary to this we see an increase in velocity perturbation activity at the lower cut-off times. As shown in Figure (3.9) we have isolated this activity into three separate low pass filter cut-off time periods: less than 12 hours (2 cycles/day or more), between 12 and 24 hours (1 to 2 cycles/day), and greater than 24 hours (<1 cycle/day). In doing so we note that there is negligible difference in the LPF cut-off times within these three frequency ranges (e.g. 15, 18 and 21 hour LPF are indistinguishable on plots) but considerable difference between each range. Based on these results, the deformation tensor components from three representative cut-off times (9, 15 and 30 hours) were selected and analyzed (Figures 3.10 to 3.12). In comparing the three we see a decrease in each components' magnitude and frequency with increased cut-off time. Comparing the 9 hour (Figure 3.10) with the 15 hour (Figure 3.11) LPF we see a decrease in both magnitude and frequency by about a factor of 2 at the 15 hour LPF time. A similar although less pronounced decrease occurs between the 15 and 30 hour cut-off times.

To get a general idea of the trends in these time series, the average and rms spread for each of these quantities is presented in Table 3.2. With regard to directional dependence, the centroid velocities at these 3 LPFs have a u velocity, x direction, which

oscillates around zero with the high frequency fluctuations almost always alternating between positive and negative on the order of Muench et al.'s 10-20 cm/s (corresponding rms is a little less than half this value) indicating strong eastward (positive) to westward (negative) fluctuations at regular intervals. The y direction on the other hand centers closer to 7.7 cm/s which is close to the 7 cm/s average northward ice drift computed by Muench et al. (1992). The 10-20 cm/s superimposed fluctuations are also present but they are of lower frequency (>30 hours) (e.g. Figures 3.10 vs. 3.12) in the y direction. These y fluctuations may be due to oceanic or atmospheric eddies (i.e. storms). The semi-diurnal fluctuations in the y direction are smaller than this, on the order of 1 to 5 cm/s as seen in the v component in Figure (3.10). This same directional dependence was seen in the buoy spectral analysis where we saw prominent power spikes at both 12 and 24 hours over the shallower western end of the array while the eastern end had a greater power but a very weak 24 hour signature.

Averages for the deformational components are centered pretty much at the origin (Table 3.2). The $\frac{\partial u}{\partial y}$ average seems to be particularly large at about 0.1×10^6 (1/s) and the next largest close to 0.04×10^6 (1/s) in the $\frac{\partial v}{\partial y}$ term. The $\frac{\partial u}{\partial y}$ term contributes to the shear in this system, as does $\frac{\partial v}{\partial x}$, while $\frac{\partial u}{\partial x}$ and $\frac{\partial v}{\partial y}$ contribute to the divergence of the system. As an initial estimate, let us define the sum of these components respectively shear ($\frac{\partial u}{\partial y} + \frac{\partial v}{\partial x}$) and divergence ($\frac{\partial u}{\partial x} + \frac{\partial v}{\partial y}$). We see in Table 3.2 that there is on average a convergence (i.e. negative divergence) of about 0.01 to 0.02×10^6 (1/s) and an overall shear of about 0.07 to 0.08×10^6 (1/s) which is about four times larger than the divergence average. This estimate suggests that shear is contributing about four times as much to the deformation process as divergence primarily due to a strong north-south variation in the u velocity field. With regard to the spread (or variability) in these averages, we see from Table 3.2 that variations in the y direction are about twice those in the x direction which we can also clearly see from Figures (3.10) to (3.12). This information combined with previous results above strongly suggests that the deformation activity is dominated by shear and has a strong y directional preference. As with the previous results the shelf slope shallowing to the west must be a main contributor to this directional dependence.

We can look at these processes of divergence and shear more closely by computing and plotting the four differential kinematic parameters (DKPs) of divergence (DV), normal deformation (ND), shear deformation (SD) and vorticity (VT) defined as (Massom, 1992)

$$DV = \frac{\partial u}{\partial x} + \frac{\partial v}{\partial y} \quad (3.1)$$

$$ND = \frac{\partial u}{\partial x} - \frac{\partial v}{\partial y} \quad (3.2)$$

$$SD = \frac{\partial v}{\partial x} + \frac{\partial u}{\partial y} \quad (3.3)$$

$$VT = \frac{\partial v}{\partial x} - \frac{\partial u}{\partial y} \quad (3.4)$$

Descriptively, the DKPs are as follows. Divergence is the change of area and is an invariant of the system. The two quantities of normal and shear deformation denote change in shape. Normal deformation is the change in shape due to stretch in one

Table 3.3: Overview of Deformation Parameters

Def Term	9 Hour LPF		15 Hour LPF		30 Hour LPF	
	Avg Mag	RMS	Avg Mag	RMS	Avg Mag	RMS
Vel Mag (cm/s)	10.7936	7.0307	10.3895	6.8876	9.6783	6.9506
Max Shr $\times 10^6$ (1/s)	0.9480	0.6949	0.6632	0.4398	0.4722	0.3504
DV $\times 10^6$ (1/s)	0.5523	0.7968	0.3603	0.4950	0.2203	0.3255
ND $\times 10^6$ (1/s)	0.6187	0.7877	0.4292	0.5161	0.3005	0.3632
SD $\times 10^6$ (1/s)	0.5831	0.7741	0.4141	0.5075	0.2990	0.3669
VT $\times 10^6$ (1/s)	0.6556	0.9871	0.4855	0.7210	0.3189	0.5127

direction and shrinking in the other without area change (i.e. elongation) while shear is due to stretching without area change of cross component terms. Finally vorticity describes the rotation of the system and does not contribute to the deformation of the system.

Figures (3.13) to (3.15) show the time series for these DKPs along with the array's centroid speed and a term formally defined as maximum shear in the literature (see for example Fung, 1977),

$$\text{Max. Shear} = \sqrt{\left(\frac{\dot{e}_{xx} - \dot{e}_{yy}}{2}\right)^2 + \dot{e}_{xy}^2} = \frac{\dot{e}_1 - \dot{e}_2}{2} \quad (3.5)$$

where

$$\dot{e}_{xx} = \frac{\partial u}{\partial x} \quad (3.6)$$

$$\dot{e}_{yy} = \frac{\partial v}{\partial y} \quad (3.7)$$

$$\dot{e}_{xy} = \frac{\frac{\partial u}{\partial y} + \frac{\partial v}{\partial x}}{2} \quad \text{or} \quad \gamma_{xy} = \frac{\partial u}{\partial y} + \frac{\partial v}{\partial x}. \quad (3.8)$$

\dot{e}_1 and \dot{e}_2 are the principal strains (see Chapter 5: Principal Axis in 2-Space). Their sum equals the divergence; when subtracted and divided by 2, the resultant magnitude equals the maximum shear. In terms of the DKPs defined above the max shear can also be expressed as

$$\text{Max. Shear} = \sqrt{\left(\frac{\text{ND}}{2}\right)^2 + \left(\frac{\text{SD}}{2}\right)^2}. \quad (3.9)$$

In looking at this last definition of max shear relative to its DKP components we see that it must be related to shear and normal deformation as these are the quantities which are physically changing the shape and deforming a given region. Like divergence, the max shear is an invariant but because of its definition, it is about half the size of the divergence which makes it difficult to compare them directly. Thus, in order to compare the magnitude of these two invariants, both plus and minus values of max shear have been plotted in Figures (3.13) to (3.15) and twice the positive value is used to determine average max shear magnitudes in Table 3.3.

Since each of these DKP components now contains both x and y differential components the directional dependence is no longer visible. Instead we see a clear distinction

between LPF cut-off times with highest frequency and largest magnitude changes at the 9 hour LPF. An overview of these results in Table 3.3 shows that each of the DKPs has about the same magnitude for a given LPF time but the 15 hour LPF result has about half the magnitude of the 9 hour LPF result and correspondingly between the 30 and 15 hour LPFs. The divergence and max shear are independent of coordinate system (i.e. invariant) so they give us a good idea of the total areal change and shape change of the system. From these we see that the shear is about twice the magnitude of the divergence so we have more shear than areal change going on. The RMS spread of the deformation components is nearly the same for a given LPF except for the vorticity which is almost a third larger.

As a final observation, the difference between the 9, 15, and 30 hour LPF deformations need to be considered in light of the total amount of deformation accomplished, the amount of work performed and the amount of energy expended. A simple thought experiment using the divergence helps to put some of this into perspective. On a daily basis the total amount of divergence done by the ice in each of the cases is actually quite similar as reflected by the divergence averages in Table 3.2. For a 9 hour LPF, a spread of -2 to $+2 \times 10^{-6}$ 1/s is typical for divergence while at 30 hour LPF the spread is more like -0.5 to $+0.5 \times 10^{-6}$ 1/s. In considering the frequency at which this spread occurs (6 hours max to min tidal frequency versus one day) we get four times the divergence over a 6 hour period for the 9 hour LPF than for the 30 hour LPF. Since the 30 hour LPF represents effects occurring over a day (24 hours being 4 times that of the 6 hour max to min tidal frequency), the total work being done to open and close a given area over a day may be the same but the energy expended in doing so through a direct versus oscillatory tidal motion is significant. Hence, when comparing the total amount of work over a given day, the 9 and 30 hour divergence rates are comparable; over a 6 hour period however, they are not and in terms of energy expended they are certainly not.

Summarizing this section we note the following four results. First, the internal ice interaction and ocean currents are driving a great deal of the ice deformation. Second, the high frequency activity, which was only a minor contributor to the total ice drift is now a major contributor to the deformation activity, particularly at diurnal and semi-diurnal frequencies. Third, as with the ice drift, the ice deformation exhibits a definite directional dependence as a result of the topographic shelf slope. Finally, with regard to specific deformation processes, shear deformation is clearly greater than the divergence.

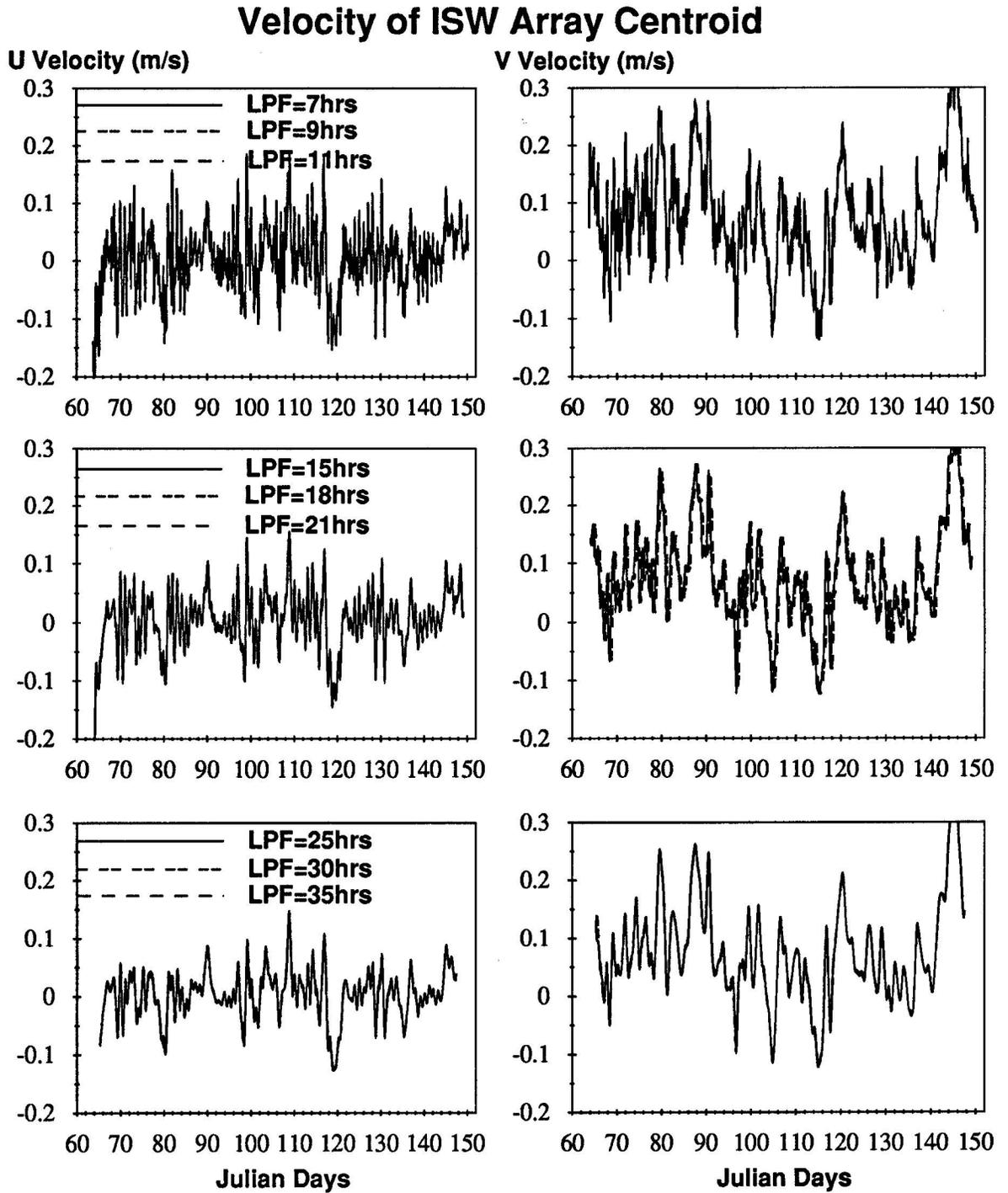


Figure 3.9: Centroid Velocity from multiple linear regression at selected low pass filters.

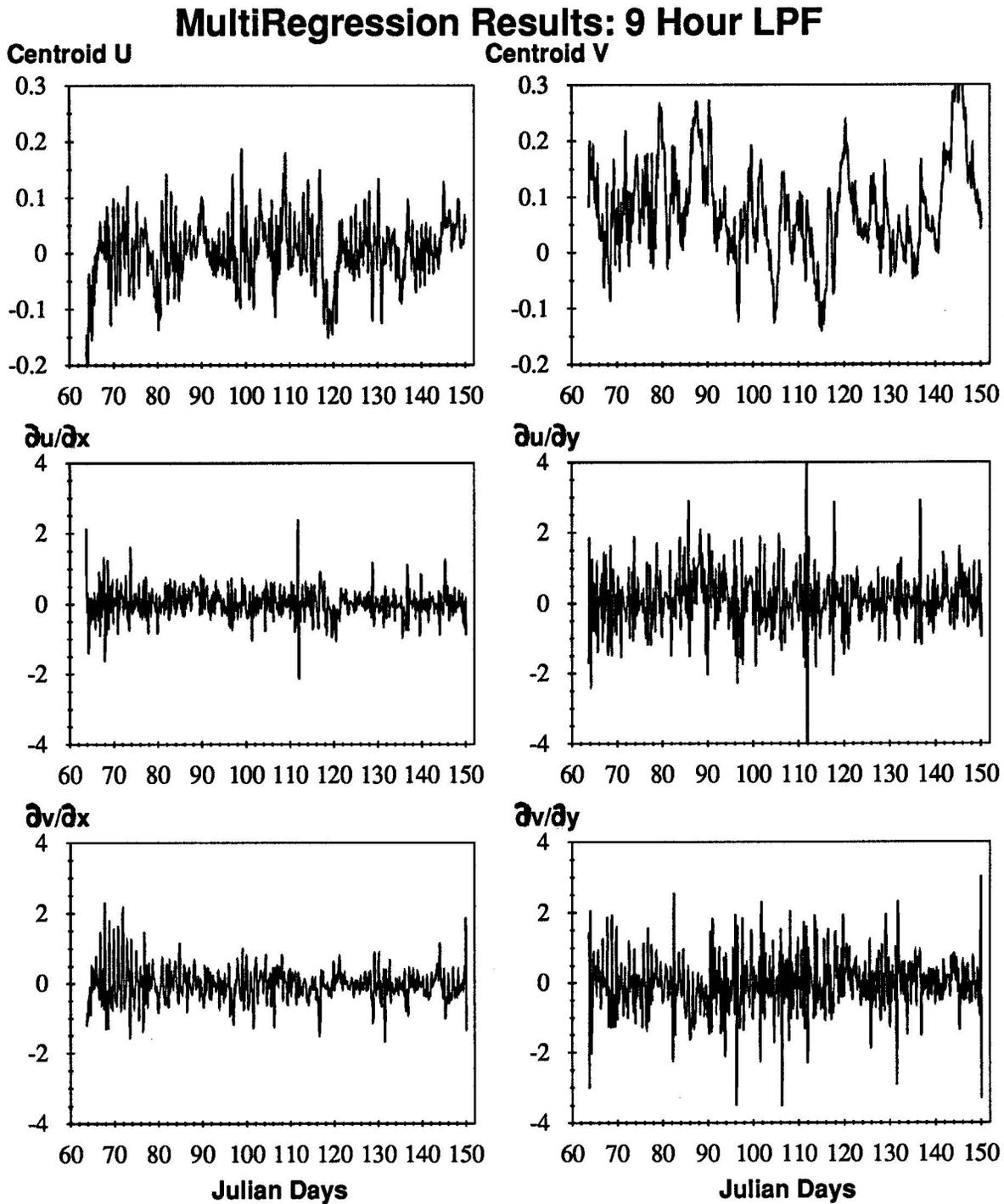


Figure 3.10: Beta parameters from multiple linear regression analysis using a 9 hour low pass filter (LPF). Velocities are in units of [m/s] and strain-rate components are in units of [$\times 10^{-6}$ (1/s)].

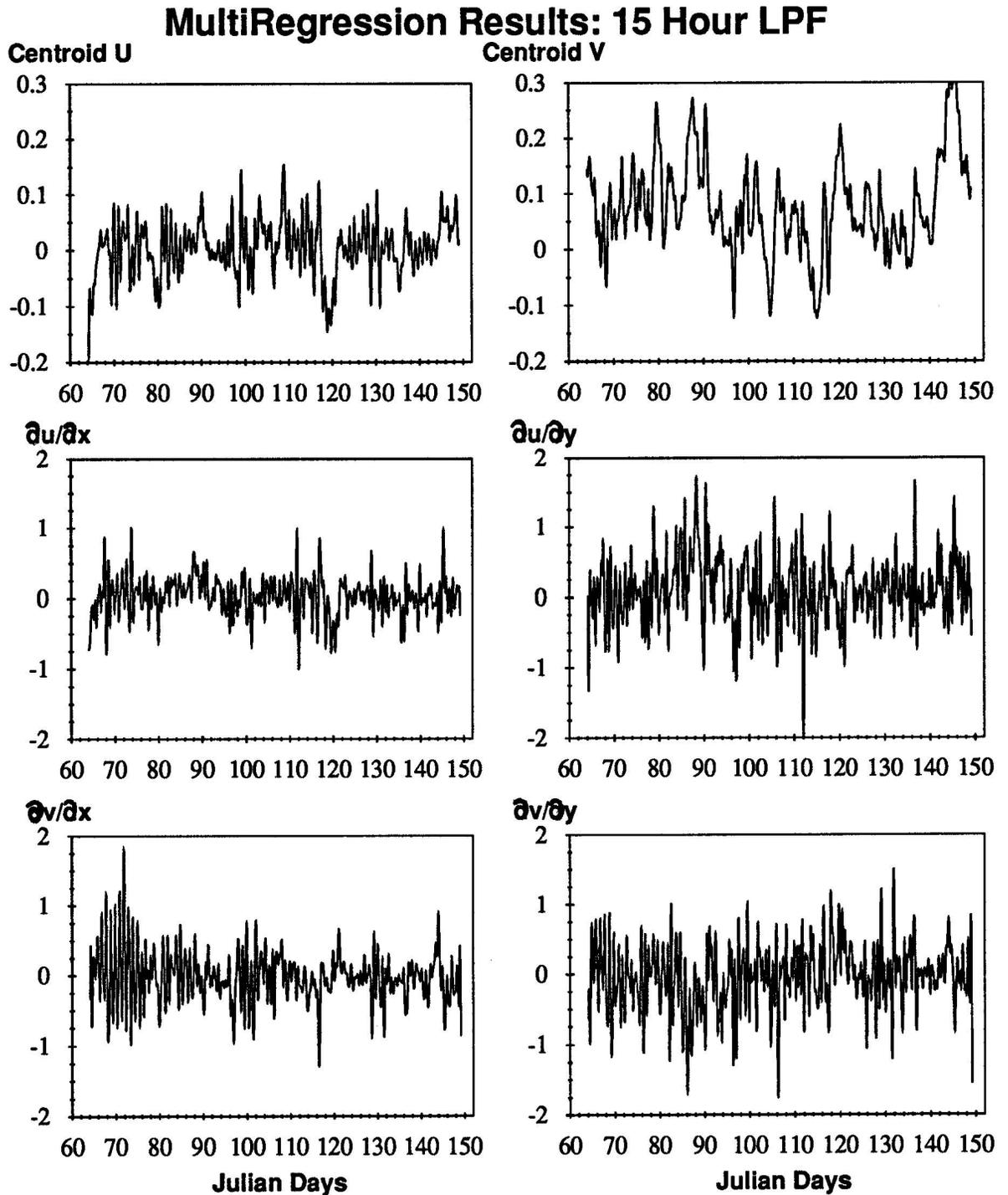


Figure 3.11: Beta parameters from multiple linear regression analysis using a 15 hour low pass filter (LPF). Velocities are in units of [m/s] and strain-rate components are in units of [$\times 10^{-6}$ (1/s)].

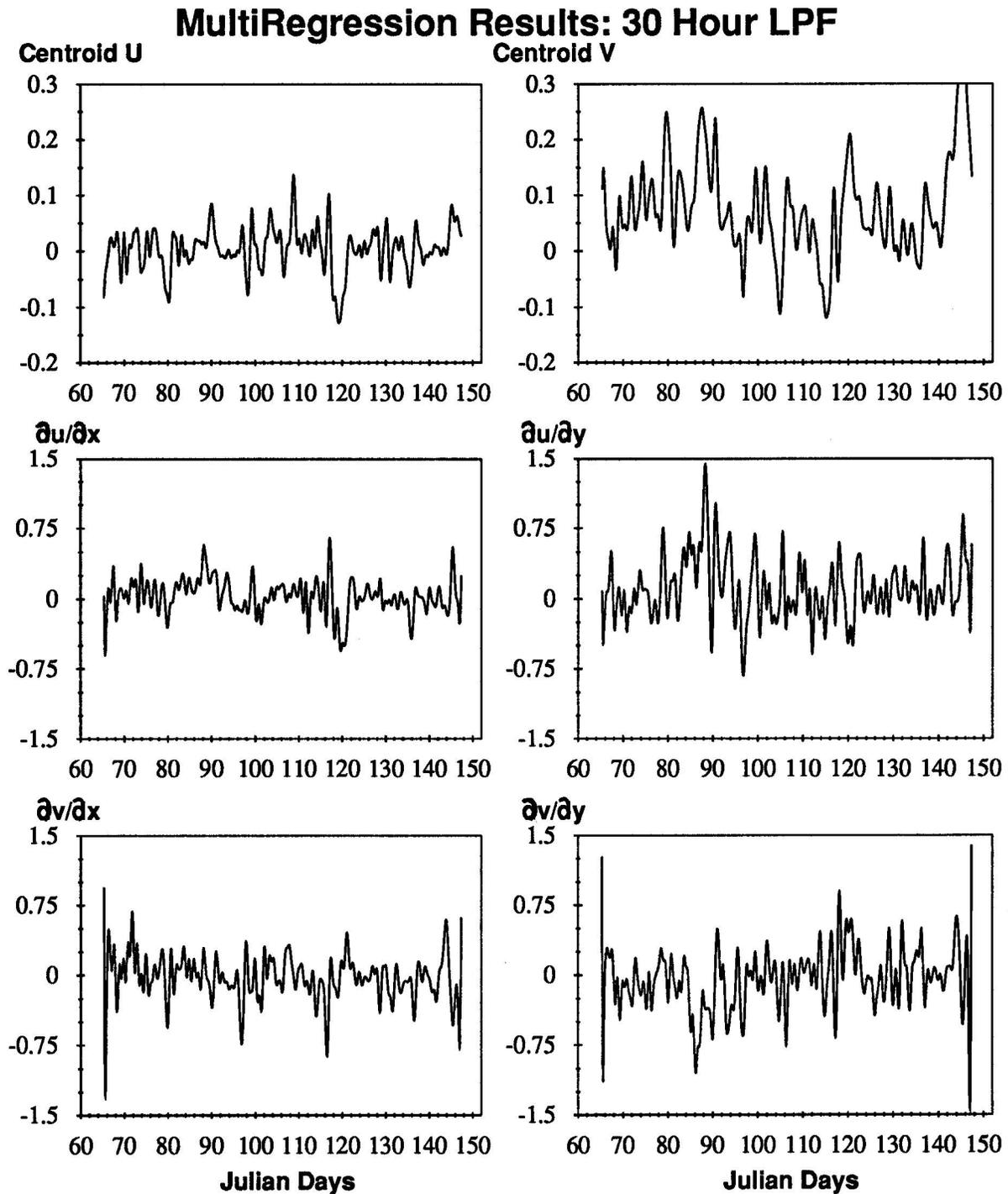


Figure 3.12: Beta parameters from multiple linear regression analysis using a 30 hour low pass filter (LPF). Velocities are in units of [m/s] and strain-rate components are in units of [$\times 10^{-6}$ (1/s)].

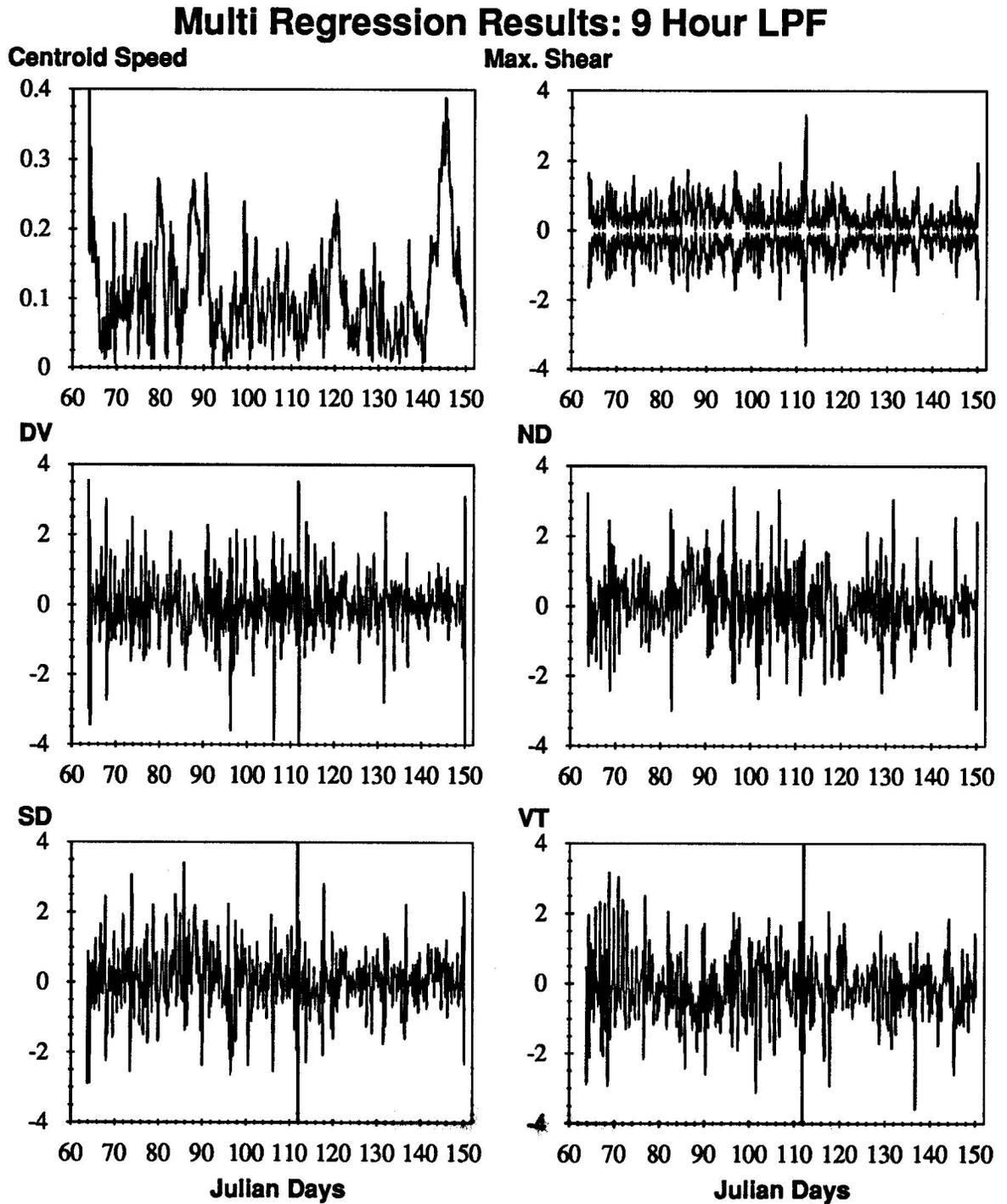


Figure 3.13: Centroid Speed, Max Shear and DKPs computed from multiple linear regression analysis using a 9 hour low pass filter (LPF). Velocities are in units of [m/s]. Max Shear and DKPs are in units of [$\times 10^{-6}$ (1/s)].

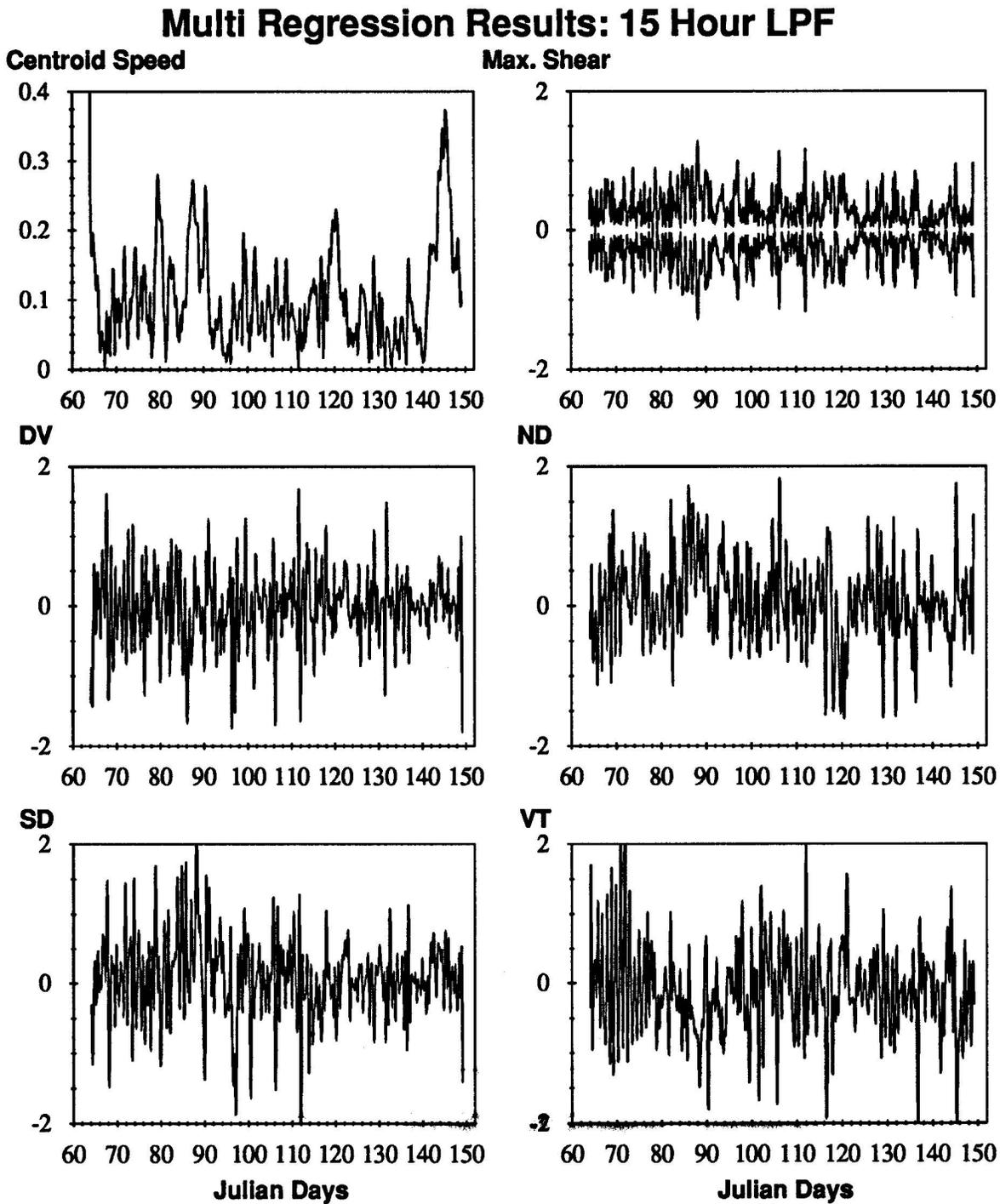


Figure 3.14: Centroid Speed, Max Shear and DKPs computed from multiple linear regression analysis using a 15 hour low pass filter (LPF). Velocities are in units of [m/s]. Max Shear and DKPs are in units of [$\times 10^{-6}$ (1/s)].

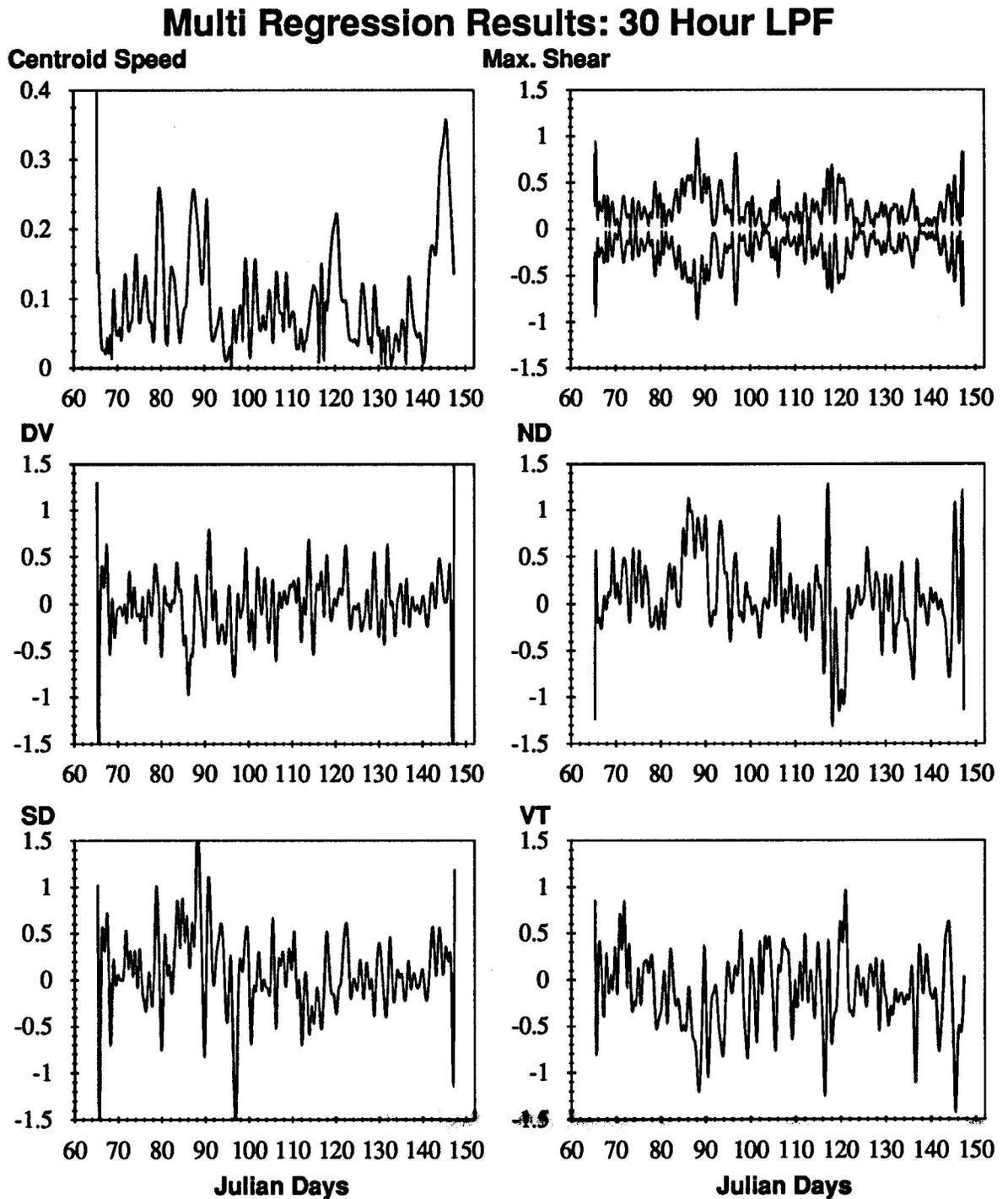


Figure 3.15: Centroid Speed, Max Shear and DKPs computed from multiple linear regression analysis using a 30 hour low pass filter (LPF). Velocities are in units of [m/s]. Max Shear and DKPs are in units of [$\times 10^{-6}$ (1/s)].

3.3.4 Error Analysis

The multiple linear regression analysis discussed in the last section included strain-rates on the order of 10^{-6} (1/s) which were computed from velocities on the order of 10 cm/s. Six sites were used and an initial instrument error analysis (Appendix A.1) estimated an instrument error of about 530 m radially and corresponding error of 375 m in the \hat{x} and \hat{y} directions. Given the very small strain-rate values, it is important to have an understanding of the errors involved in the regression procedure in order to justify the results obtained in the last section. Two types of error analyses are conducted in this section in order to determine the goodness of fit of the data. First examination of the truncation error will allow us to determine how effectively the instrument error was removed from the signal. Second, a confidence interval estimate of all 6 beta parameters will provide us with a bound on the error between the true value and what was computed. Descriptions of both types of error calculations are given in Appendix (A.4).

As described at the beginning of this chapter, buoy velocities are calculated using $\Delta x_i / \Delta t$ where Δx_i is the distance traversed by a buoy in a given direction (x or y) over a given amount of time Δt . An added distance to this is the instrument error which, when divided by Δt , also results in a velocity. Because the instrument error occurs at every time step, it shows up as a high frequency signal. More specifically, Δx_{err} produced by the instrument error is the propagated error (Beers, 1957)

$$\Delta x_{err} = \sqrt{(x[t]_{err})^2 + (x[t-1]_{err})^2} = \sqrt{2}\bar{x}_{err} \quad (3.10)$$

where \bar{x}_{err} is the average instrument error. As we increase the cut-off time in the low pass filter, the high frequency signals should decrease. Defining Δt for this case to be the low pass filter time we can estimate the propagated instrument error velocity (u_{err_i} , v_{err_i}) as follows.

$$u_{err_i} = v_{err_i} = \frac{\Delta x_{err}}{\Delta t_{LPF}} \quad (3.11)$$

$$= \frac{\sqrt{2}\bar{x}_{err}}{\Delta t_{LPF}} \quad (3.12)$$

$$= \frac{\bar{r}_{err}}{\Delta t_{LPF}}. \quad (3.13)$$

The truncation error Err_{in} in the regression analysis is computed as in Appendix (A.4) by

$$Err_{in} = Z_{in} - \hat{Z}_{in} \quad (3.14)$$

where Z_{in} is the actual velocity component value at each site and \hat{Z}_{in} is the best fit value for $i = 1$ to N buoy sites and $n = 1$ to 2 velocity components. This truncation error is a measure of the difference between the estimated linear values (\hat{Z}_{in}) and the true values (Z_{in}). Their differences account for influences not associated with the linear model. The two dominant influences responsible for these differences are 1) non-linear strains and 2) instrument error. Since the sum of both of these must be less than or equal to the total truncation error estimate, the instrument error should be less than the truncation error for the model to be believable. Since this truncation error is computed at each site we

Table 3.4: Overview of Beta Parameter Errors

Beta Term	9 Hour LPF		15 Hour LPF		30 Hour LPF	
	Avg. Mag.	S.D.	Avg. Mag.	S.D.	Avg. Mag.	S.D.
u (cm/s)	4.15	0.50	3.72	0.29	2.85	0.15
v (cm/s)	9.15	0.54	9.02	0.36	8.72	0.21
$\frac{\partial u}{\partial x} \times 10^6$ (1/s)	0.27	0.16	0.20	0.09	0.14	0.04
$\frac{\partial u}{\partial y} \times 10^6$ (1/s)	0.52	0.43	0.36	0.25	0.25	0.13
$\frac{\partial v}{\partial x} \times 10^6$ (1/s)	0.32	0.17	0.26	0.11	0.17	0.06
$\frac{\partial v}{\partial y} \times 10^6$ (1/s)	0.52	0.45	0.35	0.31	0.24	0.17

need to determine some sort of system average to compare this to the average propagated instrument error velocity. The averaging scheme used in this case is as follows. First, the truncation error at each site at each point in time is computed for each velocity component. Then, the temporal average of these values is computed at each site as is its average RMS spread. Finally, the average and RMS spread from each site are averaged for the whole system for each of the u and v velocity components.

Plots of the u and v truncation error averages are plotted together with the estimated instrument error velocity (Eq. 3.13) in Figure (3.16). The average RMS spread of the truncation error is also included to show the average range of the truncation error from all the sites. From this figure we see that the regression truncation error average decreases with increased low pass filter times as does its variability (i.e. RMS). More importantly we see that the estimated instrument error velocity for no low pass filter (1 hour) is much higher than the truncation error and well beyond the limits of the average range of that error. Hence without low pass filtering the multiple linear regression yields results which are not statistically believable. With a 3 hour low pass filter, the instrument error is at least within the bounds of the average truncation error but still significantly higher than the average truncation error. Proceeding with even larger LPF cut-off times we see that the instrument error slowly moves closer to the average truncation error but never really goes below it as theory would predict. Additional tests such as the validation case for the multiple linear regression procedure seen in Appendix Figure (A.4) indicate that there is little non-linear strain in the system at the frequencies of interest either because there are too few sites to resolve this or it just isn't very big. The decrease in magnitude from the first value of the Taylor expansion coefficient on the order of 10 cm/s to the next coefficients (strain-rate), about 10^{-6} (1/s), suggest that higher terms are several orders of magnitude smaller than strain-rate. Given these results, the instrument error is most likely the dominant error term in the system. With all the statistical averaging done to produce these results, we can at most, conclude that the regression is believable if the average instrument error is well within the range of the average truncation error RMS spread. Even then, however, there must still be noise in the system caused by instrument error and other sources which will produce errors in the results.

Using the statistical procedure described in Appendix (A.4) the standard deviation of each multiple regression term is computed and plotted as time series for 9, 15 and 30 hour LPF times in Figures (3.17) to (3.19). These terms have been computed in order

Table 3.5: Average Signal to Noise Ratio

Beta Term	9 Hour LPF	15 Hour LPF	30 Hour LPF
u (cm/s)	12.67	18.14	28.81
v (cm/s)	27.23	40.24	73.35
$\frac{\partial u}{\partial x} \times 10^6$ (1/s)	2.17	2.66	3.76
$\frac{\partial u}{\partial y} \times 10^6$ (1/s)	1.54	1.76	2.61
$\frac{\partial v}{\partial x} \times 10^6$ (1/s)	2.49	3.17	4.07
$\frac{\partial v}{\partial y} \times 10^6$ (1/s)	1.55	1.47	1.85

to estimate how close to the true value these linear regression values are. In order to get an overview of these results, the average of the magnitude of the regression values is listed in Table 3.4 together with their average standard deviation as computed from data displayed in Figures (3.17) to (3.19). Regarding the average magnitude of regression terms as the signal and the standard deviation as an estimate of the noise, a signal to noise ratio at each time interval is computed. An average of this signal to noise ratio estimate is given in Table 3.5 to get an idea of how much noise there is in the signals we are trying to analyze. From this table we find that the velocity terms are estimated quite well from the regression model while the deformation tensor components have a considerable amount of noise in them. Additionally there is more noise in the y direction components than in the x . Considering we are dealing with very small quantities these results at least show that we have more signal than noise. The error estimates are small enough to confirm that the results obtained in the last section should at least qualitatively describe true features. Overall, the velocity results have very little noise quantitatively but the deformation values must be regarded with caution since they have considerable noise in their signal, particularly for the lower low pass filter times.

The final error analysis of this section is an estimate of the power spectra amplitude error. Using the estimator derived by Welch (1967) for an FFT transformation with overlapping, the relative standard deviation (σ) of the amplitude estimate (\hat{A}) is

$$\sigma = \frac{100\%}{\sqrt{\frac{9K}{11}}} \quad (3.15)$$

$$\text{such that true amplitude} = \hat{A} \pm \sigma \hat{A} \quad (3.16)$$

where K is the number of FFT periodograms constructed from the transform (see Appendix for details). For the two cases used in this study (i.e. 64 and 128 frequency bins per periodogram), we get $K = 3$ and 5 periodograms for a three hour time sampling over the three month data period. These values produce a $\pm 49.4\%$ and 63.8% relative error, respectively, in the spectral estimate relative to amplitude. Examples for both velocity and strain-rate (Figure 3.20) show that this error is less than the prominent spikes referred to in the analysis, hence these peaked signals are quantitatively believable features.

Error Analysis of Multiple Linear Regression Method

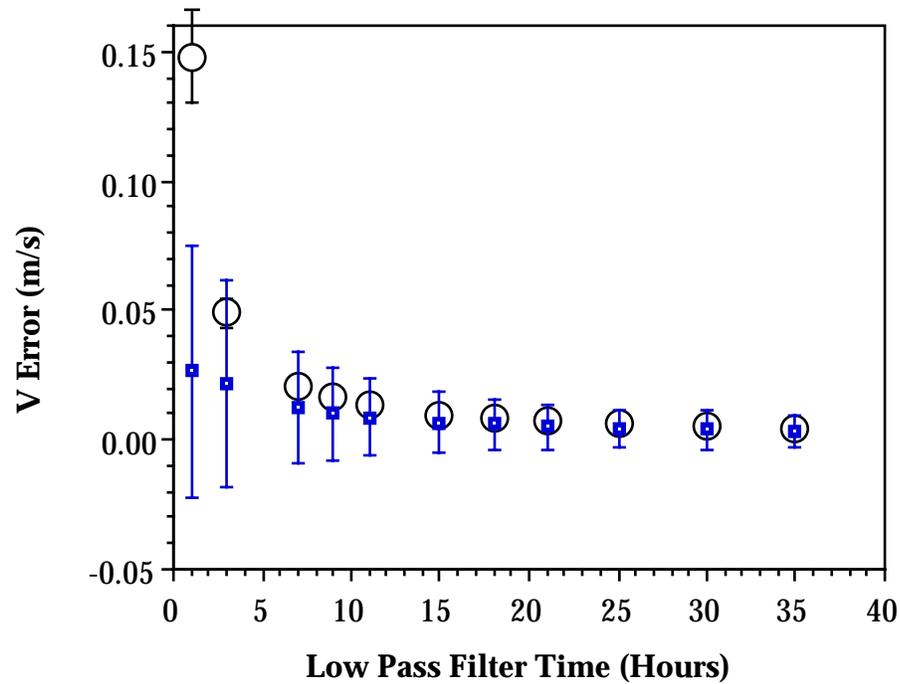
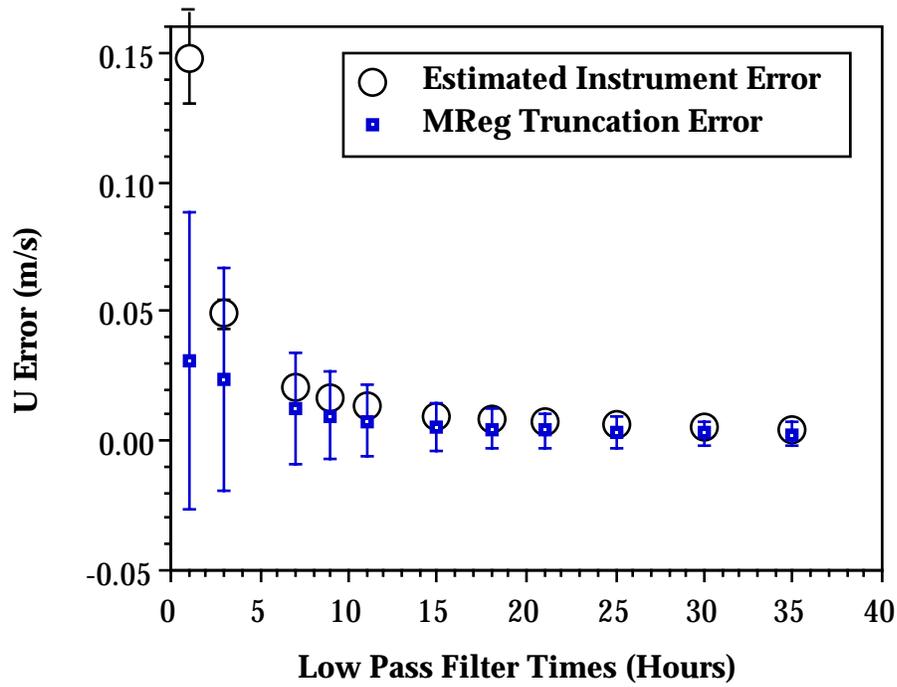


Figure 3.16: Truncation error of multiple linear regression analysis and average instrument error. Error bars are the average RMS spread computed from all site.

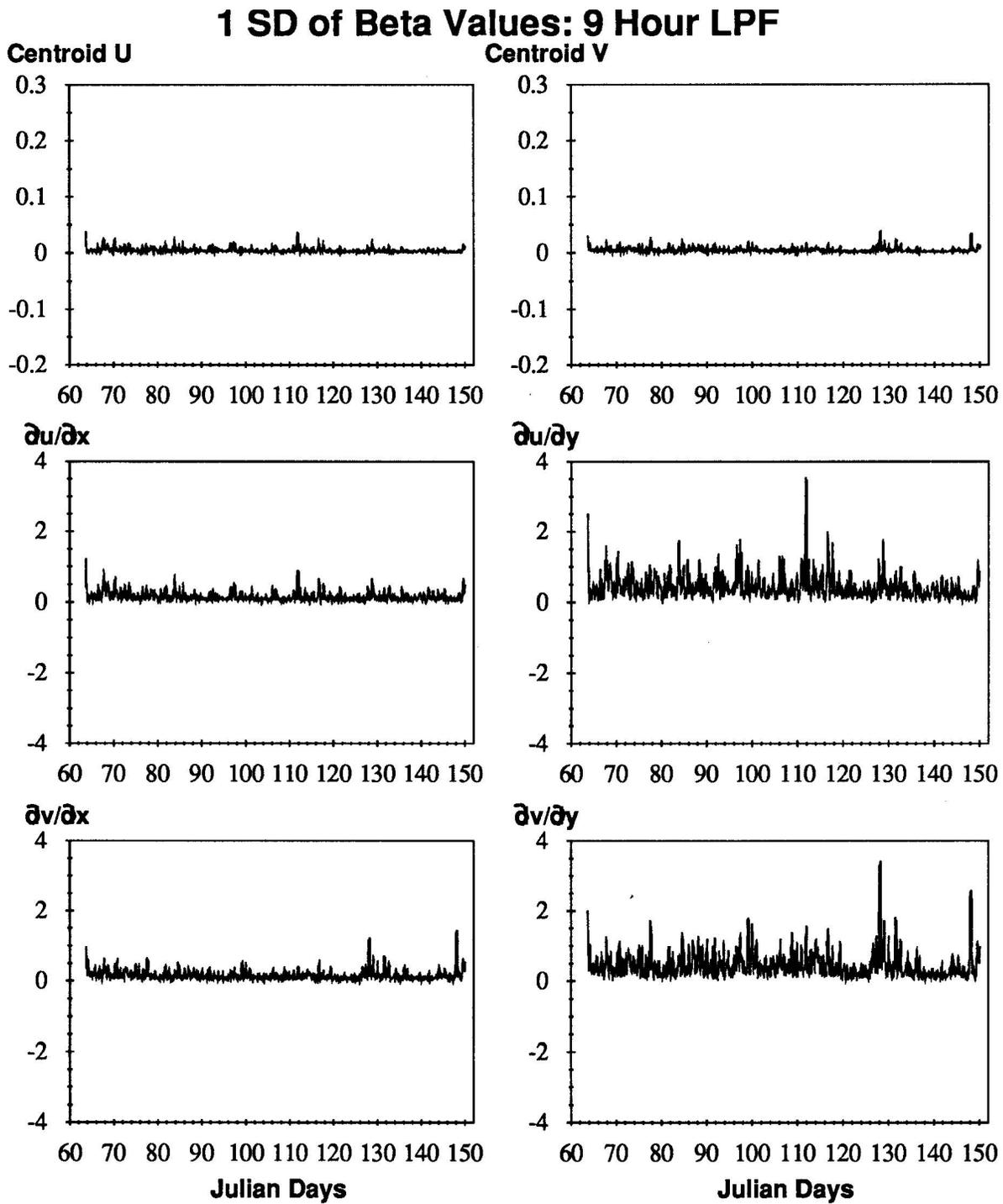


Figure 3.17: Time series of standard deviation of computed multiple linear regression variables with 9 hour low pass filter. Velocities are in units of [m/s] and strain-rate components are in units of [$\times 10^{-6}$ (1/s)].

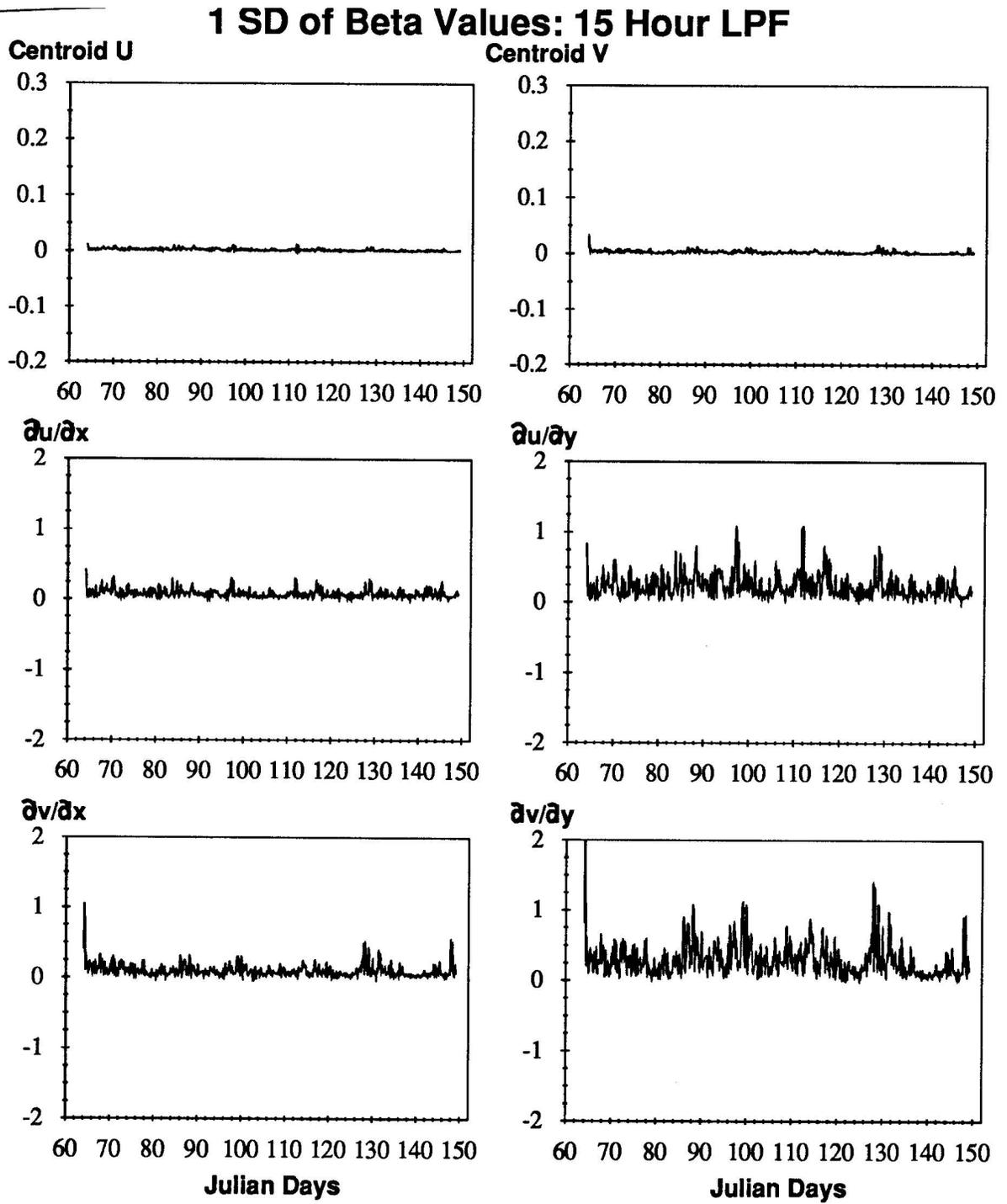


Figure 3.18: Time series of standard deviation of computed multiple linear regression variables with 15 hour low pass filter. Velocities are in units of [m/s] and strain-rate components are in units of [$\times 10^{-6}$ (1/s)].

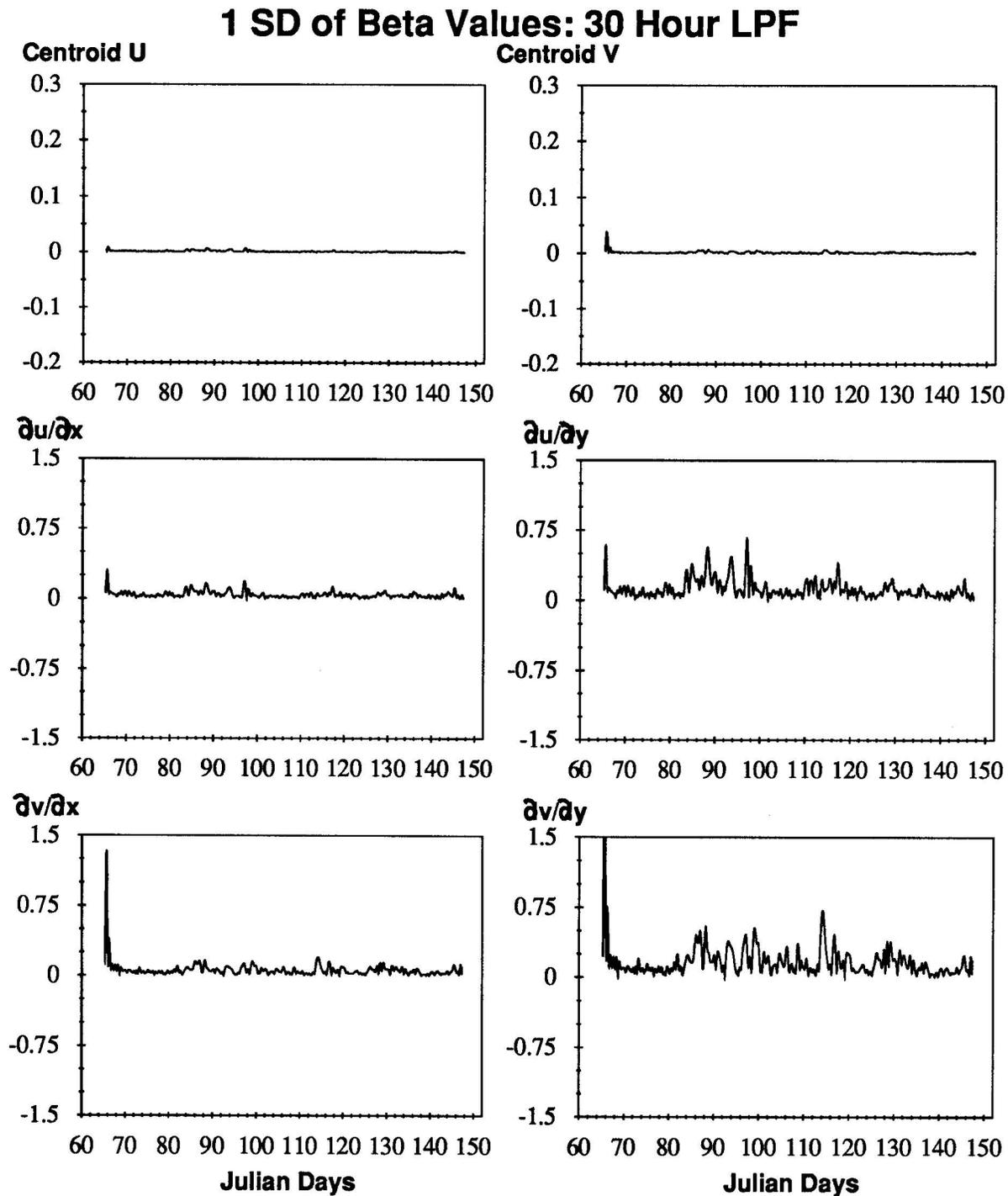


Figure 3.19: Time series of standard deviation of computed multiple linear regression variables with 30 hour low pass filter. Velocities are in units of [m/s] and strain-rate components are in units of [$\times 10^{-6}$ (1/s)].

Power Spectra with Error Estimate

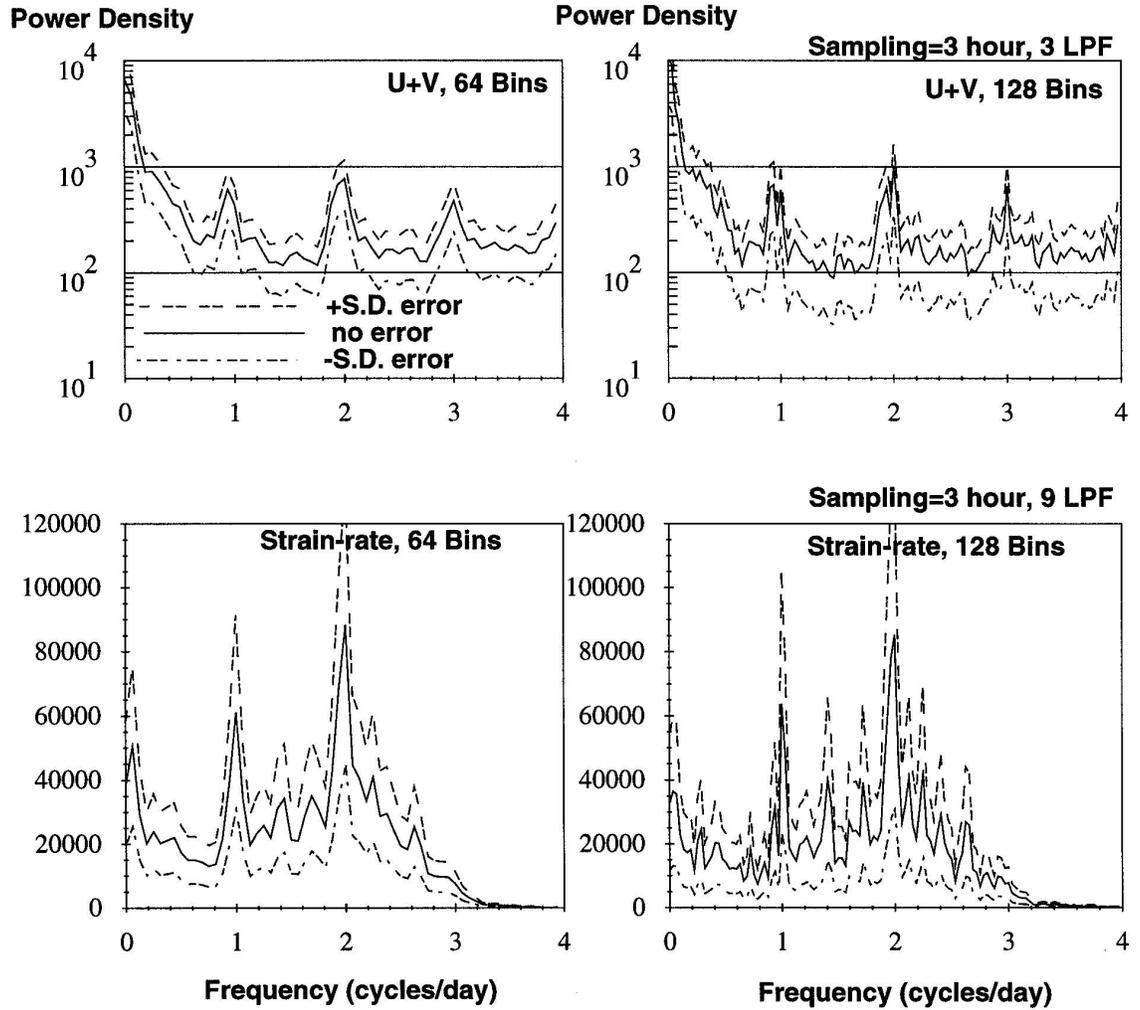


Figure 3.20: Examples of power spectra with estimates of upper and lower bounds of error. Velocity power density is given in units of $[(\text{m/s})^2/\Delta f]$.

3.4 Discussion

Analyzing the time series of the array's drift and deformation provided us with a considerable amount of information about the processes involved and gave us some idea of the forces most likely responsible for the deformation processes, but we gain even more insight by examining the power spectra of the regression terms. The first problem that arises however, is how to do this? The power spectrum of the centroid velocity is straight forward but strain-rate is not since we now have a deformation tensor.

One important property we wish to know about is the power of the total strain-rate which is defined in 2D Cartesian space by

$$(\dot{e}_{ij})^2 \equiv \dot{e}_{ij}\dot{e}_{ij} = \dot{e}_{xx}^2 + \dot{e}_{yy}^2 + 2\dot{e}_{xy}^2. \quad (3.17)$$

This expression is invariant which means that its value is independent of the coordinate system. Two additional invariant terms encountered in earlier sections are the divergence and max shear. We can compute the power density of the divergence by Fourier transforming the divergence quantity $(\dot{e}_{xx} + \dot{e}_{yy})$, squaring the transformed result and dividing by the frequency binwidth (Δf) . A similar process can be done with the max shear. Taking into account the fact that the max shear value only represents half of the magnitude of the total shear in the system we note the following interesting relationship in the frequency domain.

$$(\text{divergence})^2 + (2 \text{ max shear})^2 = (\dot{e}_{xx} + \dot{e}_{yy})^2 + (\dot{e}_{xx} - \dot{e}_{yy})^2 + (2\dot{e}_{xy})^2 \quad (3.18)$$

$$= DV^2 + ND^2 + SD^2 \quad (3.19)$$

$$= 2(\dot{e}_{ij}^2). \quad (3.20)$$

What all this is saying is that, by Parseval's theorem, the total strain-rate power is equal to half the sum of the square of the Fourier components of the three deformational DKPs (vorticity excluded). Using this information we can define the following invariant terms in the frequency domain.

- Total Strain-Rate Power = $(\dot{e}_{ij})^2 = \frac{DV^2+ND^2+SD^2}{2}$
- Total Strain-Rate Divergence Power = $\frac{DV^2}{2}$
- Total Strain-Rate Shear Power = $\frac{ND^2+SD^2}{2}$

These statements are true for individual frequencies (i.e. power spectral densities) as well as the total integrated power.

Plots of the array's centroid velocity and the above defined invariant strain-rates, shown in Figure (3.21), concur with the earlier results. The power signals in the centroid velocity contain many of the features seen in the buoy spectra including the large low frequency signature in the y direction, the two peaks at 12 and 24 hours in the x direction, and the lack of a 24 hour signature in the y direction. The signals lacking in these velocity plots are the prominent high frequency peaks near 8 hours which have purposely been filtered out. With regard to the deformation, we see that the total strain-rate power

density is, as suspected from the time series plots, dominated by high frequency peaks at 12 and 24 hours. The new information gained from these plots is that we now see that the 12 hour peak is stronger than the 24 hour and there is also a fairly strong low frequency signal which was not evident before. Looking at the two invariant subcomponents of the total strain-rate, divergence and invariant shear, we see that the shear is more than twice the divergence and therefore the greater contributor to the total strain-rate power. We also see that the low frequency signal is present in the shear but completely missing from the divergence while the 12 and 24 hour signatures are present in both.

Elaborating on this further, we can examine the non-invariant components responsible for these signatures. Power spectra for each of the deformation tensor components and half the power density of each DKP term are shown in Figure (3.22). As was the case with the velocity, the individual deformation tensor components show a clear dichotomy in power distribution. The main contributors to the total power are the y differential terms which have a number of power spikes, the largest being the 12 hour peak in the $\partial v/\partial y$ term. In the x direction, the signal is significantly less but there are two very clear 12 and 24 hour signatures in both x differential components with the $\partial v/\partial x$ term having a very strong 24 hour peak. Looking at this same information in terms of DKPs we see that the large 24 hour peak from the $\partial v/\partial x$ term shows up primarily in the vorticity (VT). The divergence (DV) is identical to that shown in Figure (3.21) but in this context we see that its 12 and 24 hour peaks are coming from both $\partial u/\partial x$ and $\partial v/\partial y$. However, the low frequency signal from both of these is not included. Contrary to this, the normal deformation (ND) which is the difference between these same two strain-rate components contains both 12 and 24 hour peaks and the low frequency peak. The large spike at 12 hours from the $\partial v/\partial y$ term is clearly the main contributor to this signal. The normal deformation is also a greater contributor to the total strain-rate than the shear deformation (SD) particularly at the 12 hour period. The shear deformation is primarily contributing an assortment of power peaks over the whole range.

The above information together with the results in the previous sections show that the 12 hour oscillations are definitely producing divergence and elongation in the ice. The shear deformation is not as periodic indicating that shear deformation for this particular coordinate system, as a process, may be a result of non-linear interaction within the ice. Comparing the vorticity with the normal deformation we see that the strongest peak is the 12 hour signature in the normal deformation while the strongest in the vorticity is the 24 hour peak. What appears to be happening here is that the 12 hour tidal oscillations are generating most of the shear activity in the form of elongation while the 24 hour oscillations are working more on the ice as a solid body to turn the whole system. Findings from Foldvik et al. (1990) concluded that diurnal tides in this region move barotropically (as a solid body at the surface) while the semi-diurnal tides are influenced by the depth. Their findings also show that all four major tidal components: O_1 , K_1 , M_2 , and S_2 move as a tidal wave around the edge of the Weddell basin in a clockwise direction. This information further supports the findings that most of the subdaily signal we are seeing here is tidal and that there is a difference in response between the diurnal and semi-diurnal signals. In close proximity to the research area, the latitude $74^\circ 28'S$ is known as a critical latitude where the inertial period matches the M_2 (semi-diurnal) tidal component. Thus there is also a strong likelihood that inertial oscillations are working either in combination with or response too the semi-diurnal tidal

signal. Such an influence is one mechanism which may be responsible for the differences in diurnal and semi-diurnal ice responses. Additionally we see that shear is more affected by high frequency inputs (12 hour tides) while translation and rotation are more effected by lower frequency forcing (one day and longer).

We can sum up the power from a specified band width ($n \Delta f$) over a single periodogram to get the integrated power density and divide that by the band width to provide information about frequency band changes with time. We will now examine results from such integrated power spectra to understand the time evolution of the three main frequency bands we have been examining all along namely, low frequency (D.C. to <0.9 cycles/day), middle frequency (0.9 to 2.7 cycles/day), and high frequency (2.7 to 4.0 cycles/day). The integrated spectra are computed from 32 frequency bins over 15 day time periods for the wind, ocean currents, each buoy site ($u + v$), centroid velocity and invariant strain-rate components as presented in Figures (3.23) to (3.28).

Looking first at the overall results from the buoys, upper panel in Figure (3.23), we see that the low frequencies (solid white bar) contribute the most to the overall average power density (solid black bar). Middle and high frequencies have nearly the same value with middle frequencies being slightly higher at earlier times (mid days 70 and 76). The overall change in time of low frequency (and hence the overall average) is an initial rise in power from mean day 70 to 84 followed by relatively moderate power from mean day 92 to 132 and finally a large increase followed by a decrease in power from mean day 140 to 148. The smaller rise and fall in power from mean day 108 to 124 corresponds to the passage of a large storm system around day 120 as discussed earlier. An overall decreasing power density for the middle and high frequencies is also seen with power density values close to $40 \text{ (m/s)}^2 / (n \Delta f)$ at the beginning near mid day 70 down to around $10 \text{ (m/s)}^2 / (n \Delta f)$ by mid days 140 and 148. With regard to regional variations (panels B and C), we see that for the average over all frequencies, the western buoy sites collectively have less power than the eastern buoy sites for the first half of the drift (from mean day 70 to 108) but then become roughly equal for the second half. Except for days 124 and 148 the more western sites (Ed and Chris), which are located on the shelf, have more energy than the camp.

The regional differences become even greater when we examine the spectra of the individual frequency bands as shown in Figure (3.24) for the western buoys and Figure (3.25) for the eastern buoys. Looking first at the low frequency band (upper most plots), we see a change in power density with time which is nearly the same as that described for the sum of the buoys. There is no substantial difference between the eastern and western part of the array both in terms of absolute magnitude and relative change in power density. Hence whatever is driving the low frequency activity of the ice, is at least as large in scale as the array. The middle and high frequency bands show a completely different picture. First, both regions show an overall trend of decreasing power density with time for both middle and high frequency bands. The western sites clearly show a regional decrease in power from west (site Ed) to east (Camp) while the eastern sites are fairly uniform in magnitude for any given integration period. The two exceptions to these trends are the Camp near mean days 124 and 148 and site Brent near mean day 70. The Camp ice floe underwent considerable deformation around day 120 (i.e. it split in half!) so the strong signal at this time is indicative of that local event. Similar types of local events may have occurred during the other unusual peaks as well. Since the western

sites traverse the steepest part of the shelf slope, their west to east decrease in power density is most likely caused by the western intensification current described earlier in Section (3.3.2). The more uniform distribution of power density to the east, where the topography is much more uniform, further supports this.

The wind in the upper plot of Figure (3.26) shows the same temporal evolution of power density as the sum of the buoys with the low frequency band clearly being the main source of that power. The ocean currents on the other hand are fairly constant with time (about 10 to $20 \text{ (m/s)}^2 / (n\Delta f)$) except at mean day 140 where the current reaches a maximum of 30 and $20 \text{ (m/s)}^2 / (n\Delta f)$ at 25 and 50 meters depth, respectively. The centroid velocity power density is in nearly all cases larger than the ocean current power density. When the wind is low the centroid power is nearly the same as the ocean current power but when the wind power is high, the centroid power is correspondingly higher than the ocean processes. This result gives us some information about the contributions of power from the wind and ocean to the ice drift. From these results we can conclude with reasonable certainty that the ocean current is providing a steady source of moderate low frequency power to the ice drift while the wind is providing an intermittent source of very high power. This conclusion supports the earlier results that the ice drifts northward as a result of the topographically steered ocean current but also that there is a large input of intermittent power coming from the wind from variable directions. The lower plot in this figure shows the local invariant strain-rate activity resulting from these forces. The general trend for these components is a sequence of 10 to 20 day increases/decreases in deformation activity (e.g. mean day 76 to 92) which does not match any temporal patterns in the ice drift, ocean current or wind.

The distribution of power density at the 3 frequency bands for the ocean current (Figure 3.27) shows that the low frequency ocean power is the main contributor to the overall power density seen in Figure (3.26). For the ocean current, the low frequency band ranges between 20 and $100 \text{ (m/s)}^2 / (n\Delta f)$. The middle and low frequency bands are much less with ocean currents only once (25m current on day 70) exceeding $10 \text{ (m/s)}^2 / (n\Delta f)$ and the high frequency band being about 10 times less than this. The centroid power density has even a larger spread with the low frequency band ranging from about 40 to over $300 \text{ (m/s)}^2 / (n\Delta f)$ while the middle frequency lies within the same range as the ocean current. The extremely low values for the centroid's high frequency band are residual signals left after a 9 hour low pass filter. The main purpose for displaying these results is to show the degree to which the high frequency signal was removed from the regression analysis.

In addition to these overall features we see that the centroid velocity follows the wind at the low frequency band but then clearly follows the ocean in the middle frequency band. In the middle frequency band, we also see the same decrease with time of power density as seen in the middle frequency band at the buoy sites. Since this middle frequency band includes frequencies from about 9 hours to a little more than a day, the reduction in power relates to a decrease in oscillation activity including both tidal and inertial periods. Since the buoy array is both drifting in space northward and advancing in time, there are two possible scenarios. First, the ocean current in this frequency band may not be as strong at the northwest end of the gyre as in the southwest possibly due to topographic changes or because stronger tidal/inertial activity may be going on at the southwest end of the basin. Second, the ice is becoming thicker and the compactness is

increasing both because the winter is progressing and the ice is flowing northward into an eastward extending land mass (Antarctic Peninsula). This creates a grid-lock at the surface which can significantly damp the ocean current below especially if the wind is working against the ocean current during this process. A combination of these scenarios is most likely the case.

With regard to the deformation activity at the different frequency bands we see in Figure (3.28) that the middle frequency band makes the largest overall contribution to total power with shear being its largest component in all cases. These results were also seen in the time series plots of the strain but now in addition to this we see that during periods of high wind or shortly after (e.g. near mean day 84 to 92 and 116) we see a substantial increase in low frequency strain-rate power in the shear but not in the divergence so there is a lot of elongation and shear deformation being produced by storm events but not as much divergence.

The middle frequency band is where the 12 and 24 hour power peaks lie and where the tides are heavily influencing. In these integrated power spectra, we do see a general decrease in the power density with time as is the case with the ocean current however, we do not see a section by section pattern emerging which clearly shows that this is the case. There are a number of possibilities responsible for this. First, as seen in the error analysis, the strain-rate data do have a considerable amount of noise in their signal so direct correspondence to current spectra is probably at best only in terms of general trends. We see, for example, that for mean day 108 there is an unusually large amount of high frequency activity which would not be significant if it were not for the fact that the high frequency signal has supposedly been filtered out. Another major influence is that non-linear internal ice interaction may propagate energy from both the high and low frequency bands into the middle band. Low frequency wind and ocean activity can induce ice processes of shear, elongation, ridge building, etc. These deformations can occur slowly at low frequencies and still emit middle frequency band responses. From the regular power spectra we did note that the SD component had no real power peak at any frequency and although ND did have a very strong 12 hour signal, there was quite a bit of low power activity in each frequency bin above the 9 hour LPF. The presence of general low power activity is a classic “symptom” associated with non-linear activity (Schuster, 1988).

Spectral Plots of MultiRegression Results

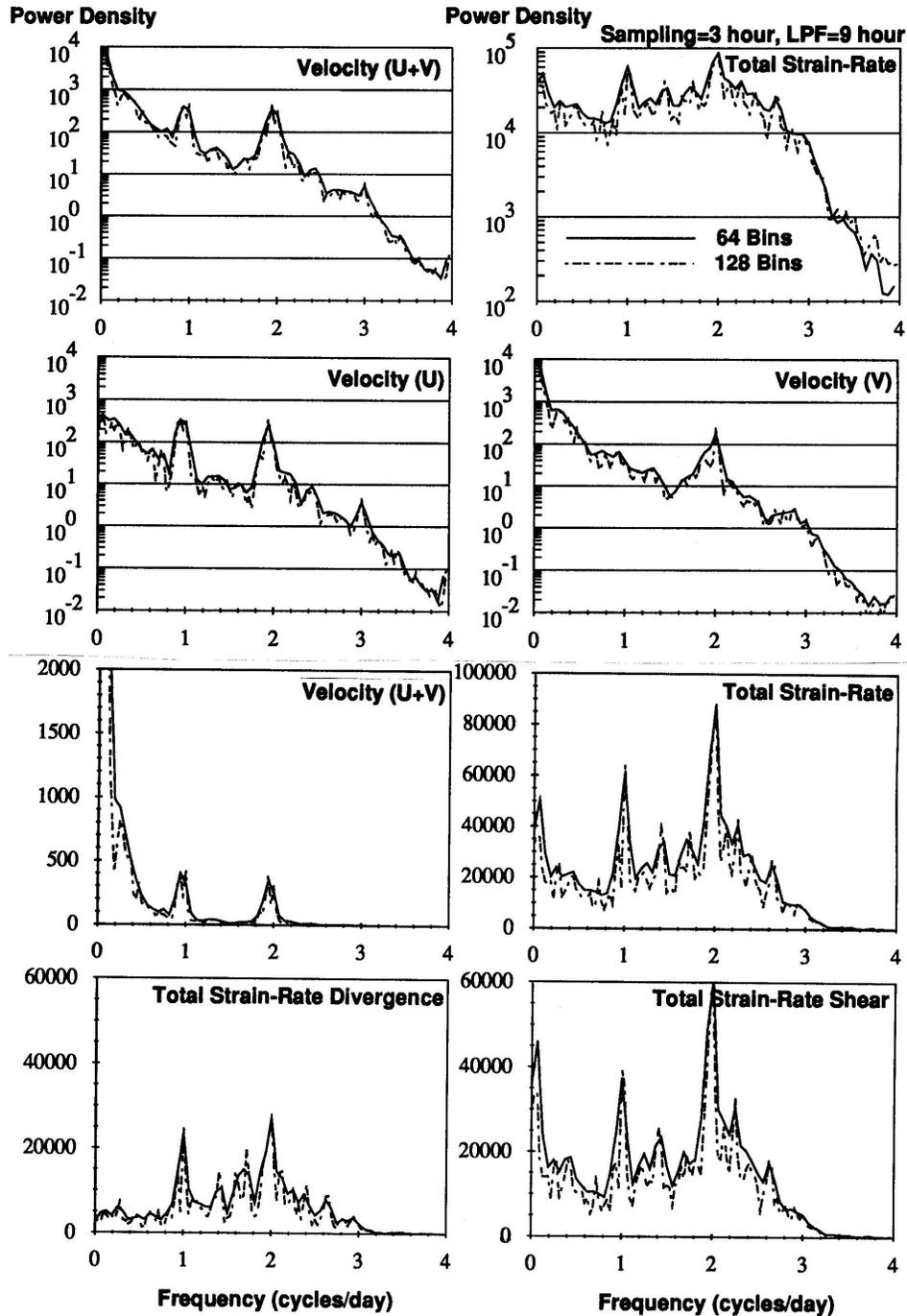


Figure 3.21: Power density of Centroid Velocity and Invariant Strain-Rates resolved to 64 and 128 frequency bins in both log and linear scales. Spectral density of velocity in units of $[(m/s)^2/\Delta f]$ and strain-rates in units of $\frac{[\times 10^{-6}(1/S)]^2}{\Delta f}$.

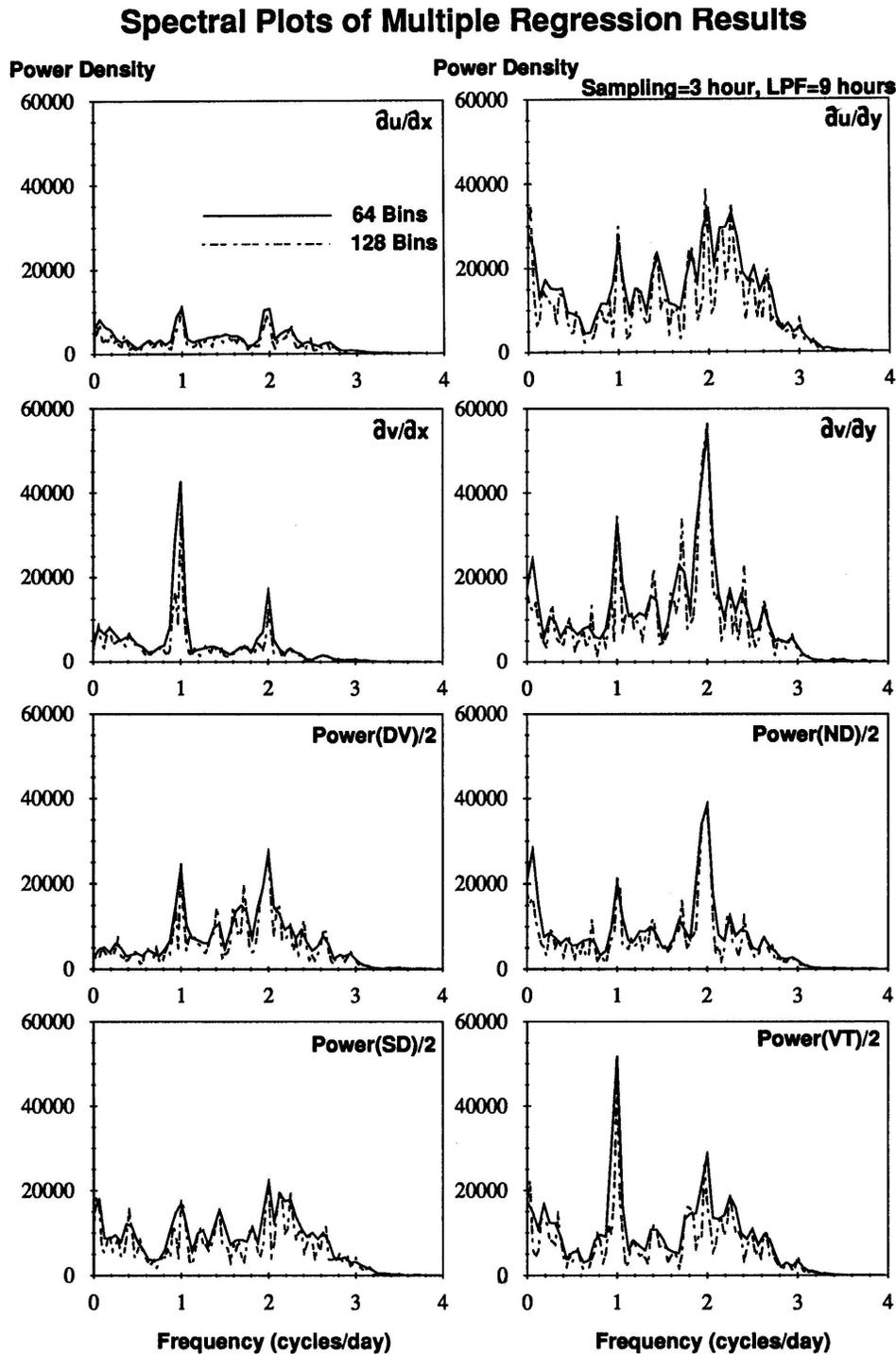


Figure 3.22: Power density of deformation tensor components and DKP terms resolved to 64 and 128 frequency bins. Power spectral density of deformation terms in units of $\frac{\times 10^{-6}(1/S)^2}{\Delta f}$.

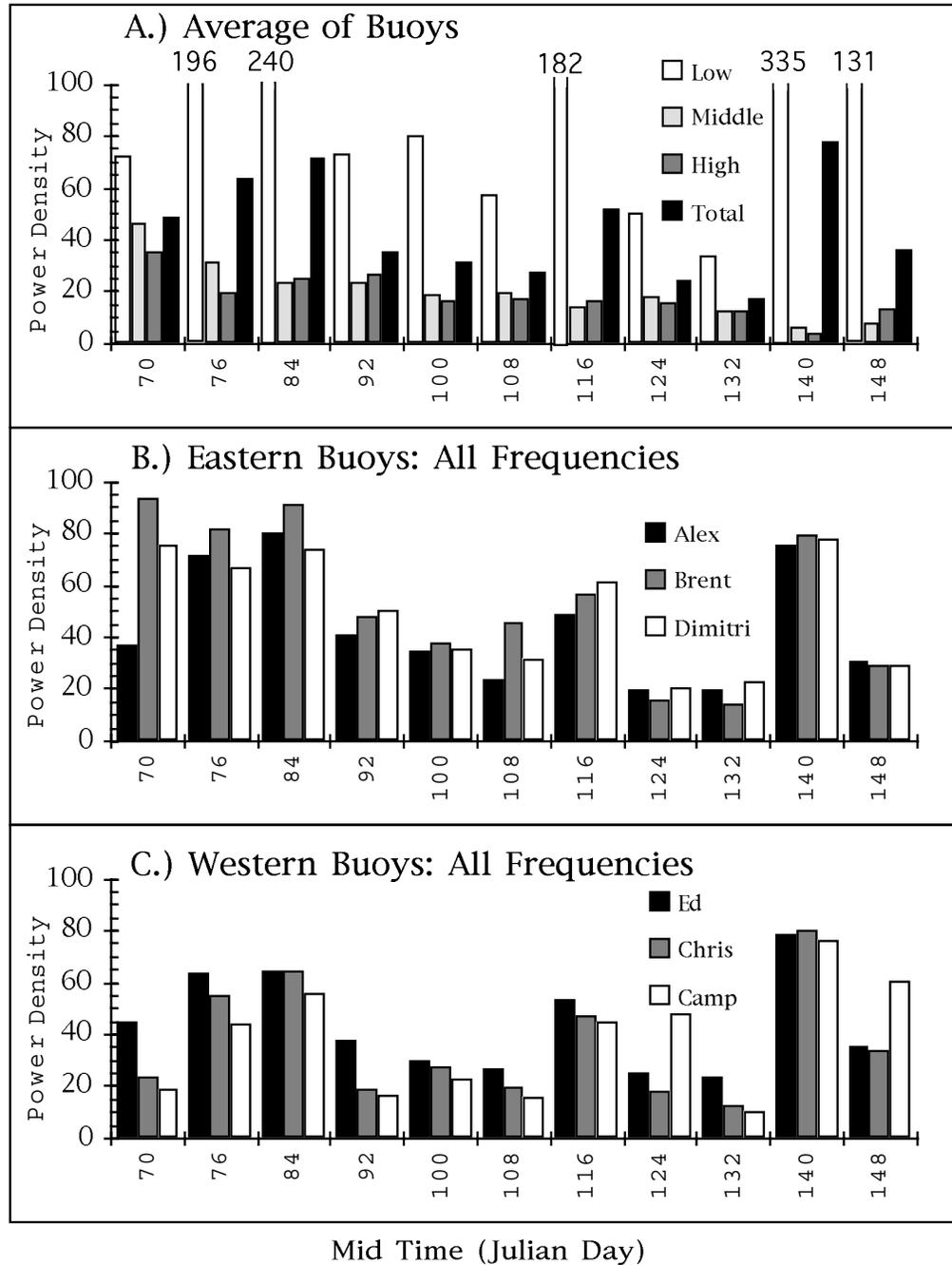


Figure 3.23: Integrated power spectra density, $u + v \text{ (m/s)}^2 / (n \Delta f)$, of all buoys resolved to 32 frequency bins. 15 day power integration labeled by central time in Julian days. Frequency subdivisions include: All (DC plus 0.125-4.0 cycles/day), Low (<0.9 cycles/day), Middle (0.9-2.7 cycles/day) and High (2.7-4.0 cycles/day).

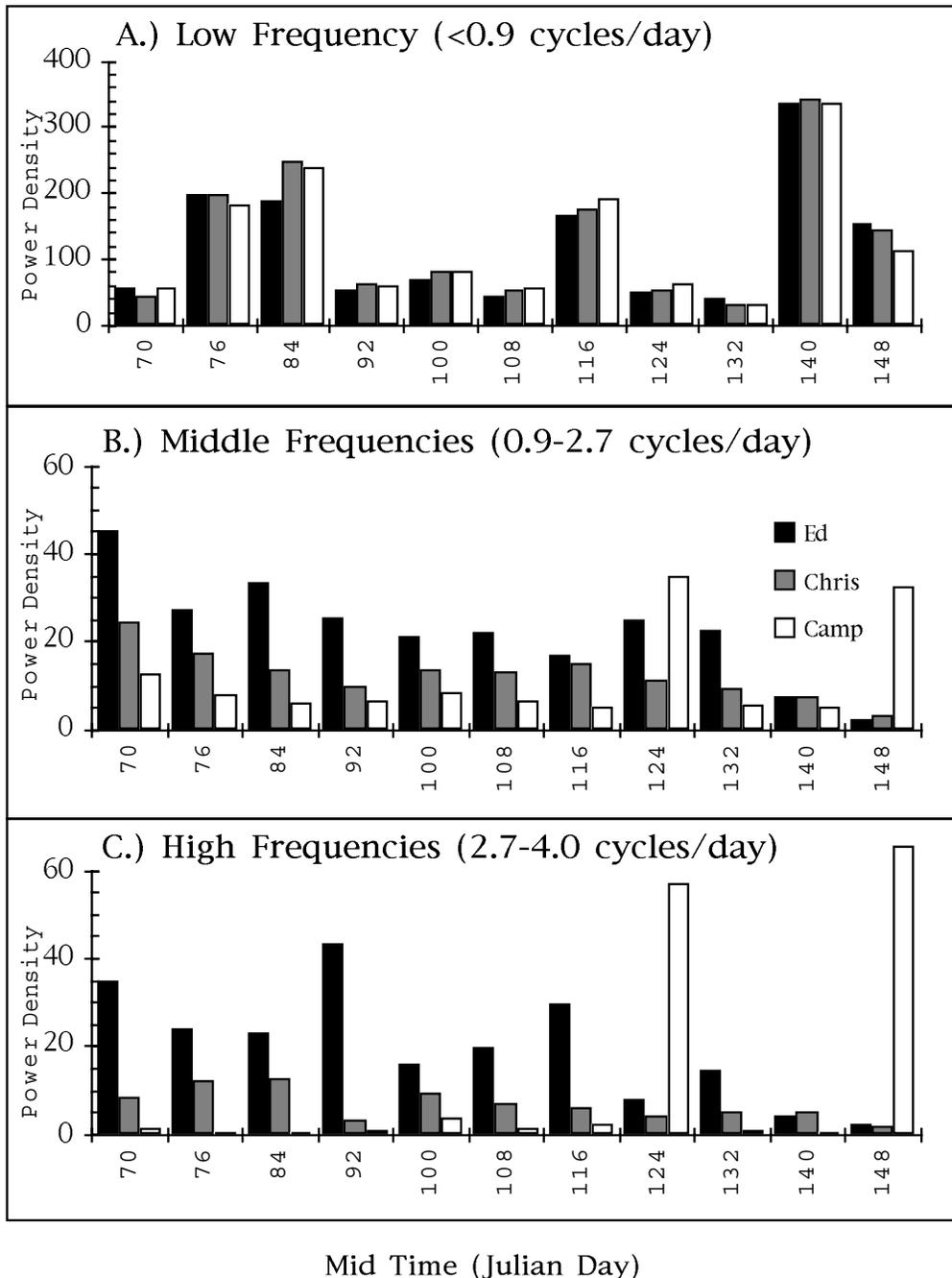


Figure 3.24: Power distribution for 15 day integrated power spectral density for western buoys, $u + v$ (m/s)²/($n \Delta f$). 15 day power integration labeled by central time in Julian days.

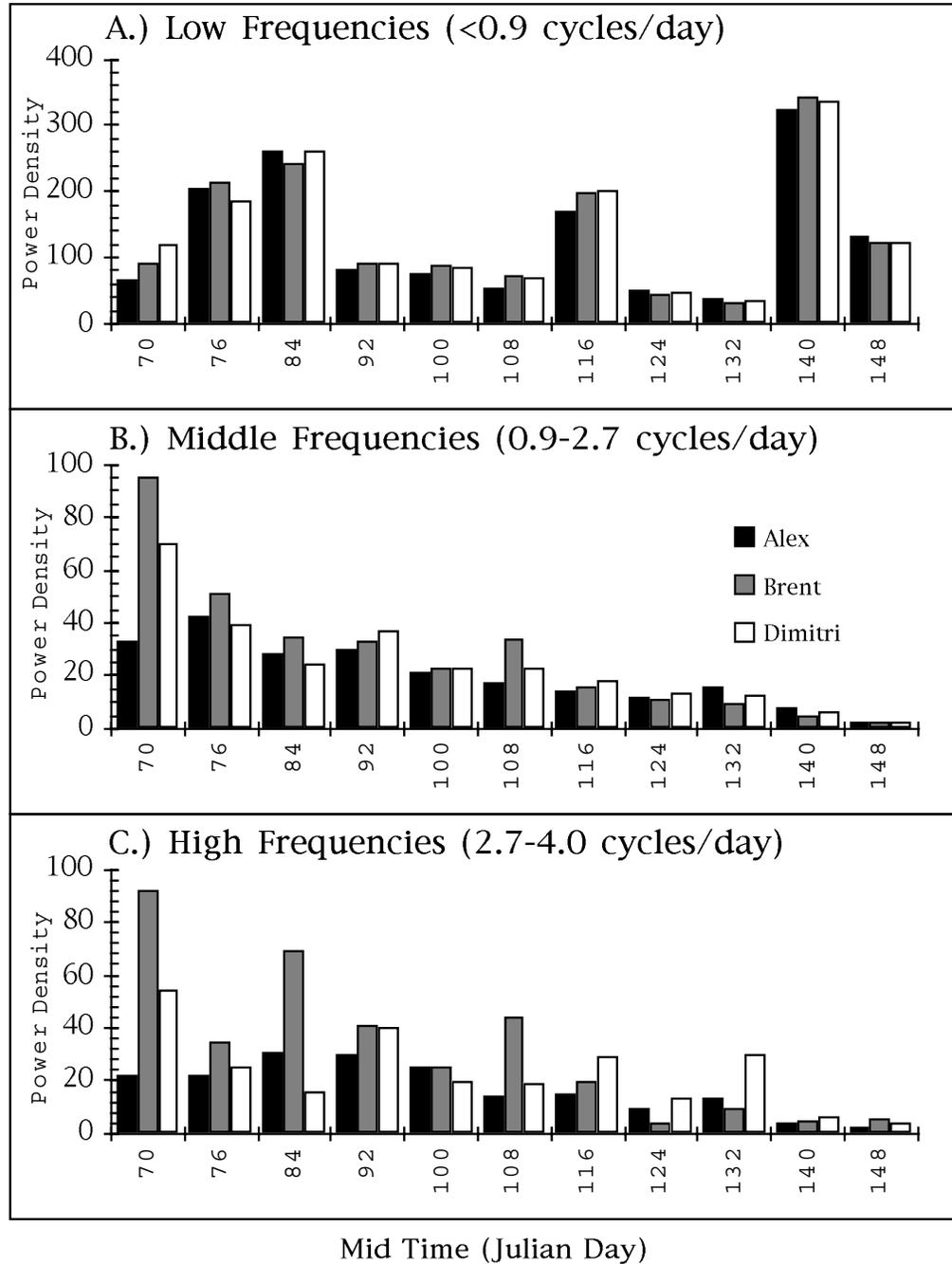


Figure 3.25: Power distribution for 15 day integrated power spectral density for eastern buoys , $u + v \text{ (m/s)}^2 / (n \Delta f)$. 15 day power integration labeled by central time in Julian days.

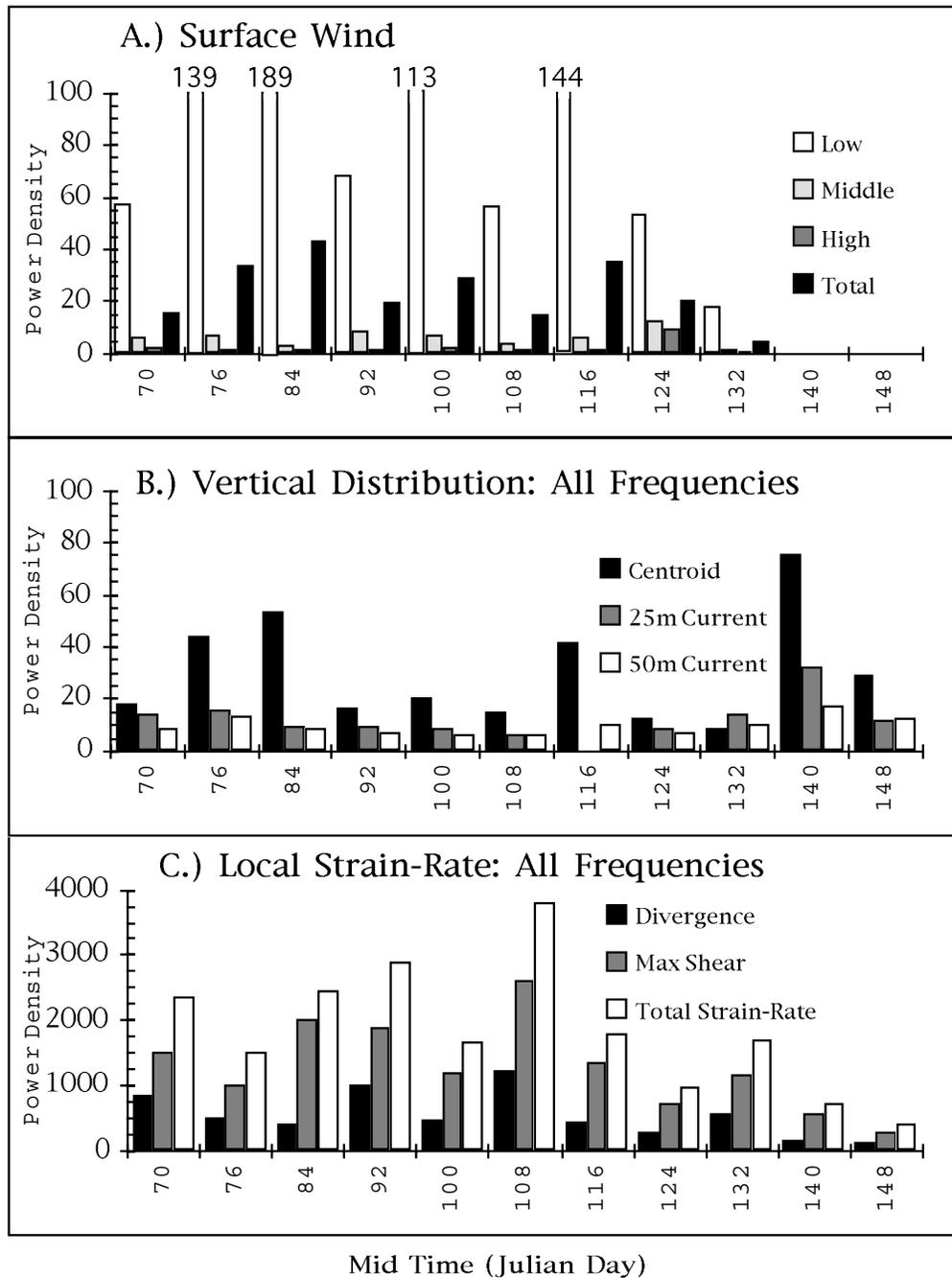


Figure 3.26: Integrated power spectral density of surface wind ($u + v$ $[(\text{m/s})^2/(1000 n \Delta f)]$), ocean current ($u + v$ $[(\text{m/s})^2/n \Delta f]$), and local strain $[(\times 10^{-6} (1/s)^2/n \Delta f)]$ resolved to 32 frequency bins. Frequency subdivisions include: All (DC plus 0.125-4.0 cycles/day), Low (< 0.9 cycles/day), Middle (0.9-2.7 cycles/day) and High (2.7-4.0 cycles/day).

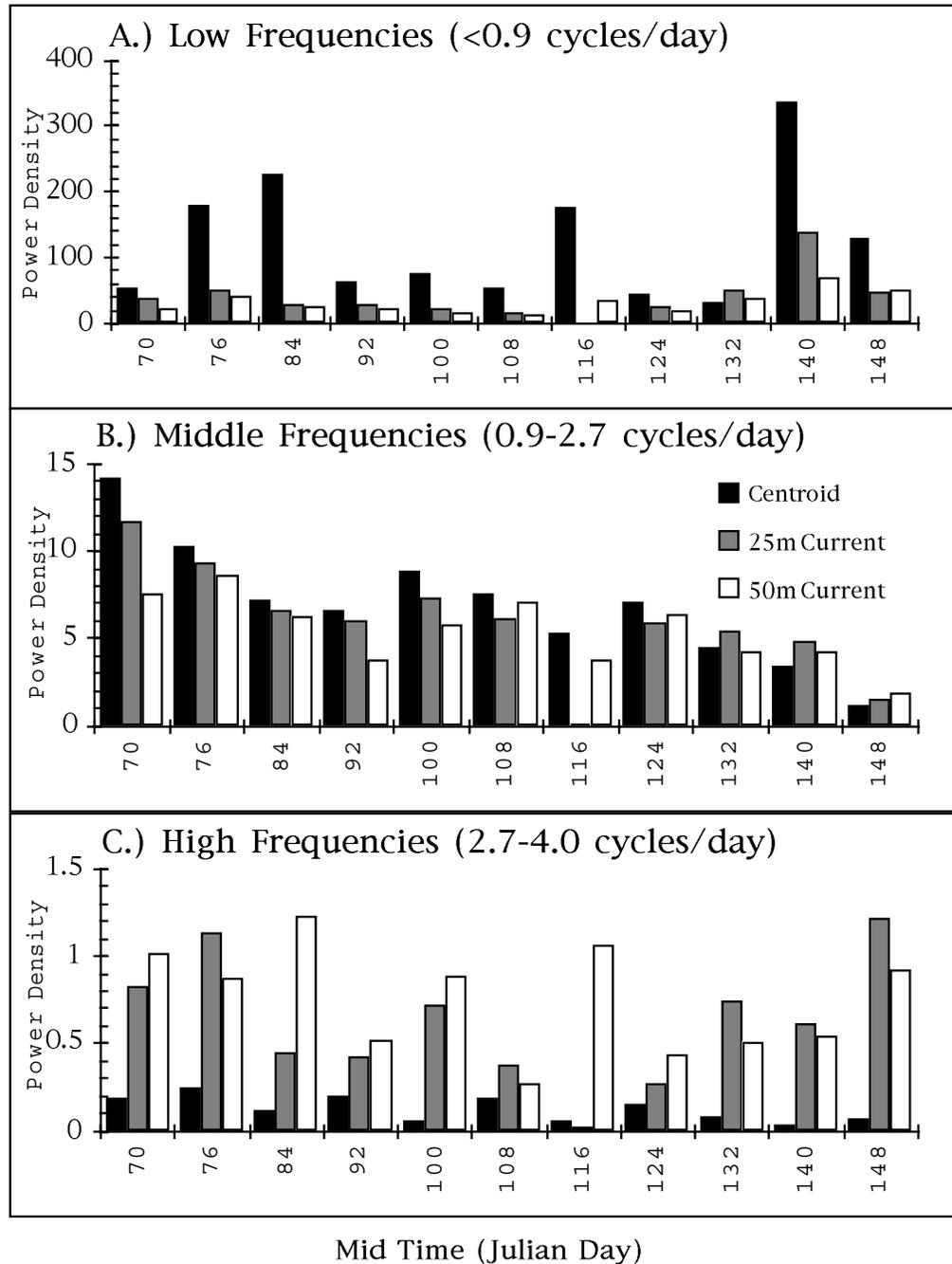


Figure 3.27: Power distribution for 15 day integrated power spectral density for array centroid and ocean current at 25 and 50 m below the Camp site. 15 day power integration with central time in Julian days. (No 25m current data around day 116.)

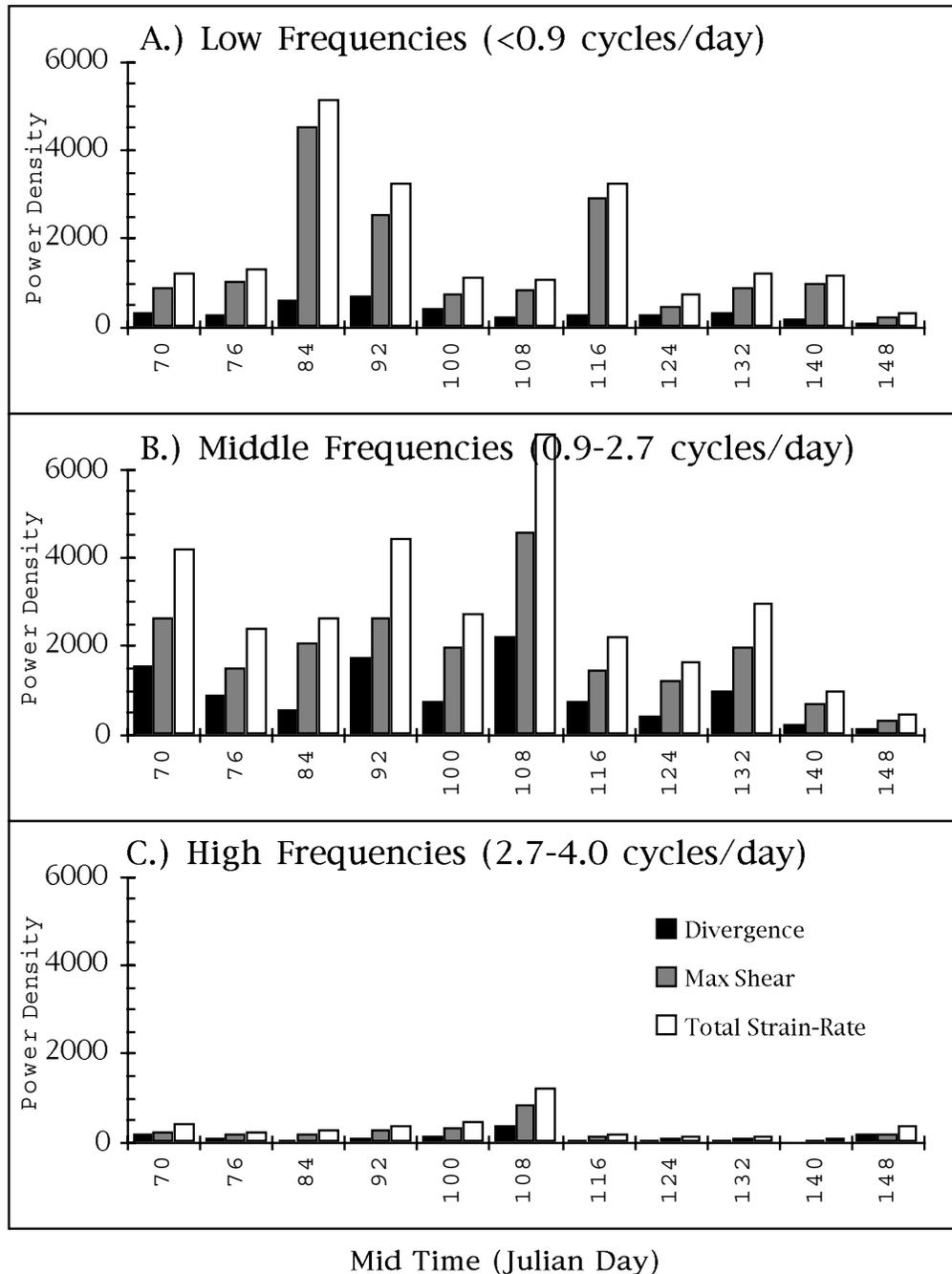


Figure 3.28: Power distribution for 15 day integrated power spectra for strain-rate variables of divergence, shear, and total strain-rate (see text for description). 15 day power integration labeled by central time in Julian days.

3.5 Chapter Summary

Data from Ice Station Weddell during 1992 has been used to examine sea ice drift and deformation activity and to identify relevant external forces responsible for driving specific processes. Use of power spectra and deformation analysis on the large scale drift velocities together with spectra of wind and current measurements have shown that the velocity, or general drift, of the sea ice pack in the Western Weddell region is driven primarily by low frequency forcing (i.e. greater than one day periods). Contrary to this, higher frequencies, specifically diurnal and semi-diurnal tidal frequencies, appear to be the main source driving sea ice deformation in this region. The local topography also plays a major role by inducing a directional dependence in both ice drift and deformation. The internal ice interaction seems to be particularly sensitive to such topographic influences, even more so than the underlying ocean current most likely due to non-linear ice interaction and inertial oscillation activity within the ice. In terms of identifying key deformation processes, comparisons using invariant quantities provide information about the total deformation process and its components of divergence and shear. The non-invariant components also provide a considerable amount of information about contributions due to specific orientations. With regard to the statistical “fitness” of the deformation information, we have provided insightful qualitative information about sea ice deformation but there is ample room for improving the quantitative value of these results. Two ways to improve this are through an increased number of sites and better instrumentation such as GPS.

With regard to specific sea ice dynamic processes and the forces most responsible for driving them, we can now identify the following two key results with reasonable certainty. First, the general drift of the sea ice pack in the Western Weddell region is a low frequency dynamic process which is driven primarily by low frequency forcing in the form of moderate but steady low frequency ocean currents and intermittent high energy storm activity from the wind. Ocean eddies are most likely acting in a similar fashion to the wind, but there is insufficient evidence from this study to verify that. Second, deformation of the sea ice pack is composed of both low (<1 cycle/day) and high (1 cycle/day or more) frequency processes with the high frequency processes clearly dominating. The low frequency processes are strongest during and after episodes of high winds. There is also evidence that moderate but steady low frequency ocean currents must also have an effect. For this region in particular divergence is clearly a high frequency process with very little low frequency contribution. Shear has large high and low frequency components with elongation deformation being the main form of deformation at low frequencies. The high frequency processes are clearly driven by 12 and 24 hour ocean oscillations with the 12 hour peak contributing most to the total shear activity while the 24 hour peak contributes more to the solid body rotation of the ice on scales at least as large as the ISW array (150 km). The previous investigation by Foldvik et al. (1990) is consistent with these results. Their conclusion that diurnal tides produce barotropic currents is synonymous with the local solid body rotation seen in the ISW array. Likewise the depth dependence they identify with the semi-diurnal tidal currents is also seen in the ISW array. These previous results also support the qualitative believability of the deformation analysis.

In terms of identifying changes in these processes with time we found that changes

in wind intensity produce parallel changes in the ice drift at low frequencies (<0.9 cycles/day) while middle (tidal) frequencies (0.9-2.7 cycles/day) change in the ice relative to the ocean, or vice versa and exhibit a decrease in power as the winter progresses. Deformation activity at middle frequencies is complicated by non-linear processes and possibly unfiltered instrument error and is therefore more difficult to relate to specific wind or ocean events in time. At low frequencies (<0.9 cycles/day), however, shear processes correlate very clearly with periods of increased wind activity while divergence changes are much smaller.

One impact of these results is the ability to monitor sea ice drift and deformation activity. Satellite imagery has a high spatial resolution but low temporal resolution (3 day pass average) so it can detect ice drift adequately but not deformation. Buoy arrays lack the high spatial resolution but do have high temporal resolution to record most of the ice deformation activity, especially differential GPS arrays. If Western Weddell region shelf break is a good indicator for other similar regions, then ice forecasting requires a combination of both techniques to correctly predict ice activity, at least in regions where subdaily forcing is very strong. Finally, in addition to these important physical results, we now have a number of observations which can serve as case studies to compare with the numerical simulations presented in later chapters.

Chapter 4

Numerical Model Hierarchy

The goal of this chapter is to examine the equations that govern the dynamics and thermodynamics of sea ice in the numerical hierarchy chosen. We will begin with an overview of the governing equations followed by a description of the boundary conditions, input fields, and numerical methods. We complete this chapter with some simple tests which ensure that the codes are functioning properly.

4.1 Governing Equations

Three general groups of equations are needed to determine the dynamics and thermodynamics of sea ice: a) momentum balance, b) constitutive relation, and c) mass conservation. The momentum balance describes the balance of forces acting on sea ice, which is

$$m \frac{D\vec{v}}{Dt} = -m f \hat{k} \times \vec{v} + \vec{\tau}_a + \vec{\tau}_w - m g \nabla H + \vec{F}_{\text{ice}}. \quad (4.1)$$

(Description of each variable in Tables 4.1 and 4.2.) The term on the left hand side represents the temporal (or inertial) and advective (or non-linear) changes of ice velocity \vec{v} (i.e. $\frac{D}{Dt}$ is the total derivative $= \frac{\partial}{\partial t} + \vec{v} \cdot \nabla$) due to the right hand side. The first term on the right hand side describes forces in the ice due to motion on a rotating system (i.e. Coriolis force). This is followed by two external forcing terms, air ($\vec{\tau}_a$) and water ($\vec{\tau}_w$) drag, which are defined through some type of drag law between air and ice, and, ice and water, respectively. The most commonly used drag law for sea ice is the two dimensional formulation

$$\vec{\tau}_a = C_a^{**} \left[\vec{V}_a \cos \theta_a + \vec{k} \times \vec{V}_a \sin \theta_a \right] \quad (4.2)$$

$$\vec{\tau}_w = C_w^{**} \left[(\vec{V}_w - \vec{v}) \cos \theta_w + \vec{k} \times (\vec{V}_w - \vec{v}) \sin \theta_w \right] \quad (4.3)$$

where it has been assumed that $\vec{V}_a \gg \vec{v}$ such that $\vec{V}_a \approx \vec{V}_a \pm \vec{v}$. C_a^{**} and C_w^{**} are empirically determined drag coefficients for air and water, respectively, and θ_a and θ_w are air and water turning angles resulting from the Ekman layer which develops at the air-ice-sea boundary interface due to the earth's rotation. Using results from McPhee (1980) an average turning angle of 25° will be used for both the air and water drag terms.

The last two terms are forces due to ocean surface tilt and internal ice force, respectively. The ocean surface tilt term, ∇H , can be replaced through the geostrophic approximation (Hibler, 1979) to

$$g \nabla H \approx -f \hat{\mathbf{k}} \times \vec{\mathbf{V}}_w, \quad (4.4)$$

whereas the internal ice force requires the inclusion of an ice rheology through a constitutive law to express the ability of the ice to resist external forces imposed on it. There is no general relationship to describe the rheology of sea ice but there are a number of tested rheologies which work well under a variety of conditions. Therefore, more discussion on this term must be addressed below in the description of specific models constructed. As for mass conservation, a general formulation is

$$\frac{Dm}{Dt} = \text{Sources} - \text{Sinks}, \quad (4.5)$$

where the left hand side expresses the temporal and spatial changes that sea ice mass can undergo while the right hand side accounts for thermodynamic processes of melting and freezing.

Pending a specific constitutive relation, this completes the equations necessary to describe sea ice, leaving us with: three equations from the momentum balance, at least one from constitutive relation, at least one from mass conservation, and several supplementary equations (drag law, geostrophic approximation, etc). There are several unknowns including $\vec{\mathbf{v}}$, $\vec{\mathbf{V}}_a$, $\vec{\mathbf{V}}_w$, m , $\vec{\mathbf{F}}_{\text{ice}}$ in addition to a number of coefficients which need to be determined. Given the complexity of this set of equations, a general solution, to date, is not possible. By imposing realistic assumptions and utilizing numerical techniques, however, we can investigate limiting cases of these coupled equations in order to obtain information about sea ice and how it responds to its environment.

The main goal of this study is to investigate the response of sea ice to specific conditions, hence all non-ice terms will be specified (i.e. $\vec{\mathbf{V}}_a$, $\vec{\mathbf{V}}_w$ are given). The non-linear advection terms in the momentum balance are significantly smaller than the other terms so we will, through scaling arguments, not include them. As shown in Chapter 2, the non-linear internal ice force is not small compared to the other terms so it can not be disregarded. Basing our numerical investigation on these conditions we will now describe the specific configuration of sea ice models to be used for this study. The remainder of this section will concentrate on the description of a hierarchy of sea ice models for both Cartesian and spherical coordinate systems for one dimensional (1D), one and a half dimensional (1.5D) and two dimensional (2D) cases. Since the fundamental set of equations for all of these systems is essentially the same, a complete description of the governing equations is given for the 2D case followed by a brief description of the equations in the other configurations.

4.1.1 2D Sea Ice Model

One 2D form of the momentum balance (Equation 4.1) can be obtained assuming a horizontal system and, through scaling arguments, neglecting the non-linear advective terms.

Table 4.1: List of Variables

Variable	Description	MKS units
f	Coriolis parameter = $2\Omega \sin \phi$	(1/s)
g	gravity =9.81	(m/s ²)
h	mean ice volume per unit area= effective ice thickness	(m)
\hat{i}	first horizontal unit vector	—
\hat{j}	second horizontal unit vector, $\hat{i} \perp \hat{j}$	—
\hat{k}	unit vector normal to sea surface = $\hat{i} \times \hat{j}$	—
m	mass of the ice	(kg)
t	time	(s)
u	ice velocity component in the \hat{i} direction, along \hat{i}	(m/s)
v	ice velocity component in the \hat{j} direction, along \hat{j}	(m/s)
\vec{v}	ice velocity = $u \hat{i} + v \hat{j}$	(m/s)
A	ice compactness	(%)
A_{min}	minimum allowable compactness = 0.01	(%)
C_a^*	wind drag coefficient	(kg/m ² s)
C_w^*	water drag coefficient	(kg/m ² s)
$\frac{D}{Dt}$	Total Derivative = $\frac{\partial}{\partial t} + \nabla \bullet$	—
\vec{F}_{ice}	force due to internal ice stress	(kg m/s ²)
$F_{\hat{i}}$	internal ice stress (force per unit area) in \hat{i} direction	(kg/m s ²)
$F_{\hat{j}}$	internal ice stress (force per unit area) in \hat{j} direction	(kg/m s ²)
H	sea surface dynamic height	(m)
$H0$	demarcation thickness between thick and thin ice = 1.0	(m)
P	internal ice pressure	(kg/s ²)
P_{max}	ice strength or maximum compressive stress	(kg/s ²)
P^*	ice strength coefficient= 27.5×10^3	(kg/m s ²)
R	radius of earth, assumed to be constant = 6366707.	(m)
U_a	geostrophic wind velocity in the \hat{i} direction	(m/s)
U_w	geostrophic water velocity in the \hat{i} direction	(m/s)
V_a	geostrophic wind velocity in the \hat{j} direction	(m/s)
V_w	geostrophic water velocity in the \hat{j} direction	(m/s)
Y_{neg}	heat storage parameter – amount of negative ice grown	(m)

Table 4.2: List of Variables (cont'd)

Variable	Description	MKS units
δ_{ij}	Kronecker Delta function	—
$\dot{\epsilon}_{ij}$	strain rate tensor	(1/s)
ζ	bulk viscosity	(kg/s)
η	shear viscosity	(kg/s)
θ_a	turning angle relative to the air/ice	(degrees or radians)
θ_w	turning angle relative to the ice/water	(degrees or radians)
λ	geographic longitude	(degrees or radians)
ϕ	geographic latitude	(degrees or radians)
ρ_a	density of air = 1.3	(kg/m ³)
ρ_i	density of ice = 930	(kg/m ³)
ρ_w	density of water = 1000	(kg/m ³)
σ_{ij}	stress tensor	(kg/s ²)
$\vec{\tau}_a$	air drag on the ice	(kg m/s ²)
$\vec{\tau}_w$	water drag on the ice	(kg m/s ²)
$\tau_{\hat{i}}$	total drag (per unit area) in the \hat{i} direction	(kg/m s ²)
$\tau_{\hat{j}}$	total drag (per unit area) in the \hat{j} direction	(kg/m s ²)

Expressing the remaining terms in component form per unit volume and multiplying by h , we arrive at the 2D momentum equations for this study which are

$$\hat{i}: -\rho_i h \frac{\partial u}{\partial t} - \alpha_w u + \beta_w v + \tau_{\hat{i}} = -F_{\hat{i}} \quad (4.6)$$

$$\hat{j}: -\rho_i h \frac{\partial v}{\partial t} - \alpha_w v - \beta_w u + \tau_{\hat{j}} = -F_{\hat{j}}. \quad (4.7)$$

Respectively, u and v are the ice velocities in the \hat{i} and \hat{j} directions for any selected orthogonal 2D coordinate system. In Cartesian coordinates, these correspond to $\hat{i} \Rightarrow x$ and $\hat{j} \Rightarrow y$ directions while in geographical spherical coordinates they correspond to $\hat{i} \Rightarrow$ longitude (λ) and $\hat{j} \Rightarrow$ latitude (ϕ). In the above form, the forces of the momentum equation are arranged to distinguish between the sources (air, water, ice) of ice forcing. The first term on the left hand side for each component is the inertial term with $\rho_i h$ being the average ice mass per unit area. The next two terms on the left hand side are the forces due to ice motion which have been extracted from the water drag term (Eq. 4.3) and the Coriolis term (Eq. 4.1). The last term on the left hand side is the sum of external air and water forces from the drag relations (Eqs. 4.2 and 4.3) which can easily be decomposed into each external force as needed. The right hand side of the equations represent the forces due to internal ice interaction.

External forcing ($\tau_{\hat{i}}$ and $\tau_{\hat{j}}$) includes the wind and water drag as follows

$$\tau_{\hat{i}} = \alpha_a U_a - \beta_a V_a + \alpha_w U_w - \beta_w V_w \quad (4.8)$$

$$\tau_{\hat{j}} = \alpha_a V_a + \beta_a U_a + \alpha_w V_w + \beta_w U_w. \quad (4.9)$$

The α and β coefficients for the air (subscript a) and water (subscript w) are

$$\alpha_a = C_a^* \cos \theta_a \quad (4.10)$$

$$\beta_a = C_a^* \sin \theta_a \quad (4.11)$$

$$\alpha_w = C_w^* \cos \theta_w \quad (4.12)$$

$$\beta_w = C_w^* \sin \theta_w + \rho_i h f. \quad (4.13)$$

h is the effective ice thickness computed as the total ice volume per unit surface area. θ_a and θ_w , the air and water turning angles, are set to 25° after McPhee (1980). C_a^* and C_w^* are the air and water drag coefficients which are computed here in both a linear and quadratic form. For the linear case the drag coefficients are constant and equal to $C_a^* = 0.0126$ and $C_w^* = 0.6524$ (Flato and Hibler, 1990) while in the quadratic case they are defined using the formulation described by McPhee (1975, 1980) as

$$C_a^* = C_a \rho_a |\vec{\mathbf{V}}_a| \quad (4.14)$$

$$C_w^* = C_w \rho_w |\vec{\mathbf{V}}_w - \vec{\mathbf{v}}|, \quad (4.15)$$

where dimensionless constants C_a and C_w equal 0.0012 and 0.0055, respectively (Hibler, 1979). Note that as in Eq. (4.2), $\vec{\mathbf{V}}_a \gg \vec{\mathbf{v}}$ is assumed for Eq. (4.14).

The ice interaction terms F_i, F_j describe the ice through a constitutive relation or ice rheology which relates the motion of the ice to its structural integrity. Two different types of rheologies have been chosen for this study: 1) cavitating fluid rheology (hereafter referred to as CAV) and 2) viscous-plastic rheology (hereafter referred to as VP). CAV assumes no shear stress, such that compressive hydrostatic pressure, P , is the only stress component (i.e. no negative P or tensile strength). VP describes an isotropic stress state whereby both compressive and tensile stresses (i.e. normal stress) and shear stress are included. The yielding criterion for this stress state can be described in principal axis space by an elliptic yield curve configuration (details in Chapter 5.2.1). CAV is computationally simple and has recently been used for climate studies involving monthly mean forcing. VP on the other hand traditionally gives more realistic results but is computationally time consuming. Used together, these models provide information about a range of internal ice responses from free drift, pressure only, to an isotropic stress state.

Mathematically these rheologies are described as

$$\vec{\mathbf{F}}_{\text{ice}} = F_i = \begin{cases} -\frac{\partial P}{\partial x_i}; & \text{Cavitating Fluid Rheology} \\ \frac{\partial \sigma_{ij}}{\partial x_j}; & \text{Viscous-Plastic Rheology} \end{cases} \quad (4.16)$$

where σ_{ij} is a stress tensor expressed in indicial notation (repeated indices sum). In this 2D system, i and j run from 1 to 2 which are the first and second coordinates of a given coordinate system. An important thing to note is that for ice in a 2D system, variables $P, P_{\text{max}}, \sigma_{ij}, \zeta$, and η are their real 3D quantities multiplied by h to form the 2D line stress and 2D bulk terms needed to represent stresses in 2D space. Hence the somewhat unusual units in Table (4.1) for stresses and pressures are in terms of Pascal meters (Pa. m) instead of Pascals because of this 2D description.

In the case of CAV, the internal ice forcing terms in Cartesian coordinates are

$$F_x = -\frac{\partial P}{\partial x} \quad (4.17)$$

$$F_y = -\frac{\partial P}{\partial y} \quad (4.18)$$

and in spherical coordinates

$$F_\lambda = -\frac{1}{R \cos \phi} \frac{\partial P}{\partial \lambda} \quad (4.19)$$

$$F_\phi = -\frac{1}{R} \frac{\partial P}{\partial \phi}. \quad (4.20)$$

These equations must satisfy the conditions (from Flato and Hibler, 1990) that

$$\nabla \bullet (\vec{v} + \vec{\tilde{v}}) \geq 0 \iff P + \tilde{P} = 0 \quad (4.21)$$

$$\nabla \bullet (\vec{v} + \vec{\tilde{v}}) = 0 \iff 0 < P + \tilde{P} < P_{\max} \quad (4.22)$$

$$\nabla \bullet (\vec{v} + \vec{\tilde{v}}) \leq 0 \iff P + \tilde{P} = P_{\max}. \quad (4.23)$$

(\tilde{P}) and ($\vec{\tilde{v}}$) are correction terms for the pressure and velocity, respectively. The divergence operator ($\nabla \bullet$) is defined in Cartesian coordinates as

$$\nabla = \frac{\partial}{\partial x} \hat{i} + \frac{\partial}{\partial y} \hat{j} \quad (4.24)$$

and in spherical coordinates as

$$\nabla = \frac{1}{R \cos \phi} \frac{\partial}{\partial \lambda} \hat{i} + \frac{1}{R \cos \phi} \frac{\partial (\cos \phi \cdot)}{\partial \phi} \hat{j}. \quad (4.25)$$

For VP in Cartesian coordinates, the stress tensor is given as in Hibler (1979) by

$$\sigma_{ij} = 2\eta \dot{\epsilon}_{ij} + (\zeta - \eta) \dot{\epsilon}_{kk} \delta_{ij} - \frac{P \delta_{ij}}{2} \quad (4.26)$$

$$\text{where: } \dot{\epsilon}_{ij} = \frac{1}{2} \left(\frac{\partial v_i}{\partial x_j} + \frac{\partial v_j}{\partial x_i} \right) \quad (4.27)$$

$$\zeta = \frac{P_{\max}}{2\Delta} \quad (4.28)$$

$$\eta = \frac{\zeta}{e^2} \quad (4.29)$$

$$P_{\max} = P^* h \exp[-C(1-A)] \quad (4.30)$$

$$\Delta = \left\{ (\dot{\epsilon}_{11}^2 + \dot{\epsilon}_{22}^2) \left[1 + \left(\frac{1}{e^2} \right) \right] + \frac{4\dot{\epsilon}_{12}^2}{e^2} + 2\dot{\epsilon}_{11}\dot{\epsilon}_{22} \left(1 - \frac{1}{e^2} \right) \right\}^{\frac{1}{2}}. \quad (4.31)$$

C is an empirical constant equal to 20, h is the ice thickness, A is the compactness or percentage of area covered by ice in a given grid cell, and e is the ratio of the major to minor axis which equals 2 for the viscous plastic rheology case. P is the pressure of sea ice for any given location while P_{\max} is the local ice strength or maximum compressive pressure the ice can withstand. In both CAV and VP yielding occurs when $P = P_{\max}$. In VP yielding also occurs whenever the elliptic yield curve is reached, P_{\max} being one point on that curve. In VP, P is defined depending on the type of closure scheme used: concentric, replacement, or truncated (more details on this in Chapter 5.2.1).

Through an assumption of constant ice density, the conservation of mass for this study becomes a conservation of effective ice thickness (h) and ice compactness (A),

$$\frac{\partial h}{\partial t} + \nabla \bullet (\vec{v} h) = \text{Growth}_h + \text{Flux}_{\text{ocean}} \quad (4.32)$$

$$\frac{\partial A}{\partial t} + \nabla \bullet (\vec{v} A) = \text{Growth}_{\text{area}}. \quad (4.33)$$

In order to clearly determine which terms in these conservation equations are due to dynamics versus thermodynamics, we separate the variables as $h = h_1 + h_2$ and $A = A_1 + A_2$ where subscript 1 refers to the dynamic part and subscript 2 to the thermodynamic part. In doing so we get the following expanded set of equations,

$$\frac{\partial h_1}{\partial t} + \nabla \bullet (\vec{v} h) = 0 \quad (4.34)$$

$$\frac{\partial (h_2 + Y_{\text{neg}})}{\partial t} = \text{Growth}_{h_2} + \text{Flux}_{\text{ocean}} \quad (4.35)$$

$$\frac{\partial A_1}{\partial t} + \nabla \bullet (\vec{v} A) = 0 \quad (4.36)$$

$$\frac{\partial A_2}{\partial t} = \text{Growth}_{A_2}. \quad (4.37)$$

The total effective ice thickness (h) equals the sum of dynamic thickness (h_1) plus thermodynamic thickness (h_2) and correspondingly for ice compactness. Additionally the growth rate term has been separated into two components with the help of

$$\text{Growth}_h = \text{Growth}_{h_2} - \frac{\partial Y_{\text{neg}}}{\partial t}. \quad (4.38)$$

Y_{neg} is a bookkeeping variable used to store the difference between the excess amount of ice thermodynamically melted and the amount of ice actually available. This variable is defined by Hibler (1979) as “negative ice”.

The surface heat budget used to compute Growth_{h_2} and Growth_{A_2} is given by

$$0 = (1 - \text{albedo}) F_{\text{sw}} + F_{\text{lw}} + F_{\text{sh}} + F_{\text{lh}} - F_{\text{bb}} + F_{\text{ice}} \quad (4.39)$$

where:

$$F_{\text{sw}} = Q (1 - 0.6 \text{ clouds}^3) \quad (4.40)$$

$$F_{\text{lw}} = D_3 T_a^4 \{1 - 0.261 \exp[-7.77 \times 10^{-4} (273 - T_a)^2]\} \\ \times (1 + 0.275 \text{ clouds}) \quad (4.41)$$

$$F_{\text{sh}} = D_1 |\vec{V}_a| (T_a - T_i) \quad (4.42)$$

$$F_{\text{lh}} = D_2 |\vec{V}_a| (q_a[T_a] - q_i[T_i]) \quad (4.43)$$

$$F_{\text{bb}} = D_3 T_i^4 \quad (4.44)$$

$$F_{\text{ice}} = \frac{K}{H} (T_w - T_i). \quad (4.45)$$

F_{sw} and F_{lw} are the short and long wave radiation terms, F_{sh} and F_{lh} are the sensible and latent heat fluxes, F_{bb} is black body radiation emitted from the ice and F_{ice} is the

conductive heat flux through the ice. T is temperature (K), q the specific humidity, and subscripts a , i , and w stand for surface air, ice (upper ice surface) and water (lower ice surface) values, respectively. Coefficients D_1 and D_2 are respectively the bulk sensible and latent heat transfer coefficients, D_3 is the Stefan-Boltzmann constant times the surface emissivity, K is the ice conductivity, and H is the ice thickness.

This budget is the same as that used in Hibler (1979) and is well described in Hibler (1980) and Parkinson and Washington (1979). Two exceptions to their formulations are as follows. First, the short wave radiation is averaged over 6 hour time periods which requires a formulation other than the daily average solar flux used in Parkinson and Washington (1979). In this case S_0 is the solar constant, E_0 eccentricity correction (Eq. (1.2.1) from Iqbal, 1983), Q is the time averaged local radiation flux defined by

$$Q = \frac{S_0 E_0}{t_2 - t_1} \int_{t_1}^{t_2} \frac{\cos Z^2}{1.085 \cos Z + (2.7 + \cos Z) ea \times 10^{-5} + 0.1} dt \quad (4.46)$$

$$\cos Z = \sin \phi \sin \delta + \cos \phi \cos \delta \cos HA \quad (4.47)$$

S_0 is the solar constant equal to 1353 W/m^2 , E_0 the eccentricity correction given in Eq. (1.2.1) in Iqbal (1983), δ the declination in degrees as given in Eq. (1.3.1) in Iqbal (1983), HA is hour angle (15° times noon-local apparent time), and ea is the vapor pressure. Monthly average cloud cover is based on Parkinson and Washington's Figure (9) and shown in Figure (4.1).

Second, the surface specific humidity, q_i , is computed using an iterative formulation in the growth subroutine to find the surface ice temperature (Hibler, 1979),

$$q_i = \frac{\epsilon ea}{P_0} \quad (4.48)$$

$$ea = 611 \exp \left[\frac{a_n (T_{\text{ice}} - 273.16)}{T_{\text{ice}} - b_n} \right] \quad (4.49)$$

where ea is the vapor pressure, $\epsilon = 0.622$ (ratio of dry to vapor gas constants), $P_0 = 101325$ Pascals (reference pressure), and a_n and b_n represent the following empirical constants, for conditions over ice ($n = 1$), $a_1 = 21.8746$, $b_1 = 7.66$, and over open water ($n = 2$), $a_2 = 17.2694$, $b_2 = 35.86$. To compute the specific humidity at 10 meters above the ice, (q_a) is computed using the air temperature (T_a), relative humidity (RH) and this same specific heat equation such that T_a is used in place of T_{ice} and Eq. (4.48) is multiplied by RH , the relative humidity, which is

$$RH = \frac{ea[T_d]}{ea[T]} \quad (4.50)$$

where ea is the vapor pressure computed using Eq. (10) in Parkinson and Washington (1979). Dewpoint was not available through ECMWF, the dewpoint temperature (T_d) and air temperature (T) used for this calculation are from the climatological 30 year monthly mean data from Taljaard et al., (1969). A representative plot of this regional relative humidity distribution for the Weddell Sea region using this method is shown in Figure (4.2).

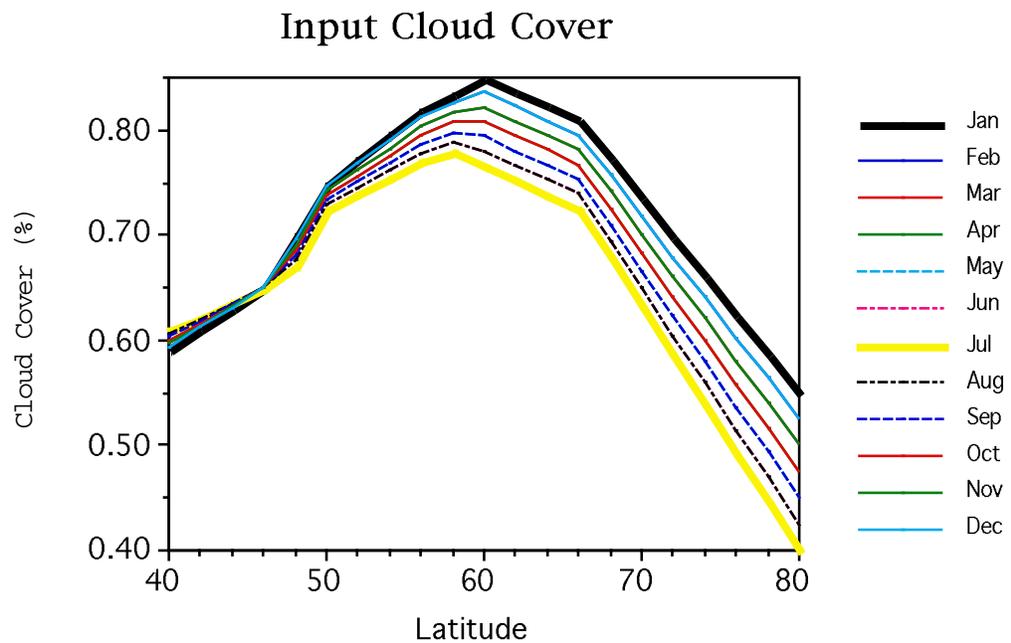


Figure 4.1: Estimate of monthly longitudinally averaged cloud cover interpolated from Figure (9) of Parkinson and Washington (1983).

Monthly Mean Relative Humidity Over Ice Surface - January

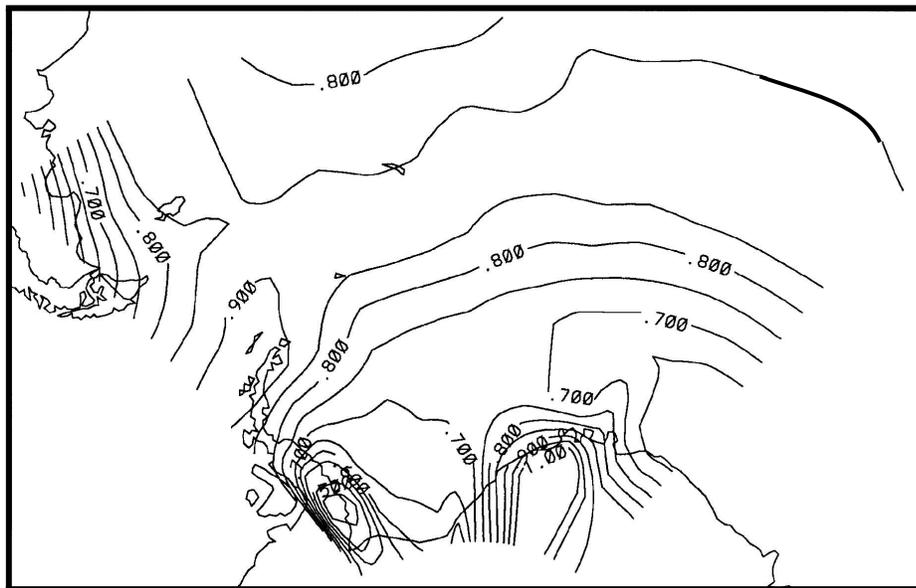


Figure 4.2: Estimate of regional relative humidity distribution based on 30 year monthly mean Taljaard et al., (1969) climatology data.

4.1.2 1D and 1.5D Sea Ice Models

In both Cartesian and spherical, 1D and 1.5D versions of CAV and VP have been constructed with a north-south orientation (i.e. latitudinally varying) in order to investigate north-south expansion and recession processes of sea ice in the Weddell Sea. The inertial term is responsible for introducing inertial oscillations to the system which are difficult to analyze in one direction, hence a steady state form will be used for these studies (i.e. no inertial term; $\frac{\partial}{\partial t} \Rightarrow 0$). The main difference between the 1D and 1.5D model is the inclusion of planetary rotation effects. The 1D model assumes no longitudinal effects (i.e. $u = 0$ and $\frac{\partial}{\partial x} = \frac{\partial}{\partial \lambda} = 0$) and no effects due to planetary rotation (i.e. θ_a, θ_w , and $f \Rightarrow 0$). The 1.5D model assumes no changes in longitudinal direction (i.e. $\frac{\partial}{\partial x} = \frac{\partial}{\partial \lambda} = 0$ while u is non-zero) but includes effects due to planetary rotation (i.e. θ_a, θ_w , and $f \neq 0$).

Incorporating these assumptions into the 2D formulations described above, the momentum balance for the 1D CAV formulation becomes

$$u = 0 \quad (4.51)$$

$$-\alpha v + \tau_j = -F_j. \quad (4.52)$$

Likewise the momentum balance for the 1.5D CAV formulation is

$$-\alpha u + \beta v + \tau_i = 0 \quad (4.53)$$

$$-\alpha v - \beta u + \tau_j = -F_j \quad (4.54)$$

which can be decoupled to

$$u = \frac{1}{\alpha^2 + \beta^2} [\beta \tau_j - \alpha \tau_i + \beta F_j] \quad (4.55)$$

$$v = \frac{1}{\alpha^2 + \beta^2} [\alpha \tau_j - \beta \tau_i + \alpha F_j]. \quad (4.56)$$

For both the 1D and 1.5D cases F_j is obtained from ∇P ($\mathbf{D}_j P$) obeying

$$\mathbf{D}_j(v + \tilde{v}) \geq 0 \iff P + \tilde{P} = 0 \quad (4.57)$$

$$\mathbf{D}_j(v + \tilde{v}) = 0 \iff 0 < P + \tilde{P} < P_{\max} \quad (4.58)$$

$$\mathbf{D}_j(v + \tilde{v}) \leq 0 \iff P + \tilde{P} = P_{\max} \quad (4.59)$$

where \mathbf{D}_j is the differential operator

$$\mathbf{D}_j = \frac{\partial}{\partial y} \hat{j} \quad (4.60)$$

in Cartesian coordinates and

$$\mathbf{D}_j = \frac{1}{R \cos \phi} \frac{\partial (\cos \phi)}{\partial \phi} \hat{j} \quad (4.61)$$

in spherical coordinates.

The 1D VP formulation in a north-south orientation is simply

$$u = 0 \quad (4.62)$$

$$-\alpha v + \tau_{\hat{j}} = -F_{\hat{j}}. \quad (4.63)$$

and 1.5D VP is

$$-\alpha u + \beta v + \tau_{\hat{i}} = -F_{\hat{i}} \quad (4.64)$$

$$-\alpha v - \beta u + \tau_{\hat{j}} = -F_{\hat{j}}. \quad (4.65)$$

The only difference at this stage between CAV and VP is the presence of an additional internal stress term in the \hat{i} direction ($F_{\hat{i}}$). This is due to the fact that the internal ice stresses are differentials of the stress tensor. In Cartesian coordinates these stresses are (as compared to Eqs. (4.16) and (4.26))

$$F_{\hat{i}} = \frac{\partial \sigma_{xy}}{\partial y} = \frac{\partial}{\partial y} \left(\eta \frac{\partial u}{\partial y} \right) \quad (4.66)$$

$$F_{\hat{j}} = \frac{\partial \sigma_{yy}}{\partial y} = \frac{\partial}{\partial y} \left((\zeta + \eta) \frac{\partial v}{\partial y} - \frac{P}{2} \right) \quad (4.67)$$

$$\Delta = \left\{ \left(1 + \frac{1}{e^2} \right) \left(\frac{\partial v}{\partial y} \right)^2 + \left(\frac{1}{e} \frac{\partial u}{\partial y} \right)^2 \right\}^{\frac{1}{2}}. \quad (4.68)$$

ζ , η , and P_{\max} are the same as for the 2D case.

A spherical version of VP is the same as above except for the internal ice force components. These quantities, as derived from the spherical 2D Zhang and Hibler (1995) formulation, are

$$F_{\lambda} = \frac{1}{R^2} \frac{\partial}{\partial \phi} \left\{ \eta \left(\frac{\partial u}{\partial \phi} + u \tan \phi \right) \right\} - \frac{2\eta \tan \phi}{R^2} \left(\frac{\partial u}{\partial \phi} + u \tan \phi \right) \quad (4.69)$$

$$F_{\phi} = \frac{1}{R^2} \frac{\partial}{\partial \phi} \left\{ (\zeta + \eta) \frac{\partial v}{\partial \phi} + (\eta - \zeta) v \tan \phi \right\} - \frac{2\eta \tan \phi}{R^2} \left(\frac{\partial v}{\partial \phi} + v \tan \phi \right) - \frac{1}{2R} \frac{\partial P}{\partial \phi}. \quad (4.70)$$

The corresponding strain-rate components are

$$\dot{e}_{\lambda\lambda} = -\frac{v \tan \phi}{R} \quad (4.71)$$

$$\dot{e}_{\phi\phi} = \frac{1}{R} \frac{\partial v}{\partial \phi} \quad (4.72)$$

$$\dot{e}_{\lambda\phi} = \frac{1}{2} \left(\frac{1}{R} \frac{\partial u}{\partial \phi} + \frac{u \tan \phi}{R} \right). \quad (4.73)$$

The only difference in 1D is that $u = 0$ so F_{λ} and $\dot{e}_{\lambda\phi}$ both also reduce to zero.

Finally, mass conservation for all of these cases reduces to

$$\frac{\partial h_1}{\partial t} + \mathbf{D}_j(v h) = 0 \quad (4.74)$$

$$\frac{\partial (h_2 + Y_{\text{neg}})}{\partial t} = \text{Growth}_h + \text{Flux}_{\text{ocean}} \quad (4.75)$$

$$\frac{\partial A_1}{\partial t} + \mathbf{D}_j(v A) = 0 \quad (4.76)$$

$$\frac{\partial A_2}{\partial t} = \text{Growth}_{\text{area}}. \quad (4.77)$$

4.2 Boundary and Initial Conditions

Boundary conditions for the 1D and 1.5D models are imposed at the first and last grid cells. Dirichlet conditions are specified at these boundaries such that values of ice velocity, thickness and compactness are set to zero. For the 2D models, Cartesian 50 and 200km resolution grids are used. A geographical layout of the area is shown in Figure (4.3) and 50 and 200 km grids are shown in Figures (4.4 and 4.5), respectively. Land point locations have Dirichlet boundary conditions specified in the same manner as in 1D and 1.5D. At outflow points (box plus cross), located along east, west and north boundaries of the grid, outflow conditions are imposed by destroying ice in these locations at the end of each time step. The inclined outflow region in the southeast corner of the grid is due to the termination of atmospheric input fields near that location. The grid cell configurations are shown in Figure (4.6).

Initial conditions include zeroing all arrays and setting all grid cells to an initial ice thickness of 1 meter, compactness of 100% and ice temperature just below freezing ($T_{\text{ice}} = 273\text{K}$). Input fields for the ocean are read in once at the beginning while atmospheric input fields are read in and interpolated spatially and temporally at the beginning of each time step using the interpolation routine described in Appendix (C.4). For VP an initial ice velocity must be computed using the dynamics routine in predictor mode with pre-set values of $\zeta = 1 \times 10^{11}h$ and $\eta = \zeta/4$. A spin-up time of one year using 1991 atmospheric forcing fields allows the system to thermodynamically equilibrate to the input fields and to remove any dependency on the initial conditions.

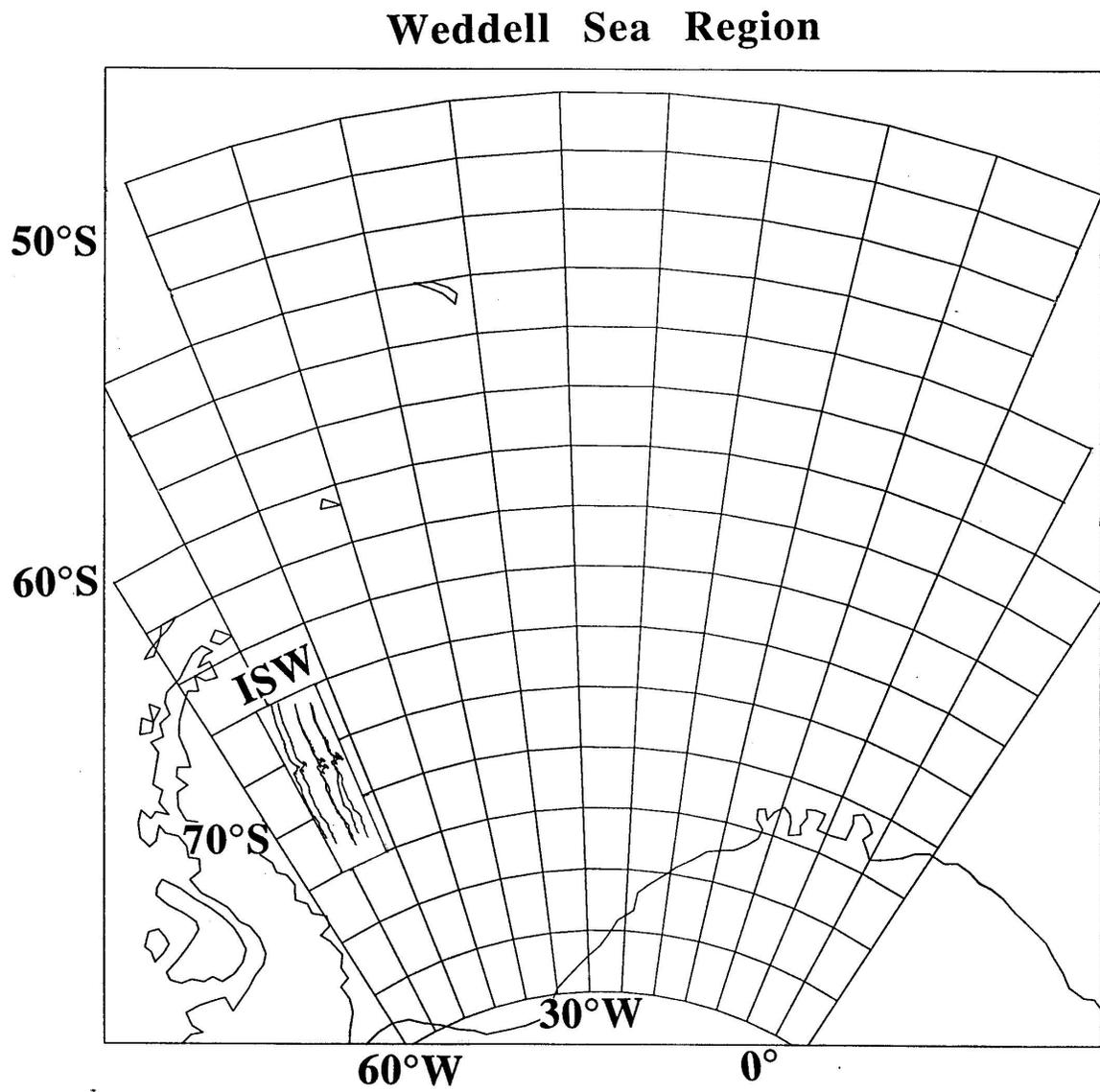


Figure 4.3: Geographical layout of the regional study area.

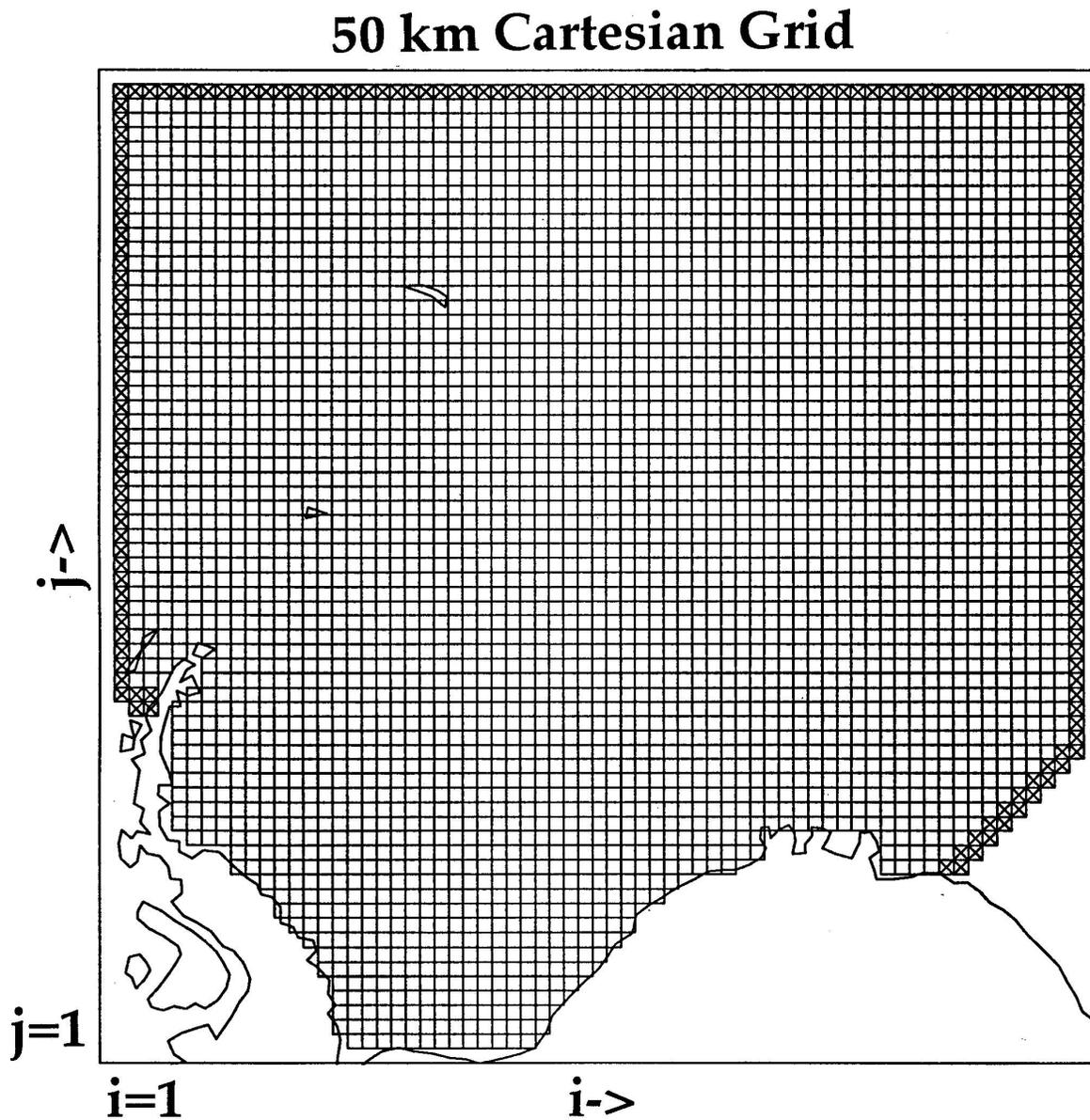


Figure 4.4: Regional study grid at 50 km resolution in Cartesian coordinates. Areas with no boxes are land points, only boxes are active ice points and boxes with crosses are outflow points.

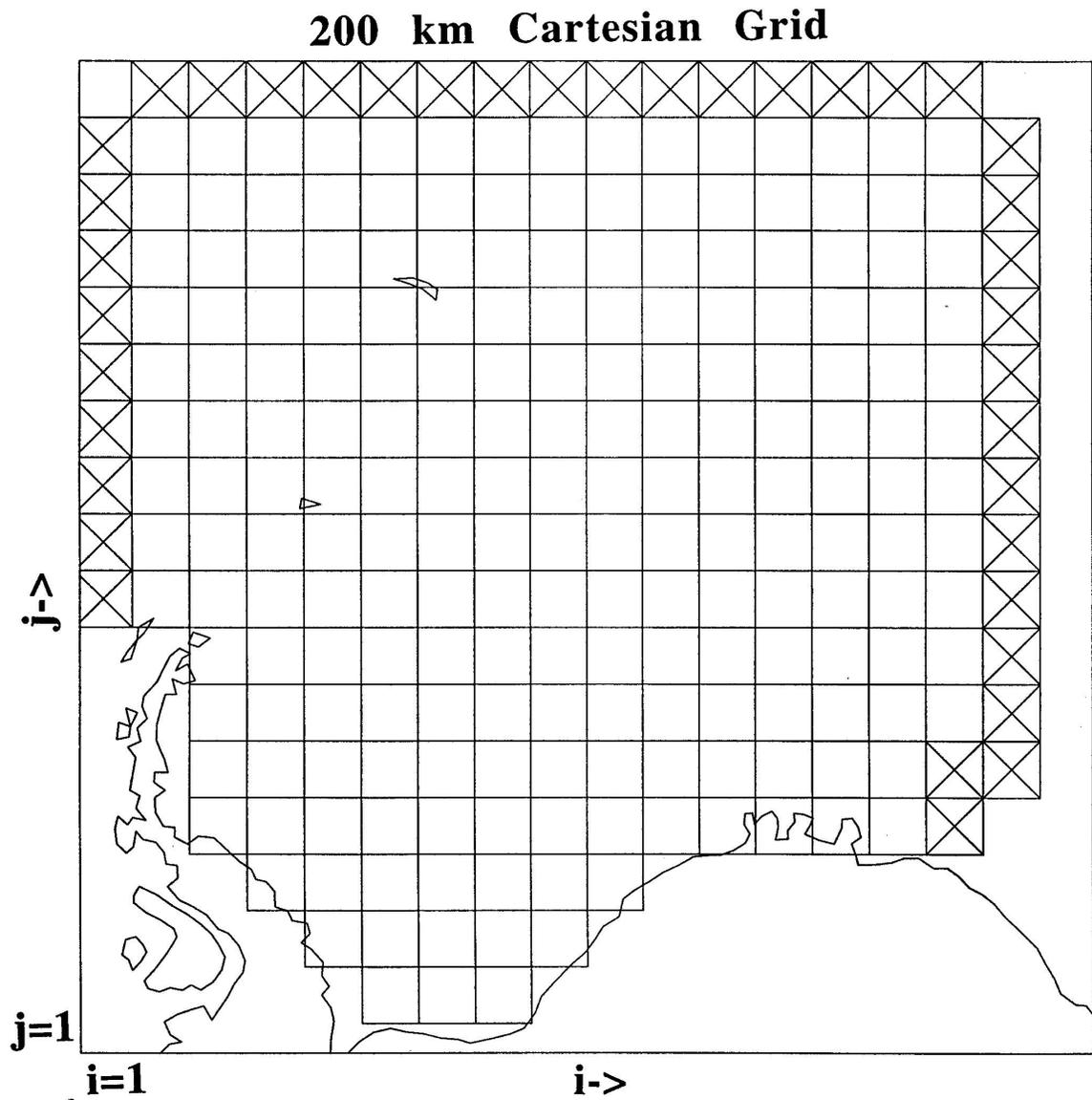


Figure 4.5: Regional study grid at 200 km resolution in Cartesian coordinates. Areas with no boxes are land points, only boxes are active ice points and boxes with crosses are outflow points.

Grid Cell Configuration

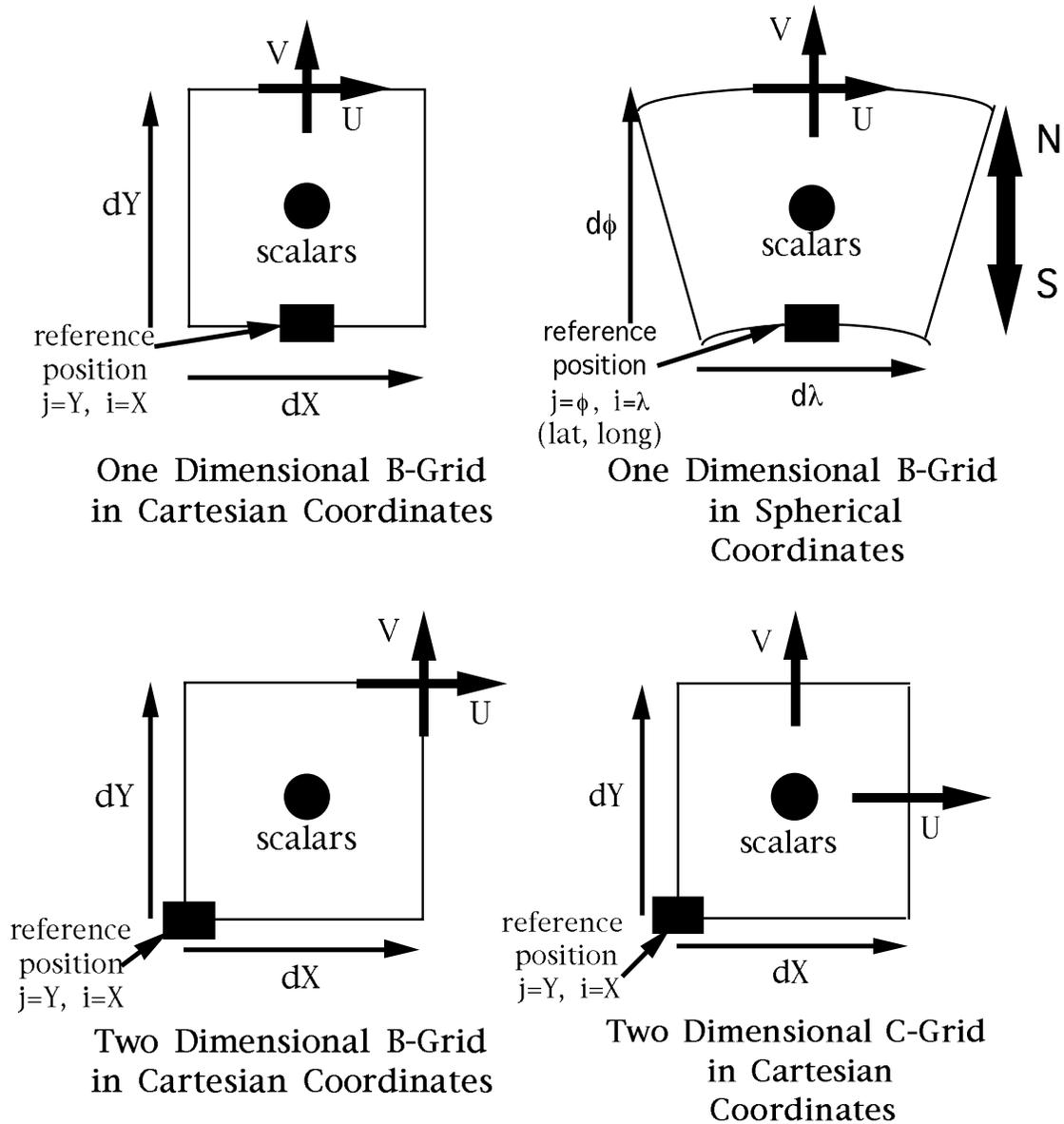


Figure 4.6: Grid cell configurations for all models in the hierarchy.

4.3 Input and Output Fields

All codes in the hierarchy use Arakawa B-grid configured atmospheric and oceanic input from preprocessed analysis fields. A linear weighted averaging scheme (Appendix C.4) is used to interpolate this B-grid information to the one dimensional fields and to C-grid for the 2D CAV code. Output includes B-grid fields (averaged from C-grid in CAV) of thickness, compactness, and ice velocities which are generated and output at the end of selected time steps. In addition properties such as velocity, stress and strain-rate are extracted from special regions as needed. Plots of these fields are generated using Northware Graf and NCAR graphics. Specifics on the atmospheric and oceanic input fields are described below.

4.3.1 Atmospheric Forcing Fields

European Center for Mid-range Weather Forecasting (ECMWF) analysis fields of 4 times daily 2 meter air temperature and sea-level pressure for the years 1991 and 1992 were made available through Christopher Kottmeier from Alfred Wegener Institute in Bremerhaven, Germany. These input fields have a resolution of 1.125° by 1.125° and extend from 79.875°S , 69.750°W to 45.000°S , 10.125°E . Information on ECMWF data is available through ECMWF Meteorological Bulletin, Research Manual 1, ECMWF Data Assimilation, 3/92.

Using these analysis fields and the heat budget equations in Section (4.1.1), five types of atmospheric input are entered into the model at every time step: long wave radiation, short wave radiation, sensible heat flux, latent heat flux, and atmospheric pressure. These inputs have been averaged to monthly (12 sets of input per year), daily (366 per year) and subdaily ($366 \cdot 4$ per year) fields which are read into the models as needed, and interpolated from the input field grid to specific model grids using the interpolation routine in Appendix (C.4). Geostrophic wind velocity is computed from the spatially interpolated atmospheric pressure (P_a in Pascals) using the geostrophic approximation

$$\text{Cartesian: } U_a = -\frac{\partial P_a}{\partial x} \quad (4.78)$$

$$V_a = \frac{\partial P_a}{\partial y} \quad (4.79)$$

$$\text{spherical: } U_a = -\frac{1}{\rho_a f R} \frac{\partial P_a}{\partial \phi} \quad (4.80)$$

$$V_a = \frac{1}{\rho_a f R \cos \phi} \frac{\partial P_a}{\partial \lambda}. \quad (4.81)$$

Computing velocity after spatial interpolation precludes the need for non-orthogonal transformation of vector components for 2D Cartesian models. Once all this is done, fields are interpolated temporally to match whatever time step is specified. Since the year 1992 is a leap year it is handled as such.

4.3.2 Oceanic Forcing Fields

Three types of oceanic input are needed by the ice model: ocean velocity, ocean heat flux, and mixed layer depth. Since this is a dynamic study the thermodynamic quantities of heat flux and mixed layer depth are not critical but reasonable estimates are needed. The mixed layer depth is used in the thermodynamics routine for heat storage. A deeper mixed layer stores more heat than a shallow one, as does a warmer mixed layer. This heat is used to melt ice or retard ice growth. The literature (e.g. Gordon and Huber, 1990) shows a range of winter mixed layer depths varying between 60 and 150 meters. In winter, warm deep water regimes have shallower mixed layers but greater deep to mixed layer heat transfer, while cold deep water regimes and areas like Maud Rise have deeper mixed layers. In the summer when stratification is strongest, the depth is considerably less (10 to 30m), as is the heat flux. We will include this information into the models in the following manner. Unless otherwise specified a constant mixed layer depth of 60m will be used for most studies. Cases involving a variable mixed layer will include a spatially constant but temporally varying mixed layer depth using sinusoidal interpolation between 20 and 100 meters as shown in the lower panel of Figure (4.7). For oceanic heat fluxes, estimates from ISW measurements (Lytle and Ackley, in press) show about 7 W/m^2 in the Western Weddell (about 60°W to 40°W) in winter. From Gordon and Huber (1990) winter heat flux values below the ice of about 37 W/m^2 is estimated for the Eastern Weddell (about 20°W to 10°E) south of 62.5°S not including the anomalous conditions over Maud Rise. In the summer an average value is about 2 W/m^2 for the entire region is typical (Parkinson and Washington, 1979). Using these values with linear interpolation in between, we get a longitudinal heat flux distribution as shown in Figure (4.7). For temporal interpolation between these values, the same sinusoidal interpolation method is used as for the mixed layer depth.

Ocean currents are important in this study as seen from the ISW field measurements in Chapter 3. Unfortunately, observational fields of ocean current for the Weddell Sea are, at the very least, difficult to acquire. We know there is a definite circulation pattern in this region including a very strong circumpolar current between 50° and 60°S and a Weddell Sea gyre circulation in the Weddell Basin. In order to provide some type of general ocean circulation field the following composite was made. First the 0-1000m steric height anomaly from this region was hand digitized from Plate 56 in Olbers' et al. (1992) Southern Ocean Atlas. Because this area is heavily lacking in winter measurements these data have a definitive summer bias. From these steric height anomalies (H_s), geostrophic flow was computed using

$$U_w = -\frac{g}{fR} \frac{\partial H_s}{\partial \phi} \quad (4.82)$$

$$V_w = \frac{g}{fR \cos \phi} \frac{\partial H_s}{\partial \lambda} \quad (4.83)$$

This method provides a reasonable circulation when compared to descriptions in the literature (Foldvik et al. 1988, Foldvik et al. 1990, Gordon, 1970). The contour information, however, is sparse around the edges of the Weddell gyre so additional information is needed there. From the ISW results presented in Chapter 3 the current meter findings by Muench et al. (1992) show a 5 cm/s northward 50 m average ocean current

in a primarily barotropic field at the western most site of the array. This decreases to 1 cm/s at the eastern most site. Matching these descriptions and their locations to the ocean grid we apply this information to produce a western boundary current along the western edge of the Weddell gyre. At the eastern edge of the gyre we know the current must close the gyre in a broad slow current. Subjective corrections to the ocean velocity field were made to ensure this and to eliminate any unusual features. An overall check of this composite was made by computing the normal transport at the perimeter of the field at the three inflow/outflow points. 1000m was chosen as the integrated depth since this is the depth the steric height anomaly data is computed for. Using these results, computed transports across the Drake passage (western inflow region between South America and Weddell Peninsula) are $97 \times 10^6 \text{ m}^3/\text{s}$ (or Sverdrups) which is quite reasonable considering estimates for the Drake passage from surface to bottom are around $130 \times 10^6 \text{ m}^3/\text{s}$ (Gordon, 1970). To the north about $25 \times 10^6 \text{ m}^3/\text{s}$ are moving southward and about $123 \times 10^6 \text{ m}^3/\text{s}$ are flowing out to the east. The sum over these boundaries is nearly in balance which provides reasonable inflow and outflow from the system with respect to ocean circulation. Figure (4.8) shows the ocean current composite in its final form.

Once the oceanic velocity field is created at the above specified grid, the field is put through a preprocessing interpolation routine (Appendix C.4) to obtain the field for each grid configuration. For the 2D Cartesian models, the velocities were additionally subjected to a non-orthogonal transform (Appendix C.3) to correct the orientation of the vectors from spherical to Cartesian coordinates. The results of that interpolation for the 50 km 2D Cartesian grid is shown in Figure (4.9).

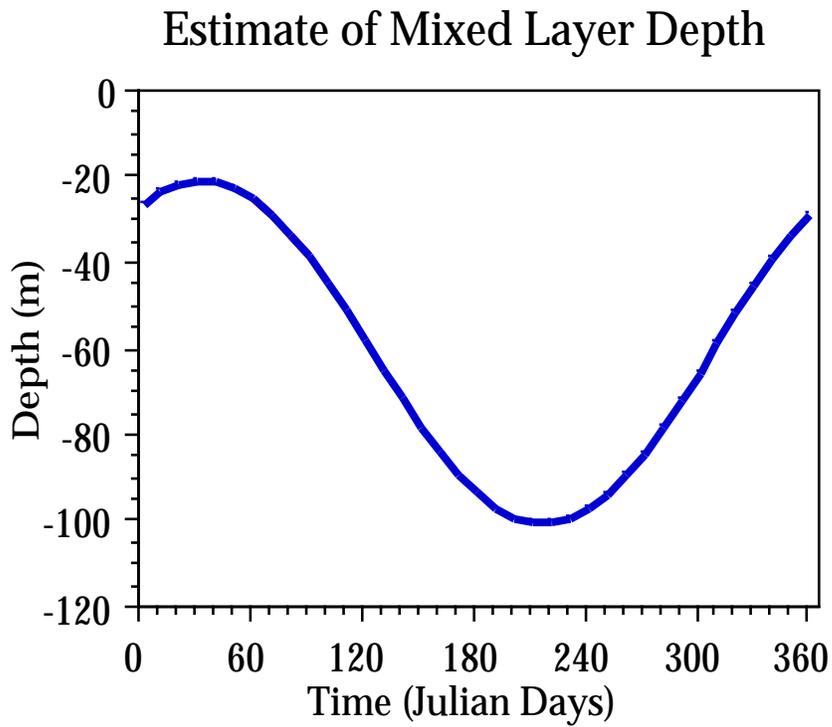
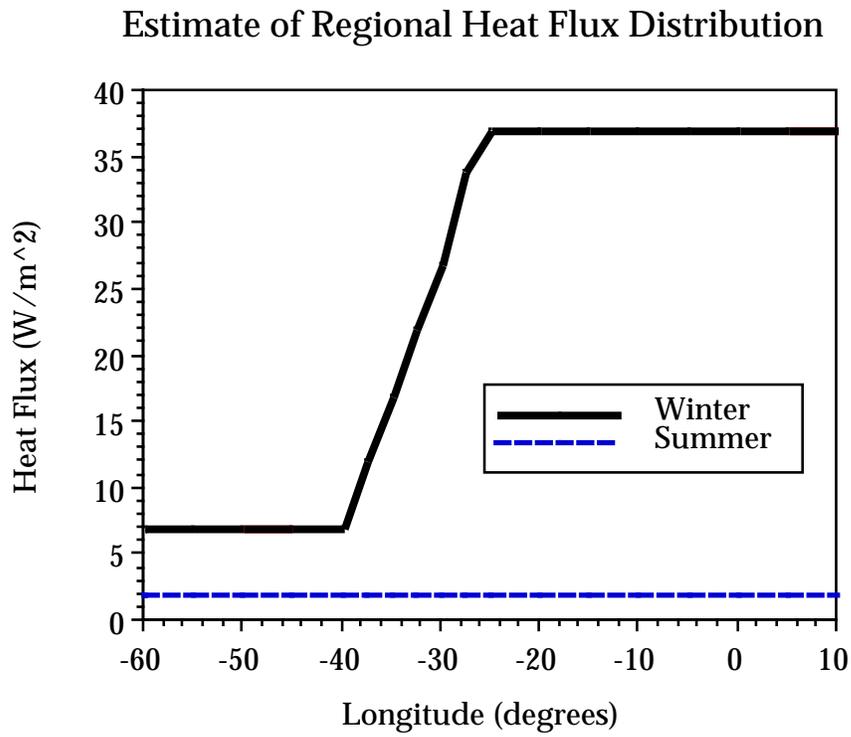


Figure 4.7: Estimated oceanic heat flux distribution for Weddell Sea area and average seasonal mixed layer depth.

Geostrophic Ocean Current Composite

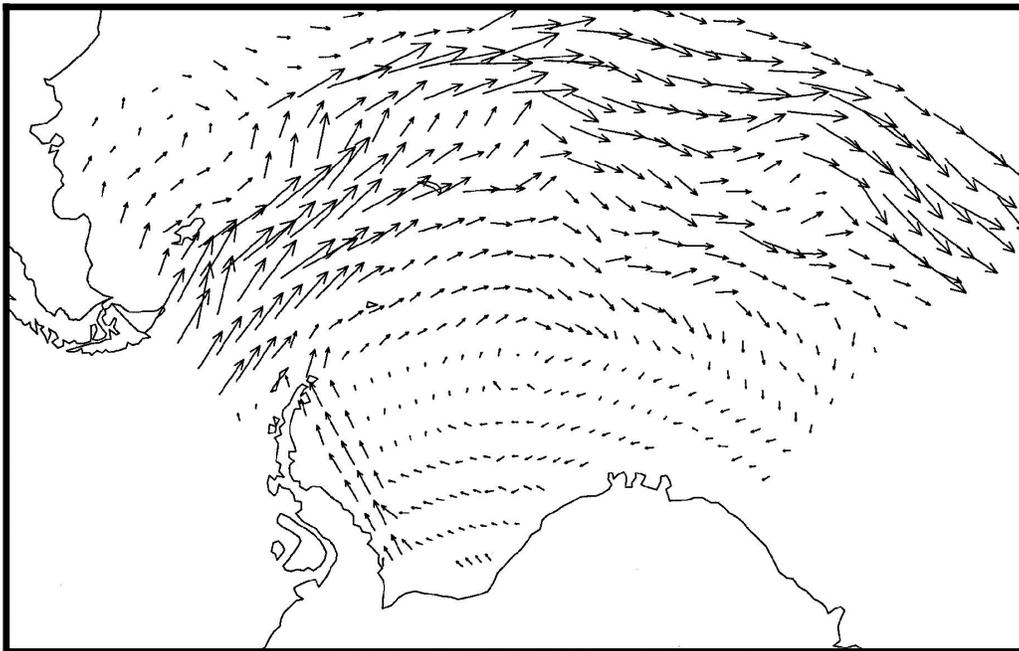
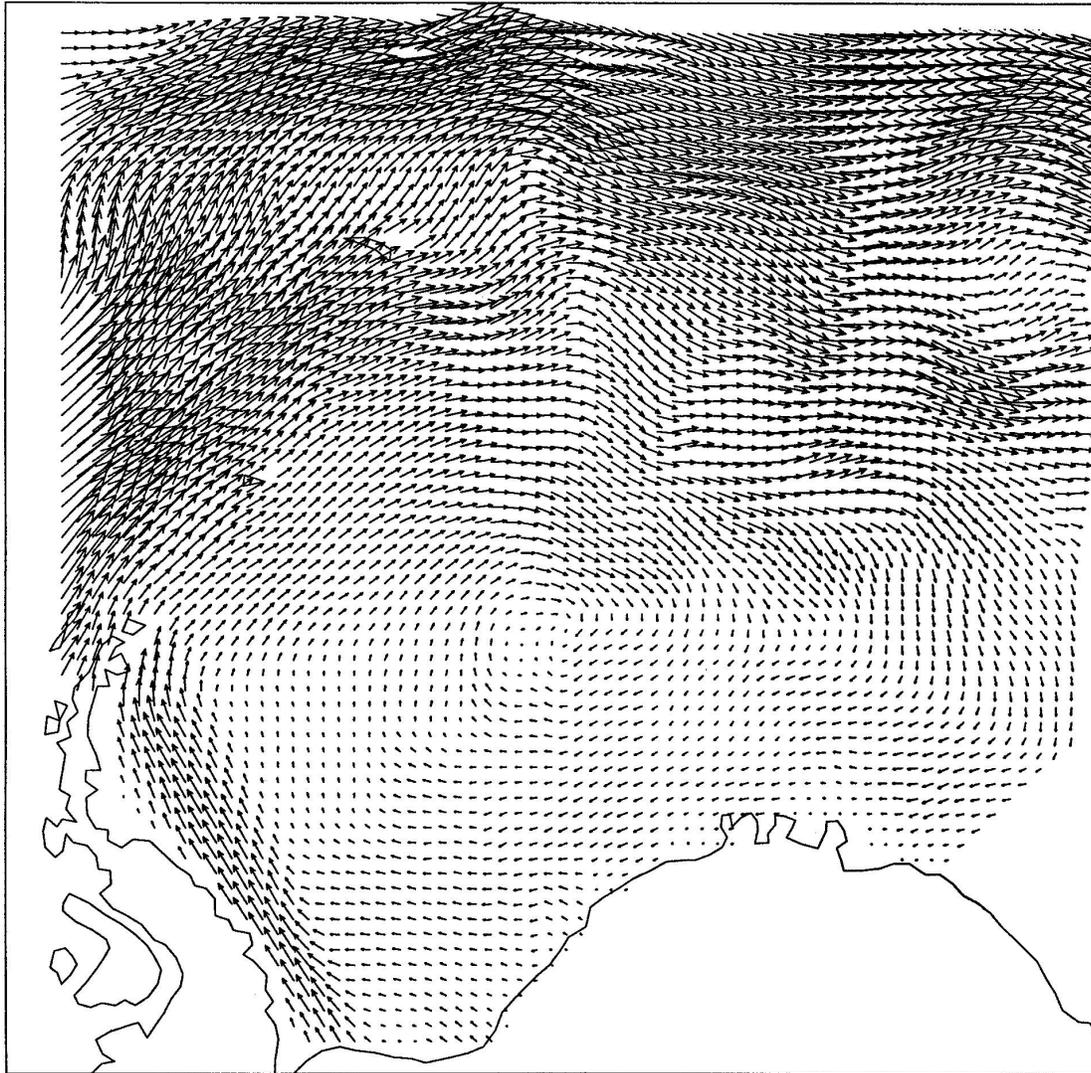


Figure 4.8: Composite of ocean circulation for Weddell Sea region based on steric height anomaly contours from Plate 56 in Olbers et al. (1992), ISW current measurements, and subjective interpretation.

Interpolated 50 km Ocean Current Field



$.200E+00$
MAXIMUM VECTOR

Figure 4.9: Ocean circulation for 50 km 2D models as interpolated from the ocean velocity field composite in Figure (4.8).

4.4 Summary of Numerical Scheme

The sea ice equations are solved numerically using a three step finite difference procedure originally designed by Hibler (1979). The basic structure in all cases is as follows.

Pseudo Code for Sea Ice Models

- Initialize system
- For each time step do
 - Setup input fields and time step conditions
 - **Step 1:** Do while not done dynamics
 - * Begin Predictor phase
 - **CAV Step i:** Solve force balance
 - **CAV Step ii:** Solve for pressure
 - **VPStep i:** Compute stress and setup force balance terms
 - **VPStep ii:** Solve force balance
 - * Begin Corrector phase
 - **CAV Step i:** Solve force balance
 - **CAV Step ii:** Solve for pressure
 - **VPStep i:** Compute stress and setup force balance terms
 - **VPStep ii:** Solve force balance
 - * Plastic solution reached predictor-corrector done
 - * **CAV Step i:** Solve force balance
 - * **VP Step i:** Compute stress and setup force balance terms
 - **Step 2:** Perform advection computation
 - **Step 3:** Perform thermodynamic growth computation
 - Output data
- Go to next time step

Within the main time loop, Step 1 solves for the momentum equations and ice rheology using a pseudo time step predictor-corrector iterative loop. Then two subdivisions of the mass conservation equations are solved in the remaining two parts as an advective routine in Step 2, using Eqs. (4.34) and (4.36), and a thermodynamic routine in Step 3, using Eqs. (4.35) and (4.37). Since most of the numerical routines used in this study have been designed by someone other than the author and since the numerical development of these codes is not the focus of this study, a detailed description of the numerical techniques will not be presented here. Instead, a summary of the methods used in each model and the main references will be given.

2D CAV was developed by Greg Flato (Flato and Hibler, 1990 and 1992) for both Cartesian and spherical coordinates for the Arctic basin at low resolution (200 km) and monthly mean forcing. Within its main time loop, the code solves the momentum balance through a relaxation procedure (Step i) for an assumed ice pressure. Then, the pressure and divergence of the field are checked against the conditional criteria in the constitutive

relation (Eqs. 4.21 to 4.23) based on the computed ice velocity field (Step ii). Corrections to the pressure (\tilde{P}) and velocity ($\tilde{\mathbf{v}}$) are made incrementally via a relaxation technique until all locations in the field meet the constitutive requirements. Iterating around this sequence of force balance and relaxation in a predictor-corrector sequence, the results converge to a mutual solution of u , v , and P satisfying both momentum balance and ice rheology constraints (i.e. achieves a plastic solution). The resultant ice velocity field is used in an upstream differencing advection scheme (see Flato and Hibler, 1990). Once the spatial adjustments to the mass balance are met through advection, the thermodynamic routine (Step 3) is used to compute the local heat budget and ice growth as developed by Hibler (1979). 2D CAV is formulated in an Arakawa C-grid (Figure 4.6) and to date can not be formulated in the B-grid due to an instability in the upstream differencing advection scheme in B-grid (Flato and Hibler, 1990). Averaging to the B-grid is done, however, at each time step for input and output information.

1D and 1.5D Cartesian and spherical versions of CAV were constructed by the author. They are nearly the same as the 2D numerical scheme except for the following changes. First, since the codes are one dimensional, the differentials in the force balance, ice rheology and advective routines are reduced to $\frac{\partial}{\partial t}$ and $\frac{\partial}{\partial y}$ components only (i.e. all Δx terms $\Rightarrow 0$). Additionally, an one dimensional Arakawa B-grid can be used without instability in the upstream differencing routine (i.e. 1D B-grid has alternating locations of scalar ($j+1/2$) and vector ($j+1$) quantities). Finally, since the momentum equations are significantly simpler (Eqs. 4.52, 4.55, and 4.56), a direct solution rather than a relaxation solution is used to solve the force balance (Step i).

VP code was originally developed by Hibler (1979) at low resolution (200 km) for the Arctic region. There are four fundamental differences between this numerical construction and that of CAV. First in Step 1, the ice rheology is more complicated but can be explicitly calculated from previous velocities rather than through a relaxation method. Second, because of the complex rheology, a relaxation procedure must be performed to solve for the force balance and ice rheology combined. Step i sets up the force balance terms and solves for the stresses, strain-rates, bulk and shear viscosities, and pressure using velocities from the previous time step. Then in Step ii the force balance is solved through a relaxation procedure. A recently improved version of the relaxation routine by Zhang and Hibler (1995) for high resolution (40km) studies has been employed. This solves for the force balance by decoupling the u and v terms and using a tridiagonal matrix solver (Thomas Algorithm). The third difference is in Step 2 in the advection scheme which uses four point finite differencing with diffusion (Hibler, 1979). The final difference is the numerical grid which is an Arakawa B-grid. The thermodynamics routine is identical to that in CAV. 1D and 1.5D versions constructed by the author use the same 1D B-grid as CAV and are capable of using either advection scheme (diffusion or upstream differencing). Upstream differencing is used in all one dimensional codes to avoid differences attributable to advection schemes.

A number of modifications had to be made to the above codes in order to investigate the Weddell Sea. First, all the codes were reconfigured into a common format so that, aside from the differences stated above, the codes have the same structural setup, initial conditions, boundary conditions, and adjustable parameters (listed in Tables 4.1 and 4.2). Second, the codes were adjusted for the Southern Hemisphere by changing the Coriolis

term and the water and air drag turning angles to negative values (i.e. negative latitudes). Third, the codes were redesigned to run at different resolution sizes (12.5 km to 222 km). This included an adjustment in the number of grid cells, resolution of the grid size, and subdaily time stepping needed for stable advection. Finally, the Coriolis parameter was explicitly defined at each grid cell; constant f plane was assumed in original Arctic codes. The field of interest ranges from 50° to 80°S where Coriolis varies considerably compared to Arctic. In spherical coordinates this is a very straightforward change;

$$f = 2\Omega \sin \phi_0 = \text{Constant} \quad (4.84)$$

is changed to

$$f = 2\Omega \sin \phi = \text{dependent on } \phi. \quad (4.85)$$

In Cartesian coordinates, the transformation is more complicated because the geographic latitude needs to be determined for the selected Cartesian grid. Since the conservation of area is so important for this type of transformation a Lambert equivalent (equal area) projection is used to determine the latitude position of the Cartesian grid points (Appendix C.2) followed by the computation in Eq. (4.85).

4.4.1 VP Numerical Scheme in Spherical Coordinates

To solve the spherical 1.5D VP equations numerically we begin by forming the force balance from Eqs. (4.64), (4.65), (4.69), and (4.70) such that the desired unknowns, u for λ and v for ϕ , are on the left hand side of the equations,

$$\begin{aligned} \alpha u - \frac{1}{R^2} \frac{\partial}{\partial \phi} \left\{ \eta \left(\frac{\partial u}{\partial \phi} + u \tan \phi \right) \right\} + \frac{2\eta \tan \phi}{R^2} \left(\frac{\partial u}{\partial \phi} + u \tan \phi \right) \\ = \tau_\lambda + \beta v \end{aligned} \quad (4.86)$$

$$\begin{aligned} \alpha v - \frac{1}{R^2} \frac{\partial}{\partial \phi} \left\{ (\zeta + \eta) \frac{\partial v}{\partial \phi} + (\eta - \zeta) v \tan \phi \right\} + \frac{2\eta \tan \phi}{R^2} \left(\frac{\partial v}{\partial \phi} + v \tan \phi \right) \\ = \tau_\phi - \beta u - \frac{1}{2R} \frac{\partial P}{\partial \phi}. \end{aligned} \quad (4.87)$$

Looking at the $\hat{\phi}$ component we rearrange terms to

$$\begin{aligned} v \left(\alpha + \frac{1}{R^2} \frac{\partial \{ (\zeta - \eta) \tan \phi \}}{\partial \phi} + \frac{2\eta \tan^2 \phi}{R^2} \right) - \frac{1}{R^2} \frac{\partial (\zeta + \eta)}{\partial \phi} \frac{\partial v}{\partial \phi} \\ + \frac{(\zeta + \eta) \tan \phi}{R^2} \frac{\partial v}{\partial \phi} - \frac{(\zeta + \eta)}{R^2} \frac{\partial^2 v}{\partial \phi^2} = \text{right hand side} \end{aligned} \quad (4.88)$$

Noting that

$$\begin{aligned} \frac{(\zeta + \eta) \tan \phi}{R^2} \frac{\partial v}{\partial \phi} - \frac{(\zeta + \eta)}{R^2} \frac{\partial^2 v}{\partial \phi^2} = \\ - \frac{(\zeta + \eta)}{R^2} \left(\frac{1}{\cos \phi} \frac{\partial \cos \phi}{\partial \phi} \frac{\partial v}{\partial \phi} + \frac{\partial^2 v}{\partial \phi^2} \right) = \\ - \frac{(\zeta + \eta)}{R^2 \cos \phi} \frac{\partial}{\partial \phi} \left(\cos \phi \frac{\partial v}{\partial \phi} \right), \end{aligned} \quad (4.89)$$

we invoke the following finite differencing scheme,

$$BT_\phi = \frac{\zeta_{j+1} + \eta_{j+1} + \zeta_j + \eta_j}{2} \quad (4.90)$$

$$DT_\phi = \zeta_{j+1} + \eta_{j+1} - \zeta_j - \eta_j \quad (4.91)$$

$$BT_\lambda = \frac{\eta_{j+1} + \eta_j}{2} \quad (4.92)$$

$$DT_\lambda = \eta_{j+1} - \eta_j \quad (4.93)$$

$$\frac{\partial \zeta}{\partial \phi} \Rightarrow \frac{\zeta_{j+1} - \zeta_j}{\Delta \phi} \quad (4.94)$$

$$\frac{\partial^2 v}{\partial \phi^2} \Rightarrow \frac{v_{j+1} - 2v_j + v_{j-1}}{\Delta \phi^2} \quad (4.95)$$

$$\text{Eq. (4.89)} \Rightarrow -\frac{BT_\phi}{R^2 \cos \phi} \frac{\cos \phi_{s_{j+1}}(v_{j+1} - v_j) - \cos \phi_{s_j}(v_j - v_{j-1})}{\Delta \phi^2} \quad (4.96)$$

The subscript s_j denotes the j th scalar point (e.g. ϕ_{s_j}). Vectors are located plus a half grid cell from this point at the vector location (e.g. ϕ_{v_j}). Rearranging Eqs. (4.86) and (4.86) one last time we form the relation

$$A_\lambda u_{j-1} + B_\lambda u_j + C_\lambda u_{j+1} = \tau_{\lambda_j} + \beta_j v_j \quad (4.97)$$

$$A_\phi v_{j-1} + B_\phi v_j + C_\phi v_{j+1} = \tau_{\phi_j} - \beta_j u_j - \frac{1}{2R} \frac{P_{j+1} - P_j}{\Delta \phi} \quad (4.98)$$

where

$$A_\lambda = \frac{DT_\lambda}{2R^2 \Delta \phi^2} - \frac{BT_\lambda \cos \phi_{s_j}}{R^2 \cos \phi_{v_j} \Delta \phi^2} \quad (4.99)$$

$$B_\lambda = \alpha + \frac{\eta_j \tan \phi_{s_j} - \eta_{j+1} \tan \phi_{s_{j+1}}}{R^2 \Delta \phi} + \frac{2BT_\lambda \tan^2 \phi_{v_j}}{R^2} + \frac{4BT_\lambda}{R^2 \Delta \phi^2} \quad (4.100)$$

$$C_\lambda = -\frac{DT_\lambda}{2R^2 \Delta \phi^2} - \frac{BT_\lambda \cos \phi_{s_j}}{R^2 \Delta \phi^2 \cos \phi_{v_j}} \quad (4.101)$$

$$A_\phi = \frac{DT_\phi}{2R^2 \Delta \phi^2} - \frac{BT_\phi \cos \phi_{s_j}}{R^2 \cos \phi_{v_j} \Delta \phi^2} \quad (4.102)$$

$$B_\phi = \alpha + \frac{(\zeta_{j+1} - \eta_{j+1}) \tan \phi_{s_{j+1}} - (\zeta_j - \eta_j) \tan \phi_{s_j}}{R^2 \Delta \phi} \quad (4.103)$$

$$+ \frac{2BT_\lambda \tan^2 \phi_{v_j}}{R^2} + \frac{4BT_\phi}{R^2 \Delta \phi^2}$$

$$C_\phi = -\frac{DT_\phi}{2R^2 \Delta \phi^2} - \frac{BT_\phi \cos \phi_{s_j}}{R^2 \cos \phi_{v_j} \Delta \phi^2}. \quad (4.104)$$

This numerical arrangement is similar to the one described in Zhang and Hibler (1995) and solved using their Thomas Algorithm matrix solver with terms on the right hand side of each equation being known; A , B , and C terms forming the components of a tridiagonal matrix; and u_j and v_j terms forming the unknown vectors to be solved for. The main difference between this and the Zhang and Hibler (1995) method is that both u and v must be solved in the \hat{j} direction.

4.5 Testing of Numerical Scheme

Test runs on the original codes are well documented and therefore need not be repeated here (see Flato and Hibler, 1990 & 1992; Hibler, 1979; and Zhang and Hibler, 1995). In the reconfigured codes, test cases in simple grids (outer grid cell boundaries only) were run to confirm that the changes discussed above were correctly implemented. Among these was a check of the numerical stability which was found to be considerably more sensitive at higher resolutions in the momentum balance and the advection routines than for the original codes.

In the momentum balance the relaxation method reaches a solution through an iterative convergence between updated ice velocities (i.e. convergence when $u_j^{k+1} - u_j^k \leq \text{tolerance}$ for $k = \text{iteration time step}$). For these codes a test to determine an acceptable tolerance can be made by running the codes under the following conditions: no thermodynamics, no advection, no ocean currents, and constant uniform wind velocity. In this case, the momentum balance is the only active part of the code. The momentum balance will progress through a series of time steps until an equilibrium has been established between the imposed wind forcing and the ice responses of velocity and stress (i.e. kinetic energy becomes constant).

Tests of this type were conducted on all codes in the hierarchy to check for conservation of total kinetic energy in each system. One representative test from each code type (VP vs. CAV) is presented in Figures (4.10) and (4.11). These runs show that at low resolution energy for tolerances as large as 10^{-5} (original codes' tolerance) converge to the same energy levels as the 10^{-7} tolerance case within a few plastic solution time steps. At higher resolution, energy for tolerances of 10^{-5} do not even come close to the 10^{-7} tolerance cases even after 365 days of running to full plastic solution. This same result occurs in both CAV and VP cases. Based on these results, decreasing the tolerance to 10^{-7} is needed in the momentum balance relaxation routines for high resolution runs to ensure numerical convergence and stability.

2D Cartesian Cavitating Fluid

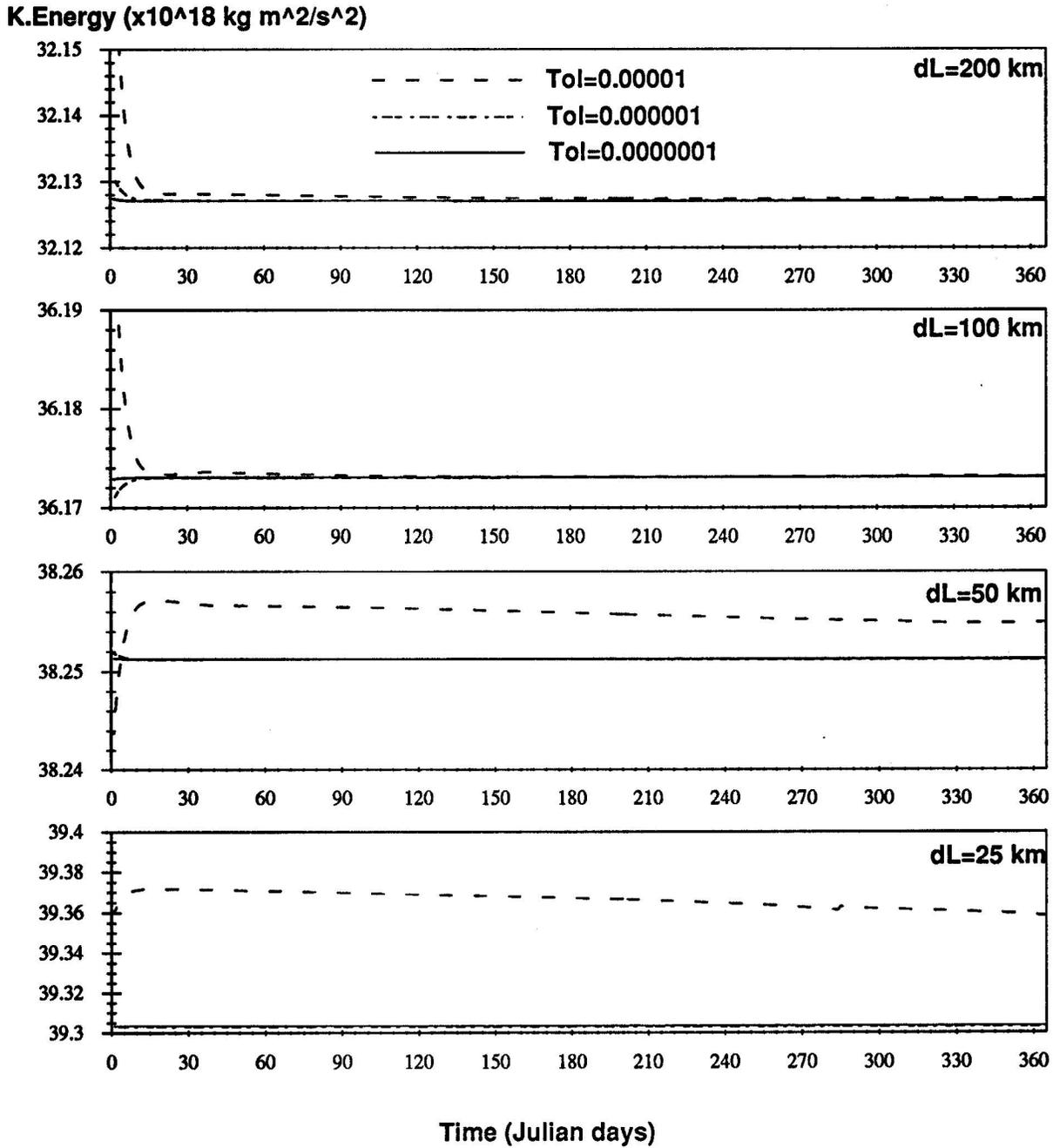


Figure 4.10: Kinetic energy during full plastic solution time steps for CAV.

2D Cartesian VP Replacement Method

K.Energy (x10¹⁸ kg m²/s²)

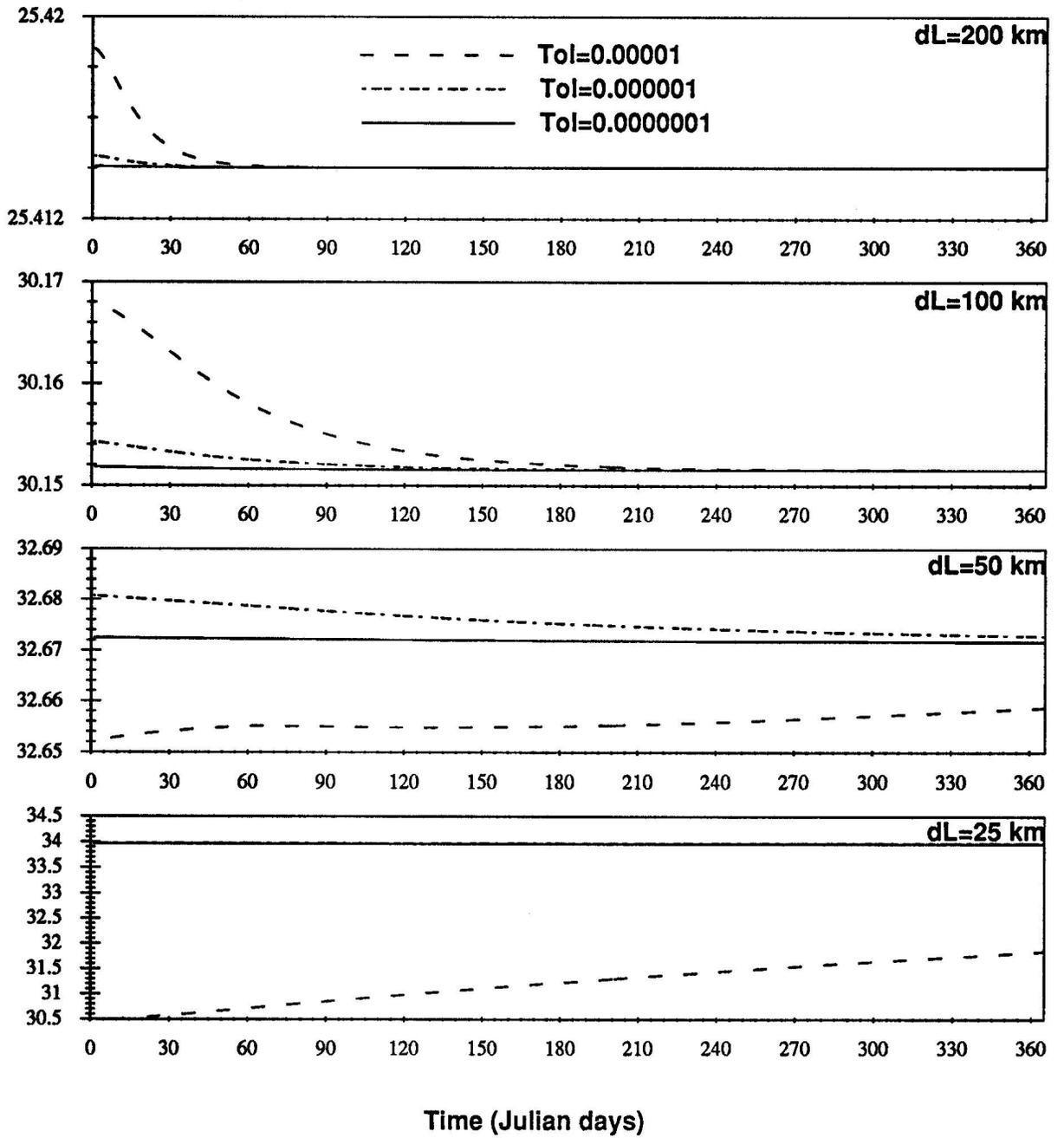


Figure 4.11: Kinetic energy during full plastic solution time steps for VP.

Chapter 5

Numerical Rheology Behavior

In this chapter we will examine ice deformation from a numerical perspective using a hierarchy of numerical sea ice models. The goal here is to assess how the numerical ice performs under a number of different ideal conditions. To do this we consider a simplified stationary, non-advective system without mass balance equations. Physically, this means that we impose forces and constitutive constraints on a system but we will not allow the system to respond to those forces (i.e. no time evolution, advection or thermodynamic response as a result of an imposed force). Computationally, this simplifies our set of equations considerably and allows us to answer a series of fundamental questions with minimal computational effort.

The chapter begins with a study of the 1D Cavitating Fluid rheology from both an analytical and numerical perspective in both Cartesian and spherical coordinates. Then we look at a series of sensitivity responses of the models and how the one dimensional models compare to 1.5D and 2D versions. A similar progression is examined for the Viscous Plastic rheology. Finally we will conclude with a summary of our findings and subsequent identification of useful model types for regional studies. As with Chapter 4 reference to the Viscous Plastic rheology is denoted by VP while the Cavitating Fluid rheology will be referred to as CAV.

The equations for all cases investigated in this chapter are the combined steady state momentum and constitutive equations described in Chapter (4.1.2). The simulation fields are 20 grid cells in the y or \hat{j} -direction (oriented south [$y = 0$] to north) for the 1D cases and the center results [at $i = 10$] of a 20 by 20 grid field for the 2D cases. There is no ocean velocity or heat flux and the windstress (τ) is determined through the wind velocity which is uniform, specified and in most cases directed southward toward a land mass such that southward wind direction gives negative velocities and wind stresses due to direction (north is positive). The boundary conditions include a wall along the perimeter of the field where the Dirichlet boundary condition of zero outward ice velocity normal to the boundary is imposed. To maintain continuity, inflow is permitted at the north boundary $j = 20$ via the Von-Neumann condition $\frac{\partial v}{\partial n} = 0$. Additionally at the ice edge, the ice strength goes to zero (i.e. no internal ice stress at the ice edge). Standard values for each variable are listed in Table 5.1.

Table 5.1: Standard Values for Rheology Study

Variable	Standard Value	Range
dY ($d\phi$)	222 km (2°)	All
dX ($d\lambda$)	222 km	All
L	$15.5 dY = 3441$ km	All
R	6303.707 km	All
h	2.0 m	$j = 1$ to 15
	0.0 m	$j = 16$ to 20
A	1.0	$j = 1$ to 15
	0.0	$j = 16$ to 20
\vec{V}_a	-10m/s \hat{j}	All
α (linear drag)	0.6524 kg/m ² s	All
τ	-0.1256 kg/m s ²	All
P_{\max}	55000. Pa m	$j = 1$ to 15
	0. Pa m	$j = 16$ to 20
BCs	$v = 0$	$j = 1$
	$\frac{\partial v}{\partial n} = 0$	$j = 20$
	$u = 0$	$i = 1, i = 20$

5.1 Basic Behavior of Cavitating Fluid Rheology

5.1.1 1D Cavitating Fluid Code vs. Analytical Solution

In this section we investigate CAV from both a numerical and analytical perspective in order to examine the physical behavior of simulated ice. The momentum balance has been reduced to a diagnostic form so the equations in 1D are a function of only one independent variable (i.e. we are dealing with ordinary differential equations). Experiments are conducted using a 1D grid with an ice thickness distribution specified as in Table 5.1 such that the southern wall is located at the first grid cell where $v[y = y_s = 0] = 0$, 2 meters of ice from $0 \leq y \leq L$ (i.e. grid cells 1 to 15), and no ice beyond $y = L$ (grid cell 15) to the northern wall $y = y_n$. For simplicity, linear drag is assumed so the variables τ and α remain constant as specified in Table 5.1. Numerical solutions are obtained under these conditions by running the CAV code without advection or thermodynamics to a full plastic solution for one time step to reach steady state. The corresponding analytical solutions are derived below. For notational clarity [] indicates the argument at which a function is being evaluated.

In Cartesian coordinates, the set of equations governing this system includes the 1D momentum balance

$$\frac{dP}{dy} = \tau - \alpha v, \quad (5.1)$$

the constitutive relation

$$\frac{\partial v}{\partial y} \geq 0 \iff P = 0; \text{ Free Drift} \quad (5.2)$$

$$\frac{\partial v}{\partial y} = 0 \iff 0 \leq P \leq P_{\max}; \text{ Incompressible Flow} \quad (5.3)$$

$$\frac{\partial v}{\partial y} \leq 0 \iff P = P_{\max}; \text{ Isotropic Yielding} \quad (5.4)$$

and boundary conditions. The presence of three constitutive cases produces three solution regions: free drift, incompressible flow and isotropic yielding. Within the free drift and isotropic yielding regions the pressure is constant so the pressure gradient vanishes and we simply get

$$P = \text{constant} \quad (5.5)$$

$$v = \frac{\tau}{\alpha} = \text{constant}. \quad (5.6)$$

For the incompressible flow case we must integrate from any arbitrary point in the field to a specified reference point $[y = y_{\text{ref}}]$ such that $P_{\text{ref}} \equiv P[y_{\text{ref}}]$. From the linear drag assumption, τ and α are constant and can be taken outside of the integral. Additionally divergence is identically zero in this region so the velocity must also be a constant which gives us the incompressible solution

$$v[y] = \text{constant} \quad (5.7)$$

$$P[y, v] = P_{\text{ref}} + (\tau - \alpha v)(y - y_{\text{ref}}). \quad (5.8)$$

To complete these solutions, boundary conditions must be satisfied for both pressure and velocity. Since there are three different solutions, a total of five possible boundaries can exist within a given field. The first two are always present and fixed at the south and north walls ($y = y_s$ and $y = y_n$) where we have imposed the Dirichlet boundary condition of no flow through the southern wall (i.e. $v[y_s] = 0$) and Von-Neumann condition $\frac{\partial v}{\partial y} = 0$ at the northern wall. The pressure at these walls is specified by the kinematic conditions created by the orientation of the wind which specifies the pressure at the wall via a reaction force per unit area that is equal but opposite to the imposed force. In this experiment the north wall has no wind or ice pushing against it so $P[y_n] = 0$. The southern wall must oppose the wind stress exerted over the ice which extends from $0 \leq y \leq L$ so (note that $\tau < 0$ is considered here)

$$P[y_s] = -\tau L. \quad (5.9)$$

The three remaining boundaries are located between free drift and incompressible flow at the internal free drift boundary (y_{fi}), incompressible flow and yielding at the internal yielding boundary (y_{iy}) and free drift and yielding (y_{fy}). At all three of these locations the boundary matching condition must be satisfied. Due to the orientation of the wind and the distribution of both the ice thickness and compactness, the free drift solution in this experiment can only exist where there is no ice which is between $L \leq y \leq y_n$. Since the ice can not advect, this also means that the location of boundary y_{fi} remains fixed at $y_{fi} = L$. The rest of the region $0 \leq y \leq L$ may include three possible combinations of the two remaining solutions, 1) incompressible flow only, 2) isotropic yielding only or 3) incompressible and yielding together .

For incompressible flow alone, if we choose $y_{\text{ref}} = L$ such that $P_{\text{ref}} = P[y_{\text{ref}} = L] = 0$ and we apply the boundary condition at the wall that $v[y = y_s] = 0$. This gives us the solutions of

$$v[0 \leq y < L] = \text{constant} = 0 \quad (5.10)$$

$$P[0 \leq y \leq L] = \tau(y - L). \quad (5.11)$$

Likewise if we choose $y_{\text{ref}} = 0$ ($P_{\text{ref}} = -\tau L$) we arrive at the same answer

$$P[0 \leq y \leq L] = P[y_s = 0] + \tau y = \tau(y - L). \quad (5.12)$$

This gives us a linear pressure profile in the incompressible region that matches the free drift pressure solution at $y = L$ provided the pressure at the wall is non-zero and does not meet or exceed P_{max} . A discontinuity in velocity results from this solution at the boundary $y = L$ which is attributable and admissible to the discontinuous thickness distribution specified there. To overcome this discontinuity the velocity at the boundary $y = L$ must be the average of the two velocity solutions (i.e. $v[y = L] = \frac{\tau}{2\alpha}$).

Consider now the effect of the boundary conditions for the yielding case. According to the initial computation above, isotropic yielding occurs at a constant pressure ($= P_{\text{max}}$) and velocity ($\frac{\tau}{\alpha}$). The boundary conditions are therefore needed to determine where the yielding solution is located. Given the orientation of the wind and the Cartesian grid which is parallel to it, the south wall must be the location where yielding starts. For the yielding to match the free drift solution at the boundary y_{fy} the pressures must match. This condition is only possible in the case $P_{\text{max}} = 0$ which is the trivial case of zero ice thickness. This means that the internal boundary we need to match is y_{iy} . Applying the constant yielding velocity and pressure to Eqs. (5.7) and (5.8) we get

$$P_{\text{max}} = P_{\text{ref}} + \left(\tau - \alpha \frac{\tau}{\alpha} \right) (y_{iy} - y_{\text{ref}}) \quad (5.13)$$

$$\implies P_{\text{max}} = P_{\text{ref}}. \quad (5.14)$$

This solution is only possible if $y_{iy} = y_{\text{ref}}$. In this case y_{ref} can not equal L except for the trivial solution $P_{\text{max}} = 0$. For $0 < y_{iy} < L$, the boundary between incompressible and yielding is inside the ice but this produces a discontinuity of velocity ($v = \tau/\alpha$ for yielding versus $v = \tau/\alpha + P_{\text{max}}/(L - y_{iy})\alpha$ for incompressible \implies discontinuous jump in velocity of $P_{\text{max}}/(L - y_{iy})\alpha$). Since inside the ice can not be discontinuities the only possible solution for this case is $y_{iy} = y_s = 0$. This means that the only solution for yielding which satisfies the boundary conditions is the one where yielding occurs only at the south wall and $P_{\text{ref}} = P_{\text{max}}$. This also means there is no solution of yielding everywhere from $0 < y \leq L$. Hence, the only two solutions which do exist are the cases of incompressible flow only (solved above) and yielding at the south wall only with incompressible flow from $0 < y < L$. To solve for this second solution we must make use of the two boundary conditions $P[y_s] = P_{\text{max}}$ and $P[L] = 0$. From this we solve for the velocity (which must be constant) by applying both conditions to Eq. (5.8) to get v and then either condition to Eq. (5.8) plus the resultant velocity to P giving us

$$v[0 < y < L] = \frac{\tau}{\alpha} + \frac{P_{\text{max}}}{\alpha L} = \text{constant} \quad (5.15)$$

$$P[0 \leq y \leq L] = \frac{P_{\text{max}}}{L}(L - y). \quad (5.16)$$

Combining these results we obtain the following set of solutions,

$$P = \begin{cases} P_{\text{icewall}} = \text{MIN}(-\tau L, P_{\text{max}}); & \text{at } y = 0 \\ \frac{P_{\text{icewall}}}{L} (L - y); & \text{at } 0 < y \leq L \\ 0; & \text{at } L \leq y \leq y_n \end{cases} \quad (5.17)$$

$$v = \begin{cases} 0; & \text{at } y = 0 \\ v_1 = \frac{\tau}{\alpha} + \frac{P_{\text{icewall}}}{\alpha L}; & \text{at } 0 < y < L \\ \frac{v_1 + v_2}{2}; & \text{at } y = L \\ v_2 = \frac{\tau}{\alpha}; & \text{at } L < y < y_n \end{cases} \quad (5.18)$$

Examining these results we see that deformation occurs at the wall when $P[0] \geq P_{\text{max}}$. The ice has a constant thickness and is assumed to behave isotropically, so it yields in a uniform manner at a constant velocity with a non-zero velocity produced from the yielding process in the following way: When the reaction pressure at the wall ($P_{\text{wall}} = -\tau L$) exceeds P_{max} , the pressure imposed on the ice that equals the internal ice stress (P_{max}) causes the ice to fail (i.e. deform). The excess pressure ($-\tau L - P_{\text{max}}$) continues to exert a force per unit length on the ice and thus moves the ice as it deforms. τ in this case is negative and from the v_1 equation we see that its magnitude must exceed P_{max}/L for yielding to occur. The velocity is also negative, in other words, directed toward the wall. This is consistent with the constitutive constraint that convergence must occur ($dv/dy < 0$) between the wall, where $v = 0$, and the ice, where v is negative. The distance between these two regions is infinitesimally small. In order for yielding to occur beyond the wall one of two things must happen; either the wind velocity must vary such that the ice further north can move faster than the yielding velocity at the wall, or the physical shape of the field must be such that the yielding velocity is constrained by some other means. If mass conservation was included a third option of ice redistribution would also cause yielding farther out.

Comparing these analytical results with the numerical linear drag results shown in Figures (5.1) and (5.2) we see how the solutions work for the different regions. For the free drift case, direct comparison of the analytical solutions with the numerical example for -10 m/s wind (the open diamond line for linear drag (LD Cartesian) case) shows that in grid cells 16 through 19 (no ice present) the internal ice pressure is zero and the ocean velocity is -0.1925 m/s. The same value is obtained for the analytical free drift solution using the values τ and α listed in Table 5.1. In these same figures, for wind speeds less than 5 m/s, we reproduce the analytical results for incompressible flow without yielding including the linear pressure profile and zero velocity. For wind speeds of 5 m/s and greater we see yielding occurring at the wall, a linear pressure profile, and an incompressible fluid between $0 < y < L$ with a constant velocity equal to the yielding velocity. For the example case of -10m/s wind, the ice velocity for the combined yielding and incompressible flow results is -0.1654 m/s in the model and -0.1680 m/s in the analytical case which is a difference of about 1.5%.

Making use of both the analytical and numerical information we can also examine the velocity discontinuity at $y = y_{fi} = L$ which results from the step function distribution for ice thickness. From a numerical standpoint this test from 2m to 0m of ice shows how stable the numerical solution is. From an analytical viewpoint, the pressure at the boundary must be zero and the velocity must be matched from both sides. Numerically,

the thickness is computed at $y = L$ which is the same location as the ice pressure and other scalar quantities so these terms as seen in the figures are continuous at the boundary. Due to the alternating numerical grid scheme between vector and scalar quantities, the jump in velocity is located on either side of the scalar locations. In order to achieve the matching conditions of velocities at the boundary L we simply need to compute the average of the two velocities in order to fulfill the matching condition. As shown in the analytical solution, it is for this reason that the velocity solution for both incompressible and free drift only extend up to but not including L . As a final note, the boundary y_{fy} can not occur for any uniform wind for this experimental setup.

Now consider the 1D case in spherical coordinates under the same conditions. The 1D momentum balance is

$$\frac{1}{R} \frac{dP}{d\phi} = \tau - \alpha v. \quad (5.19)$$

Physically there is no difference between this momentum balance and the Cartesian case. The independent variable is ϕ instead of y with the distance between any two spherical positions, $R\Delta\phi$, being equivalent to Δy so distance between grid cells is unchanged. The only difference between the spherical and Cartesian formulation occurs in the constitutive relation due to the divergence operator in spherical coordinates. In this case the constitutive constraint is

$$\frac{1}{\cos[\phi]} \frac{\partial(v \cos[\phi])}{\partial\phi} \geq 0 \iff P = 0 \quad (5.20)$$

$$\frac{1}{\cos[\phi]} \frac{\partial(v \cos[\phi])}{\partial\phi} = 0 \iff 0 \leq P \leq P_{\max} \quad (5.21)$$

$$\frac{1}{\cos[\phi]} \frac{\partial(v \cos[\phi])}{\partial\phi} \leq 0 \iff P = P_{\max} \quad (5.22)$$

As seen below, the addition of cosine terms in the spherical constitutive relation will have a considerable effect on the yielding dynamics of the system.

The boundaries for this problem are located at ϕ_s , $\phi_{fi} = \phi_L$, ϕ_{iy} , ϕ_{fy} and ϕ_n which correspond respectively to the boundaries and boundary conditions defined for the Cartesian case. Since we are dealing with the Weddell Sea, the geographical region is chosen to span 40° of latitude from the southern most part of grid cell 1 at $\phi_s = 79.875^\circ\text{S}$ to northern most part of grid cell 20 at $\phi_n = 39.875^\circ\text{S}$. The boundary where free drift is imposed is located at the scalar position $\phi_{fi} = 48.875^\circ\text{S}$ and L is still equal to the distance indicated in Table 5.1.

Within the free drift and isotropic yielding regions the pressure is again constant so the pressure gradient vanishes and we get the same answer as for the Cartesian grid,

$$P = \text{constant} \quad (5.23)$$

$$v = \frac{\tau}{\alpha} = \text{constant}. \quad (5.24)$$

As a result of spherical coordinates the constitutive condition for incompressible flow gives

$$v \cos[\phi] = \text{constant} = C \quad (5.25)$$

which gives us the incompressible flow solution that

$$v \cos[\phi] = \text{constant} = C \quad (5.26)$$

$$P = P_{\text{ref}} + R\tau(\phi - \phi_{\text{ref}}) - R\alpha C \ln \left\{ \frac{\tan\left(\frac{\pi}{4} + \frac{\phi}{2}\right)}{\tan\left(\frac{\pi}{4} + \frac{\phi_{\text{ref}}}{2}\right)} \right\}. \quad (5.27)$$

For the case of only incompressible flow in the region $\phi_s \leq \phi \leq \phi_L$, we can choose $\phi_{\text{ref}} = \phi_L$ ($P_{\text{ref}} = 0$) which gives us

$$v[\phi_s \leq \phi < \phi_L] \cos[\phi] = \text{constant} = 0 \implies v = 0 \quad (5.28)$$

$$P[\phi_s \leq \phi \leq \phi_L] = R\tau(\phi - \phi_L). \quad (5.29)$$

Since $R\Delta\phi = \Delta y$, this is essentially the same answer as with Cartesian coordinates.

Using the same argument as for the Cartesian case, the outer boundary for the yielding solution will again be the south wall. As before, the internal boundary ϕ_{fy} can not exist because the pressure can not be properly matched in this case. Hence we must determine the inner yielding boundary by locating the boundary ϕ_{iy} . We solve for this location by matching the yielding solutions ($v = \frac{\tau}{\alpha}$ and $P = P_{\text{max}}$) with those for incompressible flow (Eqs. 5.26 and 5.27) at the boundary ϕ_{iy} to give us

$$\tau = \frac{P_{\text{max}}}{R \left(\phi_{iy} - \phi_L - \cos \phi_{iy} \ln \left\{ \frac{\tan\left(\frac{\pi}{4} + \frac{\phi_{iy}}{2}\right)}{\tan\left(\frac{\pi}{4} + \frac{\phi_L}{2}\right)} \right\} \right)}. \quad (5.30)$$

With respect to ϕ_{iy} this solution is a highly non-linear non-trivial matter to solve. However with respect to τ , it is a very straightforward solution. What this equation tells us, as illustrated in Figure (5.3), is that for a given ice strength (P_{max}) we can determine the relationship between windstress and the location of ϕ_{iy} using the range of latitudes defined for the experiment. As an example, the lower image in Figure (5.3) indicates that the internal yielding boundary for a wind velocity of -10m/s is located at $\phi_{iy} = 66.103^\circ\text{S}$ which is between the pressure and velocity at numerical grid cell 7 which concurs with Figure (5.2) for the linear drag spherical case.

An important result is that the region of yielding in the spherical case actually extends beyond the wall. Given that the yielding velocity is constant and the region of yielding is now a finite quantity we can compute the amount of convergence at any point in the yielding region by noting that

$$\frac{1}{R \cos \phi} \frac{\partial v \cos \phi}{\partial \phi} = -\frac{v \tan \phi}{R}. \quad (5.31)$$

As eluded to in the Cartesian analysis, this condition is possible due to the shape of the grid. There is more surface contact (and hence a greater reaction force) so the ice will converge for a greater distance as the wind stress increases because the resistive forces are no longer confined to the south wall. There is a reaction force coming from the lateral walls of the grid whose reaction pressure at a given location ϕ is equal to

$-\tau(\phi - \phi_L)$. The point at which this pressure just equals the strength of the ice is where ϕ_{iy} is located. Points along the side walls north of this location will have a reaction force too weak to cause deformation and points further south will exceed this pressure and thus enhance the deformation process. Given a sufficiently large wind stress this solution for yielding can exist from $\phi_s \leq \phi_{iy} < \phi_L$. Note however that close to ϕ_L the pressure must return to zero to match the free drift solution so locations up to but not including ϕ_L can experience yielding. Instead a region of incompressible flow must exist for some finite distance between yielding and free drift. This is mathematically verified in Figure (5.3) where we see that in the limit as $\phi_{iy} \rightarrow \phi_L$, $\tau \rightarrow -\infty$, hence only for the case of infinite wind stress can the boundary ϕ_{fy} exist.

In summarizing these results, the analytical solution for this experiment is

$$C = \begin{cases} \frac{\tau}{\alpha} \cos \phi_{iy}; & \phi_{iy} \text{ exists} \\ 0 & ; \phi_{iy} \text{ does not exist} \end{cases} \quad (5.32)$$

$$v = \begin{cases} 0 & ; \text{ at } \phi = \phi_s \\ \frac{\tau}{\alpha} & ; \text{ for } \phi_s < \phi \leq \phi_{iy} \\ v_1 = \frac{C}{\cos \phi} & ; \text{ for } \phi_s \text{ or } \phi_{iy} \leq \phi < \phi_L \\ \frac{v_1 + v_2}{2} & ; \text{ at } \phi = \phi_L \\ v_2 = \frac{\tau}{\alpha} & ; \text{ for } \phi_L < \phi < \phi_n \end{cases} \quad (5.33)$$

$$P = \begin{cases} P_{\text{icewall}} = \text{MIN}(-\tau R(\phi_L - \phi_s), P_{\text{max}}) & ; \text{ at } \phi = \phi_s \\ P_{\text{max}} & ; \text{ for } \phi_s < \phi \leq \phi_{iy} \\ R \tau (\phi - \phi_L) - R \alpha C \ln \left\{ \frac{\tan\left(\frac{\pi}{4} + \frac{\phi}{2}\right)}{\tan\left(\frac{\pi}{4} + \frac{\phi_L}{2}\right)} \right\} & ; \text{ for } \phi_{iy} \text{ or } \phi_s < \phi \leq \phi_L \\ 0 & ; \text{ for } \phi_L \leq \phi \leq \phi_n \end{cases} \quad (5.34)$$

To make these analytical results more clear let us consider in detail the spherical linear drag case for a wind speed of 10 m/s. The diamond line under the LD spherical case in Figures (5.1) and (5.2) represents the -10m/s wind. Table 5.2 shows the corresponding point by point results of this case when solved analytically and numerically. Figure (5.3) shows the relationship between wind velocity and the internal yielding boundary. In combination these three illustrate the three main results for this experiment. First, direct comparison between numerical and analytical results in Table 5.2 shows the numerical solutions to be identical to the analytical solutions within 2 and 3 significant figures for pressure and velocity, respectively. Second, the location of the internal yielding boundary ϕ_{iy} is being predicted accurately in the numerical computations relative to the analytical solution, even at a coarse 2° grid resolution. Finally, the boundary conditions at the walls and the matching conditions at both ϕ_{iy} and ϕ_L are being dealt with numerically in a manner which is consistent with analytical expectations. This task is accomplished by the fact that for numerical solutions, the values of pressure are located at the center of each grid cell separated by a half grid cell distance (in this case one degree of latitude) from the velocities which are located at the northern end of each grid cell. As with Cartesian coordinates this grid arrangement gives us an ice pressure which is always continuous and velocity which can be averaged at the boundaries to allow for continuity.

Another interesting example is seen for the extreme cases of -200m/s wind velocity (plus square line) in Figures (5.2) and (5.4). In this case τ is such that ϕ_{iy} is close to

Table 5.2: Results from 1D Spherical Case with -10m/s Wind Velocity

Grid No.	Latitude Position	Analytical		Numerical		Constitutive Condition
		Press (Pa m)	Vel (m/s)	Press (Pa m)	Vel (m/s)	
1	-79.875	536796.	.000000	—	—	Wall
	-78.875	55000.	-.192520	—	—	Yielding
	-77.875	55000.	-.192520	502164.	.000000	Num. Bndry
2	-76.875	55000.	-.192520	55000.		Yielding
	-75.875	55000.	-.192520		-.192529	Yielding
⋮	⋮	⋮	⋮	⋮	⋮	⋮
6	-68.875	55000.	-.192520	55000.		Yielding
	-67.875	55000.	-.192520		-.192529	Yielding
7	-66.875	55000.	-.192520	55000.		Yielding
	-66.103	55000.	-.192520			Boundary
	-65.875	54981.	-.190808		-.190651	Incompr.
8	-64.875	54594.	-.183678	54728.		Incompr.
	-63.875	53713.	-.177114		-.176973	Incompr.
9	-62.875	52373.	-.171053	52475.		Incompr.
	-61.875	50611.	-.165442		-.165313	Incompr.
⋮	⋮	⋮	⋮	⋮	⋮	⋮
13	-54.875	28687.	-.135547	28713.		Incompr.
	-53.875	24437.	-.132285		-.132188	Incompr.
14	-52.875	19958.	-.129215	19973.		Incompr.
	-51.875	15263.	-.126322		-.126229	Incompr.
15	-50.875	10364.	-.123592	10371.		Incompr.
	-49.875	5273.	-.118577		-.120925	Incompr.
16	-48.875	0.	-.155549	0.		Boundary
	-47.875	0.	-.192520		-.192529	Free Drift
17	-46.875	0.	-.192520	0.	-.192529	Free Drift
	-44.875	0.	-.192520	0.	-.192529	Free Drift
19	-42.875	0.	-.192520	0.	-.192529	Free Drift
20	-40.875	0.	.0	0.	.0	Boundary

the velocity point at grid cells 14 and 15, respectively. As discussed in the analytical solution, the boundary y_{fy} can not exist, so for extremely high wind velocities there are two boundaries (ϕ_{iy} and ϕ_{fi}) very close to each other. In the quadratic (non-linear) drag case (Figure 5.4), the two regions are located on either side of the velocity point at grid cell 15. Although the velocity profile may seem somewhat unusual, the conditions responsible for this state are consistent with the need to maintain a continuous pressure distribution, as shown in the analytical results.

In addition to these three results we note the following. For the spherical grid configuration, the free drift case has the same velocity solution (Figure 5.2) as the Cartesian grid. For wind speeds less than 5 m/s only incompressible flow exists from $\phi_s \leq \phi \leq \phi_L$ while for wind speeds of 5 m/s and greater a combination of yielding and incompressible flow results as is the case for the Cartesian grid solutions. Contrary to this, the linear pressure profile and constant velocity seen in the Cartesian grid cases do not exist for the spherical case due to the presence of cosine terms in the divergence operator in the spherical constitutive relation. Physically, this means that the shape of the grid is no longer bound laterally by two walls parallel to the wind stress. Rather, the grid contains two lateral bounds which converge southward. Hence, the internal yielding boundary can extend beyond the location of the wall through the presence of a reaction force by the inclined longitudinal side walls.

1D Study: $h=2.0\text{m}$, $A=1.0$, Day=10

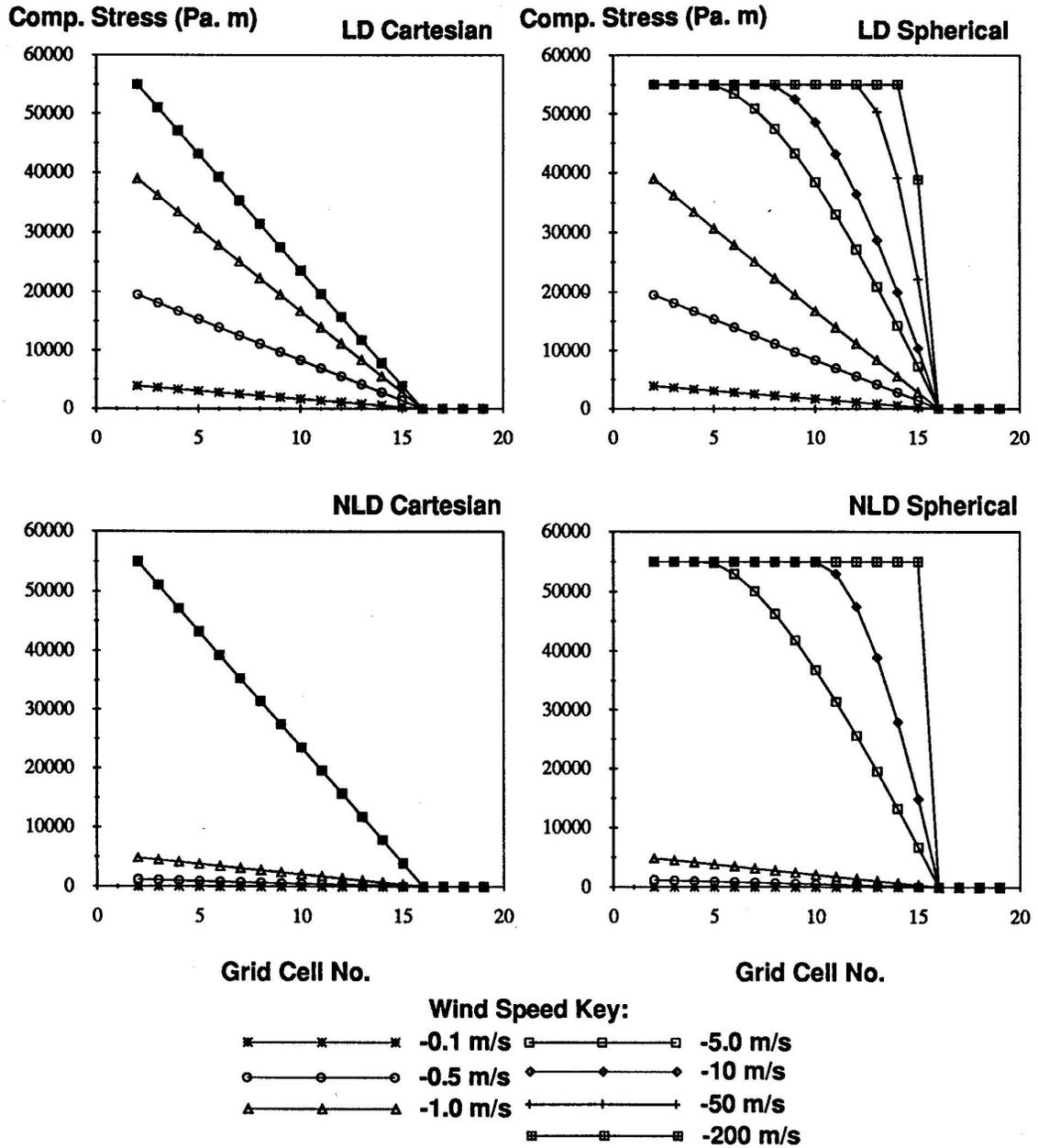


Figure 5.1: Compressive Stress of 1D CAV in Cartesian and spherical coordinates for both linear drag (LD) and quadratic drag (NLD). Specified wind blows from north to south (right to left on page). Additional details given in text.

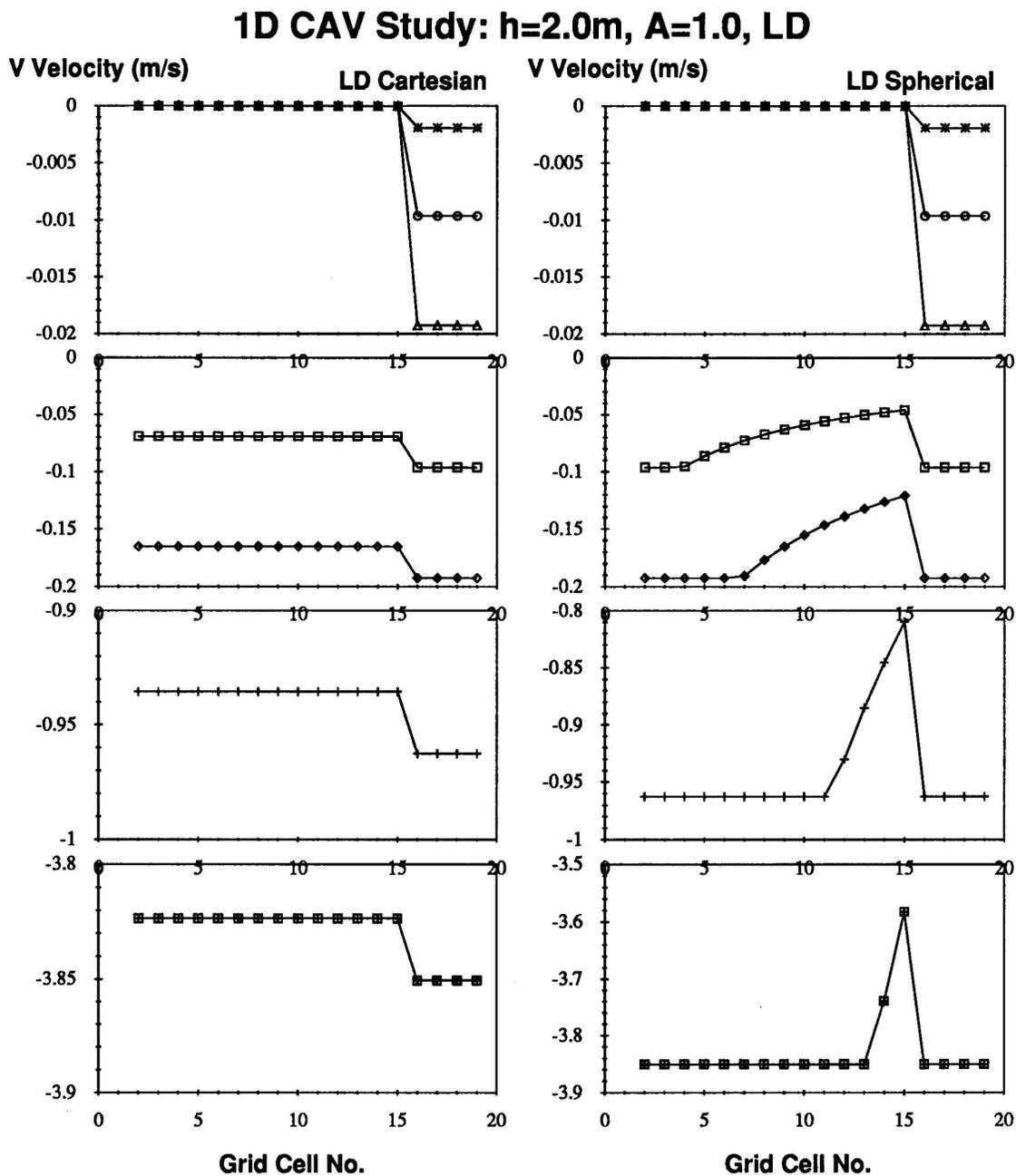


Figure 5.2: V velocity of 1D CAV in Cartesian and spherical coordinates for linear drag (LD). Specified wind blows from north to south (right to left on page). Additional details given in text.

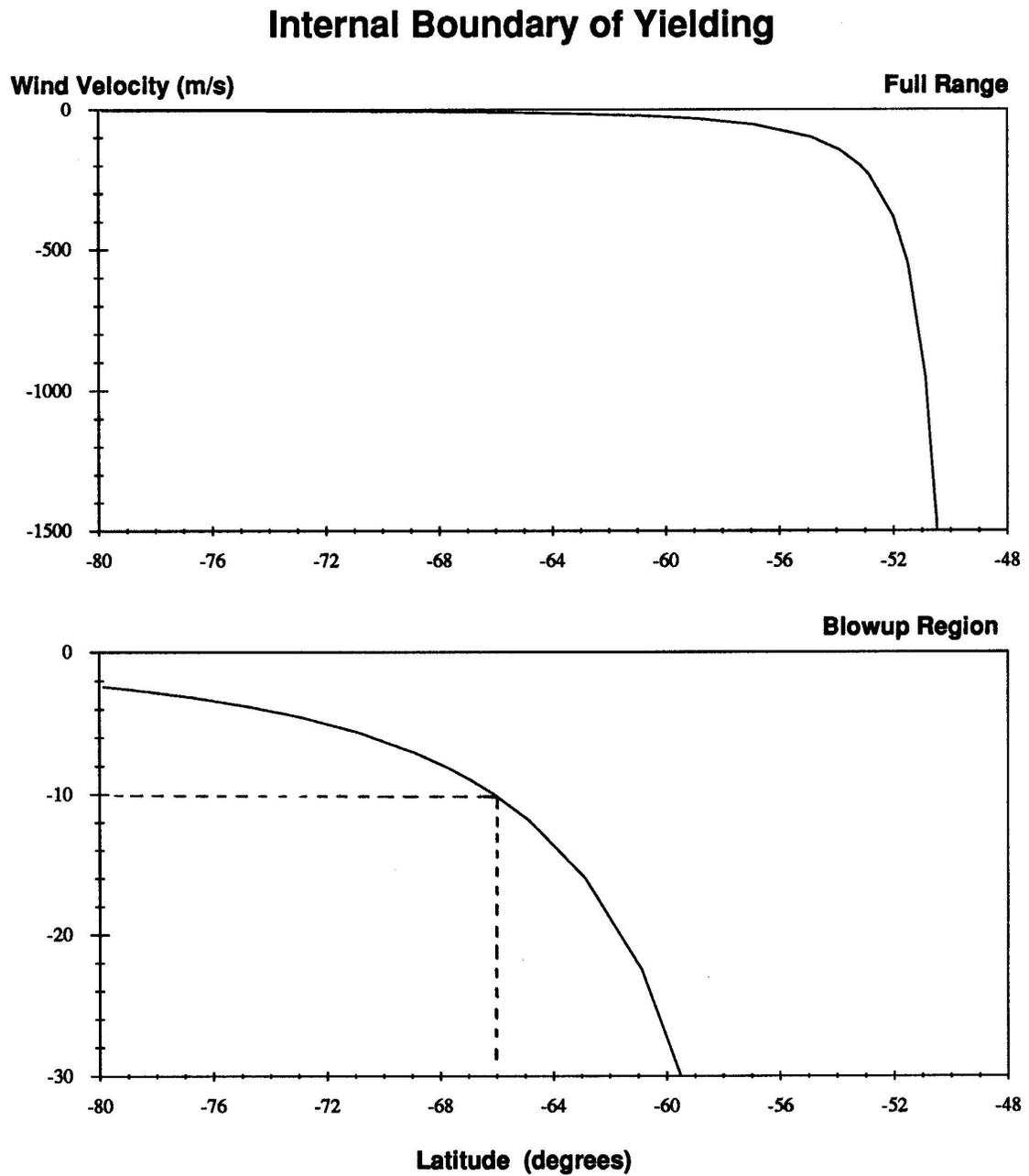


Figure 5.3: Relationship between the latitudinal position of the internal yielding boundary (y_{iy}) and a specified uniform wind velocity (north to south oriented) based on the spherical grid specified in text.

5.1.2 Sensitivity of 1D Ice Dynamics

Except for wind speed, all the coefficients listed in Table 5.1 were fixed at one representative value in the analytical study. In this section we will investigate what happens for different values of these coefficients. In other words we will examine the sensitivity of the 1D models with respect to specific conditions.

Beginning first with the wind stress we see from Figures (5.1) and (5.2) that as the wind increases in magnitude so does the wind stress and resultant internal ice pressure. Once the wind stress exceeds the internal ice strength the ice will yield and an ice velocity in the direction of the wind will result from the excess stress. A detailed investigation of this process was examined in the last section. When using a simple ice rheology like cavitating fluid, researchers often include additional simplifications such as monthly mean forcing and the simple linear wind stress drag law (Rothrock, 1975) as was done here to obtain the analytical solutions. From field observations (McPhee, 1975, 1976a) however, it has been clearly shown that momentum transfer from the wind and ocean to the ice is more a function of the square of the wind speed rather than a linear relationship. In the non-linear drag case, α also depends on wind speed. The question now is how do these stress relations behave in a numerical model.

For CAV the impact of choosing a quadratic versus linear drag relation is clearly seen in both the internal ice stress and velocity profiles in Figures (5.1) to (5.4). Consider first the relatively low wind velocity of -1 m/s in a Cartesian grid (open triangle in Figures 5.1 and 5.2). For the internal ice stress (Figure 5.1) a linear drag law produces an internal ice pressure around 40000 Pa m close to the wall while the non-linear drag produces an internal ice pressure eight times less than this, around 5000 Pa m. The ice velocity on the other hand is barely affected at such low wind speeds because any region with ice exhibits incompressible flow and no ice velocity. Only in the region of free drift do we notice a small difference. Conversely, at higher wind speeds (5 m/s or greater), we see no difference for the internal ice stress because it is subject to yielding at the wall which dominates the internal ice pressure distribution. In the velocity however, we see how the excess pressure is used to move the ice towards the wall at different magnitudes. In Figures (5.2) and (5.4) we see that a wind speed of 10m/s differs in the linear versus quadratic drag by only about 0.01 m/s while at 50m/s the ice velocities differ by about 0.1 m/s and in the extreme case of 200m/s winds the ice velocity differs by almost 0.5 m/s. The extreme case is a physical impossibility (200m/s \approx 450 miles/hour) but it has been included for illustrative purposes because it shows that the transfer of momentum from the wind to the ice differs considerably at higher wind speeds with the quadratic drag. Note also that for the linear drag case, once yielding occurs, the absolute difference between the free drift and yielding velocity remains unchanged (about 0.02 m/s) because the yielding velocity is a linear combination of the free drift velocity and a function of the ice strength which does not change in the current experimental setup. In the quadratic case however, the term α is no longer constant but a function of the magnitude of the ice velocity. Hence at higher wind speed, the difference between free drift and incompressible/yielding regions decreases from 0.02 m/s for 5 m/s wind to 0.002 m/s at 50 m/s wind to 0.0004 m/s at 200 m/s wind. This means that the effect of a discontinuous thickness at the ice edge virtually disappears at higher wind speeds with quadratic drag.

In the spherical grid, the differences between linear and quadratic drag are even

more pronounced because we see differences in both pressure and velocity at both low and high wind speeds. From Figure (5.1) we see that the internal ice pressure at low velocities behaves similar to that in the Cartesian grid but at high wind speeds the pressure is no longer constrained to a linear profile. For 5 m/s wind (open squares), the internal ice pressure using quadratic drag is less than for the linear case while for a 10 m/s wind (open diamonds) the reverse is true. As was the case for the Cartesian grid, we see in Figure (5.4) that for a given wind speed the difference between ice velocities using a quadratic versus a linear drag become more severe as the wind speed increases. In addition, we see that the location of the internal boundary of yielding is located farther from the wall when using non-linear drag. As with the Cartesian grid, the range of velocities for the incompressible solution in the non-linear drag case is considerably reduced as well as the yielding velocity at the wall. In the spherical case, however, the differences are much more pronounced. An analytical solution to the non-linear drag case is far more complicated than the solutions computed in the previous section and has not been attempted here. However, for numerical investigations non-linear drag is the preferred drag relation because it is more consistent with observations. The differences in response of the simulated sea ice between these two drag relations especially at higher wind speeds make it necessary to choose compatibility with reality rather than computational convenience.

Up to now we have only examined the effect of wind velocity in one direction. For the Cartesian grid, the effect of a wind blowing north or south gives redundant results. For the spherical grid, however, a change in wind direction also means a change in the constraints imposed by the grid. So let us now consider the spherical grid case of linear drag wind stress over the same range of wind speeds but oriented in the direction due north (meteorologists call this a south wind). In order to do this we need to reconfigure the ice thickness distribution so that we have 2m of ice from grid cells 5 to 19 (70.875°S to 41.875°S) and no ice in grid cells 1 through 4 (78.875°S to 71.875°S). Figure (5.5) shows the results for both pressure and velocity. For low wind speeds (less than 5 m/s) we see the same results as those for a wind blowing southward. For higher wind speeds (5 m/s and greater) we see free drift in the southern region, incompressible flow to the north, and yielding right at the north wall only. Since the wall is located at a velocity point, pressure is not available numerically there, so we must refer back to the analytical results to clearly see the case of yielding at the wall. These analytical results are indicated by dashed lines in Figure (5.5).

The grid is laterally increasing as ice flows from south to north so ice can only yield at the wall. Note that in this case despite the fact that we have a fixed ice thickness distribution, the boundary ϕ_{fi} moves northward with increasing wind speed. This result comes about by the fact that the incompressible region is subject to an expanding area as it moves northward. At some point ϕ_{fi} the expansion of the grid and the wind stress combine to allow for free drift. Since ice resistance of any form (yielding or incompressible) slows down the ice velocity an increase in wind stress will increase the free drift region and move the boundary ϕ_{fi} northward. We can determine the location of this internal free drift boundary (ϕ_{fi}) using the results from Section 5.1.1 as follows. For yielding at the wall, the equations for velocity and pressure in the incompressible region are

$$v \cos[\phi] = \text{constant} = C \quad (5.35)$$

$$P = P_{\text{ref}} + R\tau(\phi - \phi_{\text{ref}}) - R\alpha C \ln \left\{ \frac{\tan\left(\frac{\pi}{4} + \frac{\phi}{2}\right)}{\tan\left(\frac{\pi}{4} + \frac{\phi_{\text{ref}}}{2}\right)} \right\}. \quad (5.36)$$

In this case we choose the reference location at the fixed boundary $\phi_{\text{ref}} = \phi_{iy} = \phi_n$ and look at the internal boundary solution at $\phi = \phi_{fi}$ so that $P[\phi_{if}] = 0$ and $P_{\text{ref}} = P[\phi_n] = P_{\text{max}}$. In doing so we also have the condition that $v[\phi_{fi}] \cos[\phi_{fi}] = \frac{\tau}{\alpha} \cos[\phi_n]$. Combining these results we get,

$$\tau = \frac{P_{\text{max}}}{R \left(\cos[\phi_{fi}] \ln \left\{ \frac{\tan\left(\frac{\pi}{4} + \frac{\phi_{fi}}{2}\right)}{\tan\left(\frac{\pi}{4} + \frac{\phi_n}{2}\right)} \right\} + \phi_n - \phi_{fi} \right)}. \quad (5.37)$$

This is the same type of relationship found with Eq. (5.30) and as can be seen in Figure (5.6), the above result produces a similar profile only this time for positive wind velocities. As an example, the 10 m/s wind speed numerical results (open diamond) shows the boundary ϕ_{fi} near the pressure value at grid cell 10 (60.875°S) which is very close to the value shown in Figure (5.6) (60.973°S). Note here the excessive wind speeds have been included to consider the full range of the solution. The lower (blow up) graph in Figures (5.3) and (5.6) show the range of results for realistic wind speeds.

From these results and those found in Section 5.1.1 we begin to see a pattern emerging. In the Cartesian case, both internal boundaries ϕ_{fi} and ϕ_{iy} were fixed. In the spherical grid with wind in the converging direction, there is a fixed free drift internal boundary but an internal yielding boundary positionally dependent on the wind stress. With wind in the diverging direction, the reverse is true. There is a fixed internal yielding boundary but an internal free drift boundary dependent on the wind stress. In summary, it appears that the physical states of free drift, incompressible flow and yielding are much more sensitive to wind stress in the spherical grid due to the shape of the grid. Since this shape is also representative of the physical shape of the circumpolar Southern Ocean, we can take this result one step further and suggest that the physical shape of the region is responsible for some of the ice dynamics we see there. For example, the results of high winds which force the ice toward the continent can create situations where large expanses of north-south oriented regions of sea ice can undergo deformation all at once due to the converging shape of the Southern Ocean. Likewise, during periods of northward ice expansion, greater regions of free drift and potentially an increased amount of open water may be present due to the diverging shape of the region.

The ice thickness and distribution clearly play an important role in determining ice strength. In order to examine this effect more closely we will consider a set of numerical runs where we keep the same distribution and compactness of ice but vary the ice thickness. In effect we are varying the value of P_{max} (Eq. 4.30). Figure (5.7) shows results for ice thicknesses ranging from 0.1 to 20 meters for wind speed 10 m/s. For both Cartesian and spherical grids the results are similar to those we have already seen. Looking at the Cartesian grid however, we note a few additional things. First, in the pressure profiles we have included lines without symbols (solid and dashed) which correspond to the ice strength for a given thickness (i.e. P_{max}). The non-symbol lines match their corresponding pressure curve at the wall except for the 20 m thickness case which correspond to the

upper solid line. Because the ice pressure up to 10 m thick corresponds to its strength (P_{\max}) at the wall, it is yielding there. Conversely, the 20 m thick ice pressure only reaches a pressure of 500000 Pa at the wall rather than the corresponding ice strength of 560000 Pa. This case is obviously unrealistic but it does illustrate the fact that the wind stress (specified at -10 m/s) has only enough energy to produce yielding in ice that is around 10 m or less while ice exceeding that will remain incompressible and in this case not move at all. The same is true for the spherical case only now we see that due to the converging shape of the grid, yielding occurs not only at the south wall but from the wall out to a specified distance y_{iy} and ϕ_{iy} . The thicker the ice, the smaller the distance from the south wall. This again exemplifies the significance of the shape of the spherical grid in enhancing the ice dynamics. Note that h is divided out to go from line pressure to pressure, Figure (5.7) looks like Figure (5.1), with the incompressible case produced by the 20m thickness and yielding for the 4m thickness case.

Extending these results to realistic field conditions we see that the dynamic state of the ice (free drift, incompressible, yielding) is highly dependent on its thickness. Hence, a region of uniform ice thickness must respond differently than a region with a collection of ice floes varying in size and shape. In the Weddell Sea ice floes are formed as a result of pancake ice which grows and sticks together to become larger floes. Ridges and deep keels typical of the Arctic are not as prevalent. From this, we expect the ice in the Antarctic to behave quite differently from Arctic ice due to the range of ice thicknesses concentrated within a given area (like a grid cell). It is for this reason that the use of a two level model for this study has been chosen rather than a computationally very slow multilevel version.

In addition to ice thickness, the dynamics of sea ice are quite dependent on the ice compactness. Results from an ice compactness sensitivity studies using -10 m/s wind are shown in Figure (5.8) for compactness values ranging from 70 to 100%. From these results we note that for an ice compactness near or below 70% the ice essentially exhibits free drift. Above this point yielding is experienced because the wind speed is great enough to force floes into each other across the open water region. The amount of yielding that results for regions with more open water is less since a proportionally larger amount of energy has to be used to move the floes together prior to yielding. An interesting result is seen when comparing the two grids. For the Cartesian grid the yield velocities are less in magnitude than free drift velocities and become even lower the greater the compactness. In the spherical grid this is true of the incompressible region but the yielding velocity remains fixed like the free drift region. Another interesting result in the spherical grid is seen when comparing the velocity profile for 95 versus 100% compactness. For a 95% compactness the internal yielding boundary is near grid cell 12 while the 100% compactness internal yielding boundary is near grid cell 10. This means that as the compactness decreases the region affected by yielding is greater. In this case, the response is due to the absence of a proper mass balance, but it is interesting to see that the region affected by the momentum balance is different and this will have an impact on the solution even with the mass balance included. Each of these results again must be due to the converging shape of the spherical grid.

The final sensitivity study is relevant to any numerical simulation namely, the effect of resolution on both the Cartesian and spherical grids. Figures (5.9) and (5.10) show the results made for both grid configurations in a region a little over twice that defined

in Table 5.1. The total distance is 10000 km with resolutions extending from 500 km (20 grid cells) to 1/2 km (20000 grid cells) which covers geophysical sizes from large to small scale ¹. Quadratic drag has been used and the values specified in Table 5.1 have been used with the exception of the distance and resolution. In the spherical grid, resolutions were computed based on distances in kilometers as follows:

$$dL = \text{Resolution} \quad (5.38)$$

$$\text{KmPerDegree} = 1.852 * 60 \quad (5.39)$$

$$\phi_{\text{ref}} = 60^\circ\text{S} \quad (5.40)$$

$$d\phi = \frac{dL}{\text{KmPerDeg}} \quad (5.41)$$

$$d\lambda = \frac{dL}{\text{KmPerDeg} * \cos[\phi_{\text{ref}}]} \quad (5.42)$$

For further details see Appendix B.

Looking first at the Cartesian grid results (Figure 5.9), we see that a convergence tolerance (as described in Chapter 4) of 10^{-7} is probably sufficient for resolutions above 10 km. For 10 km resolution and below, however, the expected results are not achieved. By increasing the tolerance to 10^{-10} we are able to reach a correct solution up to at least 2.5 km. Because of the increased computation time, results for the higher tolerance at 1 km and 1/2 km resolutions are not included. The simple steady state solution in 1D for one time step at these two resolutions takes over two weeks of simulation time.

For the spherical grid (Figure 5.10), we have looked at the sensitivity to resolution for both northward and southward blowing winds for the standard tolerance of 10^{-7} . For the southward blowing winds we see that resolutions up to 2.5 km can now be fairly well resolved at the standard tolerance. Results such as these were achieved for the Cartesian case when the tolerance was orders of magnitude less. Again the converging shape of the grid plays an important role, namely to decrease the sensitivity of the model to resolution. This is a comforting result since spherical grid cells closer to the pole are at a higher resolution in terms of physical distance compared to grid cells closer to the equator. With a northward blowing wind we see that the results at the standard tolerance give a correct solution for resolutions lower than 5 km. Although this is twice the distance for the converging wind case it is half that for the Cartesian case so as a general result the resolution achievable with the spherical grid appears to be at least twice that possible with the Cartesian given the same convergence tolerance.

In looking at this more closely, we recall that a spherical grid in one dimension provides many of the physical constraints felt by the circumpolar field of Southern Ocean sea ice. For the numerical simulations, this physical narrowing is having an effect on the convergence of the numerical iteration scheme. The fact that the grid cells are not all of uniform size in the x or \hat{z} -direction seems to have a stabilizing effect on the convergence rate. Output from model runs allowed to converge to a full plastic solution show that approximately the same number of iterations are performed in both Cartesian and spherical grids at modest resolutions. However, for the Cartesian runs the iterative solution is determined more or less in one pseudo time step of the dynamics routine while

¹A resolution of 1 km or less is considered small scale in geophysical fluid dynamics

the spherical grid requires a number of pseudo time steps to achieve the same plastic solution. The result is that Hence, for low resolution, the amount of computational time for a spherical run is slightly greater than for the Cartesian solution. At high resolution, however, the incremental stepping through a few pseudo time steps each with only a few relaxation iterations converges much faster toward the solution than does one very long iteration step.

In summarizing this section we note the following. First, from a numerical point of view we now have a better understanding of how the dynamics of CAV works and to what degree it compares to analytical results. Second, for analytical understanding of CAV, a simple linear drag model provides a considerable amount of information regarding the dynamics of the system and is fairly close to the results found using the quadratic drag. However, in terms of realistic simulations, the inclusion of the quadratic drag provides additional dynamics which correspond to more realistic conditions. Third, the shape of the spherical grid plays a significant role in increasing the sensitivity of the model and enhancing sea ice dynamics. Finally, although the Cartesian version of CAV is physically simpler and easier to understand, certain advantages exist when using the spherical grid including a physical similarity to the Antarctic region and an increased resolution capability.

1D Study: $h=2.0m, A=1.0, Day=10, NLD$

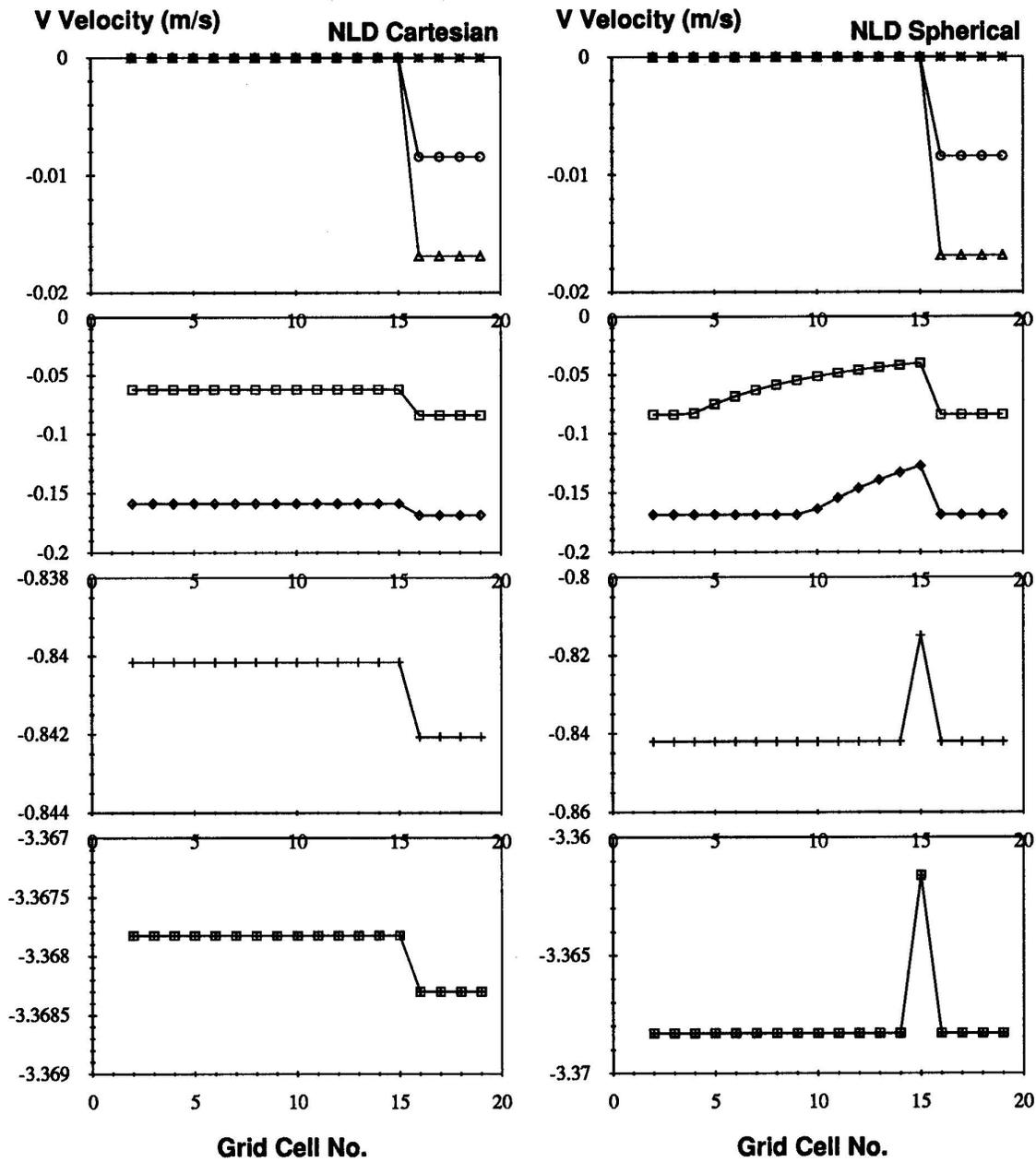


Figure 5.4: V velocity of 1D CAV in Cartesian and spherical coordinates for quadratic drag (NLD). Specified wind blows from north to south (right to left on page).

Spherical Wind Study: $h=2.0\text{m}$, $A=1.0$, Day=10, LD

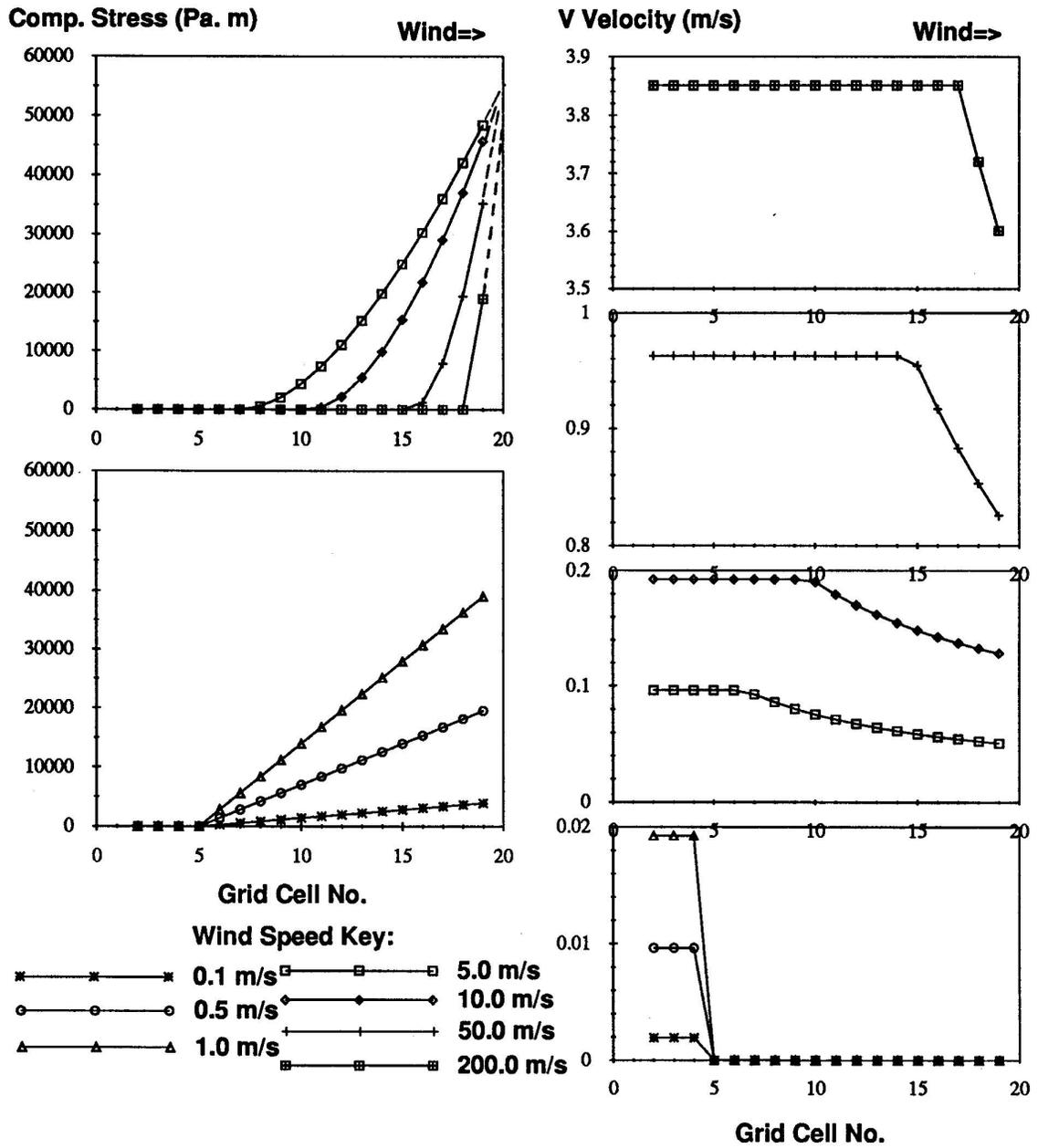


Figure 5.5: Results of 1D CAV in spherical coordinates for linear drag (LD). Wind blowing in direction of spherical grid expansion south to north (left to right on page).

Internal Boundary of Free Drift

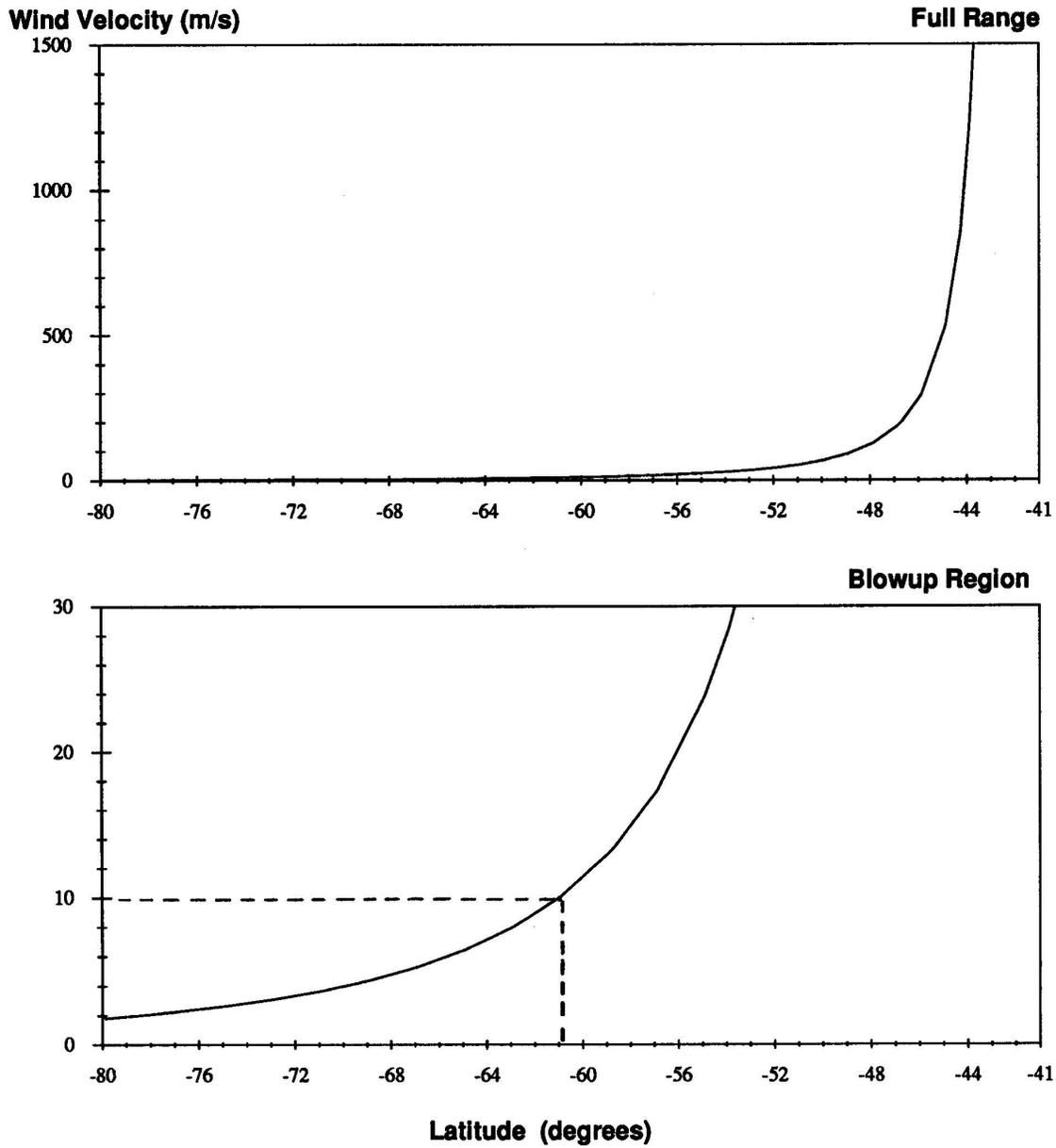


Figure 5.6: Relationship between the latitudinal position of the internal free drift boundary (y_{fi}) and a specified uniform wind velocity (south to north oriented) for the spherical grid specified in text.

Thickness Study: A=100%, Day=10, V=-10m/s, NLD

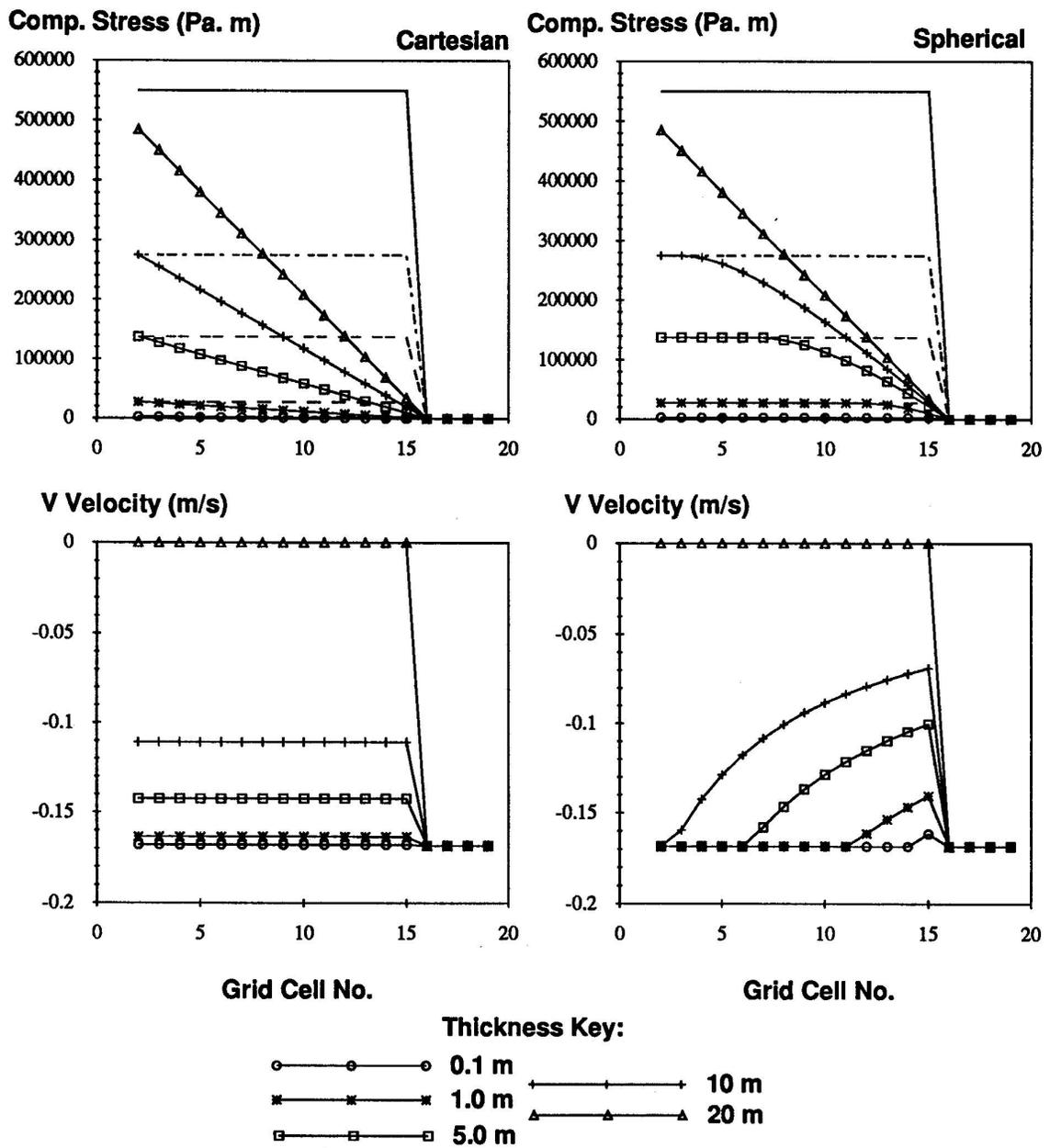


Figure 5.7: Response of 1D CAV in Cartesian and spherical coordinates with quadratic drag (NLD) to different uniform ice thicknesses.

Compactness Study: $h=2$ m, Day=10, $V=-10$ m/s, NLD

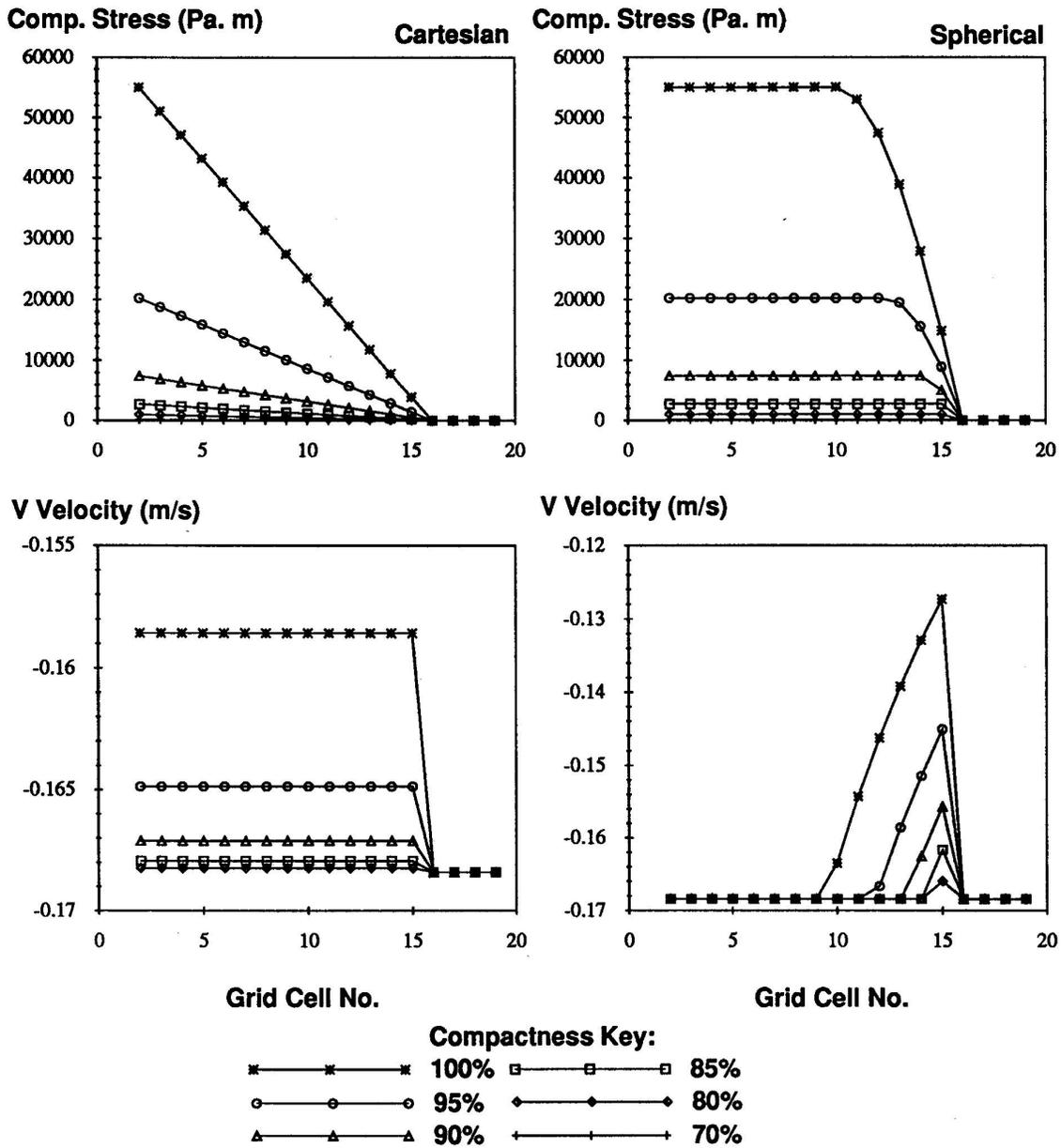


Figure 5.8: Response of 1D CAV in Cartesian and spherical coordinates with quadratic drag (NLD) to different uniform ice compactnesses.

Cartesian Res. Study: $h=2.0\text{m}$, $A=1.0$, Wind= -10m/s , NLD

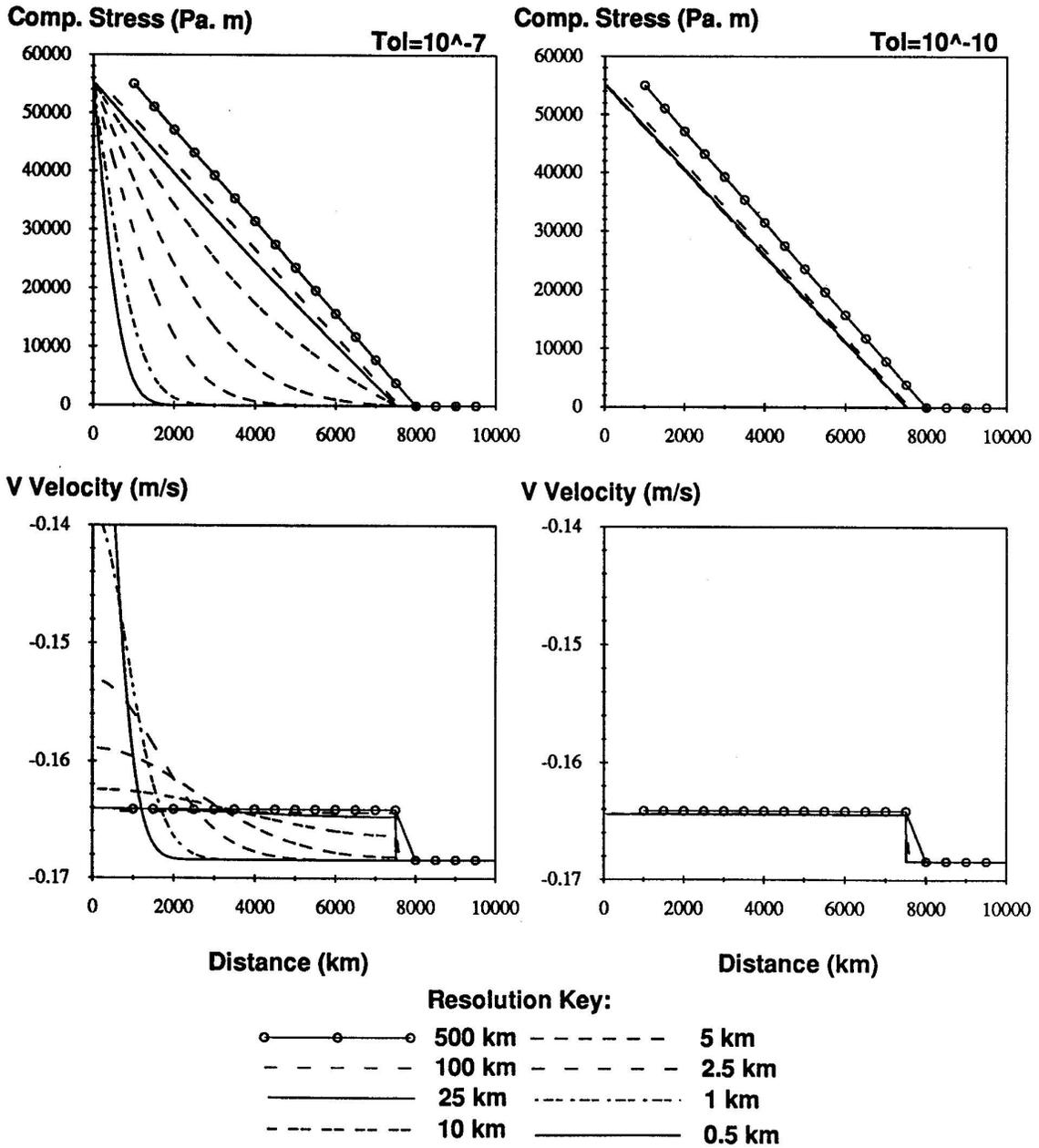


Figure 5.9: Response of 1D CAV in Cartesian coordinates to different resolutions at two different convergence tolerances ($\text{Tol.} = 10^{-7}$ and 10^{-10}). Because of the increased computation time, results for the higher tolerance at 1 km and 1/2 km resolutions are not included.

Spherical Res. Study: $h=2.0m$, $A=1.0$, Wind= $10m/s$, NLD

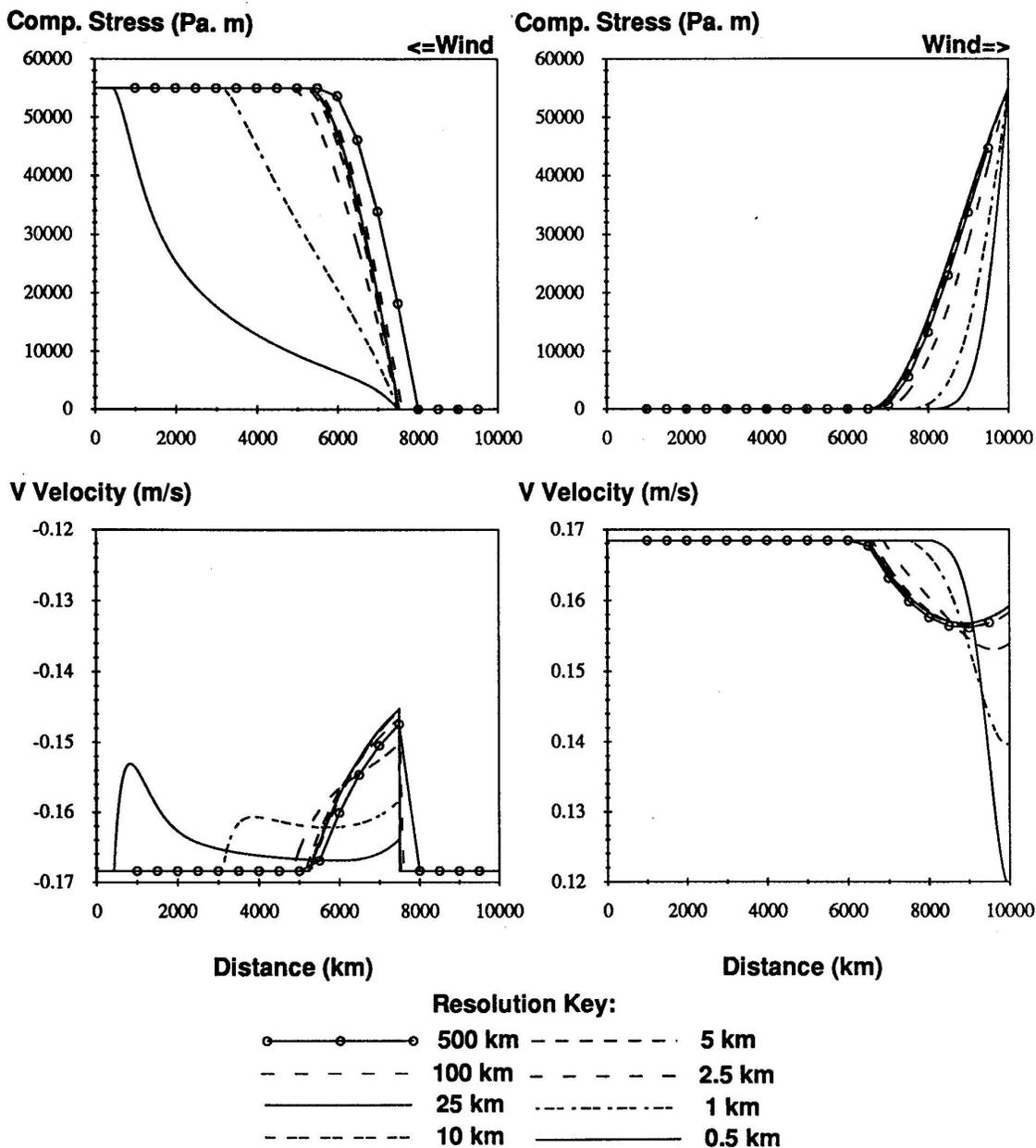


Figure 5.10: Response of 1D CAV in spherical coordinates to different resolutions for both wind directions at a convergence tolerance of 10^{-7} .

5.1.3 Dimensional Sensitivity of Cavitating Fluid Rheology

The 1D investigation above provided quite a bit of insight into the basic dynamics of sea ice as it would behave for example, without shear in a channel. In order to investigate the ice in a manner more relevant to the Weddell Sea, we need to expand on these results and look at two additional forms of the momentum balance equations, namely 1.5D and 2D forms which are described in Chapter 4. The one and a half dimensional (1.5D) form is still a one dimensional model but now the effect of planetary rotation is also included. Using this form we can look at changes in time of a representative south-north transect while the two dimensional (2D) form can be used to look at field values at specific time periods. These in combination with input fields should provide information about the temporal and spatial events occurring in the region.

As a first step we consider the simple momentum balance with CAV constitutive constraints to see how these additions affect the dynamics of the modeled ice. Using the values in Table 5.1 and the quadratic drag relation, steady state runs were made in 1.5D and 2D Cartesian and spherical coordinates for a range of wind velocities from -0.1 to -200 m/s. Test cases of a 1D run using the 2D numerical methods and a 2D run with no rotation for both Cartesian and spherical coordinates produce the same results as those seen in Section 5.1.1. Once rotation is included however, the results change considerably as shown in Figures (5.11) to (5.13). Beginning first with the 1.5D Cartesian case we see in Figure (5.11) that the internal ice stress for wind speeds as high as 5 m/s behaves essentially the same as for the 1D case. At higher wind speeds however, the rotation is clearly imposing an additional constraint on the system such that yielding can now occur at locations other than the wall.

In order to understand this better let us return to the equations themselves. If we cast the 1.5D momentum balance (described in Chapter 4.1.2) into the same form as the 1D case we get

$$\frac{dP}{dy} = \tilde{\tau} - \tilde{\alpha}v \quad (5.43)$$

$$u = \frac{\beta v + \tau_x}{\alpha} \quad (5.44)$$

$$\text{where: } \tilde{\tau} = \tau_y - \frac{\beta\tau_x}{\alpha} \quad (5.45)$$

$$\tilde{\alpha} = \frac{\alpha^2 + \beta^2}{\alpha}. \quad (5.46)$$

Due to rotation, the direction of the applied wind stress is no longer oriented north to south so the side walls of the grid now act as regions of constraint in addition to the north and south walls. As a result, a velocity (u) in the x direction also exists. The pressure in spherical coordinates undergoes a similar effect but is far less sensitive due to the fact that the side walls are not parallel to the wind even without rotation so this effect has already been included in the 1D system.

The corresponding velocity profiles shown in Figure (5.12) concur with these results. For both Cartesian and spherical coordinates, velocity profiles for winds up to 5 m/s show no change. However in both cases once wind speeds reach about 10 m/s we see that the difference between the free drift solution and the yielding solution is greater

in the Cartesian case and for the spherical case the yielding velocity at the wall is now slower, rather than equal to the free drift solution. Additionally we see a new feature, namely at -50 m/s and -200 m/s winds the spherical and Cartesian grid solutions are similar in magnitude and shape except for the ice edge boundary.

For 2D grids with rotation similar features can again be identified. Looking first at Figure (5.11) we see that increased wind velocity increases the wind stress, but this is no longer parallel to either axis. As a result, the walls in both the x and y -directions impose constraints. An additional pressure gradient force in the x or \hat{i} -direction is created which produces yielding, incompressible flow and free drift from a second direction. So now, at high winds speeds (like -50m/s) the ice experiences additional yielding at the east wall which creates a region of incompressible flow and free drift east to west along the south wall. For the spherical grid, we notice these effects show up by a change in the location of the internal yielding boundary, but this grid is clearly far less sensitive. In the velocity profile (Figure 5.13) differences between the two coordinate systems are significantly less especially at very low and very high wind speeds. Only at moderate wind speeds (5 to 10 m/s) do we see discernible differences. We also see that the pressure drop along the south wall corresponds to an increased velocity there which further supports the idea that yielding along the east wall is causing incompressible flow and free drift east to west. As an important side note, in the case of an open boundary to the east this effect does not occur.

In summary, we see that at higher dimensions the wind stress is able to exert forces at angles relative to the grid which in turn produce dynamic effects created by the side walls of the grid. The earth's rotational force is the main factor responsible for the change in orientation not only of the wind stress but also the rotational adjustment of the moving ice through the Coriolis term (f). Finally, we note that results from the higher dimensions in the spherical grid are similar to those in 1D because of the grid shape (i.e. the constraining effects of the side walls are already included in the 1D grid shape). Although more difficult to interpret, simulations in 1D and 1.5D using a spherical grid provide results most similar to those seen in 2D for the non-rotational and rotational cases, respectively. Given the proper outflow boundary conditions in 2D, these solutions can be made even more similar.

Higher Dim. Study: $h=2.0\text{m}$, $A=1.0$, Day=10, NLD

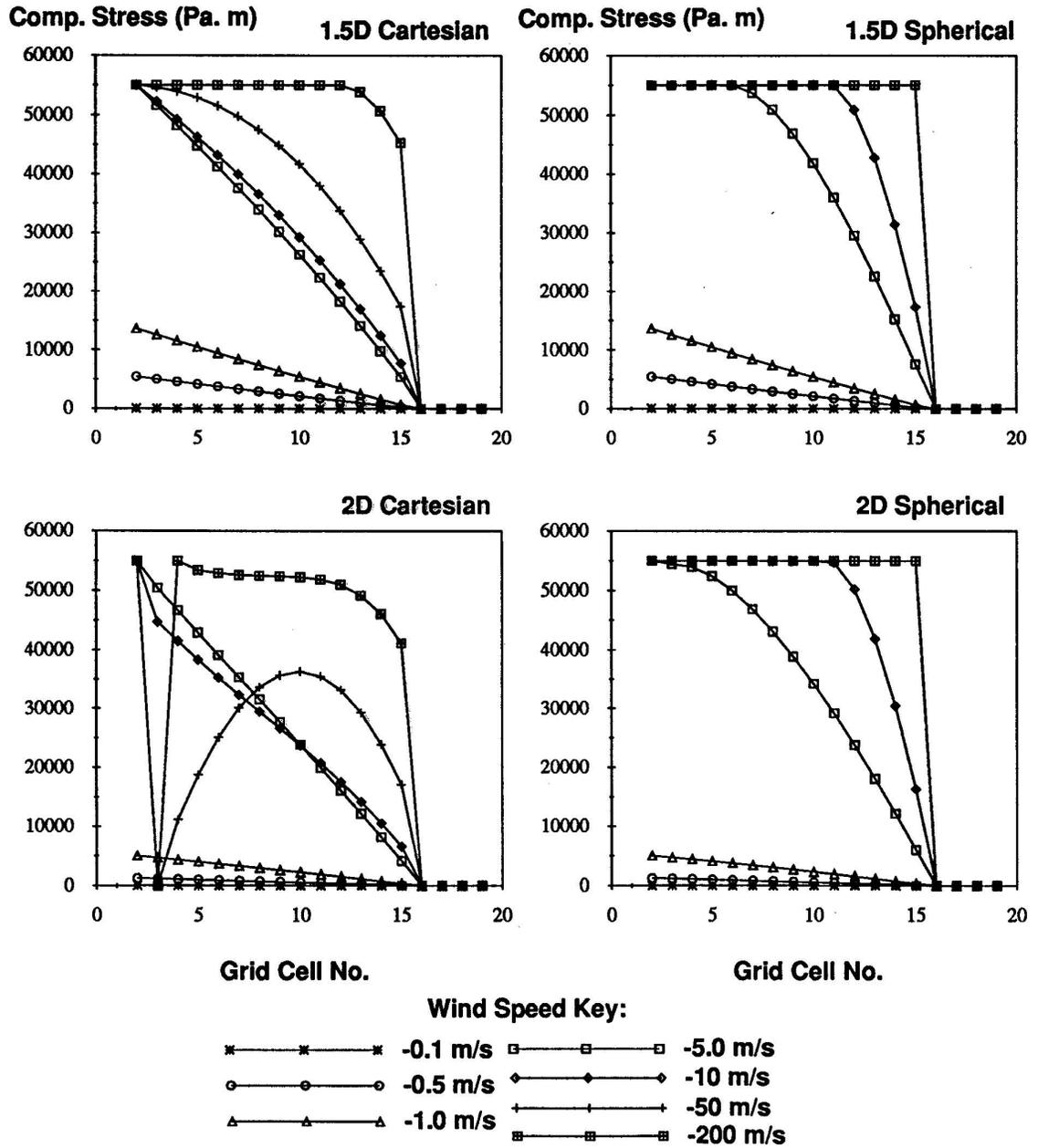


Figure 5.11: Compressive Stress of 1.5D and 2D CAV in Cartesian and spherical coordinates for quadratic drag (NLD). Specified wind blows from north to south (right to left on page).

1.5D Study: $h=2.0m$, $A=1.0$, Day=10, NLD

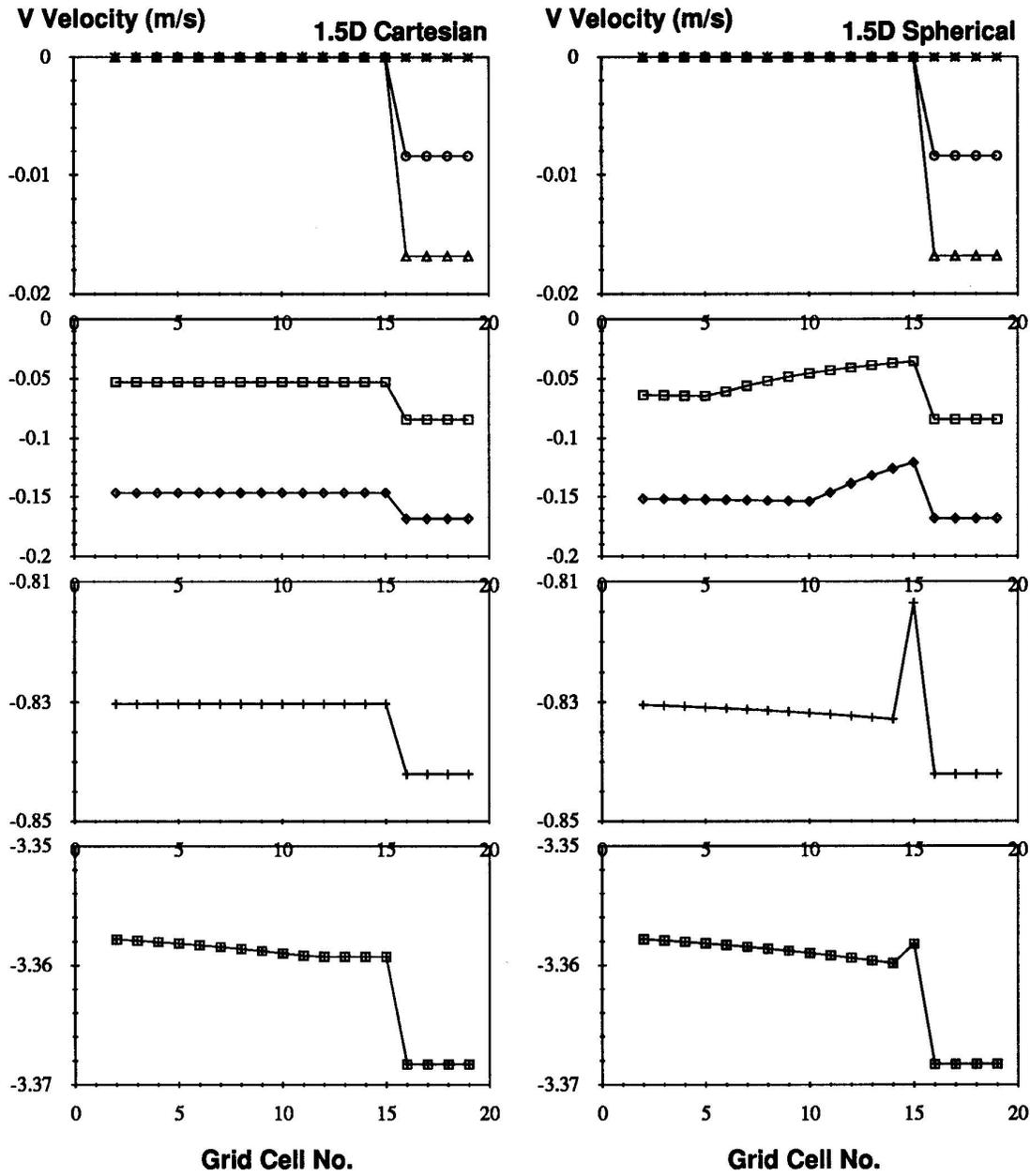


Figure 5.12: V velocity in 1.5D CAV Cartesian and spherical coordinates for quadratic drag (NLD). Wind blows from north to south (right to left on page).

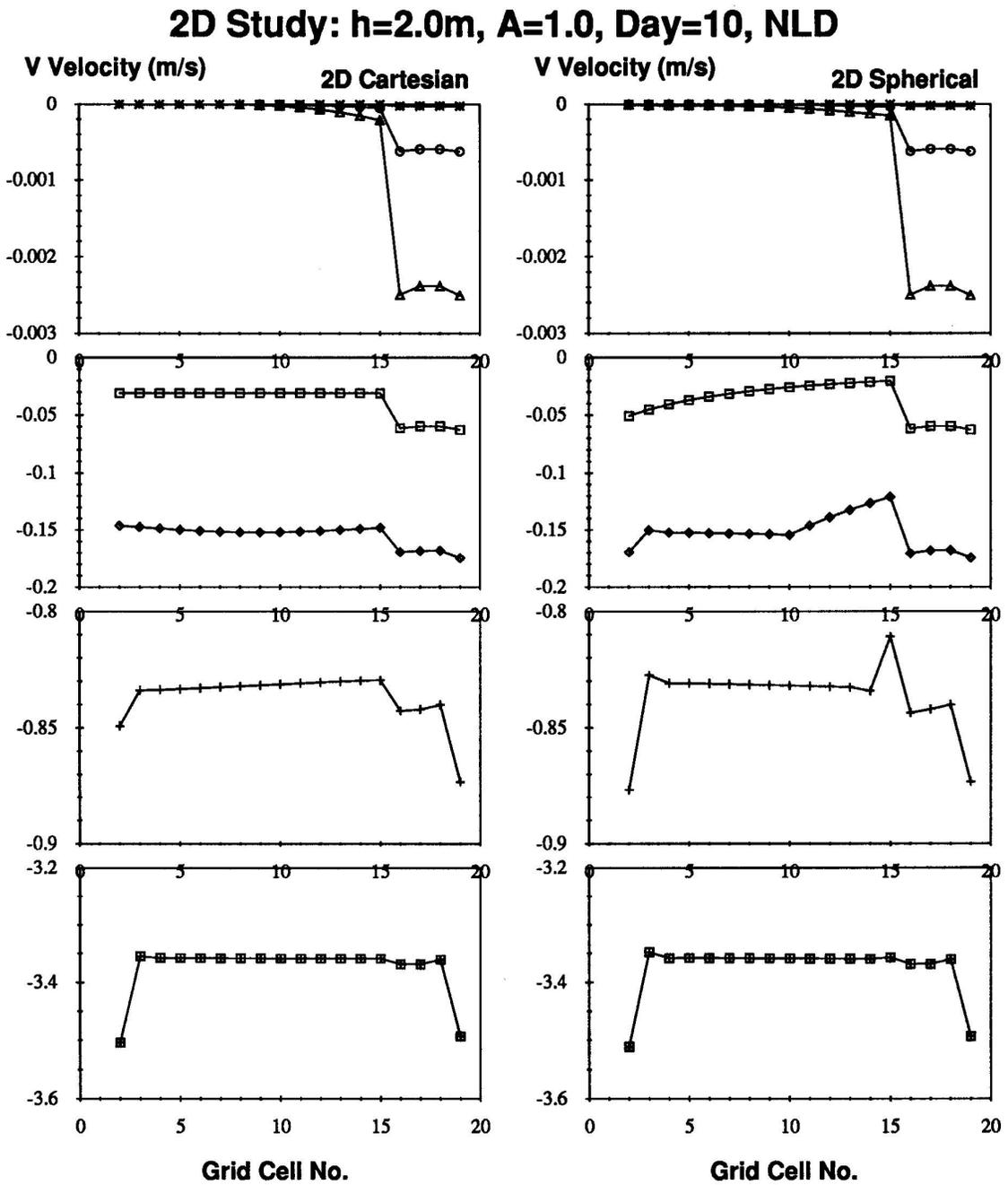


Figure 5.13: V velocity in 2D CAV Cartesian and spherical coordinates for quadratic drag (NLD). Wind blows from north to south (right to left on page).

5.2 Basic Behavior of Viscous Plastic Rheology

One important thing not included in CAV is the ability of ice to undergo shear. As we saw in Chapter 3, this is an important process which occurs whenever floes come into sliding contact with other floes or a boundary. In this section we will examine how this process behaves in VP under the same simple conditions used to examine CAV.

5.2.1 Principal Axes in 2-Space

In order to compare VP with CAV we need some way of examining both in a common frame of reference. In addition to the coordinate systems chosen for this study a coordinate system known as Principal Axis space will also be used. Since the sea ice models we are dealing with are 2 dimensional, a 2-space Principal Axis will be used.

From basic continuum mechanics (see for example Fung, 1977), principal stress axes in 2-space are defined relative to any stress tensor (σ_{ij}) by

$$\sigma_1 = \frac{\sigma_x + \sigma_y}{2} + \sqrt{\left(\frac{\sigma_x - \sigma_y}{2}\right)^2 + \sigma_{xy}^2} \quad (5.47)$$

$$\sigma_2 = \frac{\sigma_x + \sigma_y}{2} - \sqrt{\left(\frac{\sigma_x - \sigma_y}{2}\right)^2 + \sigma_{xy}^2} \quad (5.48)$$

where σ_1 and σ_2 are respectively the maximum and minimum principal stresses oriented at an angle θ relative to the X -axis (for $\sigma_x > \sigma_y$, and Y -axis for $\sigma_y > \sigma_x$) determined by

$$\tan 2\theta = \frac{2\sigma_{xy}}{\sigma_x - \sigma_y}. \quad (5.49)$$

Additionally,

$$\begin{aligned} \tau_{\max} &= \pm \sqrt{\left(\frac{\sigma_x - \sigma_y}{2}\right)^2 + \sigma_{xy}^2} \\ &= \pm \frac{\sigma_1 - \sigma_2}{2} \end{aligned} \quad (5.50)$$

is the maximum shear stress whose direction is located at an angle $+45^\circ$ (anticlockwise is positive) from σ_1 and -45° from σ_2 . Noting the similar structure in Eqs. (5.47) and (5.48) and the fact that the expression for τ_{\max} is the same as the square root terms in them, we can decompose the expression for the principal axes into two parts,

$$\sigma_I = \frac{\sigma_x + \sigma_y}{2} \quad (5.51)$$

$$\sigma_{II} = |\tau_{\max}| \quad (5.52)$$

such that

$$\sigma_1 = \sigma_I + \sigma_{II} \quad (5.53)$$

$$\sigma_2 = \sigma_I - \sigma_{II} \quad (5.54)$$

or conversely that

$$\sigma_I = \frac{\sigma_1 + \sigma_2}{2} \quad (5.55)$$

$$\sigma_{II} = \frac{\sigma_1 - \sigma_2}{2}. \quad (5.56)$$

σ_I and σ_{II} are the first and second stress invariants² of maximum stress and maximum shear, respectively. This same procedure can be applied to both the strain and strain-rate tensors.

The invariants for the VP rheology are

$$\sigma_I = \zeta \dot{\epsilon}_I - \frac{P}{2} \quad (5.57)$$

$$\sigma_{II} = \eta \dot{\epsilon}_{II} \quad (5.58)$$

where $\dot{\epsilon}_I$ and $\dot{\epsilon}_{II}$ are the strain-rate invariants

$$\dot{\epsilon}_I = \frac{\partial u}{\partial x} + \frac{\partial v}{\partial y} \quad (5.59)$$

$$\dot{\epsilon}_{II} = \sqrt{\left(\frac{\partial u}{\partial x} - \frac{\partial v}{\partial y}\right)^2 + \left(\frac{\partial u}{\partial y} + \frac{\partial v}{\partial x}\right)^2} \quad (5.60)$$

derived using the same procedure as for the stress tensor only without the 1/2 factor (see for example Fung, 1977). Note that the first strain-rate invariant is simply the divergence of the flow field while the second strain-rate invariant is the maximum shear deformation which is a combination of two of the four DKPs, normal and shear deformation, described in Chapter 3. Since divergence is also a DKP, the fourth of these, being vorticity, is the only DKP component not included in these invariants.

If we plot the two invariants (σ_I and σ_{II}) for VP in principal axis space (σ_1 vs σ_2) we note two very important things (Figure 5.14A). First the invariants reside in the quadrant of principal axis space where both the major and minor axes are negative indicating that ice is a compressive material with very little tensile strength. Second the orientation and position of the two invariants in both the stress and strain serve as major and minor axes of an ellipse we can create through the following relations in the principal stress plane and principal strain plane, respectively as follows. In the principal stress plane

$$\frac{\left(\sigma_I + \frac{P}{2}\right)^2}{\left(\frac{P}{2}\right)^2} + \frac{\sigma_{II}^2}{\left(\frac{P}{2e}\right)^2} = 1. \quad (5.61)$$

In the principal strain plane

$$\frac{(\zeta \dot{\epsilon}_I)^2}{\left(\frac{P}{2}\right)^2} + \frac{(\eta \dot{\epsilon}_{II})^2}{\left(\frac{P}{2e}\right)^2} = 1. \quad (5.62)$$

These two sets of axes are compatible due to a condition known as the normal flow rule (Zubov, 1943) where the direction of the strain flows perpendicular to lines of constant

²Invariant of a tensor is by definition independent of any coordinate system.

stress. e is the ratio between the major and minor axis. The squared terms in the denominator of each term on the left hand side are the radii of the major and minor axes, respectively. The size and scaling of these radii are a function of P and e . In the numerator, the addition of the pressure term for the stress invariant (or major axis) determines the physical position of the ellipses relative to each other. In VP this ellipse serves as the yield curve with $e = 2$ being the empirical value determined by Hibler because the presence of twice as much shear versus divergence in the observed Arctic ice pack (Hibler, 1979). The ice flows plastically at any point on the yield curve and flows as a viscous fluid everywhere inside the ellipse. Note that by assuming an elliptical shape, the bounds of the yield curve allow for a small amount of tensile strength.

CAV has compressive strength only (no shear) so $\sigma_{II} = 0$ for this rheology. In principal axis space this rheology appears as a straight line equal to σ_I as shown in Figure (5.14B) with yielding occurring only at the point where $\sigma_1 = \sigma_2 = -P_{\max}$. At any point between P_{\max} and $\sigma_1 = \sigma_2 = 0$ the flow is incompressible and at the origin it experiences free drift as described in Section (5.1.1).

For VP, ellipses with the same e value as the yield curve describe regions of constant viscosity. However, depending on the closure method specified, these viscous ellipses can be oriented in a number of different ways inside the elliptical yield curve. Two methods are considered here. The first method, as shown in Figure (5.14C) is that devised by Hibler (1979) which defines concentric ellipses about the point $\sigma_1 = \sigma_2 = -P/2$. In this case the bulk viscosity (ζ) is computed from the pressure as

$$\zeta = \frac{P}{2\Delta} \quad (5.63)$$

and then checked against a maximum bulk viscosity and correspondingly adjusted, $\zeta = \text{Min}(\zeta, \zeta_{\max})$, to ensure that it never exceeds a given maximum. A second method used by Ip et al. (1991) and Ip (1993) includes an additional step after the adjustment of ζ wherein the pressure is also corrected so that Eq. (5.63) is once again satisfied as

$$P = 2\Delta\zeta. \quad (5.64)$$

Physically this means that the pressure can only be equal to or less than its initial value. From Eq. (5.61) we see that this causes two effects. First from the denominator of this equation we see that this method decreases the size of the viscous and yielding ellipses. Secondly due to the pressure dependence in the numerator of the major axis term, a shift of the ellipses toward the origin along the stress invariant axis will occur. The result as seen in Figure (5.14D) is that the viscous ellipses are no longer centered at $\sigma_I = P_{\max}/2$ but are now forced to make contact with the origin. The advantage of this second method (also called the Replacement Method) is that in the absence of forcing, the ice experiences no motion which is more realistic. Previous work by Ip (1993) and Song (1994) also indicate that the replacement method compares statistically better with buoy data than the Concentric Ellipse Method in Arctic simulations. For this study in particular, use of the replacement method in VP is a better suited method to use when making comparisons against CAV as the maximum stress invariant (σ_I) at any instant in VP is directly compatible to P_{\max} in CAV. The main disadvantage is the extended amount of computer time needed to determine the solution, since a number of pseudo time steps are needed for the pressure to undergo the necessary adjustment.

On the large-scale, tensile stress is not believed to exist between systems of ice floes. Building from the replacement method an additional improvement to the rheology can be achieved by removing the effect of tensile stress through the condition

$$|\sigma_1 - \sigma_2| < |\sigma_1 + \sigma_2| \quad (5.65)$$

$$\text{such that } \sigma_1 \leq 0. \quad (5.66)$$

In numerical models this is accomplished by constraining the shear viscosity to the condition that

$$\eta \leq \frac{P/2 - \zeta(\dot{\epsilon}_1 + \dot{\epsilon}_2)}{|\dot{\epsilon}_1 - \dot{\epsilon}_2|} \quad (5.67)$$

From Figure (5.14E) the effect of this condition is seen in principal axis space. The regions where σ_1 or σ_2 become positive are removed and hence the name Truncated. An interesting facet to this final closure method is that it quite closely resembles the yield curve shapes derived from laboratory experiments (Schulson, personal communication).

For the 1D and 1.5D cases, this same 2-space principal axis coordinate system still applies since we are dealing with 2-space stress states. In the 1D case, the stresses applied can only be in the same direction or perpendicular to the coordinate system chosen and hence are lacking any σ_{xy} cross term, so the stress is in a principal axis orientation. Because of rotation, the 1.5D stresses can be oriented in any direction. In both cases a number of regions within the ellipse can be reached because shear is present. Its bounds can vary however, depending on the type of closure scheme chosen for the pressure (i.e. concentric ellipse vs. replacement method). We will examine these bounds in 2-space principal axis in more detail below.

Rheologies in 2D Principal Axis Space

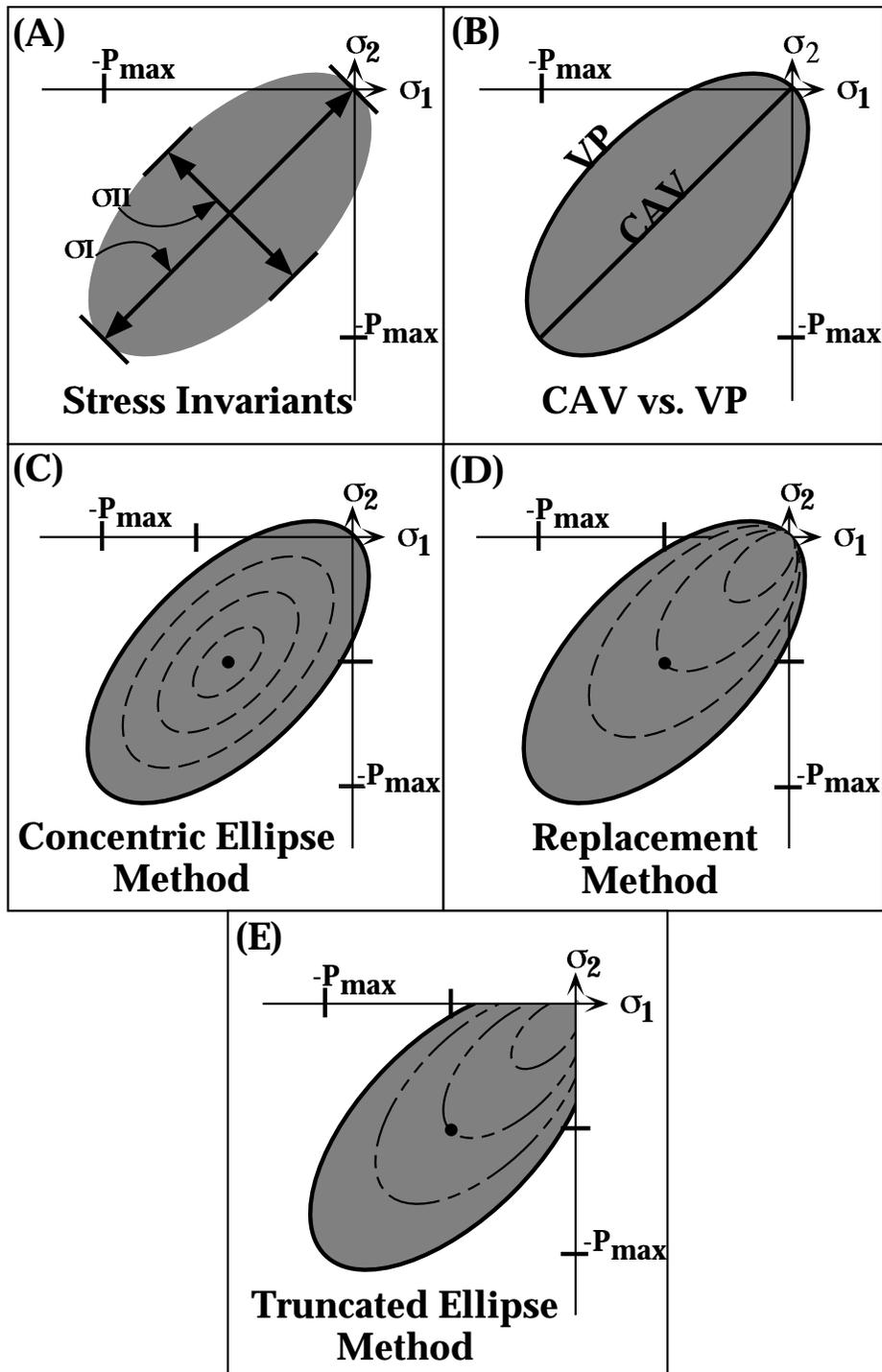


Figure 5.14: Stress Invariants and Rheologies in 2D principal axis space. P_{\max} is a positive pressure term and both P_{\max} and all σ values are in units of (Pa m).

5.2.2 1D Viscous Plastic Code vs. Analytical Solution

The Cartesian 1D VP momentum balance oriented parallel to the Y -axis is

$$u = 0 \quad (5.68)$$

$$-\alpha v + \tau = -\frac{d}{dy}\sigma_{yy} \quad (5.69)$$

$$\sigma_{xx} = (\zeta - \eta)\frac{dv}{dy} - \frac{P}{2} \quad (5.70)$$

$$\sigma_{yy} = (\zeta + \eta)\frac{dv}{dy} - \frac{P}{2} \quad (5.71)$$

$$\sigma_{xy} = 0. \quad (5.72)$$

Using the same configuration as for CAV we have a step function ice thickness distribution with the values specified as in Table 5.1. $P_{\max} = 55000$ (Pa m) is constant for a region with uniform ice thickness of 2 m at 100% compactness, hence $P = P_{\max}$ where there is ice and also a constant in the region where no ice is present (i.e. $P_{\max} = P = 0$).

Starting with the simplest case of free drift with no ice, we have the condition of no ice stress, so $\sigma_{ij} = 0$ as are the differentials and therefore we obtain the same free drift solution as for CAV, namely,

$$\sigma_{xx} = 0 \quad (5.73)$$

$$\sigma_{yy} = 0 \quad (5.74)$$

$$v = \frac{\tau}{\alpha}. \quad (5.75)$$

To solve for the ice region from $y_s \leq y \leq L$, we will consider the case of $\zeta =$ constant. Since $\eta = \zeta/4$ ($e = 2$), this is also constant. From this assumption we see that in the region $y_s \leq y \leq L$ the momentum balance reduces to the second order ordinary differential equation

$$(\zeta + \eta)\frac{d^2v}{dy^2} - \alpha v = -\tau \quad (5.76)$$

where τ in this case is the non-homogeneous term. To solve this we separate the equation into two parts, homogeneous (v_1) and non-homogeneous (v_2), and seek solutions for each of these such that $v = v_1 + v_2$. Looking first at the homogeneous equation

$$(\zeta + \eta)\frac{d^2v_1}{dy^2} - \alpha v_1 = 0, \quad (5.77)$$

we get the general solution for v_1 that

$$v_1 = C_1 e^{\psi y} + C_2 e^{-\psi y} \quad (5.78)$$

$$\text{where: } \psi = \sqrt{\frac{\alpha}{\zeta + \eta}}. \quad (5.79)$$

Plugging this back into the original equation we find through process of elimination a constant solution for v_2 to be

$$v_2 = \frac{\tau}{\alpha} \quad (5.80)$$

which is the free drift solution for this problem. Thus the general solution to our original equation is

$$v = C_1 e^{\psi y} + C_2 e^{-\psi y} + \frac{\tau}{\alpha}. \quad (5.81)$$

In order to obtain a particular solution we must determine and apply boundary conditions. As with CAV, the velocity at the wall must be zero if yielding is not occurring. If yielding is occurring we will assume a velocity function similar to that for CAV namely,

$$v = \frac{\tau}{\alpha} + \frac{\sigma_{\max}}{\alpha L} \quad (5.82)$$

where σ_{\max} is some maximum stress value to be determined. At the ice edge location $y = L$, the ice stress must be zero so the boundary condition requires the additional consideration that

$$\begin{aligned} \sigma[L] &= \sigma_{yy}[L] \\ &= (\zeta + \eta) \frac{dv}{dy} - \frac{P_{\max}}{2} = 0 \end{aligned} \quad (5.83)$$

$$\frac{dv}{dy} = \frac{P_{\max}}{2(\zeta + \eta)}. \quad (5.84)$$

In terms of velocity, we see that a zero stress condition at $y = L$ produces the Von Neumann boundary condition such that the velocity gradient at the boundary is constant.

Applying these boundary conditions to the general solution we get values for the coefficients of

$$C_1 = \frac{P_{\max}}{4\sqrt{\alpha(\zeta + \eta)} \cosh[\psi L]} + \frac{\sigma_{\max} e^{-\psi L}}{2\alpha L \cosh[\psi L]} \quad (5.85)$$

$$C_2 = -\frac{P_{\max}}{4\sqrt{\alpha(\zeta + \eta)} \cosh[\psi L]} + \frac{\sigma_{\max} e^{\psi L}}{2\alpha L \cosh[\psi L]}. \quad (5.86)$$

Applying these to the general solution we obtain the particular solution

$$v[y_s \leq y < L] = \frac{P_{\max} \sinh[\psi y]}{2\sqrt{\alpha(\zeta + \eta)} \cosh[\psi L]} + \frac{\sigma_{\max} \cosh[\psi(y - L)]}{\alpha L \cosh[\psi L]} + \frac{\tau}{\alpha}. \quad (5.87)$$

Because of the assumption $\zeta = \text{constant}$, the above solution is only an approximation to the force balance in Eq. (5.69). So unlike CAV we do not have an analytic solution which corresponds exactly to the numerical results. Instead we have an approximate solution with one undetermined constant σ_{\max} which can be used as a tuning parameter to solve for the case where these two solutions are nearly the same and compare these responses. For the case of wind = -10m/s we get a solution for v which matches the numerical solution's velocity to 4 significant digits when $\sigma_{\max} = 1.24P_{\max}$. As seen in Figure (5.15) in both σ_1, σ_2 space and σ_{xx}, σ_{yy} space, the approximate solution also matches the stress state close to the wall at $[j = 2]$ and follows along the same stress state path as the numerical solution, up to the center point of the ellipses $(-P_{\max}/2, -P_{\max}/2)$. The analytical solution then jumps immediately to the free drift

state located at the origin while the numerical solution continues from the center point along a path to the origin.

There are four interesting things to note at this point. First, the yield point for this case is located at the very bottom of the ellipse at the point $\sigma_1^{min}, \sigma_2^{min}$ which is where σ_2 and σ_{yy} are at their maximum possible compressive value. Using simple geometry, this location is equal to

$$\sigma_1^{min} = \sigma_{xx}^{min} = -\frac{P_{max}}{2} \left(1 + \frac{e^2 - 1}{e \sqrt{1 + e^2}} \right) \quad (5.88)$$

$$\sigma_2^{min} = \sigma_{yy}^{min} = -\frac{P_{max}}{2} \left(1 + \frac{\sqrt{1 + e^2}}{e} \right). \quad (5.89)$$

For $P_{max} = 55000$ and $e = 2$ these values give $\sigma_1^{min} = -64395$ Pa m, $\sigma_2^{min} = -58246$ Pa m. Second, using the shape of the ellipse, a trial and error guess of $\sigma_{max} = 1.24P_{max}$ fits the empirical relation

$$(2\sigma_{max})^2 = \left(\sigma_{xx}[j = 2] + \frac{P_{max}}{2} \right)^2 + (e\sigma_{yy}[j = 2])^2 \quad (5.90)$$

with about a 1% error for the 10m/s wind case (i.e. $1.25 P_{max}$). This together with the first point indicates that the yielding occurring at the wall is at the maximum possible compressive stress oriented normal to the wall (i.e. the ice is deforming with everything it's got).

Third, the path of the stress state in σ_{xx}, σ_{yy} space is from the maximum yield location to the exact opposite end of the ellipse at the point where σ_{yy} has a tensile strength maximum. This is located at the point

$$\sigma_1^{max1} = \sigma_{xx}^{max1} = -\frac{P_{max}}{2} \left(\frac{\sqrt{1 + e^2}}{e} - 1 \right) \quad (5.91)$$

$$\sigma_2^{max1} = \sigma_{yy}^{max1} = +\frac{P_{max}}{2} \left(1 - \frac{e^2 - 1}{e \sqrt{1 + e^2}} \right). \quad (5.92)$$

Finally, the path in principal axis space proceeds from the yield point to the center point then is deflected towards the maximum σ_1 tensile stress point located at

$$\sigma_1^{max2} = \sigma_{xx}^{max2} = +\frac{P_{max}}{2} \left(1 - \frac{e^2 - 1}{e \sqrt{1 + e^2}} \right) \quad (5.93)$$

$$\sigma_2^{max2} = \sigma_{yy}^{max2} = -\frac{P_{max}}{2} \left(\frac{\sqrt{1 + e^2}}{e} - 1 \right). \quad (5.94)$$

Although σ_{xx}, σ_{yy} are not principal axes they do represent the stress state of the 1D field since σ_{xy} is zero. From these two stress states we see the following condition developing. Yielding occurs at the wall, oriented towards the wall and normal to the wall. As yielding occurs at the wall and the numerical ice is a continuum, it is being pulled away from points located at a distance from the wall. Because of this, consecutive non-yielding grid cells head towards the maximum tensile point in the stress plane. Once the compressive state

Approximate Analytical vs. Numerical Solution
CON, Wind=-10m/s, LD, Sigma_max=1.24*Pmax

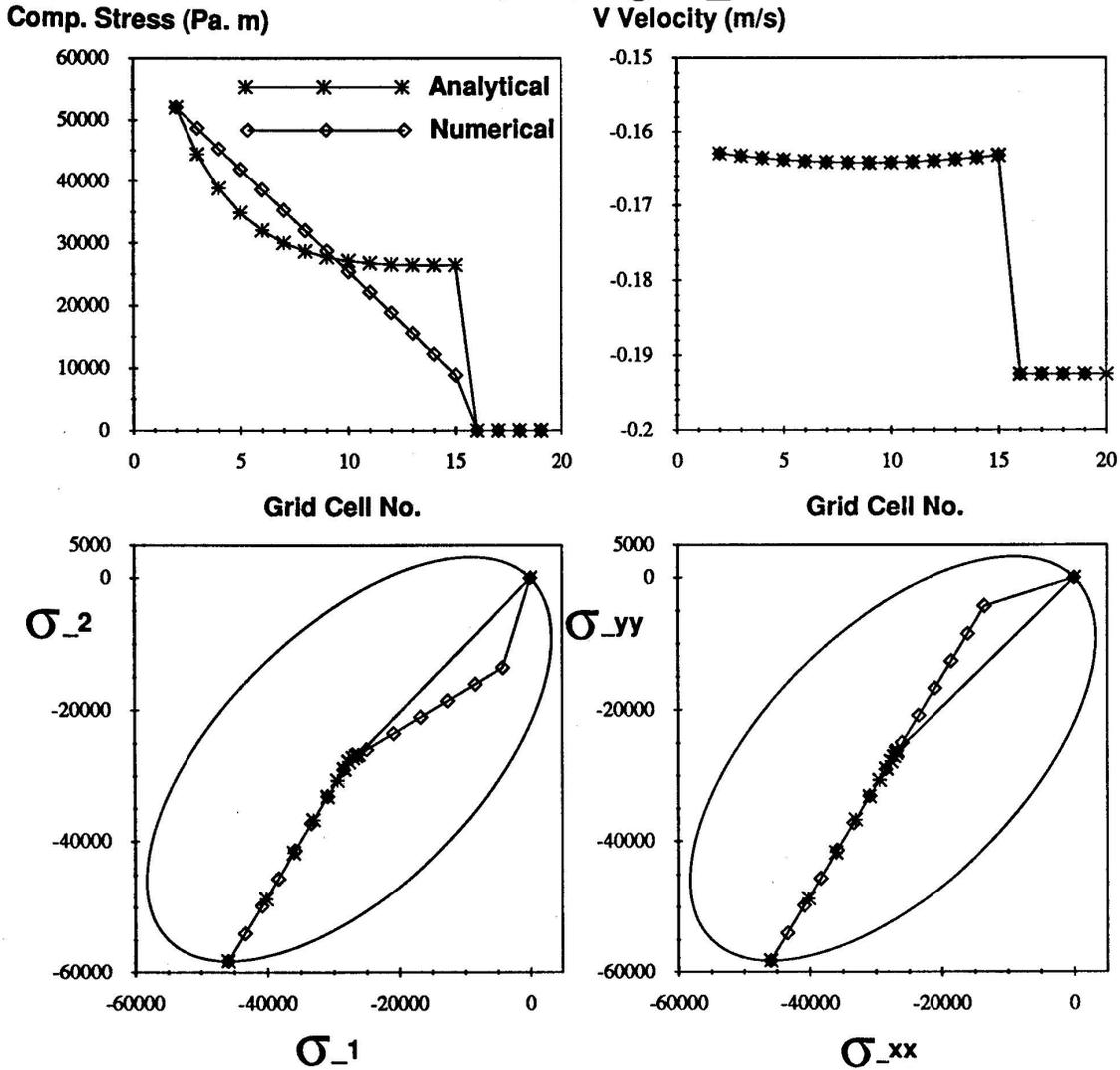


Figure 5.15: Comparison between analytical solution of momentum balance and corresponding numerical case. σ_1 and σ_2 are the coordinates for principal axes space.

reaches the center of the elliptical yield curve the σ_{yy} compressive stresses become smaller than the σ_{xx} stresses and hence the orientation of the stress state flips 90° in principal axis space so that σ_{xx} now becomes the dominant compressive stress. A schematic of this process is shown in Figure (5.16). Since the momentum balance is 1D, these are the only two possible stress states which can exist. If we introduce a rotation to the system, as in the 1.5D model, this same transition occurs but more gradually with the orientation of the stress states moving through several degrees of orientation as one proceeds from the wall to the ice edge. Hence, in the VP simulations, planetary rotation creates a torque on the ice from points of yielding at the coast lines to the open water regions.

Schematic of 1D Grid Stress State

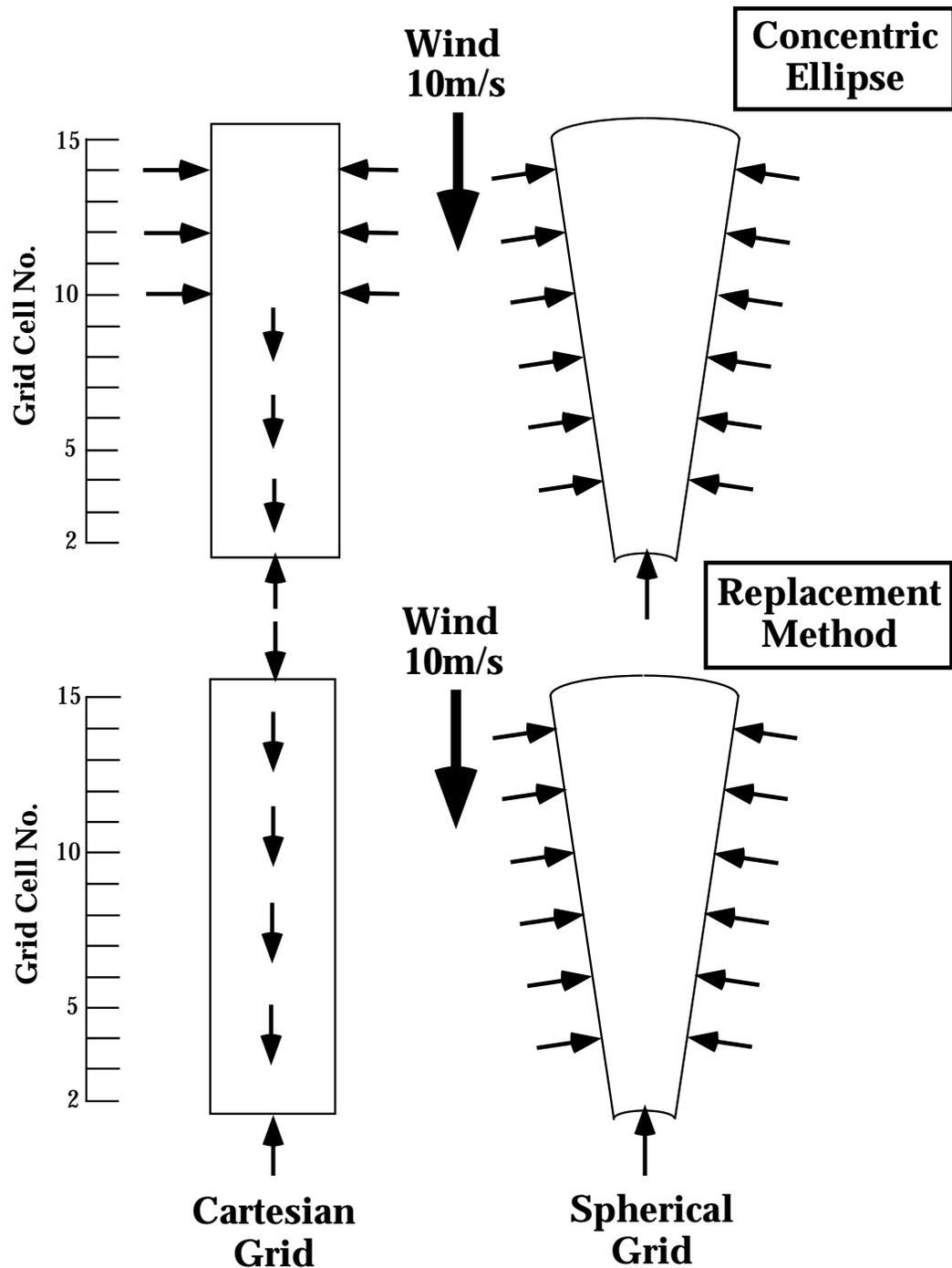


Figure 5.16: Schematic of the stress distribution for the 1D VP 10m/s wind case with Concentric Ellipse closure method. Arrows toward the grid indicate compression, arrows away from the grid indicate tension.

5.2.3 Sensitivity of 1D Viscous Plastic Rheology

In the previous section, we examined the basic dynamic ice responses in the numerical VP model using both analytical and numerical solutions for a very specific case. In this section we will examine how these responses change as we change the various dynamic parameters within the model. Beginning first with the wind speed, we see in the upper left panel of Figure (5.17) that the compressive stress of the VP simulated ice is similar to that for CAV. The only difference is a jump right at the ice edge between ice and no ice, but the linear pressure gradient from the wall to the edge occur just as in CAV as does a zero stress state in the free drift region. Additionally we see in the lower left panel that for representative wind speeds of -0.1, -1.0, and -10.0 m/s winds, the principal axis path is nearly the same. For a very low wind speed where there is no yielding (-0.1m/s are the stars), the stress state path proceeds from the origin to a path oriented from σ_1^{\max} to the center of the ellipse but only extends a short distance. As the wind increases (-1.0m/s triangles) the path extends along this same line, reaches the center of the yielding ellipse then turns toward σ_2^{\min} but never reaches the yield curve. The final case of yielding is the one discussed in the previous section. This stress state path is the same for all wind velocity cases shown here. The only difference from case to case is how far along the path they reach which is a function of how strong the wind is.

The corresponding velocities, shown in Figure (5.18), are nearly identical to those in CAV. The only difference is a very slight downward bend in the non-free drift velocities in all cases and the presence of positive velocities in the non-yielding cases. These positive values are due to the initial jump in compressive stress right at the ice edge (grid cell 15) which is caused by the concentric ellipse closure scheme. Since the viscous ellipses (as described in Section 5.2.1) are concentric in this closure scheme, even when there is no yield stress imposed on the ice, it moves as if it was yielding. Since the yielding velocity at the wall is zero, it moves positively away from the wall. This response is caused by the presence of viscosity which moves the ice even when it shouldn't be moving and when viscosity should have no effect. As seen from these figures the main side effects of this closure are small motions at low wind speeds when the ice should be stopped, and a discontinuity at open boundaries.

In spherical coordinates the response is also similar to CAV in the compressive stress and velocities except for the conditions just described. What is new is the information we get in looking at the stress state in principal axis space. As seen in the lower right hand panel of Figure (5.18), unlike the Cartesian VP CON case, the spherical case does not have a straight line path through principal axis space. Instead at low wind speeds without yielding it jumps from the origin to a curved path in principal axis space which is no longer oriented toward any specific yield curve point. When yielding occurs, however, the stresses jump from the origin to some location along the yield curve and move along the curve toward the bottom of the curve. Examining these same responses in $\sigma_{\lambda\lambda}$, $\sigma_{\phi\phi}$ space (Figure 5.19) we see that yielding does occur at the wall at $\sigma_{\phi\phi}^{\min}$ as was the case in Cartesian. Immediately after that, however, the stress state flips and it is the side walls of the grid which impose lateral stresses due to the fact that the grid side walls are no longer parallel to the imposed wind (see Figure (5.16) for schematic description).

The behavior due to viscosity at low wind speeds has been investigated by Ip (1993, 1994) who devised a closure scheme whereby the viscous ellipses were moved to the origin

rather than being concentric (see Chapter 4 for details). Using this method we see in Figures (5.20) and (5.21) that we obtain solutions which are more in agreement with those in CAV and which satisfy the condition of stress continuity at the ice edge. We also see identical paths in principal axis space and σ_{xx}, σ_{yy} space so the process of the stress states flipping part way through in Cartesian coordinates has also been removed. Additionally we see that the jump from the origin to the non-free drift grid cells is now continuous in principal axis space as well. The differences in spherical coordinates are only slight and the flip in stress orientation is still present, but this is also consistent with previous findings. Given these results, this closure scheme is fundamentally more realistic than the concentric ellipse scheme.

An approximation to CAV using VP is made possible by setting the ratio of the major to minor axis to some large value such that the ellipse of the elliptical yield curve approaches a straight line oriented along σ_I . Results from this run (Figures 5.22 and 5.23) come very close to reproducing the results in CAV. There is some difference in the compressive stress at the point just beyond the wall in spherical coordinates and the velocity in spherical coordinates is a bit different. From principal axis space we see that the yield point in this approximation (VP→CAV) is actually less than the yield point in the other two closure methods in VP. Furthermore the difference in response in spherical coordinates is due to the fact that only the wall point is allowed to yield through this approximation even in spherical coordinates. So while this method is very good for reproducing Cartesian responses it is lacking in the ability to yield at points away from the wall which is present in spherical CAV runs.

Comparing the three closure types just presented above, one very important process becomes clear, namely the effect of shear on the different configurations. In CAV and in VP→CAV we see that the shear stress (σ_{II}) is zero. In the concentric ellipse case the shear stress is at a minimum in Cartesian coordinates at the center of the ellipse but then as one proceeds along the Cartesian stress state path in either direction away from that center shear stress increases linearly. This means that when ice is present there is an increasing amount of shear with increasing compressive stress but also an increase amount of shear with decreasing compressive stress which seems counter intuitive with real ice behavior. Contrary to this the Replacement Method forms a stress state path from the origin to the $\sigma_{xx}^{min}, \sigma_{yy}^{min}$ which produces a linearly increasing amount of compressive stress and a linearly increasing shear stress which is fundamentally more consistent with real ice behavior. In spherical coordinates, the stress state with yielding at the wall is accompanied by yielding of interior grid cell points due to the effects of the grid configuration. With respect to shear there is actually an increase in shear away from the wall and a corresponding decrease in compressive stress. This means that as the compressive stress decreases with distance from the south wall, it acts to relieve the pressure in the ice and to encourages shear. When yielding is not achieved there is still a non-linear increase in shear stress for grid cells closer to the wall. Hence in a 1D formulation, the spherical coordinate allows most of the states of shear to exist while the Cartesian coordinate only allows shear over a far more limited range along a set stress state path determined by the closure scheme. In light of this information, the Replacement Method closure scheme and spherical coordinate grid configuration provide the best combination for examining ice dynamics in one dimensional models.

In Cartesian coordinates, the 1D model will maintain the same stress state path

regardless of northward or southward wind. The effect of wind direction in spherical coordinates, however, is substantial. As seen in Figure (5.24), a south wind (blowing northward) will produce a very small compressive stress and velocities approaching those of free drift close to the wall. This response is due to the fact that in spherical coordinates the lateral walls are getting wider northward and hence the entire field is expanding. Yielding is occurring at the north wall for wind velocities in these examples of 5 m/s and greater but due to the spherical grid shape a tensile yielding is occurring. As seen in principal axis space all the wind cases are experiencing a positive stress in the $\sigma_1 = \sigma_{\lambda\lambda}$ direction and a negative stress in the $\sigma_2 = \sigma_{\phi\phi}$. In comparing amounts of compressive versus shear stress we see that in this state most of the yielding is occurring due to shear and not compressive stress. This condition of yielding at points away from the wall in spherical coordinates was seen in CAV, only now, the presence of tensile strength and shear in VP allows for additional processes to develop which were not possible with CAV.

Examining the response to these same conditions for the truncated ellipse provides the best example of its effectiveness. As seen in Figure (5.25), the primary difference between the Truncated Ellipse and the Replacement method is under conditions where tensile stress can arise. Contrary to the previous case we see from this figure the stress path of the transect to be bound to the σ_2 axis hence fulfilling the requirement discussed in Section (5.2.1) that $\sigma_1 \leq 0$. The compressive stresses are general higher. The velocities are very similar but the truncated ellipse has a more uniform velocity characteristic in the ice region due to the fact that the stress state has changed from tensile yielding to incompressible flow.

Responses using quadratic drag versus linear drag are shown in Figures (5.26) and (5.27). As with CAV, at lower wind speeds the ice responses are less and at higher wind speeds responses are greater than for linear drag with the difference between free drift and non-free drift being reduced as wind speed increases. An additional effect not seen before is that at very high wind speeds, the ice velocity moves slower near the yielding region at the wall than in regions away from the wall (Figure 5.27). Additionally the high wind speed case of 50m/s (+ symbol) is shown in principal axis space. For Cartesian we see that the response is similar to the 10m/s wind speed case except for the positioning of specific values along the same stress state path. In spherical coordinates however, we see that as wind speed increases yielding begins at a greater compressive stress on the yield curve. This illustrates an important point with respect to the amount of shear stress present. For the 10m/s wind speed case yielding begins at the ice edge with a compressive stress equal to about $-\sqrt{2}P_{\max}/2$ but at the maximum σ_{II} value which is the maximum possible shear value so all of the yielding occurring there is due to shear. Wind speeds below this will reach the yield curve at a compressive stress less than $-\sqrt{2}P_{\max}/2$, then proceed along the yield curve through the maximum shear point and onward. This means that yielding is occurring at the wall due primarily to compressive forces exceeding the ice strength but then within the field, regions are also yielding due to a combination of shear and compression with effects of shear dominating at moderate wind speeds at distance far from the wall.

Finally with respect to resolution sensitivity, from Figure (5.28) we see that VP is extremely robust in both Cartesian and spherical coordinates. For a relaxation iteration tolerance of 10^{-7} , a resolution of 222km down to 200m yields the same results making this numerical method far more robust for high resolution studies than CAV.

Reviewing these sensitivity studies we see that the best choice for one dimensional studies is a spherical coordinate system using VP with the Replacement method and for realistic drag relations, the quadratic drag formulation. This choice covers most of the principal axis elliptical yield curve region which means it covers most yielding and deformation states that a full 2D model would cover and it is fundamentally more realistic than the Concentric method. Given the robust resolution capability of VP compared to CAV and the improved numerical method of Zhang and Hibler (1995), this code is very utilizable for investigating sea ice processes at high resolution. With regard to the processes of deformation we also see that the presence of shear in the system allows for yielding to occur at distances far from the south wall in spherical coordinates due the grid configuration.

1D VP Study: h=2.0m, A=1.0, LD, CON

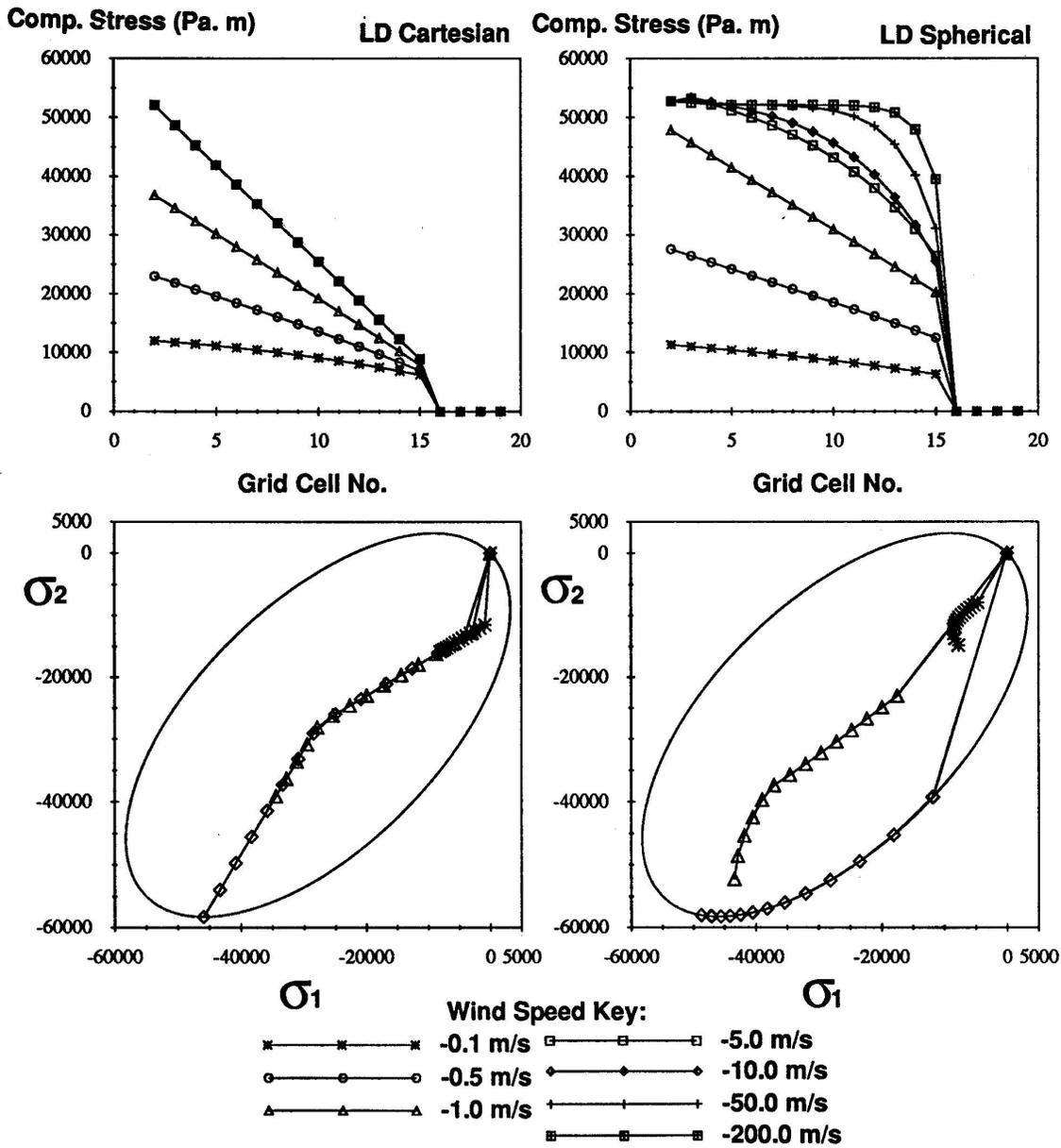


Figure 5.17: Stress state for 1D viscous plastic rheology using linear drag and the concentric ellipse closure method. Representative responses at -0.1, -1.0 and -10.0 m/s winds are included in the principal axis space (σ_1 and σ_2).

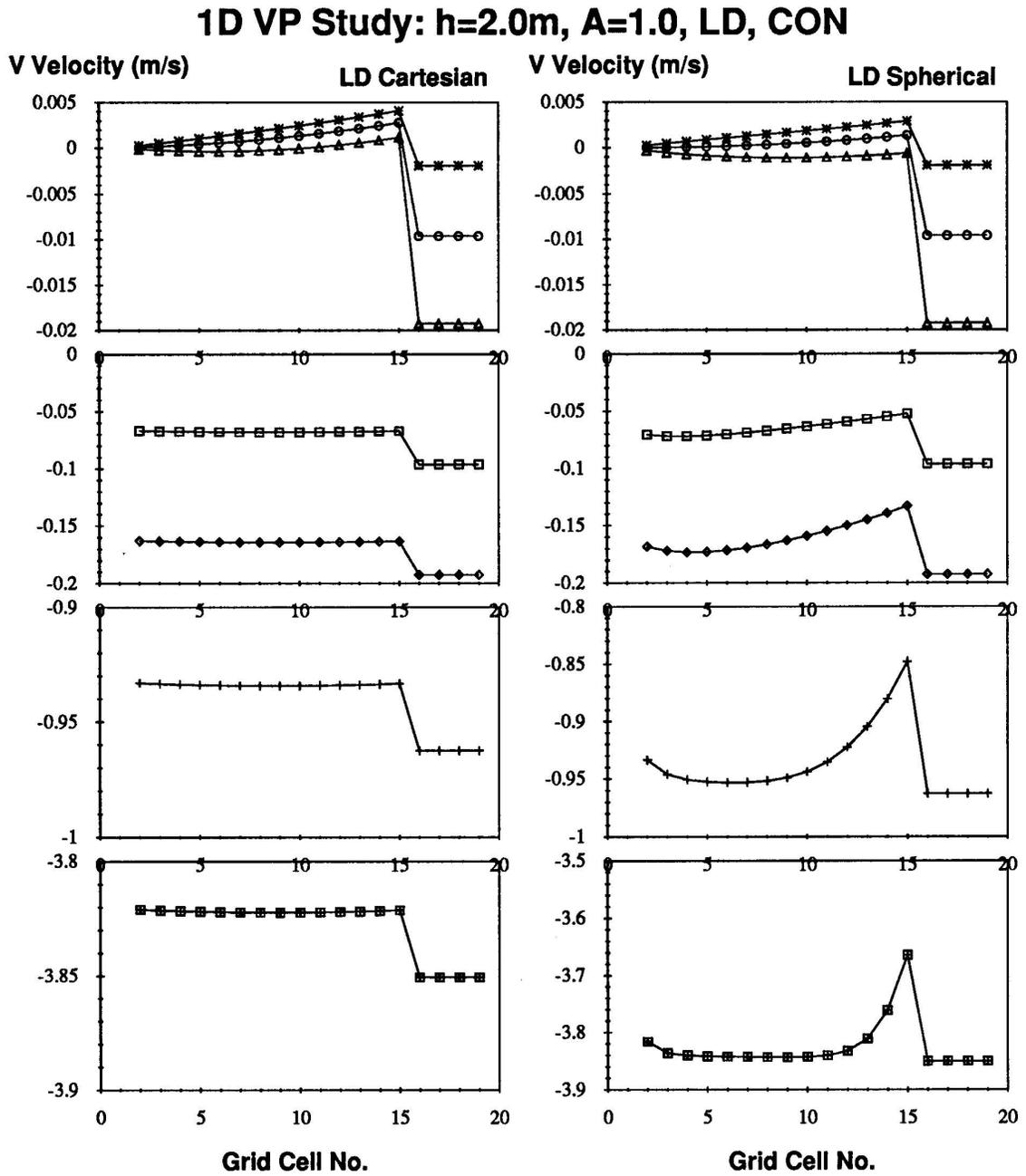


Figure 5.18: Velocity for 1D viscous plastic rheology using linear drag and the concentric ellipse closure method.

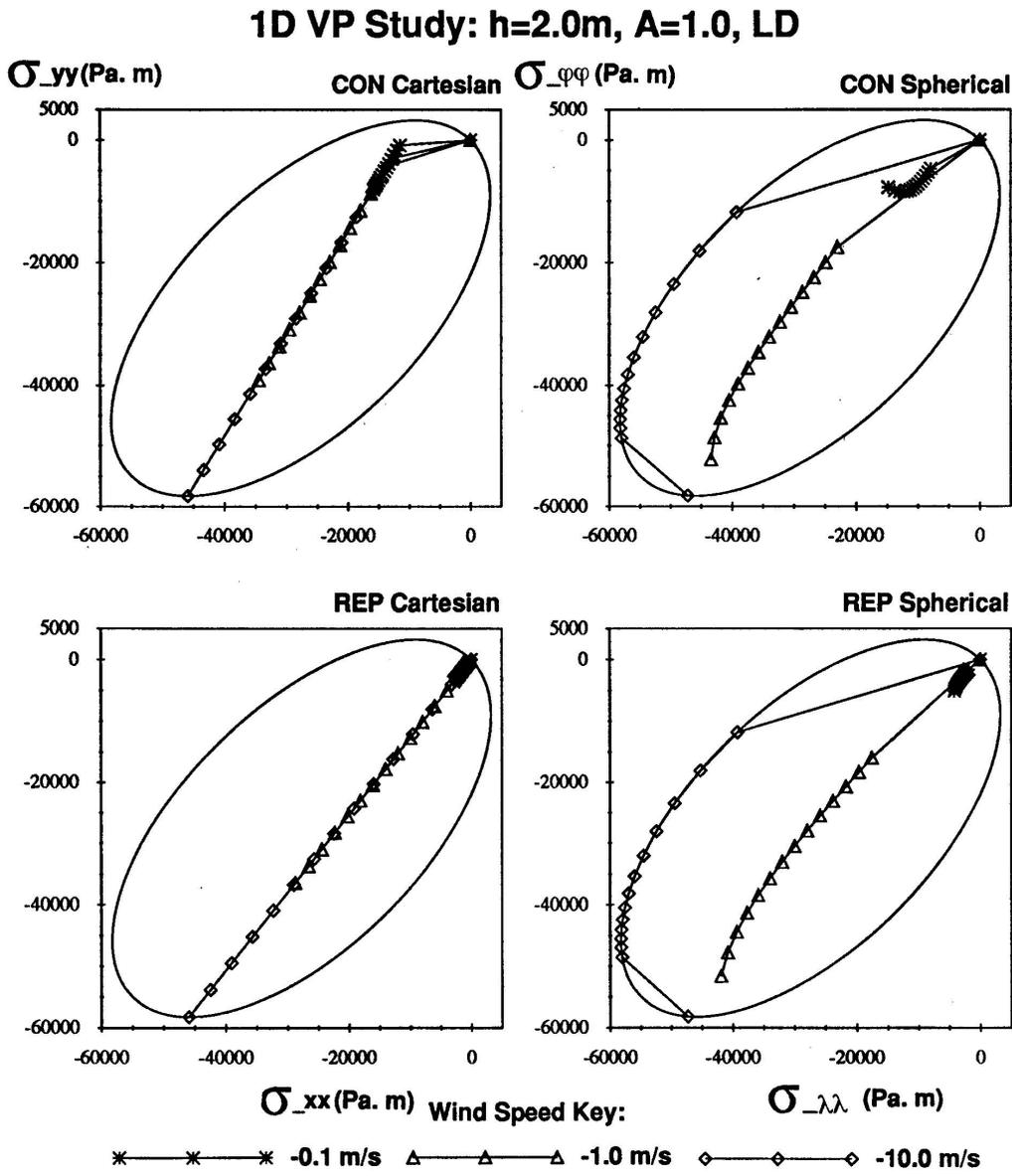


Figure 5.19: Stress states for 1D VP closure methods in σ_{xx}, σ_{yy} space.

1D VP Study: $h=2.0\text{m}$, $A=1.0$, LD, REP

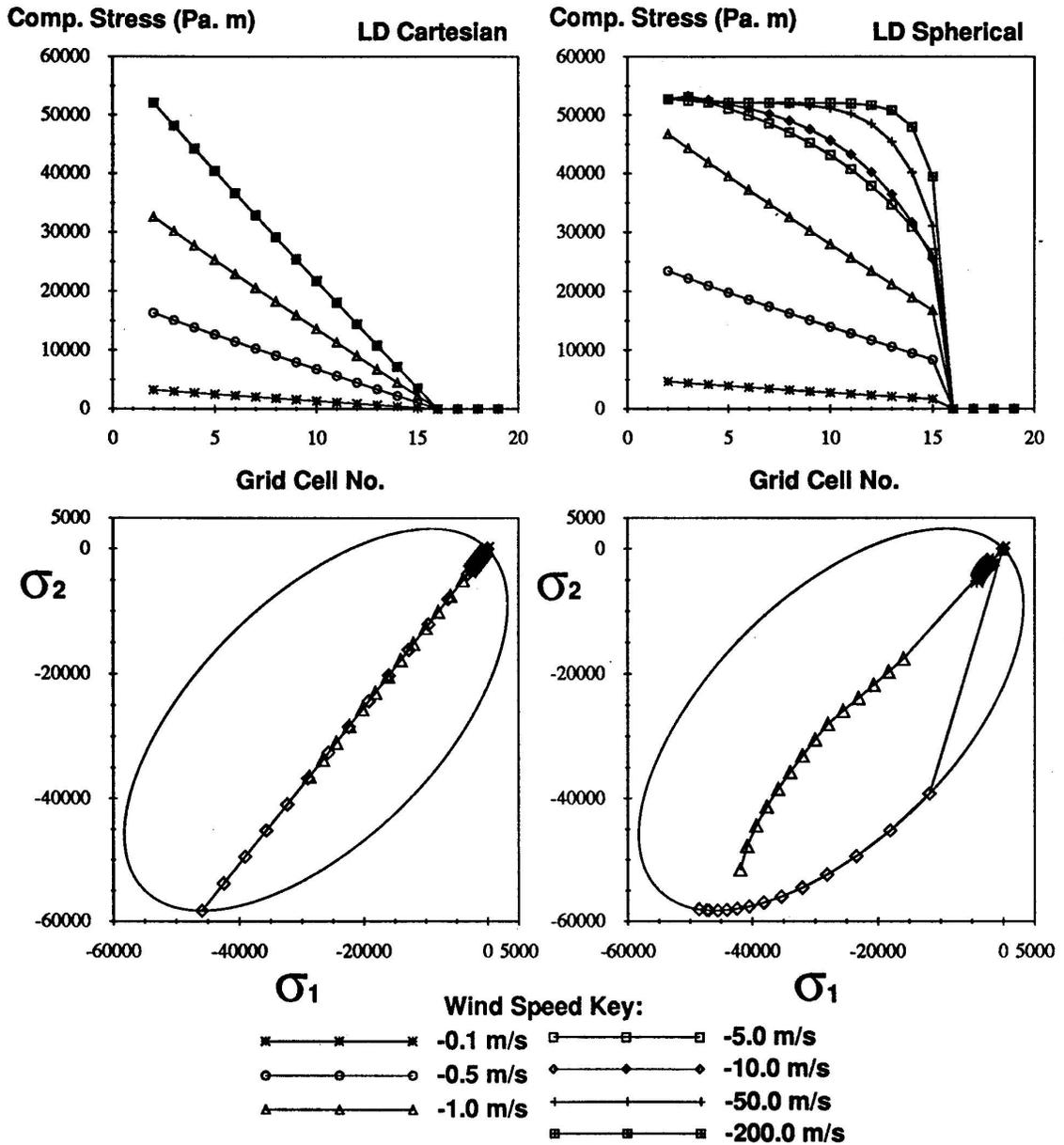


Figure 5.20: Stress state for 1D viscous plastic rheology using linear drag and closure scheme with ellipses to the origin (Replacement Method). Representative responses at -0.1, -1.0 and -10.0 m/s winds are included in the principal axis space (σ_1 , σ_2).

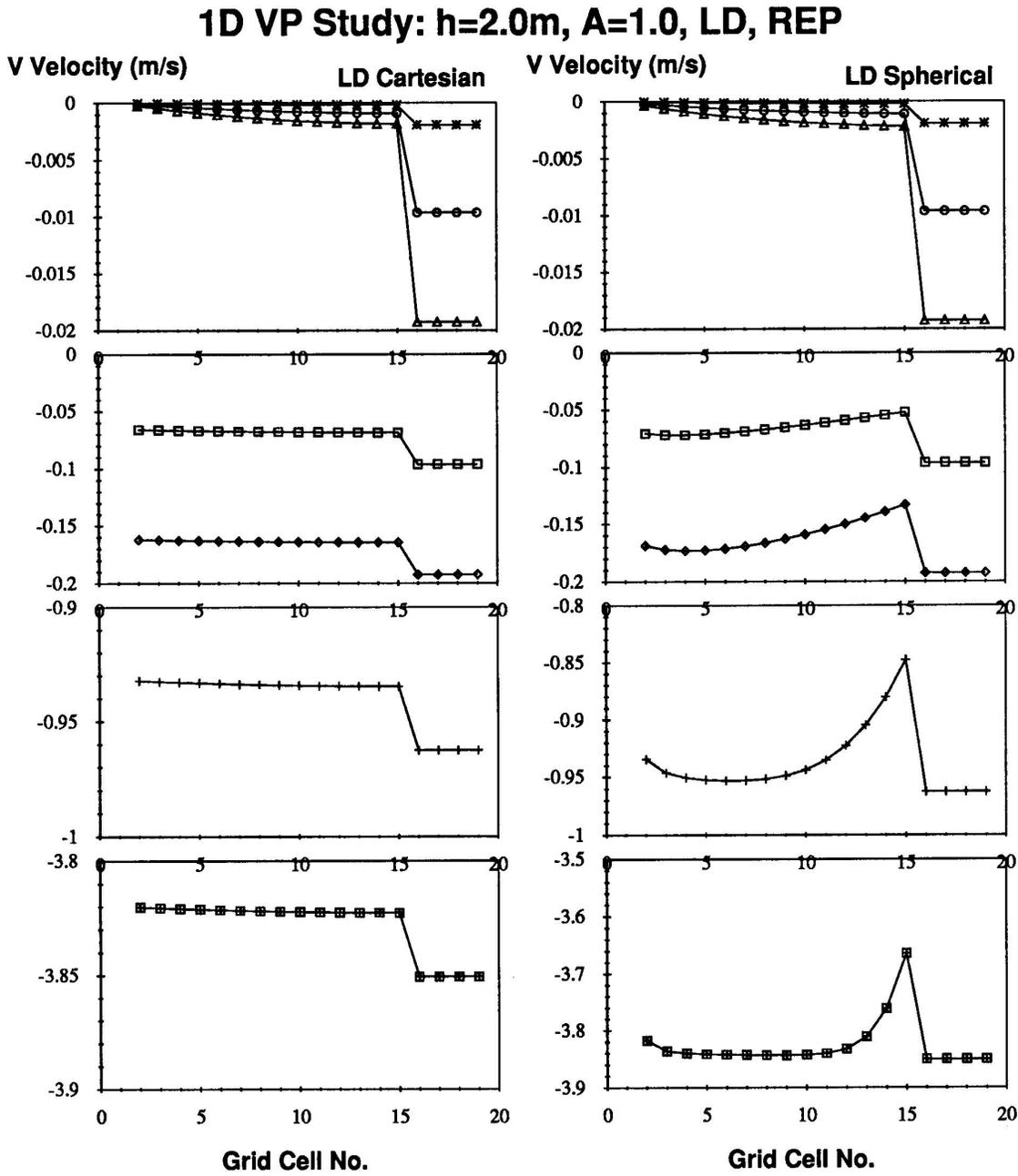


Figure 5.21: Velocity for 1D viscous plastic rheology using linear drag and closure scheme with ellipses to the origin (Replacement Method).

1D VP Study: $h=2.0m, A=1.0, LD, VP \rightarrow CAV$

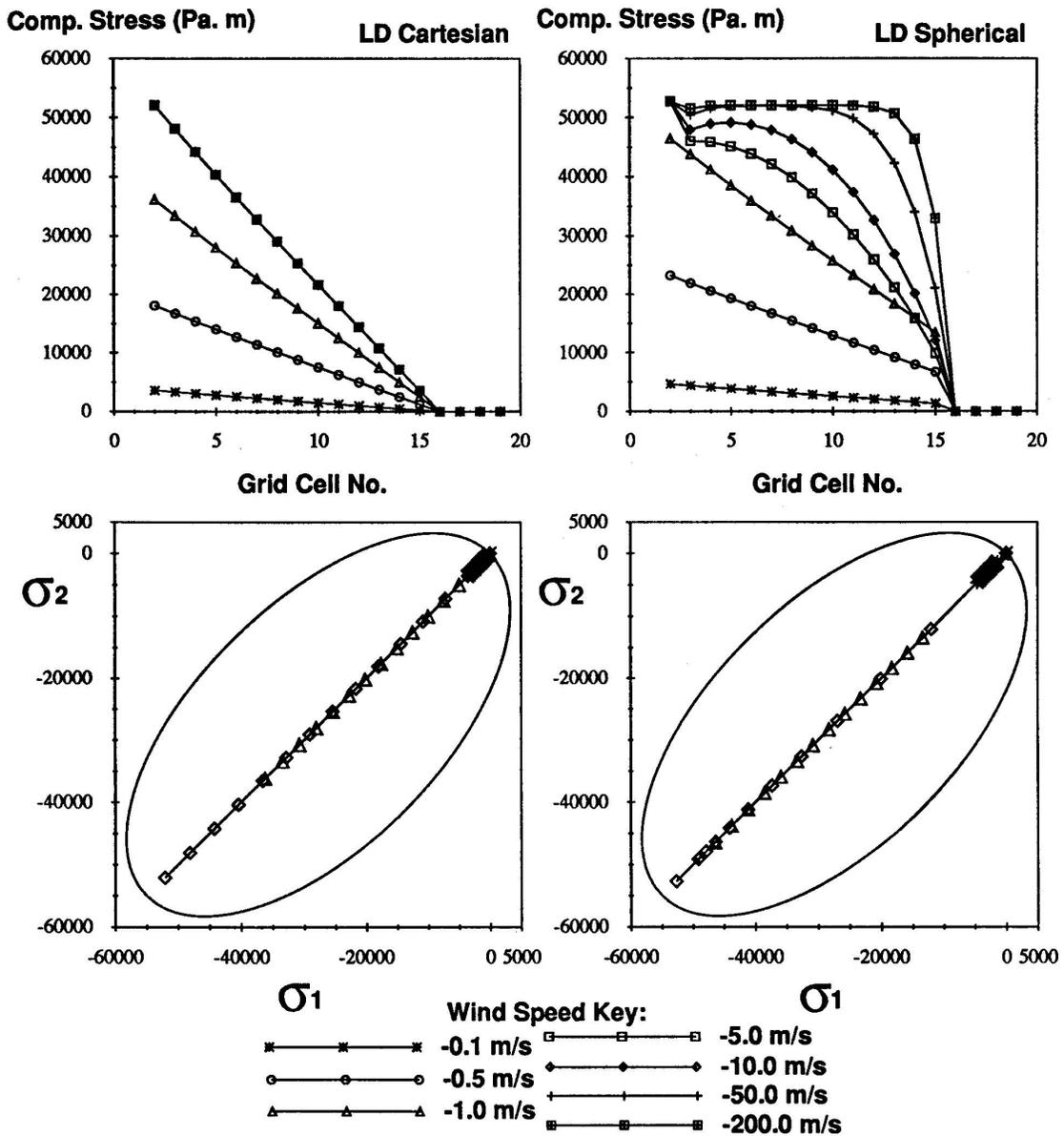


Figure 5.22: Stress state for 1D viscous plastic rheology with closure method approximate to CAV (i.e. $VP \rightarrow CAV$ is VP with ellipse ratio of 1000 for major to minor axis). Representative responses at -0.1, -1.0 and -10.0 m/s winds are included in the principal axis (σ_1, σ_2).

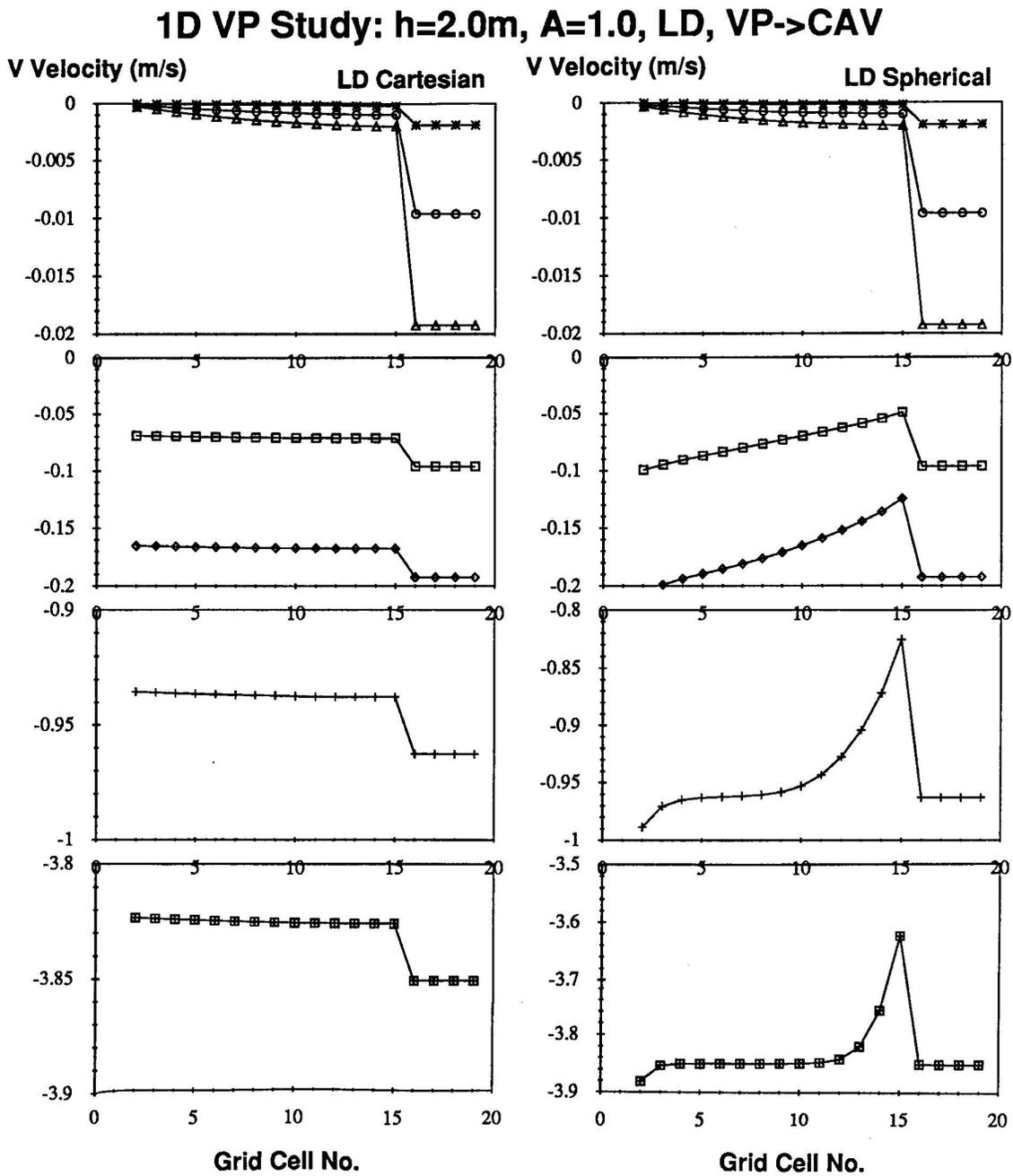


Figure 5.23: Velocity for 1D viscous plastic rheology with closure method approximate to CAV (i.e. VP→CAV is VP with ellipse ratio of 1000 for major to minor axis).

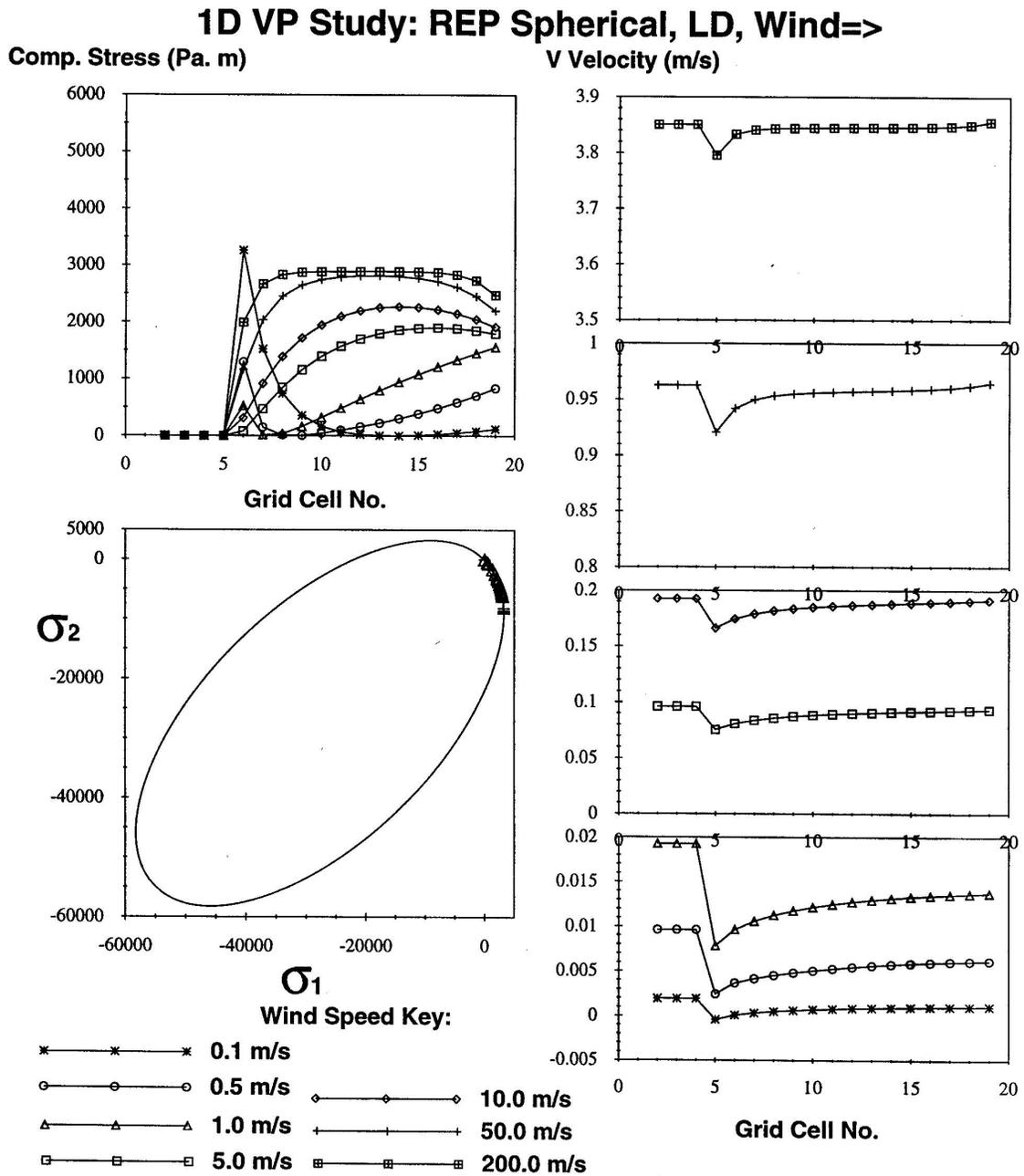


Figure 5.24: Stress state and velocity of 1D VP spherical case with linear drag and Replacement Method for a south wind (i.e. wind=+10m/s). Representative responses at -0.1, -1.0 and -10.0 m/s winds are included in the principal axis space (σ_1, σ_2).

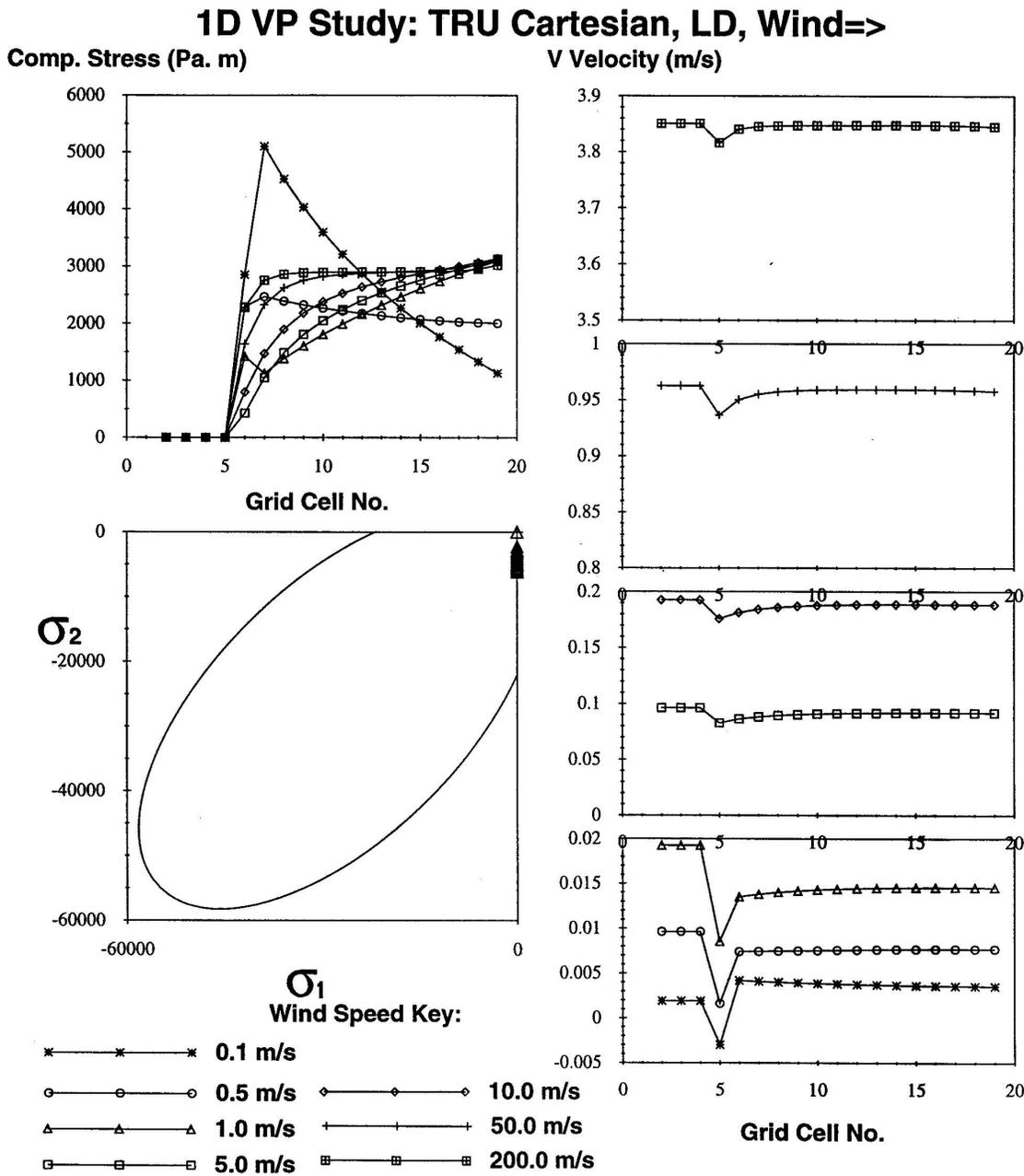


Figure 5.25: Stress state and velocity of 1D VP spherical case with linear drag and Truncated Ellipse for a south wind i.e. wind=+10m/s). Representative responses at -0.1, -1.0 and -10.0 m/s winds are included in the principal axis space (σ_1, σ_2).

1D VP Study: Replacement Method, NLD

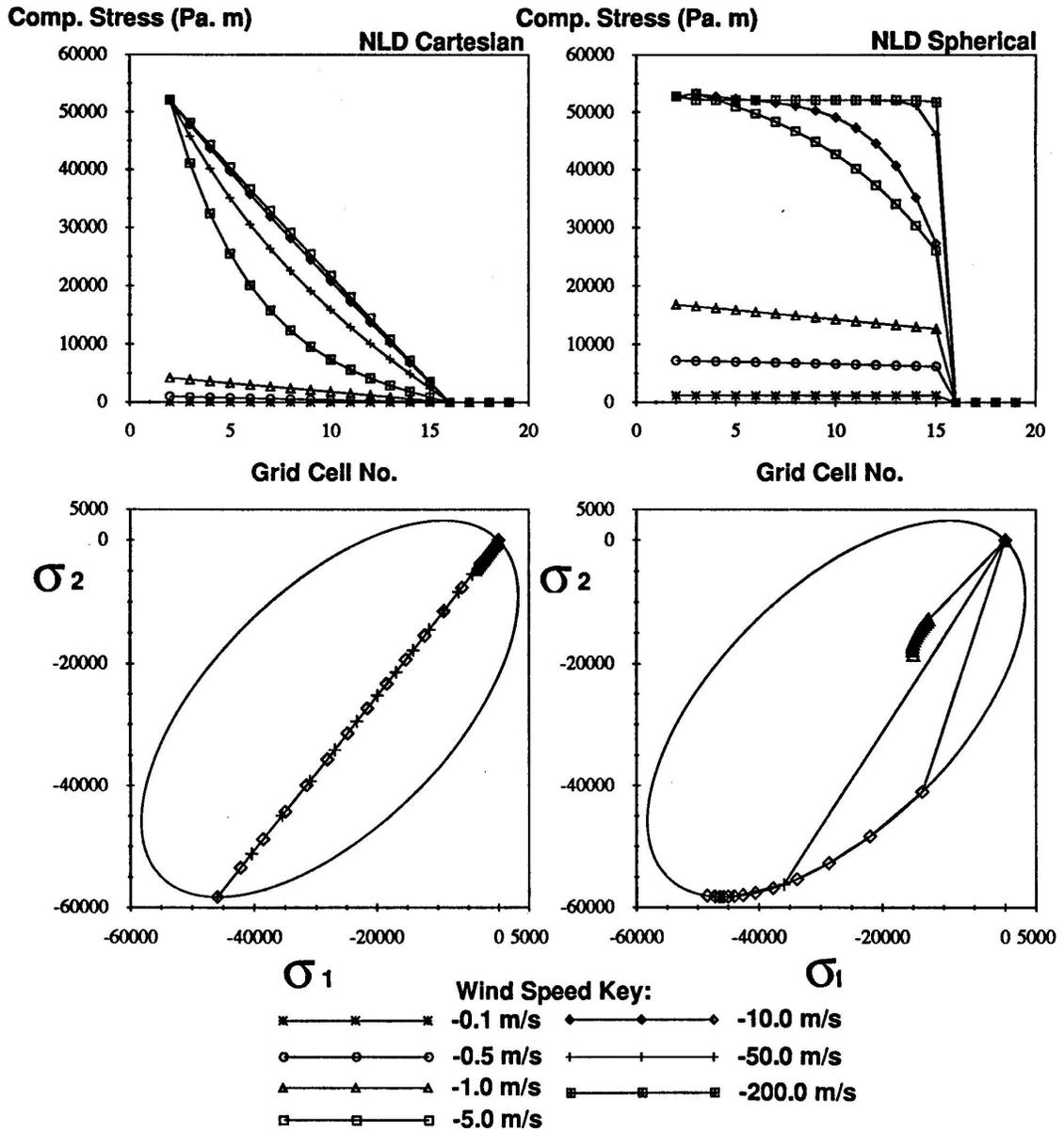


Figure 5.26: Stress state for 1D viscous plastic rheology using quadratic drag and closure scheme with ellipses to the origin (Replacement Method).

1D VP Study: $h=2.0m$, $A=1.0$, NLD, REP

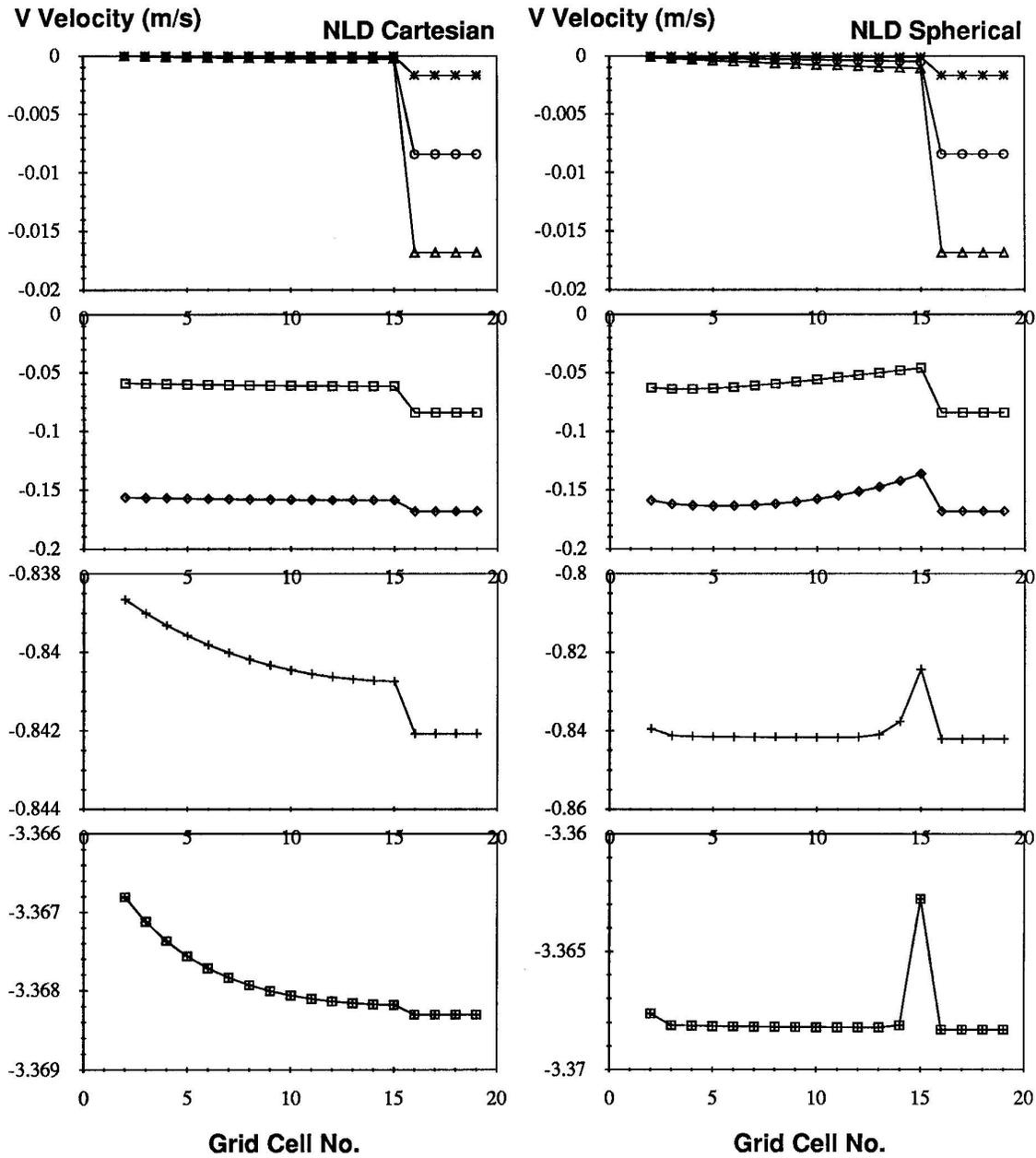


Figure 5.27: Velocity for 1D viscous plastic rheology using quadratic drag and closure scheme with ellipses to the origin (Replacement Method). Representative responses at -1.0 , -10.0 , and -50 m/s winds are included in the principal axis space (σ_1, σ_2) .

VP Resolution Study: Wind=-10m/s, NLD, REP

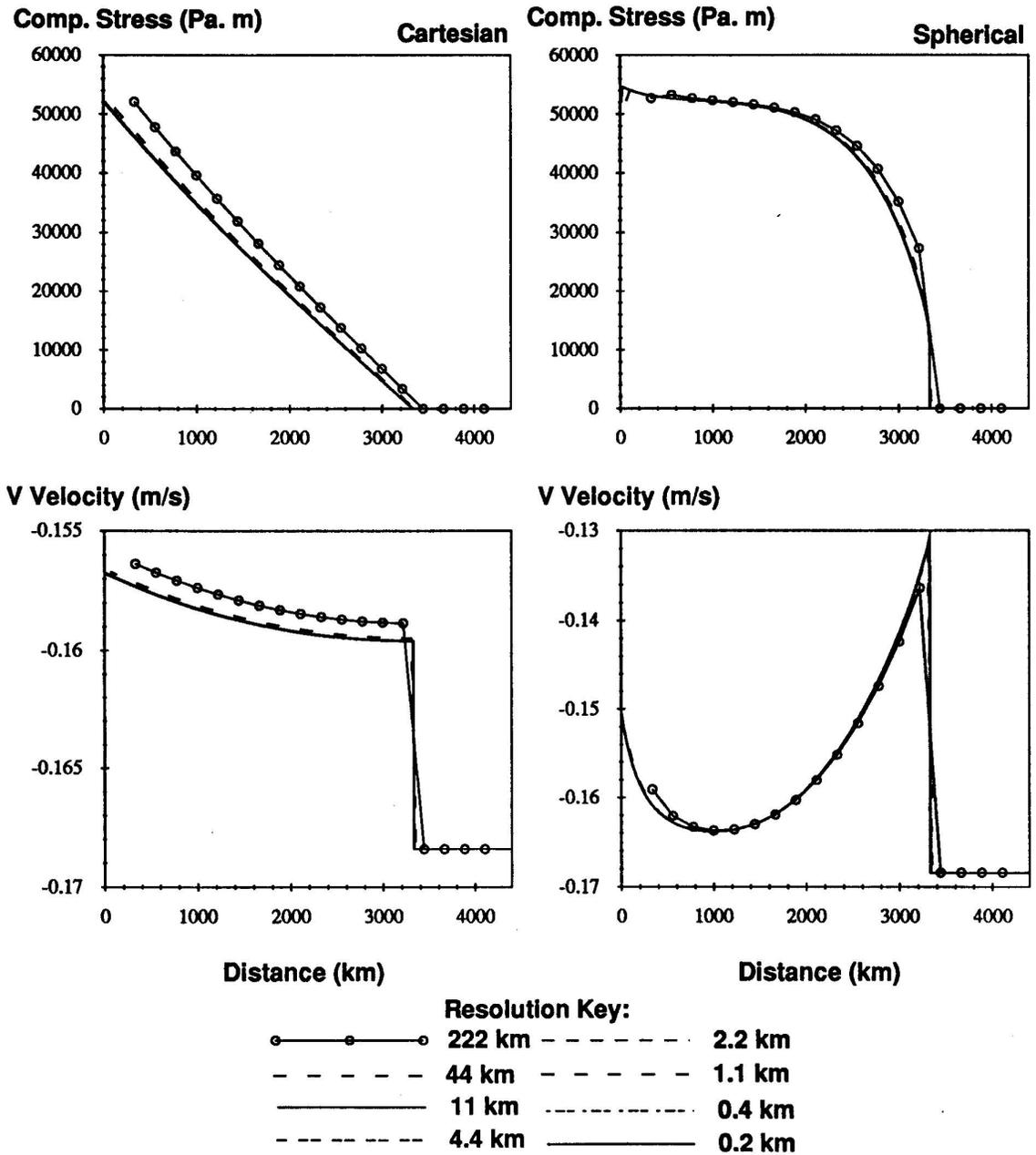


Figure 5.28: Effects of resolution on 1D VP for a relaxation tolerance of 10^{-7} for a range of 222km to 200m.

5.2.4 Dimensional Sensitivity of Viscous Plastic Rheology

The main difference between the 1D and 1.5D VP codes is the inclusion of rotation into the system. With the wind coming from the north and rotation included, the u velocity component no longer vanishes and so forces which in the 1D case were zero now contribute to the force balance of the system. Beginning with the stress state we see in Figure (5.29) for the spherical case that there is little change compared to Figure (5.26) in the compressive stress. In principal axis space the only difference is a slight increase in shear for the intermediate non-yielding case of -1m/s. In the Cartesian case, the compressive stresses are the same as in Figure (5.26) except for the two extreme yielding cases where we see a jump at the ice edge in compressive stress for the -50m/s case and in addition for the -200m/s case there is a notable S-shaped curvature. What is happening here becomes clear in principal axis space as seen for the 50m/s wind speed case (+ symbol). The jump at the ice edge occurs because there is yielding there due to shear. Referring back to the schematic made for the 1D cases (Figure 5.16) with rotation, we create the same situation for Replacement Method as was present in the 1D VP concentric ellipse case in Cartesian. Because of rotation we now have lateral forces impacting on the stress state. With the compressive forces oriented north south and the shear stresses oriented east west, we reach a point close to the ice edge where the compressive stress is low but the shear stresses dominate but then decrease as compressive stress increases toward the south wall.

In the v velocity component in Figure (5.30) we see that compared to the 1D case in Figure (5.27), the rotation reduces the leveling off effect on the wall velocities in Cartesian for high wind speeds. This also reduces the high wind speed ice velocities in spherical coordinates so that now the two cases of Cartesian and spherical are very similar which was also the case in CAV. From the u velocity in Figure (5.31) we also see that at low wind speeds (-0.1,-0.5, -1.0m/s cases) there is a small westward velocity, due to the Coriolis force; the velocity is greatest at the ice edge where the compressive stress is weakest. Once yielding begins at moderate wind speeds (e.g. -5m/s and -10m/s cases, square and diamond symbols), the u velocity direction shifts eastward due to the interaction of the compressive stress at the south wall and primarily shear stresses due to the east and west walls. At very high wind speed (e.g. -50m/s, and -200m/s +, plus square symbols) we see that the u velocity is now eastward with the largest magnitudes at the south wall. The u velocity is nearly uniform in the ice in these cases with most of the yielding due to compressive stress at the south wall and due to shear at the ice edge.

When we increase the system to a 2D momentum balance we introduce forces caused by $\partial/\partial x$ terms which are the normal stress (σ_{xx}) in the X direction and the cross stress (σ_{yx}) in the Y direction. For reasons described in Chapter 4, we are only dealing with Cartesian coordinates in 2D. Looking at the stress state in Cartesian coordinates for both linear and quadratic drag, we see from Figure (5.32) that the 2D system behaves somewhat between the 1.5D Cartesian and spherical responses. The compressive stress in 2D behaves similar to the Cartesian 1.5D compressive stress for quadratic drag except for the presence of a sharp peak in the middle at grid cell 7. Looking at this in principal axis space we see that this spike arises from a maximum in shear stress in both linear and quadratic drag. The shear response in this 2D case is similar to the 1.5D spherical in that yielding in the form of shear occurs at the ice edge and except for the high wind

cases, the ice is yielding at all ice points as it moves along the yielding ellipse along a path from the origin to the minimum σ_2 value. The main difference in 2D is that there are now two locations, right at the ice edge and one in the middle of the field (grid cell 7) where yielding due to mostly shear is reached. The v velocity (Figure 5.33) due to the effect just described, experiences a jump and a reduction in velocity from the shear yield point to the south wall. Except for this jump the v velocity looks like the 1.5D Cartesian velocities. The u velocity exhibits a similar velocity jump near the shear stress peak (Figure 5.34), only the jump is more pronounced. Energetically this means that shear is pulling kinetic energy out of the system between the south wall and the middle yield point (at grid cell 7). This process is analogous to the observed process where land fast ice is being separated by the pack ice through a shear zone.

1.5D VP Study: Replacement Method

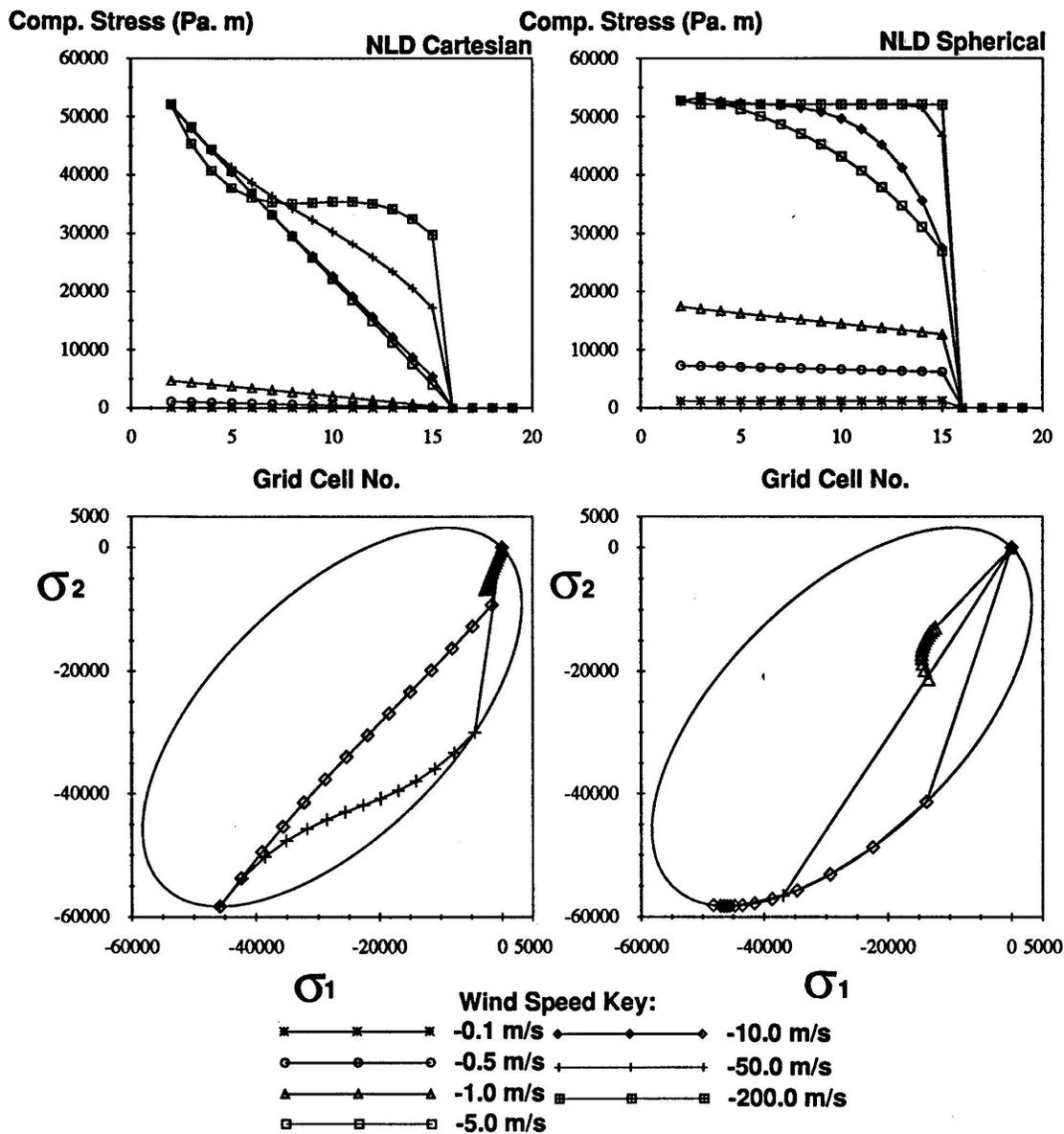


Figure 5.29: Stress state for 1.5D viscous plastic rheology using quadratic drag and closure scheme with ellipses at origin (Replacement Method). Representative responses at -1.0, -10.0, and -50 m/s winds included in principal axis space (σ_1, σ_2).

1.5D VP Study: $h=2.0m$, $A=1.0$, NLD, REP

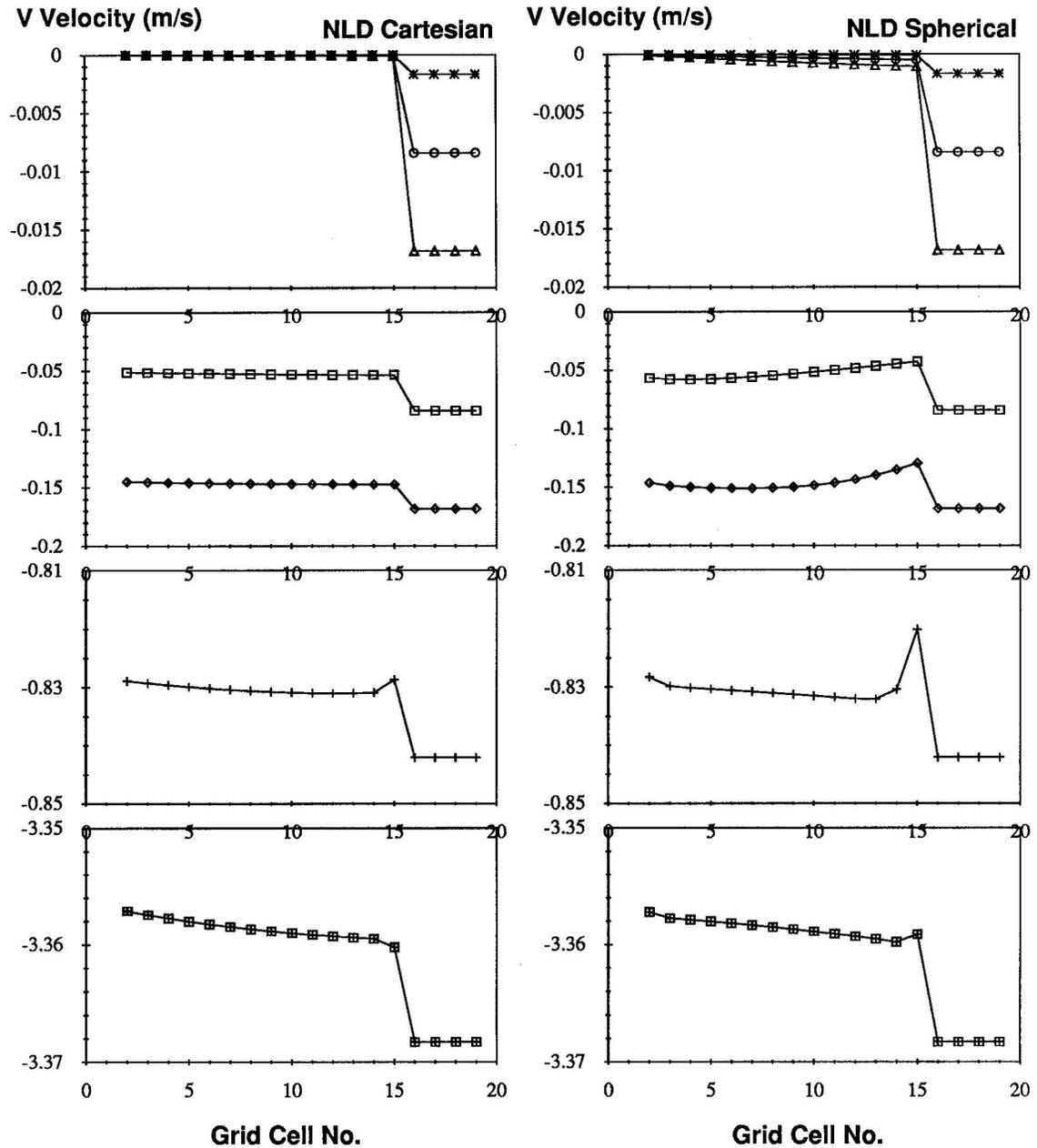


Figure 5.30: V Velocity for 1.5D viscous plastic rheology using quadratic drag and closure scheme with ellipses to the origin (Replacement Method).

1.5D VP Study: $h=2.0m, A=1.0, NLD, REP$

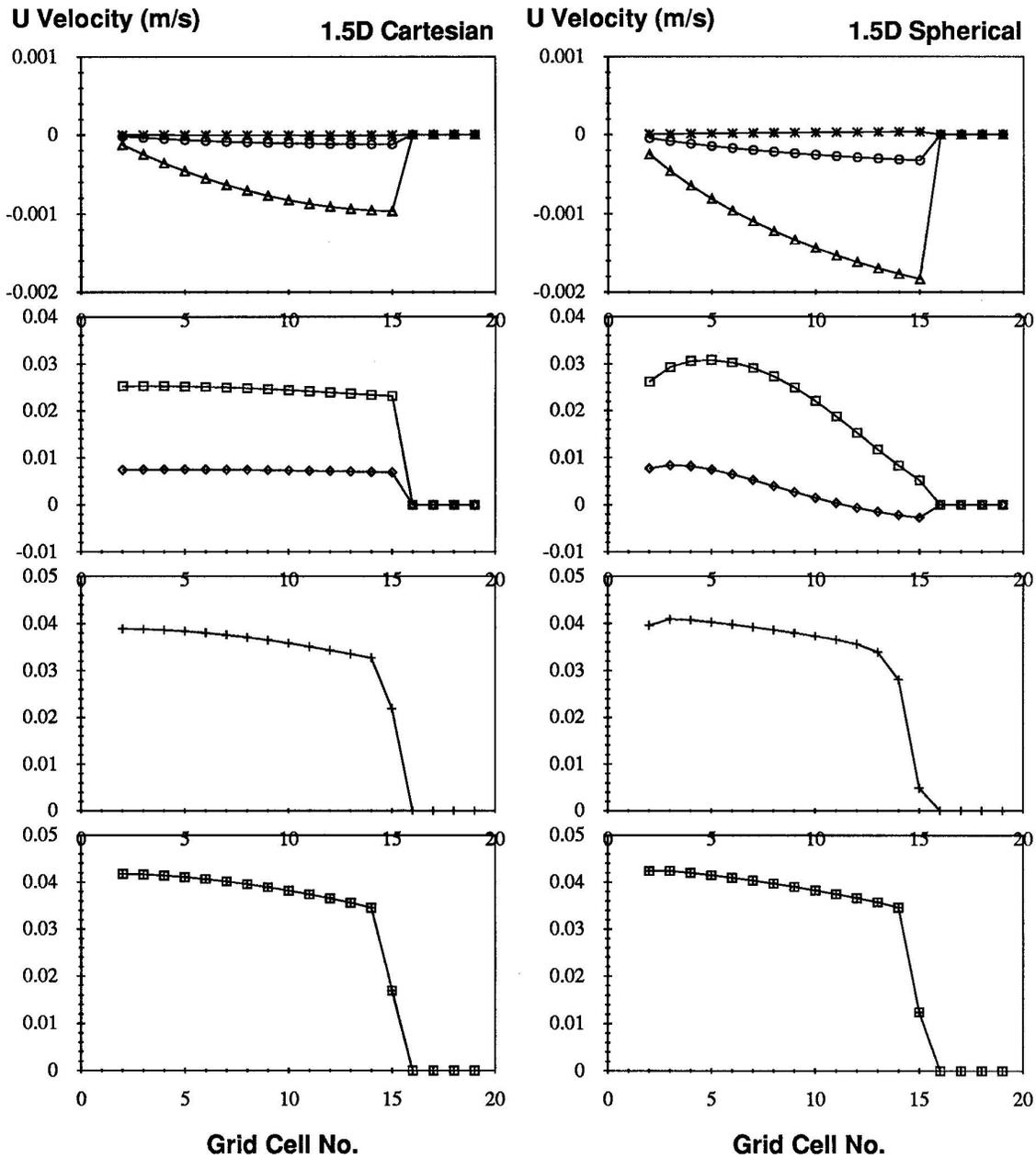


Figure 5.31: U Velocity for 1.5D viscous plastic rheology using quadratic drag and closure scheme with ellipses to the origin (Replacement Method).

2D VP Study: Cartesian, Replacement Method

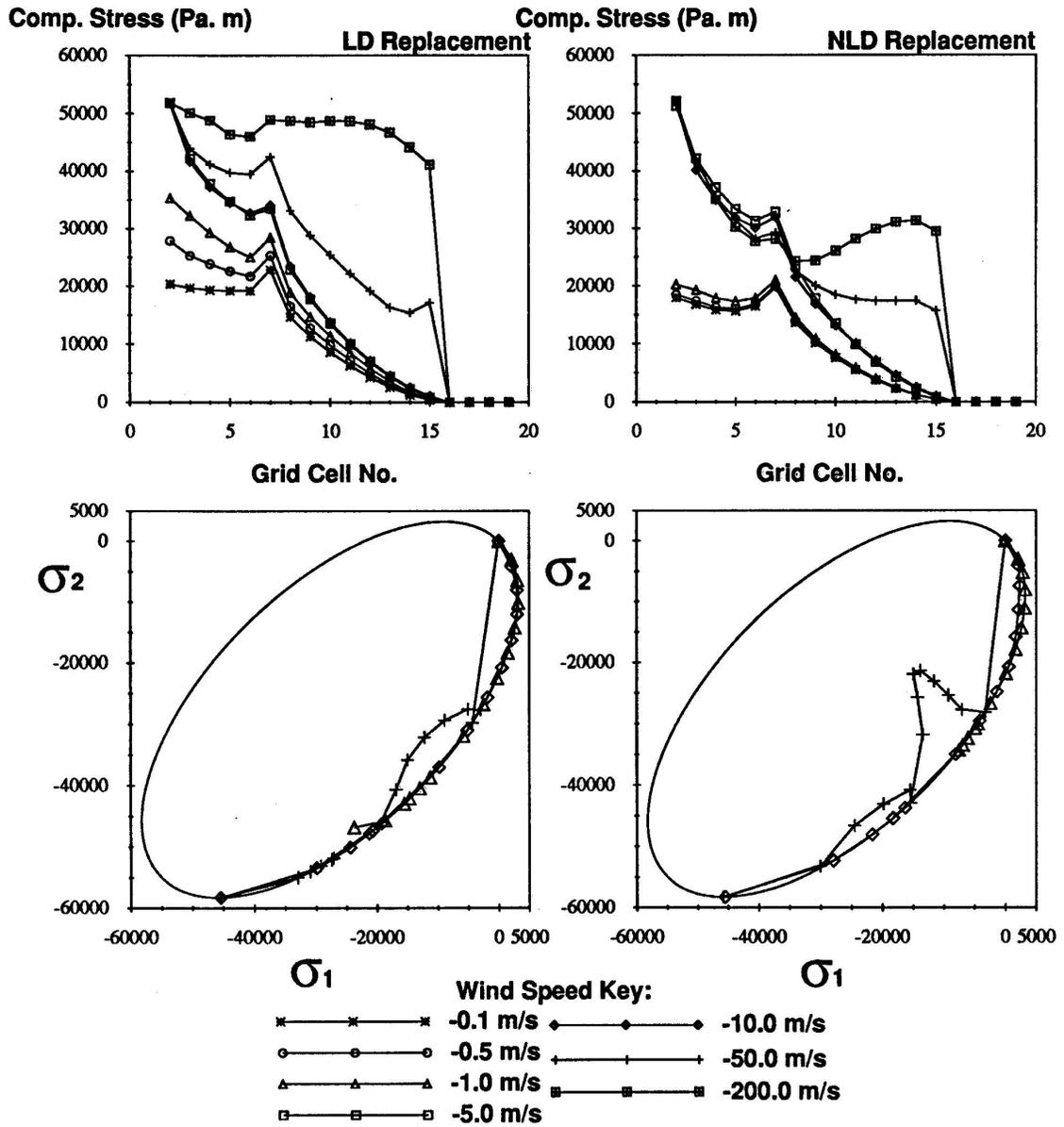


Figure 5.32: Stress state for 2D viscous plastic rheology using closure scheme with ellipses to the origin (Replacement Method). Representative responses at -1.0, -10.0, and -50 m/s winds are included in the principal axis space (σ_1, σ_2).

2D VP Study: Cartesian, Replacement Method

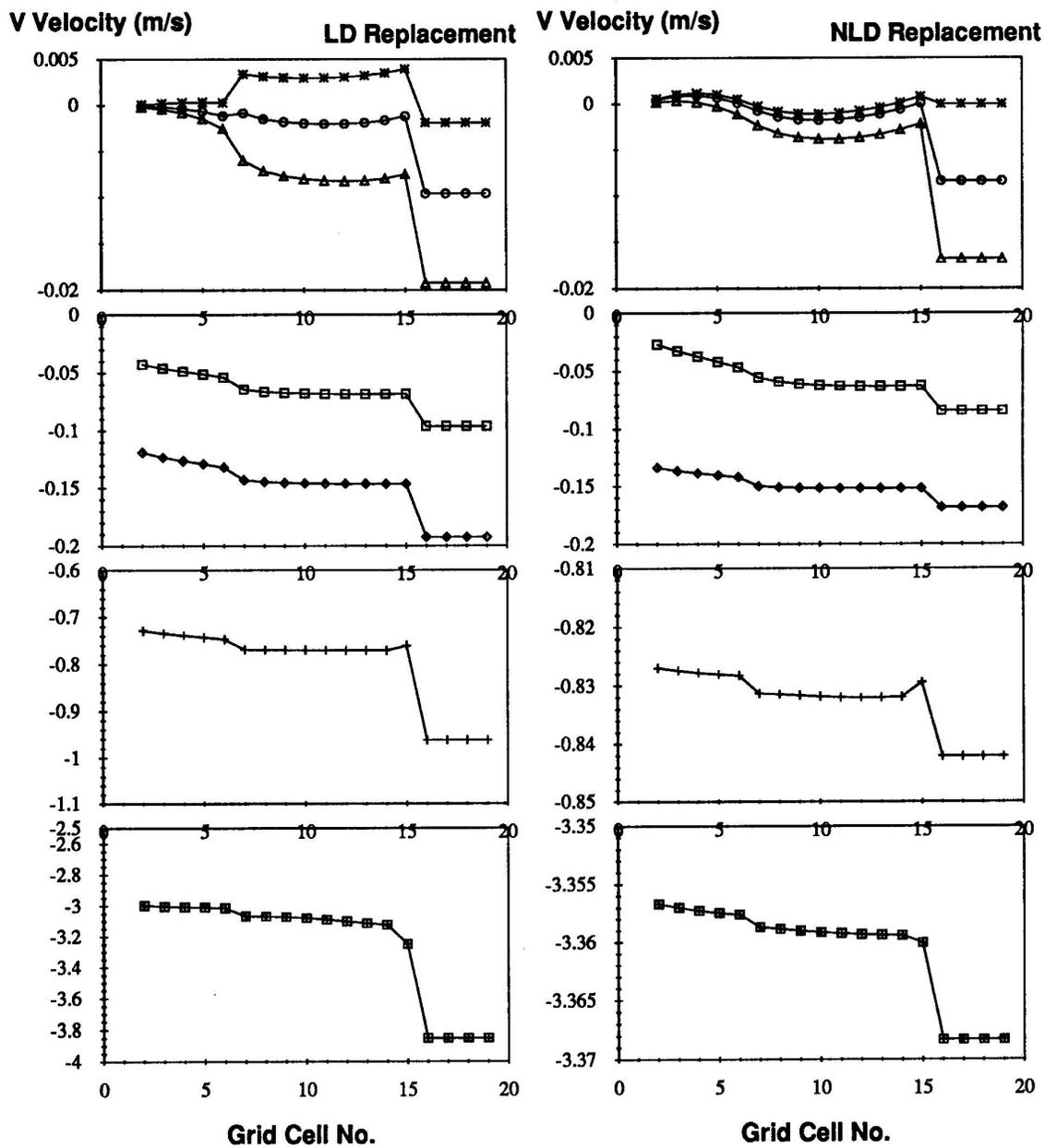


Figure 5.33: V Velocity for 2D viscous plastic rheology using closure scheme with ellipses to the origin (Replacement Method).

2D VP Study: Cartesian, Replacement Method

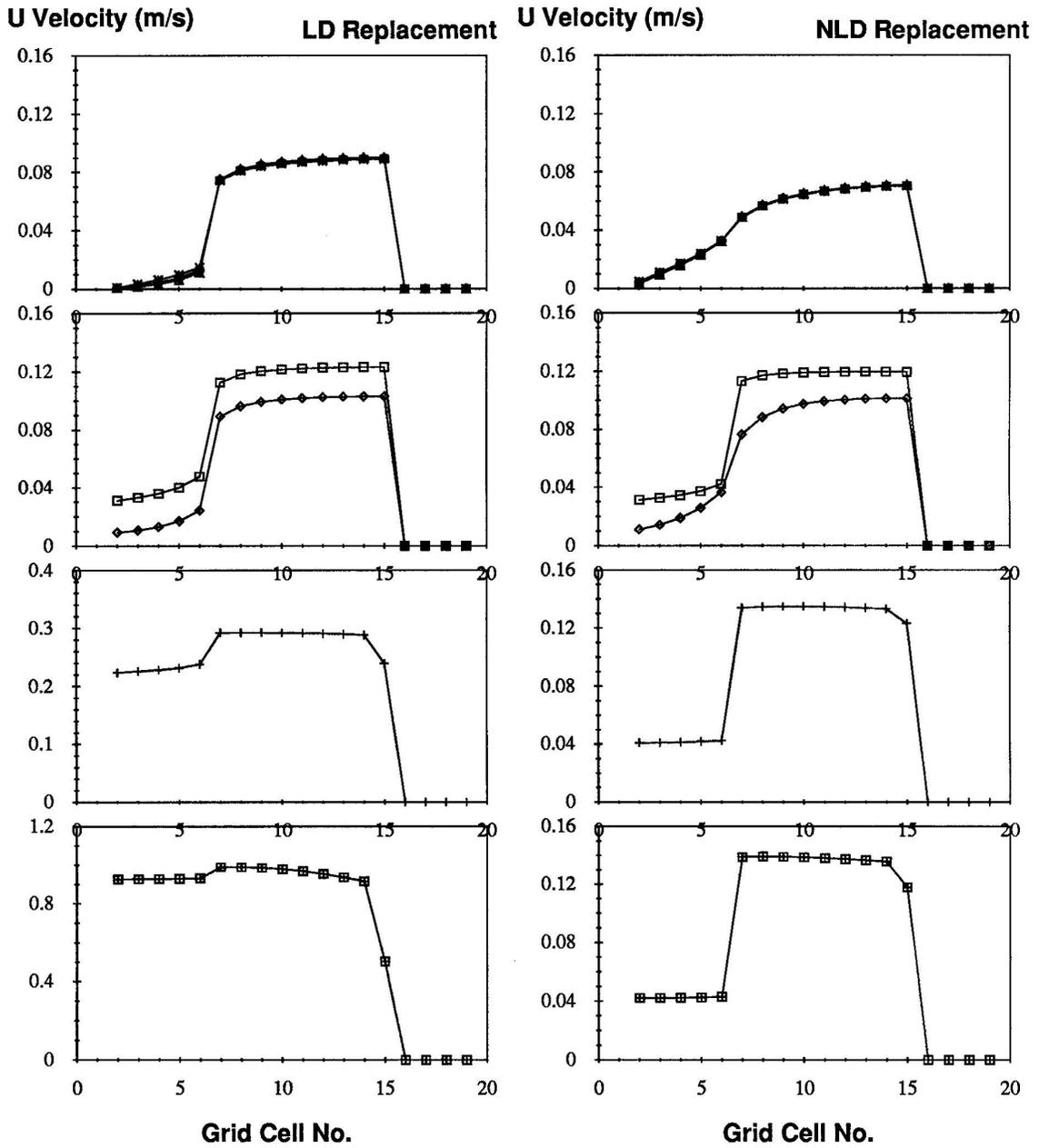


Figure 5.34: U Velocity for 2D viscous plastic rheology using closure scheme with ellipses to the origin (Replacement Method).

5.3 Chapter Summary

We have examined the mechanical behavior of sea ice as depicted by two of the most widely used models in the large-scale sea ice community. Within this framework, two major goals have been achieved. First, given the circumpolar configuration of Antarctic sea ice, we found that 1.5D spherical models in both CAV and VP using the Replacement Method and Truncated Ellipse closure schemes, are the most realistic choices for isolating and examining temporal changes in north-south growth and decay processes in the Weddell region. These models exhibit many of the features that full 2D models have but are computationally much faster and provide an excellent source for examining the temporal changes of individual north-south transects of selected regions. Given that spherical and Cartesian results in 2D are nearly the same, and due to the complexity of VP in spherical, 2D Cartesian models, using CAV and VP with the Replacement Method/Truncated Ellipse lets us look at regional variability at select times to assess the annual cycle and to compare with field observations. This combination makes use of 1.5D spherical transect models to examine temporal north-south variations in the annual cycle and 2D field models to look at spatial variations in the annual cycle for the Weddell Sea region.

The second major result of this chapter is an improved understanding of how the simulated ice performs under a number of different idealized dynamic conditions. Working in a hierarchical fashion we have analyzed deformation processes utilizing both analytical and numerical means to achieve this goal. Beginning with the simple 1D pressure-only CAV models we saw the impact that spherical versus Cartesian grid cell configurations have on the yielding property of the ice, and interpreted the results by comparing them to analytical solutions, how the numerical yielding works, and some of the basic responses. Next we examined the sensitivity of yielding under a number of simple forcing conditions to determine how the simulated ice responds to conditions of ice thickness, compactness, drag relations, wind direction and numerical resolution. At higher dimensions the forces introduced due to rotation had the biggest impact on yielding due to the reaction from the side walls at the 1.5D level, and at the 2D level we were able to establish that Cartesian and spherical solutions are nearly the same. Overall we found that the spherical solution changed very little from 1D to 1.5D to 2D because the spherical grid configuration provides converging side walls relative to north-south winds which allowed yielding to occur over a larger region of the grid rather than only at one end. It is for this reason that the 1.5D spherical was chosen over the Cartesian grid for analyzing temporal effects in the annual cycle.

In the VP study we introduced the process of shear into our idealized system to examine how shear affected the yielding process. In the initial 1D cases we saw that shear made a small contribution to the overall yielding process in Cartesian coordinates but had an immediate impact right out to the ice edge in the spherical cases. Using both numerical and analytical results we found out two important features. First, the point of yielding at the wall is also equal to the minimum value of σ_2 at the bottom of the elliptical yield curve (greatest magnitude) which is primarily a compressive state with a small amount of shear. Second we found that the path taken within principal axis space to reach this yield point is dependent on the closure method and grid configuration chosen. Under wind conditions conducive to tensile stress the distinction between the

Replacement method and Truncated Ellipse became most clear with the Truncated ellipse proving the most realistic in terms of large-scale dynamics. With regard to the impact of shear on the process of yielding we found that the spherical grid contained considerably more shear than the Cartesian grid without rotation. With rotation, both Cartesian and spherical grids exhibit yielding in the form of shear at the open boundary region (ice edge) and in 2D regions at the open boundary and in the interior, due primarily to shear. Given these results we saw characteristics similar to the fast land, pack ice, shear zone situations and concluded that the presence of shear was contributing to a reduction in kinetic energy in the system. Finally, we were able to conclude that shear stress was capable of producing yielding under stress situations with far less external forcing than for compressive stress systems alone.

Chapter 6

Regional Model Study

At the end of Chapter 2, the following two questions were posed. First, how do the external forces and internal ice dynamic processes affect the ice expansion and decay cycle in a region as variable as the Weddell Sea? Second, what external forces are responsible for the development of specific drift and deformation processes, and how well can we simulate (and eventually predict) such events? In pursuit of answers to these questions we consider the following issues. In Section 6.1, a sensitivity study of ice models to external forcing terms is conducted by examining the ice edge location and thickness distribution in high (25 km) and low (100 km) resolution 1.5D and low (200 km) resolution 2D cases against observed properties. In Section 6.2, sensitivity of low (200 km) resolution 2D ice models to internal ice parameters is studied using the same sensitivity variables as in Section 6.1. In Section 6.3, an evaluation of modeled ice advance and decay processes is conducted using high resolution (50 km) 2D models. In Section 6.4, we examine ice drift and deformation processes by statistically comparing the high resolution 50 km cases with Western Weddell Sea ISW buoy array observations.

The point of this chapter is not to create a “tuned” reproduction of the observed ice field but to identify in relative terms how external and internal factors affect sea ice drift, deformation, expansion and decay processes. The reason for this focus will become clear as we proceed through this chapter. As a preview of the results, we will see below that ice features such as ice edge extent and overall drift can be reproduced to a reasonable degree in most models because they are observed frequently and, the physical processes that drive them are fairly well understood and included in the models. Contrary to this, we will find that ice properties for which we have little observational data (e.g. ice thickness distribution and deformation) are much more sensitive and more difficult to reproduce in numerical models. What is even more disheartening is that when we try to collectively compare combinations like ice drift and deformation versus observations we are unable to correctly model both despite efforts to “tune” internal ice parameters. One important reason for this is that we have a reasonable understanding of how air and water impact ice but are significantly more deficient in understanding how ice impacts the air, water and itself. It is important to keep these points in mind when examining the case studies used in this chapter.

6.1 Model Sensitivity to External Input

A number of sensitivity studies are presented in this section to determine how the annual advance and decay cycle of the modeled ice responds to input field conditions and how well these responses compare to observations. Variations in the position of the ice edge and the ice thickness distribution will be used to quantify the “sensitivity” of the ice. The section is broken into three sensitivity categories: resolution, air and ocean with a fourth sensitivity category, ice, investigated in Section 6.2. The resolution study is strictly a modeling issue while sensitivities to air and ocean examine the major input variables on an individual basis to determine how they impact the annual cycle of sea ice. A final Subsection summarizes these studies and proposes a number of scenarios occurring within the annual ice cycle in the Weddell Sea.

6.1.1 Sensitivity to Resolution

The first constraints imposed when implementing a model include size of the region, spatial resolution, time stepping, and time resolution of the input fields. To examine the effect of these resolution categories, 1.5D spherical versions of VP (viscous plastic rheology with replacement closure method) and CAV (cavitating fluid rheology) are used at relatively low (100 km) and high (25 km) resolutions with monthly, daily, and subdaily (4 times a day) atmospheric input fields all of which have been averaged from the subdaily fields. The 1.5D codes are well suited for this type of testing because they are quick and give the basic overview needed for resolving general annual features without including complicated effects associated with boundaries. For these studies the 1.5D code is located in the center of the 2D grid at 28°W longitude.

Starting with the VP monthly 100 versus 25 km runs, we see in the upper two panels of Figure (6.1) similar ice edge extents, with the higher resolution case displaying finer detail, as expected. In the interior of the pack, however, the ice thickness distribution is much different. From the ice edge to the first 1.0m contour, a common thickness distribution evolves at both low and high resolution. At high resolution, however, there is a thinner interior (i.e. more seasonal melting) during the decay period, a thinner interior during the winter, and greater ice growth near the continent during the expansion period. These differences in ice thickness distribution are not just a matter of resolving thinner ice because of higher resolution. There is also a resolution effect on the evolution of the model dynamics which is sufficient to change the ice thickness distribution within the field with time.

Unlike VP, CAV 100 vs. 25 km have nearly the same ice edge extent and thickness distribution (lower panels of Figure 6.1). The slight differences at any given time are resolution dependent but do not alter the ice thickness distribution with time. For both CAV cases, the decay period is longer in duration and extends further southward than for VP. The ice thickness distribution is about the same in CAV as VP from the ice edge to the 1.0 m contour but then CAV is generally thicker in the interior relative to VP. The striking difference in resolution response with monthly forcing (both thermal and wind forcing) is one of the reasons why VP is not desired for climate modeling where monthly mean forcing may be used. The reason for this is that a monthly averaged wind field is

too weak, both in magnitude and variability, to produce a strong enough forcing field to induce the necessary shear responses in the VP model (Hibler, personal communication).

Looking now at the low resolution (100km) VP with daily input (upper left panel in Figure 6.2), we note that the summer decay does not extend as far south, by about 200 km, at the minimum extent. Also the time of minimum extent is not as long, about 56 days at the 1250 km mark with monthly input versus about 30 days at the 1450 km mark with daily input. While the maximum extent is about as long (ca. 110 days) with daily input, its extent is about 100km further north (at 55°) for the entire period of the maximum extent (day 221-330) rather than for only a short period of time (day 251-282) as in the monthly case. The change in interior pack ice thickness is also temporally more smooth in the daily case despite the presence of a four times daily weighted interpolation routine to compute input field values at every time step independent of input field sampling. At higher resolution (25km), the same effect is seen (upper right panel of Figure 6.2) as with monthly input, namely more decay during melt season at the ice edge and thinner ice in the interior with higher resolution. In this case, however, the ice decays about 100km further south than for the 100km resolution, rather than earlier in the season as was the case with monthly input. There is also greater similarity between high and low resolution than for the monthly input case primarily due to the presence of a daily varying wind field which is critical to the VP rheology as noted above. CAV is more similar to VP when daily input fields are applied (lower panels in Figure 6.2) versus monthly. Among the differences, ice melts back sooner and further with CAV. Also the interior pack of CAV at low resolution is slightly thinner at the south end versus VP but thicker than VP at high resolution; this was the reverse with monthly input.

The low resolution VP case using subdaily input (upper panel in Figure 6.3) shows the same minimal extent, 1450 km distance, as with the daily input, only the duration of this minimum is much shorter, about 12 days with subdaily input versus about 30 days with the daily input case. The maximum extent with daily input is reached about 10 days earlier than with the subdaily input. The subdaily extends about 100km further north for a little over 30 days. There is no significant difference within the pack between daily and subdaily at low resolution; the only real difference is in the ice edge extent which is resolved in finer detail. At higher resolution (25 km VP case) the maximum ice extent is about the same as for the daily input case of the same resolution. The main difference between VP high resolution (25 km) daily versus sub daily forcing is an increased ice thickness in the interior at the south end, particularly the 1.5, 2.0 and 2.5 meter contours. CAV at low resolution with subdaily forcing is similar to VP. The differences observed between the two with daily forcing are still present with subdaily forcing, only these differences are less pronounced with the subdaily forcing.

Summarizing the above cases, we can identify the following resolution dependencies in these models. First, monthly forcing, specifically monthly mean winds, has a strong effect on VP. Depending on the resolution used, a substantial difference in ice thickness distribution results despite only minor differences in ice edge extent. Second, the ice edge extent and duration of maximum and minimum are quite sensitive to the time sampling of the input fields. Finer time stepping (subdaily versus daily forcing) affects the maximum and minimum of the ice edge primarily in duration of extent with the subdaily minimum being shorter (by about 20 days) and the maximum occurring earlier (by about

10 days). The ice thickness distribution of the interior pack has a similar sensitivity to spatial resolution with VP being the more sensitive of the two (VP vs. CAV), and the higher resolution producing a thinner interior especially during the summer melt-back period. Finally, as input fields become more temporally resolved (subdaily versus daily or monthly), the differences in spatial resolution become less pronounced. This last point indicates that an increase in input field temporal resolution is more critical than the model's spatial resolution in terms of the overall evolution of decay and expansion processes in the ice. The physics behind these findings will be examined in the next section. In terms of computation, this last point can lead to considerable saving on run time.

1.5D Spherical Resolution Study Ice Thickness using Monthly Atmospheric Forcing

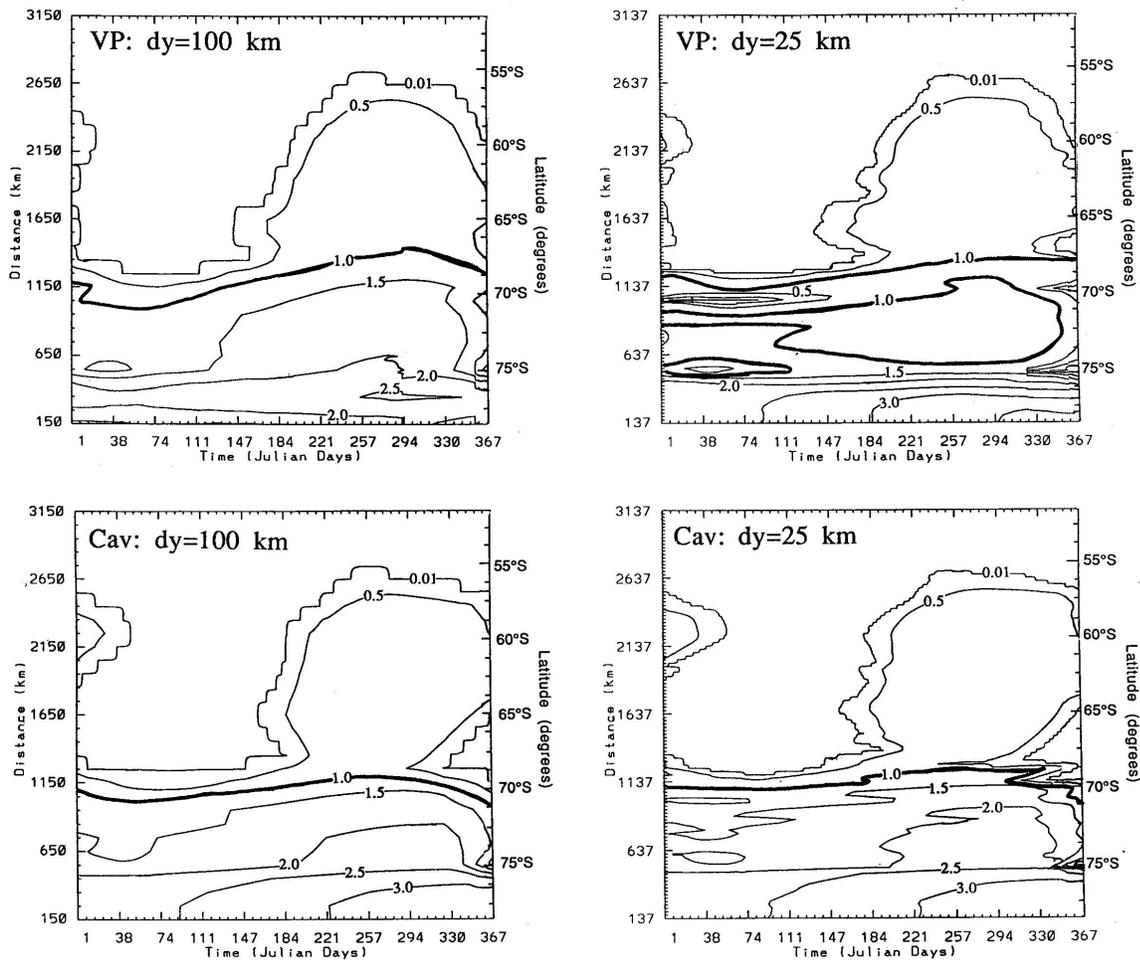


Figure 6.1: Ice thickness (m) sensitivity to monthly atmospheric input fields at relatively low (100 km) and high (25 km) resolution using 1.5D models.

1.5D Spherical Resolution Study Ice Thickness using Daily Atmospheric Forcing

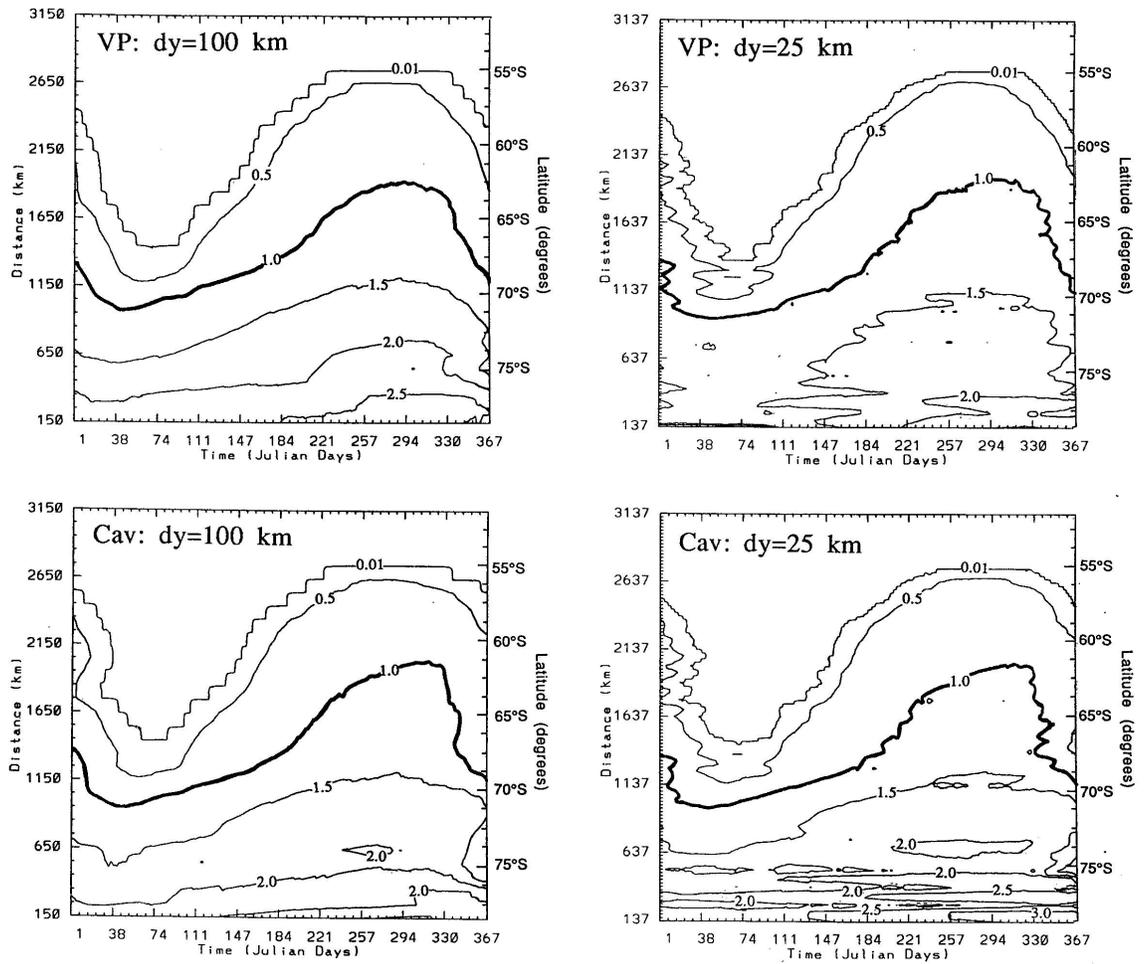


Figure 6.2: Ice thickness (m) sensitivity to daily atmospheric input fields at relatively low (100 km) and high (25 km) resolution using 1.5D models.

1.5D Spherical Resolution Study Ice Thickness using 4xDaily Atmospheric Forcing

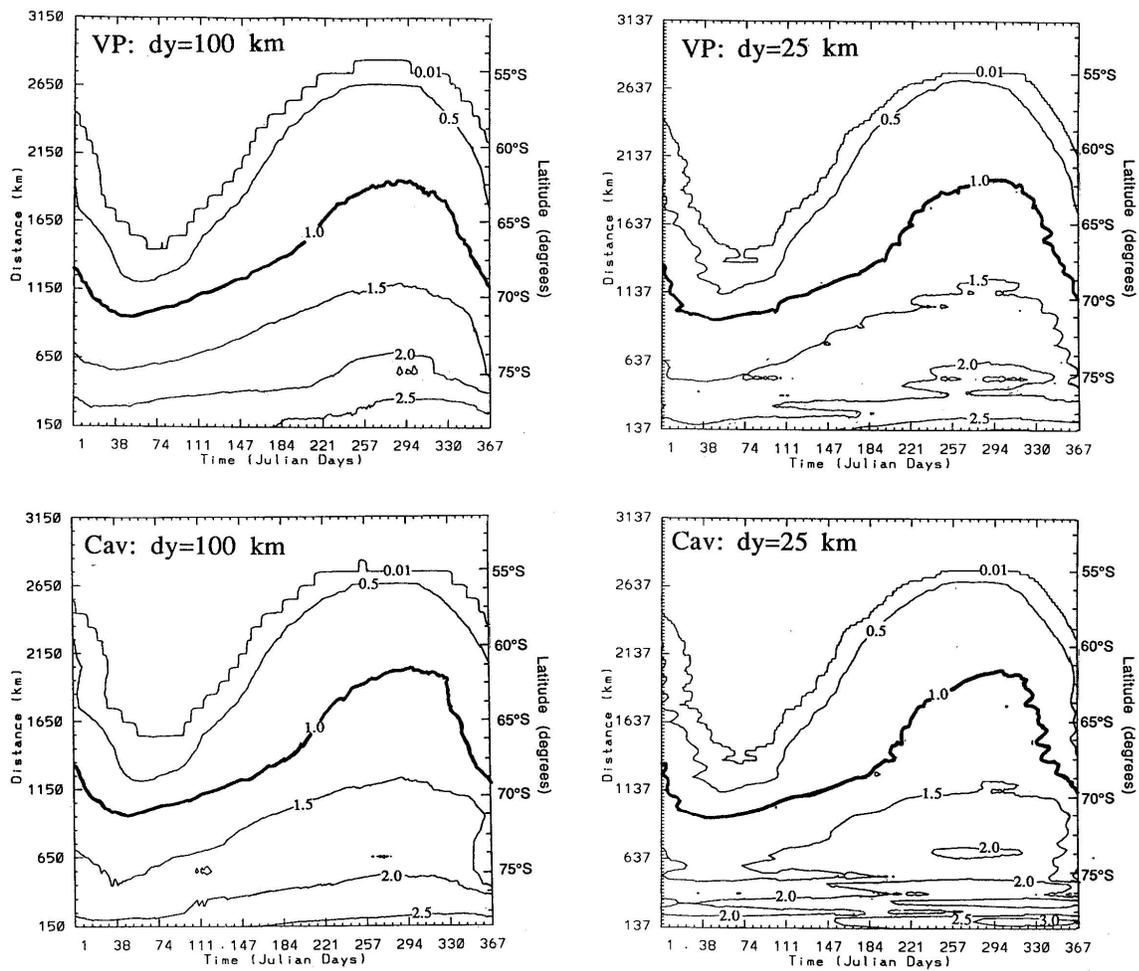


Figure 6.3: Ice thickness (m) sensitivity to 4 times daily atmospheric input fields at relatively low (100 km) and high (25 km) resolution using 1.5D models.

6.1.2 Sensitivity to Atmospheric Forcing

Data fields from the atmosphere which are used as input forcing for sea ice in the models include air temperature, wind velocity, sensible and latent heat fluxes, long and short wave radiation, albedo, and cloud cover. Since the dynamic responses of the ice are the key issue in this study we will only examine three of these: air temperature, wind velocity and relative humidity (latent heat flux parameter) in order to assess how they affect the annual expansion and decay cycle of the ice.

Air Temperature

Thermal contributions to the expansion and decay of sea ice depends on its freezing and melting point, which are not the same. Sea ice freezes with the onset of winter at a freezing point, depending on salinity, around -2°C or 271K. During the winter season the ice undergoes a continuous leaching process expelling salt from the ice so that by spring melt, the ice thaws at a temperature closer to 0°C or about 273K, which is the melting point of fresh water. This dichotomy in phase change produces a hysteresis which is critical to the thermal annual decay and expansion of sea ice, especially in relation to its sensitivity to air temperature. From the results of the 1.5D spherical study, we can examine this impact via air temperature by looking at two examples: VP with 100km resolution with monthly forcing and VP with 25km resolution with subdaily forcing (upper panels of Figure 6.4) which were the extremes from the previous section. Added to these figures are the monthly averaged air temperature contours of 271K (freezing point of sea ice) and 273K (melting point of fresh water).

The pattern that emerges is an ice edge decay and expansion with an annual cycle which is offset (phase shifted) from a similar cycle in air temperature and, not shown here, an additional phase shift from the solar cycle (maximum at day 356, minimum at day 173). During expansion, the ice edge is south of the freezing line while during the decay, the ice edge lies between the air temperature lines where ice melts and freezes. A number of other experiments (e.g. Figures 6.15 and 6.16) confirm this type of behavior for thermodynamic only model (Thermo Only), free drift (FD) and cavitating fluid (CAV) models with the thermodynamic only model ice (Figure 6.15) oscillating the least. These annual cycle oscillations are analogous to a coupled spring and dashpot (or resistor and capacitor, respectively) with the air temperature moving about 1.5 to 3 months ahead of the ice edge depending on the resolution, heat fluxes and rheology used. Superimposed on top of this annual cycle are a number of higher frequency oscillations in the air temperature ranging from daily (lower left panel of Figure 6.4) to subdaily (lower right panel of same). These higher frequency oscillations are what create many of the differences in ice edge extent as the input field time resolution increases. In addition to air temperature, long and short wave radiation cycles, cloud cover cycles, and latent and sensible heat fluxes also contain daily and subdaily frequencies which work similar to the air temperature. The impact of this on the ice edge and thickness distribution was described in the section above. Based on this more physical information and eluding to results seen later in this section, we find that the increased resolution of input fields dominates the ice field more so than the rheology chosen and hence similar ice edge extents and thickness distributions were found for the subdaily input field cases examined

in the last section.

Low resolution (200 km) 2D studies without and with ocean heat flux and currents show this same effect of phase lag in ice extent versus air temperature (also in the other atmospheric terms discussed above). The main difference between 1.5D and 2D is the presence of spatial variability in the 2D field due to boundaries (open water and land). When only atmospheric forcing is used (Figure 6.5), we see the ice catching up, and at times passing, the freezing line in the mid-eastern portions of the grid during the expansion part of the cycle (March and June in upper two panels). During the decay, the air temperature lines move southward first from their maximum extent (near end of June) while the ice continues through August to extend northward up to the air temperature equal to the melt line. Even with the addition of ocean heat fluxes and currents (Figure 6.6), the air temperature still dominates the ice edge, but inclusion of an ocean heat flux produces an ice edge closer to the observed during the minimal extent periods (November - March). More noticeably, the ocean heat flux has a significant effect on the ice thickness distribution which exhibits an overall thinning in the field when an ocean heat flux is included. This is clearly seen by examining the highlighted 1.0 meter ice thickness contours in the two sets of figures. This effect is present during both summer and winter months. With respect to the impact on global climate, this sensitivity to ocean heat flux is significant: While the ice edge expansion and decay are changing only marginally due to ocean warming, ice thickness is decreased substantially. Overall thinning of ice can pre-condition the entire pack such that wide spread melting can occur very quickly. Extrapolating this response to a global warming situation, an increase in air temperature can lead to ice edge changes, but, more critically, ocean warming can lead to overall thinning (which is much more difficult to detect) followed by catastrophic melt-back.

Wind Velocity

The main difference between the thermodynamic only model and the others is the inclusion of dynamics. With respect to atmospheric forces this means the inclusion of wind velocity. Figure (6.7) shows the 7-day average winds for the same four periods covered in the previous two Figures (6.5) and (6.6), as well as the observed ice edge and two air temperature lines at the melting and freezing points of ice. Looking first at the upper left panel we see that during days 87-93 of 1992, the wind field over the ice is moving north; buoys from ISW also show a northward drift of the ice. The ice thickness relative to the freezing temperature line however appears to be expanding more northeast. In Section 6.3 below we will look closer at this issue of northeastward ice expansion versus northward drift using high resolution (50 km) transects.

We see that the March episode has wind blowing over the ice more or less in a south to north direction. The air temperature associated with this is below freezing (dotted line in Figure 6.7) and thus helps it to advance. In the December example, a west wind dominates the field to the north of the ice, the winds are weak to the south, and the air temperature over the ice is mostly above freezing (i.e. most of ice field is between the dashed and dotted lines in Figure 6.7). In this case, the wind is expanding the ice and then the local air temperature melts it. In the other two cases (June and August) a cyclonic low is moving over the ice, most likely due to the passage of storms. There is

no preferred wind direction over the ice edge in the June case but a definite west wind over the ice edge in the August case. The presence of the storms means increased wind activity and thus greater surface heat transfer, either cooling or warming, which will also enhance freezing and melting. More on the effects of the wind velocity on the ice expansion and decay processes will be examined further in Section 6.3.

Relative Humidity

A lack of humidity data prompted two sets of fortuitous simulations. Initial runs were made assuming a constant relative humidity based on previous modeling efforts done in the Arctic (Hibler, 1979). This assumption proved inadequate for Antarctic studies for both low (40%) and high (90%) values of relative humidity as seen in Figure (6.8). While the lower humidity seemed to produce reasonable results along the coast, it overshoots in the ice edge elsewhere, especially in the winter months. Contrary to this, the high humidity case does a fairly good job in reproducing the ice edge results during the winter months but drastically reduces the ice in the summer months. This problem was corrected using the dewpoint and air temperatures from the climatological 30 year monthly mean data of Taljaard et al. (1969), as described in Section 4.1.1 and the relative humidity Eq. (4.50). Using this information, a monthly average regional distribution of relative humidity was computed as seen for example in Figure (4.2).

Making use of the Bowen ratio (B), we can examine the difference between Arctic and Antarctic ice growth sensitivity to humidity. The Bowen ratio (Andreas and Ackley, 1982) is the ratio of sensible to latent heat. Using the terms defined in Eqs. (4.48, 4.42, 4.43) this ratio becomes (Note: $q[T]$ means q as a function of T)

$$B = G \frac{T_a - T_i}{RH q_a[T_a] - q_i[T_i]} \quad (6.1)$$

$$G = \frac{D_1}{D_2} \quad (6.2)$$

where D_1 , D_2 and other terms are those described in Section 4.1.1. Plots of this ratio, shown in Figure (6.9), for low and high relative humidities show that lower values of relative humidity (RH) reduce the Bowen ratio (i.e. increase the latent heat). This result comes about because differences in specific humidity are much smaller than differences in temperature (values of q are of order 10^{-3}) such that $q_a \approx q_i$ relative to changes in temperature. For RH close to 1 this yields a small latent heat flux relative to the sensible heat flux because $(RH - 1)$ approaches zero. Conversely as RH decreases, $(RH - 1)$ becomes an increasingly larger negative number and the latent heat magnitude increases. Since the sensible heat flux is unaffected by RH the change in latent heat is responsible for the ice growing too rapid at lower relative humidities and not enough at higher humidities.

In terms of physical ice growth, the large negative latent heat is a loss of heat from the sea water due to the phase transition from water to ice. A smaller RH in regions of sub-freezing temperatures, therefore, means a higher conversion from the liquid to the solid state. This explanation of the effect on phase state is further supported by the fact that the ice thickness and distribution in the interior of the pack during winter (August

in Figure 6.8) is only marginally different at 40% versus 90% RH for thicknesses of 1.0 meter or more, but the ice edge and thinner ice (< 0.6 meters) are much further north in the $RH = 40\%$ case. Therefore, it is the thin ice and water during the advance, and the thin ice during the decay, which are being impacted by the humidity in the annual cycle. As seen in Figure (4.2), the regions of low relative humidity are located along the dry continent of Antarctica, while the more moist air is located closer to the ice edge. Because of the presence of a dry central continent in the Antarctic region, the seasonal ice cycle in the Antarctic is subjected to a greater range of humidity than in the Arctic. This result substantially increases the need for high quality humidity data in input fields, more so than for the Arctic.

A test to illustrate this effect is shown in Figure (6.10) using the standard model. From Figure (4.2) we see that the climatological monthly average relative humidity at the tip of the Antarctic Peninsula ranges from 80% to over 90%. Also in this region the model poorly predicts the northward ice margin near the peninsula coast during the summer months, a difficulty not atypical of ice models in the Weddell Sea (Hibler and Ackley, 1983). Running a test whereby we reduce the humidity along the continent in the first 4 grid cells wide by 10 grid cells high (Figure 4.5) to 40%, we notice a considerable increase in ice growth in summer along the peninsula which is more like the observed ice edge. As will be seen below in the ocean sensitivity, the northward ocean current in this region is also capable of increasing the northward expansion of ice growth, as is a lower ocean heat flux and to a small degree a deeper mixed layer. While the humidity may not be the only reason for the lack of good correlation in summer months between the models and observed ice at the northern tip of the peninsula, it seems to be one ingredient not well understood in current models. In the next section we will compare these ice responses to relative humidity against other likely candidates associated with the ocean.

1.5D VP Sensitivity Study to Air Temperature

- - - - Air Temp at Melting Point of Fresh Water
 Air Temp at Freezing Point of Sea Water

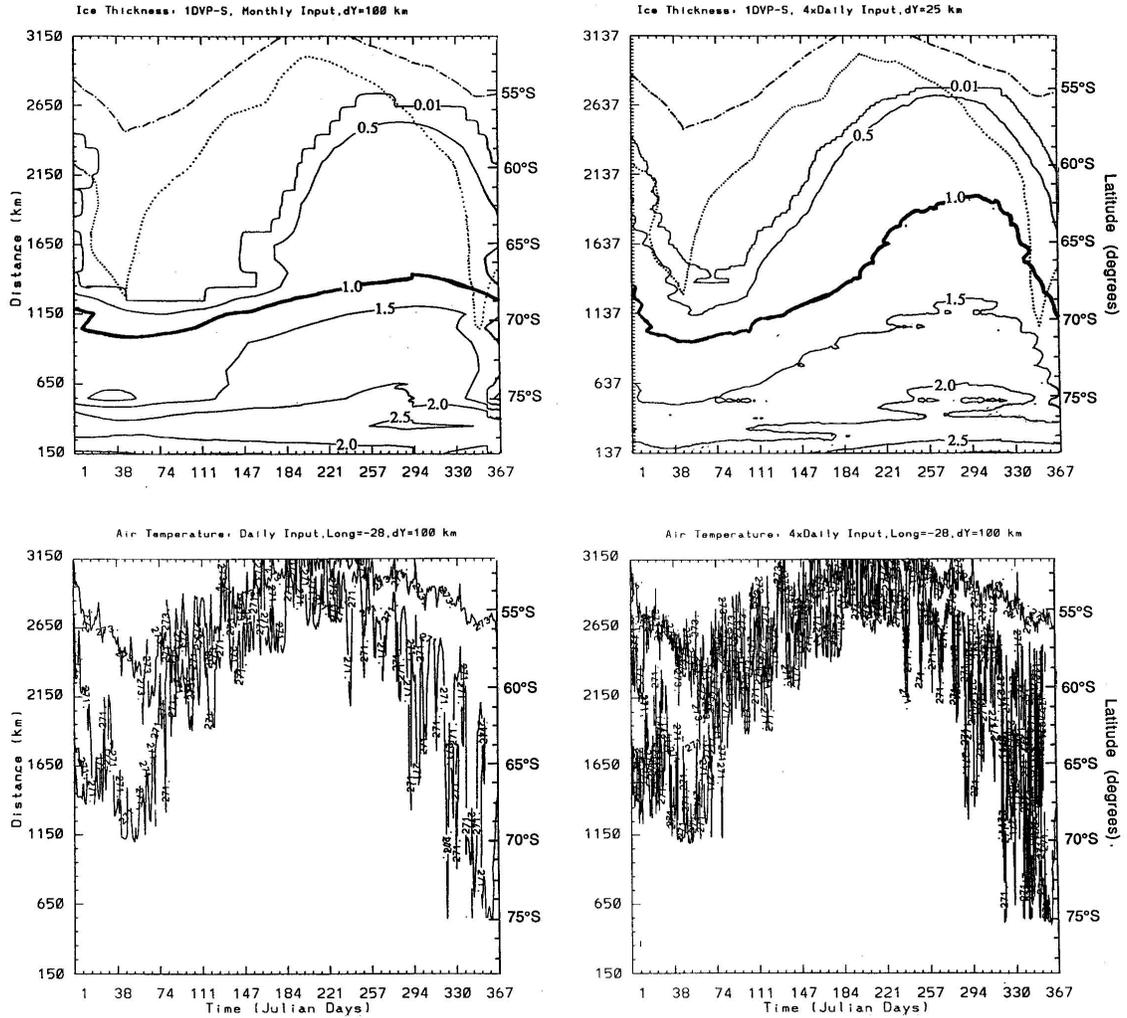


Figure 6.4: Sensitivity of sea ice thickness (m) to air temperature on an annual cycle using 1.5D models.

**VP Low Resolution (200km)
7 Day Mean Ice Thickness (m)
Control Case (Atmospheric Input Only)**

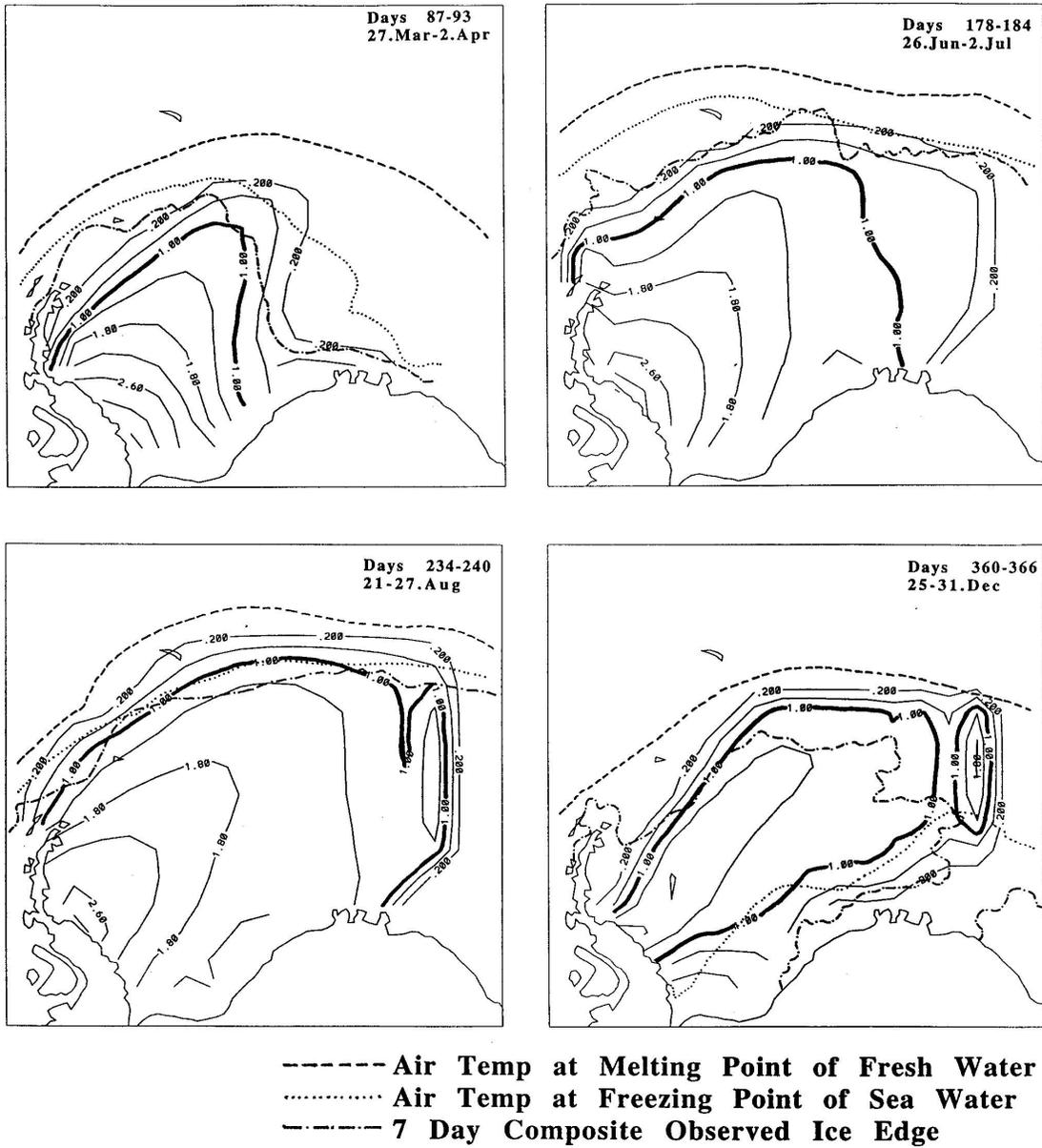


Figure 6.5: Control case for 2D low resolution sensitivity study on 1992 annual cycle in Weddell Sea.

**VP Low Resolution (200km)
7 Day Mean Ice Thickness (m)
Standard Case (Atmospheric and Ocean Input)**

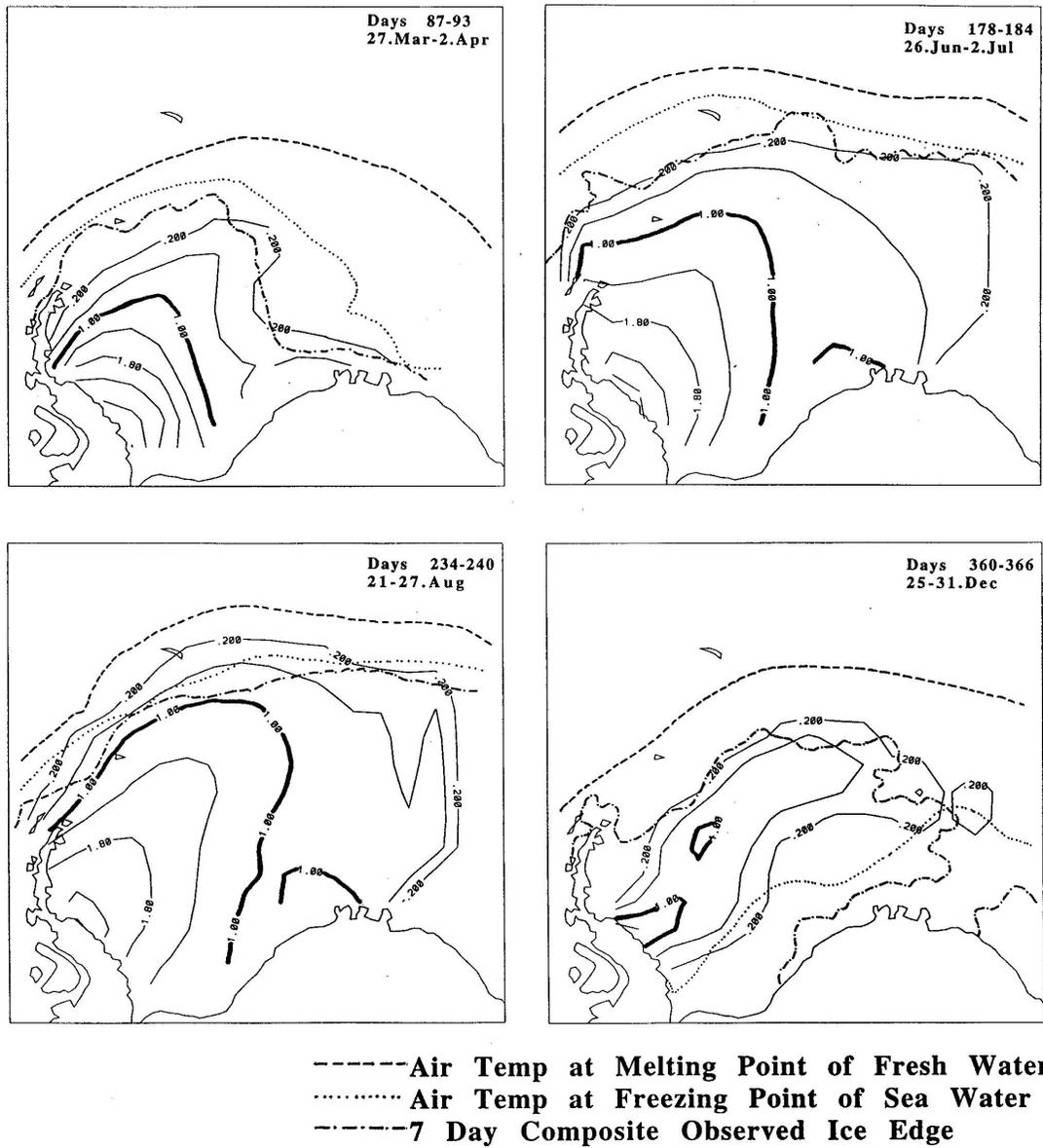


Figure 6.6: Standard case for 2D low resolution sensitivity study on 1992 annual cycle in Weddell Sea.

VP Low Resolution (200 km) Sensitivity Study 7 Day Mean Ice Thickness (m)

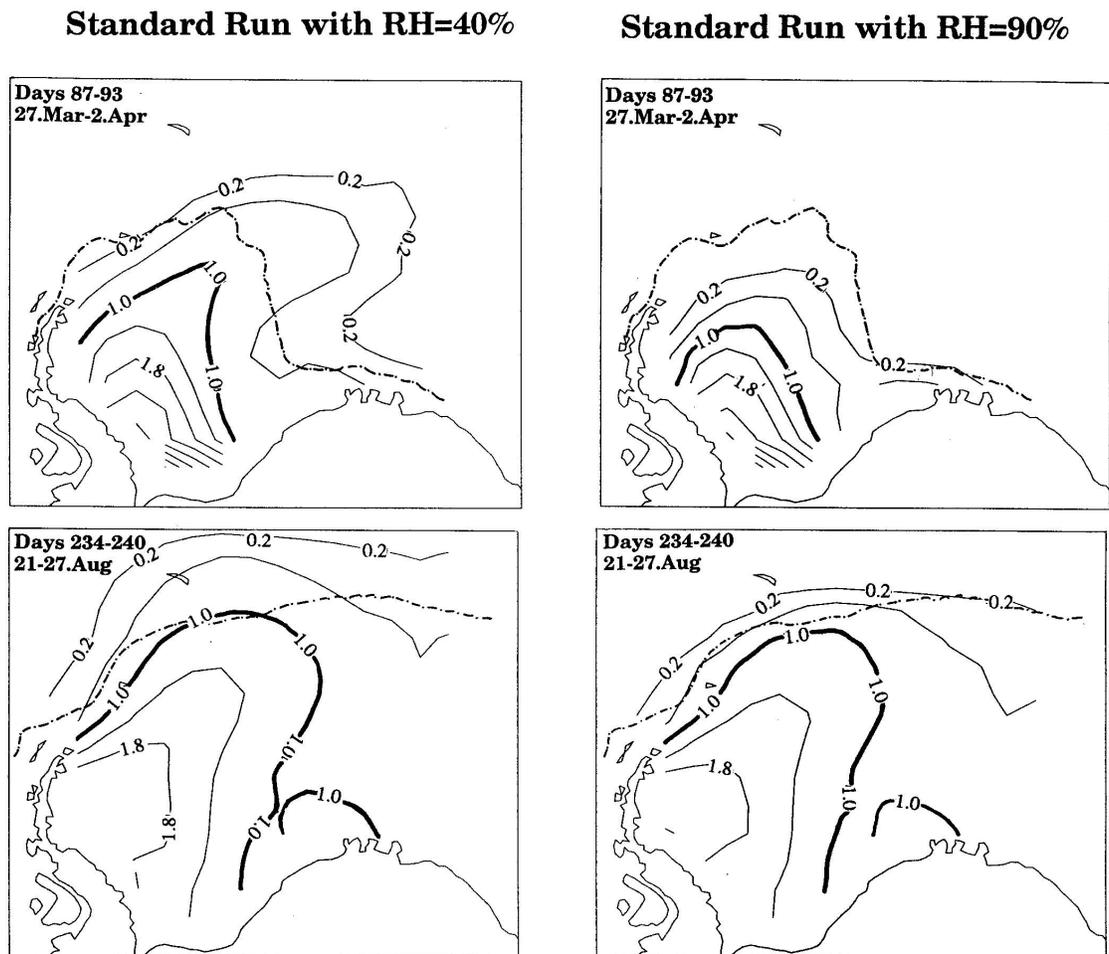


Figure 6.8: Standard run with 2 cases of constant relative humidity. Dot-dash line is NSIDC observed 7 day composite ice edge from same 7 day period as the model.

January Monthly Mean Bowen Ratio

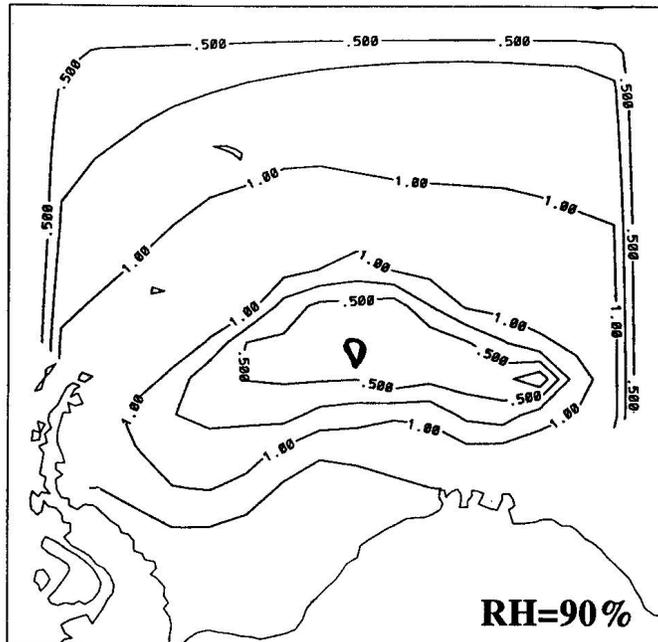
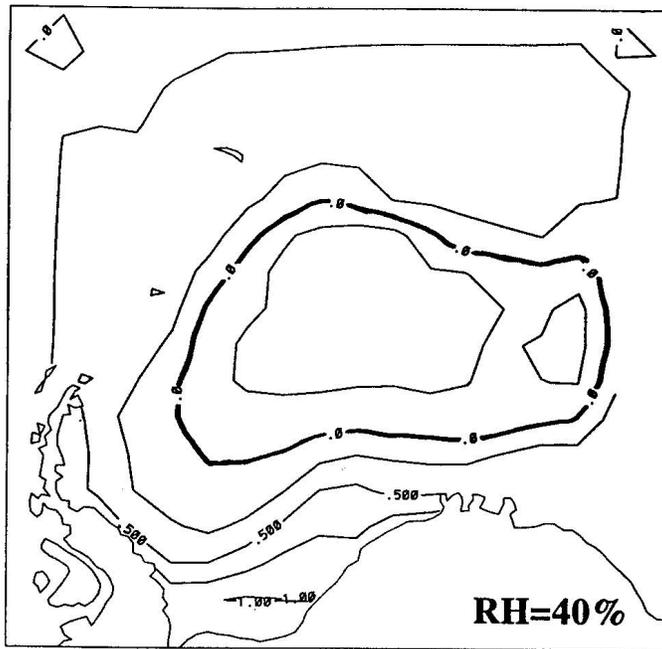


Figure 6.9: Examples of Bowen ratio distribution during summer in Weddell Sea under low and high relative humidity.

VP Low Resolution (200km) Sensitivity Studies 7 Day Mean Ice Thickness (m)

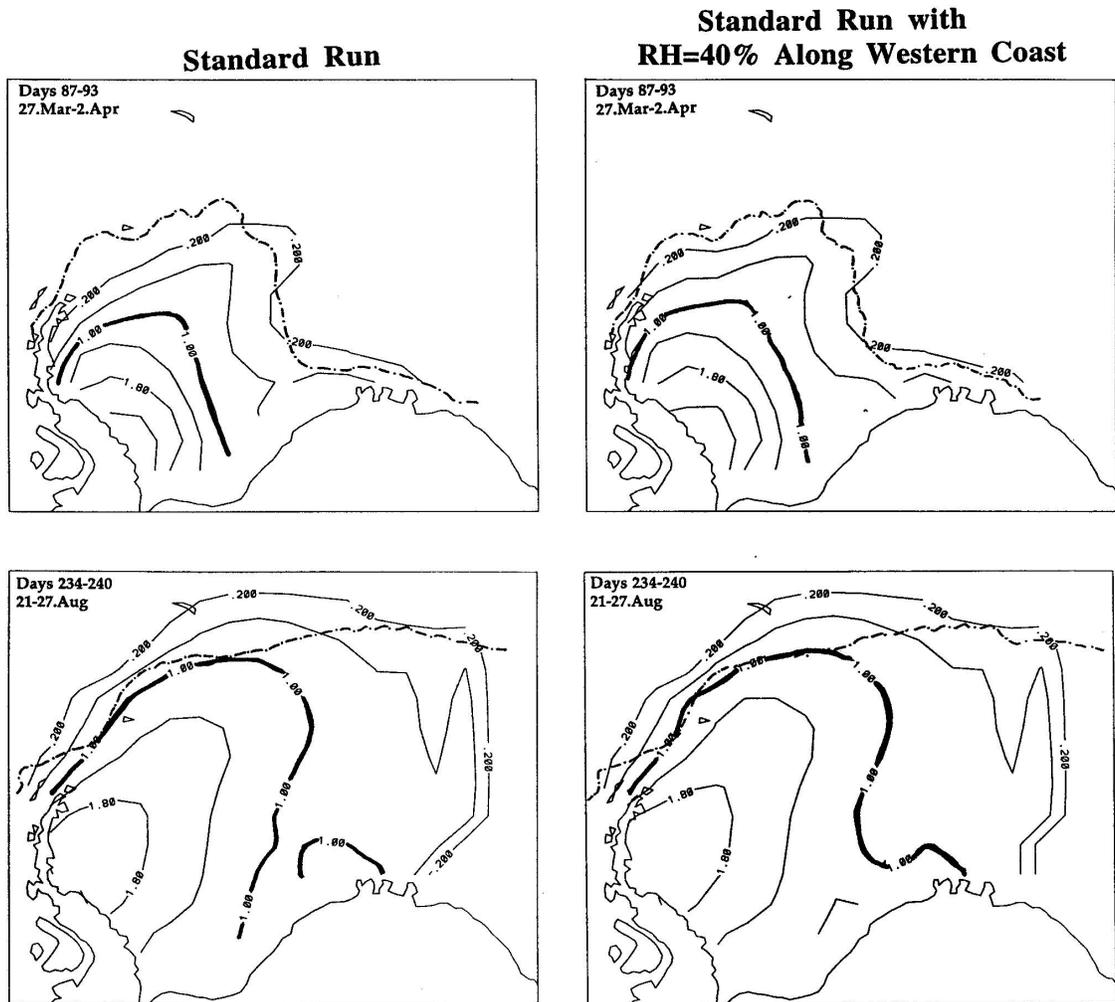


Figure 6.10: Sensitivity to low relative humidity along the Antarctic Peninsula during 1992. Dot-dash line is the NSIDC observed 7 day composite ice edge from the same 7 day period as the model.

6.1.3 Sensitivity to Ocean

In this section we examine the effects of the ocean on the ice growth and decay using a full 2D model at low resolution (200km) which is about the same as the 222km model used in Hibler and Ackley (1983). We will highlight a series of runs using representative 7 day mean ice thickness fields near minimum (March) and maximum (August) seasonal ice extent to compare ice edge extent and interior thickness distributions under different conditions. The three dominant effects on the ice by the ocean are ocean heat flux, mixed layer depth and velocity field. As a control case, we select the standard model configuration defined in Chapter 4 using the replacement method closure, but we remove ocean heat flux, ocean current, and use the fixed mixed layer depth of 60 m. Everything else is as described in Chapter 4. From this control case we add effects like heat flux and ocean current and examine the thickness distribution in order to assess the impact of these processes on the annual ice expansion and decay.

Beginning with the control case (two left panels in Figure 6.11), we see that the modeled ice overshoots the observed 7 day composite ice edge to the northeast in March and in general during the maximum extent in August. Including a variable mixed layer (as described in Chapter 4) has almost no noticeable effect (two right panels in Figure 6.11) versus an average fixed mixed layer. However, introducing even a small amount of ocean heat flux does, as seen in the left panels in Figure (6.12) for the 2 W/m^2 case. There is a slight impact on the ice edge and an even more noticeable impact on the ice thickness distribution during both minimum (e.g. 1.0 m contour) and maximum (e.g. 2.6 m contour) ice extent periods. With a 10 fold increase in ocean heat flux (20 W/m^2 , right panels in Figure 6.12) the differences in ice edge extent become very obvious in March during the onset of ice growth but less obvious during the winter maximum. The interior ice thickness, however, becomes uniformly thinner everywhere during both minimum and maximum extent, making the ice thickness distribution much more sensitive to ocean heat flux than the ice edge advance and retreat. This is clearly seen when comparing relative changes in the 0.2 m and 1.0 m contours, and reaffirms the results seen when comparing Figures (6.5) and (6.6).

Using the variable heat flux described in Chapter 4, we see that the low heat flux in March (upper left panel, Figure 6.13) produces an ice edge which compares well to the observed everywhere except close to the Antarctic Peninsula. The interior ice is also thinner than the control case near both minimum and maximum extent. Adding just ocean current to the control case (right panels, Figure 6.13), we see a much stronger northeast extent of ice early in March. There is little difference in ice thickness distribution close to the peninsula but there is more build up of ice at the eastern outflow in winter (August). From these descriptions, the interior pack seems to be propagating northeastward from 2 primary sources: thermodynamic growth from atmospheric forcing and ocean advection. The principal component hindering this expansion appears to be ocean heat flux.

Combining all three of the above effects, variable mixed layer, variable heat flux, ocean current (left panel, Figure 6.14), comes close to reproducing the observed ice edge with the lowest correspondence located along the northeast shore of the Antarctic Peninsula. As shown in the humidity study above, one way of improving the representation in this region is to obtain accurate humidity data along the continent throughout the year. Another is to include a western intensification current along the coast as done in

the Standard Model case (western intensification input explained in Chapter 4). From the right panels of Figure (6.14) we see that this does improve the northward extent of ice relative to the VHF+VML+OcA case. Using two consecutive contours at 1.4 and 1.8 meters as a guide in both March and August to compare between the VHF+VML+OcA Case and Standard Run, we see from the thickness distribution that additional ice edge expansion is achieved through advection as the thickest ice in the southwest corner of the grid is getting thinner while more ice appears near the north end of the peninsula.

Comparing this with the ice response to the earlier relative humidity test (right hand panels in Figure 6.10) shows that the relative humidity had a greater impact on advancing the ice northward in March (early ice advance period) than either ocean current or heat flux, while there is little difference with or without the inclusion of lower humidity during the maximum extent. The relative humidity ice growth is thermodynamic and therefore highly dependent on the amount of open water or thin ice. Open water is effected the most by low relative humidity and latent heat removal close to shore. Further testing using improved humidity values and accurate coastal current information is needed to define these sensitivities more, but this is a task beyond the scope of this work.

VP Low Resolution (200km) Sensitivity Studies 7 Day Mean Ice Thickness (m)

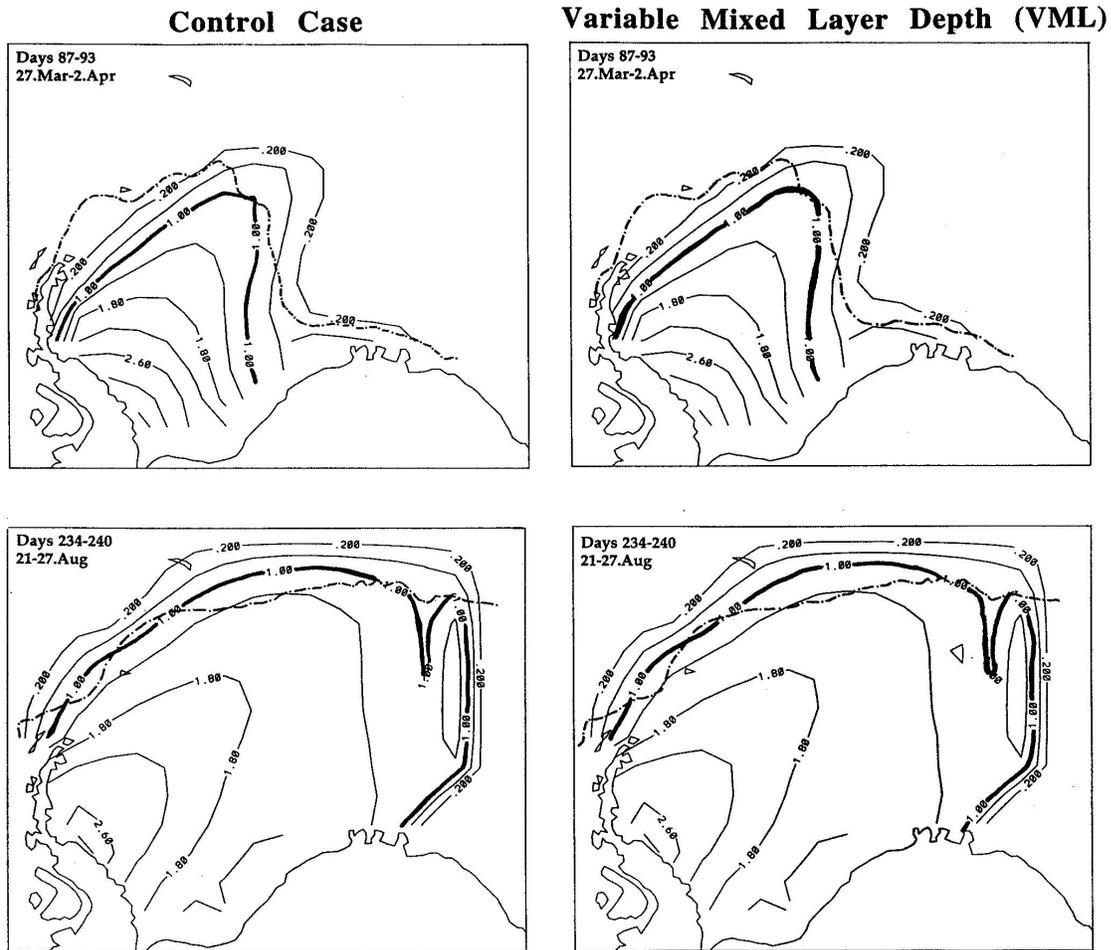


Figure 6.11: Control case versus variable mixed layer case (VML) for 2D low resolution sensitivity study. Dot-dash line is the NSIDC observed 7 day composite ice edge from the same 7 day period as the model.

VP Low Resolution (200km) Sensitivity Studies 7 Day Mean Ice Thickness (m)

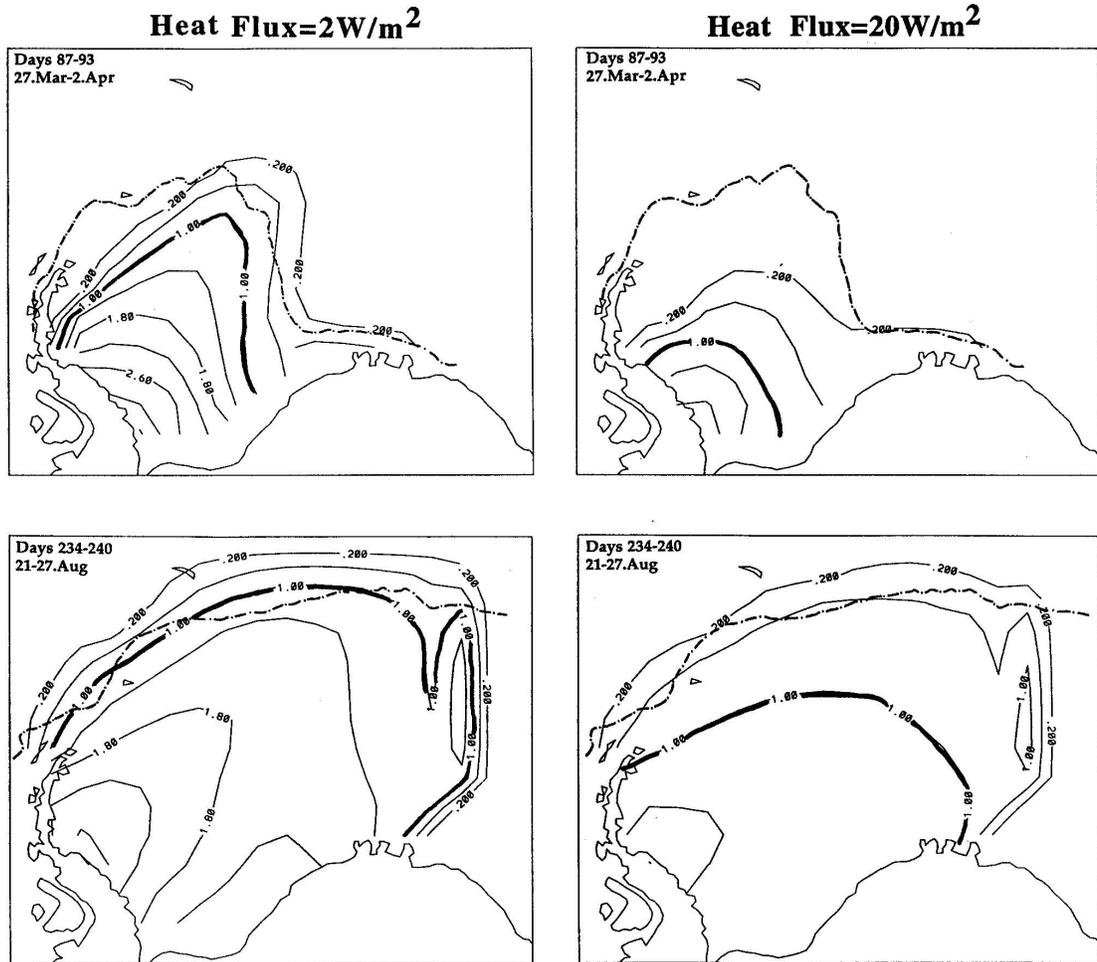


Figure 6.12: Sensitivity to low and high constant ocean heat flux for 2D low resolution sensitivity study. Dot-dash line is the NSIDC observed 7 day composite ice edge from the same 7 day period as the model.

**VP Low Resolution (200km) Sensitivity Studies
7 Day Mean Ice Thickness (m)**

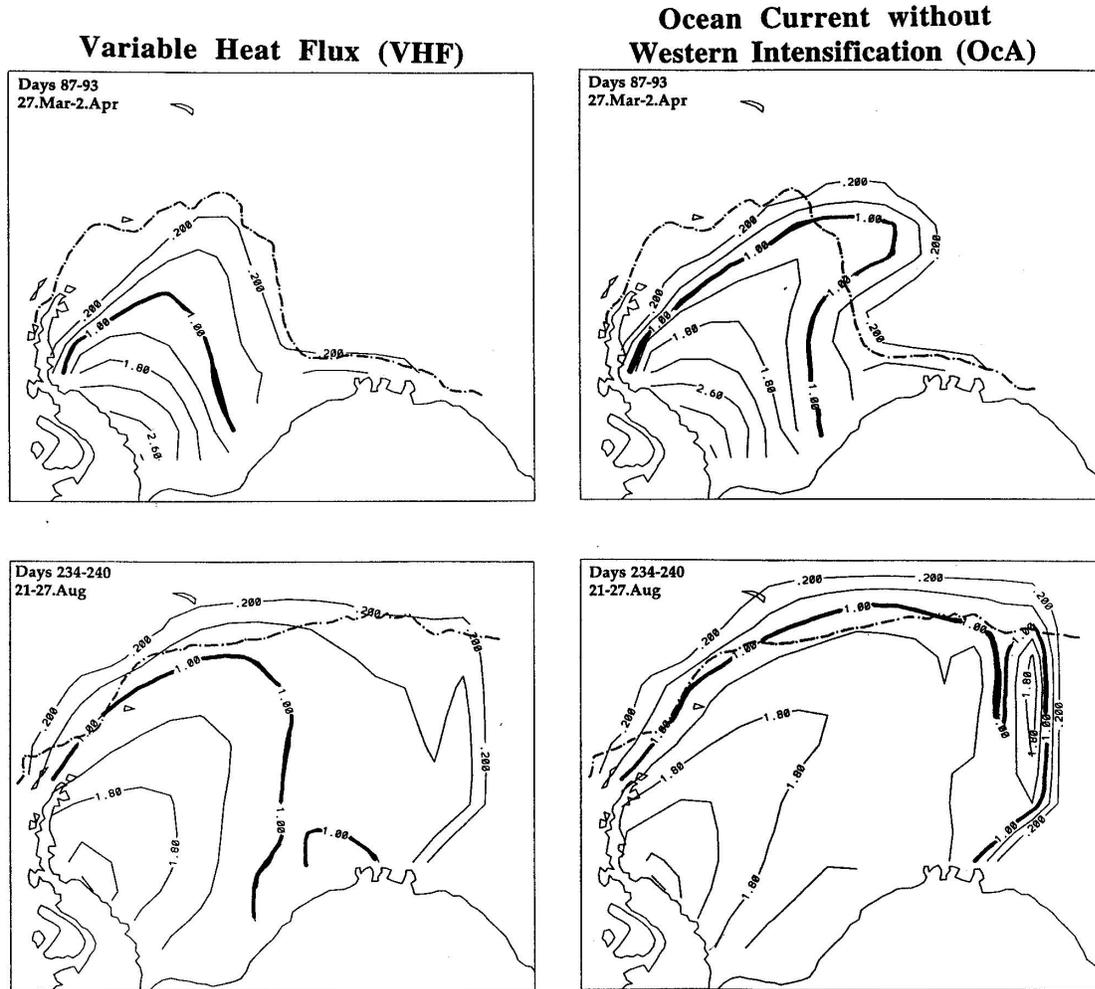


Figure 6.13: Sensitivity to variable ocean heat flux (VHF) and ocean currents (OcA). Dot-dash line is the NSIDC observed 7 day composite ice edge from the same 7 day period as the model.

**VP Low Resolution (200km) Sensitivity Studies
7 Day Mean Ice Thickness (m)**

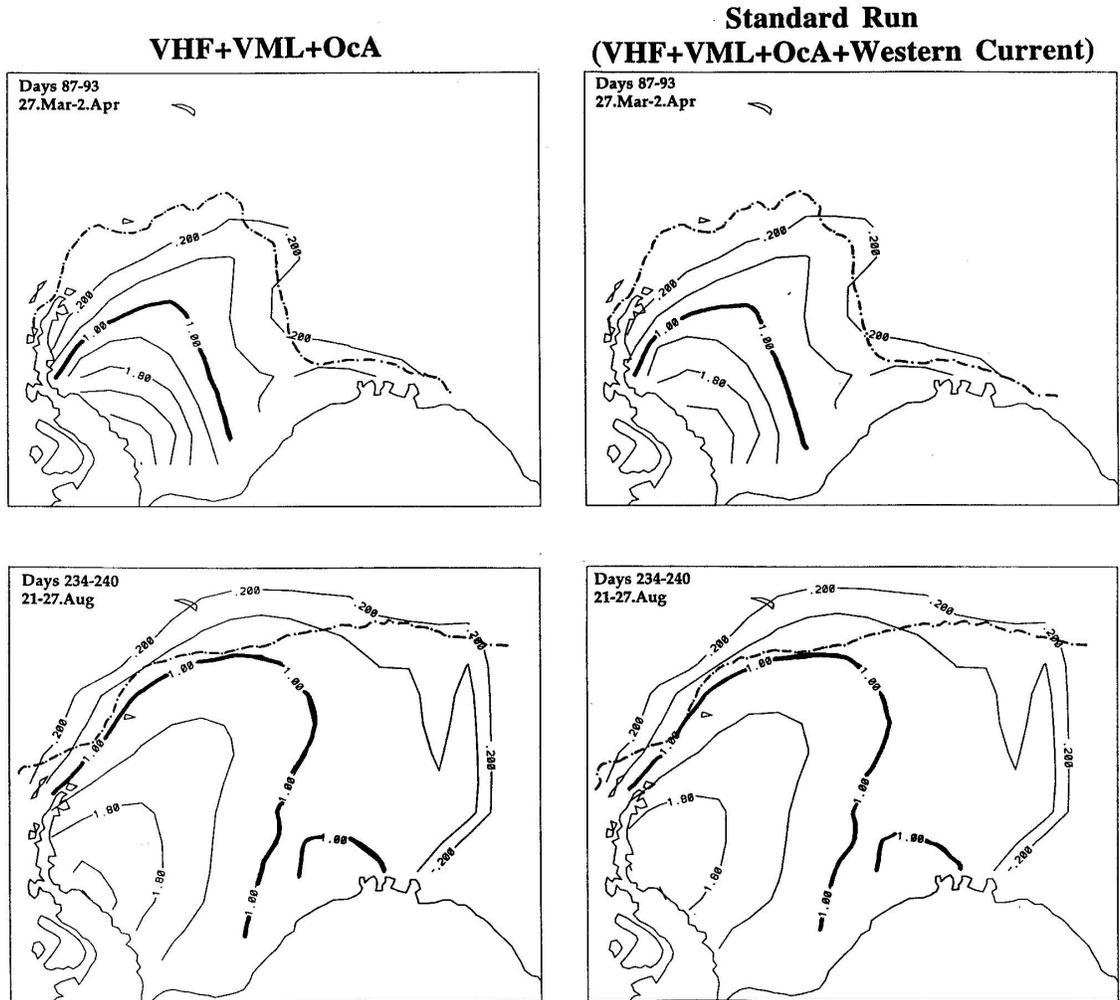


Figure 6.14: Sensitivity to a combination of input fields. Dot-dash line is the NSIDC observed 7 day composite ice edge from the same 7 day period as the model.

6.1.4 Summary of Ice Sensitivity to External Forcing

In this section we have used ice edge and thickness distribution to determine in qualitative terms relative differences in the field caused by specific input variables. In summarizing this section we note the following. First, with regard to model resolution, the ice edge extends further north with increased input field time resolution (e.g. subdaily versus daily); the overall ice thickness is less with increased spatial resolution; and thickness distribution and extent become more are most similar for any spatial resolution. Second, ice thermodynamic growth is dominated by air temperature during the winter months with additional increases achieved with the reduction of relative humidity in open water and thin ice areas. The relative humidity issue is most noticeable along the Antarctic Peninsula such that the standard case with $RH = 40\%$ along the coast gives the best results for this study relative to observed ice edge composites. Third, with regard to ocean activity, ice extent and thickness is thermodynamically reduced by ocean heat flux while advective activity increases with the inclusion of ocean current, as expected.

Casting these results in terms relative to the annual cycle in the Weddell Sea, we conclude that the period of ice edge expansion and decay from April to September is dominated by the air temperature (and wind velocity for heat flux), while the later stages of ice edge retreat and early stages of expansion are very sensitive to a number of other thermodynamic variables (particularly relative humidity/latent heat and ocean heat flux) and dynamic variables (e.g. wind and ocean currents). Contrary to this, ice thickness distribution is more sensitive to both dynamic and thermodynamic inputs year round. The main exception to this is the northern half of the Antarctic Peninsula which is very sensitive at the ice edge to ocean heat flux and especially relative humidity. The relative humidity and ocean heat flux responses are also critical climatic issues. On the one hand, increased ocean heat due to events like global warming can lead to increased ocean heat flux which in turn reduces the overall ice thickness distribution with little effect to the ice edge. This type of scenario is very difficult to detect using ice edge extent as the principal monitor and can lead to catastrophic melt back once the ice becomes critically thin overall. On the other hand, an impact of increased atmospheric temperatures can lead to an overall increase in atmospheric moisture which effects the latent heat transfer from air to ice. In this scenario ice edge extent is changed considerably and is more detectable by visual inspection. Currently, both these scenarios are potential candidates in the event of global warming.

Given these findings, quantification of a model's predictability solely on the reproducibility of ice edge extent can be very misleading. A more stringent criterion of model validation is the comparison of both ice edge location and interior ice thickness distribution with the ice thickness distribution being the more critical variable. With regard to model construction, the need for more frequent input fields outweighs the need for higher resolution; this is a useful result in terms of computer utilization.

6.2 Model Sensitivity to Ice Components

Continuing with model sensitivity, we now investigate responses of the ice due to modeled constitutive design (i.e. ice response due to ice). We will focus on two categories using ice

edge extent and thickness distribution from low (200 km) resolution 2D models. In the first category we examine the response of ice to a hierarchy of ice rheologies which proceed from a totally stationary ice field or thermodynamic only (Thermo Only) response to no ice interaction or free drift (FD) model to a pressure resistance only or cavitating fluid (CAV) rheology and finally a viscous-plastic (VP) rheology involving both pressure and shear resistance to ice. The second category includes VP ice response to yielding closure methods, brittle vs. ductile behavior, energy transfer from air and water to ice, and ice strength. Recalling the purpose of this chapter, results from this section will not be used to declare a definitive “tuned” condition under which sea ice is to internally behave, but it will provide us with a better understanding of how specific ice components affect ice edge extent and thickness distribution.

6.2.1 Responses due to Rheology

Using a hierarchy of rheologies, we now assess the constitutive and mass balance components of the modeled ice. Beginning with a thermodynamic only (Thermo Only) model at 100% ice compactness (left panels, Figure 6.15), we see that the ice edge overpredicts relative to the observed edge in the summer months, but does reasonably well during the maximum extent. This is primarily due to the thermodynamic response of the ice to air temperature, as discussed in Section 6.1.2. Compared to the Standard Model (right side panels in Figure 6.14) the ice is thicker in the southwest corner of the grid, thicker in general in the summer, extends further north in the summer and not as much in the winter. All of these differences arise because of the lack of ice dynamics and advection, both of which work to move the ice around and locally to create leads and ridges. This comparison clearly shows that ice motion and ice-ice interaction are responsible for moving ice out of the southwest corner of the Western Weddell Sea and propagate it in a northeastward direction. In doing so the ice moves further north along its northern perimeter, as seen in the winter example of the Standard Model (lower right panel in Figure 6.14). In summer, this must also be happening but there is less ice in the Standard Model which means there must be more melting going on in the summer months when advection and ice-ice interaction are included. Hence, thermodynamic interaction with these dynamics must also be very important.

An additional feature seen in the thermodynamic only run is the thermal sensitivity of ice compactness. With 95% compactness (right panels, Figure 6.15), the Thermo Only ice edge has the same extent in summer and is only slightly further north in winter than for the 100% compactness case. The interior ice thickness, however, almost doubles in winter (and is about 1.5 times as thick in summer) due to the presence of only 5% open water. Open water fractions of this magnitude are fairly typical values in the field. This means that accurate computation of open water fraction is essential to proper thermodynamic heat exchange in models. It is for this reason that both thermal and dynamical considerations need to be included when examining, for example, the northeastward advance of ice seen in the Standard model versus Thermo Only comparison just made above. In all of the models used for this study compactness is computed as an artifact of the effective ice thickness (volume/area) but it is not treated as a conserved property. This is a real problem in ice modeling since it requires a thickness distribution function such as that of Rothrock et al. (1975) which is computationally very intensive. The lack of high

quality compactness data in observations also precludes the ability at this time to obtain compactness estimates for models. In the mean time, improved model parameterization of this term is needed so the compactness can be computed in a computationally efficient and conserved manner.

Adding to the thermodynamic only model the ability of ice to move without resisting (so called free drift (FD) model) lets us see how advection works together with thermodynamics to affect the ice thickness field response. As seen in comparing the Thermo Only models (Figure 6.15) to the Free Drift model shown in the two left panels of Figure (6.16), the inclusion of advection improves the ice edge location in summer compared to the observed, but overshoots the observed in winter. More noticeably, however, there is an overall decrease in the interior ice thickness to the more typical values of 1 to 2 meters, except for the southwest corner in the Weddell where ice builds up along the Antarctic Peninsula. This abnormally high build up is due to the fact that this type of passive modeled ice can move but can not resist due to the lack of structural integrity. The fact that the winter extent of the ice edge changes only slightly between Thermo Only and Free Drift models supports the fact that air temperature thermodynamics plays the dominant role in ice edge expansion during the winter months even more so than the advective processes. Conversely, thickness distribution is far more sensitive to the dynamic process of advection even in the presence of thermodynamic processes. The introduction of advection to the model also produces the northeastward orientation of ice thickness distribution seen in the Standard Model. Since both thermodynamics and advection are present at this point, it is difficult to say which of the two is the more prominent process responsible for this ice response. A combination of both is certainly needed.

Including pressure resistance to the ice using CAV (right panels, Figure 6.16) we see a considerable decrease in ice edge extent at the northeast end of the ice edge in March but more northward advection of ice along the Antarctic Peninsula. In winter there is very little change in ice edge extent between FD and CAV. As before however, the interior ice thickness changes considerably everywhere, especially close to the Antarctic Peninsula. The reason for this, as shown in the 1D mechanistic CAV model in Chapter 5, is that the ice is forced into the southwest corner of the basin but the internal ice pressure resists this force and therefore keeps the ice from piling up along the coast. Differences in the total amount of ice in these two cases reveal that there is considerably less ice in the basin for the CAV model than for the FD model in both winter and summer. There are two sources in these models for this type of loss. Either the ice is advected as a result of ice-ice interaction into warmer regions of the field where it is melted, or it is advected out the open boundary regions to the east and west.

The VP case (standard run, right panels, Figure 6.14) reacts quite differently from CAV because of the presence of shear. First, the VP modeled ice extends more northward and eastward than CAV in March and the ice edge extent is more like that in the Free Drift (FD) model. Second, the ice is overall thicker with VP than CAV but not as thick as FD. The difference between FD, CAV and VP are the degrees of resistance in the ice, so the difference in overall thickness and thickness distribution is caused by the amount of open water creation and advection created by resistance of the ice. Like CAV, VP is able to resist under pressure but it will also shear and this can create additional open water (and ridges). Hence more ice is present in VP than in CAV due to shear processes.

During maximum extent (August) CAV and VP are similar in ice edge extent but VP has about 0.4 meters more ice in its interior thickness. Again this difference is attributable to either advection out of the model domain and/or thermodynamic melt.

The reoccurring points of thermodynamic growth versus advective processes, their interactive role and the impact of the rheology on these processes is a fundamental issue which merits further examination. Prompted by these results, a study is considered in Section 6.3.2 using higher (50 km) resolution models in order to better understand the interaction between advection, thermodynamics and ice rheology on the annual cycle mass balance in the region.

6.2.2 Responses to Internal Ice Parameters

We now look at specific internal ice parameters in the full ice rheology case (VP) to determine how the ice is responding to specific ice-ice internal forcing. First in considering a few of the closure methods, we find that comparing the Standard Model with replacement method (Figure 6.14) with concentric method (not shown—graphically identical to Figure 6.14) and with a truncated ellipse (left panels in Figure 6.17) that there are only minor differences in ice edge extent or thickness distribution. This is due to the fact that there are only small differences in the rheological description of each of these closure types (see 5.2.1).

Second, the maximum bulk viscosity (ζ_{max} or Z_{max}) determines how brittle (high ζ_{max}) or ductile (low ζ_{max}) the ice is. Plots of ζ_{max} reduced by a factor of 100 ($\zeta_{max}/100$), presented in the right panels of Figure (6.17), show a small increase in ice thickness in the southwest corner of the Weddell Sea where we noted the high build up of ice in the Free Drift case. This difference is subtle but important because it is due to the fact that reduced bulk viscosity causes the ice to move more ductile, experiencing more creep flow from increased viscous motion, rather than experiencing brittle yielding as examined in the mechanistic studies of Chapter 5. These differences are difficult to see in the annual cycle changes because they have their greatest effect at low velocities where creep flow prevails. A better way to understand the effects due to ductility is through buoy drift observations which will be examined in Section 6.4.

Next we compare the Standard Run which has an air drag coefficient of $Ca^* = 0.0012 \text{ kg/m}^2 \text{ s}$ and water drag of $Cw^* = 0.0055 \text{ kg/m}^2 \text{ s}$ (right panels, Figure 6.14) to a run with drag coefficients determined by Fisher and Lemke (1994) of $Ca^* = 0.0015 \text{ kg/m}^2 \text{ s}$ and $Cw^* = 0.0030 \text{ kg/m}^2 \text{ s}$ (right panels, Figure 6.18). The ice edge extent is less in the northeast and the interior ice thickness is greater along the coast in March in the new drag case. The ice extent is only marginally different in August but has a thicker interior (see for example the 1.8 m contour). The reason for these differences is a proportional increase and decrease in the air and water drags, respectively, producing a corresponding increased and decreased transfer of both heat and momentum from the air and water to the ice. In areas with cold air temperature this means more/thicker ice is created due to an increased heat extraction from water/ice to air. Additionally, the increased air drag produces a higher momentum/energy transfer from the wind to the ice resulting in more drift and deformational activity which can create more open water regions for freezing. The lower water drag correspondingly means that there is

less ocean resistance such that the wind dominates more than the water in this modified drag case. This is particularly noticeable in the northeastward expansion of the ice. In March this feature is non-existent in the modified drag case but is even larger in the August example. These differences further complicate the northeast expansion to not only include advection (horizontal) and thermodynamics (vertical) processes but also this feature is governed by an energy transfer (vertical) process from air to ice to water.

From the mechanistic study in Chapter 5, we also learned that the ice strength (P^*) is the bulk parameterization used to determine the yield point of the ice. Reducing ice strength from the standard value (27500N/m^2) to 20000N/m^2 as used in Table 1 of Fisher and Lemke (1994) we see (right panels, Figure 6.18) only slightly thicker ice (about 0.4 meters more) right at the coast along the Antarctic Peninsula. This difference is due to a reduction in the ice strength which allows it to yield sooner under high wind conditions, thus creating leads (open water) and produce more ice locally. As with the study conducted in Chapter 5, modification of the ice strength seems only to have an impact on areas close to the coast because yielding usually begins in conjunction with a boundary like the Antarctic Peninsula. As a preliminary conclusion then, the southwest corner of the Weddell Sea in these model studies appears to be the dominant region for deformational activity. Field experiments (e.g. Wadhams, 1994) and other numerical models (Harder and Lemke, 1994) confirm this as well.

6.2.3 Summary of Sensitivity to Ice

In summarizing these internal ice sensitivity studies, we find that a proper description of the ice interaction is important for predicting sea ice mass balance, ice edge extent and thickness distribution. We also find that ice interaction processes are coupled to thermodynamic and advective processes and that this issue needs to be further assessed (in Section 6.3.2). As with the external forcing sensitivity studies, the thickness distribution is the more sensitive for all the components examined. Additionally, we find that there is a deficit in the mass balance accounting in terms of ice compactness and that this must be rectified. Some attempts have been made to improve the compactness (Flato and Hibler, 1991; Flato and Hibler, 1995; Stern et al. 1995) but they are few and observations of this ice property are still very limited and inexact making compactness an important property to further examine in both modeling and observations. Finally, we saw how changes within the VP rheology of “tuning” parameters produced only subtle changes in ice edge extent and thickness distribution except for the modified drag study. This finding in conjunction with the results of the external forcing and ice rheology suggests that dynamic external forcing terms including energy transfer processes like the modified drag study, thermodynamics and a proper rheology to account for advective and deformational processes is necessary to get an ice thickness distribution close to the true field. The effects of “tuning” model parameters like ice strength, ductility, and details of closure schemes are secondary issues relative to these.

VP Low Resolution (200km) Sensitivity Studies 7 Day Mean Ice Thickness (m)

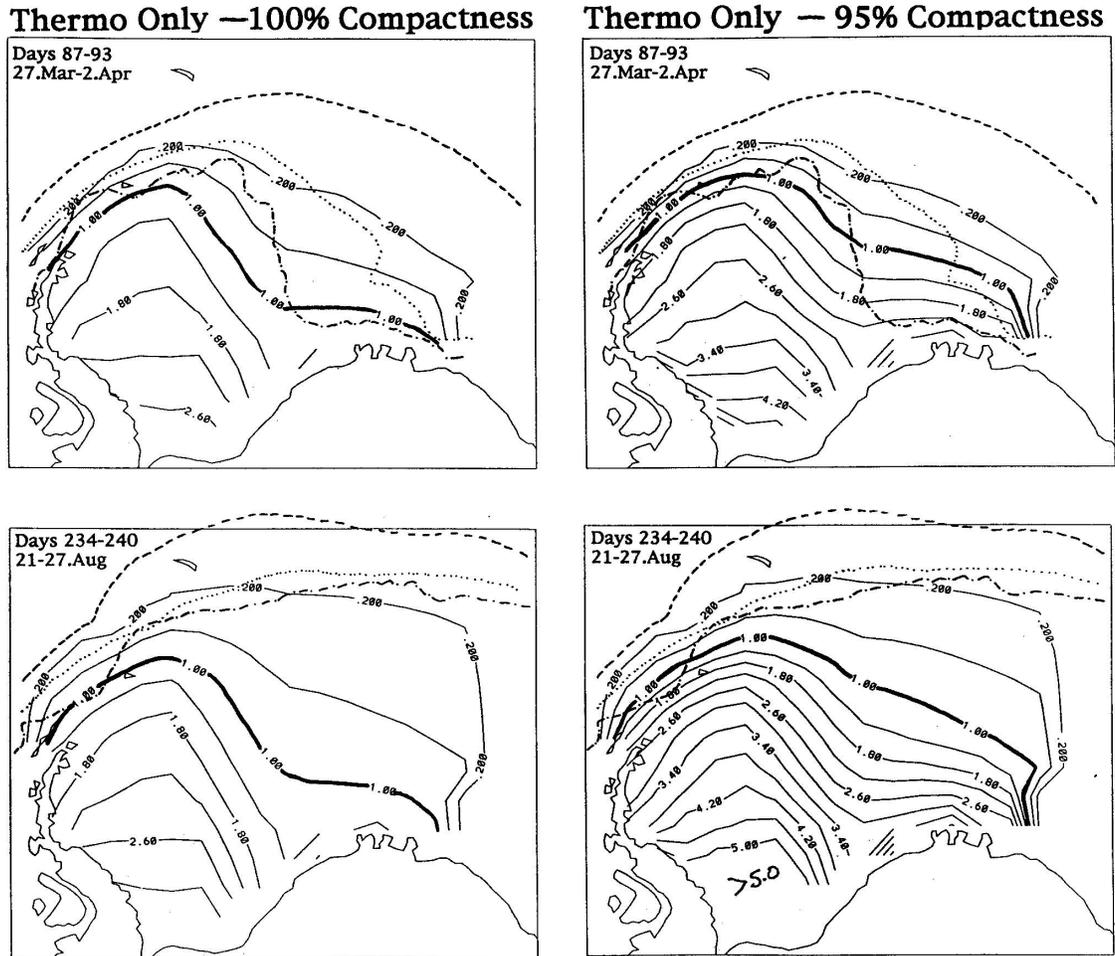


Figure 6.15: Sensitivity to thermodynamics only model under conditions of 100% compactness and 5% open water. Dot-dash line is the NSIDC observed 7 day composite ice edge from the same 7 day period as the model. Dotted and dashed lines are the air temperature at 271 and 273K, respectively.

VP Low Resolution (200km) Sensitivity Studies 7 Day Mean Ice Thickness (m)

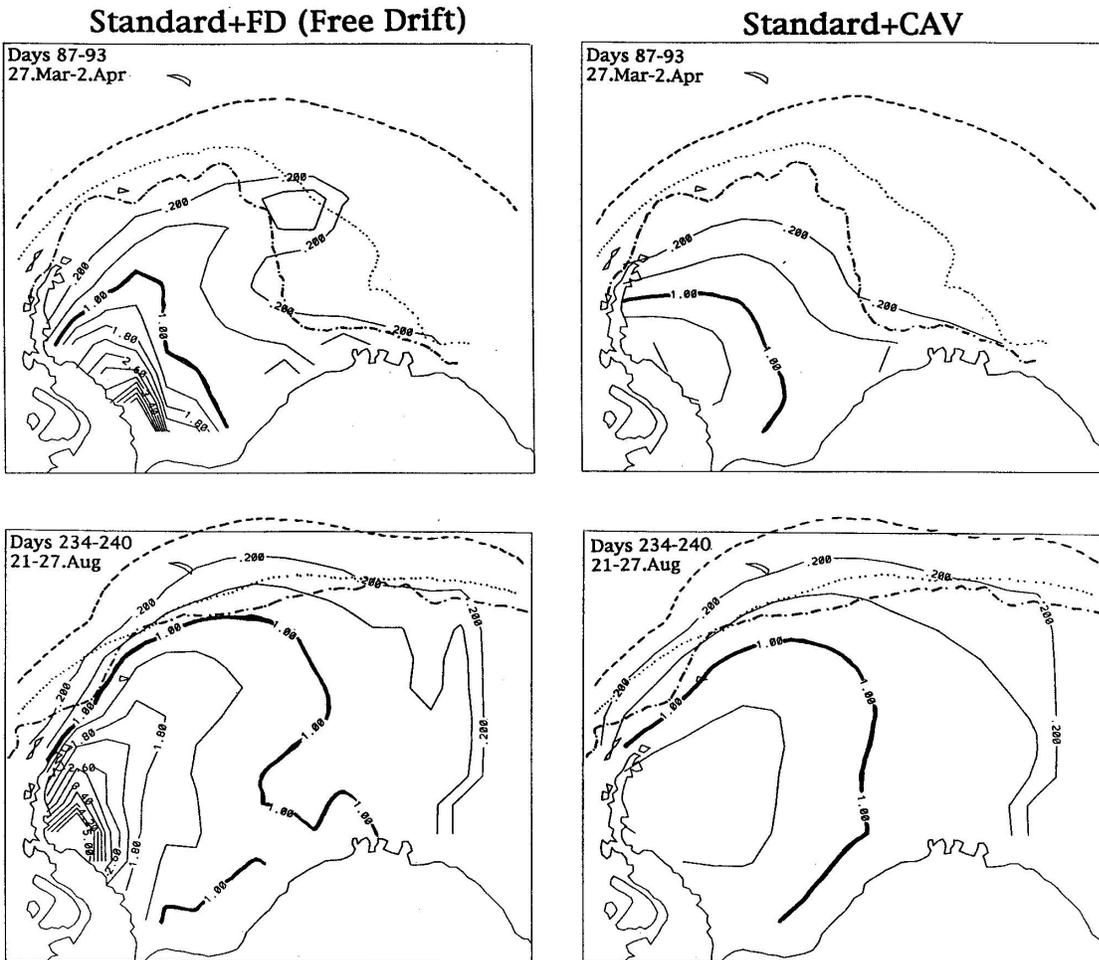


Figure 6.16: Sensitivity to no ice rheology (Free Drift-FD) and pressure resistance only (Cavitating Fluid-CAV). Dot-dash line is the NSIDC observed 7 day composite ice edge from the same 7 day period as the model. Dotted and dashed lines are the air temperature at 271 and 273K, respectively.

**VP Low Resolution (200km) Sensitivity Studies
7 Day Mean Ice Thickness (m)**

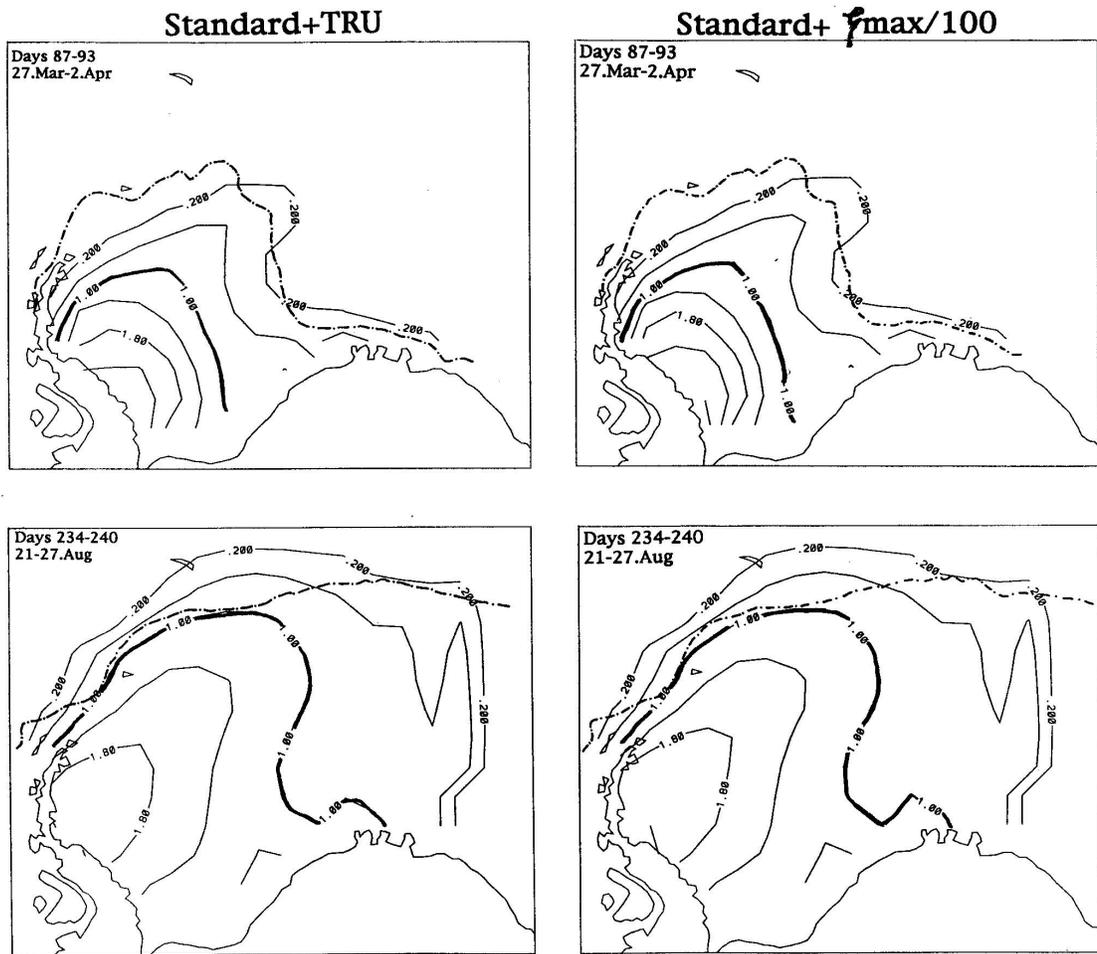


Figure 6.17: Sensitivity to ice truncated ellipse closure method (TRU) and increased ductility ($Z_{max}/100$). Dot-dash line is the NSIDC observed 7 day composite ice edge from the same 7 day period as the model. See text for details.

**VP Low Resolution (200km) Sensitivity Studies
7 Day Mean Ice Thickness (m)**

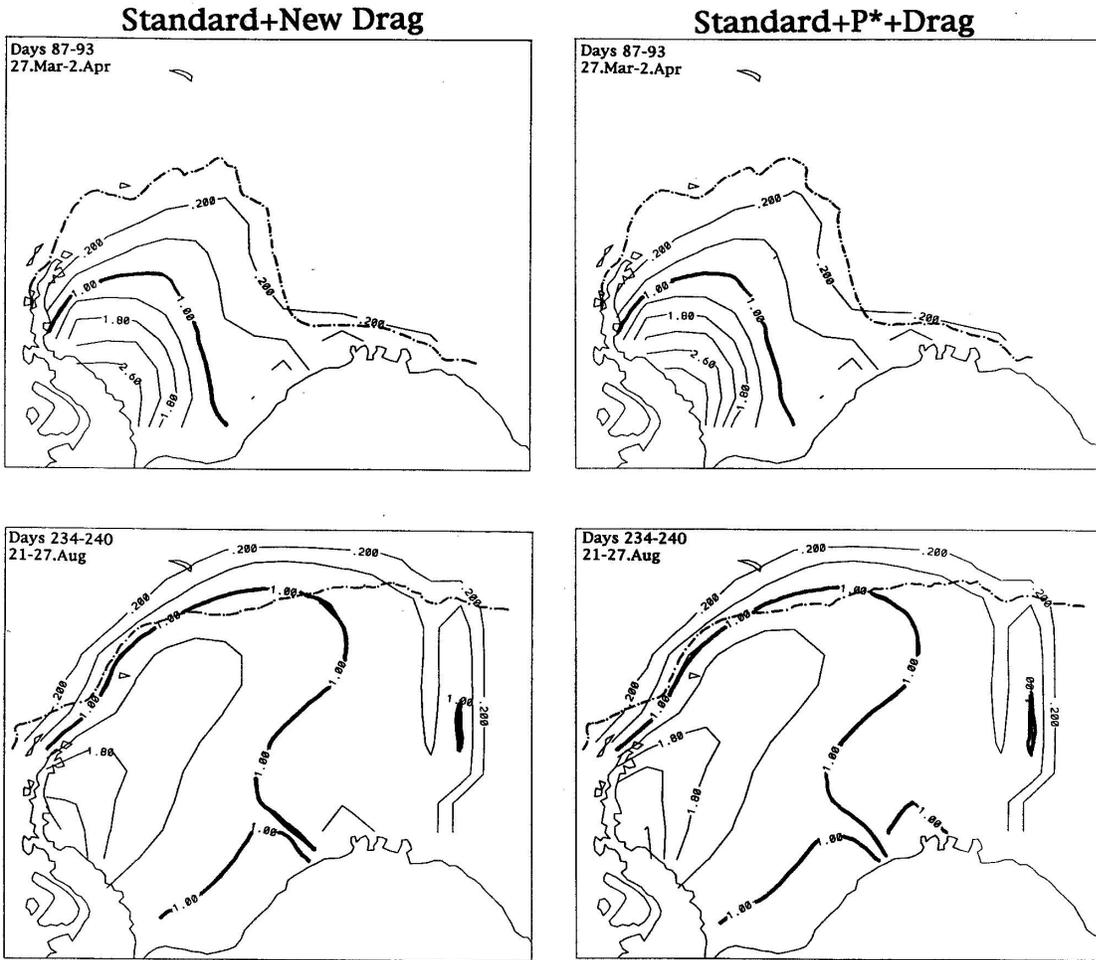


Figure 6.18: Sensitivity to internal ice parameters of drag and ice strength (P^*). Dot-dash line is the NSIDC observed 7 day composite ice edge from the same 7 day period as the model. See text for details.

6.3 Weddell Sea Annual Cycle for 1992

In the first two sections, sensitivity studies were conducted on modeled annual cycle ice edge extent and thickness distribution in order to understand responses to specific input field variables. While a number of important processes were identified in those sections, two important issues remain unclear. First, what is the importance of advection versus thermodynamic growth to annual cycle extent and decay? Second, with the responses to rheology being so subtle in the processes of ice edge extent and decay, what other measurable parameters reveal the effects of rheology more clearly and what results do those give?

In considering the first issue of advection versus thermodynamic growth to annual cycle extent and decay, the goals of this section will be to identify growth and advection as they work in simulations, and then compare these results with observations. The model results will be examined in four different ways in order to understand how growth and advection work in the simulations. In the first Subsection we will examine the modeled annual cycle versus the observed ice edge extent using a 50 km resolution model covering the same region as the 200 km sensitivity runs and using the same subdaily forcing. In the second Subsection, a balance of the regional ice extent and volume will be used to examine growth and advection. In the third Subsection, a regional distribution of the monthly integrated growth and advection will be examined while in the fourth Subsection, case studies of drifting particles within the model field and their local exposure to growth and advective processes will be investigated.

6.3.1 Modeled Annual Cycle versus Observed Ice Edge

Three simulations were made to examine the annual cycle of the ice edge and field thickness distribution using 50 km resolution models. The first case assumes no ice interaction (free drift model-FD), the second includes pressure only resistance (cavitating fluid model-CAV), and the third includes pressure and shear resistance (viscous plastic with truncated closure scheme-TRU). Figures (6.19)-(6.24) show representative 7 day mean ice thickness from each month for each rheology case. Beginning with the free drift case (Figures 6.19 and 6.20), we see that there is far more ice in this case than in the other two (CAV and TRU). This was also true in the low resolution sensitivity study (Figure 6.16) but the buildup becomes even more distinct at higher resolution. Not only is there buildup along the Antarctic Peninsula and continental coastline, as was the case with low resolution. Also at the northwestern edge of the field during the winter months there is anomalous buildup at the ice edge. This is due to the high resolution model's ability to resolve small scale features like South Orkney Island located northeast of the Antarctic Peninsula tip. The inclusion of this tiny island creates a barrier in the circumpolar current. Without ice resistance, this barrier collects so much ice that it leaves a residual ice island that remains into the next annual cycle. This high resolution result in particular illustrates how important the inclusion of some form of ice interaction is to the annual cycle particularly in higher resolution models.

Looking next at the case of pressure resistance only (CAV – Figures 6.21 and 6.22) versus pressure plus shear (TRU – Figures 6.23 and 6.24), the ice edge in both of these

is quite similar, much more so than in the lower resolution 200km cases (Figures 6.16 and 6.17, respectively); this was also found in the 1.5D spherical resolution study at the beginning of the chapter. The thickness distribution within the pack ice of these two cases is similar from the ice edge to a thickness of about 1 meter (see for example the boldfaced 1m contour lines in all 12 months in both cases). Greater than 1 meter, TRU produces more ice particularly along the Antarctic Peninsula (compare for example the 1.8 and 2.6 meter contours for each case). Additionally there is no noticeable buildup of ice during any part of the year in the CAV model near South Orkney Island while there is buildup in TRU from June to November (as exemplified by the 1m contour in June–August). The difference in these two models comes from the fact that TRU allows for shear in addition to pressure resistance while CAV only allows for pressure resistance. Given this information, it seems that the effects of shear on the ice are greater in the thicker ice than in the thinner ice, for these two models.

In terms of how well these models reproduce the observed ice edge, a number of factors not included in the models may be responsible for the poor ice edge correspondence in January and February. As can be seen in the annual cycle, the observed ice edge (dot-dashed line) contains a considerable amount of meandering not seen in the models. This may be due to the fact that the observations are a composite over a 7 day period, and hence more variable than the model which is a 7 day average. Another possibility, given that the observations are realistic, is the lack of wave action processes along the ice edge in the model. Particularly in the circumpolar current, the wave action along the ice edge due to storm activity is a huge factor not considered in large scale ice models. As seen from the 273K (dashed line) and 271K (dotted line) contours in these Figures, the air temperature is the major governor for the ice edge extent throughout the annual cycle even at higher resolution. Given this result, the input radiation balance to these models seems to be particularly critical with regard to simulated ice edge extent. As demonstrated in Section 6.1.2, more accurate humidity data in the input fields particularly along the Antarctic Peninsula may also resolve some of these discrepancies, especially for the summer months.

With regard to the dynamics, the wind velocity and its impact on the ice velocity and deformation seems to be particularly important. In Figure (6.25) we see this interaction quite clearly for a late summer (March) and winter (August) example. The ice velocities move in a general circulation pattern similar to that of the wind with a slight turn to the left of the wind due to the Coriolis interaction in the Southern Hemisphere. Near the coastal boundaries however, the ice velocity is greatly reduced despite the presence of rather high wind velocities as seen in the August example near the northern tip of the Antarctic Peninsula. Instead, along these coastal regions, the wind energy is being used to drive deformational processes as seen in the lower panels of Figure (6.25). South Orkney Island is also a region of high deformational energy ($\sigma_{ij}\dot{\epsilon}_{ij}$) in the winter months as is South Georgia (northernmost island in the center of the model). A regional dependence in the transfer of energy from the wind to ice velocity and deformation is present with the areas closest to land producing a greater transfer of wind energy to deformational processes rather than drift.

Summarizing these results, we find that as models increase in resolution, the need to include realistic ice interaction becomes more critical. This is particularly true of the inclusion of finer land boundaries which have a considerable impact on the distribution of deformational energy in models. Visual inspection of these plots showed that a free

drift model has considerably more total ice than pressure resistance (CAV) and pressure plus shear resistance (TRU) models which means that FD has a greater percentage of thermodynamically grown ice. Additionally, the TRU model produces more ice in the thicker regions of the field than does CAV due to the inclusion of shear processes in addition to pressure resistance. In terms of total ice production from least to greatest the order is CAV, TRU and FD. An important question evolving from this result is, how does the presence of ice interaction change the thermodynamic growth in the field (i.e. what is the specific process responsible for this)? Below, we will examine this question in detail.

50 km FD Standard Run: 7 Day Mean Ice Thickness (m)

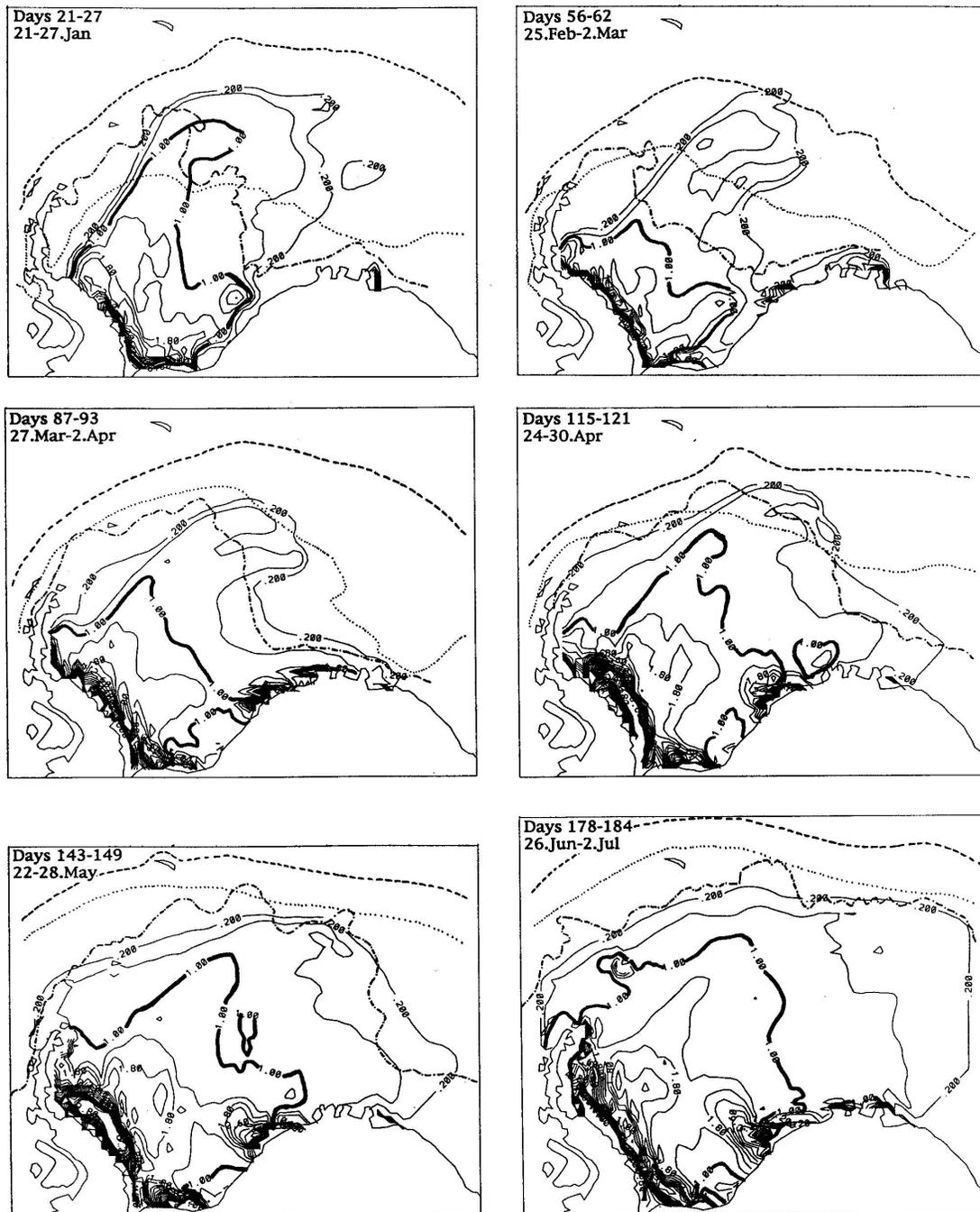


Figure 6.19: First half of the 1992 annual cycle using the 50 km resolution free drift model (FD). Dash-dot lines are the observed NSIDC ice edge composites collected over the same 7 day period as the model time indicated. The 1m ice thickness contour is highlighted for clarity and the dashed and dotted lines are the air temperature at 273 and 271K, respectively.

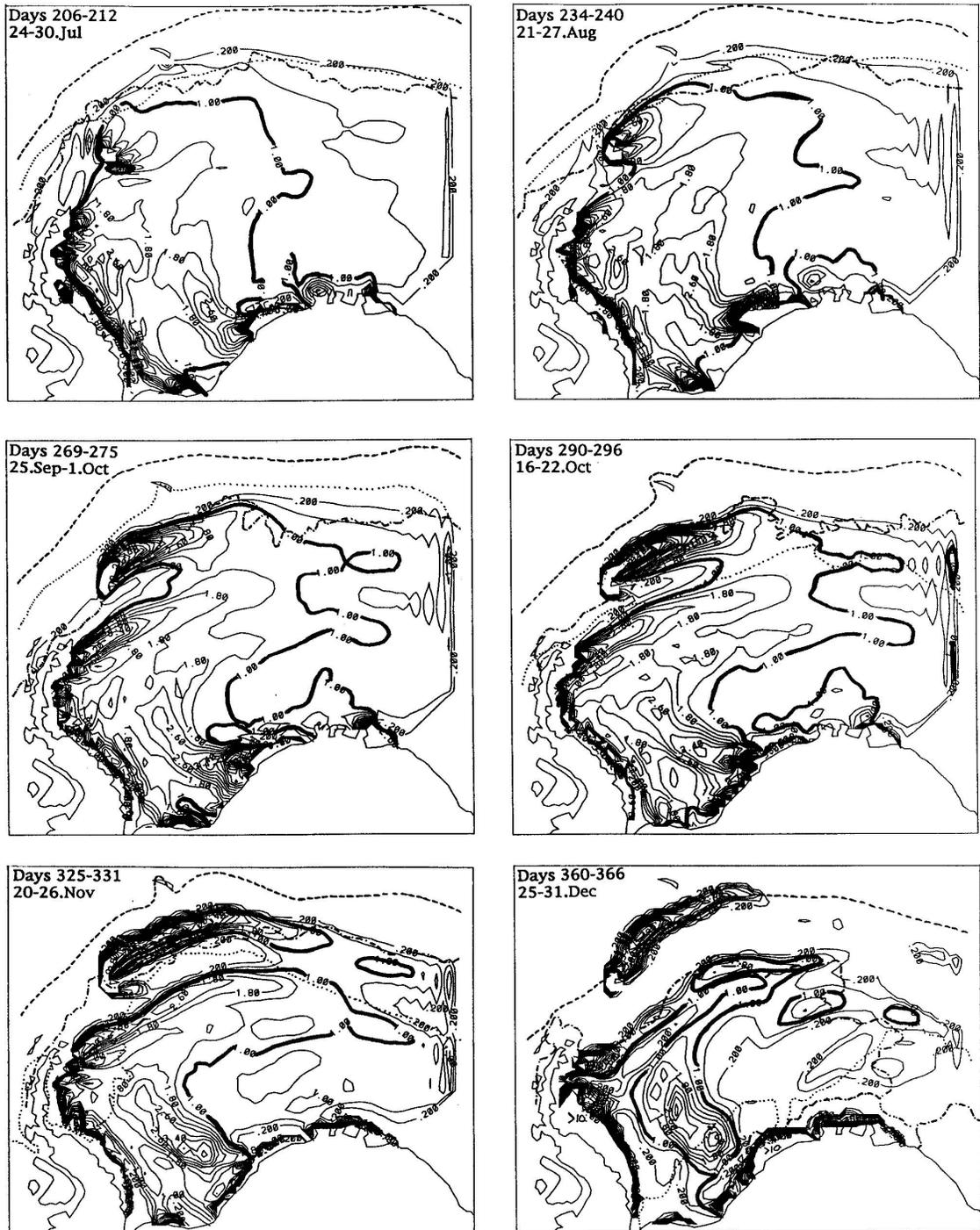
50 km FD Standard Run: 7 Day Mean Ice Thickness (m)

Figure 6.20: Second half of the 1992 annual cycle using the 50 km resolution free drift model (FD). See Figure (6.19) for key.

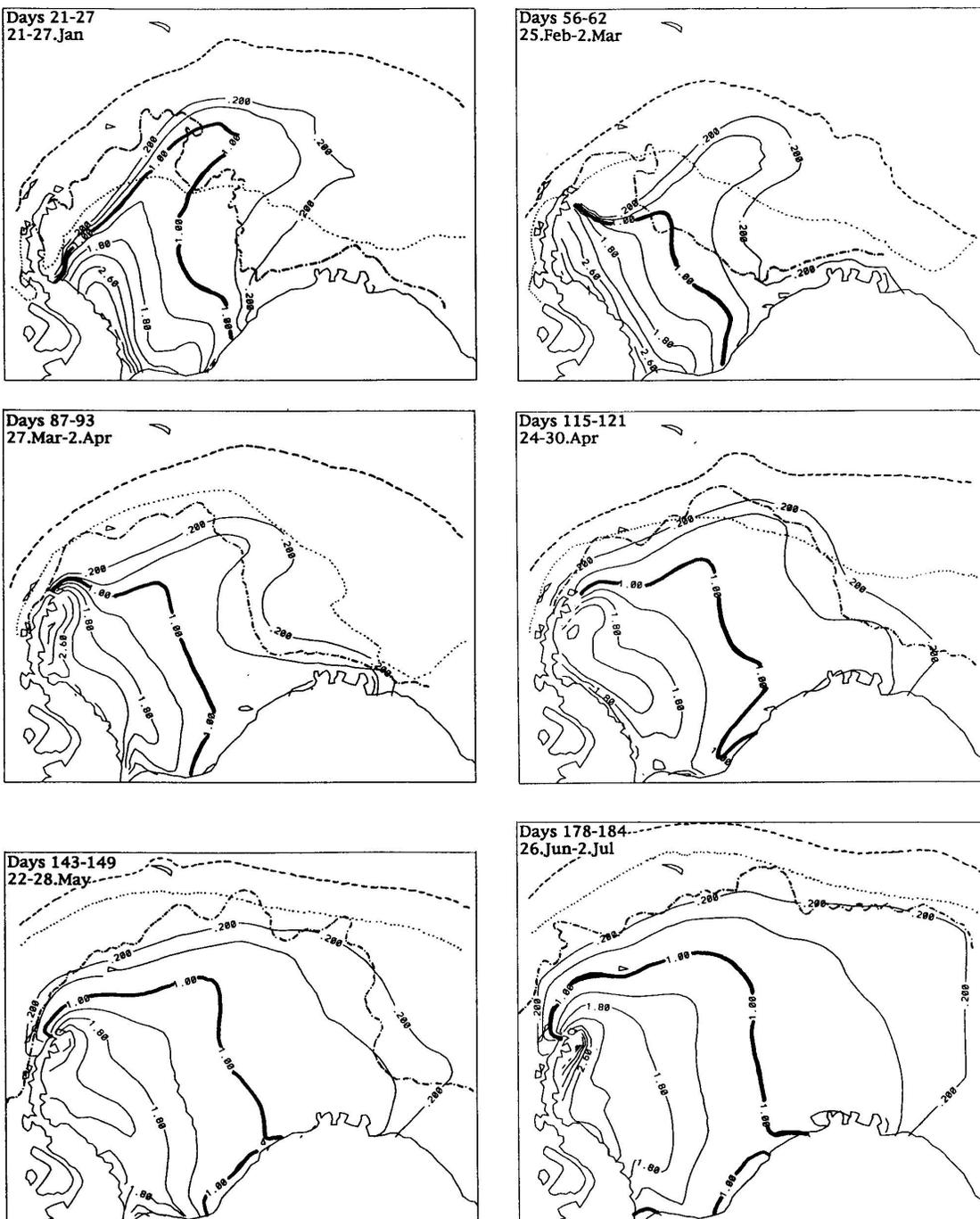
50 km CAV Standard Run: 7 Day Mean Ice Thickness (m)

Figure 6.21: First half of the 1992 annual cycle using the 50 km resolution cavitating fluid model (CAV). See Figure (6.19) for key.

50 km CAV Standard Run: 7 Day Mean Ice Thickness (m)

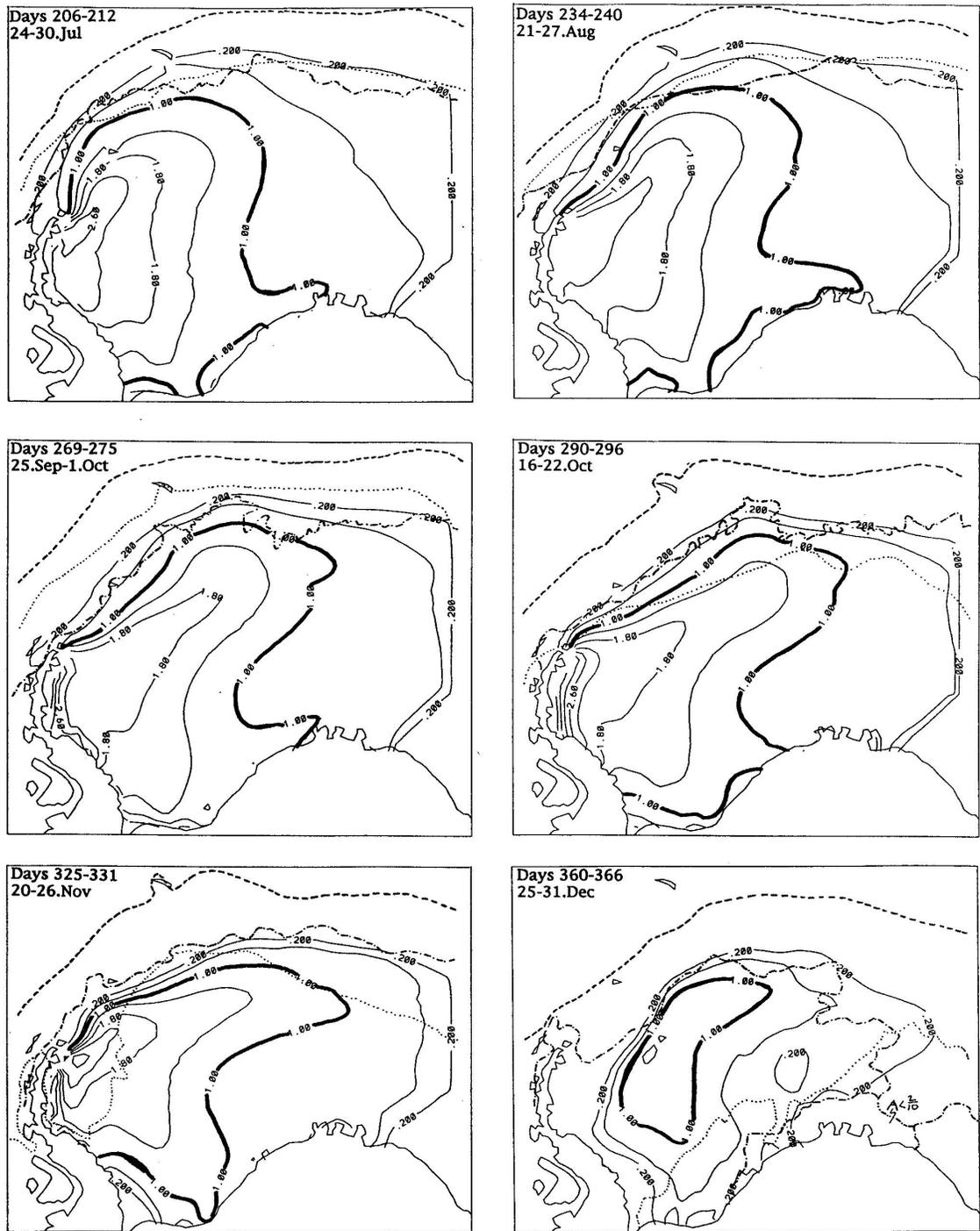


Figure 6.22: Second half of the 1992 annual cycle using the 50 km resolution cavitating fluid model (CAV). See Figure (6.19) for key.

50 km TRU Standard Run: 7 Day Mean Ice Thickness (m)

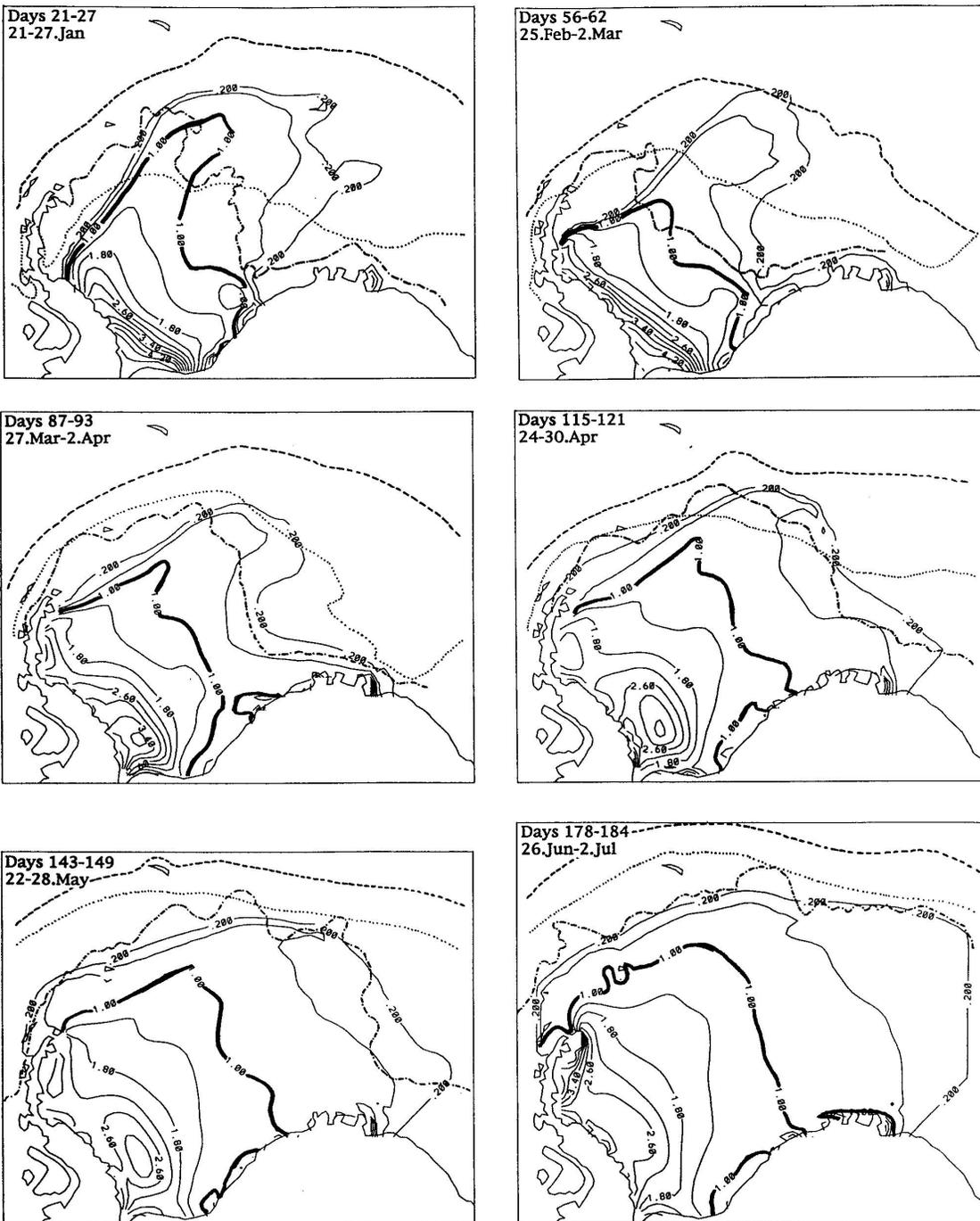


Figure 6.23: First half of the 1992 annual cycle using the 50 km resolution viscous-plastic with truncate ellipse closure model (TRU). See Figure (6.19) for key.

50 km TRU Standard Run: 7 Day Mean Ice Thickness (m)

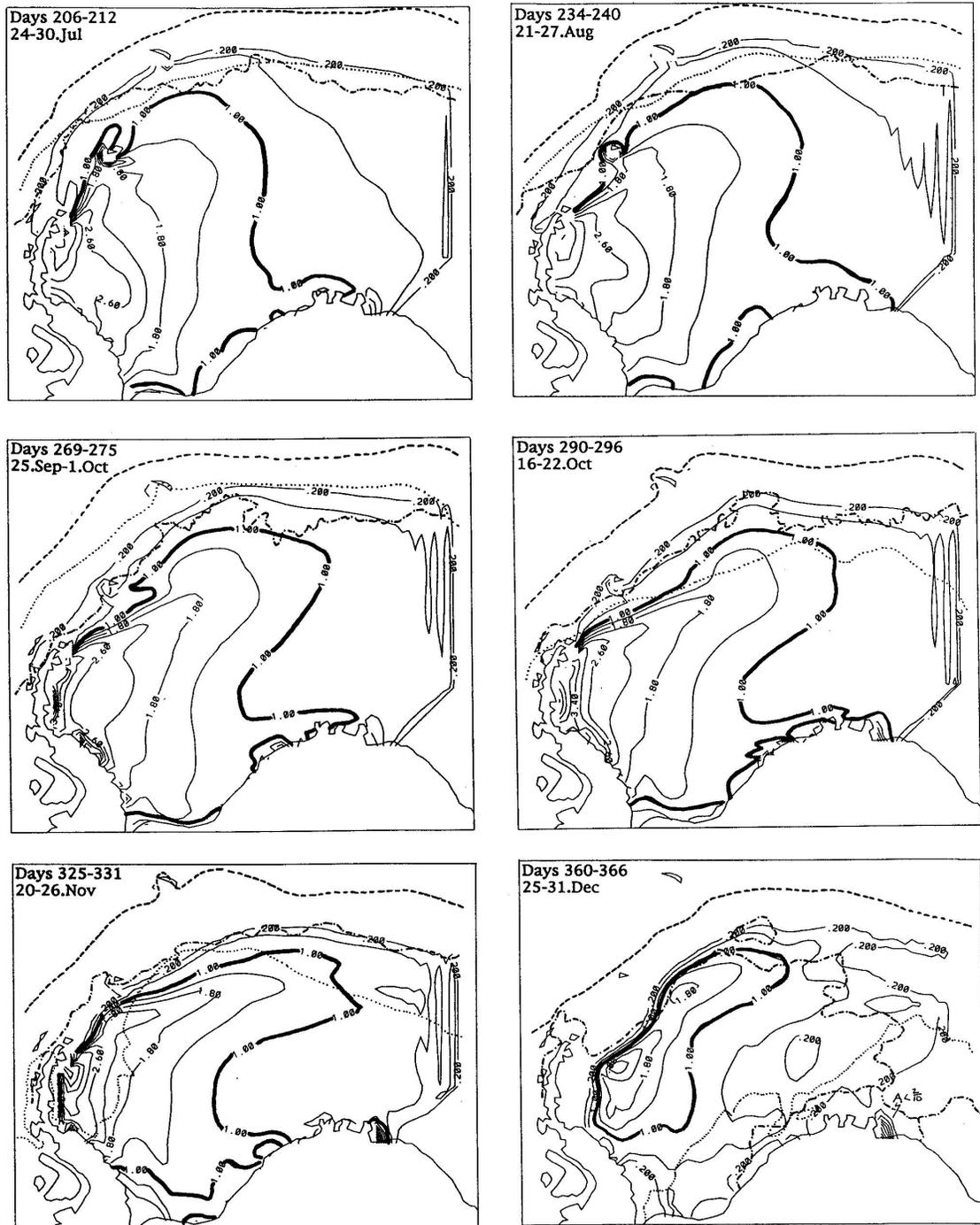


Figure 6.24: Second half of the 1992 annual cycle using the 50 km resolution viscous-plastic with truncate ellipse closure model (TRU). See Figure (6.19) for key.

50 km TRU: 7 Day Mean

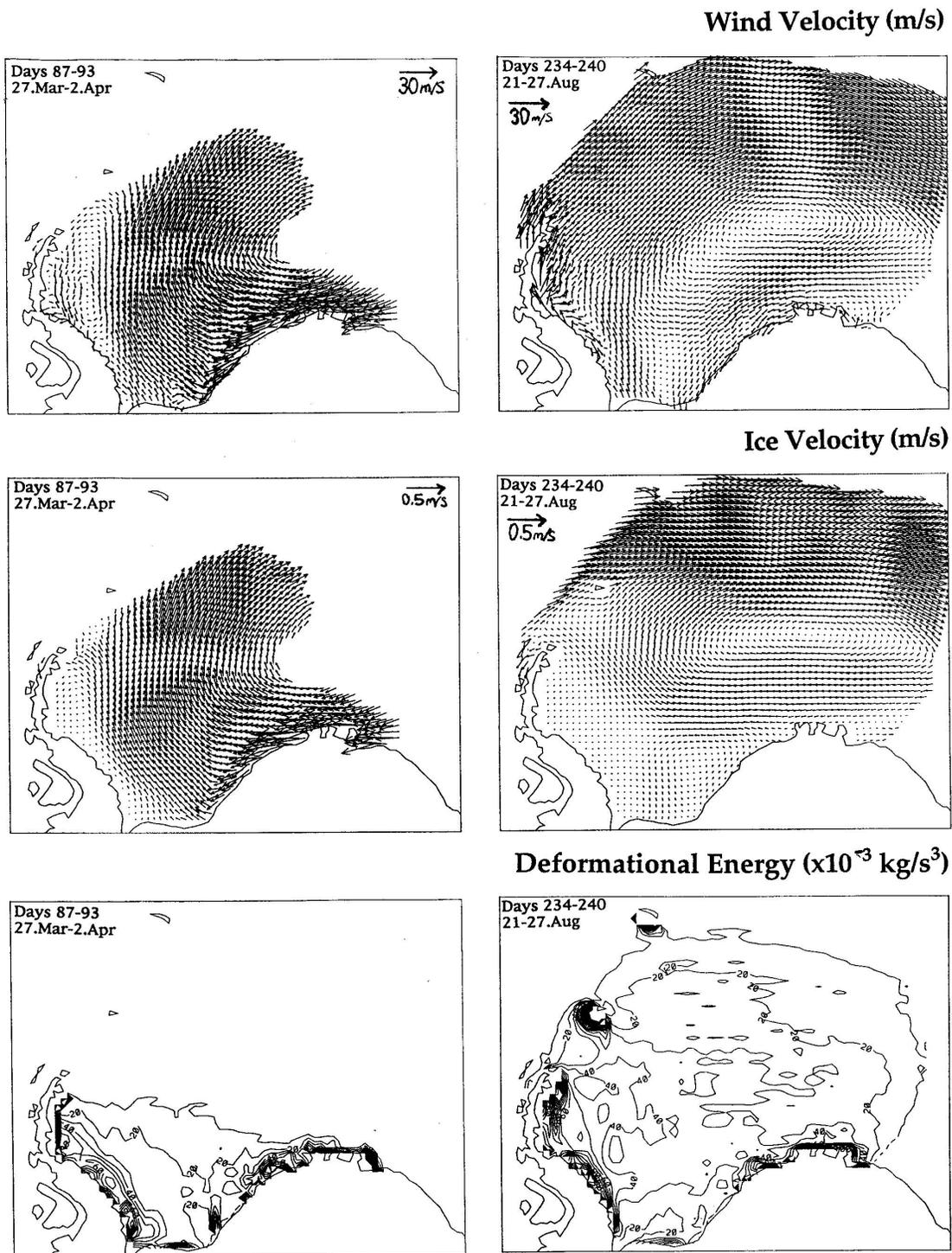


Figure 6.25: 7 day mean wind velocity, ice velocity and deformational energy near the onset of winter (end of March) and near maximum ice edge extent (end of August).

6.3.2 Regional Balance

For this study, h_{eff} is the effective ice thickness per grid cell. This value represents the volume of ice per grid cell divided by the area of the grid cell. Hence, multiplying h_{eff} by the grid area gives the volume of ice per grid cell. This can be integrated over the model domain to give the total ice volume present at a given time. Likewise an estimate of areal extent can be computed by summing up all the grid cells containing ice and multiplying this by the grid cell area. Mathematically these two regional estimates are computed from the model output as follows,

$$\text{Regional Ice Volume} = \sum_{ij} (h_{eff})_{ij} \Delta X \Delta Y \quad (6.3)$$

$$\text{Regional Ice Areal Extent} = \sum_{ij} (\text{QueryIce})_{ij} \Delta X \Delta Y \quad (6.4)$$

where i and j are indices for grid cells in the x and y directions and *QueryIce* is a logical variable equal to 1 if ice is present in a grid cell and 0 if no ice is present.

Ice density is assumed constant so the conservation equation for each grid cell is simplified to a volume conservation. As described in Chapter 4, the numerical code first computes the force balance, from the momentum balance and constitutive relations, followed by the advection and finally a thermodynamic growth locally within each grid cell. The difference between the amount of ice in each grid cell at the beginning of the time step and at the end of the advection routine gives the amount of ice advected locally in each grid cell. Likewise the difference in effective ice thickness between the beginning and end of the thermodynamic routine gives a bulk value for local growth into each grid cell. Using this information, a local balance of ice production in each grid cell equals

$$(h_{eff})_{ij}^{k+1} = (h_{eff})_{ij}^k + (\text{growth})_{ij}^k + (\text{advect})_{ij}^k \quad (6.5)$$

where superscripts k and $k + 1$ stand for the current and next time steps, respectively. By assuming this balance we consider two simple grid cell types, those with ice (where some open water may be present) and those without ice.

For a regional balance, the total ice volume at the end of a time step must equal the amount of ice at the beginning of that time step plus all the local growth within the field, minus any ice that may have flowed out through open boundaries. Mathematically this is represented by

$$\sum_{ij} (h_{eff})_{ij}^{k+1} = \sum_{ij} (h_{eff})_{ij}^k + \sum_{ij} (\text{growth})_{ij}^k - \sum_{ij} (\text{advect}_{[\text{outflow}]})_{ij}^k. \quad (6.6)$$

This regional balance is not demanded by the model and is therefore a very good check of model performance. For the cases run here, a residual between the left and right hand sides of this equation did not exceed $10^{-12} \times 10^3 \text{ km}^3$ for any time step in any of the three cases (FD, CAV, TRU) when run in double precision. This check confirms the simple black box local balance assumed in Eq. (6.5). Conservation for total regional growth is constructed from the following subcomponents,

$$\sum_{ij} \text{growth}_{ij}^k = \sum_{ij} (\text{growth}_{ij}^k)_{\text{ice} > \text{ice}} + \sum_{ij} (\text{melt}_{ij}^k)_{\text{ice} > \text{ice}}$$

$$\begin{aligned}
& + \sum_{ij} (\text{growth}_{ij}^k)_{\text{open} \rightarrow \text{ice}} + \sum_{ij} (\text{melt}_{ij}^k)_{\text{ice} \rightarrow \text{open}} \quad (6.7) \\
& + \sum_{ij} (\text{growth}_{ij}^k)_{\text{open} \rightarrow \text{ad} \rightarrow \text{melt/grow} \rightarrow \text{open}}
\end{aligned}$$

where the subscripted terms *open* and *ice* indicate the state of a local grid cell at the beginning and end of each time step. Residuals between left and right hand sides of this balance also did not exceed $10^{-12} \times 10^3 \text{ km}^3$ for any time step in any of the cases run.

Overall results from the above conservation equations are shown in the upper most panel of Figure (6.26). The total ice extent for the three cases of no ice interaction (free drift - FD), pressure only interaction (cavitating fluid - CAV), and pressure plus shear ice interaction (viscous plastic rheology with truncated elliptical closure - TRU) all yield about the same ice areal extent throughout the annual cycle. A minimal extent near $3 \times 10^6 \text{ km}^2$ reached around day 50 and a maximum around $7 \times 10^6 \text{ km}^2$ reached around day 230 are reasonably close to the general estimate of $2 \times 10^6 \text{ km}^2$ and $8 \times 10^6 \text{ km}^2$, respectively given in the literature (see Chapter 1).

Contrary to this, the total volume behaves differently with the different rheology types. From the upper middle panel in Figure (6.26), we see that the free drift case, where no ice rheology is used, produces about 3 times as much ice as the other two cases and that this volume does not reach a maximum until day 320 (late austral spring). The ice volume involving pressure resistance (CAV) is only slightly less than the TRU model with both pressure and shear resistance. The common volume at the beginning of the year is due to the fact that all three models were started from the same initial conditions (see Chapter 4). An interesting point in comparing the ice volume to the ice areal extent is that the minimum ice volume is about $3 \times 10^3 \text{ km}^3$ and the maximum for TRU and CAV is about $8 \times 10^3 \text{ km}^3$. A regional average for the effective thickness (total volume/total areal extent) is about 1 meter in the summer months and just a little over 1 meter in the winter months, which means that nearly all the distribution of the growth goes into the surface expansion of the ice, as expected. It is for this reason that the 2D planar approach to ice mechanics works so well.

The two lower panels of Figure (6.26) show the time integrated regional growth and outflow, respectively. From the total integrated growth (middle lower panel in Figure 6.26), we see that the source of the annual cycle's ice volume comes from the ice growth, as expected, such that the only difference between the cycle of total ice volume and total integrated thermodynamic growth is an offset, in this case about $5 \times 10^3 \text{ km}^3$. In the bottom panel of Figure (6.26), we see that the outflow, through the western and eastern sides of the grid are about 10 times smaller than the growth for the free drift case, but for CAV and TRU the difference between maximum and minimum ice volumes is about $5 \times 10^3 \text{ km}^3$ which is only about 2.5 times greater than the amount that flows out the eastern and western boundaries.

Another important point with the outflow condition is that most of the outflow occurs during the winter months when the ice has the greatest contact with the open boundaries. Conversely, most of the melt back occurs in the Austral spring following that. Using the ratios of 10 for FD and 2.5 for CAV and TRU, we estimate that respectively, 10 and 2.5 times as much ice is lost to ice melt processes in the Austral spring than outflow through the open boundaries. This means that even though outflow can occur sooner

than melt back of the annual pack, the melting process dominates (about 2.5 times greater when an ice rheology used) over the outflow process in the numerical models. As will be seen in the advective balance in Figure (6.29) outflow through the eastern boundary is much greater than the outflow to the western boundary and thus the outflow pattern greatly resembles that in nature where outflow to the eastern boundary is caused by the presence of the circumpolar current moving ice eastward. In nature there is also virtually no ice entering the system through the western boundary. Therefore, while there are no computed values of observed ice transport out of the Weddell Sea, the numerical outflow is reasonable given what information is known about the circulation in this area.

A final point is with regard to the free drift model's outflow which actually is negative during the onset of winter months. FD is run using the TRU numerical code and simply setting the ice strength to zero. As seen in the outflow however, in the FD case this leads to a flow of negative ice from the outflow cells back into the active ice area. The numerical code is set up to handle this by transferring negative ice quantities into heat in the mixed layer. While this amounts to bookkeeping in the interior of the simulation, in regions near the outflow and possibly in regions near the ice edge, the possibility of negative ice advecting is not realistic. With the inclusion of a viscous-plastic rheology, this effect goes away. In CAV, this problem is completely avoided by using an upstream differencing advection scheme, but this requires a C-grid to work in and the viscous-plastic models currently operate in a B-grid because of the complexity of the rheology. In creating a more realistic numerical scheme, methods to remove advection of negative ice (such as in the upstream differencing scheme) should be considered for the viscous-plastic models.

In Figure (6.27), the areal extent, volume, growth and outflow increments at each time step ($\Delta t = 3$ hours) for FD and TRU are shown (CAV not shown as it appears in these plots quite similar to TRU). In addition to the nice smooth temporally integrated curves in Figure (6.26), we see the subdaily, daily and longer period changes in the total field over the course of one annual cycle. The change in areal extent varies at nearly every time step and this is fairly consistent throughout the year with the least variation occurring from about day 90 to 230 (primarily the winter months). More distinctly, the volume and growth changes from days 1-90 and 230-366 coincide with periods of greatest melting with fluctuation in the growth varying at the frequency of the thermal input fields. Contrary to this, the ice growth during the winter months (90-230) is fluctuating more at the storm frequency (5-8 days) with only very small sub-daily variations.

These differences confirm that two separate mechanisms are involved in the seasonal evolution of the ice pack. During the melt back period, the solar radiation and corresponding daily and sub-daily temperature and radiation fluxes are melting the ice, while the winter expansion is due to sensible/latent heat losses where wind velocity has the greatest impact. While these processes are well known observationally, in the models their effect is seen at two distinct frequencies, namely as daily/sub-daily radiation forcing in the summer months versus weekly high wind sensible heat losses in the winter months. This dichotomy is interesting because the winter months' ice edge is better simulated in the models compared with observed than is the summer ice edge. The fact that the summer melt is primarily regulated by radiation fluxes at daily/sub-daily rates suggests that the radiation balance used in these models may be something to improve upon in terms of better simulating summer ice extents. Parameters such as relative humidity, as

discussed in Section 6.1.2, seem to be critical components to examine in next generation models.

These thermal differences are seen in all three rheology cases with CAV and TRU being very similar. In the case of FD, however, there is about a 10 fold increase in growth during the winter months over the other rheologies. This is occurring due to weekly storm systems at high winds passing through the area. From Figure (6.28) we see that this increased growth rate is coming primarily from open water regions. Furthermore, if we look at the advection of ice into these same open water regions (bottom panel in Figure 6.29), we also see that there is close to a 15 fold increase in ice advection into open water cells for the FD case over TRU. This difference reveals the process responsible for the high ice production in the case of no ice resistance; namely the lack of ice resistance allows the ice to move freely into the coast where it builds up with increasing thickness. As it does this, open water regions are created. Since the ice edge is of similar extent in FD and TRU in winter, the open water regions must be located between the ice edge region and the coast (i.e. a regional divergence with opening in the center must be occurring in FD). The open regions are quickly cooled and more ice is formed and advected into the coast where it builds up even further.

With ice resistance (TRU as representative in Figures 6.28 and 6.29), advection into open water is greatest during the onset of winter; in free drift the reverse is true, the greatest advection is during winter and melt periods. Looking at the magnitudes of these different growth and advective processes in terms of contributions to the annual cycle, we see in FD that advection into open water contributes about three times as much to the ice increase versus the growth in ice cells (primarily in the open water partitions of ice grid cells). Growth of ice in open water cells is about two orders of magnitude smaller than both of these. In terms of processes in the free drift model, ice moves toward the coast and open water is created behind it producing a conveyor belt of ice production not found when the ice resists motion and insulates the water below from the cold air. The process of internal ice pressure resistance therefore, is a key mechanism to insulating the ocean. In the cases where ice resistance is incorporated into the model, the largest source of new ice production comes from growth in open water regions of ice cells followed by advection into open water regions (about an order of magnitude smaller) and then growth in open water regions (an additional order of magnitude smaller-Figure 6.28).

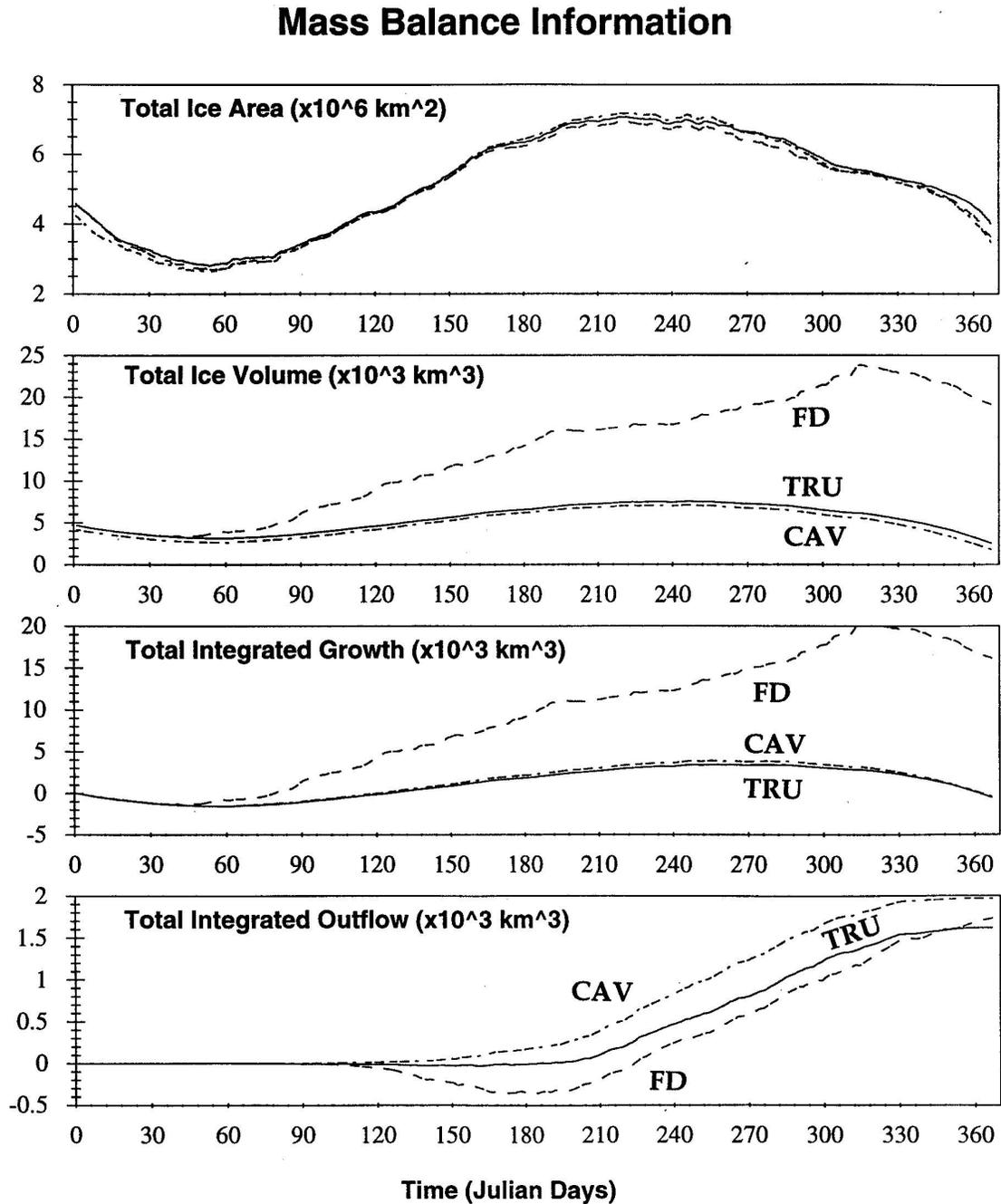


Figure 6.26: Overview of the annual cycle regional mass balance (density assumed constant) in the form of regional areal ice extent, total ice volume, time integrated ice growth, and integrated outflow through the western and eastern ends of the model. Symbols: free drift model (FD), cavitating fluid model (CAV), viscous-plastic with truncated ellipse model (TRU).

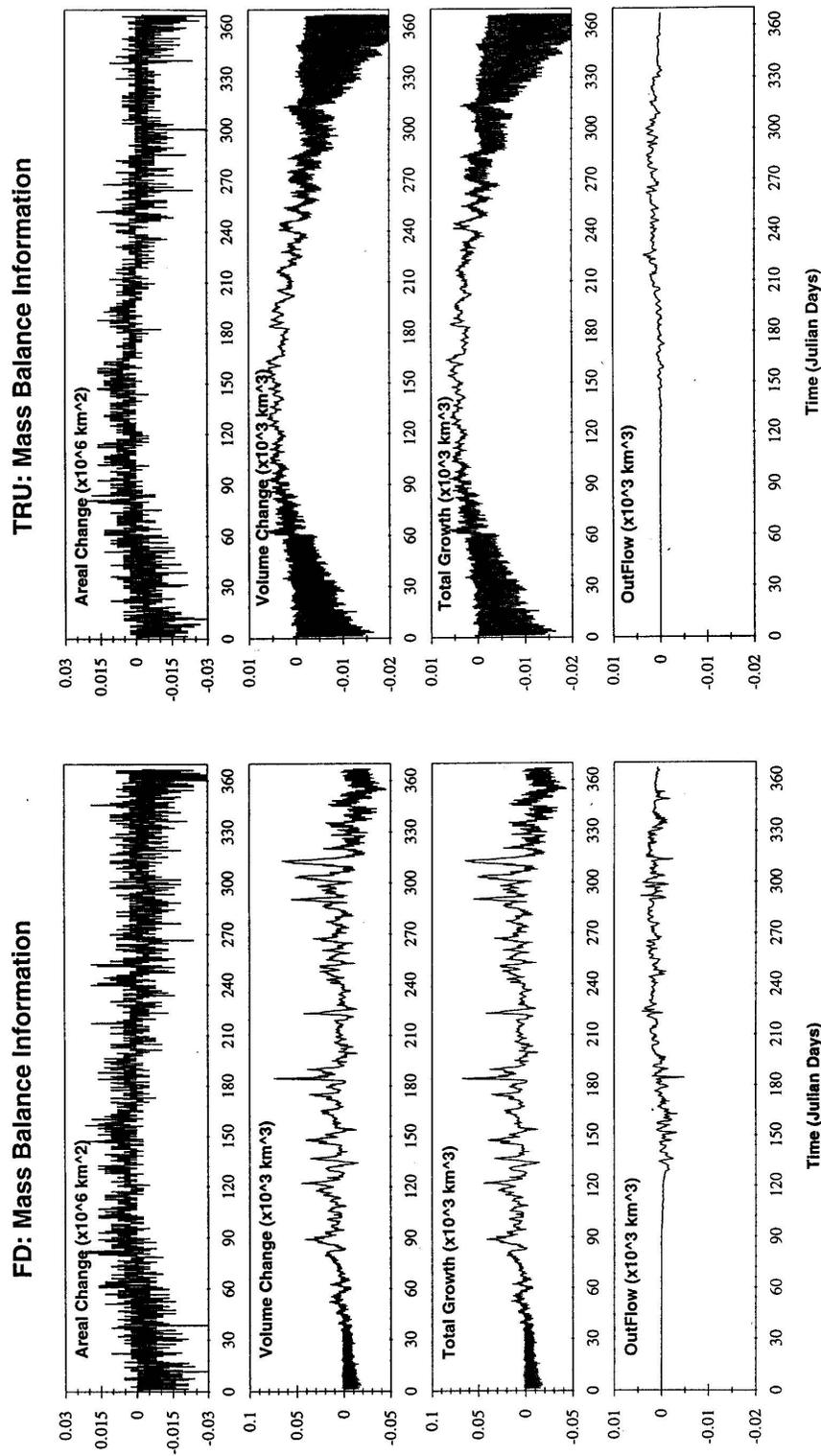


Figure 6.27: Changes in areal ice extent and ice volume, thermodynamic growth and advected outflow are shown for each time step ($\Delta t = 3$ hours) for the free drift (FD) and viscous-plastic with truncated ellipse (TRU) models.

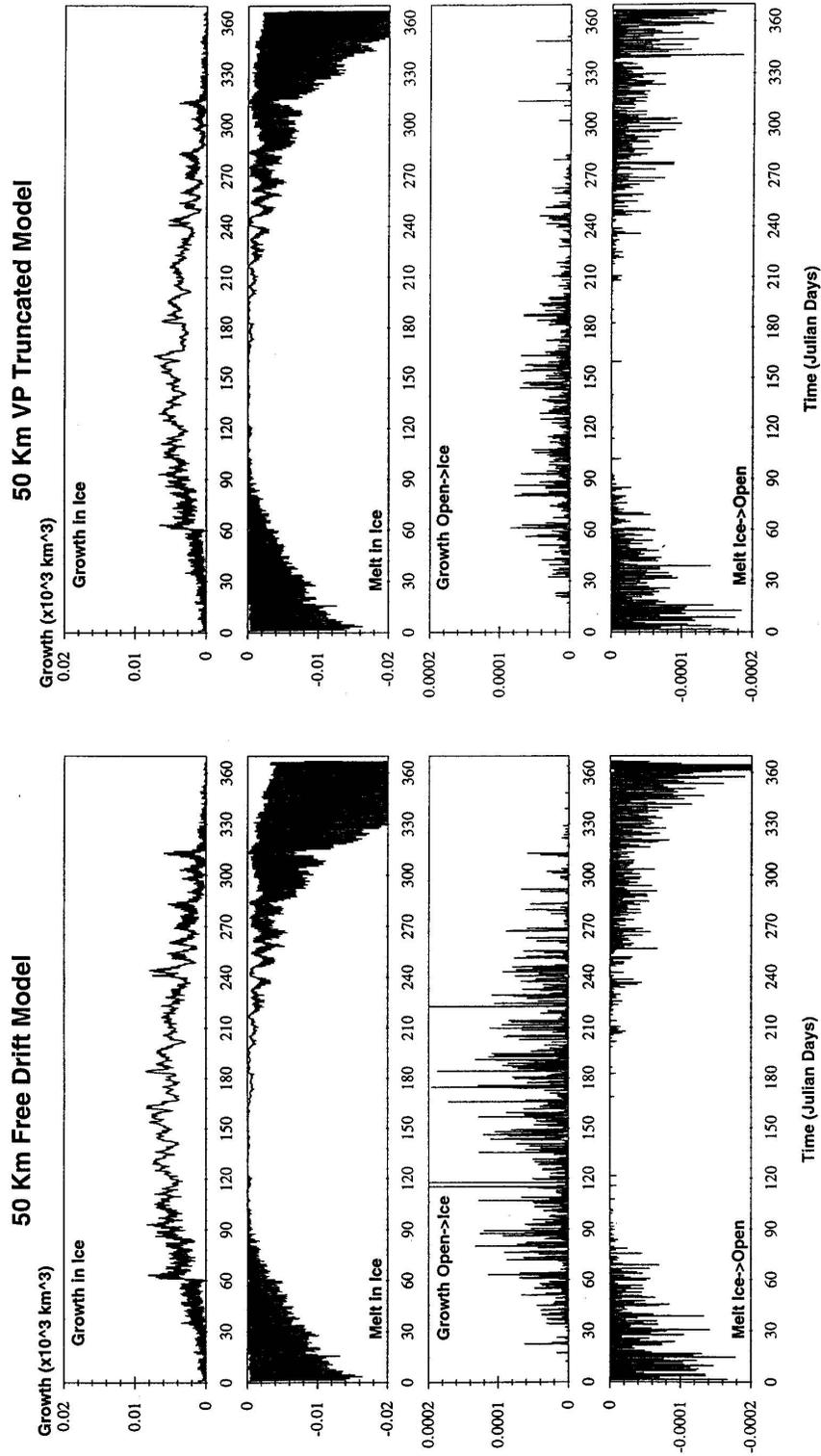


Figure 6.28: Regional growth balance for each time step ($\Delta t = 3$ hours).

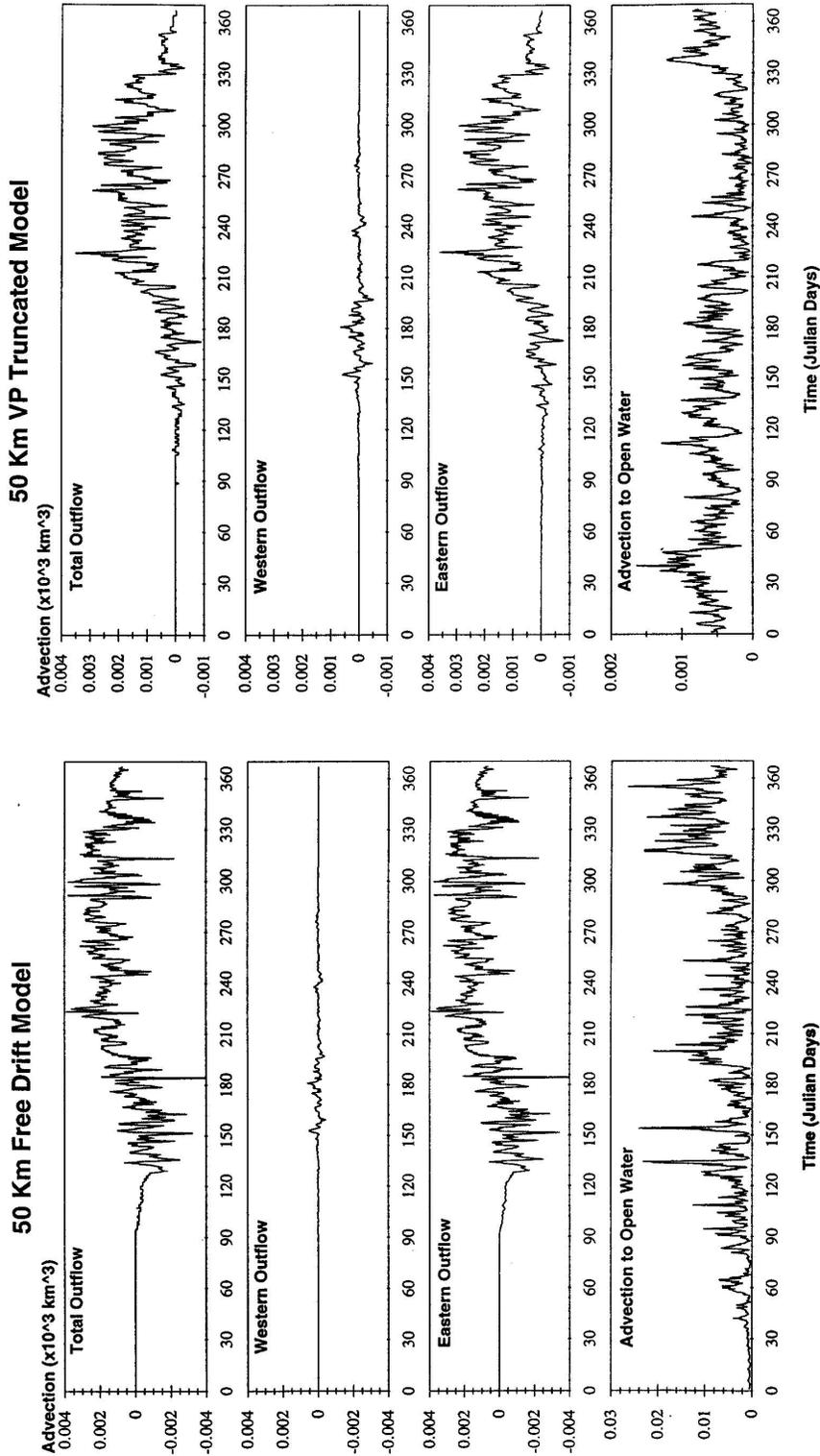


Figure 6.29: Regional advective balance for each time step ($\Delta t = 3$ hours).

6.3.3 Regional Distribution of Growth and Advection

In order to understand the results from the regional balance more clearly, a regional distribution of growth and advection is presented using the TRU model as this is the most realistic case based on what we found from the previous two sections. The change in ice thickness, ice growth and advection in each grid cell is integrated over one month periods (i.e. January = 31 days, February = 29 days, etc.) and plotted on regional contour charts. Additionally, LOG_{10} of the ratio of the magnitude of growth to advection is also computed; taking the LOG_{10} of this ratio produces more linear distribution of contours. Since we are interested in changes over the annual cycle, the three months of January-March and July-September are selected and shown in Figures (6.30)-(6.35) because they illustrate changes in the region from the decaying to growing period and growing to decaying period, respectively.

Beginning with the summer months (January-March), we see from the upper left panels in Figures (6.30)-(6.32), transition from primarily decaying ice in January to producing ice beginning along the coastline and moving outward through February and March. Three interesting occurrences of ice production during this time period are the increased production of ice along the Antarctic Peninsula in January, and the two decaying tongues along the southern coast during February and March. From the lower right panel in these Figures we see a strong resemblance to these anomalies in the advection yet no signal in the ice growth. The thermodynamic growth proceeds during this time from primarily melt back in January to some growth along the Maud Rise coastal region in the Eastern part of the Weddell from February to March. The advection is primarily into ice edge regions and the coast during January and February and then primarily away from the coast during March.

The January and February distribution exhibit a divergence oriented in a southwest to northeast direction which may be due to the pressure resistance from the Antarctic Peninsula to which this orientation is normal. The same is true of the advection away from the coast in March. In terms of which component is greater, we see from the lower left panel in these Figures that regions closer to land have more dashed contours which means advection is the dominant process here while for January and February thermodynamic melting dominates in areas away from the coast, including the ice margin. In March, this picture changes to include a strong advective tongue of ice near the northwest ice margin oriented in a northeast to southwest direction. Within this tongue advection dominates over thermodynamic growth.

The regional picture six months later starts in July (Figure 6.33) with ice decay at the southwest end of the region and ice production everywhere else, particularly in the region between South Georgia and South Orkney Islands. The islands themselves appear to be important contributors to the buildup of ice in that region. By August ice production is minimal while decay along the western end of the region is on the rise. This pattern continues into September. During this period it is the advection which dominates the field (lots of dashed lines in the ratio images) with most of the advection moving away from the coast in a northeasterly direction. Both thermodynamic growth and melt are very low through this period (July-September) except for growth along the continental margins and the two islands of South Georgia and South Orkney.

From the regional balance in the previous section and this regional distribution, we find that localized daily/sub-daily thermodynamic melt is the dominant process during the summer months while advection induced by storm activity and thermodynamic growth processes related to high wind drag and accompanying heat transfer are the dominant processes in the winter. We also find that the shape of the region, specifically the location and orientation of the Antarctic Peninsula, plays a very important role in the ice interaction and advection processes such that the ice orients itself in a northeast to southwest direction in its advective pattern.

VP Truncated Model Monthly Integrations: February

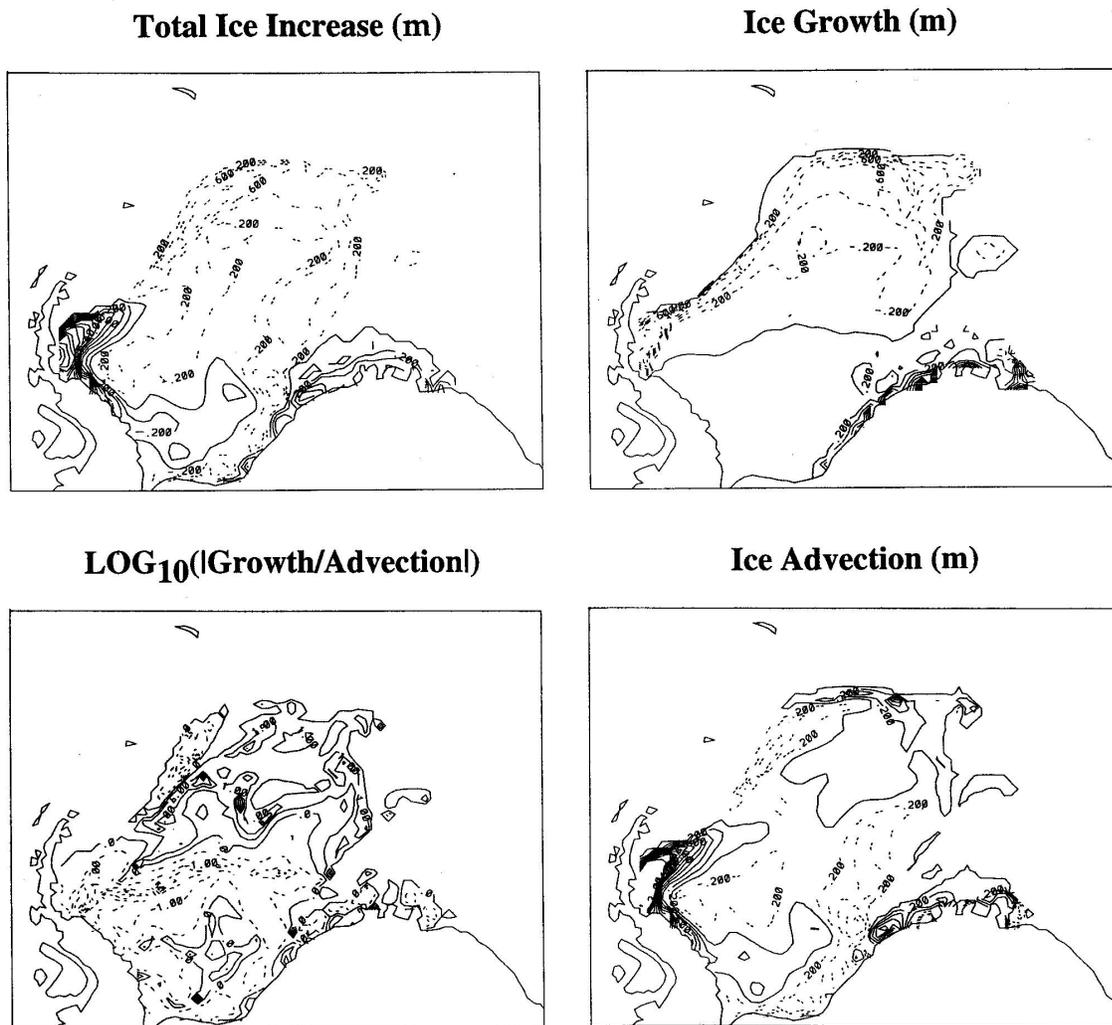


Figure 6.31: Monthly integrated regional distribution for February of ice thickness change, ice growth, ice advection and LOG_{10} of the ratio of growth to advection (see text for clarification).

VP Truncated Model Monthly Integrations: March

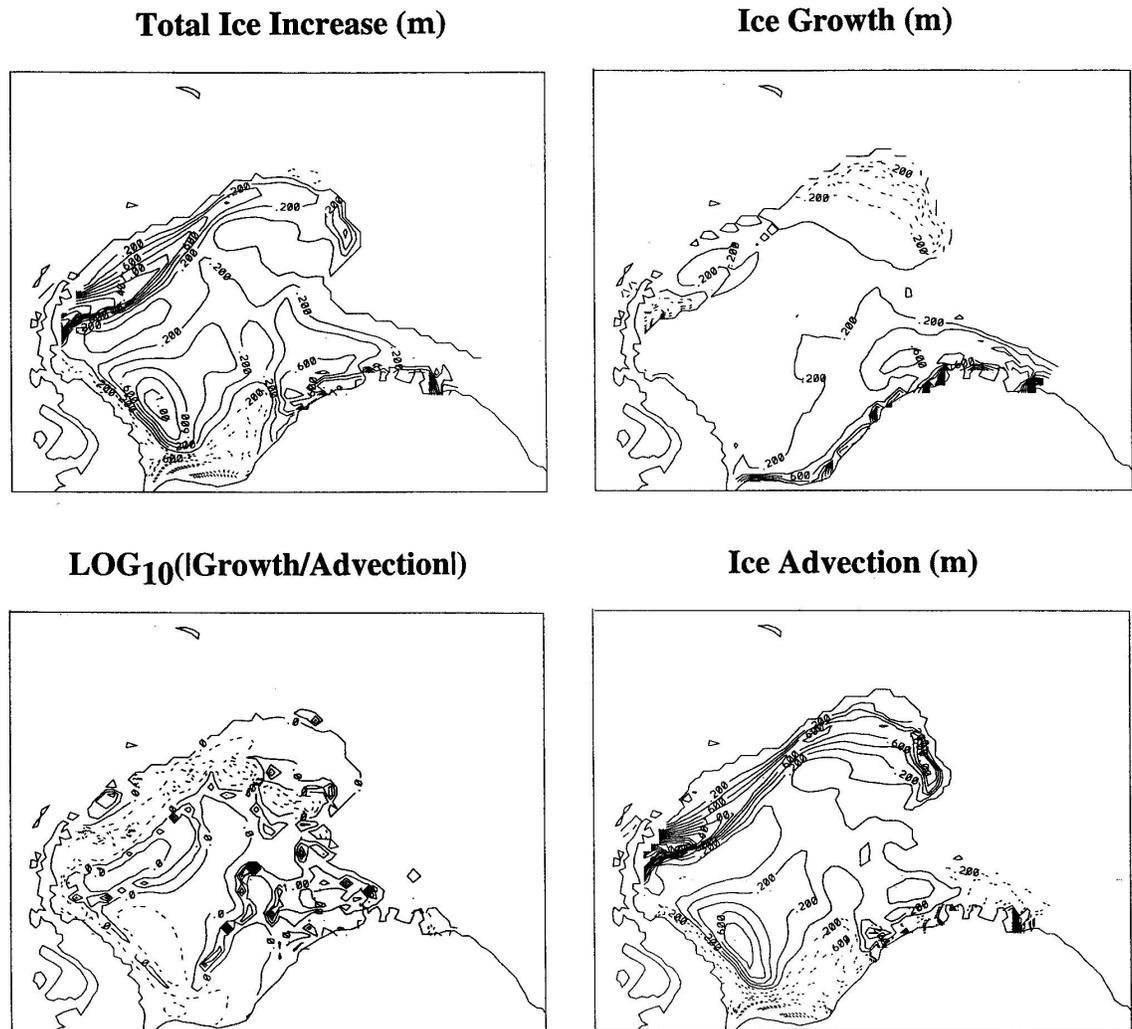


Figure 6.32: Monthly integrated regional distribution for March of ice thickness change, ice growth, ice advection and LOG_{10} of the ratio of growth to advection (see text for clarification).

VP Truncated Model Monthly Integrations: July

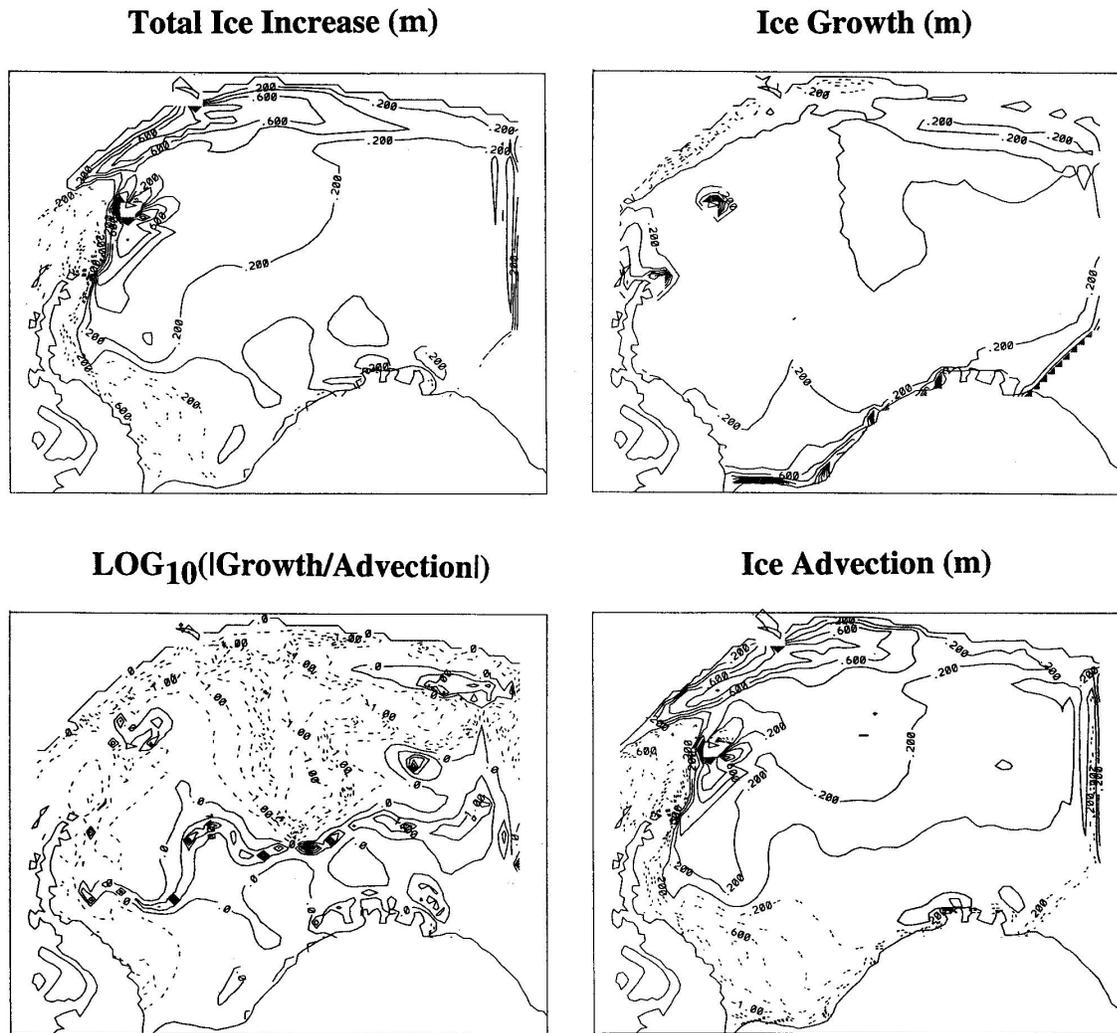


Figure 6.33: Monthly integrated regional distribution for July of ice thickness change, ice growth, ice advection and LOG_{10} of the ratio of growth to advection (see text for clarification).

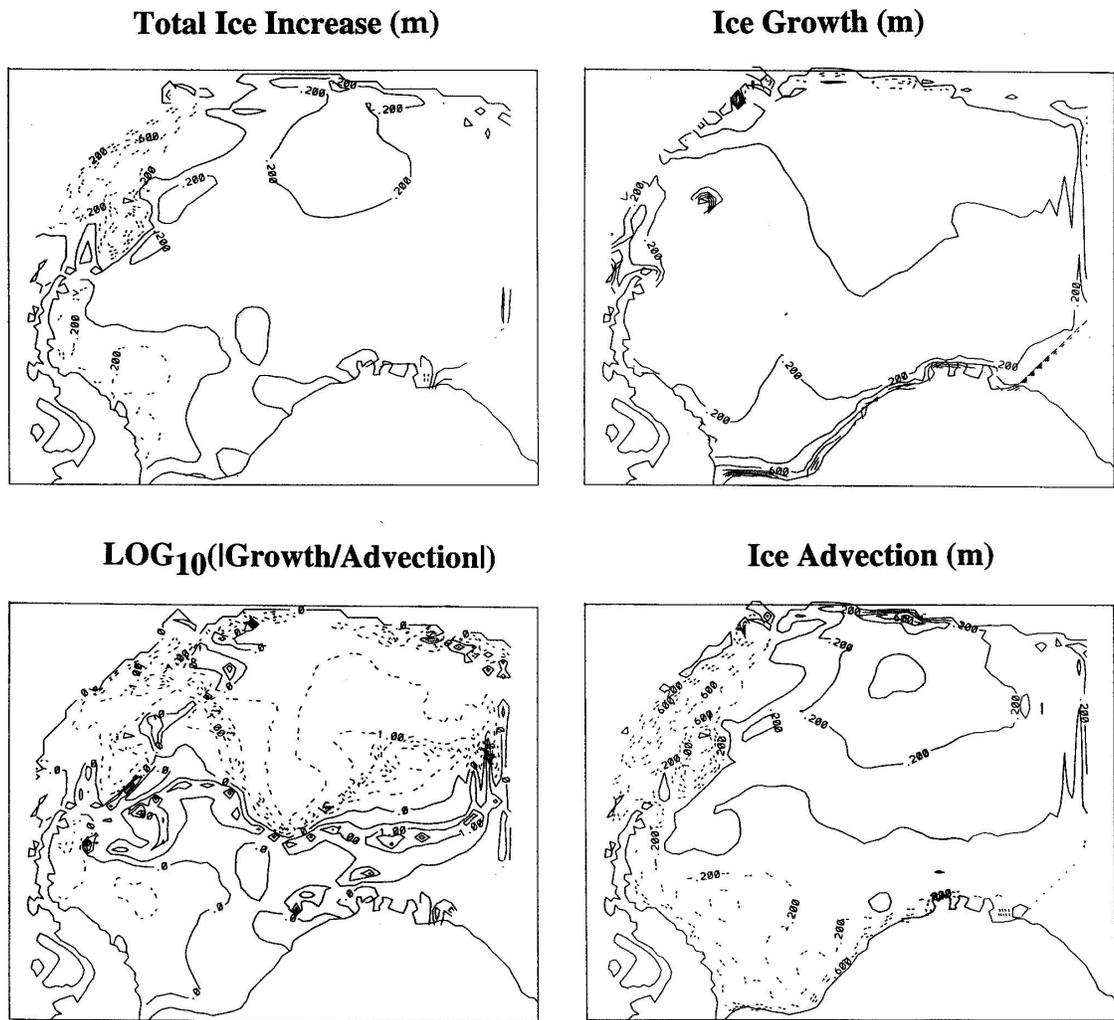
VP Truncated Model Monthly Integrations: August

Figure 6.34: Monthly integrated regional distribution for August of ice thickness change, ice growth, ice advection and LOG_{10} of the ratio of growth to advection (see text for clarification).

VP Truncated Model Monthly Integrations: September

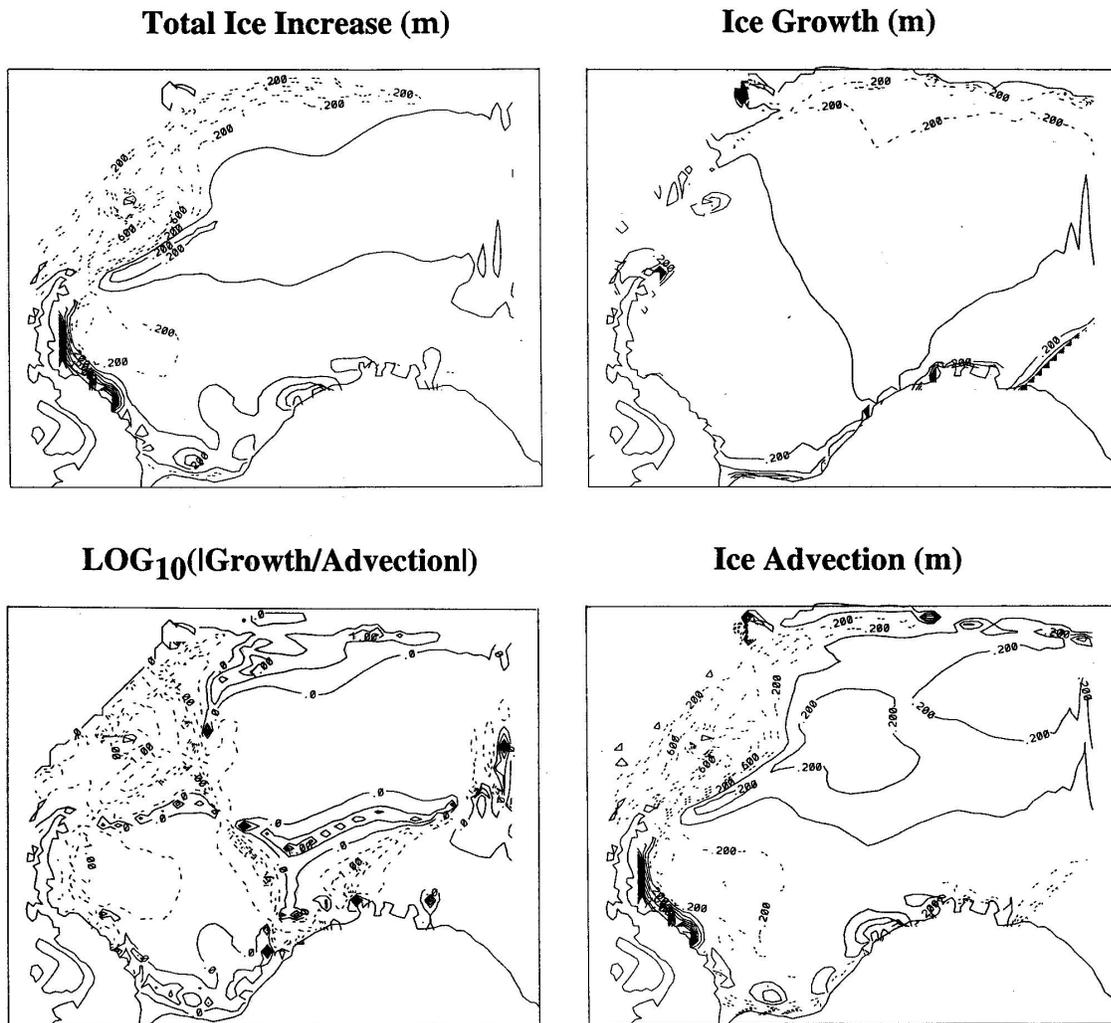


Figure 6.35: Monthly integrated regional distribution for September of ice thickness change, ice growth, ice advection and LOG_{10} of the ratio of growth to advection (see text for clarification).

6.3.4 Particle Case Study

So far we have examined the ice edge and field thickness distribution and computed a regional balance and distribution of growth and advective processes. As a final contribution, we look at local changes as seen by individual particles to assess how, at the case study level, different particles are exposed to these growth and advective processes. To do this, 12 locations were chosen from the model grid as shown in Figure (6.36). Since March is the starting time of the expansion phase of the ice, Julian day 91.0 was chosen as the start time to track these particles (in Figure 6.36 this location is the solid circle closest to the particle identification number). Trajectories of these particles (Figure 6.36) show that ice in the west and central part (particles 1-6) of the basin drifts northward from end of March to end of June or July. At this point the particles have drifted far enough north that the Antarctic Peninsula no longer provides a shielding against the circumpolar current. The particle trajectories change due to winds and currents of the circumpolar region to a northeasterly and then primarily easterly direction and eventually out of the model's field of view. Particles which start in more northerly and easterly parts of the basin (particles 8-12) are not shielded by the Antarctic Peninsula and are quickly dragged into the circumpolar current. In the southeast corner of the Weddell near the Maud Rise coast, westward flow of the gyre takes particles (e.g. particle 7) through a more meandering route either back through the Weddell Gyre (no particle in this case was able to make that journey) or gradually drift northward and eventually get caught up in the circumpolar current.

Additional information on the 4 particles closest to the ice edge (particles 1,2, 11, and 12) are shown in Figures (6.37) and (6.38). For each of these particles, local ice thickness, growth and an averaged local advection are compiled. Since the particles are sample drifters moving through an Eulerian grid, the advection is computed as a weighted average at the particle point relative to four nearest grid cell centers. This sampling method is chosen over the Lagrangian calculation because this particle study is meant for growth and advection sampling in different regions of the field. Looking first at trajectories of particles 1 and 2 (Figure 6.37), particle 2 sees little local advective activity (lowest panels in figure) compared to particle 1, which is the closer of the two to the ice edge. Additionally there is increased advective activity in the winter months near particle 1 and the now familiar increased thermodynamic melting of the summer months. The relatively smaller advection in particle 2 is also typical for particles 3,4,5,6 which are all located fairly deep in the pack ice. From this we find further evidence to support results in the regional balance of high advective activity near the ice edge.

Particles 11 and 12 were fortuitously placed so that they would pass through both open water and ice regions during their trajectory. From Figure (6.38) we see that particle 11 started in ice then moved into open water from about day 120 to 190, then back into the ice until it left the model region around day 210. Conversely particle 12 started in open water and was intercepted by the advancing ice edge around day 180 where it continued in the ice until it left the model region around day 230. In the case of particle 11, high advection of ice toward the particle followed by even higher melt rates results in its initial entry into open water during a period of advancing ice. At this point in time, atmospheric thermal conditions are hindering ice edge advance despite sufficient dynamic conditions to support ice advancement. Later in that season (days 180-210),

the same particle is subjected to conducive thermodynamic growth and advection of nearby ice. Although these processes are not as intense as during days 90-130, the ice remains because the dynamics and thermodynamics both work toward ice growth rather than against each other. In the case of particle 12, initial contact with the ice edge is seen during days 90 to 105 in the advection and growth panels (middle panels) but the amount of ice advecting toward the particle is met with conditions too warm to sustain it and so the ice melts before it can establish itself and advance further. Later in the season, however, a fluctuating period of melt and growth with advection both converging towards and diverging from the particle resolves itself to a net positive growth such that ice survives. This second case again illustrates how both dynamic and thermodynamic processes must be conducive to ice growth at the ice edge for advance to take place, at least for numerical models.

From these 4 particle case studies, we find that except for the summer melt back, much of the advancing activity happens close to the ice edge with the highest advection values and greatest melting rates occurring there. Additionally we see from particles 11 and 12 that the advance of ice in these models is heavily dependent on a sufficient positive feedback and coupling between ice advecting into open water regions and sustainable thermodynamic conditions. In field studies, the ice edge is expanding due to rapid growth of ice through frazil and pancake growth which occurs at a sub-grid scale relative to these models. The question that arises then is, are the growth-advective responses seen in these geophysical scale models consistent with the observed ice edge sub-grid scale processes of frazil and pancake cycle growth? Furthermore, how can next generation models be parametrized in order to validate this multi-scalar response at the ice edge.

Trajectories using VP Truncated Model

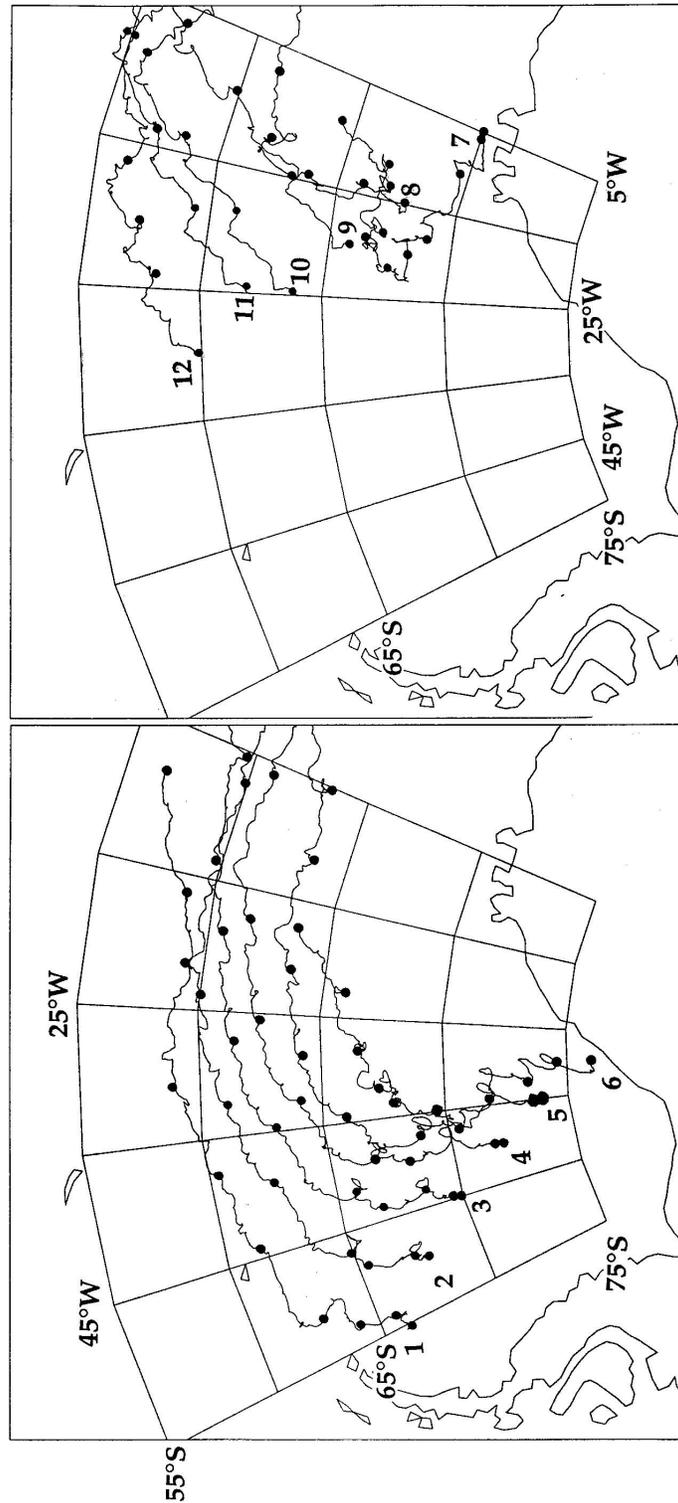


Figure 6.36: The 12 particle positions are prescribed and initialized at day 90.0 The start point is located closest to the reference number for each particle and the solid dots mark the end of each month starting with the end of March at day 91.

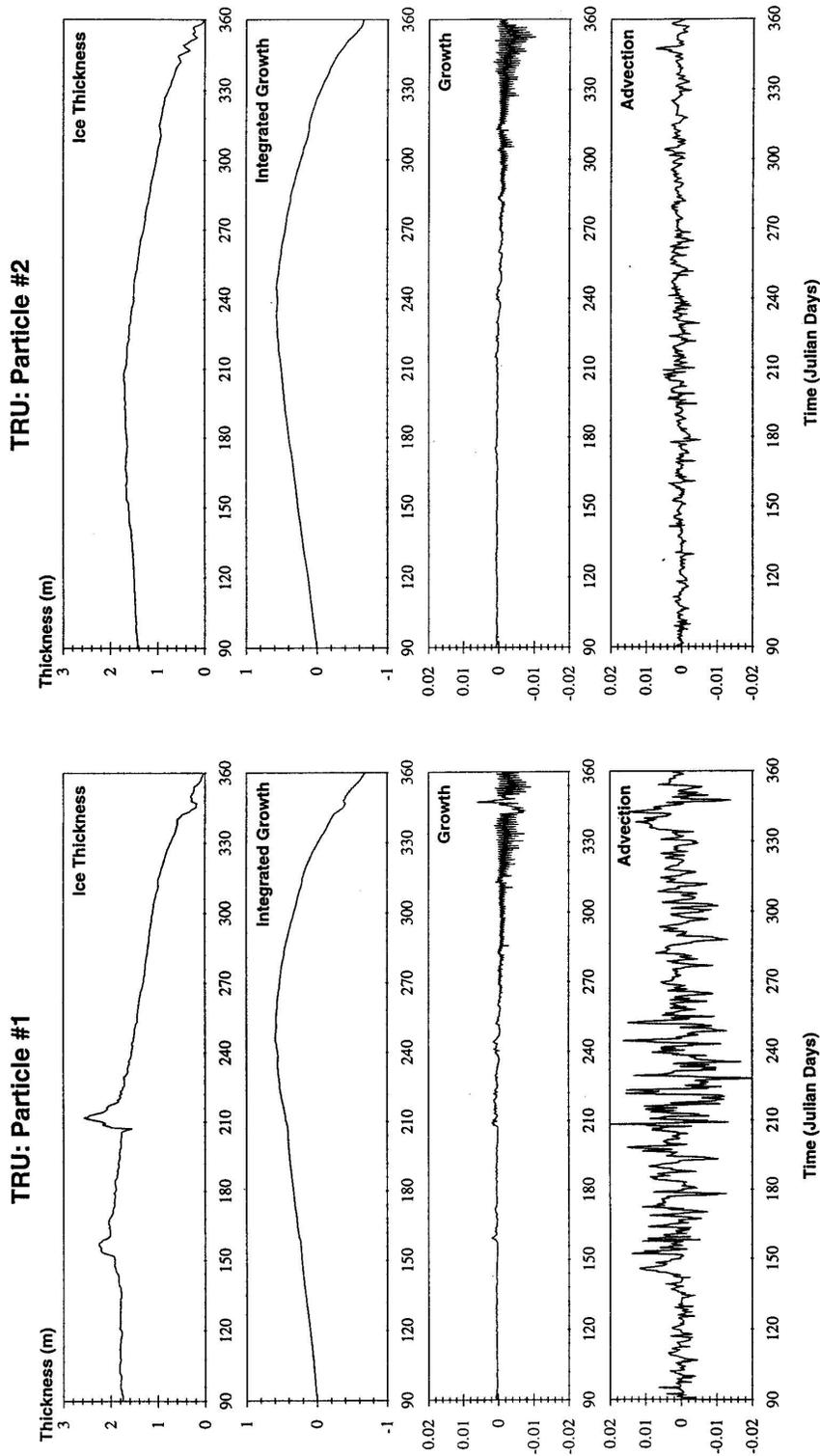


Figure 6.37: Mass balance information for VP with truncated ellipse model (TRU) along the trajectories of particles 1 and 2 shown in Figure (6.36).

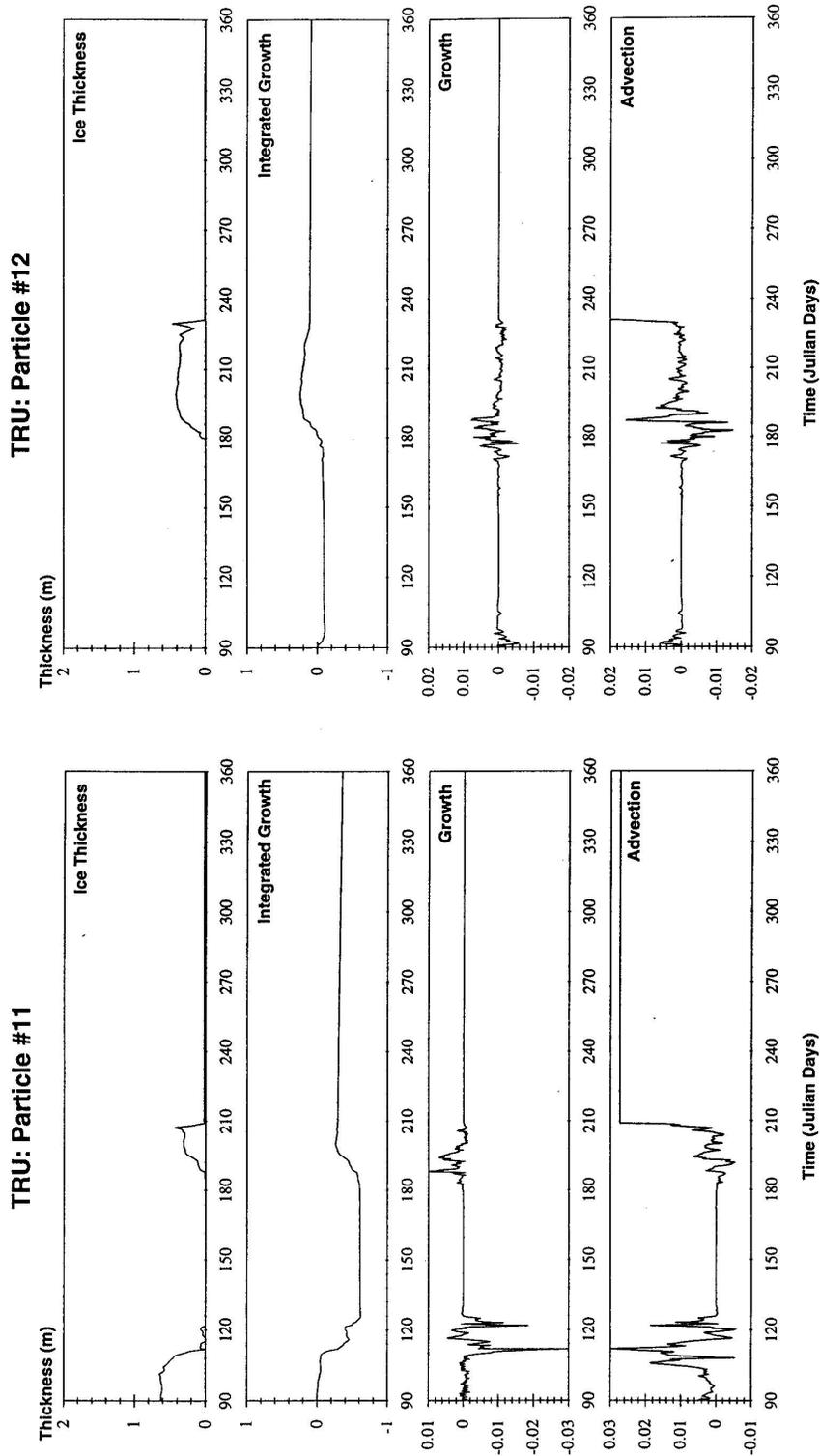


Figure 6.38: Mass balance information for VP with truncated ellipse model (TRU) along the trajectories of particles 11 and 12 shown in Figure (6.36).

6.3.5 Summary of Simulated Results

In summarizing this section, we found first that ice interaction is very important for realistic modeling of the annual cycle and that this point becomes increasingly more critical as the resolution in models increases. Second, from a modeling perspective the processes of growth and advection are such that daily/sub-daily thermodynamic melt dominates the summer decay while advection and wind drag related sensible/latent heat losses dominate the winter expansion in the interior of the pack and close to the ice edge. The processes at the ice edge which evolve using these models are consistent with those observed in nature. However, the responses in the large scale models need to be validated against the sub-grid scale physical processes of frazil and pancake growth to ensure a proper link between these two scales. Finally, the processes of drift and deformation in general seem to be evolving in a manner consistent with observations both in terms of choice of a pressure and shear resistant ice rheology and in terms of producing results which resemble the annual expansion and decay cycle of the ice in the Weddell Sea.

6.4 Buoy Comparison

The viscous-plastic (VP) and cavitating fluid (CAV) ice models were designed to simulate internal ice pack dynamics and thermodynamics using conservation laws and constitutive relations to relate ice response to imposed forces. Traditionally comparison of observed ice edge location with model results has served as one of the standard checks for validating these models, primarily because ice edge location is widely available. But, as we saw in the first three sections of this chapter, ice edge location is not very sensitive in these models compared to ice thickness distribution and compactness. Additionally from the second section, we found that spatial contours of ice thickness are not a good parameter to examine sensitivity to internal ice variables primarily for 2 reasons. Firstly, there is a lack of regionally observed thickness distribution and secondly, for many of the internal ice parameters, differences in ice thickness between models were not very pronounced. The end result is that a better way to examine responses of the internal ice interaction is needed.

Since the foundation of ice models is the constitutive relation, a more rigorous examination of internal ice interaction must include direct examination of drift and deformation observations. In this study, we accomplish this using the geographical positions from the observed ISW buoys. The ISW positions are located within the model grid every three hours between Julian days 63 and 150. At these locations, velocities are extracted from the model's Cartesian grid and transformed spatially and with respect to vector orientation of the ISW observed array. These velocities, together with the observed positions, are subjected to the same deformation analysis described in Chapter 3. In addition, cross-spectral density function, cross-correlation, probability density distribution, and chi-square (χ^2) analyses are used to make a statistical comparison of drift and deformation responses between the models and the observations. These methods compare buoy drift in the frequency domain, the time domain, and with respect to distribution categories including principal axis space, scatter plots and probability distribution functions. An overview of each statistical function is provided in Appendix (B)

with additional information found, for example, in Bendat and Piersol (1971) and Hines and Montgomery (1990).

As alluded to at the outset of this chapter, the end result of this study will not unveil the ideal rheology that will allow us to correctly reproduce all the ice interaction features seen in the observations. On the contrary, it will show how many different aspects of the modeled ice interaction we (ice research community as a whole) need to examine in greater detail. This is an important contribution however, because VP with concentric ellipse closure and CAV are currently the most widely used ice rheologies in the sea ice, ocean and climate research communities. They are constantly being modified, updated and tuned to fit each new study region. The information gained through this section can be used in future research efforts so that the next generation of these models can be equipped to handle more of the observed physical processes and thus predict sea ice response more realistically. It is important to keep these points in mind when examining the case studies in this section.

6.4.1 Comparison in the Frequency Domain

To get an overview of the different models, results in the frequency domain are examined using power spectra from observations and three basic model types: no rheology using free drift (FD), pressure resistance using cavitating fluid rheology (CAV), and pressure plus shear resistance using the viscous plastic (VP) rheology with truncated ellipse closure scheme (TRU). Comparing each of the three total velocity and strain-rate power spectra with those observed, we see in Figures (6.39)-(6.41) that the models exhibit a fairly smooth red-shift signal in the model drift and deformation spectra as opposed to the tidal-peaked signals in the observed (OBS) velocity and jagged unsloped spectra of OBS deformation. These general trends in all the models show a lack of daily and sub daily (high frequency) activity despite the presence of an inertial term in the model's momentum balance and subdaily forcing.

The primary reason for this lies in the construction of the boundary layer in the current model types which damp subdaily oscillation activity in the ice. The primary source of this damping is the fact that the boundary layer formulation is set up to transfer energy between the air and ocean through the Ekman formulation, and then ice is embedded into this (Hibler, personal communication). Correcting this requires a new boundary layer formulation which includes ice embedded in the boundary layer before computing the energy transfer processes between air and water. This type of correction is currently being considered as a new research topic.

Two examples of some of that research are as follows. In Figure (6.43), we see results from an experimental run where the density has been amplified by a factor of 30 to enhance the inertial force. In doing this, we see from the Figure that a small peak does occur at the 2 cycles/day frequency at all the stations. The overall energy in the system is also reduced by a factor of 10 compared to the standard run (Figure 6.41) because of the increased density which slows all the other processes down. While this preliminary experiment is merely a numerical trick, it confirms the presence of inertial oscillations in the ice models. With a reformulation of the boundary layer, an inertial peak should also appear as an undamped sub-daily process in the model in a manner coherent with

nature.

The second example is an experiment to separate tidal and inertial signals via rotary spectra (see Appendix A.2.1 for a description of rotary spectra). Preliminary results of this method are shown in Figures (6.44 and 6.45) for the left and right turning rotational frequencies of the observed buoy data. Inertial oscillations can only turn to the left in the southern hemisphere so they can only be present in Figure (6.44). As seen in this Figure versus the right turning case (Figure 6.45), the spectral peak around 2 cycles per day is broader at most of the sites for left turning than right turning spectra and in the 128 bin case there does appear to be more peaks in the left direction than in the right. The inertial period is close to that of the M2 and S2 tides for this region, so longer time records than 3 months are needed to look at these small frequency differences with confidence. Use of this method together with year long simulations, for example, may allow us to develop a method to separate the inertial from the tidal signal and hence understand the coupling of these two processes better. A tidal ice model is needed in order to achieve this however, and this requires that the first problem of a properly constructed boundary layer be resolved. While these two examples are only preliminary, they do provide a direction for including some of these important sub-daily processes into the models.

Because of the difficulties just mentioned above in modeling the sub-daily features in the ice, the remainder of this section focuses on the low frequency signals present. From the power spectra, we see that there is some similarity in the frequency signatures smaller than 1 cycle per day, particularly in the velocity spectra which show a peak cross-spectral correlation between 0.8 to 0.9 in the range of D.C. to 0.2 cycles/day in all the models. This strong correlation corresponds to such processes as the 5 day storm cycles that move through the area and which are included in the ECMWF analysis fields used to drive the model. It is these low frequency correlations that we will examine in this section by considering outputs from observations (OBS) and the models after exposure to a 30 hour LPF to remove the daily and subdaily oscillations.

The spectrum in the lower frequencies for free drift (FD) velocity reaches a maximum cross-spectra value between D.C. and 0.2 cycles/day of about 0.8, while CAV and TRU (VP rheology with truncated ellipse closure scheme) models successively improve from this to almost 0.9. The total strain-rate power is far less encouraging with a maximum value of 0.2 at 0.4 cycles/day for FD and similarly for CAV. Only TRU shows some positive results at low frequencies for deformation with a maximum correlation of 0.4 in the lowest frequencies. Closer examination of the two major invariants of the strain-rate, divergence and maximum shear for the TRU case (Figure 6.42), shows a much higher correlation between TRU and OBS for invariant shear (about 0.5 at the D.C.) versus divergence which does not exceed 0.2. In the two remaining evaluations (time domain and category domain) we will evaluate these correlations more closely in order to understand how and why the different codes correlate as such.

Spectral Plots of FD vs. Observation

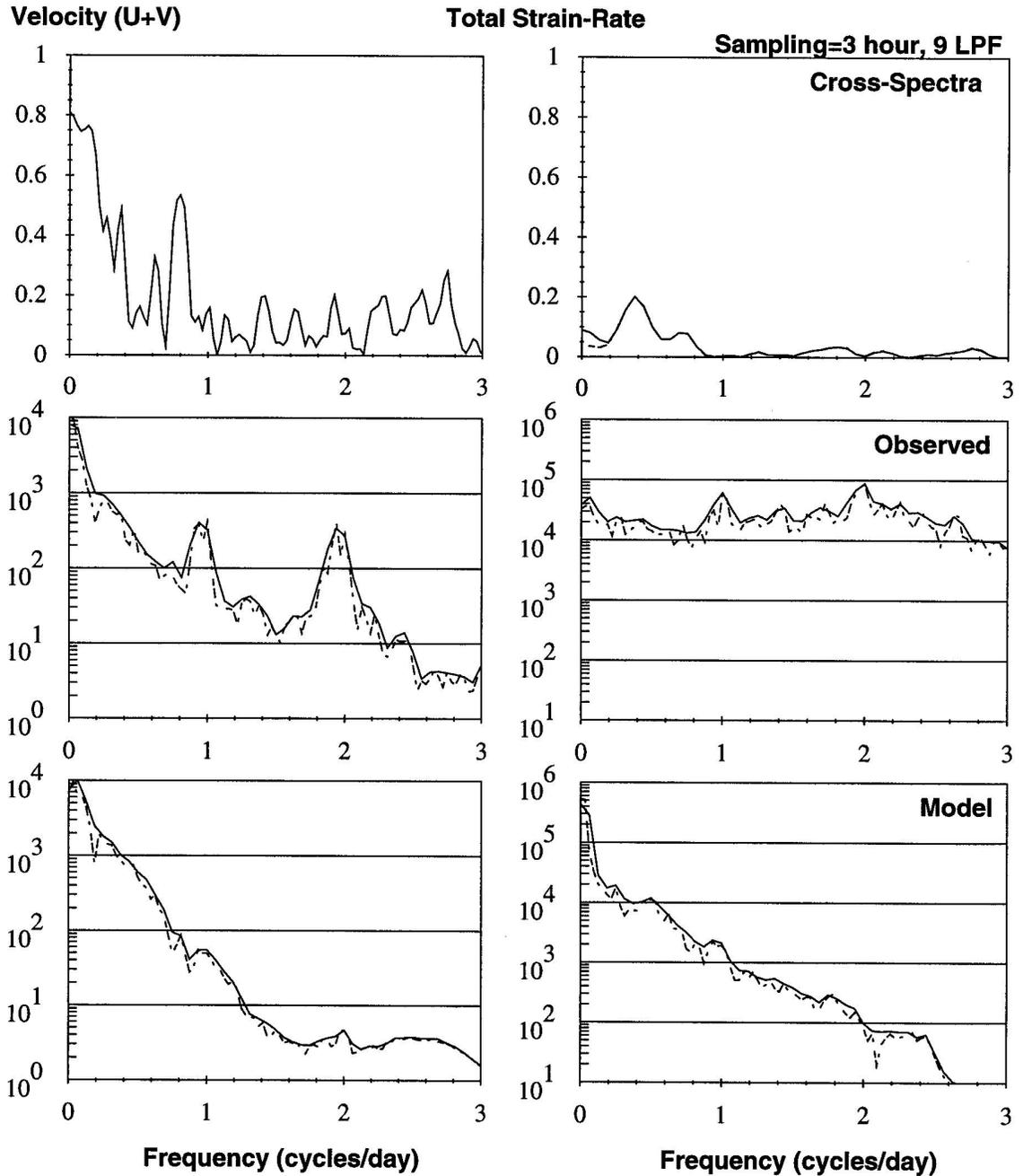


Figure 6.39: Power density of velocity and total strain-rate ($\dot{\epsilon}_{ij}^2$) from Free Drift (FD) Model versus Observed resolved to 64 (solid) and 128 (dashed) frequency bins. Power spectral density of velocity in units of $\frac{[m/s]^2}{\Delta f}$ and strain-rate in units of $\frac{\times 10^{-6}(1/S)^2}{\Delta f}$. Cross-spectra are normalized as described in Appendix (B).

Spectral Plots of CAV vs. Observation

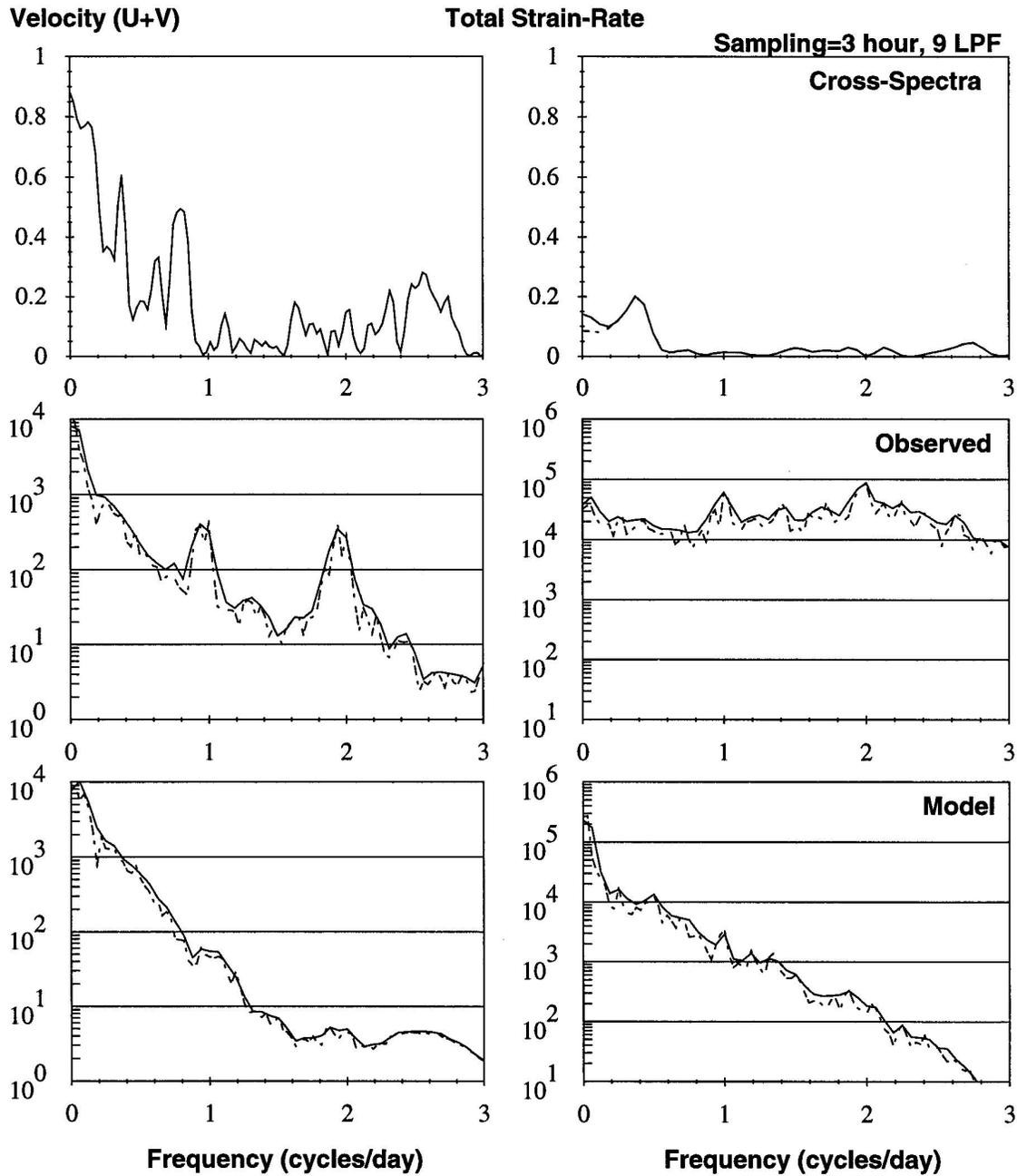


Figure 6.40: Power density of velocity and total strain-rate from Cavitating Fluid (CAV) Model versus Observed resolved to 64 (solid) and 128 (dashed) frequency bins. Power spectral density of velocity in units of $\frac{[m/s]^2}{\Delta f}$ and strain-rate in units of $\frac{\times 10^{-6}(1/s)^2}{\Delta f}$. Cross-spectra are normalized as described in Appendix (B).

Spectral Plots of Tru vs. Observation

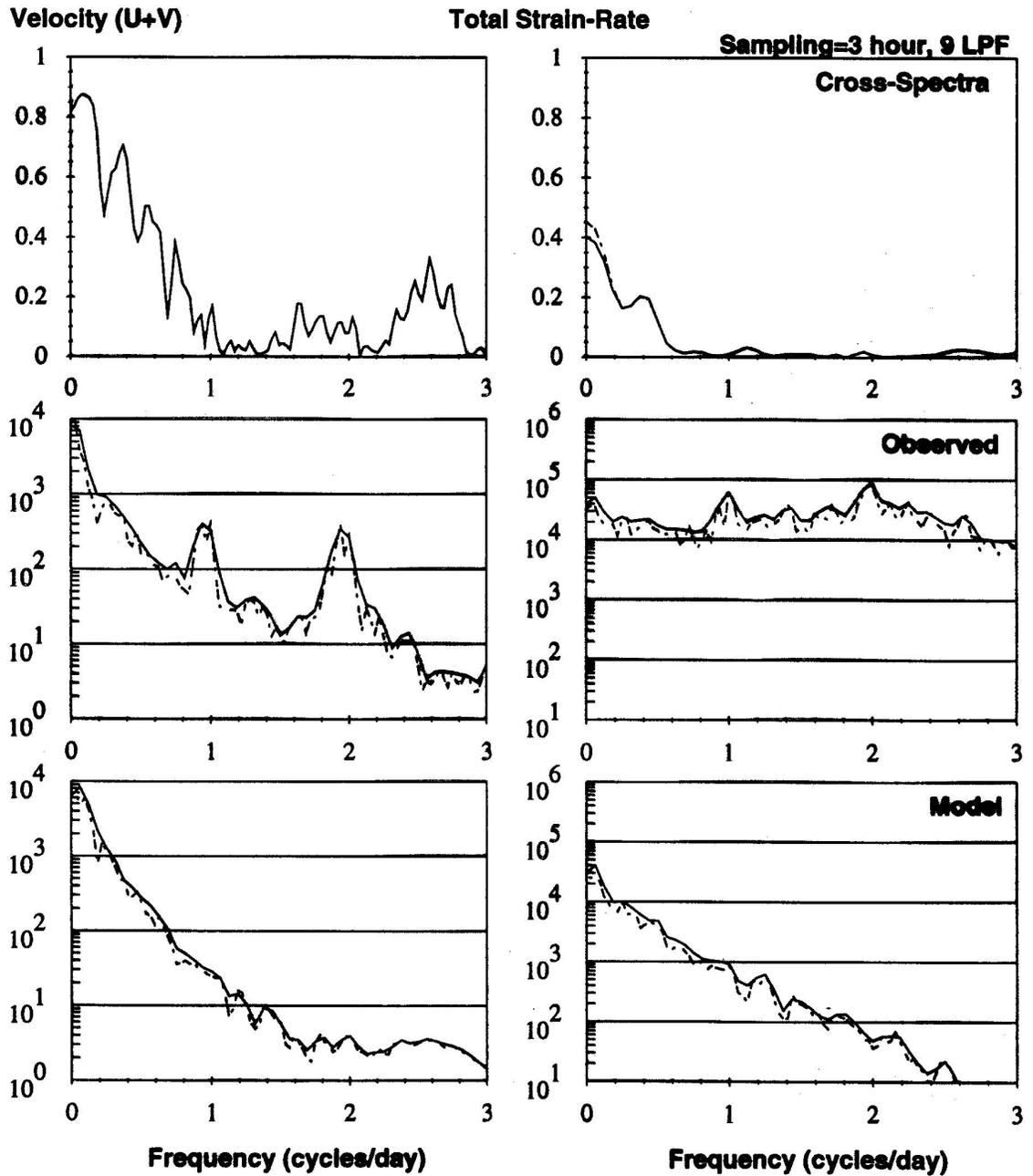


Figure 6.41: Power density of velocity and total strain-rate from VP with Truncated Ellipse (TRU) Model versus Observed resolved to 64 (solid) and 128 (dashed) frequency bins. Power spectral density of velocity in units of $\frac{[m/s]^2}{\Delta f}$ and strain-rate in units of $\frac{\times 10^{-6}(1/S)^2}{\Delta f}$. Cross-spectra are normalized as described in Appendix (B).

Spectral Plots of Tru vs. Observation

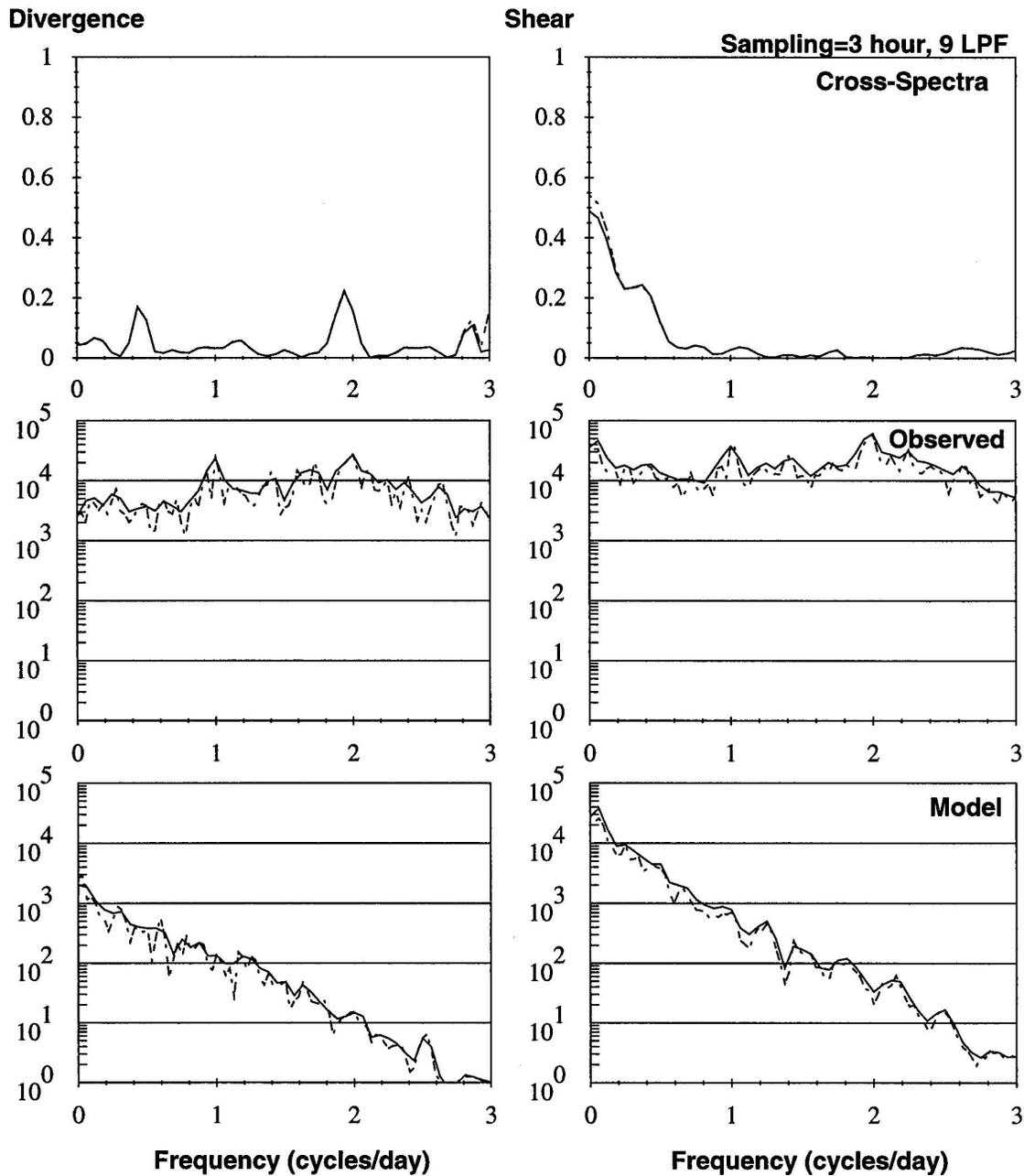


Figure 6.42: Power density of divergence and shear strain-rates from VP with Truncated Ellipse (TRU) Model versus Observed resolved to 64 (solid) and 128 (dashed) frequency bins. Power spectral density of strain-rate in units of $\frac{\times 10^{-6}(1/S)^2}{\Delta f}$. Cross-spectra are normalized as described in Appendix (B).

Spectra of Zero Dimensional Test Model

Normalized Power Density (U+V)

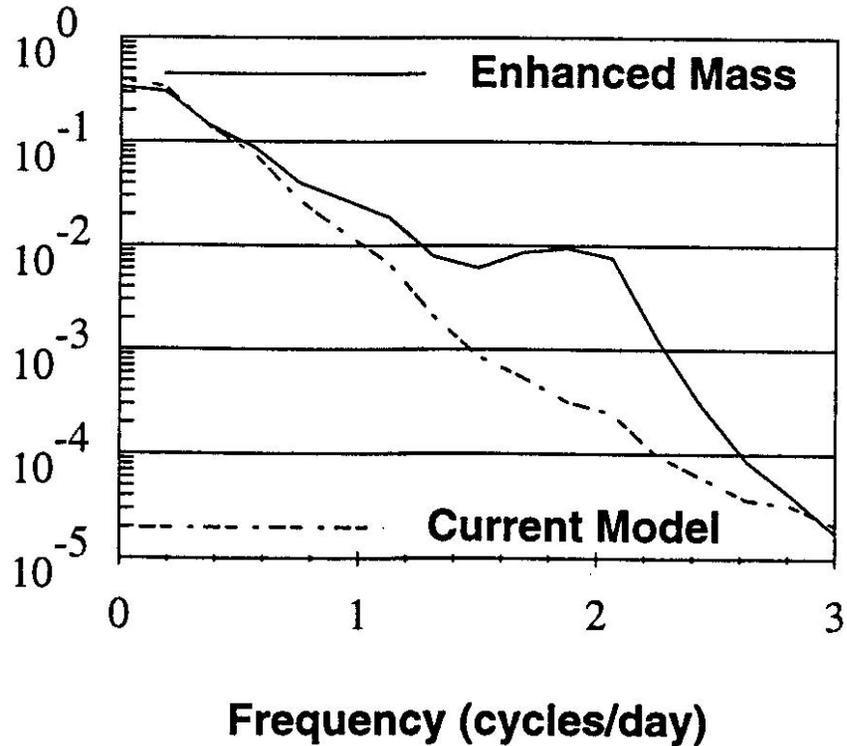


Figure 6.43: Power density for the zero dimensional experimental case of TRU both without and with an increased density ($30 \times \rho_{ice}$) to magnify inertial oscillation signal. Velocity in units of $\frac{[m/s]^2}{\Delta f}$.

Rotary Spectra of Buoy Data

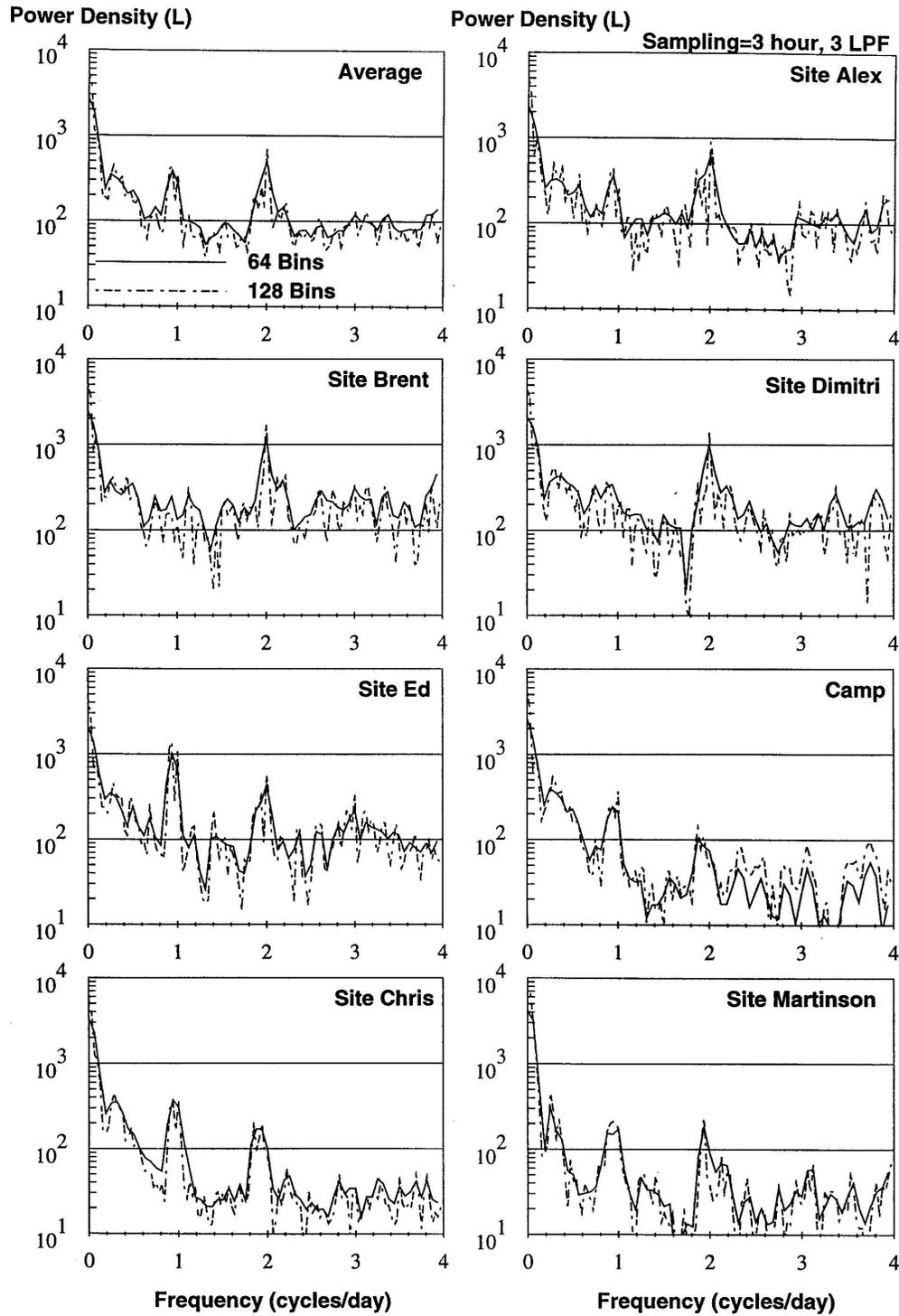


Figure 6.44: Power density at each of the observed buoy sites of left rotary velocity (L). Velocity in units of $\frac{[m/s]^2}{\Delta f}$. See text for details.

Rotary Spectra of Buoy Data

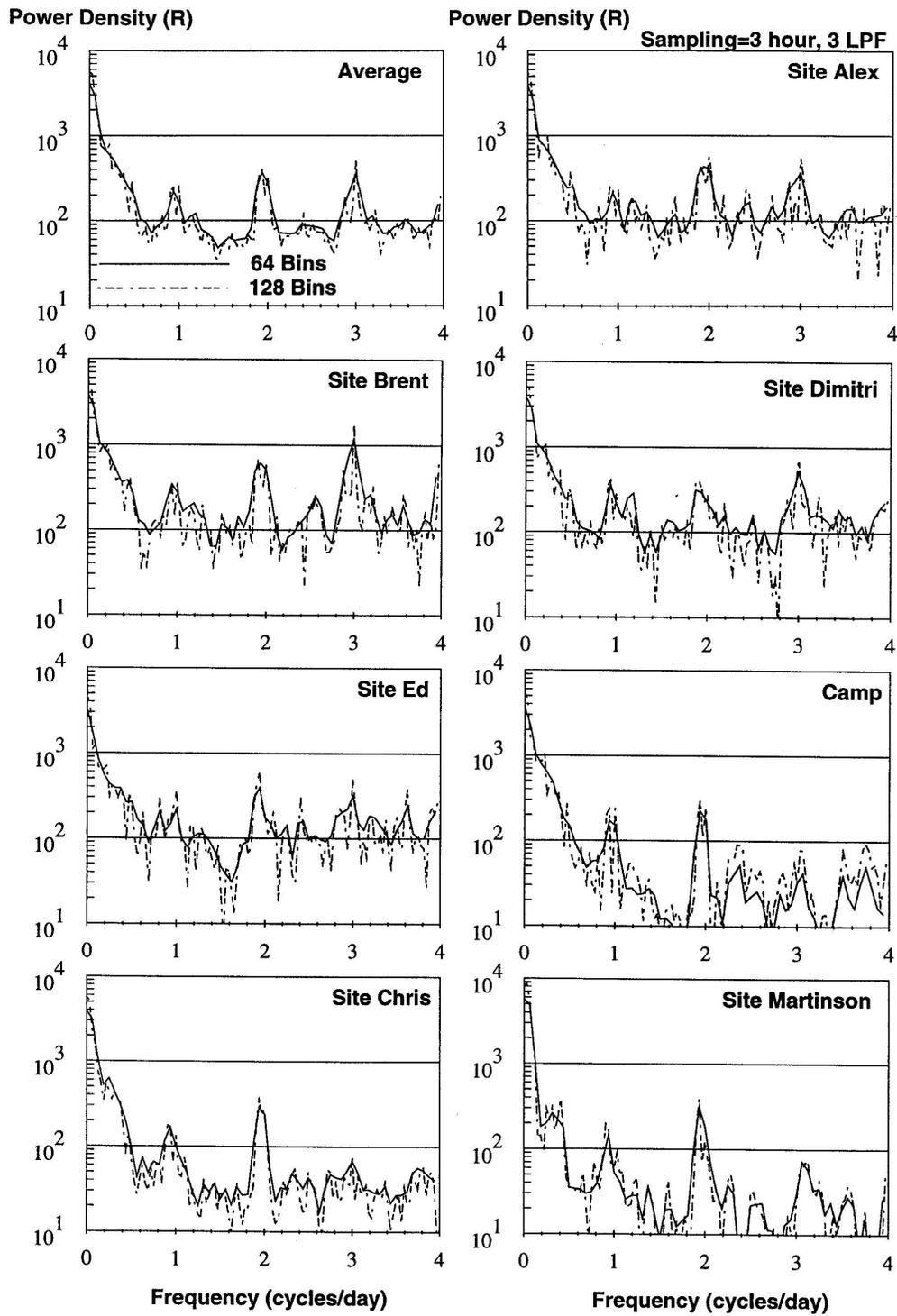


Figure 6.45: Power density at each observed buoy site of right rotary velocity (R). Velocity in units of $\frac{[m/s]^2}{\Delta f}$. See text for details.

6.4.2 Comparison in the Time Domain

Time series plots of velocity and deformation components for each of the three model types are shown in Figures (6.46)-(6.51). These figures contain the same information at the same scale as the 30 hour LPF observed data shown in Figures (3.12) and (3.15) in Chapter 3. Looking first at the output of the multiple linear regression analysis terms (velocity and deformation components) in the observed case (Figure 3.12) versus model results (Figures 6.46, 6.48, and 6.50), we see high correspondence in the velocity time series, particularly for the v velocity with specific high velocity events (peaks and valleys on the plot) coinciding in time very closely between models and observations. The deformation components have a similar range of deformation values but it does a poor job at matching specific time episodes (although there are some). The zero mean in deformation components seen in OBS is reproduced in TRU but not in the FD and CAV cases which exhibit a number of strong very low frequency signals from 5 to 60 day periods which were not seen in the observations.

Combining regression velocity and strain-rate components, we can identify terms like velocity magnitude, DKPs and maximum shear which describe specific drift and deformation processes as predicted by the models. Comparing these derived terms in the observations (Figure 3.15) with those in Figures (6.47), (6.49), and (6.51) we see that the divergence rates compare poorly in all three model types either in terms of magnitude (as with TRU) or because of very low frequency oscillations (ca. 60 day period) seen in FD and CAV. FD in particular (Figure 6.47) experiences a strong convergence (ca. $1 \times 10^{-6}(1/s)$ or $\approx 10\%$ per day) from about day 90 to 120. This is a behavior not seen in the observations which relates to the piling up of ice along the coast in the FD model. CAV is not as extreme as FD in the divergence but large low frequency oscillations in the shear components of normal (ND) and shear (SD) deformation are comparable to FD. TRU appears devoid of such low frequency events, suggesting that both pressure and shear resistance inhibit the development of low frequency (60 day period) oscillations. Of all the deformation components, maximum shear comes closest to reproducing the observed time series information. Although it is missing specific higher frequency events (0.2 to 1 cycle/day), the general time evolution of maximum shear for TRU is remarkably similar to that observed, hence the correlation of 0.6 on the cross-spectral analysis in Figure (6.42).

Multiplying velocity vectors by the time interval between each result (in this study 3 hours), we can compute local displacements resulting from the velocity field. Using the first ($t = 1$) observed position as an initial reference, these displacement vectors can be connected head to tail on a geographic projection to generate a trajectory of the buoys. This method of comparing trajectories works well because the positions that the modeled velocities are extracted from are those of the observed, while the velocities and their resultant displacements are those determined by the model at that location. In oceanography this method is called progressive vector plotting. Generating progressive vector plots for the observed (OBS), FD, CAV, VP truncated ellipse (TRU) and TRU with modified drag (DRAG) cases, we see how the spatial drift of the ice field changes with time. Comparing observations to FD (Figure 6.52), we see that FD drifts faster northward in the west than east as seen in the observed, but the drift pattern is distorted especially at the 4 eastern sites. This distortion produces the poor deformation outcome

seen in the time series plots. CAV compares somewhat better than FD to the observed with the 2 western buoys drifting more similar to that seen in the observed than for any other case shown in this comparison. The 4 eastern sites, however, are still poorly reproduced.

TRU¹ versus the observed in Figure (6.53) shows many of the short term features in the observations and a trajectory which is overall the closest of the three rheologies. However, particulars of the drift are distorted, specifically the intermittent drift perturbations (wiggles in the observed 30 hr LPF drift) and the observed strong west to east shear in the net northward drift which is reversed in the TRU model. In an attempt to see if the drag coefficient might be responsible for the stronger northward flow in the west, the drag coefficients were modified according to Lemke and Fischer (1994) to include a reduced ocean drag ($C_w^* = 0.0030$ down from $C_w^* = 0.0055$ kg/m²s) and increased wind drag ($C_a^* = 0.0015$ up from $C_a^* = 0.0012$ kg/m²s). Unfortunately this leads to an overall northward flow which greatly exceeds observed and proportionally increases the east to west shear with the eastern buoys still moving too fast northward relative to the western buoys.

Overall assessment using progressive vector plots shows that none of these models properly reproduces all the features observed, but CAV best reproduces the general western intensification flow seen in the observations while VP (due to inclusion of shear) spatially drifts similar to the observed except for the western intensification. This is occurring despite the fact that a simple western intensification ocean current is added in the models as prescribed by the observations (see Chapter 4 for complete description).

¹CON (concentric ellipse closure) and REP (replacement method) nearly identical to TRU (truncated ellipse closure) in progressive vector plots.

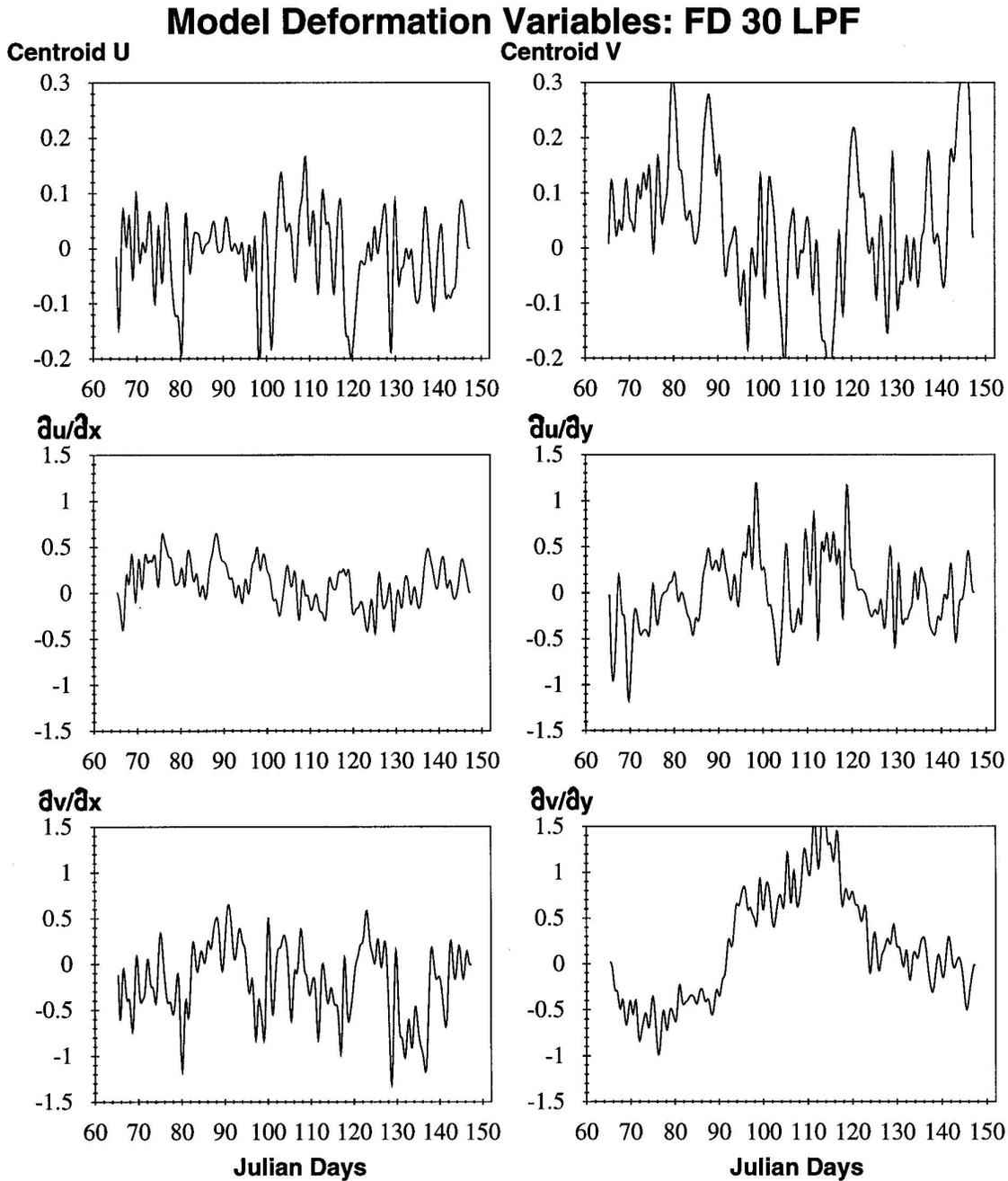


Figure 6.46: Beta parameters from regression analysis on Free Drift (FD) model output subjected to 30 hour LPF. Velocities are in units of [m/s] and strain-rate components are in units of [$\times 10^{-6}$ (1/s)].

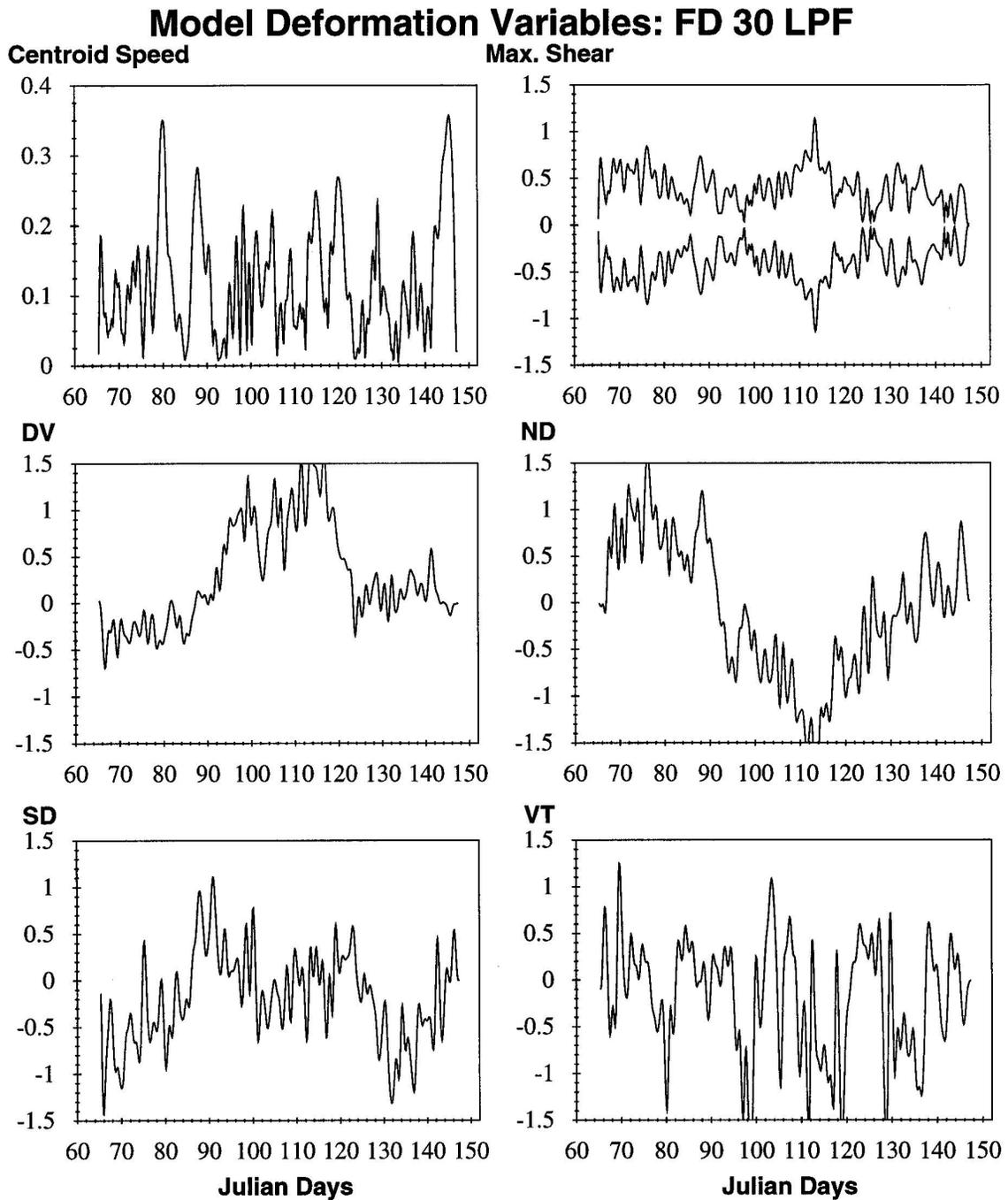


Figure 6.47: Centroid Speed, Max Shear and DKPs of Free Drift (FD) model computed from multiple linear regression analysis using 30 hour low pass filter (LPF). Velocities in units of [m/s] and Max Shear, DKPs in units of [$\times 10^{-6}$ (1/s)].

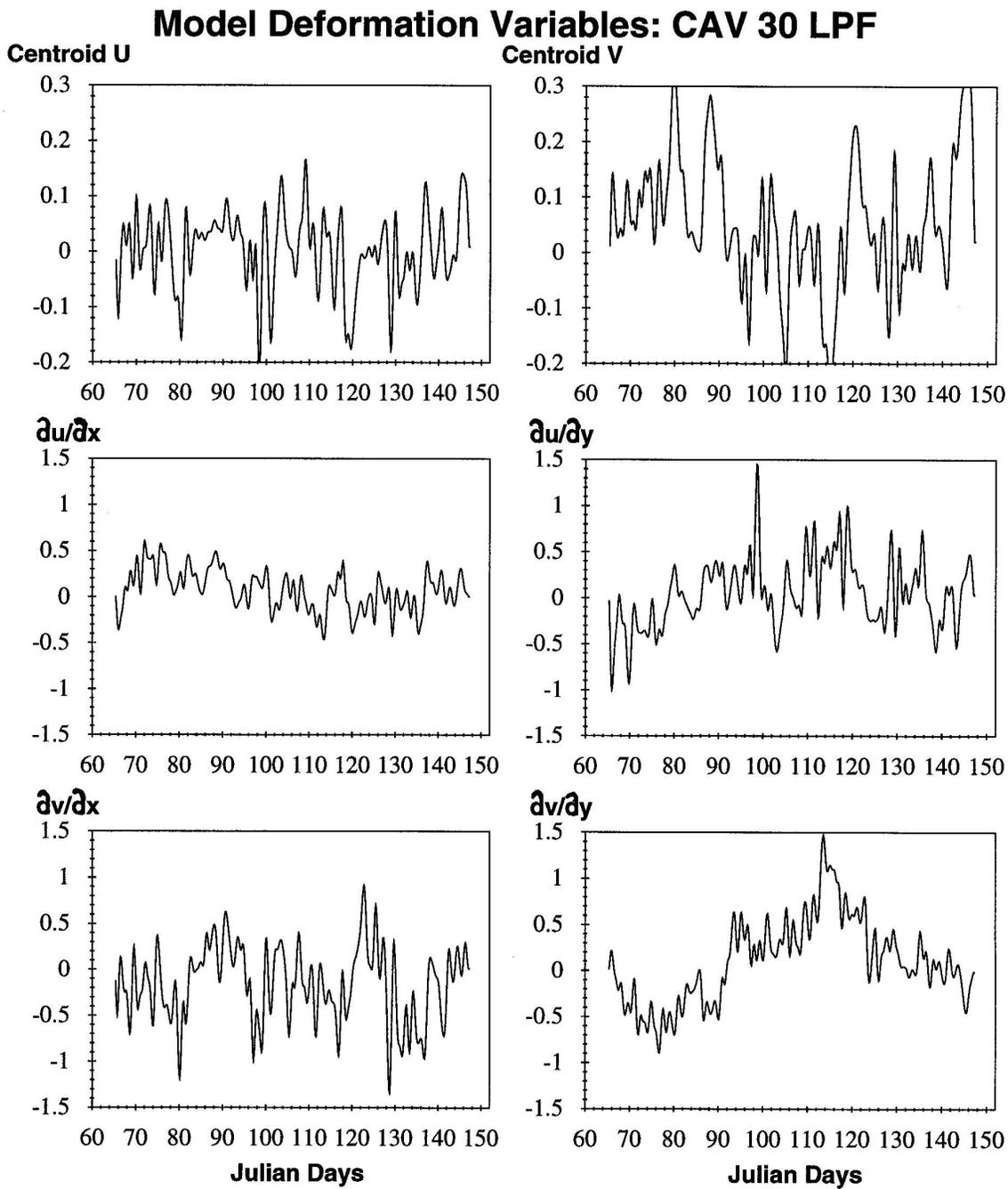


Figure 6.48: Beta parameters from regression analysis on Cavitating Fluid Rheology (CAV) model output subjected to 30 hour LPF. Velocities are in units of [m/s] and strain-rate components are in units of [$\times 10^{-6}$ (1/s)].

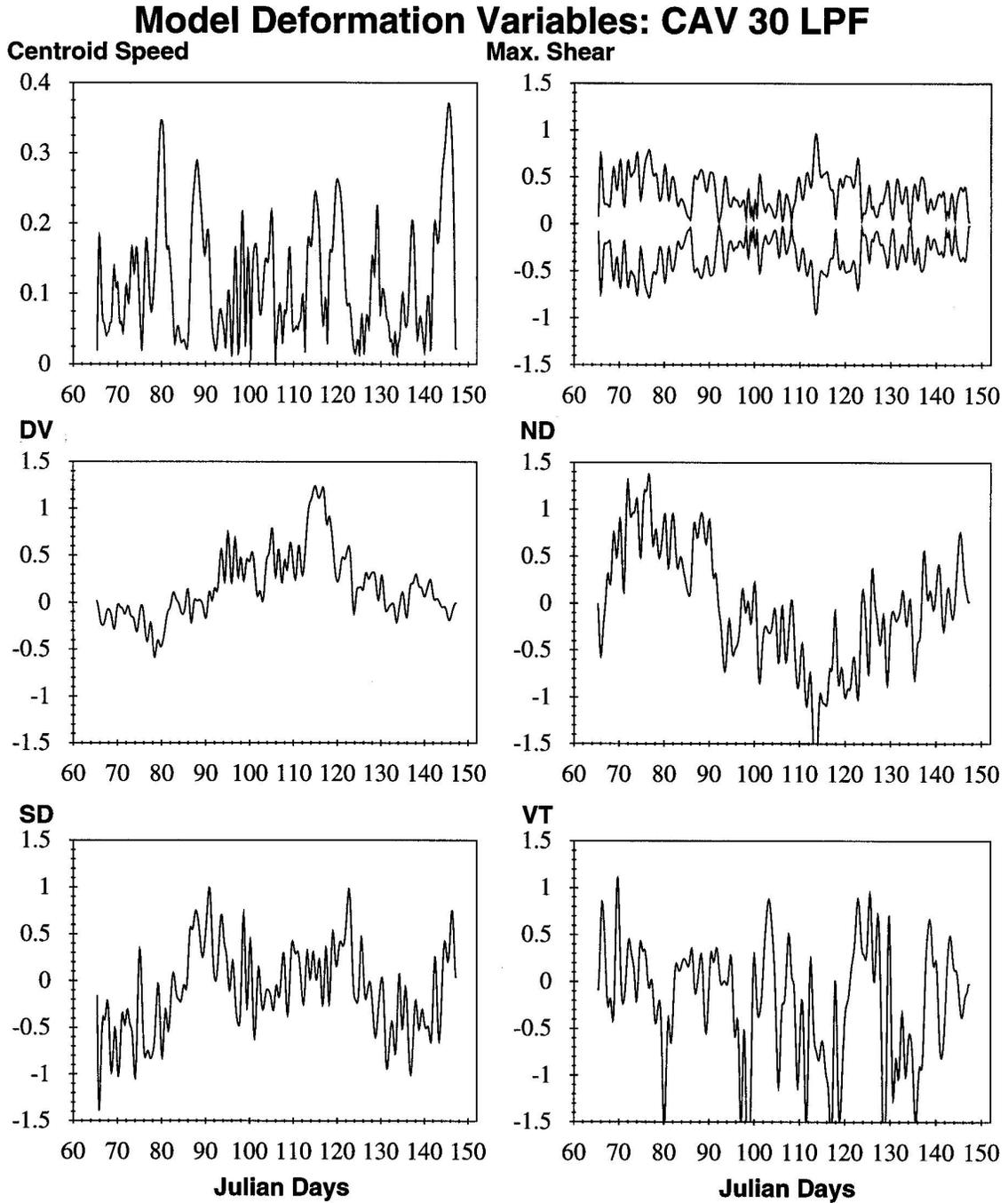


Figure 6.49: Centroid Speed, Max Shear and DKPs from Cavitating Fluid Rheology (CAV) model as computed from multiple linear regression analysis using a 30 hour low pass filter (LPF). Velocities are in units of [m/s]. Max Shear and DKPs are in units of [$\times 10^{-6}$ (1/s)].

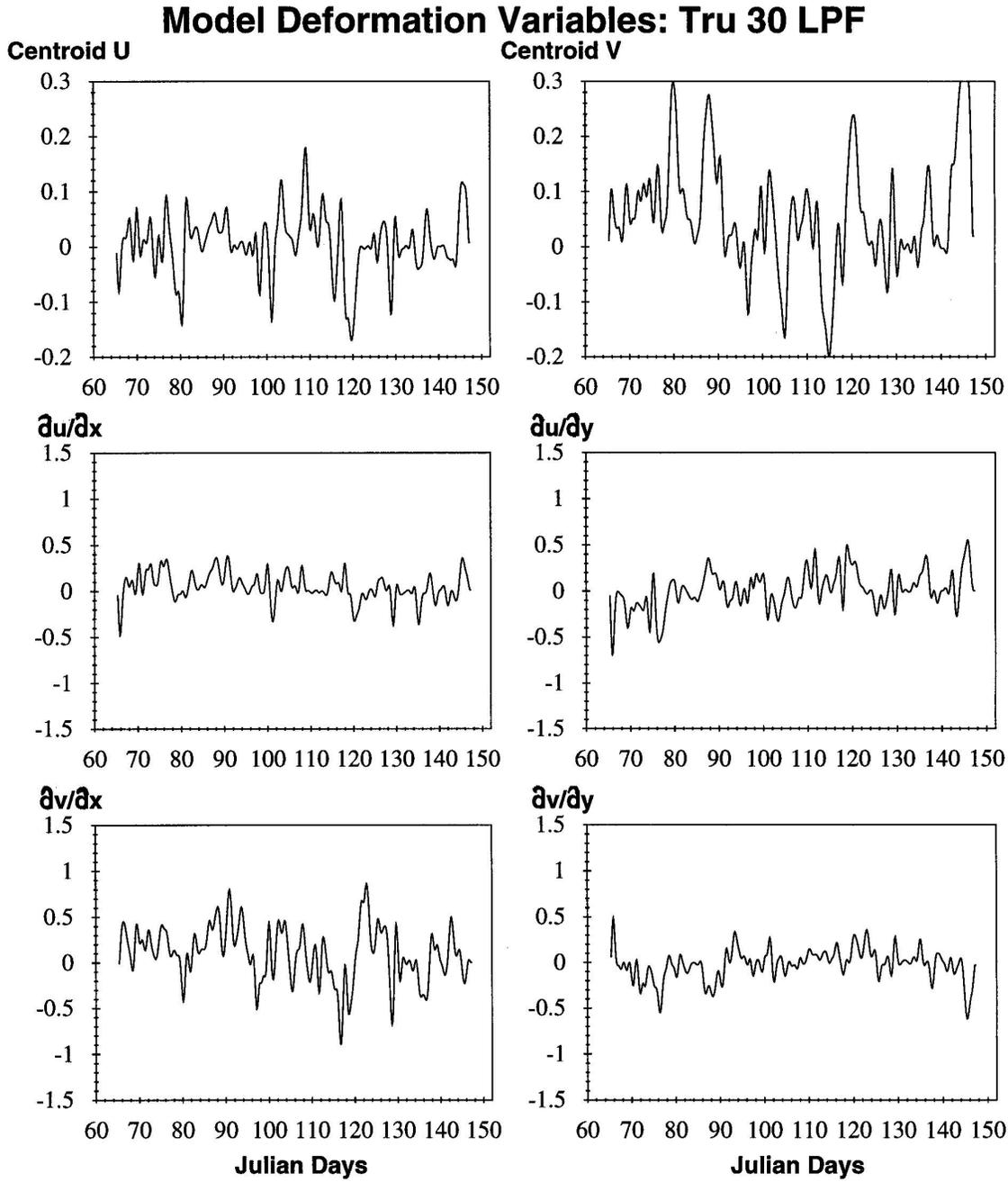


Figure 6.50: Beta parameters from regression analysis on Viscous Plastic Rheology with Truncated Ellipse (Tru) model output subjected to 30 hour LPF. Velocities are in units of [m/s] and strain-rate components are in units of [$\times 10^{-6}$ (1/s)].

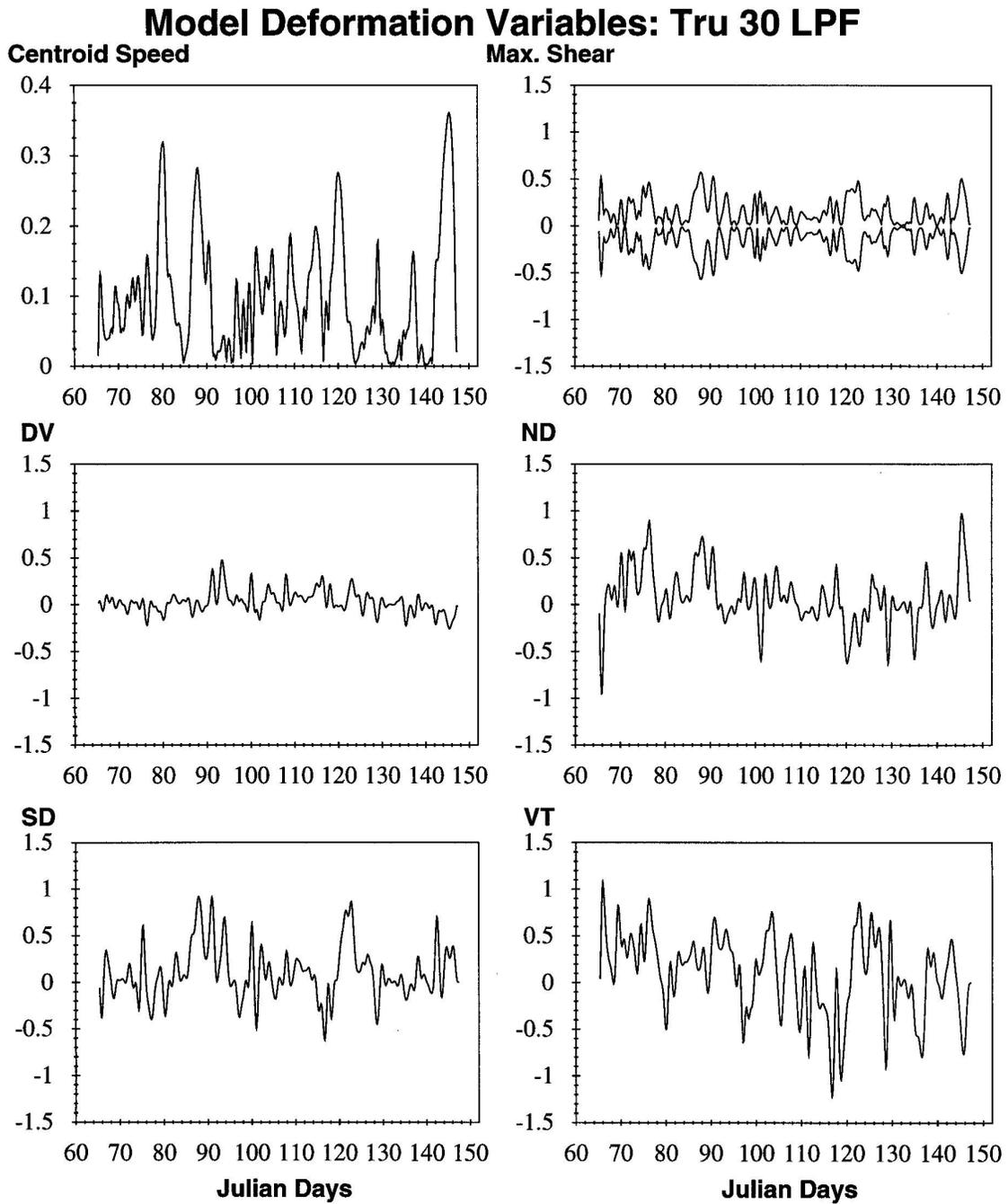


Figure 6.51: Centroid Speed, Max Shear and DKPs from VP with Truncated Ellipse (Tru) model as computed from multiple linear regression analysis using a 30 hour low pass filter (LPF). Velocities are in units of [m/s]. Max Shear and DKPs are in units of [$\times 10^{-6}$ (1/s)].

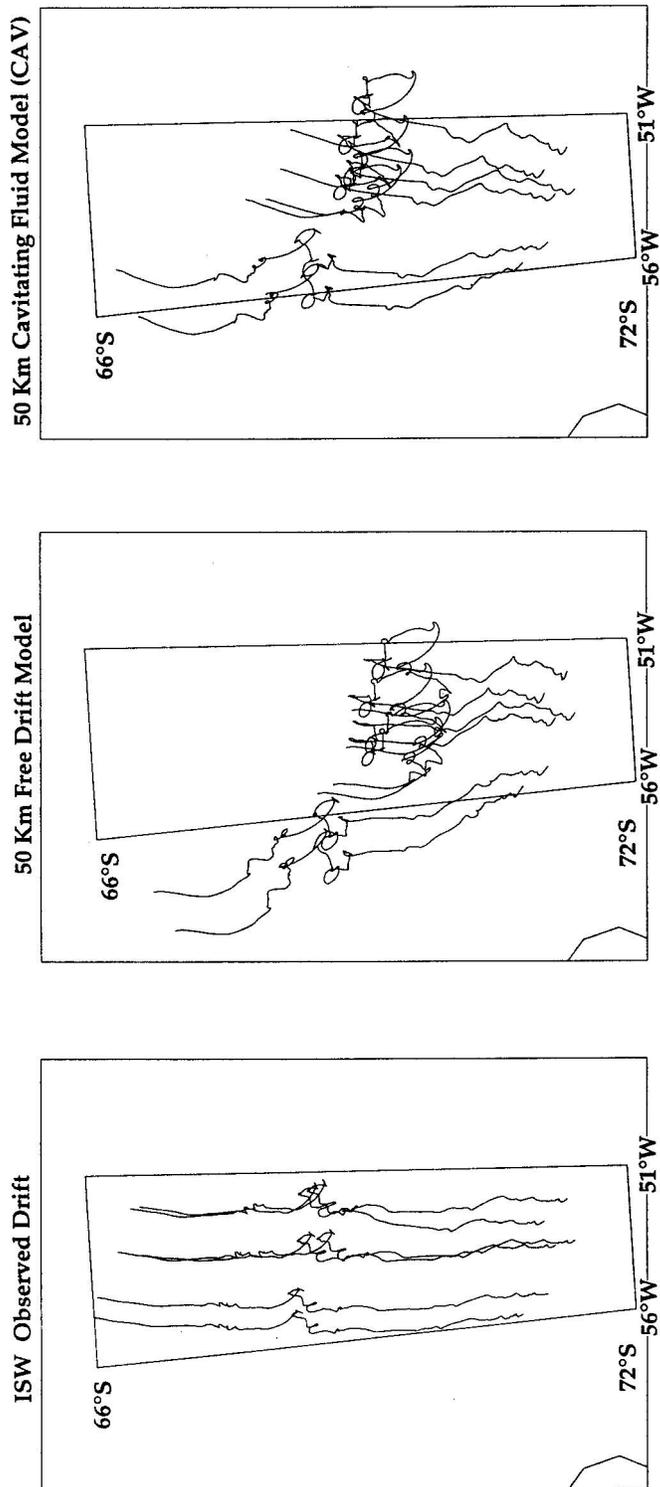


Figure 6.52: Progressive vector plots using velocities from ISW Sites at 30 hour LPF Observed, No LPF FD and CAV models.

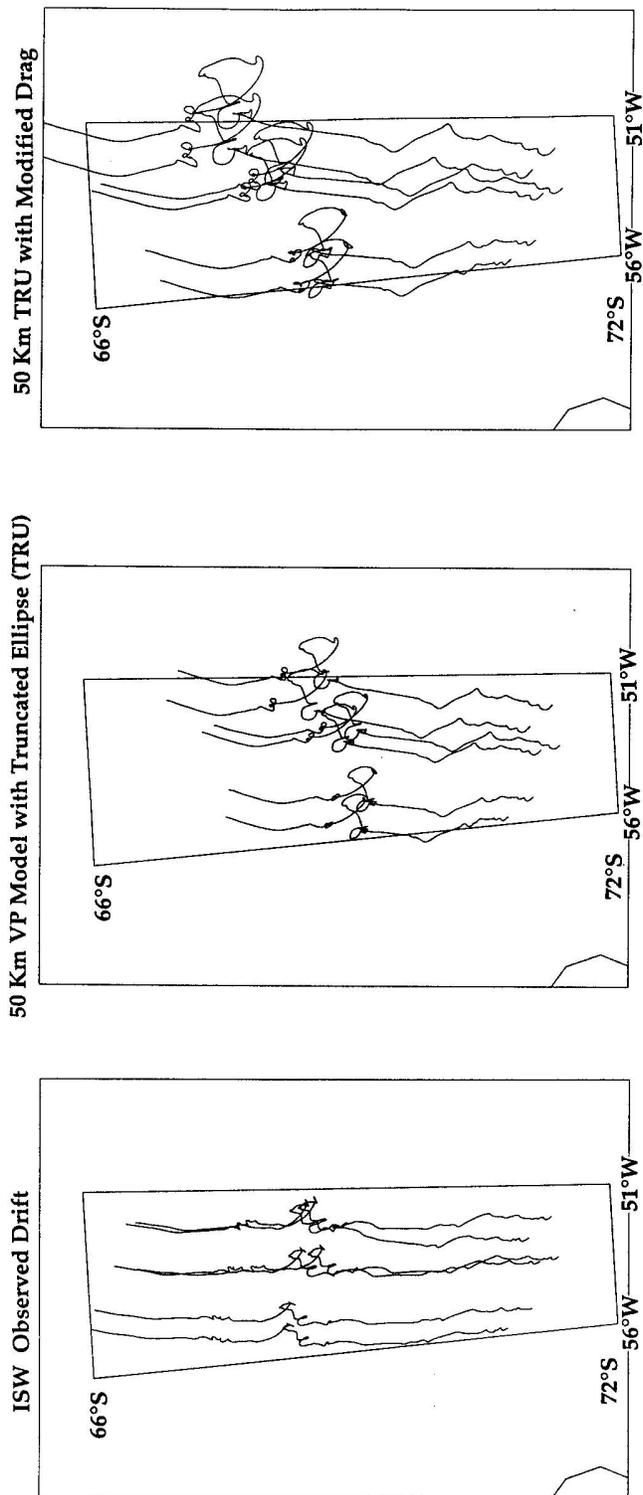


Figure 6.53: Progressive vector plots using velocities from ISW Sites at 30 hour LPF Observed, No LPF VP TRU and VP TRU with modified drag models.

6.4.3 Comparing Category Distributions

In Figure (6.54), we see how each modification to the viscous-plastic rheology affects deformation in principal axis space. At 3-hour intervals, the modeled stress state is computed at the ISW centroid location and plotted in principal axis space for the following models: VP concentric ellipse closure model (CON), VP truncated ellipse (TRU), increased ductility (Zmax/100) and modified drag (DRAG). The truncated ellipse case (TRU; upper right panel of Figure 6.54), as the name implies, truncates the stresses from reaching any tensile regime. Increasing the ductility (TRU+Zmax/100 case) creates fewer stress states along the yield curve where brittle failure occurs (lower left panel in Figure 6.54), and instead creates more ductile or viscous states such that more events occur in the interior of the yield curve. Modifying the drag after Lemke and Fischer (1994) (lower right panel in Figure 6.54) changes the stress states only slightly such that for a few points the compression stress lies further down the yield curve closer larger $-\sigma_I$ values. There are also a few more point within the yield curve (in the viscous regime) then with TRU.

Returning to the ductile versus brittle issue, the increases in ductility also increases the ice thickness in the area of the ISW array as seen in Figure (6.55), with the greatest increases in thickness occurring closer to shore (sites Ed and Chris). A possible explanation for this may be that ice moves faster with increased ductility (i.e. the very slow 0-2 km/day drift experienced under TRU is no longer present). As a result there is greater potential for open water creation and consequently more freezing at open water sites (hence overall thicker ice). A desirable comparison to observations would be a time series of the local average ice thickness in an area comparable with that in the models. Experimentally, however, this is a very difficult task even at the individual ice floe level.

Information from the ISW cruise reports (Ackley, Gow, et al. 1992) for the Camp ice floe exemplifies some of the difficulties including a variety of ice types from new thin lead ice, medium thick first year, thick deformed old ice with thicknesses of 0.5-4.0 m. The Camp had an areal extent of about 2 to 3km² and was composed mostly of a matrix of first-year ice interspersed with cakes of multiyear and first-year ice breccia. Estimates from Churun et al. (1992) found the first-year ice thicknesses on the floe to range from 0.9-1.5m of ice and 0.2-1.3m of snow cover. Multi-year floes (8-10m across) had thicknesses up to 1.8m and 0.5-0.6m of snow cover. From these descriptions, we see that the ability to tell which of the two modeled rheologies (brittle or ductile) above is closer to reality is not possible in terms of the time series measurements. Instead statistical methods involving probability distributions must be used. This will be examined below but its application will be for drift and deformation rather than ice thickness. About all we can identify for now is some rough estimates. First in terms of the model reproducing the correct thickness, we are at the high end of the observed ice thickness in the model (1.7-1.9m modeled). Snow cover is considerable in this area but not considered in this study, so the modeled results should be higher from a thermodynamics perspective. There is also the issue of ice formed from snow, caused by the weight of the snow sinking the ice below freeboard, swamping and refreezing into congelation ice. This process is significant in the Antarctic and almost non-existent in the Arctic. In short, there are a lot more considerations to be included in these models in order to achieve good high resolution predictability.

Use of correlation diagrams is another way to realistically compare observed drift and deformation with model cases. In Figures (6.56)-(6.60), the cases of free drift (FD), cavitating fluid (CAV), truncated ellipse closure method (TRU), TRU with higher ductility (Z/100), and TRU with modified drag (DRAG) are plotted for the centroid of the array. As opposed to the time series representation, this type of display provides a more quantitative measure of how well a specific model variables compare to observations. Beginning with the velocity in FD (Figure 6.56) we see that magnitude is clustered mostly between 0 and 0.2 m/s with the data scattered by about 0.1 m/s about a 45° slope, as desired. Differences in velocity magnitude for this case versus CAV (Figure 6.57) are small, but there is an improved correlation in TRU (Figure 6.58) (i.e. velocity magnitudes have less scatter relative to observed in this case). While there is only negligible change when introducing more ductility (Figure 6.59), modifying the drag coefficient to those of Lemke and Fischer (1994) modifies the drift such that the model predicts too great a velocity at most points in time versus observed, and hence the scatter slope increases to an angle of about 60° indicating systematic deviations.

The velocity magnitude is the best correlated variable from all drift and deformation terms compared. Velocity direction in each of these cases is clustered fairly densely along the 45° slope, but there is considerable scatter at the top and bottom of the direction plots such that the observations points in a northward direction while the model predicts these same points heading in a southwesterly to southeasterly direction. This seems to be the dominant source of error in the models with regard to predicting drift. At this point in time the reasons for this lack of correspondence are unclear, but it is something repeatably occurring in all cases to about the same degree. The atmospheric input fields used to drive these models is one possible source for this error, as is the boundary layer formulation problem presented earlier.

Selecting the two invariant strain-rates of divergence (DV), maximum shear, normal (ND) and local (SD) shear deformation (see 5.2.1), we see that max. shear is predicted much better than divergence in all cases with the amount of scatter decreasing as the model hierarchy progresses from free drift (FD) to a full pressure and shear rheology (TRU). Considering the ice to be more ductile (Figure 6.59) decreases the scatter in both divergence and shear components but the magnitudes in the model are considerably lower than the observed such that the orientation of the scatter is close to 30° for shear and nearly 0° for divergence. Using the modified drags (Figure 6.60) suggested by Lemke and Fischer (1994) improves the magnitudes of the model deformation versus observed (i.e. slope close to 45°) but the scatter has increased. Combining these last two improves the results seen in Figure (6.60) only slightly.

Subjecting the data to a correlation analysis gives an overview of these results in bar graph form (Figure 6.61). From the upper panels, we see that the models do fairly well, independent of rheology, in predicting the ice velocity with the greatest weakness being the ability to properly predict drift direction. From the scatter plots we further know that it is a shift in the number of northerly versus southerly directions which are poorly predicted. Since the dominant drift is due north, the presence of modeled southerly flow is opposite the dominant drift track. These tendencies reoccur in all the presented models (upper left panel) and at all buoy sites (upper right panel of Figure 6.61). In contrast, inclusion of pressure and shear resistance in an ice rheology has a considerable effect on the predictability of ice deformation. The two major highlights seen in this comparison

are that the divergence is poorly predicted in all the models while shear is predicted better than divergence in all cases and better predicted with the more extensive VP type rheology. Additionally, there is evidence that small improvements (i.e. tuning) in predictability can be made within the VP model for deformation and drift by adjusting internal ice parameters of ductility and ice strength as well as boundary layer transfer terms such as drag coefficients and turning angles. In terms of the directionally dependent strain-rate variables (lower left panel in Figure 6.61), $\dot{\epsilon}_{22} = \partial v / \partial y$ is the least correlated strain-rate component with the derived quantities of vorticity and divergence following with increasingly poorer results. Since the vorticity is a drift rotational effect, the poor correlation in this is most likely linked to the low correlations in velocity direction.

Examining this from a probability distribution perspective, we see first in the ice drift (Figure 6.62), that the primary lack of correlation between observed and modeled velocity direction is an underestimated number of northward flowing outcomes in the models versus observed which complements the findings from the scatter study. In the probability distributions, however, there is a noticeable gap in the 4-6 km/day peak velocity magnitude. This information is hidden in the spread of the scatter of the smaller velocity magnitudes in Figures (6.56)-(6.60).

This point is important for the following reason. The dominant drift speed categories of 4-5 and 5-6 km/day each occurs about 11 to 12% of the time in the observations but only about 7 to 8% of the time in the models. Collectively this means that for almost 25% of the time the drift speed observed is between 4-6 km/day while in the model it is only 14 to 16% of the time. This means there is about a 10% difference in predominant drift speed between models and observations. This sort of error is not clearly reflected in the Chi-Square because these differences are small relative to cases where the observed is small and the model is only somewhat larger (e.g. FD/CAV 12-18 km/day category). Commensurate with this, the velocity magnitudes in FD and CAV are shifted relative to observed from 4-8 km/day to 10-20 km/day (upper panels). In TRU (lower panels) there is a considerable improvement in this shift but an increase in the 0-2 km/day range. This slower 0-2 km/day range is improved by increasing the ductility (ζ_{max} reduced by 100) such that there is almost no difference in this 0-2 km/day range between the observed and the ductile case (Z100 in Figure 6.62). Using the modified drag of Lemke and Fischer (1994) makes the distribution for velocity worse and is therefore not shown). Putting this all together we find that there is comparable probability distribution error in both velocity magnitude and direction but only the directional error is clearly evident in the scatter, correlation, and chi-square statistical methods.

When we examine the deformation we see for FD and CAV (Figure 6.63) that $\partial u / \partial x$ and $\partial u / \partial y$ terms are probabilistically quite close to observed but that $\partial v / \partial x$ and $\partial v / \partial y$ are not. The inclusion of pressure resistance in the case of CAV only improves the former. Inclusion of shear (Figure 6.64) improves the distribution further although TRU overpredicts three of the four peak categories in the smaller deformation events (-0.1 to 0.1×10^{-6}). Unlike with velocity, increasing the ductility of the ice does little to change these deformation distributions relative to TRU (therefore Figure not shown); but use of the modified drag greatly improves the prediction of smaller deformation events. The only exception to this is the distribution of the $\partial v / \partial x$ term which is very poorly reproduced in these distributions.

As seen in the probability Figures, better fit between modeled and observed values means smaller chi-square components (reverse of the correlation analysis). With this in mind we look at the total chi-square results of the probability distributions in Figures (6.65)-(6.67). For the velocity magnitude (Figure 6.65), FD and CAV behave similarly, so the inclusion of pressure resistance actually does little to affect the overall drift behavior of the ISW buoys. For almost all the buoys, TRU has the least effective rheology especially for the buoys closest to the coast (Ed and Chris) but increasing the ductility in TRU (by $\zeta_{max}/100$) rectifies this producing the best results at all but one station (Dimitri) and comes in a close tie with CAV at site Ed. This result is not reflected in the progressive vector plots, primarily because the biggest improvement in these distributions comes from the slowest speeds (0-2 km/day range). From the middle panel in Figure 6.65 we see that inclusion of a truncated ellipse and further increasing the ductility improves the viscous-plastic rheology behavior at all buoy sites; adjustments to parameters such as drag coefficient and ice strength does not, even in combination with increased ductility .

In terms of velocity direction (Figure 6.66), the inclusion of pressure resistance (through CAV) and then shear resistance (through TRU) increases the ability of the models to predict velocity direction. Unfortunately, modifications to improve TRU (increased ductility, reduced drag, decreased ice strength, and combinations) produce less effective results (lower 2 panels in Figure 6.66). The same is true of vorticity (all panels Figure 6.67). As for deformation, inclusion of both pressure and shear improves the predictability of the model versus observed (upper panel Figure 6.67) but modifications to the viscous-plastic rheology produce both positive and negative effects in different deformational processes such that good predictability of model deformation is far from achieved. While increased ductility improves shear processes, it does worse than TRU or even CON and REP in predicting divergence. Modifying the drag coefficient improves divergence and normal deformation but does not do as well in the local shear deformation (lower panel Figure 6.67).

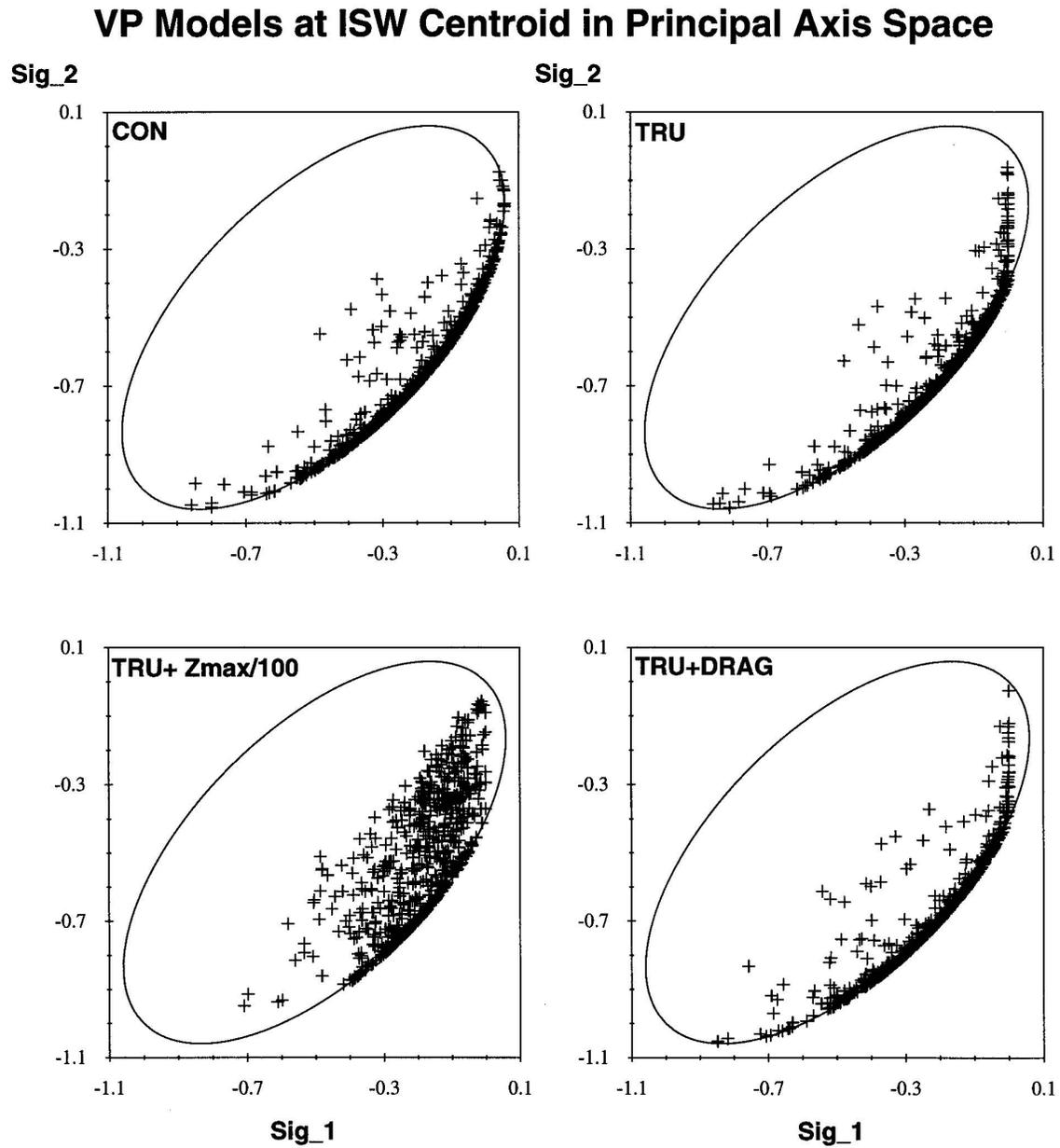


Figure 6.54: Scatter plots in normalized principal axis space of 3-hour ISW centroid location in VP Models with concentric ellipse closure (CON), truncated ellipse closure (TRU), TRU in more ductile state (TRU+Zmax/100), and TRU with modified drag (TRU+DRAG).

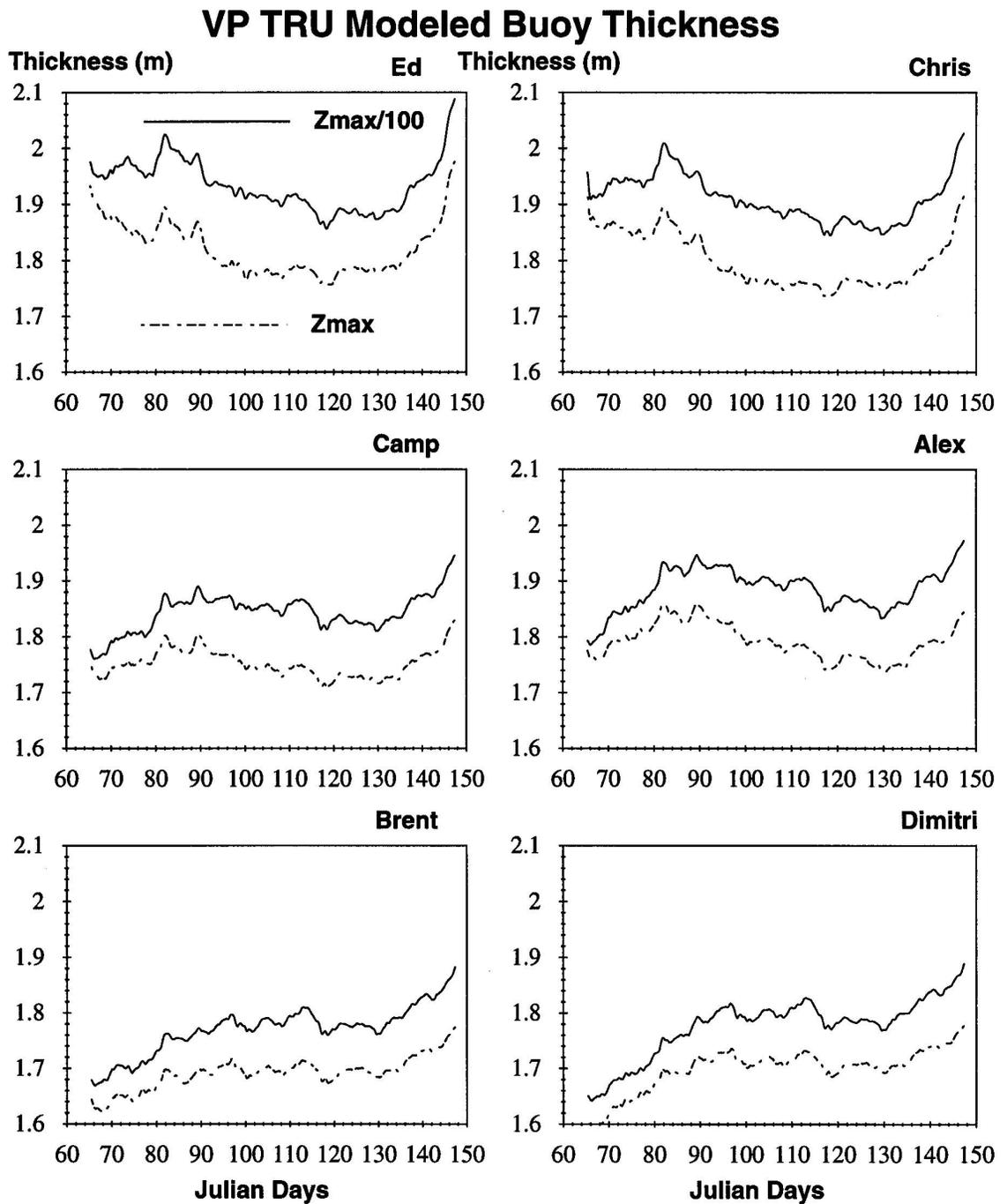


Figure 6.55: Time series of ice thickness at ISW sites under ductile ($Z_{max}/100$) and brittle (Z_{max}) states.

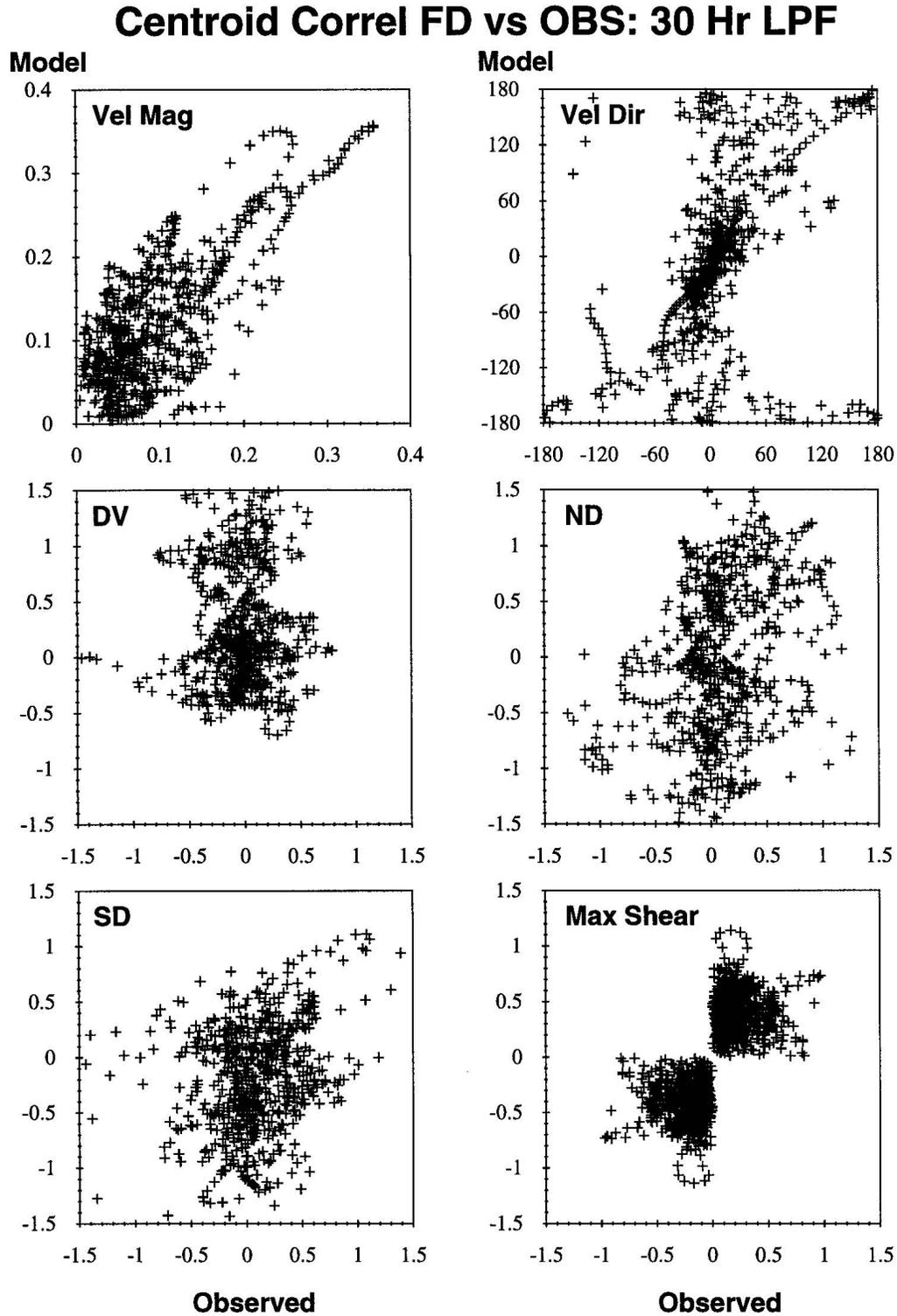


Figure 6.56: Scatter plot of correlation between 3 hour ISW centroid observations (OBS) and free drift (FD) for velocity magnitude (m/s), direction (degrees), and selected deformation terms ($\times 10^{-6}$ 1/s).

Centroid Correl CAV vs OBS: 30 Hr LPF

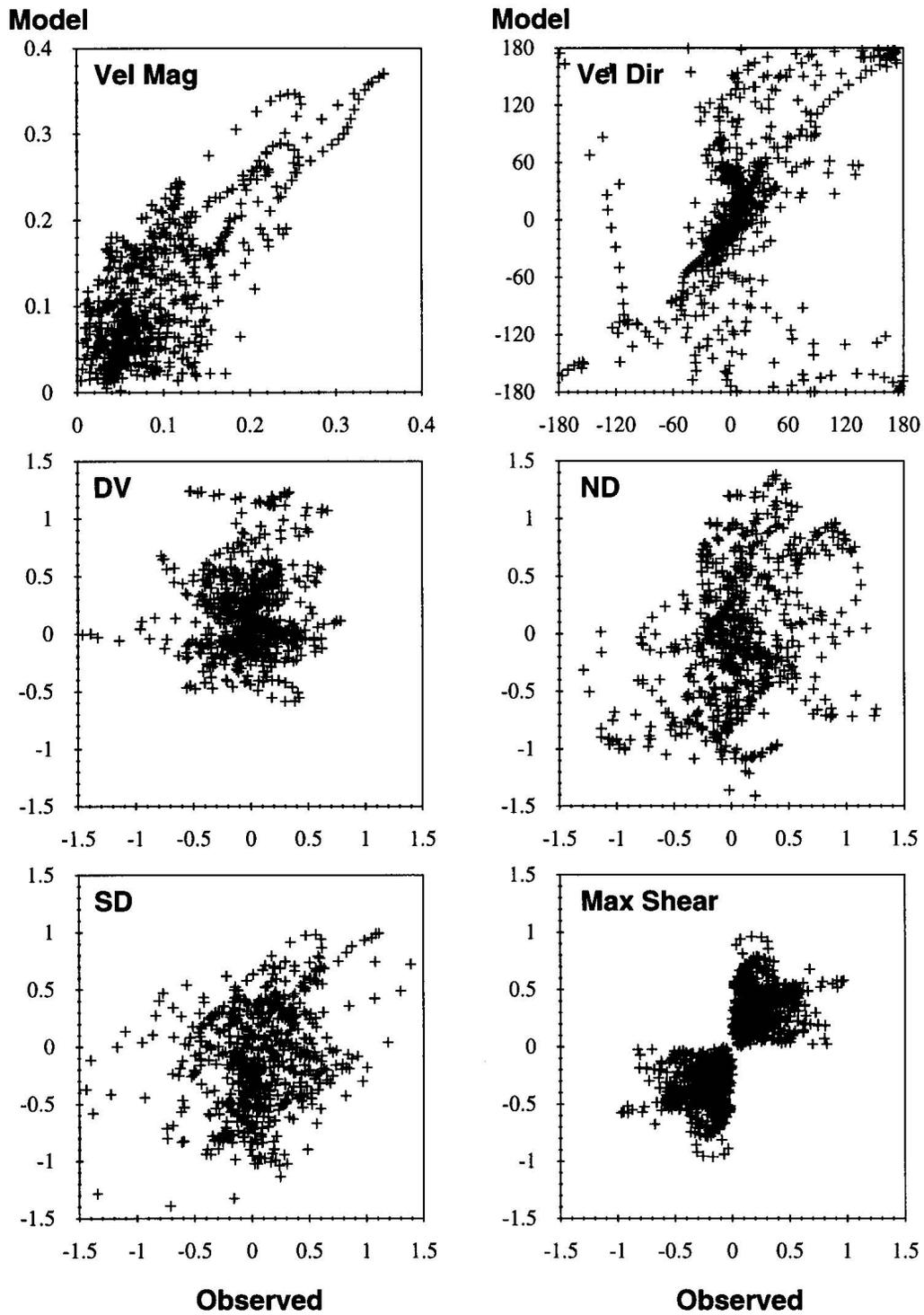


Figure 6.57: Scatter plot of correlation between 3-hour ISW centroid observations (OBS) and cavitating fluid (CAV) for velocity magnitude (m/s), direction (degrees), and selected deformation terms ($\times 10^{-6}$ 1/s).

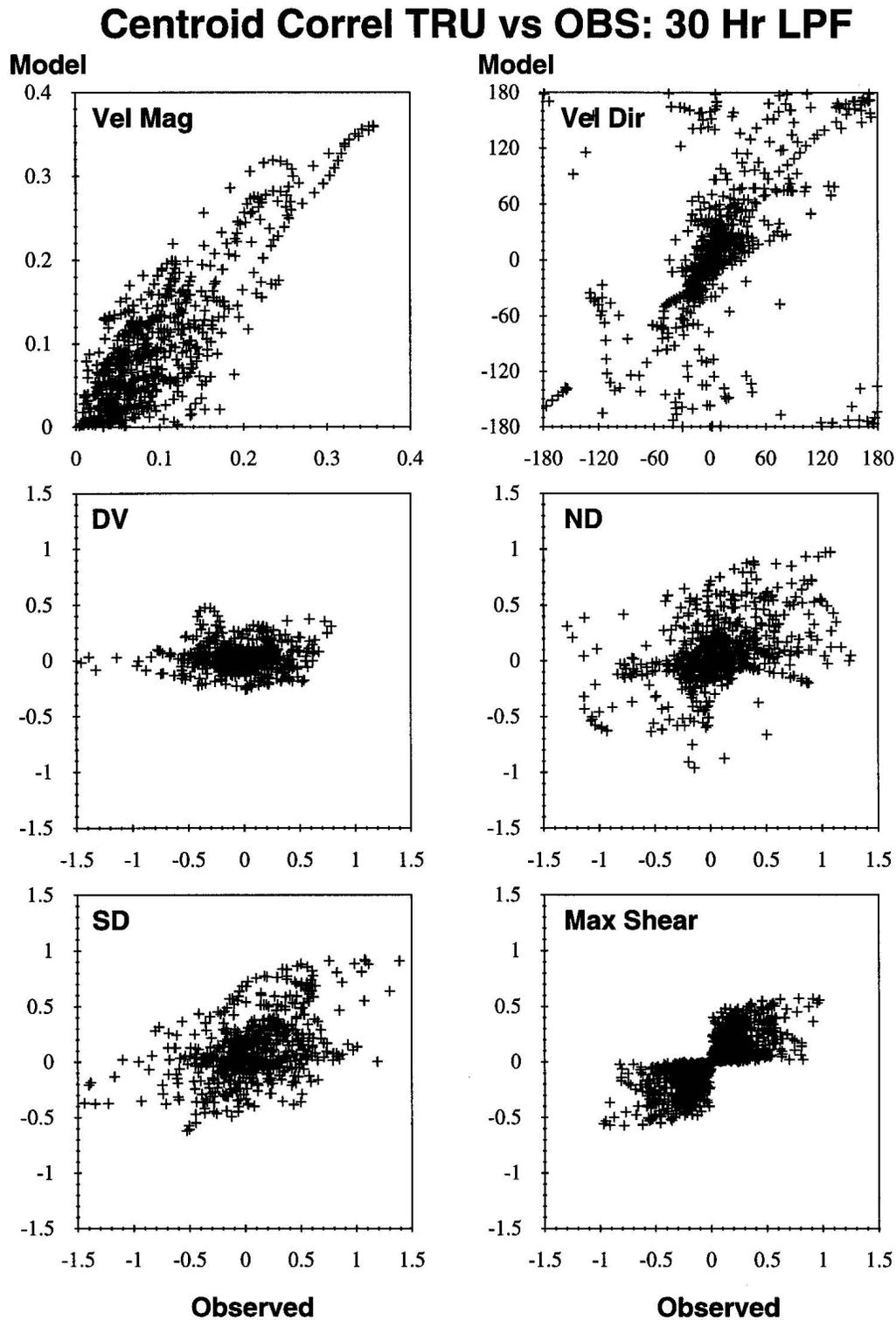


Figure 6.58: Scatter plot of correlation between 3-hour ISW centroid observations (OBS) and VP with truncated ellipse (TRU) for velocity magnitude (m/s), direction (degrees), and selected deformation terms ($\times 10^{-6}$ 1/s).

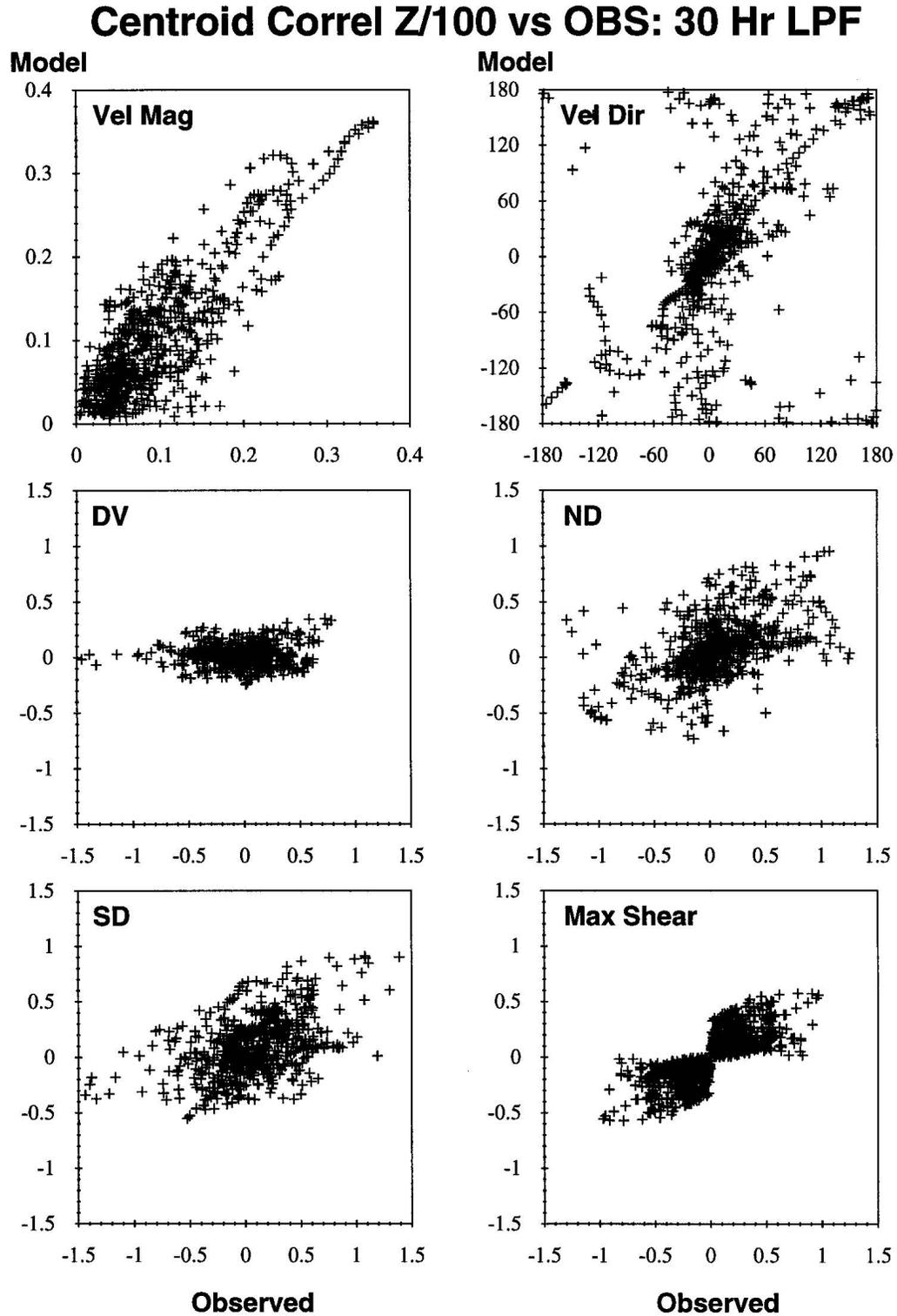


Figure 6.59: Scatter plot of correlation between 3-hour ISW centroid observations (OBS) and VP TRU under ductile flow (Z/100) for velocity magnitude (m/s), direction (degrees), and selected deformation terms ($\times 10^{-6}$ 1/s).

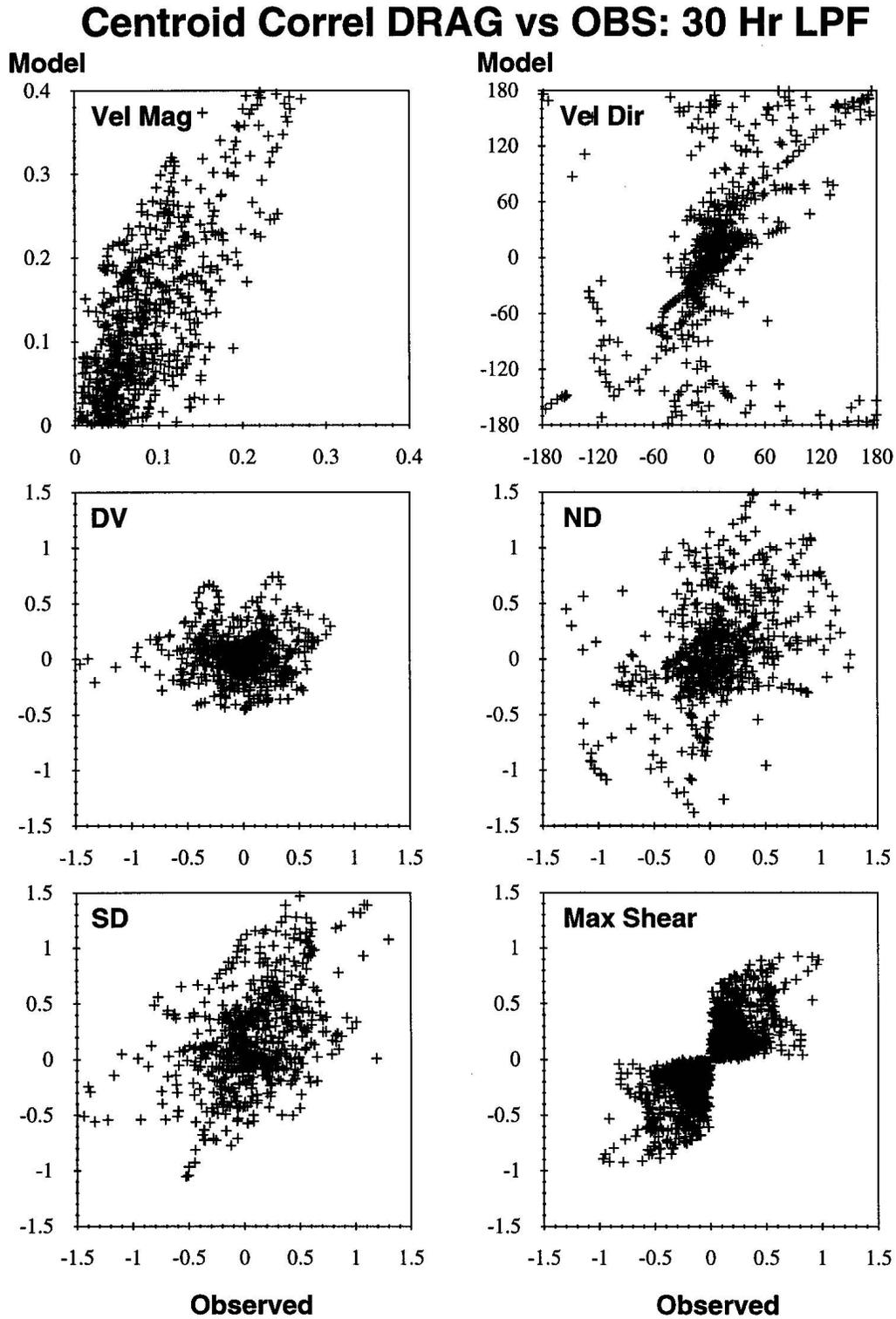
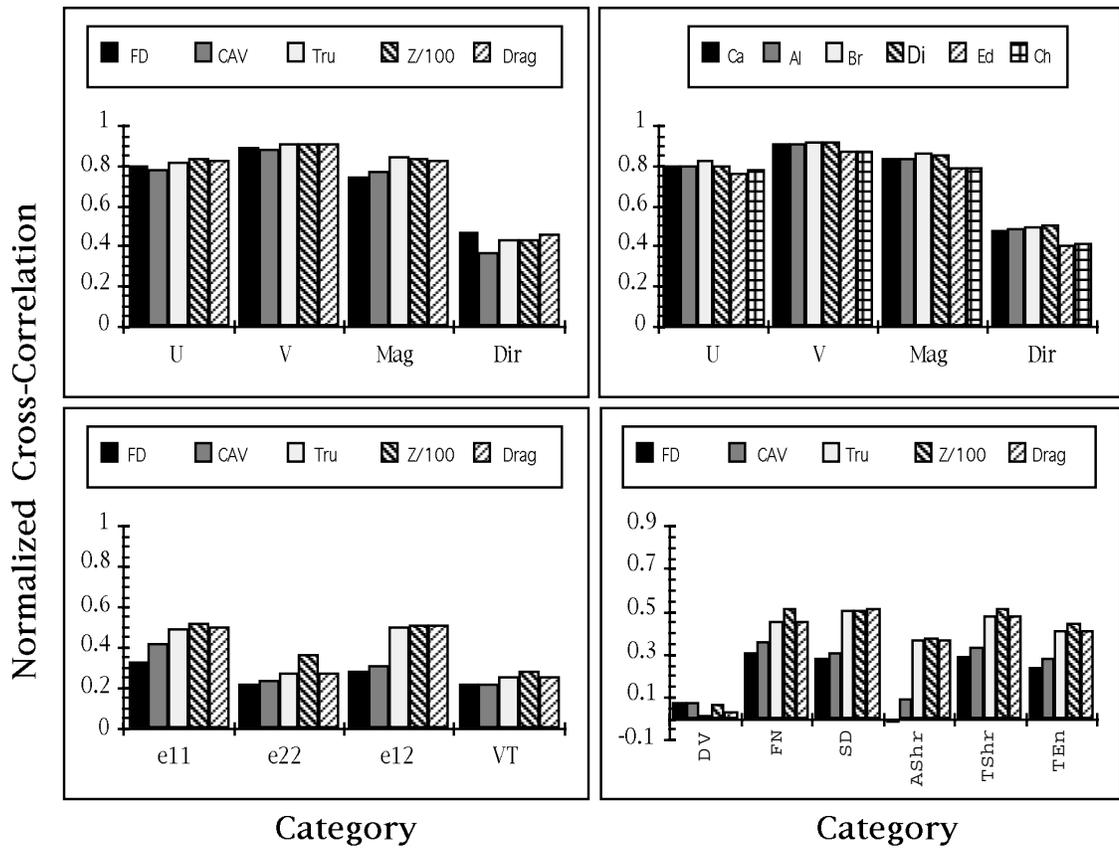


Figure 6.60: Scatter plot of correlation between 3-hour ISW centroid observations (OBS) and VP TRU with modified drag (DRAG) for velocity magnitude (m/s), direction (degrees), and selected deformation terms ($\times 10^{-6}$ 1/s).

Cross-Correlation Results for Velocity and Deformation



Note: Mean removed from velocity terms
Mean not removed from deformation terms

Figure 6.61: Cross-correlation between observations and models of free drift (FD), cavitating fluid (CAV), VP with truncated ellipse (TRU), TRU under ductile state (Z/100), TRU with modified drag (Drag). Camp (Ca), Alex (Al), Brent (Br), Dimitri (Di), Ed, Chris (Ch) computed for TRU. AShr uses absolute value of max. shear; TShr is for total max. shear (positive and negative incl.); TEn is Total Energy; and DV, FN (ND), SD, VT are DKPs (see text).

Distribution of Velocity

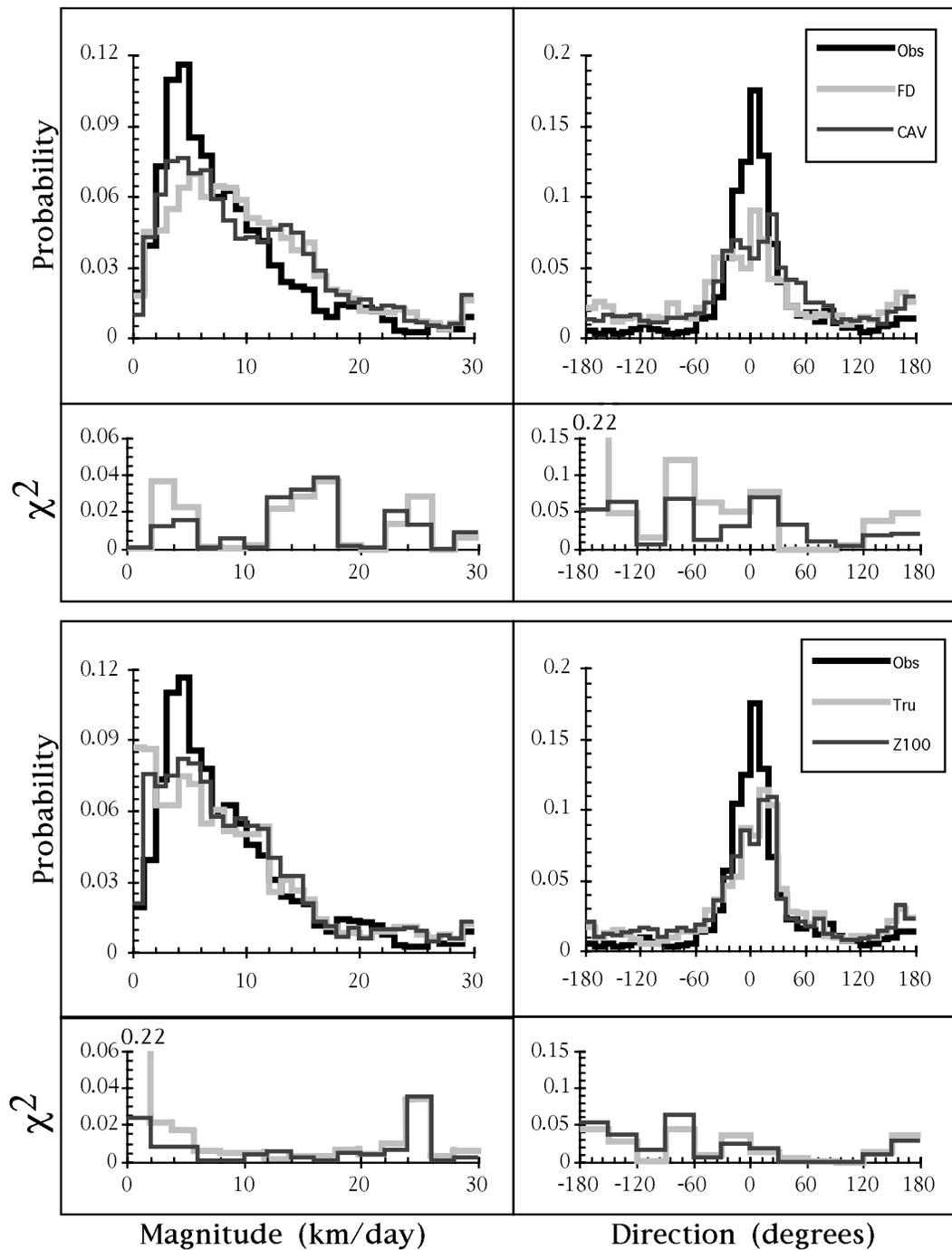


Figure 6.62: Normalized probability distribution and unsummed Chi-Square terms for velocity using observations (OBS) versus the 4 model types of Free Drift (FD), Cavitating Fluid (CAV), VP with Truncated Ellipse (TRU) and VP TRU with reduced bulk viscosity (ductile case $Z100 = \zeta_{max}/100$).

Distribution of Deformation Components

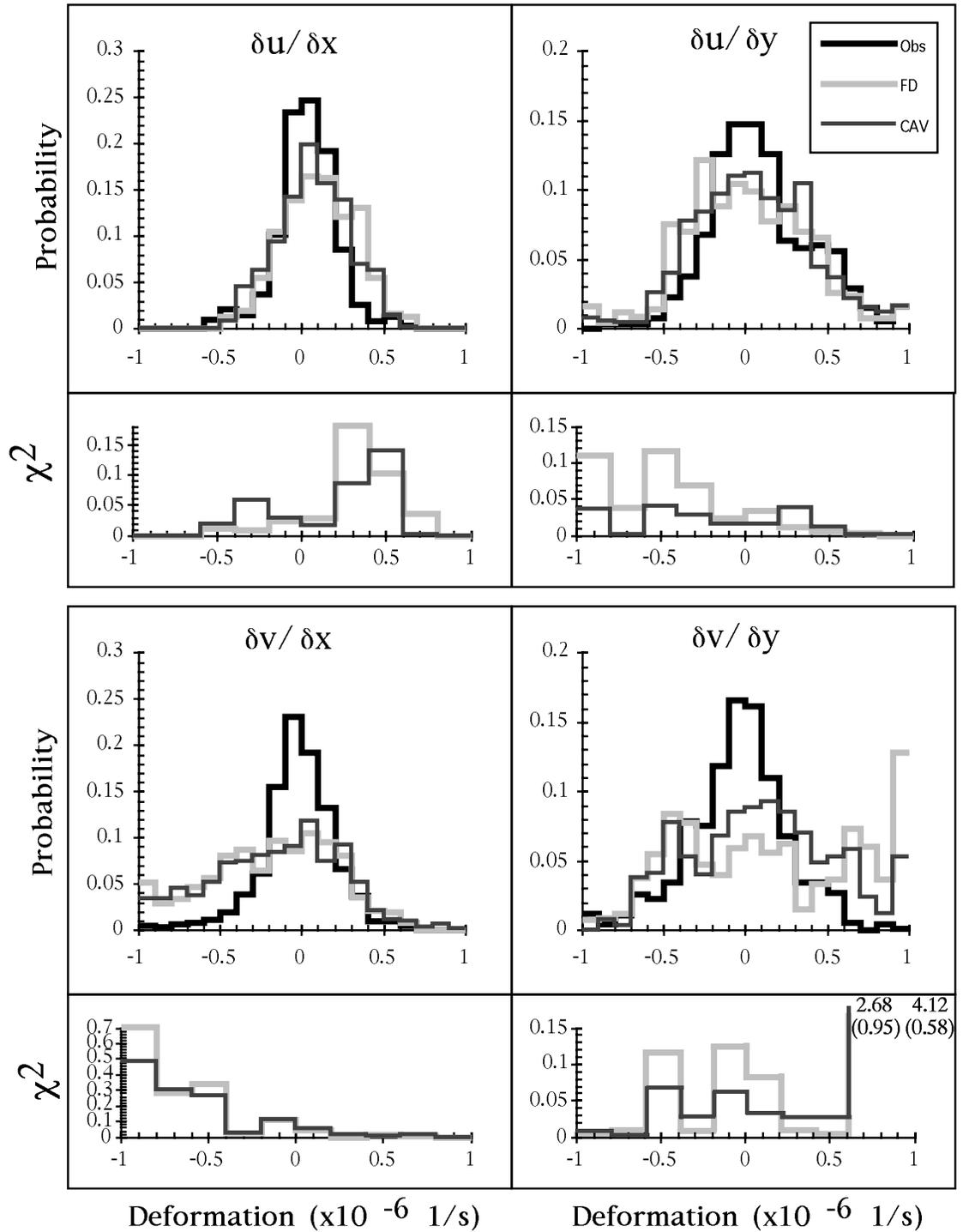


Figure 6.63: Normalized probability distribution and unsummed Chi-Square terms for deformation components using observations (OBS) versus the 2 model types of Free Drift (FD) and Cavitating Fluid (CAV).

Distribution of Deformation Components

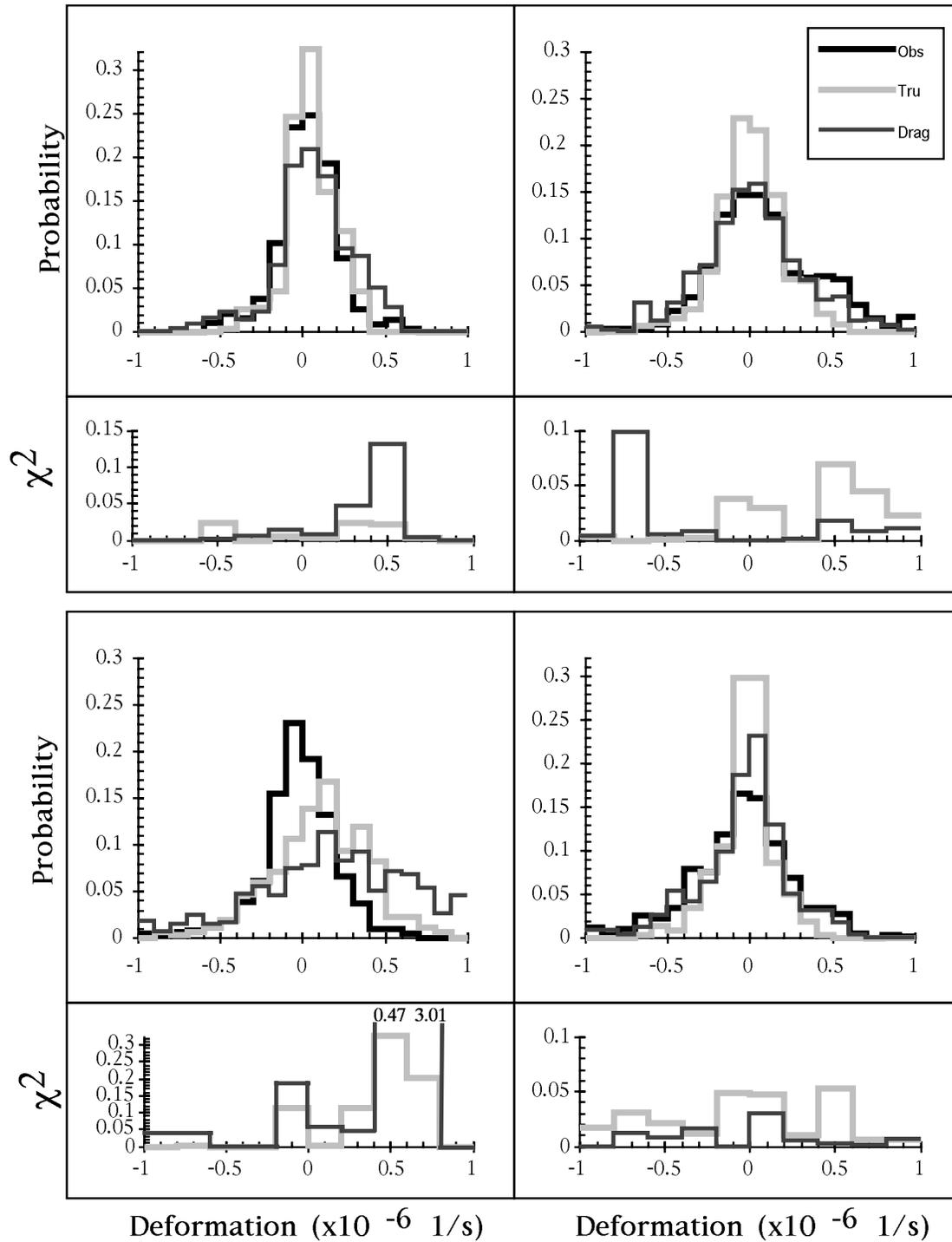


Figure 6.64: Normalized probability distribution and unsummed Chi- Square terms for deformation components using observations (OBS) versus the 2 model types of VP with truncated ellipse (TRU) and VP TRU with modified drag (DRAG).

Chi-Square Results for Velocity Magnitude

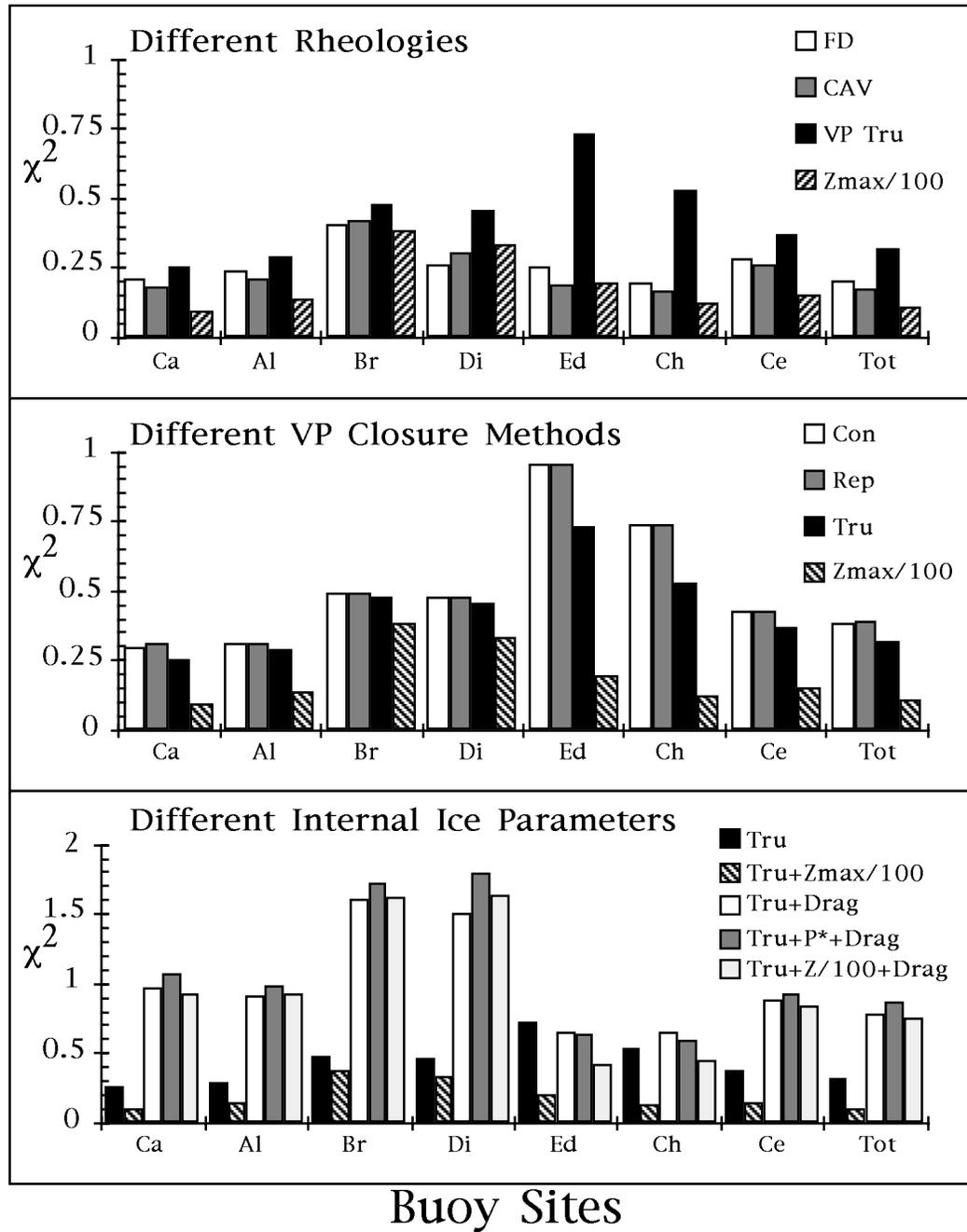


Figure 6.65: Chi-square velocity magnitude between observed buoy sites and model outputs. *Key:* Free drift (FD), cavitating fluid (CAV), VP with truncated ellipse (TRU), VP TRU under ductile state (Zmax/100 or Z/100), VP TRU with modified drag (Drag), VP TRU with reduced ice strength (P*), Camp (Ca), Alex (Al), Brent (Br), Dimitri (Di), Ed, Chris (Ch), All (Tot).

Chi-Square Results for Velocity Direction

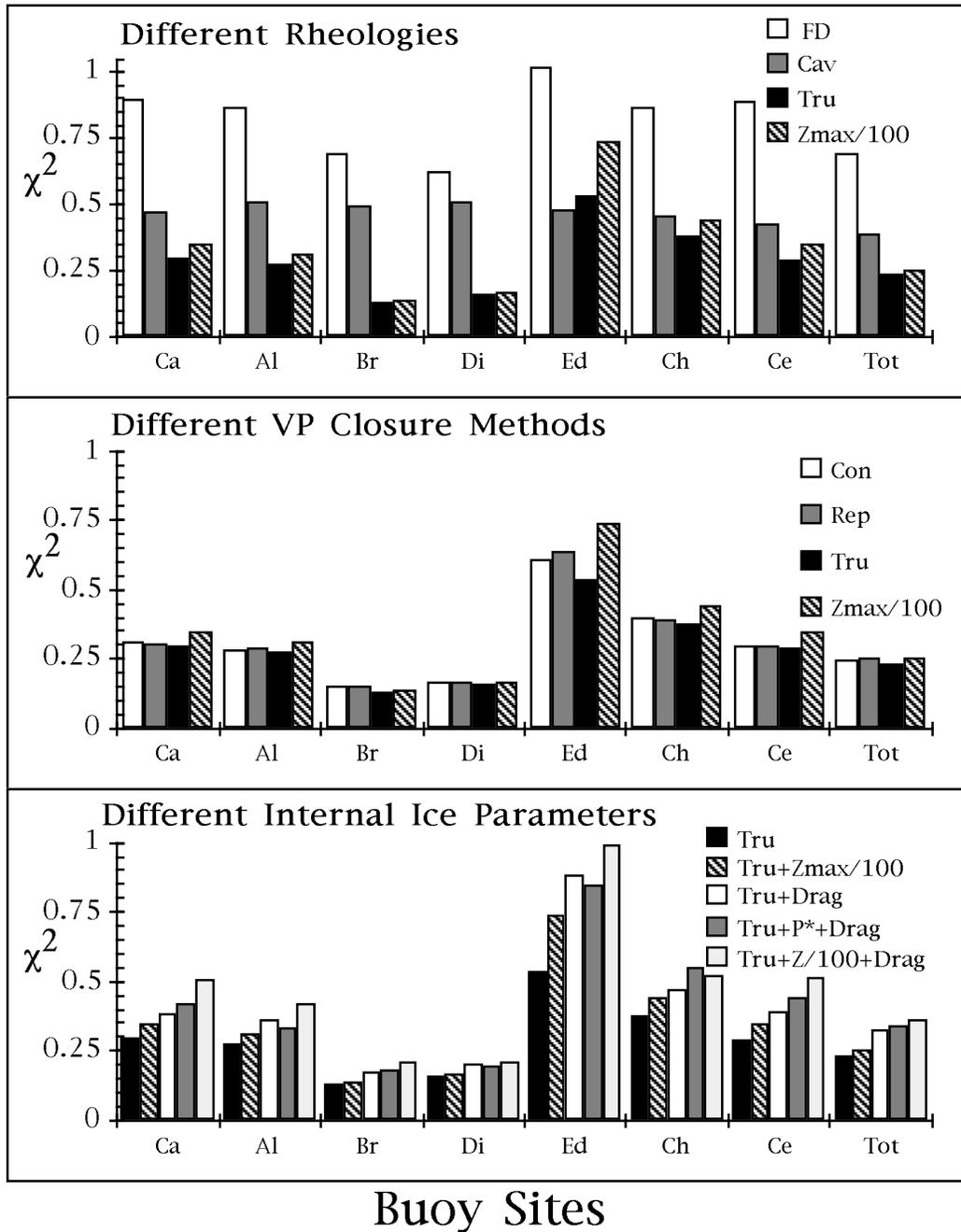


Figure 6.66: Chi-square velocity direction between observed buoy sites and model outputs. *Key:* Free drift (FD), cavitating fluid (CAV), VP with truncated ellipse (TRU), VP TRU under ductile state (Zmax/100 or Z/100), VP TRU with modified drag (Drag), VP TRU with reduced ice strength (P*), Camp (Ca), Alex (Al), Brent (Br), Dimitri (Di), Ed, Chris (Ch), All (Tot).

Chi-Square Results for Deformation Terms

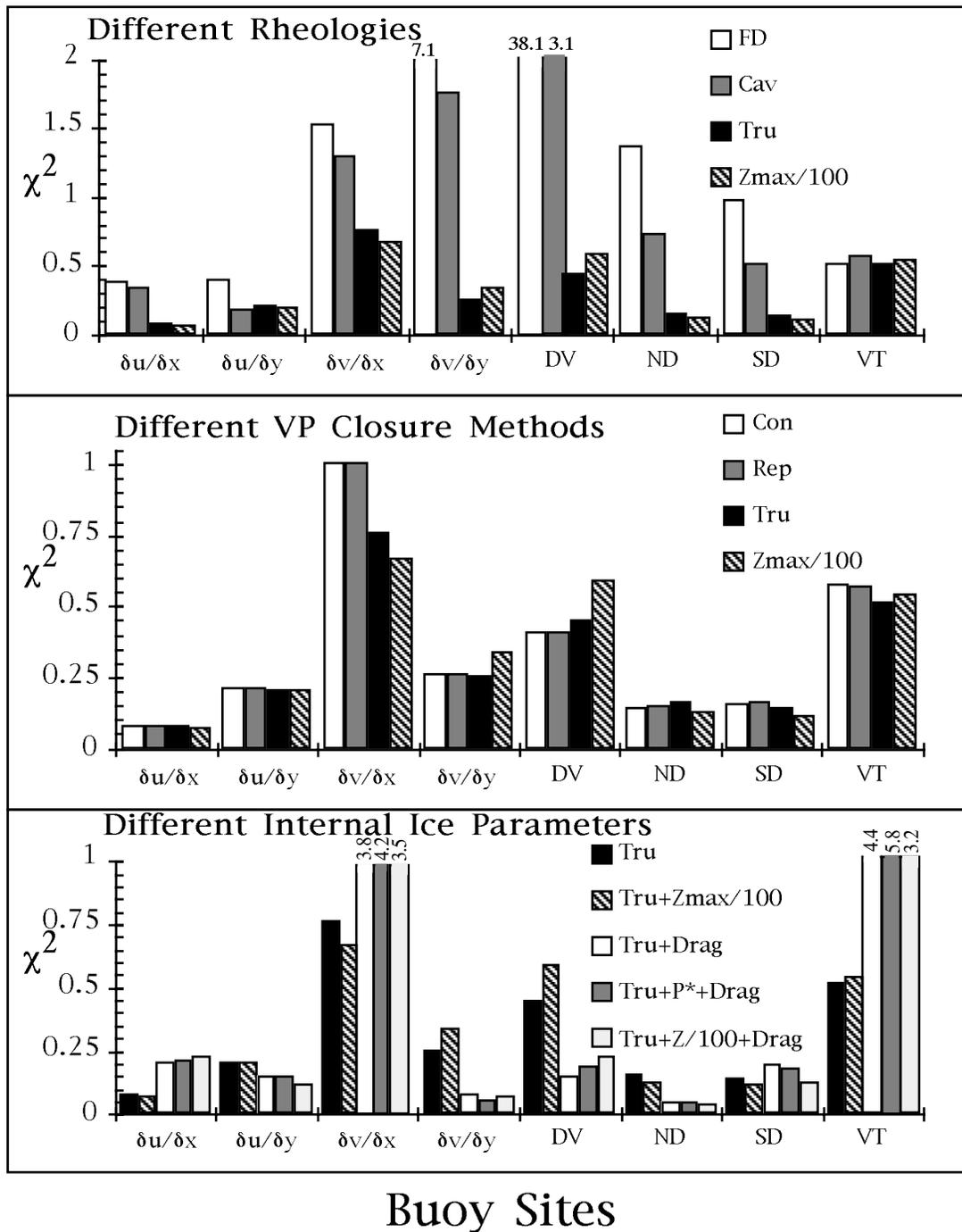


Figure 6.67: Chi-square of deformation terms between observed centroid and models. *Key:* Free drift (FD), cavitating fluid (CAV), VP with truncated ellipse (TRU), VP TRU under ductile state (Zmax/100 or Z/100), VP TRU with modified drag (Drag), VP TRU with reduced ice strength (P*).

6.4.4 Summary of Buoy Comparison

The key results seen in this buoy comparison are as follows. First, while none of the models completely reproduce the buoy behavior observed in the field, the use of a rheology with both pressure and shear resistance is the best solution to date. Second, with regard to sensitivity to these models, predictability of ice deformation is far more difficult to achieve than drift and is much more sensitive in terms of response to the tuning of internal ice parameters than velocity. Third, one major disappointment in the attempts made in this study is that an adequate model improving both drift and deformation was not achieved. While use of increased ductility in VP models greatly improved drift statistics, modifying the drag coefficients was far more successful at improving the deformation components; however a combination of these failed to produce a positive effect. Fourth, the sensitivity of the different deformation terms (both directional and invariants) is such that some parameters seem to improve while others do not, depending on the modifications made to the models.

Overall, shear is reproduced much better than divergence and velocity magnitude is predicted much better than direction in most cases. A combination of improved input fields and the need for an improved boundary layer formulation provide a means to correct some of the differences found in this comparison study. In the meantime, the methods presented here now serve as useful processing tools for analyzing and testing model modifications in a way which directly compares observed drift and deformation behavior with numerically constructed constitutive assumptions.

6.5 Chapter Summary

In summary, we again ask the questions posed at the beginning of this chapter. How do the external forces and internal ice dynamic processes affect the ice expansion and decay cycle in the Weddell Sea region? What external forces are responsible for the development of specific drift and deformation processes and how well can we simulate (and eventually predict) such events? In response to these questions we can now say that through this study we have at least identified in relative terms how external forcing and internal ice dynamics and thermodynamics affect sea ice drift, deformation, expansion and decay processes in the current models and to what degree we are able to predict and reproduce the observed events. Specifics to these conclusions are as follows.

First, sensitivity of ice models to external and internal forcing is investigated using a hierarchy of numerical models which include high (25 km) and low (100 km) resolution 1.5D and high (50 km) and low (200 km) resolution 2D cases. The results of ice edge location and thickness distribution, were compared to each other and additionally to observed ice edge locations. In these comparisons, it was found that the inclusion of a properly formulated ice rheology is critical to producing a realistic annual cycle in the Weddell Region. This is particularly important in terms of ice thickness distribution and with respect to the current trend to produce higher resolution models. As seen in Section 6.3 for example, the impact of ice interaction becomes increasingly important as finer resolution models with features like islands and detailed land boundaries are developed. Producing realistic ice edge extent is more linked to the air temperature and

atmospheric input fields.

Looking specifically at ice edge expansion, we found from this study that the expansion as reproduced in the models occurs between about days 90 and 230 (March to August). It is dominated by the air temperature at the ice edge and wind related sensible and latent heat fluxes at the storm frequencies of 5 to 8 days in the interior pack. From the sensitivity studies in Section 6.2 and the mass balance study of Section 6.3, we also find the primary source of ice production in models during the expansion is thermodynamic growth in the leads within the pack ice, secondary sources include the advection of ice into open water regions (an order of magnitude smaller regionally) and thermodynamic growth in open water cells (an additional order of magnitude less). A closer look at each of the ice production mechanisms reveals that, lead parameterization is accounted for in these models through the compactness term such that, a proper accounting of the compactness is critical for accurately reproducing ice thickness distributions within the field. There is also the issue of the development of a northeast-southwest oriented divergence associated with the ice resistance and advective processes in the models. This divergence and its orientation is resulting from the shape of the Weddell Region and, in particular, the presence and orientation of the Antarctic Peninsula. Finally, the process of thermodynamic growth at the ice edge are underestimated compared with observation, because the observed processes of frazil and pancake ice formation which naturally dominate this region are lacking in these models. Parametrization of these processes and feedback between the ocean and air to the ice should rectify this inconsistency in the models. In the meantime, the models use a process of high interior growth in leads coupled with divergent advection towards the open water regimes to expand the ice pack in winter.

During the warmer months (September to February), we found that a number of thermodynamic variables were particularly important to the ice edge retreat. Specifically, daily/subdaily thermal variations in the atmosphere, relative humidity/latent heat and ocean heat flux were identified in Sections 6.1, 6.2 and 6.3 as the sources responsible for the rapid decay of the ice pack in summer. These same processes also act as a dashpot or capacitor to retard the initial expansion phase into the next growing season. Additionally we found that the thickness distribution was much more sensitive to both dynamic and thermodynamic inputs year round than the ice edge. The major exception to this is at the northern end of the Antarctic Peninsula where we found the ice edge to be very sensitive to ocean heat flux and especially relative humidity. These relative humidity and ocean heat flux responses were also found to be critical climatological issues. On the one hand, increased ocean heat due to events like global warming can lead to increased ocean heat flux which in turn reduces the overall ice thickness with little effect to the ice edge. This type of scenario is very difficult to detect using ice edge extent as the principal monitor and can lead to catastrophic melt back once the ice becomes critically thin overall. On the other hand, an impact of increased atmospheric temperatures can lead to an overall increase in atmospheric moisture which affects the latent heat transfer from air to ice. In this scenario ice edge extent is changed considerably and is more detectable by visible inspection. Currently, both these scenarios are potential candidates in the event of global warming.

In the last Section, 2D high resolution (50 km) simulations were used to compare drift and deformation time series versus the 150 km Argos buoy array from Ice Station

Weddell 1992. Modeled ice drift and deformation both exhibit red-shift spectra with small contributions from subdaily forcing. In contrast, observed drift and deformation have significantly greater high frequency content with dominant power spikes around 12 and 24 hours. Part of the discrepancy between high frequency results in the models versus observed is attributed to the model formulation of the boundary layer which currently suppresses subdaily processes such as inertial oscillations. Reformulation of the boundary layer allows high frequency (subdaily) ice processes, which are important at the smaller scales, to evolve. In terms of correlation between the models and observations at lower frequencies, significant coherence in cross-spectral analysis is found between simulated and 30 hour low pass filter observed velocity and strain rates with shear characteristics significantly better modeled than divergence rate. In contrast to buoy drift velocity, the deformation is dependent upon the type of ice rheology assumed and significantly degrades when either free drift or a cavitating fluid sea ice model is utilized versus a full viscous-plastic pressure plus shear resistance model.

In addition to the standard rheology runs of free drift, pressure resistance and pressure plus shear resistance, simulations were carried out with a truncated elliptical rheology which more closely resembles laboratory based yield curves. Additionally, simulations were carried out for different cases of ductile versus brittle flow, ice strength, and air-ice-sea energy transfer parametrized through the drag coefficients. These simulations were run and compared to the observed ISW results in an attempt to gain insight into the constituents needed to formulate a more realistic ice rheology for use in next generation of sea ice models. From these investigations, we found that none of the rheological configurations tried completely reproduce the buoy behavior observed in the field but, the use of a rheology incorporating both pressure and shear resistance is the most realistic direction to take. With regard to sensitivity to these models, predictability of ice deformation is far more difficult to achieve than for drift and is much more sensitive in terms of response to the tuning of internal ice parameters than velocity.

One major disappointment in the attempts made in this study is that an adequate model improving both drift and deformation was not achieved. While use of increased ductility in VP models greatly improved drift statistics, modifying the drag coefficients was far more successful at improving the deformation components and a combination of these failed to produce a positive effect. The sensitivity of the different deformation terms (both directional and invariant) is such that some parameters seem to improve while others do not depending on the modifications made to the models. Overall however, shear is reproduced much better than divergence and velocity magnitude is predicted much better than direction in most cases. The most significant contribution from Section 4 in terms of improving future models, is the construction of a set of useful statistical processing tool for analyzing and testing new model modifications in a way which directly compares observed drift and deformation behavior with numerically constructed constitutive assumptions.

Chapter 7

Summary

In this thesis, the dynamic sea ice processes of drift, deformation, annual cycle expansion and decay are examined. The processes of drift and deformation have been examined using an observational deformation array, mechanistic studies and regional models, while sensitivity studies, regional mass balances, and particle analysis were used to understand the annual cycle expansion and decay processes that currently exist in ice models. A summary of these findings are as follows.

First in terms of observations, data from Ice Station Weddell during 1992 has been used to examine sea ice drift and deformation activity and to identify relevant external forces responsible for driving specific processes. Use of power spectra and deformation analysis on the large scale drift velocities together with spectra of wind and current measurements have shown that the velocity, or general drift, of the sea ice pack in the Western Weddell region is driven primarily by low frequency forcing (i.e. periods greater than one day). Contrary to this, higher frequencies, specifically diurnal and semi-diurnal tidal frequencies, appear to be the main source driving sea ice deformation in the Western Weddell Sea region. The local topography also plays a major role by inducing a directional dependence in both ice drift and deformation. The internal ice interaction seems to be particularly sensitive to such topographic influences, even more so than the underlying ocean current most likely due to non linear ice interaction and inertial oscillation activity within the ice. In terms of identifying key deformation processes, comparisons using invariant quantities provide information about the total deformation process and its components of divergence and shear. The non-invariant components also provide a considerable amount of information about contributions due to specific orientations. With regard to the statistical “fitness” of the deformation information, this study has provided insightful qualitative information about sea ice deformation but there is ample room for improving the quantitative value of these results. Two ways to improve this are through an increased number of sites and better instrumentation such as GPS.

The results of this study can also be used to identify the following important sea ice dynamic processes. First, the general drift of the sea ice pack in the Western Weddell region is a low frequency dynamic process which is driven primarily by low frequency forcing in the form of moderate but steady low frequency ocean currents and intermittent high energy storm activity from the wind. Ocean eddies are most likely acting in a similar fashion to the wind, but there is insufficient evidence from this study

to verify that. Second, deformation of the sea ice pack is composed of both low (<1 cycle/day) and high (1 cycle/day or more) frequency processes with the high frequency processes clearly dominating. The low frequency processes are strongest during and after episodes of high winds. There is also evidence that moderate but steady low frequency ocean currents must also have an effect. For this region in particular divergence is clearly a high frequency process with very little low frequency contribution. Shear has large high and low frequency components with elongation deformation being the main form of deformation at low frequencies. The high frequency processes are clearly driven by 12 and 24 hour ocean oscillations with the 12 hour peak contributing most to the total shear activity while the 24 hour peak contributes more to the solid body rotation of the ice on scales at least as large as the ISW array (150 km). These results concur with previous findings by Foldvik et al. (1990).

One impact of these results is the ability to monitor sea ice drift and deformation activity. Satellite imagery has a high spatial resolution but low temporal resolution (3 day pass average) so it can detect ice drift adequately but not deformation. Buoy arrays lack the high spatial resolution but do have high temporal resolution to record most of the ice deformation activity, especially GPS. If the Western Weddell shelf break is a good example of other similar regions, then ice forecasting requires a combination of both techniques to correctly predict ice activity, at least in regions where subdaily forcing is very strong.

Choosing the two most widely used ice models in the large-scale sea ice, ocean and climate communities to examine the modeled mechanical behavior of sea ice, this study has achieved two major goals. First, given the circumpolar configuration of Antarctic sea ice, we found that 1.5D spherical models in both the cavitating fluid rheology model (CAV) and the viscous-plastic rheology models (VP) with a Replacement Method (REP) and Truncated Ellipse (TRU) closure scheme, are the realistic for isolating and examining temporal changes in north-south growth and decay processes in the Weddell region. These models exhibit many of the features that full 2D models have but are computationally much faster and provide an excellent source for examining the temporal changes of individual north-south transects of selected regions.

The second major result of the mechanistic study is an improved understanding of simulated ice performance under a number of different idealized dynamic conditions. Working in a hierarchical fashion we have analyzed deformation processes utilizing both analytical and numerical means to achieve this goal. Beginning with the simple 1D pressure-only CAV model, we saw the impact that spherical versus Cartesian grid cell configurations have on the yielding property of ice. The results were interpreted by comparing numerical output to analytical solutions in order to understand how the numerical yielding worked. The sensitivity of yielding under a number of simple forcing conditions was also examined to determine how the simulated ice responds to conditions of ice thickness, compactness, drag relations, wind direction and numerical resolution. At higher dimensions the forces introduced due to rotation had the biggest impact on yielding due the reaction from the side walls at the 1.5D level, and at the 2D level, Cartesian and spherical solutions became nearly identical. Overall, the spherical solution changed very little from 1D to 1.5D to 2D because the spherical grid configuration provides converging side walls relative to north-south winds which allowed yielding to occur over a larger region of the grid rather than only at one end. It is for this reason that the 1.5D spherical

models were chosen over the Cartesian grid for analyzing temporal effects in the annual cycle.

In the viscous-plastic (VP) mechanistic study, the process of shear was introduced into the idealized system to examine how shear affected the yielding process. In the initial 1D cases, shear made a small contribution to the overall yielding process in Cartesian coordinates, but had an immediate impact right out to the ice edge in the spherical cases. Using both numerical and analytical results two important features were found from this VP study. First, the point of yielding at the wall is also equal to the minimum value of σ_2 at the bottom of the elliptical yield curve (greatest magnitude) which is primarily a compressive state with a small amount of shear. Second, the path taken within principal axis space to reach this yield point is dependent on the closure method and grid configuration chosen. Under wind conditions conducive to tensile stress the distinction between the Replacement method and Truncated Ellipse become most clear with the Truncated ellipse proving the most realistic in terms of large-scale dynamics. With regard to the impact of shear on the process of yielding, the spherical grid contains considerably more shear than the Cartesian grid without rotation. With rotation, both Cartesian and spherical grids exhibit yielding in the form of shear at the open boundary region (ice edge) and in 2D regions at the open boundary and in the interior. Characteristics similar to the observed distribution of fast land, pack ice, and shear zone situations were reproducible. Additionally, the presence of shear was found to contribute to a reduction in kinetic energy in the system. Finally, it was shown that shear stress was capable of producing yielding under stress situations with far less external forcing than for compressive stress systems alone.

Building on the knowledge from the mechanistic study, 2D high resolution (50 km) simulations were used to compare drift and deformation time series versus the 150 km Argos buoy array from Ice Station Weddell 1992. Modeled ice drift and deformation both exhibit red-shift spectra with small contributions from subdaily forcing. In contrast, observed drift and deformation have significantly greater high frequency content with dominant power spikes around 12 and 24 hours. Part of the discrepancy between high frequency results in the models versus observed is attributed to the model formulation of the boundary layer which currently suppresses subdaily processes such as inertial oscillations. Reformulation of the boundary layer allows high frequency (subdaily) ice processes, which are important at the smaller scales, to evolve. In terms of correlation between the models and observations at lower frequencies, significant coherence in cross-spectral analysis is found between simulated and 30 hour low pass filter observed velocity and strain rates with shear characteristics significantly better modeled than divergence rate. In contrast to buoy drift velocity, the deformation is dependent upon the type of ice rheology assumed and significantly degrades when either free drift or a cavitating fluid sea ice model is utilized versus a full viscous-plastic pressure plus shear resistance model.

In addition to the standard rheology runs of free drift, pressure resistance and pressure plus shear resistance, simulations were carried out with a truncated elliptical rheology which more closely resembles laboratory based yield curves. Additionally, simulations were carried out for different cases of ductile versus brittle flow, ice strength, and air-ice-sea energy transfer parametrized through the drag coefficients. These simulations were run and compared to the observed ISW results in an attempt to gain insight into the constituents needed to formulate a more realistic ice rheology for use in next genera-

tion of sea ice models. From these investigations, we found that none of the rheological configurations tried completely reproduce the buoy behavior observed in the field but, the use of a rheology incorporating both pressure and shear resistance is the most realistic direction to take. With regard to sensitivity to these models, predictability of ice deformation is far more difficult to achieve than for drift and is much more sensitive in terms of response to the tuning of internal ice parameters than velocity.

An adequate model statistically agreeing with both drift and deformation observations was not achieved. While use of increased ductility in VP models greatly improved drift statistics, modifying the drag coefficients was far more successful at improving the deformation components and a combination of these failed to produce a positive effect. The sensitivity of the different deformation terms (both directional and invariant) is such that some parameters seem to improve while others do not, depending on the modifications made to the models. Overall however, shear is reproduced much better than divergence and velocity magnitude is predicted much better than direction in most cases. The most significant contribution from the buoy study in terms of improving future models, is the construction of a set of useful statistical processing tool for analyzing and testing new model modifications in a way which directly compares observed drift and deformation behavior with numerically constructed constitutive assumptions.

In terms of annual cycle expansion and decay processes, sensitivity of ice models to external and internal forcing were compared to ice edge location and thickness distribution between a hierarchy of numerical models including high (25 km) and low (100 km) resolution 1.5D and high (50 km) and low (200 km) resolution 2D cases. A comparison between these results and observed ice edge locations were also made. In these comparisons, it was found that the inclusion of a properly formulated ice rheology is critical to producing a realistic annual cycle in the Weddell Region. This is particularly important in terms of ice thickness distribution and with respect to the current trend to produce higher resolution models wherein, the impact of ice interaction becomes increasingly important as finer meshes with smaller features like islands and detailed land boundaries are included. Producing realistic ice edge extent is more linked to the air temperature and atmospheric input fields.

Looking specifically at ice edge expansion, this study shows that the expansion as reproduced in the models occurs between about days 90 and 230 (March to August). It is dominated by the air temperature at the ice edge and wind related sensible and latent heat fluxes at the storm frequencies of 5 to 8 days in the interior pack. From the sensitivity and mass balance studies in Chapter 6, the study shows that, for the models, the primary source of ice production during the expansion is thermodynamic growth in leads within the pack ice, followed by advection of ice into open water regions (an order of magnitude smaller regionally) and finally thermodynamic growth in open water cells (an additional order of magnitude less). A closer look at each of the ice production mechanisms reveals that, lead parameterization is accounted for in these models through the compactness term such that, a proper accounting of the compactness is critical for accurately reproducing ice thickness distributions within the field. There is also the development of a northeast-southwest oriented divergence in the field, associated with the ice resistance and advective processes in the models. This divergence and its orientation result from the shape of the Weddell Region and, in particular, the presence and orientation of the Antarctic Peninsula. Finally, the process of thermodynamic growth

at the ice edge seems to be highly underestimated compared with observation, because the observed processes of frazil and pancake ice formation which naturally dominate this region are lacking in these models. Parametrization of these processes and feedback between the ocean and air to the ice should rectify this inconsistency in the models. In the meantime, the models use a process of high interior growth in leads coupled with divergent advection towards the open water regimes to expand the ice pack in winter.

During the warmer months (September to February), a number of thermodynamic processes were identified in relation to the ice edge retreat. Specifically, daily/subdaily thermal variations in the atmosphere, relative humidity/latent heat and ocean heat flux were identified in the numerical regional study as the sources responsible for the rapid decay of the ice pack in summer. These processes are analogous to dashpots or capacitors as they work to retard the initial expansion phase into the next growing season. Additionally, the thickness distribution was much more sensitive to both dynamic and thermodynamic inputs year round than the ice edge. The major exception to this is at the northern end of the Antarctic Peninsula where the ice edge is quite sensitive to ocean heat flux and especially relative humidity. These relative humidity and ocean heat flux responses were also found to be critical climatological issues. On the one hand, increased ocean heat due to events like global warming can lead to increased ocean heat flux which in turn reduces the overall ice thickness with little effect to the ice edge. This type of scenario is very difficult to detect using ice edge extent as the principal monitor and can lead to catastrophic melt back once the ice becomes critically thin overall. On the other hand, an impact of increased atmospheric temperatures can lead to an overall increase in atmospheric moisture which affects the latent heat transfer from air to ice. In this scenario ice edge extent is changed considerably and is more detectable by visible inspection. Currently, both these scenarios are potential candidates in the event of global warming.

Appendix A

Data Processing Tools

A series of data processing algorithms had to be developed by the author in order to analyze the ISW large scale array. This Appendix addresses the technical aspects of these algorithms including their verification test runs. The results of these methods when applied to the ISW array are described in Chapter 3 of the main text.

A.1 Estimate of Instrument Error

The Global Positioning System (GPS) used on the ice camp is supposedly accurate to within 100 meters (with active dithering) and Argos buoys to within 500 meters. Linear interpolation of raw satellite positions to hourly positions may introduce additional error. It is possible to estimate these errors by taking advantage of 2 time periods when the Argos buoys and the camp's GPS unit were stationary relative to each other. The first occurrence is in February when 4 of the buoys were actively transmitting but still sitting at the camp waiting to be deployed. The second is when two buoys were residing on the same ice floe from Julian day 116 to 154. Personal communication with the ISW personnel reveals that under both situations there was no observed intrafloe activity between the instruments (i.e. no ice ridging, lead openings or other structural changes) making these ideal conditions for conducting an error analysis.

Following linear interpolation of the data to hourly time intervals, 11 pairs of buoy-buoy and camp-buoy east-west (x) and north-south (y) distances were computed during the two stationary periods (Table A.1). In order to remove effects caused by rotation between the pairs, the radial distance ($r = \sqrt{x^2 + y^2}$) was also computed. The time series from each buoy pair for each directional distance (x , y and r) was then entered into the matrix form r_{jk} for $j = 1$ to $N = 11$ pairs and $k = 1$ to T_j times. Statistically, the time average for each pair (\bar{r}_j) should be close to the true distance ($r_{j(actual)}$) while its RMS value (Δr_j) should represent the RMS instrument error associated with each pair. In other words,

$$r_{jk} = \bar{r}_j \pm \Delta r_j \tag{A.1}$$

$$\bar{r}_j = \frac{1}{T_j} \sum_{k=1}^{T_j} r_{jk} \tag{A.2}$$

Table A.1: Instrument Pairs for Error Estimate

Pair	Instrument	Start		Stop		Total
No.	Pair	Day	Time	Day	Time	(hours)
1	Camp-1430	44	18:00	48	15:00	93
2	Camp-1431	44	18:00	61	08:00	398
3	Camp-1432	44	18:00	61	08:00	398
4	Camp-1433	44	18:00	50	13:00	139
5	1430-1431	41	20:00	48	13:00	161
6	1430-1432	41	16:00	48	17:00	169
7	1430-1433	41	15:00	48	17:00	170
8	1431-1432	41	19:00	61	07:00	468
9	1431-1433	41	19:00	50	14:00	211
10	1432-1433	41	16:00	50	13:00	213
11	1435-6440	116	11:00	154	13:00	914

$$\Delta r_j = \left[\frac{1}{T_j} \sum_{k=1}^{T_j} (r_{jk} - \bar{r}_j)^2 \right]^{\frac{1}{2}} \quad (\text{A.3})$$

$$r_{j(\text{actual})} = \bar{r}_j \pm CI(\bar{r}_j) \quad (\text{A.4})$$

$$CI(\bar{r}_j) = tVal_{\left(\frac{\alpha}{2}, T_j - 1\right)} \frac{1}{T_j} \left[\sum_{k=1}^{T_j} (r_{jk} - \bar{r}_j)^2 \right]^{\frac{1}{2}}. \quad (\text{A.5})$$

$CI(\bar{r}_j)$ is the confidence interval for the average (\bar{r}_j) and $tVal$ is the statistical t value for a 90% confidence level (α) with $T_j - 1$ degrees of freedom (see Table IV, page 679 Hines and Montgomery, 1990). We can take this one step further and estimate the RMS instrument error ($E_{(\text{actual})}$) from the average instrument errors of each pair (\bar{E}) and the variations of that average (ΔE , $CI(\bar{E})$). In other words,

$$\Delta r_j = \bar{E} \pm \Delta E \quad (\text{A.6})$$

$$\bar{E} = \frac{1}{N} \sum_{j=1}^N \Delta r_j \quad (\text{A.7})$$

$$\Delta E = \left[\frac{1}{N} \sum_{j=1}^N (\Delta r_j - \bar{E})^2 \right]^{\frac{1}{2}} \quad (\text{A.8})$$

$$E_{(\text{actual})} = \bar{E} \pm CI(\bar{E}) \quad (\text{A.9})$$

$$CI(\bar{E}) = tVal_{\left(\frac{\alpha}{2}, N - 1\right)} \frac{1}{N} \left[\sum_{j=1}^N (\Delta r_j - \bar{E})^2 \right]^{\frac{1}{2}}. \quad (\text{A.10})$$

The overall results of this analysis for the radial distance (r), shown in Table A.2, indicate that there is a 90% confidence instrument error of 0.5309 ± 0.0882 km in pair distances. For the other components (not shown in table) the average instrument error is 0.4919 ± 0.0849 km in the x direction and 0.4889 ± 0.0735 km in the y direction. Given

Table A.2: Results of Error Analysis

Estimate of Instrument Error ($r = \sqrt{x^2 + y^2}$)				
Pair No.	Average Distance (km)	90% CI of Average (km)	RMS Error (km)	RMS-Avg RMS (km)
1	0.6327	0.0118	0.4460	-0.0849
2	0.6133	0.0035	0.7497	0.2187
3	0.6416	0.0039	0.8771	0.3462
4	0.8667	0.0129	1.2093	0.6784
5	0.4242	0.0069	0.4679	-0.0630
6	0.2955	0.0060	0.3832	-0.1477
7	0.2964	0.0053	0.3096	-0.2213
8	0.4015	0.0026	0.5361	0.0051
9	0.4084	0.0048	0.3841	-0.1468
10	0.2631	0.0041	0.2776	-0.2533
11	1.5612	0.0008	0.1994	-0.3315
Average RMS Error = 0.5309 km				
90% CI of Average RMS Error = 0.0882 km				

the confidence intervals, the magnitudes for the x and y RMS errors are statistically the same, indicating no directional dependence in the error. However the sum of the squares of these two values (0.6935 km) is significantly greater than the radial error, the difference of which must be coming from rotation between the buoy pairs. According to ISW researcher Vicky Lytle (personal communication), the camp underwent a rotation of about 10 to 15° during the early period of the experiment. Since there seems to be no directional preference in the error we can use the radial error distance to estimate the non-rotational instrument error for the x and y directions respectively by $e_x = e_y = e_r/\sqrt{2} = 0.3754$ km. It is interesting to note that the largest errors occur between pairs which include the GPS unit on the Camp. This indicates that there is a significant difference between absolute positions recorded using GPS versus Argos. One reason for this difference is deliberate dithering put in for military security reasons in the GPS unit (i.e. there is noise deliberately put into the signal). This noise can be removed by those with special equipment and military access. For scientists and civilians not involved in military and classified research, this is not the case except with the use of differential GPS which was not an available technology in 1992.

A.2 FFT Power Spectra

Visual inspection of time series data on time series plots ($property(t)$ vs. t) is one way to identify dominant or unusual changes in a signal. Another way of examining this same information is to transform the data from the time domain to the frequency domain in order to view the signal as a function of frequency. In particular, the power spectral density (i.e. magnitude of the transformed quantity squared per unit frequency) provides information about the power at different frequencies. Such a determination is quite useful

in the case of the ISW strain array since we wish to know which frequencies contain the strongest signals.

The transform procedure differs depending on the type of data. For mathematically continuous data of infinite length or strictly periodical data one makes use of a Fourier transform and then directly computes the square of the magnitude of the transformed signal in the frequency domain. This is probably the most direct method; unfortunately, it only holds for the most unrealistic cases. In the case of the ISW large scale strain array, the data are discretely sampled and finite in length hence, we need to consider both of these matters.

First, let us consider transforming discretely sampled data. For a sequence of discrete points taken at regular time intervals, a fast Fourier transform (FFT) can be used to transform information from the time domain to the frequency domain. Since this is not a continuous transform it is also not an exact one because the transformation is missing information between signals. To approximate a continuous signal, the discrete signal is regarded as a series of piecewise constant square functions of finite amplitude and width equal to the magnitude of the signal and width of the sampling interval (Δt), respectively. This sequence of square functions Fourier transforms into a sequence of sinc functions, one for each frequency bin. The sinc function is composed of a main lobe, or peak signal, surrounded by a series of decreasing side lobes which extend away from the main lobe in both directions. The main lobe is centered at the frequency f_k ¹ with each frequency bin separated by Δf .

The ideally desired discrete transform is one in which the width of the main lobe, D , is made as thin as possible while the height of the side lobes, $A(db)$, are made as small as possible; in essence we desire a delta function located at each f_k in the frequency domain. Unfortunately this condition is not possible. Additionally, the extension of the side lobes makes the width of the sinc function greater than Δf resulting in an effect known as *leakage* where information destined for a specific frequency bin actually extends into neighboring bins. In order to minimize leakage and maximize the desired transform shape, a technique called *data windowing* is employed (see, for example, Oppenheim et al. 1975).

Several types of data windows are available, each of which have advantages and disadvantages in minimizing one or both of the D and A parameters. One particularly robust window type is the *Kaiser Window* which allows the user to physically select the shape of the window via a shape factor (a). The primary advantage of this window construction is that it is adjustable and therefore adaptable over a large range of applications. This window is also capable of reproducing many of the other standard window types such as the Hamming, Blackman, and Square windows (Hamming, 1989) making it a robust general purpose window function.

The Kaiser window in the time domain is equal to (from equation 9.3-1 in Hamming, 1989)

$$w(n) = \begin{cases} \frac{I_0\left(a \sqrt{1 - \left[\frac{n}{N}\right]^2}\right)}{I_0(a)}, & |n| \leq N \\ 0, & |n| > N \end{cases} \quad (\text{A.11})$$

¹ k is the number of the frequency bin for $k = 1$ to K total bins

where N is the total number of discrete data points for $n = 1$ to N and I_0 is the zeroth order Bessel function of the argument specified in parenthesis. The window function is applied by multiplying the window function by the time series data and then FFT'ing their product into the frequency domain where the signal is now concentrated into specific frequencies with selectively minimal leakage between frequency bins and minimal side effects due to the windowing function.

Typical values for the shape function (a) range between 0 and 11 which varies as a function of main lobe width (D) and side lobe height (A). A small a produces small side lobes (A small) and a wide main lobe (large D) while a large a value produces shapes with characteristics opposite of this (i.e. A large and D small). Examples of Kaiser windows in the time domain for different values of a are shown in the upper image of Figure A.1. Notice in this figure that a shape factor of $a = 0$ makes the classic square window, while an intermediate value of 5 produces closer to a Hamming window. An initial investigation of the range of a values using the ISW buoy velocity data shows that the more moderate values near $a = 5$ produce the best balance between modest side lobe height and relatively centralized main lobes. The value of $a = 5.4414$ was chosen for the final analysis of the ISW data as this matches the standard Hamming window.

Let us now consider the problem of frequency resolution for finite and discrete data. There are three major constraints associated with such data. First, the width of the frequency bins, Δf , is inversely proportional to the length of the time sampled record, T . Second, the time sampling interval, Δt , determines the total range of frequencies, F . Third, the frequencies to be resolved cannot exceed the Nyquist frequency ($f_c = 1/2\Delta t$). In other words, the resolution of the power spectrum we wish to produce is directly related to the length of the sampled time series while the overall range of calculable frequencies is directly related to the sampling interval of that data. For the ISW data set, we are bound by a set of data which is sampled on average every 3 hours and extends about 3000 hours in length. We are specifically interested in frequencies from the sampling rate down to frequencies on the order of mesoscale meteorological events. Given these constraints we can examine frequencies as high as the Nyquist frequency of 4 cycles/day (6 hour periods) and low frequencies on the order of 1/5 cycles/day (5 day periods) or so which is the frequency of atmospheric storm activity. A minimum of 32 bins is needed to achieve this range, given that for the FFT algorithm used here, the number of bins has to be a power of 2.

Some important nomenclature to consider at this point is as follows. The total power of a time signal is the integral over the quantity squared over all times. Since for most signals this quantity diverges, and moreover, one has only a finite stretch of signal over the time interval, T , it is customary to divide the integrated power by T to obtain the power per unit time, which can be identified with the term *mean squared amplitude*. In this thesis, power stands for power per unit time, and the power spectral density is actually a power per unit frequency per unit time.

In deciding on the number of frequency bins, it is necessary to consider one additional statistical difficulty associated with finite data sets. One finite time series is one sample from an infinitely long time series of the true situation being investigated (i.e. a sample from an entire population). Since it is only a sample, the resultant power spectrum is only one probable estimate of the true power spectrum for that system. In order

to have a power spectrum which is more representative of the true situation, replicate samples under the same conditions need to be taken. Since time series data rarely have the luxury of being collected in a replicate manner, increased confidence in the resultant power spectra can be achieved by transforming subsets or segments of the time series data (i.e. perform κ separate FFT transforms). The generated power spectra is then summed and normalized relative to the number (κ) of periodograms (transformed segments) and the windowing function. The main advantage of subdividing the data in this fashion is to increase the probability that the estimated power amplitude is close to the true value. The main drawback is that this partitioning reduces the number of frequencies which can be resolved.

A robust power spectrum algorithm which deals with all of the concerns expressed above has been constructed by Press et al. (1992) and used here with some modification. In addition to the inclusion of data windows, multiple periodograms, and restraint between the Nyquist frequency ($-f_c$ to f_c), this algorithm uses an overlapping scheme to increase the number of periodograms by a factor of 2 (i.e. for no overlap $\kappa = \frac{N}{4*M}$ and with overlap $\kappa = \frac{\frac{N}{2}-1}{M}$ where N = number of total data and M = number of desired frequencies). For the ISW data two values have been chosen for M , 64 and 128, and plotted as a function of frequency (cycles/day). With 64 bins we get a little more than 7 periodograms per time series while we get around 3 periodograms for 128 bins for a sampling rate of 3 hours over a 3000 hour time series. This yields a sampled time series of about 1000 points which is padded with zeros at the end to reach the next power of 2 for a total of 1024 points. The advantage of the 64 bins is a better estimate of the true amplitude while the 128 bins have greater resolution on the number of frequencies. Therefore plots of both bin sizes let us see the case of higher frequency resolution versus higher amplitude accuracy for comparison.

Modifications to the Press et al. algorithm include the use of a Kaiser window instead of those prescribed by the program, a special modification for reading two input variables (u and v), adjustment to the power spectrum calculation to add the power of the two variables, and normalizing per band width (Δf) to obtain the power spectral density. Output of the normalized power spectra density is computed as both a function of frequency (in cycles/day) and period (in hours/cycle) for physical interpretation. The images in Figure (A.1) serves as a verification for the code by showing the resultant power spectra of an input white noise velocity signal ² in the time domain which should, theoretically, transform to a square function in the frequency domain. As seen in Figure(A.1), the algorithm reproduces the proper square function regardless of the value of the shape function. The effect of the shape function is seen in the lower figure for this normalized case. For large values of (a) the power at each bin is large (approaching 1) while for smaller values the amplitude is smaller. This is caused from the width of the main lobe which is high and narrow for large numbers and, low and wide for low numbers.

²Test sinc function input velocity $U = A \frac{\sin(\lambda k)}{\lambda k}$ where amplitude $A = 30$, $\lambda = \pi$ and $k = -(\frac{K}{2})$ to $(\frac{K}{2})$ for K =total length of time series = 2562 hours. Numerical values were chosen for convenience of illustration.

A.2.1 Rotary Spectra

Rotary spectra was developed from the principles of optics (Born and Wolf, 1975; Hecht, 1988; Dr. Eric Hansen, personal communication) from the fact that a planar oscillation can not only be described by a two component orthonormal (unit) vector such as \hat{x} , \hat{y} , but also in terms of two rotational directions (Hecht, 1988), dextrorotatory (right turning or clockwise) and levorotatory (left turning or counterclockwise) which also form an orthonormal vector. The unit vectors \hat{x} , \hat{y} can also be written as the basis vectors

$$\hat{x} \equiv \begin{bmatrix} 1 \\ 0 \end{bmatrix} \quad (\text{A.12})$$

$$\hat{y} \equiv \begin{bmatrix} 0 \\ 1 \end{bmatrix}. \quad (\text{A.13})$$

The relationship between these and the rotary basis vectors is

$$\begin{bmatrix} 1 \\ 0 \end{bmatrix} = \frac{1}{2} \begin{bmatrix} 1 \\ i \end{bmatrix} + \frac{1}{2} \begin{bmatrix} 1 \\ -i \end{bmatrix} = \frac{1}{\sqrt{2}} \hat{L} + \frac{1}{\sqrt{2}} \hat{R} \quad (\text{A.14})$$

$$\begin{bmatrix} 0 \\ 1 \end{bmatrix} = \frac{-i}{2} \begin{bmatrix} 1 \\ i \end{bmatrix} + \frac{i}{2} \begin{bmatrix} 1 \\ -i \end{bmatrix} = \frac{-i}{\sqrt{2}} \hat{L} + \frac{i}{\sqrt{2}} \hat{R} \quad (\text{A.15})$$

where

$$\hat{L} \equiv \frac{1}{\sqrt{2}} \begin{bmatrix} 1 \\ i \end{bmatrix} \quad (\text{A.16})$$

$$\hat{R} \equiv \frac{1}{\sqrt{2}} \begin{bmatrix} 1 \\ -i \end{bmatrix} \quad (\text{A.17})$$

such that \hat{L} , \hat{R} are respectively the right turning and left turning unit vectors in rotary space.

The relationship between velocity components described using \hat{x} , \hat{y} and \hat{L} , \hat{R} is

$$\vec{v} = u\hat{x} + v\hat{y} \quad (\text{A.18})$$

$$u[t]\hat{x} = \frac{1}{\sqrt{2}} u[t](\hat{L} + \hat{R}) \quad (\text{A.19})$$

$$v[t]\hat{y} = \frac{-i}{\sqrt{2}} v[t](\hat{L} - \hat{R}). \quad (\text{A.20})$$

Because the unit vectors are not a function of time $[t]$, this relationship also holds in the frequency $[\omega]$ domain such that

$$U[\omega]\hat{x} = \frac{1}{\sqrt{2}} U[\omega](\hat{L} + \hat{R}) \quad (\text{A.21})$$

$$V[\omega]\hat{y} = \frac{-i}{\sqrt{2}} V[\omega](\hat{L} - \hat{R}). \quad (\text{A.22})$$

Combining the two components in the frequency domain we get

$$U[\omega]\hat{x} + V[\omega]\hat{y} = \frac{1}{\sqrt{2}}(U[\omega] - iV[\omega])\hat{L} + \frac{1}{\sqrt{2}}(U[\omega] + iV[\omega])\hat{R} \quad (\text{A.23})$$

$$= L[\omega]\hat{L} + R[\omega]\hat{R} \quad (\text{A.24})$$

and so the power of the rotary spectra becomes

$$|L[\omega]|^2 = \frac{1}{2} |U[\omega] - iV[\omega]|^2 \quad (\text{A.25})$$

$$|R[\omega]|^2 = \frac{1}{2} |U[\omega] + iV[\omega]|^2. \quad (\text{A.26})$$

A result of the Fourier Transform from the time domain to the frequency domain is that

$$u[t] = u_R[t] \iff U[\omega] = U_R[\omega] + iU_I[\omega] \quad (\text{A.27})$$

$$v[t] = v_R[t] \iff V[\omega] = V_R[\omega] + iV_I[\omega] \quad (\text{A.28})$$

where subscripts R and I refer to real and imaginary components such that the power spectral components, in Section A.2 are

$$|U[\omega]|^2 = |U_R + iU_I|^2 = U_R^2 + U_I^2 \quad (\text{A.29})$$

$$|V[\omega]|^2 = |V_R + iV_I|^2 = V_R^2 + V_I^2. \quad (\text{A.30})$$

So it is simply a matter of recombining the real and imaginary components of each of these to get the rotary spectral components $|L[\omega]|^2, |R[\omega]|^2$ which are

$$|L[\omega]|^2 = \frac{1}{2}(U_R^2 + U_I^2) + \frac{1}{2}(V_R^2 + V_I^2) + (U_R V_I - U_I V_R) \quad (\text{A.31})$$

$$|R[\omega]|^2 = \frac{1}{2}(U_R^2 + U_I^2) + \frac{1}{2}(V_R^2 + V_I^2) - (U_R V_I - U_I V_R). \quad (\text{A.32})$$

A test of the algorithm is shown in Figure (A.2) for both the left and right rotating cases.

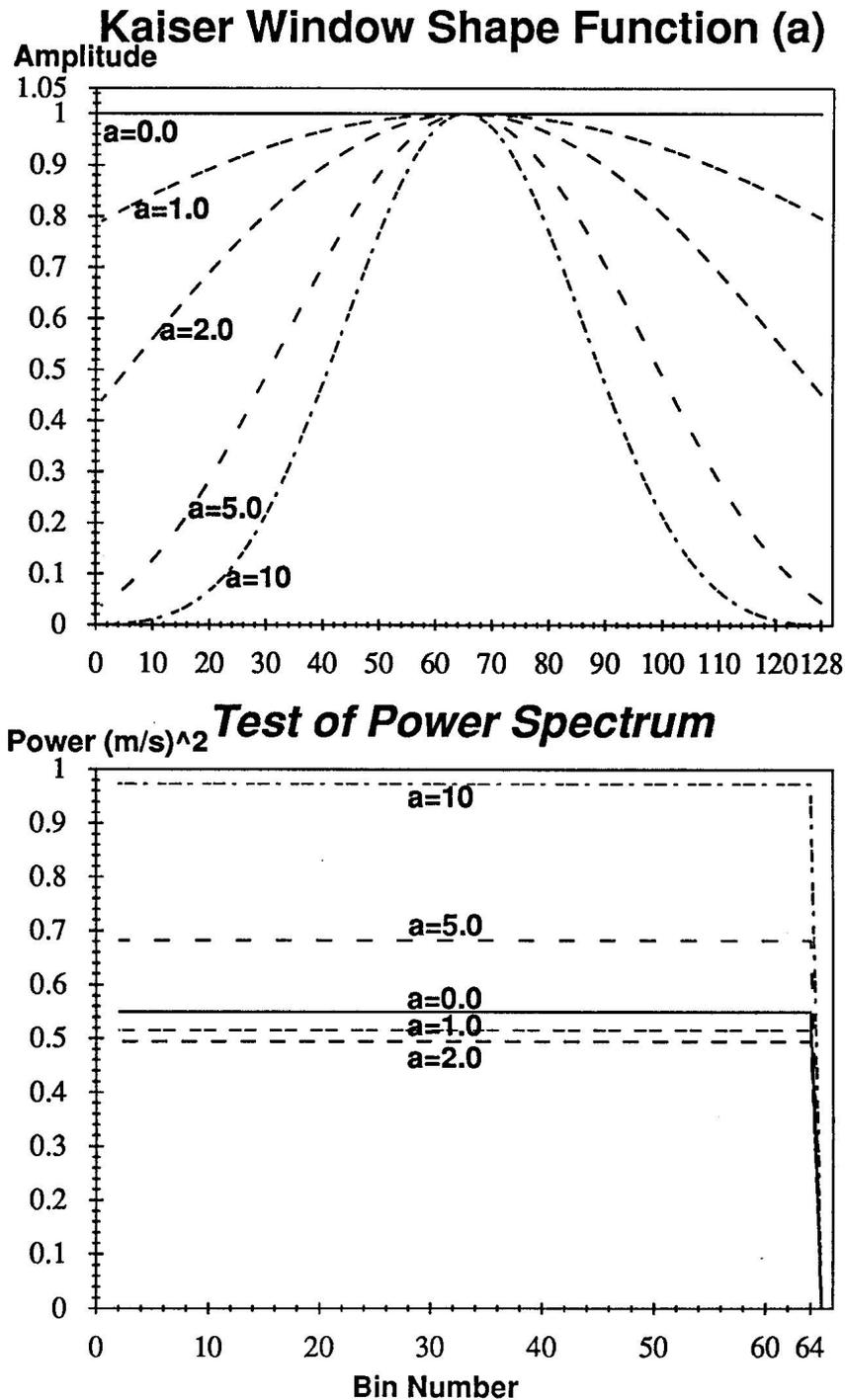
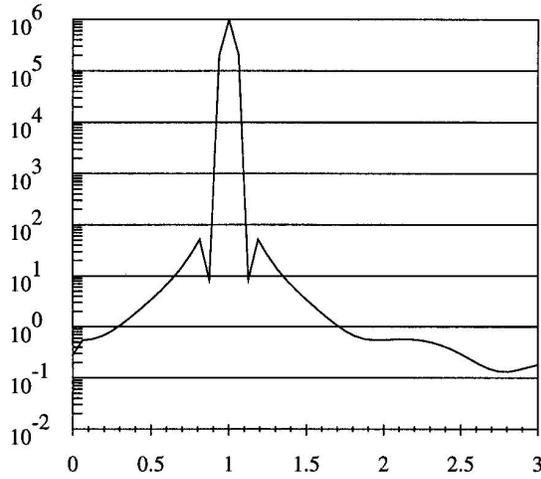


Figure A.1: Test results for power spectrum algorithm. The upper image shows the shape of the Kaiser windows in the time domain for a range of shape function values (a). The lower image shows the results of test runs using white noise (sinc function) as the input time signal.

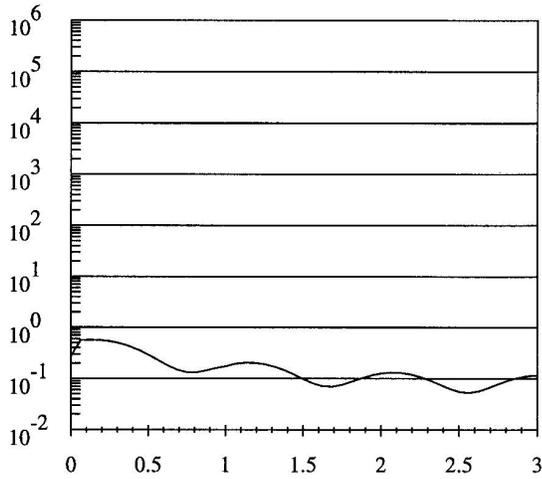
Test of Rotary Spectra Algorithm

Left Turning Case

Power Density (Left)

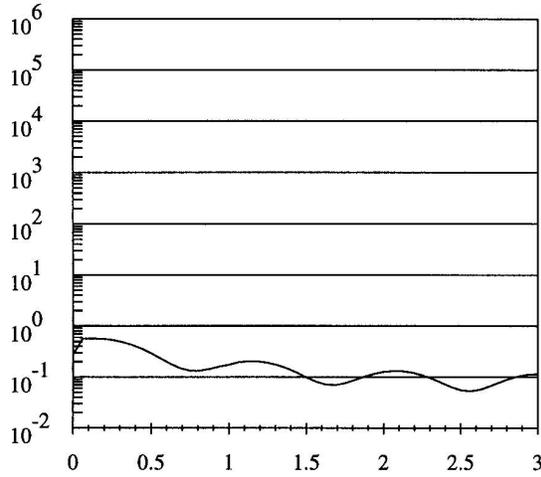


Power Density (Right)

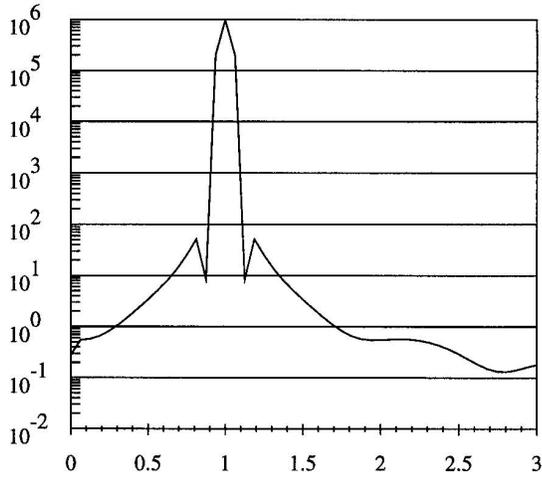


Right Turning Case

Power Density (Left)



Power Density (Right)



Frequency(cycles/day)

Frequency(cycles/day)

Figure A.2: Test results for rotary spectrum algorithm. Upper images show the spectra for left turning function $U = \cos[\frac{2\pi t(\text{hrs})}{24(\text{hrs})}]$, $V = \sin[\frac{2\pi t(\text{hrs})}{24(\text{hrs})}]$. Lower images show results for right turning function $U = \cos[\frac{2\pi t(\text{hrs})}{24(\text{hrs})}]$, $V = -\sin[\frac{2\pi t(\text{hrs})}{24(\text{hrs})}]$.

A.3 Low Pass Filter (LPF)

In order to remove measurement error and other high frequency signatures a squared four-pole Butterworth low pass filter was designed to filter out high frequencies in the buoy time series. The filter was designed using the principles described by Roberts et al. (1978) and technical notes received from Researcher Brian Farrelly while at the University of Bergen (for additional reference see also Oppenheim et al. 1975).

The Butterworth filter for discrete systems is the squared transfer function

$$|H_B(j\omega)|^2 = \left[1 + \frac{\tan(\frac{\omega T}{2})}{\tan(\frac{\omega_c T}{2})}\right]^{2n} \quad (\text{A.33})$$

where j is the complex value $\sqrt{-1}$, ω_c is the cutoff frequency (T_c is the cutoff period), T is the discrete sampling interval and n is the number of poles in the complex plane located at the polar coordinate angles $\pm\theta_1$ and $\pm\theta_2$ (described below). A Z transform allows us to produce the discrete filtered signal (y_k) for any given time (k) through the two step recursive formula

$$y_k^{(1)} = b_1 (x_k^{(1)} + 2x_{k-1}^{(1)} + x_{k-2}^{(1)}) - (a_{11}y_{k-1}^{(1)} + a_{12}y_{k-2}^{(1)}) \quad (\text{A.34})$$

$$y_k^{(2)} = b_2 (x_k^{(2)} + 2x_{k-1}^{(2)} + x_{k-2}^{(2)}) - (a_{21}y_{k-1}^{(2)} + a_{22}y_{k-2}^{(2)}) \quad (\text{A.35})$$

where $x_k^{(1)}$, $x_{k-1}^{(1)}$, $x_{k-2}^{(1)}$ are the initial input signals at times k , $k-1$, and $k-2$; $y_k^{(1)}$ is the output from the first half of the filter; $x_k^{(2)}$, $x_{k-1}^{(2)}$, $x_{k-2}^{(2)}$ are the inputs to the second half of the filter (output results from the first half - see below); and $y_k^{(2)}$ is the output from the second half of the filter. The a and b coefficients are results from the Z transform of the filter (see Roberts et al., 1978) which are equal to

$$b_i = \frac{\hat{\omega}_c^2}{1 + 2\hat{\omega}_c \cos\theta_i + \hat{\omega}_c^2} \quad (\text{A.36})$$

$$a_{i1} = \frac{-2 + 2\hat{\omega}_c^2}{1 + 2\hat{\omega}_c \cos\theta_i + \hat{\omega}_c^2} \quad (\text{A.37})$$

$$a_{i2} = \frac{1 - 2\hat{\omega}_c \cos\theta_i + \hat{\omega}_c^2}{1 + 2\hat{\omega}_c \cos\theta_i + \hat{\omega}_c^2} \quad (\text{for } i = 1, 2), \quad (\text{A.38})$$

where

$$\hat{\omega}_c = \tan\left(\frac{\omega_c T}{2}\right) \quad (\text{A.39})$$

$$\omega_c = \frac{2\pi}{T_c} \quad (\text{A.40})$$

$$\theta_1 = \frac{\pi}{8} \quad (\text{A.41})$$

$$\theta_2 = \frac{3\pi}{8} \quad (\text{A.42})$$

The recursive nature of this setup produces an unwanted phase shift in the output signal which can be removed by running the filters over a time series of length K (i.e. time length $\{k\} = 1, 2, 3, \dots, K$) in the following sequence:

1. Run entire original signal through Eq. (A.34)
2. Run the output signal of Eq. (A.34) through Eq. (A.34) backwards (i.e. $y_k^{(1)}$ for $k = 1$ to $K \Rightarrow x_k^{(1)}$ for $k = K$ to $1 \Rightarrow$ Eq. (A.34))
3. Invert the time sequence of this output back to forward (i.e. $k = 1$ to K)
4. Run the output from step 3, now the new input signal, through equation (A.35)
5. Run the output signal of equation (A.35) back through equation (A.35) backwards (i.e. $y_k^{(2)}$ for $k = 1$ to $K \Rightarrow x_k^{(2)}$ for $k = K$ to $1 \Rightarrow$ equation (A.35))
6. Invert the time sequence of this final output (back to forward as $k = 1$ to K).

To minimize high frequency signals, this LPF method must be passed over the hourly positions (latitude and longitude) prior to computing relative distances and velocities. The resultant velocity from test runs with actual hourly data versus 3 hour and 7 hour LPF'ed data are shown in Figure (A.3). Since this is a three point recursive system the first and last two positions are lost, but this is a relatively minimal loss of data.

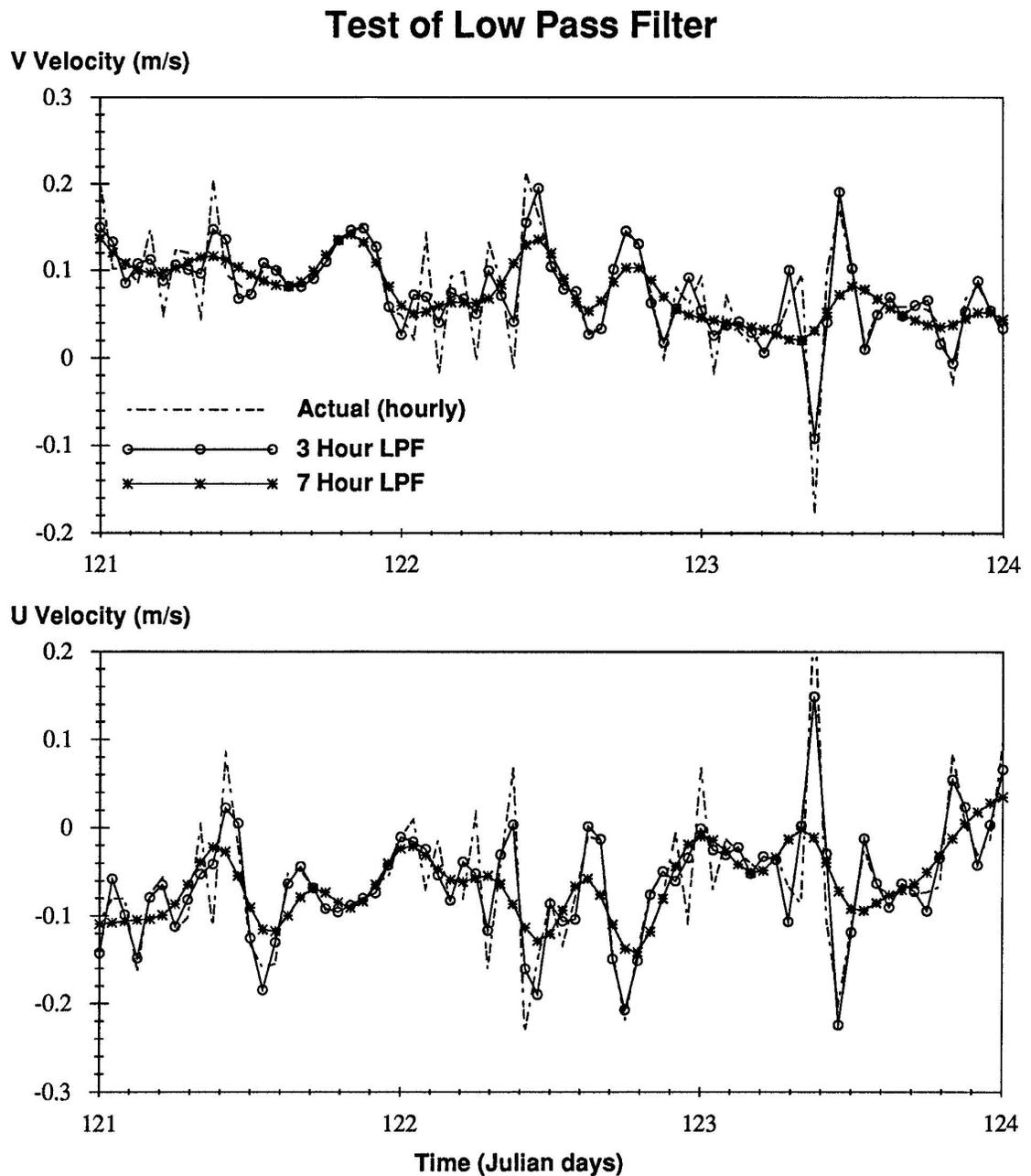


Figure A.3: Example output from test results of low pass filter runs on the linearly interpolated hourly time series from site Alex (1430). The velocities shown are a result of the LPF run over the position data prior to computing the velocity.

A.4 Ice Deformation using Multiple Regression

Two sets of variables, position [$\vec{x} = (x, y)$] and velocity [$\vec{v} = (u, v)$], can be obtained from buoy data. From these, we can determine the translation and deformation of the local ice field using the following method developed by Hibler et al. (1974) and modified for this study.

Consider the components of velocity (u_i, v_i) from observation site i at the position (x_i, y_i) relative to a co-moving reference velocity (u_0, v_0) at (x_0, y_0) . The relationship between the co-moving reference point and site i can be described mathematically using the following two dimensional Taylor expansion,

$$u_i = u_0 + \left(\frac{\partial u}{\partial x}\right) \Delta x_i + \left(\frac{\partial u}{\partial y}\right) \Delta y_i + Err_{u_i} \quad (\text{A.43})$$

$$v_i = v_0 + \left(\frac{\partial v}{\partial x}\right) \Delta x_i + \left(\frac{\partial v}{\partial y}\right) \Delta y_i + Err_{v_i} \quad (\text{for } i = 1 \text{ to } N). \quad (\text{A.44})$$

N is the number of measured sites at any given time in the field (in this case $N =$ number of buoys including the camp), $\Delta x_i = x_i - x_0$, $\Delta y_i = y_i - y_0$, and Err_{u_i}, Err_{v_i} are the truncation errors for each expansion. The co-moving reference is the geometric center of the array determined by

$$x_0 = \frac{1}{N} \sum_{j=1}^N x_j \quad (\text{A.45})$$

$$y_0 = \frac{1}{N} \sum_{j=1}^N y_j. \quad (\text{A.46})$$

The first order derivatives are also the elements of the linear deformation tensor from which the four differential kinematic parameters (*DKPs*) can be described as follows.

$$\text{Divergence} = D = \frac{\partial u}{\partial x} + \frac{\partial v}{\partial y} \quad (\text{A.47})$$

$$\text{Normal Deformation} = N = \frac{\partial u}{\partial x} - \frac{\partial v}{\partial y} \quad (\text{A.48})$$

$$\text{Shear Deformation} = S = \frac{\partial v}{\partial x} + \frac{\partial u}{\partial y} \quad (\text{A.49})$$

$$\text{Vorticity} = V = \frac{\partial v}{\partial x} - \frac{\partial u}{\partial y}. \quad (\text{A.50})$$

Packing the system of Eqs. (A.43) and (A.44) into the form shown below, we can use a linear multiple regression method to solve for the needed differential terms and the co-moving reference velocities (i.e. the translation of the system) using the known quantities of u, v, x , and y .³ This yields the equation

$$Z_{in} = X_{ij} \beta_{jn} + Err_{in} \quad (\text{A.51})$$

³Note: Indicial notation used here, repeated indices sum.

for $i = 1$ to N (Number of buoy sites)
 $j = 1, 2, 3$ (Number of β 's for each velocity component)
 $n = 1, 2$ (Number of velocity components $\Rightarrow u, v$),

where

$$Z_{i1} \Rightarrow \{u_1, u_2, \dots, u_N\} \quad (\text{A.52})$$

$$Z_{i2} \Rightarrow \{v_1, v_2, \dots, v_N\} \quad (\text{A.53})$$

$$X_{ij} \Rightarrow \begin{Bmatrix} 1 & \Delta x_1 & \Delta y_1 \\ 1 & \Delta x_2 & \Delta y_2 \\ \vdots & \vdots & \vdots \\ 1 & \Delta x_N & \Delta y_N \end{Bmatrix} \quad (\text{A.54})$$

$$\beta_{j1} \Rightarrow \left\{ u_0, \frac{\partial u}{\partial x}, \frac{\partial u}{\partial y} \right\} \quad (\text{A.55})$$

$$\beta_{j2} \Rightarrow \left\{ v_0, \frac{\partial v}{\partial x}, \frac{\partial v}{\partial y} \right\} \quad (\text{A.56})$$

$$Err_{i1} \Rightarrow \{error_{u_1}, error_{u_2}, \dots, error_{u_N}\} \quad (\text{A.57})$$

$$Err_{i2} \Rightarrow \{error_{v_1}, error_{v_2}, \dots, error_{v_N}\}. \quad (\text{A.58})$$

The unknown set of j by n parameters in the β_{jn} matrix can be solved by the multiple regression approximation (Hines and Montgomery, 1990- Chapter 15)

$$\hat{\beta}_{jn} = (X_{ji} X_{ij})^{-1} X_{ji} Z_{in} \quad (\text{A.59})$$

where X_{ji} is the transpose of the X_{ij} matrix and $\hat{\beta}_{jn}$ are the least squares best fit solutions for each β_{jn} term. Two additional calculations allow us to determine how well this regression model fits the data. First, an estimate of the truncation error (Err_{in}) can be determined by computing the difference between the actual data and the regression results using Eq. (A.60). Second, a confidence interval associated with the $\hat{\beta}_{jn}$ term can be determined using equation (A.62):

$$Err_{in} = Z_{in} - \hat{Z}_{in} \quad (\text{A.60})$$

$$\text{where: } \hat{Z}_{in} = X_{ij} \hat{\beta}_{jn} \quad (\text{A.61})$$

$$\beta_{jn} = \hat{\beta}_{jn} \pm CI_{jn} \quad (\text{A.62})$$

The truncation error is a measure of the difference between the estimated linear values (\hat{Z}_{in}) and the true values (Z_{in}). Their differences must account for influences not associated with the linear model. Two of the most likely and dominant influences responsible for these differences are 1) non-linear strains and 2) measurement errors. Since the sum of both of these must be less than or equal to the total truncation error estimate, the measurement error must be less than the truncation error for the model to be believable. As can be seen in Chapter 3, we use this argument to identify a reasonable Low Pass Filter cut-off time that has minimal measurement error effect.

In Eq. (A.62), CI_{jn} is used to establish a range within which the true values of β_{jn} should be. We would like this value to be as small as possible. This is formally referred to as the confidence interval which can be determined using the following procedure:

1. Calculate the Variance between Z_{in} and \hat{Z}_{in} ,

$$Var_n = \frac{1}{DoF} \sum_{i=1}^N (Z_{in} - \hat{Z}_{in})^2 \quad (A.63)$$

$$\begin{aligned} DoF &= 2N - (\text{number of } \beta \text{ terms} + 1) \\ &= \text{Degrees of Freedom} \end{aligned} \quad (A.64)$$

2. Calculate CI for each β parameter

$$CI_{jn} = tVal_{(\frac{\alpha}{2}, DoF)} \sqrt{(Var_n) (C_{jj})} \quad (A.65)$$

$$C_{jj} = \text{Main diagonal of matrix } (X_{ji} X_{ij})^{-1} \quad (A.66)$$

$$\begin{aligned} tVal &= t \text{ value at a specified confidence} \\ &\quad (\text{table IV, pg 679 Hines and Montgomery, 1990}) \end{aligned}$$

$$\alpha \Rightarrow (1 - \alpha)100 = \text{percent confidence}$$

Another statistical indicator is the standard deviation, which depends more on the number of sites. This is defined by

$$SD_{jn} = \sqrt{(Var_n) (C_{jj}) / (N - 1)}. \quad (A.67)$$

The standard deviation is roughly equivalent to the 68% confidence interval. In estimating errors for the strain data in Chapter 3, this statistic will be used.

To ensure that the numerical coding of this multiple regression method is functioning properly, a test case was run with the co-moving reference set at the camp (which is near the center of the array). This test uses both positions and velocities from the distant buoys but only the position from the camp (x_0, y_0). The relative distances of the buoys from the camp, at any given time, were used to determine the $\Delta x_i, \Delta y_i$ values for the X_{ij} matrix while the buoys' low pass filter velocities were put into the Z_{in} matrix. The resultant $\hat{\beta}_{jn}$ matrix includes the deformation tensor for the region near the camp and, more important to this test run, the camp's velocity as estimated by the multiple regression. The camp velocity calculated using this method was compared to the camp's low pass filter velocity to verify the code. A test case using four buoys with a 7 hour low pass filter (Figure A.4) shows that the velocities correspond quite well hence verifying the code.

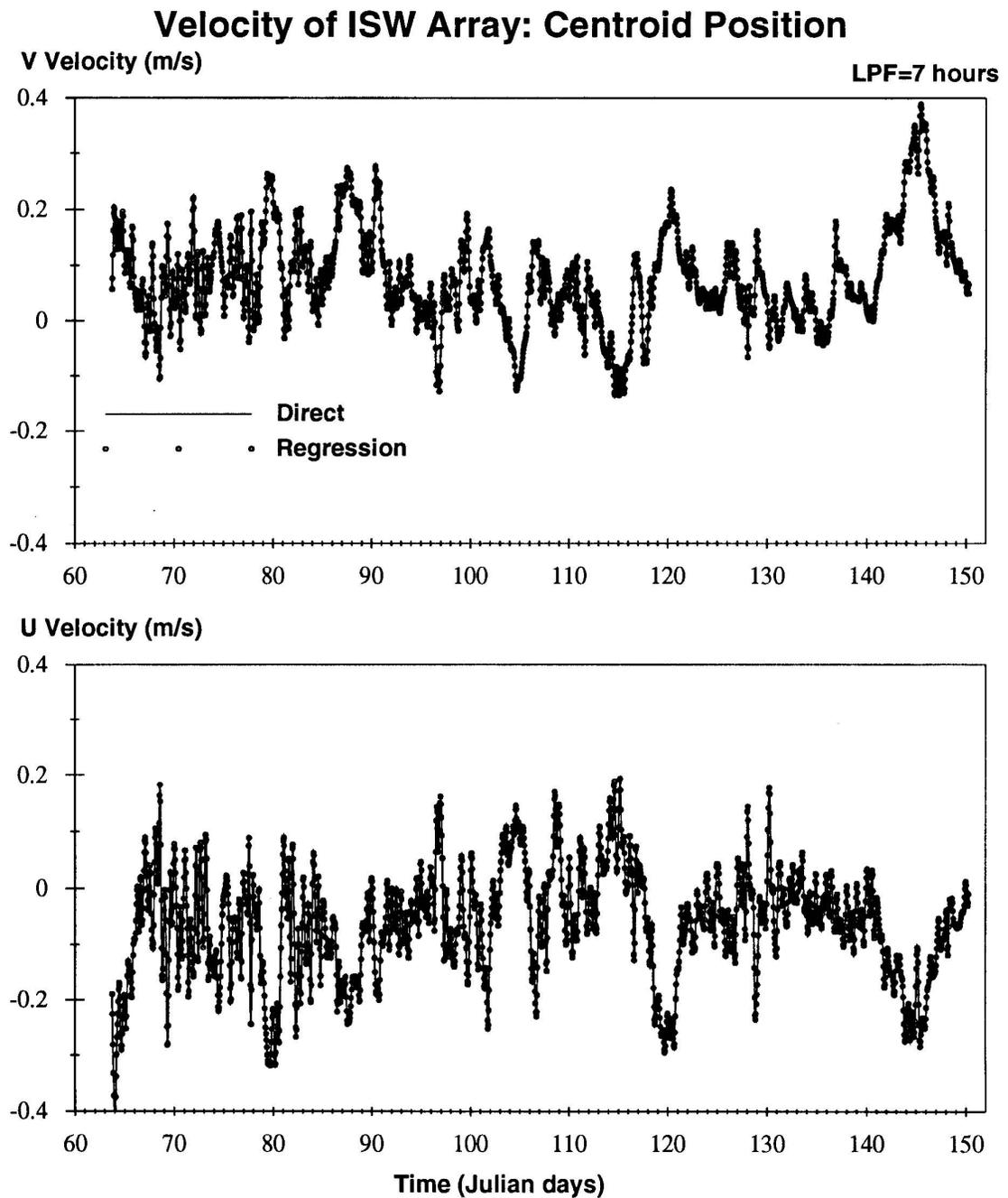


Figure A.4: Test results from the multiple regression strain algorithm using sites Alex (1430), Brent (1431), Dimitri (1432), Ed (1433) and the camp (1400) after being subjected to 7 hour low pass filtering. The camp velocity is calculated from the regression and compared here with 7 hour low pass filter camp velocity.

Appendix B

Statistical Methods for Comparison

In addition to the data processing tools developed for Chapter 3, four types of statistical analysis are used to compare modeled versus observed results in Chapter 6.4. These include probability density distribution, chi-square (χ^2) analysis, correlation coefficient, and cross-spectral density function. A brief overview of each of these functions is provided below with additional information found, for example, in Bendat and Piersol (1971) and Hines and Montgomery (1990).

B.1 Probability Density Distribution

The probability density distribution is computed by sorting a data series into normalized probability categories. To illustrate this method consider the time series of velocity magnitude with values ranging from 0 to 20 km/day. Subdividing this range into categories of 1 km/day intervals (0 to 0.99, 1 to 1.99, 2 to 2.99,...) creates 20 slots wherein any data value may reside. Keeping track of the number of data which fall into each category we can sort the data by category and normalize these categories relative to the total length of the data set. Plotting these normalized counted values against their respective category provides a useful geometric interpretation of how the data are sorted. Since the data are a sample of what is really going on in the total population, this information is referred to as a probability distribution. By normalizing the data (dividing by the total number) it is possible to compare data sets of different lengths by examining them on a common normalized scale (i.e. probability density distribution).

B.2 Chi-Square Analysis

χ^2 analysis between the modeled and observed probability density distribution allow us to determine how well the model distribution matches the observed. The χ^2 value for each category of the probability density distribution (χ_k^2) is

$$\chi_k^2 = \frac{(M_k - O_k)^2}{O_k} \quad (\text{B.1})$$

where M_k and O_k are the probability density distributions from the model results (M) and observations (O) in category k , respectively. The total χ^2 is the sum of each (χ_k^2) component for $k = 1$ to N categories. Individual (χ_k^2) components and the resulting total are used in this study to provide information about the “goodness of fit” for each category and the overall result.

B.3 Correlation Coefficient

The correlation coefficient is another statistical method which determines how well two data sets compare in time. This is computed for discrete systems using the estimator (repeated indices do NOT indicate sum here!!)

$$\hat{\rho}_{ij}[\tau] = \frac{\hat{R}_{ij}[\tau]}{\sqrt{\hat{R}_{ii}[0]}\sqrt{\hat{R}_{jj}[0]}} \quad (\text{B.2})$$

$$\hat{R}_{ij}[\tau] = \frac{1}{N-r} \sum_{n=1}^{N-r} (x_{i,n} - \bar{x}_i)(x_{j,n+r} - \bar{x}_j) \quad (\text{B.3})$$

$$\bar{x}_i = \frac{1}{N} \sum_{n=1}^N x_{i,n}. \quad (\text{B.4})$$

For discrete data $\hat{R}_{ij}[\tau]$ is an estimate of the covariance while $\sqrt{\hat{R}_{ii}}$ and $\sqrt{\hat{R}_{jj}}$ are the discrete standard deviations for the two time series each with N data points. $x_{i,n}$ is the n th data point of variable x from time series i and \bar{x}_i is the mean for that time series. This method can be used to compare one series at any point relative to the other with τ being the offset time or time lag ($\tau = r\Delta t$) between the two series; $r = 0, 1, 2, 3, \dots, m$ being the phase lag number and m being the total number of phase lags in each time direction. $\hat{R}_{ii}[0]$ is the autocorrelation of a time series without any time lag (i.e. $\tau = 0$). The correlation coefficient can be plotted versus the lag time to form a cross-correlogram with correlations ranging from -1 to 1. The inclusion of the mean is optional depending on the type of analysis performed. For the analysis here the mean is included unless otherwise specified.

B.3.1 Correlation of Max Shear

Since Max Shear is a positive definite quantity, the formulation above works fine for the magnitude of Max Shear but does not tell us about the correlation in absolute terms. The following method allows us to compute the correlation of Max Shear in absolute terms.

Using Eq. (3.17) from the Discussion section of the Observations we find that the total strain-rate power equals

$$(\dot{\epsilon}_{ij})^2 = \frac{DV^2 + ND^2 + SD^2}{2} \quad (\text{B.5})$$

$$= \frac{DV^2}{2} + 2(\text{Max Shear})^2 \quad (\text{B.6})$$

Solving for Max Shear using this and the strain-rate tensor in coordinate specific terms we get

$$(\text{Max Shear})^2 = \frac{(\dot{e}_{ij})^2}{2} - \frac{\dot{e}_{ii}\dot{e}_{jj}}{4}. \quad (\text{B.7})$$

Both quantities on the right hand side are invariant (total strain-rate and divergence). Furthermore terms like $(\dot{e}_{ij}^m)(\dot{e}_{ij}^o)$ are also invariant provided that the tensors represented by matrix superscript m and superscript o are both in the same coordinate system. Designating m for model and o for observed we can form the following invariant correlation of Max Shear

$$\hat{R}_{mo}[\tau] = \frac{\dot{e}_{ij}^m[\tau]\dot{e}_{ij}^o[\tau]}{2} - \frac{\dot{e}_{ii}^m[\tau]\dot{e}_{jj}^o[\tau]}{4} \quad (\text{B.8})$$

where

$$\dot{e}_{ij}^m\dot{e}_{ij}^o = \dot{e}_{11}^m\dot{e}_{11}^o + \dot{e}_{22}^m\dot{e}_{22}^o + 2\dot{e}_{12}^m\dot{e}_{12}^o \quad (\text{B.9})$$

$$\dot{e}_{ii}^m\dot{e}_{jj}^o = \dot{e}_{11}^m\dot{e}_{11}^o + \dot{e}_{22}^m\dot{e}_{22}^o + \dot{e}_{11}^m\dot{e}_{22}^o + \dot{e}_{22}^m\dot{e}_{11}^o. \quad (\text{B.10})$$

In principal coordinate space this reduces to

$$\hat{R}_{mo} = \frac{\dot{e}_1^m\dot{e}_1^o + \dot{e}_2^m\dot{e}_2^o}{2} - \frac{(\dot{e}_1^m + \dot{e}_2^m)(\dot{e}_1^o + \dot{e}_2^o)}{4} \quad (\text{B.11})$$

$$= \frac{(\dot{e}_1^m - \dot{e}_2^m)(\dot{e}_1^o - \dot{e}_2^o)}{4}. \quad (\text{B.12})$$

(See Section 5.2.1 in Mechanistic Study for notation description)

Finally noting that

$$2\dot{e}_{II} = \dot{e}_1 - \dot{e}_2 = 2(\text{Max Shear}) \quad (\text{B.13})$$

we can produce the normalized correlation

$$\hat{\rho}_{mo}[\tau] = \frac{\hat{R}_{mo}[\tau]}{\dot{e}_{II}^m[0]\dot{e}_{II}^o[0]} \quad (\text{B.14})$$

$$= \frac{\hat{R}_{mo}[\tau]}{\sqrt{\hat{R}_{mm}[0]}\sqrt{\hat{R}_{oo}[0]}}. \quad (\text{B.15})$$

Correlations of Max Shear in both magnitude and absolute terms are computed in the main text.

B.4 Cross-Spectral Analysis

The cross-spectral density function is the Fourier transform of the cross correlation function and is defined as the complex function

$$G_{ij}[f] = C_{ij}[f] - \mathbf{j}Q_{ij}[f] \quad (\text{B.16})$$

$$= |G_{ij}|e^{-\mathbf{j}\theta_{ij}} \quad (\text{B.17})$$

$$|G_{ij}| = \sqrt{C_{ij}^2 + Q_{ij}^2} \quad (\text{B.18})$$

$$\theta_{ij} = \tan^{-1}\left(\frac{Q_{ij}}{C_{ij}}\right) \quad (\text{B.19})$$

where C_{ij} is the real or coincident spectral function, Q_{ij} is the imaginary or quadrature spectral density function and \mathbf{j} is the imaginary value $\sqrt{-1}$ in Cartesian space. In polar coordinates, $|G_{ij}|$ is the magnitude of the function and θ_{ij} is the phase. When normalized the magnitude,

$$\gamma_{ij}^2[f] = \frac{|G_{ij}|^2}{G_{ii}G_{jj}}, \quad (\text{B.20})$$

is known as the coherence function (γ_{ij}^2). We can compute the real and imaginary components, following Bendat and Piersol (1971), by separating the cross-correlation into even and odd parts,

$$\text{even part: } \hat{A}_r = \hat{A}_{ij}[\tau] = \frac{1}{2} (\hat{R}_{ij} + \hat{R}_{ji}) \quad (\text{B.21})$$

$$\text{odd part: } \hat{B}_r = \hat{B}_{ij}[\tau] = \frac{1}{2} (\hat{R}_{ij} - \hat{R}_{ji}) \quad (\text{B.22})$$

such that

$$C_{ij} \approx \hat{C}_k \quad (\text{B.23})$$

$$Q_{ij} \approx \hat{Q}_k \quad (\text{B.24})$$

where the Hanning smoothing functions

$$\hat{C}_0 = 0.5 \times \tilde{C}_0 + 0.5 \times \tilde{C}_1 \quad (\text{B.25})$$

$$\hat{C}_k = 0.25 \times \tilde{C}_{k-1} + 0.5 \times \tilde{C}_k + 0.25 \times \tilde{C}_{k+1}; \text{ for } k = 1, \dots, m-1 \quad (\text{B.26})$$

$$\hat{C}_m = 0.5 \times \tilde{C}_{m-1} + 0.5 \times \tilde{C}_m \quad (\text{B.27})$$

are used for both \hat{C}_k and \hat{Q}_k where

$$\tilde{C}_k[f] = 2\Delta t \left(\hat{A}_0 + 2 \sum_{r=1}^{m-1} \hat{A}_r \cos \left[\frac{\pi r k}{m} \right] + (-1)^k \hat{A}_m \right) \quad (\text{B.28})$$

$$\tilde{Q}_k[f] = 4\Delta t \sum_{r=1}^{m-1} \hat{B}_r \sin \left[\frac{\pi r k}{m} \right]. \quad (\text{B.29})$$

$f = kf_c/m$ is the given frequency for $k = 0, 1, 2, 3, \dots, m$ and $f_c = 1/2\Delta t$ is the cut-off/Nyquist frequency.

Appendix C

Coordinate System Transforms

Two types of coordinate systems are used in this investigation: 1) geographical (λ, ϕ), and 2) Cartesian (X, Y). The geographical grid is located along the earth's surface which is assumed to be a perfect sphere, at sea level, with radius R . It is locally orthonormal with unit vectors, expressed in radians, along the $\hat{\lambda}, \hat{\phi}$ directions.¹ Longitude (λ) is the equatorial angle relative to Greenwich, U.K. and latitude (ϕ) is complementary to the spherical polar angle. The Cartesian coordinate system is a grid fixed to a regional location on the globe with orthonormal unit vectors, in kilometers, along \hat{x} and \hat{y} directions.

Transfer of information between these two systems is the focus of this Appendix. In the first section a description of distance transforms is presented. In the second section, an area preserving projection is examined followed by a discussion of vector transforms using this projection in third section. Finally in fourth section, we examine an efficient numerical scheme for interpolating information between grids of different shapes and sizes.

C.1 Distance Transforms

C.1.1 Arc Length Distance

The geographical grid described in the last section is expressed in terms of radian measure. Since we wish to transform properties between this and a Cartesian grid which has metric distances, the first thing needed is a description of geographical distances which are the same as Cartesian distances (e.g. in kilometers). In the current formulation we have assumed the shape of the earth to be spherical. The shortest distance between two points on the surface of a sphere is the arc length of a Great Circle through those two points. This length is equal to the radius (R) of the sphere times the angle, Θ , made between two vectors of length R that originate at the center of the earth and extend to the two points. Given the angular distances λ and ϕ , a Great Circle distance (S) is

¹To be specific, $\hat{\lambda}, \hat{\phi}$ pertain no longer to the surface of the sphere, but to a local tangential plane in contact with the location under investigation.

determined by

$$S = R \Theta \quad (\text{C.1})$$

where for any two arbitrary points λ_1, ϕ_1 and λ_2, ϕ_2 , it can be shown using spherical trigonometry that

$$\cos \Theta = \cos \phi_2 \cos \phi_1 \cos(\lambda_2 - \lambda_1) + \sin \phi_2 \sin \phi_1 \quad (\text{C.2})$$

The distance between lines of latitude is an example of a Great Circle distance so as a special case we get for

$$\lambda_2 = \lambda_1 \implies \cos(\lambda_2 - \lambda_1) = 1 \quad (\text{C.3})$$

$$\cos \Theta = \cos \phi_2 \cos \phi_1 + \sin \phi_2 \sin \phi_1 \quad (\text{C.4})$$

$$= \cos(\phi_2 - \phi_1) = \cos(\Delta \phi)$$

$$\Theta = |\Delta \phi| \quad (\text{C.5})$$

The distance between two lines of longitude is the special case

$$\phi_2 = \phi_1 = \phi \quad (\text{C.6})$$

$$\cos \Theta = \cos^2 \phi \cos(\lambda_2 - \lambda_1) + \sin^2 \phi. \quad (\text{C.7})$$

Only at the equator, where $\phi = 0$ does this distance equal that of a Great Circle so that $\Theta = |\Delta \lambda|$. Hence, in general, distances along lines of constant latitude are not the shortest or true distance between two points on the surface of a sphere.

C.1.2 Local Projection

Consider now the issue of transferring these metric spherical distances to a flat Cartesian grid. As an example let us consider the geographical area of the ISW drift station. The expanse of the entire research domain is $\Delta \phi \approx 6^\circ$, $\Delta \lambda \approx 5^\circ$. Within this space we wish to transfer distance along the geographical grid to a local Cartesian grid. We can position the origin of the Cartesian grid, X_0 and Y_0 , over a central point on the earth's surface, in this case for example $\phi_0 = 69^\circ\text{S}$, $\lambda_0 = 54^\circ\text{W}$. The X, Y plane is tangent to the earth's surface at this point with \hat{x} and \hat{y} oriented at the origin parallel to the geographical coordinates λ and ϕ , respectively. Since the region is geographically small (i.e. local spherical curvature is small) increasing longitudes (lines of constant latitude) are parallel to X and increasing latitudes are approximately parallel to Y .

From the discussion above we know that changes in latitude equal the arc length of a Great Circle so given the current configuration between coordinate systems, we can immediately compute the distance Y from latitude. Employing an effective radius equal to $R \cos \phi$, which is the distance from the earth's polar axis to a latitude line containing $\Delta \lambda$, we can also estimate a relationship between X and longitude such that lines of Y remain parallel to lines of latitude. In other words,

$$X = R(\lambda - \lambda_0) \cos \phi \quad (\text{C.8})$$

$$Y = R(\phi - \phi_0) \quad (\text{C.9})$$

This is a standard navigational distance formula whereby a minute of latitude is equal to 1 nautical mile which by international standards equals 1.852 km. For consistency in the calculations we can use this relationship to determine a corresponding value for the radius R by putting Eq. (C.10) into Eq. (C.9) yielding Eq. (C.11).

$$Y = 1 \text{ (degree)} \times 60 \frac{\text{(nautical miles)}}{\text{(degrees)}} \times 1.852 \frac{\text{(kilometers)}}{\text{(nautical miles)}} \quad (\text{C.10})$$

$$\begin{aligned} &= 111.12 \text{ (kilometers)} \\ R &= \frac{Y \text{ (kilometers)}}{\frac{1 \text{ (degree)} \times \pi \text{ (radians)}}{180 \text{ (degrees)}}} \quad (\text{C.11}) \\ &= 6366.7 \text{ (kilometers)} \end{aligned}$$

This value of R has a relative error of about 0.2% from the radial constant used, for example, in Pearson's (1990) Lambert Equal Area Projection. Since there is a considerable range of values that R tends to have in the literature, the above definition is reasonable and will serve as the value of the earth's radius in all cases for this study.

C.1.3 Comparison

The local nautical method deviates somewhat from the Great Circle distance determination which is the correct one for computing distances. However, this second method is effective at flattening out the region without angular distortion along X , a major drawback with Great Circles. Using the bounds of the ISW field as test inputs, we can estimate how well the navigational method works. Distances for both these methods are listed in Table C.1. A point by point comparison shows that the Great Circle distances are indeed smaller as expected but there is a relative error of only about 0.01% between the two methods which is very low. This good correspondence is due to the fact that $\Delta\lambda$ is quite small so $\cos(\lambda - \lambda_0)$ is close to 1. Comparing these results with the case of $\Delta\lambda = 90^\circ$ along $\phi = 45^\circ$ we get respective values of 7071.63 versus 6667.20 km which has a 5% relative error. With respect to angular distortion along Y , a difference of 16.12 km in X over a Y distance of 333.36 km, which is half the ISW length, yields a distortion in angle of 2.77° at the outer corners of the specified grid. Since angular distortion increases with horizontal distance, X , from the central latitude and since all the buoys are considerably closer than this, distortion in angle for determining buoy distance is considerably smaller than the maximum distortion angle determined above. The angular distortions incurred when trying to use Great Circle calculations are far greater as angle

Table C.1: Navigational versus Great Circle Distance

$\Delta\lambda = 3^\circ$	Longitudinal Distance (km)	
ϕ	Eq. (C.8)	Eq. (C.7)
66°S	135.5897	135.5768
69°S	119.4655	119.4537
72°S	103.0139	103.0032

is not a conserved quantity in this calculation, only distance. Given these results, the navigational distance transformation described above is quite effective for determining distances provided the longitudinal distance is very small. This transform is thus used in this investigation for local numerical grid manipulations and processing of the ISW strain array.

C.2 Equal Area Transforms

In this section we will consider the area of the Weddell Sea. Based on the available sources of input fields, the region of interest is bound from 80°S to 45°S latitude and 70°W to 10°E longitude. The region is used to run numerical two dimensional sea ice models with resolutions in grid size from 2° to 1/8°. Quantities such as ice thickness, compactness, ice velocity, and stress-strain relations are computed. The scalar quantities represent average values within a specified grid cell. When multiplied by the corresponding grid cell area and integrated over the entire domain, these values are used to determine properties such as total ice mass and regional ice thickness distribution. In order to conserve these properties during coordinate transformations, the area of each grid cell must be conserved, hence an equal area projection must be used when transforming information between geographical and Cartesian grids.

C.2.1 Basic Formulation

The transformation chosen for the numerical study is based on Alber's projection with one parallel (Pearson, 1990) because of its area conserving property. The projection is a conical plotting surface tangent to the earth's surface at a selected origin (ϕ_0, λ_0) . For the desired 2D model Cartesian orientation in this study, the transformation from geographical to Cartesian coordinates using Alber's projection with one parallel is

$$x = \rho \sin \theta \quad (\text{C.12})$$

$$y = \rho \cos \theta - R(\phi_0 - \phi_{00}) \quad (\text{C.13})$$

where:

$$\rho = R \sqrt{2(1 + \sin \phi)} \quad (\text{C.14})$$

$$\theta = \Delta \lambda = \lambda - \lambda_0 \quad (\text{C.15})$$

$$\phi_{00} = \text{latitudinal tangent to earth's surface} = 90^\circ \text{S} \quad (\text{C.16})$$

$$\phi_0 = \text{latitude of Cartesian grid origin} = 64.6^\circ \text{S} \quad (\text{C.17})$$

$$\lambda_0 = \text{longitude of grid origin, tangent to earth's surface} = 28.0^\circ \text{S} \quad (\text{C.18})$$

$$R = \text{radius of the earth} = 6,366,707. \text{ m.} \quad (\text{C.19})$$

The inverse transform from Cartesian to geographical coordinates is

$$\lambda = \lambda_0 + \Delta \lambda \quad (\text{C.20})$$

$$\phi = \sin^{-1} \left\{ \frac{1}{2 \sin \phi_{00}} + \frac{\sin \phi_{00}}{2} - \frac{\sin \phi_{00}}{2 R^2} \kappa^2 \right\} \quad (\text{C.21})$$

where:

$$\kappa = \sqrt{x^2 + y^2} \quad (\text{C.22})$$

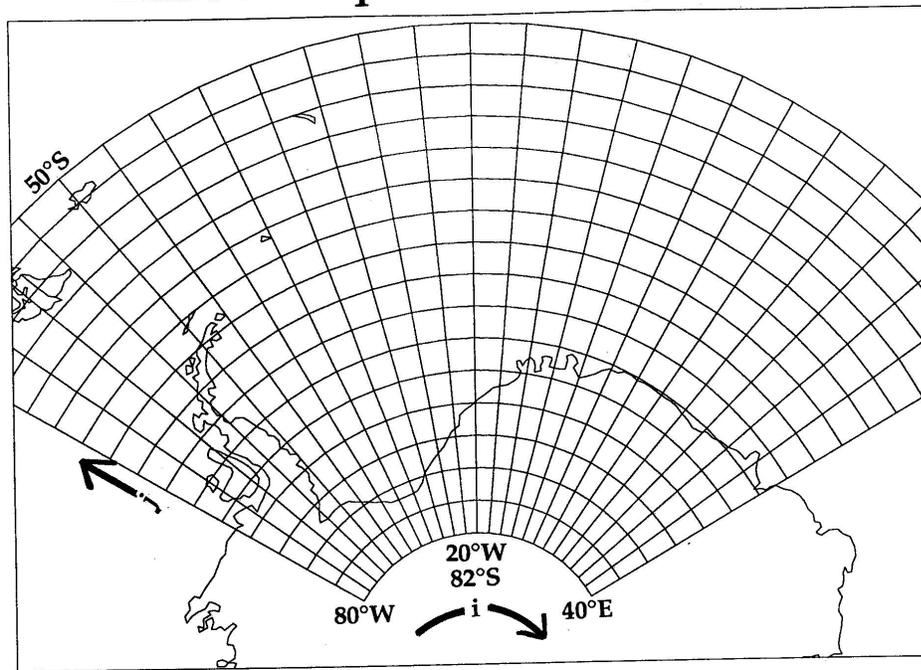
$$\Delta\lambda = \sin^{-1}\left(\frac{x}{\kappa}\right) \quad (\text{C.23})$$

$$x = i * dX - x_0 \quad (\text{C.24})$$

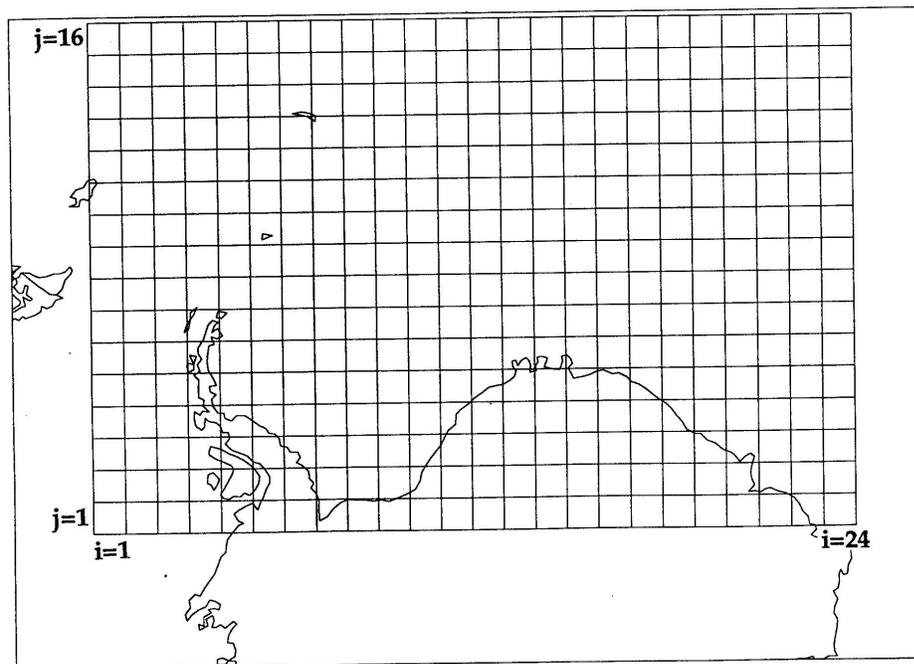
$$y = j * dY - y_0 + R(\phi_0 - \phi_{00}). \quad (\text{C.25})$$

This projection of both the geographical and Cartesian grids for the Weddell Sea region is shown in Figure (C.1) for a grid resolution of 2° latitude in geographical coordinates and correspondingly 222 km in Cartesian coordinates.

Lambert Equivalent Projection



Geographical Grid



Cartesian Grid

Figure C.1: Geographical (upper image) and Cartesian (lower image) grids on Lambert Equivalent Projection. Grids are 2° and 222 km in latitude and y directions, respectively. Origin for Cartesian grid set at Y° latitude and X° longitude.

C.3 Non-Orthogonal Transformations

The Lambert Equal Area Projection described in the last section has two major drawbacks; it is neither distance nor angle conserving. In order to conserve area while projecting a sphere onto a flat surface, distances between lines of latitude must decrease away from ϕ_0 while distances between lines of longitude proportionally increase. This produces a deformation in shape which in turn destroys the local orthogonality between the two coordinates. In order to transform properties such as ice velocity and stress states which are distance and direction dependent, a general non-orthogonal transform can be used to correctly transfer vector and tensor components between the two grids.

C.3.1 Basic Formulation

The general formula for a transform using summation notation (Arfken, 1985) is as follows.

For a vector,

$$\tilde{V}^i = V^r \frac{\partial \tilde{x}^i}{\partial x^r} \quad (\text{C.26})$$

and for a tensor,

$$\tilde{T}^{ij} = T^{rs} \frac{\partial \tilde{x}^i}{\partial x^r} \frac{\partial \tilde{x}^j}{\partial x^s} \quad (\text{C.27})$$

Letting $x^1 = x$, $x^2 = y$, $\tilde{x}^1 = R \cos \phi \Delta\lambda$, and $\tilde{x}^2 = R\phi$, this transformation, in expanded component form, corresponds to

$$\begin{pmatrix} V_x \\ V_y \end{pmatrix} = \begin{pmatrix} \frac{\partial x}{\partial R \cos \phi \Delta\lambda} & \frac{\partial x}{\partial R\phi} \\ \frac{\partial y}{\partial R \cos \phi \Delta\lambda} & \frac{\partial y}{\partial R\phi} \end{pmatrix} \begin{pmatrix} V_\lambda \\ V_\phi \end{pmatrix} = [\mathbf{A}] \begin{pmatrix} V_\lambda \\ V_\phi \end{pmatrix} \quad (\text{C.28})$$

for a geographical to Cartesian transform and

$$\begin{pmatrix} V_\lambda \\ V_\phi \end{pmatrix} = \begin{pmatrix} \frac{\partial R \cos \phi \Delta\lambda}{\partial x} & \frac{\partial R \cos \phi \Delta\lambda}{\partial y} \\ \frac{\partial R\phi}{\partial x} & \frac{\partial R\phi}{\partial y} \end{pmatrix} \begin{pmatrix} V_x \\ V_y \end{pmatrix} = [\mathbf{B}] \begin{pmatrix} V_x \\ V_y \end{pmatrix} \quad (\text{C.29})$$

for a Cartesian to geographical grid vector transform. The matrices $[\mathbf{A}]$ and $[\mathbf{B}]$ containing the partial differentials are called Jacobian matrices which resolve to

$$[\mathbf{A}] = \begin{pmatrix} \frac{\rho \cos \theta}{R \cos \phi} & \frac{-R \cos \phi \sin \theta}{R \cos \phi \cos \theta} \\ \frac{\rho \sin \theta}{R \cos \phi} & \frac{\rho}{R \cos \phi \cos \theta} \end{pmatrix} \quad (\text{C.30})$$

$$[\mathbf{B}] = \begin{pmatrix} \frac{R \cos \phi y}{\kappa^2} & \frac{R \cos \phi x}{\kappa^2} \\ -x & y \\ \kappa \sqrt{1 - \left(\frac{\kappa}{2R}\right)^2} & \kappa \sqrt{1 - \left(\frac{\kappa}{2R}\right)^2} \end{pmatrix} \quad (\text{C.31})$$

using the nomenclature developed in the previous section. The only drawback to this method is a singularity at the pole. The singularity arises because, at the pole, ρ and κ vanish in the denominator of the Jacobian matrices $[\mathbf{A}]$ and $[\mathbf{B}]$, respectively. This can easily be corrected with negligible distortion by adding a very small value of ϵ to each of these quantities. This problem doesn't arise in any situation encountered in this Thesis.

C.3.2 Test Case

In order to check these transformations the following tests were devised. First matrix [A] and [B] were multiplied together to confirm that as inverses they equal the identity matrix. Second, a 17×14 point Cartesian grid, similar to the one shown in Figure (C.1), with 200 km resolution was set up to cover the Weddell Sea Region. Using NCAR graphics as a visual aid, a uniform velocity field (e.g. $U_x = 0$, $V_y = 1$) is plotted over the field. The length ($|\vec{v}|$) and angle of orientation (α) of the vectors are equal to

$$|\vec{v}| = \sqrt{U_x^2 + V_y^2} \quad (\text{C.32})$$

$$\alpha = \arctan\left(\frac{V_y}{U_x}\right) \quad (\text{C.33})$$

which equal 1 and 90° , respectively for the example case. These values can be used to check the transform from Cartesian to geographical and back to Cartesian. If the transformation has worked correctly it should be able to reproduce the original vector with the correct orientation and length. Since the length of the vector is independent of coordinate system, an additional intermediate check can be done to insure that the length of the velocity vectors in the geographical coordinates, when expressed in kilometers, is also conserved.

As a comparison, the case where we assume the geographical grid remains locally orthogonal under the Lambert Equal Area Transform is also considered. In this case the transformation need be nothing more than the Lambert projection described in Section B.2 and a simple rotational formula, derived from law of cosines,

$$\psi = \lambda - \lambda_0 \quad (\text{C.34})$$

$$U_\lambda = \cos\psi U_x - \sin\psi V_y \quad (\text{C.35})$$

$$V_\phi = \cos\psi V_y + \sin\psi U_x. \quad (\text{C.36})$$

When we run this case, the original vector length is numerically conserved but there is some angular distortion. Depending on the direction of the vector and its position in the field, this angular distortion can vary from 0° to more than 5° . For tasks such as plotting this may be tolerable but for interpolation routines for input and output fields to numerical models, this introduces a considerable amount of variable error. If we perform this same test using the Lambert projection described in Section B.2 combined with the non-orthogonal transformation described above we introduce a maximum distance and angular distortion of 10^{-6} using single precision on an IBM RS/6000 computer. Hence, the distance and direction of the vectors are, within numerical limits, conserved.

C.4 Interpolation of Data

C.4.1 Basic Formulation

The purpose of a data interpolation routine is to determine the value of a continuous function, f , at a selected point given information from other points. In this study a

collection of functions (e.g. wind velocity, radiation, temperature) are known at regularly spaced locations, or nodes, on orthogonal grid cells. We can determine the value of these functions at any other point in the field by averaging the known values near the desired point in the following weighted manner,

$$f[x, y] = \sum_{i=1}^n \omega_i f_i \quad (\text{C.37})$$

where $f_i \equiv f[x_i, y_i]$ are known values of the function at the points (x_i, y_i) and ω_i are weight functions relating the relative distance of the point (x, y) where f is unknown to the points where f_i is known.

There are two difficulties associated with this method. First, we need to find a specified number of nearest points and second we need to define the weight functions. A computationally efficient method for doing this is described in Chapter 3 of Taylor et al. (1981) where a second local coordinate system (ζ, η) is placed on the individual grid cell containing the location (x, y) . The local system is set up in such a way that the known nodes are located on its perimeter, the origin is located in the center of the grid and its values are normalized from -1 to 1 for both ζ and η (Figure C.2). For this study, 4 values are located at the corners of a quadrilateral which by convention (Taylor et al., 1981) are numbered sequentially from 1 to 4 in a counterclockwise manner. Given this configuration the location of the nearest points is simply the values at the four corners of a specified grid cell whose lower left location is (Figure C.2)

$$i = \text{integer} \left[\frac{x - x_{ref}}{\Delta x} \right] + 1 \quad (\text{C.38})$$

$$j = \text{integer} \left[\frac{y - y_{ref}}{\Delta y} \right] + 1 \quad (\text{C.39})$$

for i and j going from 1 to I_{max} and J_{max} , respectively and where x_{ref} and y_{ref} are a reference point somewhere on the global coordinate system (e.g. global coordinate system origin in lower left corner). The center location of the selected grid cell, and hence the origin of the local coordinate system, is defined by

$$x_0 = x_{ref} + (i - 1/2) \Delta x \quad (\text{C.40})$$

$$y_0 = y_{ref} + (j - 1/2) \Delta y. \quad (\text{C.41})$$

Furthermore with this definition,

$$\zeta = \frac{x - x_0}{\Delta x/2} \quad (\text{C.42})$$

$$\eta = \frac{y - y_0}{\Delta y/2}. \quad (\text{C.43})$$

The weight functions can now be determined in terms of the local coordinate system (see Taylor et al., 1981 for detail) as

$$\omega_i[\zeta, \eta] = (1 + \zeta_i \zeta) (1 + \eta_i \eta)/4 \quad (\text{C.44})$$

which is governed by the constraints that

$$\sum_{i=1}^n \omega_i = 1 \quad (\text{C.45})$$

$$\text{and at corners } i; \quad \omega_i[\zeta_i, \eta_i] = \delta_{ij}. \quad (\text{C.46})$$

Hence, given the weight functions from Eq. (C.44) and their respective known f_i values, the unknown value of function f at position x, y can now be solved using Eq. (C.37).

This method has been applied to both the Cartesian and spherical coordinate systems used in this study. To apply this method to a spherical coordinate system simply substitute x with longitude ($x \rightarrow \lambda$ and $\Delta x \rightarrow \Delta \lambda$) and y with latitude ($y \rightarrow \phi$ and $\Delta y \rightarrow \Delta \phi$). To interpolate data from one of these coordinate systems to the other using this method simply transform the location of the requested value in the new system to the old known system, then interpolate that value using the method just described. The interpolated value is now known in both coordinate systems at the desired location.

Transformation for Interpolation Routine

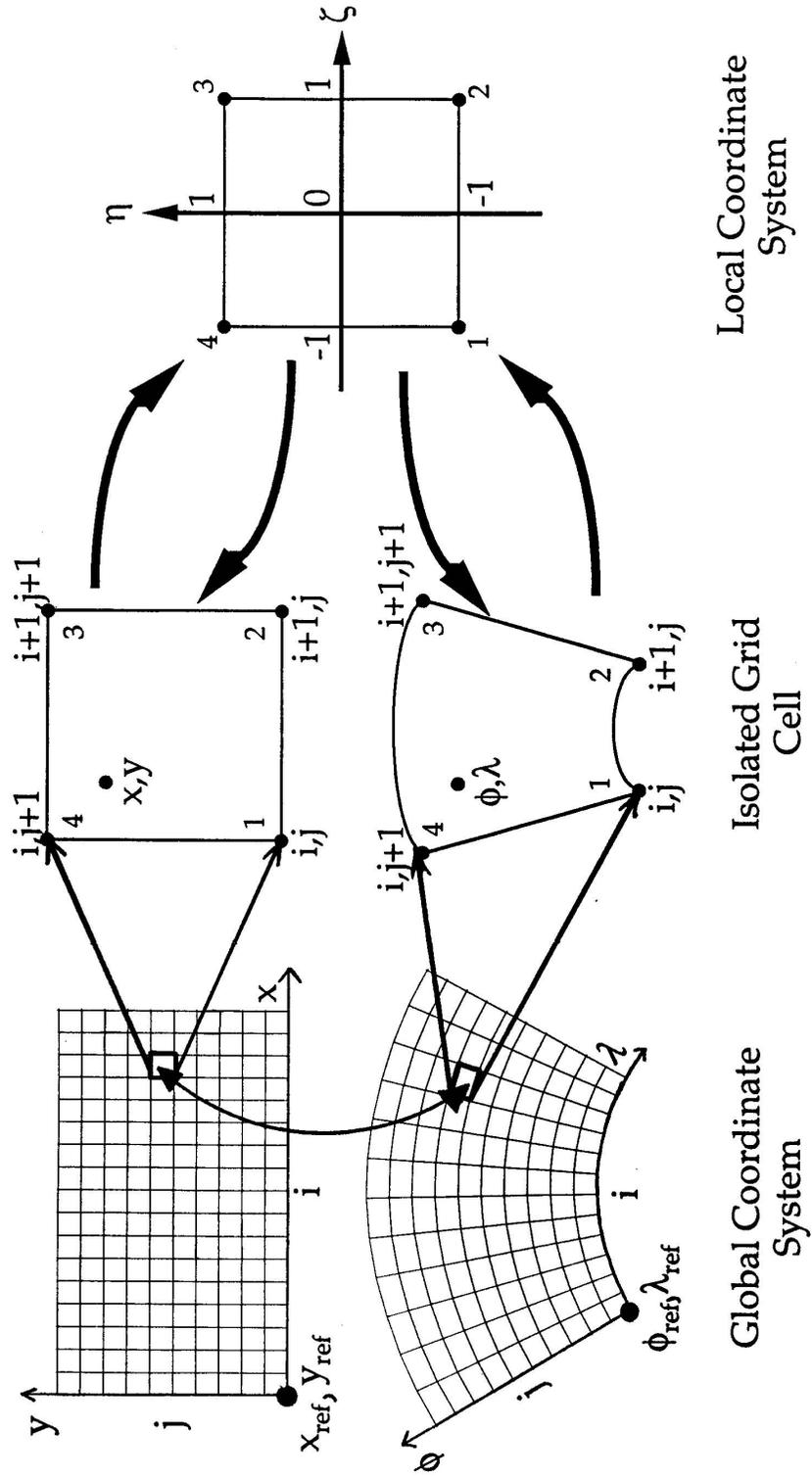


Figure C.2: Pictorial outline of procedure for interpolating data between coordinate systems of different shapes and sizes.

C.4.2 Example Case

A simple test case for verifying the interpolation routine, specifically in spherical coordinates, is as follows. The input analysis fields are given in geographical coordinates but we wish to determine them on a Cartesian grid. First we select the i, j point in the Cartesian grid and transform it to the corresponding latitude (ϕ), longitude (λ) location using the method described in Appendix B.2. Consider a point at 52.5°S , 62.5°E on a spherical grid with 10° resolution, nodes of the grid cells at $0^\circ, 10^\circ, 20^\circ, \dots$ etc. and an origin at 80°S , 0° . Using Eq. (C.38) and (C.39) we determine the specific grid cell where the data point is bound by the four points of (1) 60°S , 60°E ; (2) 60°S , 70°E ; (3) 50°S , 70°E ; and (4) 50°S , 60°E which are located in grid cell $i = 7$, $j = 3$. Using Eq. (C.40) and (C.41) we determine that the center of that grid cell is 55°S , 65°E which gives us $\zeta = -0.5$ and $\eta = 0.5$. At the corner points the known values of the function are given, hypothetically, as (1) 1, (2) 2, (3) 2, (4) 1. From Eq. (C.44) the weight functions are $\omega_1 = 0.1875$, $\omega_2 = 0.0625$, $\omega_3 = 0.1875$, $\omega_4 = 0.5625$ (check: $\sum \omega_i = 1$) and hence the value of the function is $f = 1.25$ which is intuitively correct.

Just to be sure that things work correctly in the spherical coordinates we choose any value within the selected grid cell which is along the 62.5°E longitude line (e.g. at 50°S , 52.5°S , 55°S , 57.5°S , 60°S). Due to the data distribution of known values of f_i for this case, the value of f should be the same along any line of longitude. Anywhere along our chosen line $\zeta = -0.5$ but η will vary (respectively, 1.0, 0.5, 0.0, -0.5, -1.0). $f_1 = f_4$ and $f_2 = f_3$ in this example so for the specific grid cell

$$f = f_1(\omega_1 + \omega_4) + f_2(\omega_2 + \omega_3). \quad (\text{C.47})$$

In order for f to be constant, the terms in parenthesis must be constant (e.g. $\omega_1 + \omega_4 = \text{constant}$). Running through the same procedure we find that the value inside both sets of parenthesis always adds up to 0.75 and 0.25, respectively, and thus the f value is constant along the longitude line.

We can apply this same procedure for one dimensional interpolation in, for example, the y or ϕ direction. Equations (C.39), (C.41) and (C.43) are used to determine the correct grid cell, center of that grid cell and η in the local coordinate system, respectively. The only difference is the use of only two weight functions (i.e. f_i and ω_i are for $i = 1, 2$) which are defined as

$$\omega_i = (1 + \eta_i \eta) / 2. \quad (\text{C.48})$$

References

Ackley, S.F., V.I. Lytle, B. Elder, D. Bell. 1992. Sea Ice Investigations on Ice Station Weddell #1. I. Ice Dynamics. *Preliminary Reports: Sea Ice Studies on Ice Station Weddell and Cruise NBP92-2, N.B. Palmer January - June 1992.* pgs. 2-12.

Ackley, S.F., A.J. Gow, V.I. Lytle, M.N. Darling, N.E. Yankielun. 1992. Sea Ice Investigations on Nathaniel B. Palmer: Cruise 92-2. *Preliminary Reports: Sea Ice Studies on Ice Station Weddell and Cruise NBP92-2, N.B. Palmer January - June 1992.* pgs. 2-12.

Andreas, E.L. and S.F. Ackley. 1982. *On the Differences in Ablation Seasons of Arctic and Antarctic Sea Ice.* Journal of Atmospheric Sciences. Vol. 39, No. 3, pp 440-447.

Beers, Y. 1957. Introduction to the Theory of Error. *Chapter 5: Propagation of Error.* Addison-Wesley Publishing Co. Reading, Mass. pgs 26-36.

Bendat, J.S. and A.G. Piersol. 1971. Random Data: Analysis and Measurement Procedures. Wiley and Sons Publishing. 407 pages.

Born, M. and E. Wolf. 1975. Chapter 1.4 Vector Waves. Principles of Optics 5th Edition. Pergamon Press. pgs 23-36.

Breitenberger, E. and G. Wendler. February 1990. Variations in Antarctic Sea Ice. *Sea Ice Properties and Processes: Proceedings of the W.F. Weeks Sea Ice Symposium.* Monograph 90-1. pgs 173-177.

Churun, V., V. Grichenko, V. Lukin, A. Provorkin. 1992. The Structure and Drift of the Ice Floe of Ice Station Weddell I. (abstract no. 041D-3). *EOS Trans. AGU* Vol. 73, pg 300.

Dingman, S.L. 1994. Appendix D in *Physical Hydrology.* MacMillan Publishing Co. pp 516-517.

Ekman, V.W. 1905. On the influence of the earth's rotation on ocean currents. *Arkiv för Matematik, Astronomi och Fysik*, Vol. 2, No. 11, pg 52.

Fischer, H. and P. Lemke. 1994. On the required accuracy of Atmospheric Forcing Fields for Driving Dynamic-Thermodynamic Sea Ice Models. *The polar oceans and their role in shaping the global environment: The Nansen Centennial Volume*. pgs 373-397.

Flato, G. and W.D. Hibler III. 1990. On a simple sea ice dynamics model for climate studies. *Annals of Glaciology: International Glaciological Society*. Vol. 14, pgs 72-77.

Flato, G. and W.D. Hibler III. 1991. An Initial Numerical Investigation of the Extent of Sea-Ice Ridging. *Annals of Glaciology: International Glaciological Society*. Vol. 15, pgs 31-36.

Flato, G. and W.D. Hibler III. 1992. Modeling Pack Ice as a Cavitating Fluid. *Journal of Physical Oceanography*. Vol. 22 (6), pgs 626-651.

Flato, G. and W.D. Hibler III. 1995. Ridging and strength in modeling the thickness distribution of Arctic sea ice. *Journal of Geophysical Research*. Vol. 100, No. C9. pgs. 18,611-18,626.

Foldvik, A., and T. Gammelsröd. 1988. Notes on Southern Ocean Hydrography, Sea-Ice, and Bottom Water Formation. *Paleogeography, Paleoclimatology, Paleoecology*. Vol. 67 pg 3-17.

Foldvik, A., J.H. Middleton, T.D. Foster. 1990. The Tides of the Southern Weddell Sea. *Deep Sea Research*. Vol. 37, No. 8 pp. 1345-1362.

Fung, Y.C. 1977. *A First Course in Continuum Mechanics* Second Edition. Prentice-Hall, Inc. Englewood Cliffs, New Jersey. 340 pages.

Gordon, A. 1970. Oceanography of Antarctic Waters. *Oceanology* (Ed. J. Reid). Antarctic Research Series American Geophysical Union. Vol. 1, No. 15, pg 169-203.

Gordon, A.L. and Ice Station Weddell Group of Principal Investigators and Chief Scientists. 1993. Weddell Sea Exploration from Ice Station. EOS Transaction AGU Vol. 74, No. 11. 16. March. Pages 121 and 124-126.

Hamming, R.W. 1989. *Digital Filters*. 3rd Edition. Prentice-Hall Inc. Chapter 9 pgs 185-207.

Harder, M. and P. Lemke. 1994. Modeling the Extent of Sea Ice Ridging in the Weddell Sea.. *The Polar Oceans and Their Role in Shaping the Global Environment*. AGU Geophysical Monograph 85. pages 187-197.

Hecht, E. 1988. Chapter 8.10 Optical Activity. *Optics* 2nd Edition. Addison-Wesley Publishing Co. pgs.309-313.

Hibler, W.D. 1979; A Dynamic Thermodynamic Sea Ice Model; *Journal of Physical Oceanography*. Vol 9, pgs 815-846.

Hibler, W.D. 1980. Modeling a variable thickness sea ice cover. *Monthly Weather Review*. pp. 1943-1973.

Hibler, W.D. and S.F. Ackley. March 30, 1983. Numerical Simulation of the Weddell Sea Pack Ice. *Journal of Geophysical Research*. Vol. 88 (C5), pgs 2873-2887.

Hibler, W.D. III. W.B. Tucker, W.F. Weeks. 1975. Measurement of Sea Ice Drift Far From Shore Using Landsat and Aerial Photographic Imagery. *Proceedings: Third International Symposium on Ice Problems*. 18-21 August CRREL. Hanover, New Hampshire pgs. 541-554.

Hibler, W.D., W.F. Weeks, A. Kovacs, S.F. Ackley. 1974. Differential Sea-Ice Drift. part 1: Spatial and Temporal Variations in Sea-Ice Deformation. *Journal of Glaciology*. Vol. 13 (69). pgs 437-455.

Hines, W.W, and D.C. Montgomery. 1990. Chapter 15: Multiple Regression. in *Probability and Statistics in Engineering and Management Science* (3rd Edition). pgs. 487-558.

Ip, F.C. 1993. Numerical investigation of different rheologies on sea-ice dynamics. Ph.D. Thesis. Dartmouth College. 242 pages.

Iqbal, M. 1983. Chapter 1: Sun-Earth Astronomical Relationships. *An Introduction to Solar Radiation* Academic Press pg 1-28.

Koch, C. 1988. A Coupled Sea Ice - Atmospheric Boundary Layer Model Part I: Description of the Model and 1979 Standard Run. *Beitr. Phys. Atmosph*. Vol 61 (4). pgs 344-354.

Lemke, P., W.B. Owens and W. D. Hibler III. 1990. A coupled Sea Ice - Mixed Layer - Pycnocline Model for the Weddell Sea. *Journal of Geophysical Research*. Vol. 95 (C6), pgs 9513-9525.

Lewis, E.L. and W.F. Weeks. 1970. Sea Ice: Some Polar Contrasts. *Proc. Tokyo Symp. Antarctic Ice and Water Masses*. Cold Regions Research and Engineering Laboratory. pgs 23-34.

Lytle, V. and S.F. Ackley. In Press. Heat Flux through Sea Ice in the Western Weddell Sea. *Journal of Geophysical Research*.

Massom, R.A. 1992. Observing the Advection of Sea Ice in the Weddell Sea Using Buoy and Satellite Passive Microwave Data. *Journal of Geophysical Research*. Vol. 97 (C10), pgs. 15559-15572.

Maykut, G.A. and N. Untersteiner. 1971. Some Results from a Time Dependent, Thermodynamic Model of Sea Ice. *Journal of Geophysical Research*. Vol. 76. pgs. 1550-1575.

McPhee, M.G., 1975. Ice-ocean momentum transfer for the AIDJEX ice model. *AIDJEX Bulletin*. Vol. 29, pgs93-111.

McPhee, M.G. 1980. An analysis of pack ice drift in summer. *Sea Ice Processes and Models*. edited by R.S. Pritchard, University of Washington Press. Seattle, Washington, pages 62-75.

McPhee, M.G. 1982. Ice-ocean momentum transfer for the AIDJEX ice model. *AIDJEX Bulletin* Vol. 29, pgs. 93-111.

Muench, R.D. and A.L.Gordon. 1995. Circulation and transport of water along the western Weddell Sea margin. *Journal of Geophysical Research*. Vol. 100. No. C9. pgs. 18,503-18,515.

Muench, R.D., J.T. Gunn, and M.D. Morehead. 1992. Upper Layer Current Observations in the Western Weddell Sea (abstract no. 041D-5). *EOS Trans. AGU* Vol. 73, pg 301.

Nansen, F. 1906. Northern Waters: Captain Roald Amundsen's Oceanographic Observations in the Arctic Seas in 1901. *Videnskapslige-Selskap Skrifter. I. Mat. Natur. Kl.* Dybwad, Christiania 1, 145 pages.

Olbers, D.,V. Gouretski, G. Seiß, J. Schroter. 1992. *Hydrographic Atlas of the Southern Ocean*. Alfred-Wegener-Institute, Bremerhaven.

Oppenheim, A.V. and R.W. Schafer 1975. Digital Signal Processing. Englewood Cliffs, N.J. Prentice Hall.

Owens, W.B. and P. Lemke. 1990. Sensitivity Studies with a Sea Ice - Mixed Layer - Pycnocline Model in the Weddell Sea. *Journal of Geophysical Research*. Vol. 95 (C6), pgs 9527-9538.

Parkinson, C.L. and W.M. Washington. 1979. A Large-Scale Numerical Model of Sea Ice. *Journal of Geophysical Research*. Vol. 84, pgs 311-337.

Pearson, F. 1990. Albers projection with one parallel. **Map projections: Theory and Applications**. CRC Press Inc, United States. pgs. 103-129.

Pinder, G.F. and W.G. Gray. 1977. Finite Element Simulations in Surface and Subsurface Hydrology. Academic Press. New York.

Press, W.H., S.A. Teukolsky, W.T. Vetterling, B.P. Flannery. 1992. *Numerical Recipes in Fortran: The Art of Scientific Computing*. Cambridge University Press. Second Edition. Chapter 13, pgs 530-602.

Roberts, J. and T.D. Roberts. 1978. Use of the Butterworth Low-Pass Filter for Oceanographic Data. *Journal of Geophysical Research*. Vol. 83 No. C11 pgs. 5510-5514.

- Rowe, M.A., C.B. Sear, S.J. Morrison, P. Wadhams, D.W.S. Limbert, D.R. Crane. 1989. Periodic Motions in the Weddell Sea Pack Ice. *Annals of Glaciology*. Vol. 12. pgs 145-151.
- Schuster, H.G. 1988. Chapter 1: Experiments and Simple Models. *Deterministic Chaos: An Introduction*. 2nd Edition. Verlagsgesellschaft. Weinheim. pages 7-19
- Segerlind, L.J. 1984. *Applied Finite Element Analysis*. John Wiley and Sons Publishing.
- Semtner, A. J. 1976. A Model for the Thermodynamic Growth of Sea Ice in Numerical Investigation of Climate. *Journal of Physical Oceanography*. Vol. 6, pgs 379-389.
- Stern, H.L., D.A. Rothrock, R. Kwok. 1995. Open Water Production in Arctic Sea Ice: Satellite Measurements and Model Parameterization. *Journal of Geophysical Research*. Vol. 100 (C10), pgs 20,601-20,612.
- Stössel, A., P. Lemke, and W.B. Owens. 1990. Coupled Sea Ice - Mixed Layer Simulations for the Southern Ocean. *Journal of Geophysical Research*. Vol. 95 (C6), pgs 9539-9555.
- Taljaard, J.J., H. van Loon, H.L. Crutcher, and R.L. Jenne. 1969. Climate of the upper air. I: Southern Hemisphere. Vol. 1: Temperature, Dew Points, and Heights at Selected Pressure Levels. NAVAIR. Report No. 50-IC-55. 135 pages. U.S. Naval Weather Service. Command, Washington, DC.
- Taylor, C. and T.G. Hughes. 1981. Chapter 3: Basic Concepts. *Finite Element Programming of the Navier-Stokes Equations*. Pineridge Press, LTD. Swansea, UK. pp 30-57.
- Thorndike, A.S., D.A. Rothrock, G.A. Maykut, and R. Colony. 1975. The thickness distribution of sea ice. *Journal of Geophysical Research* Vol. 80. pgs 4501-4513.
- Untersteiner, N. 1986. *The Geophysics of Sea Ice*. Plenum Press, NATO ASI Series-B, New York/London.
- van Ypersele, J.P. 1986. A Numerical Study of the Response of the Southern Ocean and its Sea Ice to a CO₂ - Induced Atmospheric Warming. *Ph.D. Thesis* Fac. des Sci., Univ. Cath. de Louvain, Louvain la Neuve.
- Wadhams, P. 1994. Sea Ice Thickness Changes and Their Relation to Climate. *The Polar Oceans and Their Role in Shaping the Global Climate*. AGU Monograph 85. pages 337-361.
- Wadhams, P. 1986. The Seasonal Ice Zone. *The Geophysics of Sea Ice: chapter 14* (editor N. Untersteiner). Plenum Press, NATO ASI Series-A, pgs 825-992.

Wadhams, P., M.A. Lange, and S.F. Ackley. 1987. The Ice Thickness Distribution Across the Atlantic Sector of the Antarctic Ocean in Midwinter. *Journal of Geophysical Oceanography*. Vol. 92 (C13), pgs 14535-14552.

Welch, P.D. 1967. A Use of Fast Fourier Transform for the Estimation of Power Spectra: A Method Based on Time Averaging Over Short, Modified Periodograms. *IEEE Trans Audio and Electroacoust.* Vol. AU-15 pp70-73. June 1967.

Zhang, J. 1993. A High Resolution Ice-Ocean Model with Imbedded Mixed Layer. Ph.D. Thesis. Dartmouth College. 229 pages.

Zhang, J. and W.D. Hibler III. 1994. On an Efficient Numerical Method for Modeling Sea Ice Dynamics. *submitted to Journal of Geophysical Research*.

Zubov, N.N. 1943. L'dy Arktiki (Arctic Ice). Izdatel'stvo Glavsevmorputi, Moscow. 360 pages. (US Navy Hydrographic Office, Translation 217, 1963; Available as AD426972 from NTIS, Springfield, Va.).

Zwally, H.J., J.C. Comiso, C.L. Parkinson, W.J. Campbell, F.D. Carsey, and P. Gloersen. 1983. *Antarctic Sea Ice, 1973-1976: Satellite Passive-Microwave Observations*. NASA Scientific and Technical Information Branch. Supt of Docs. no.: NAS 1.21:459, 206 pages.